IPP-Report

Max-Planck-Institut für Plasmaphysik

Christian Linsmeier

Surface chemistry of fusion first wall materials

IPP 17/19
September 2010

Surface chemistry of fusion first wall materials

Vorgelegt dem

Department Chemie

der

Technischen Universität München

als Habilitationsschrift für das Fachgebiet

“Physikalische Chemie”

von

Dr. rer. nat. Christian Linsmeier

September 2009

To
Helmut Knözinger
and
Edmund Taglauer

my scientific mentors and friends.

Contents

1 Introduction

Modern societies rely on a virtually unlimited and reliable energy supply. The energy consumption is directly related to the standard of living. In a reference scenario [1], the IEA predicts a worldwide increased primary energy demand by almost 50% for 2030. The strong economic growth in China and India only will account for half of this increase. The present world energy supply relies to more than 80% on burning of fossil fuels, and based on current trends the energy-related emission of carbon dioxide and other greenhouse gases will lead to an increase of the average global temperature of 6 °C in the long run. According to the 2007 IPCC report [2], even the harshest scenario leading to a long term mitigation of climate change effects (requiring a 50–80% reduction of the CO_2 emission in 2030 compared to 2000) still predicts a global mean temperature increase of 2.0–2.4 °C. Although resources for oil, gas and coal are sufficient for the next decades or even centuries, their availability is limited, as it is for fuels for nuclear fission power plants. Fast breeder fission technologies, moreover, are not likely to be acceptable, since waste disposal, safety and proliferation issues are unsolved. Renewable energy sources (solar, geothermal, tidal, wind, biomass etc.) are hardly an alternative to replace the bulk majority fossil sources, due to limited continuous availability and lack of energy storage technologies [3]. The only new sustainable energy source which is able to secure long-term energy supply while avoiding any greenhouse gas emission is nuclear fusion.

1.1 Nuclear fusion

In a nuclear fusion power plant the same physical processes as in the sun are used to generate energy: the fusion of light nuclei. For a reactor, the reaction between deuterium (^{2}H, D) and tritium (^{3}H, T) is most suitable, since it has a maximum cross-section at lowest temperatures: given a sufficient particle density (approximately 10^{20} m^{-3}), a temperature of approximately 10^8 K is

necessary to efficiently use the reaction:

$$D + T \longrightarrow {}^4He + n + 17.6\ MeV$$

At such temperatures, hydrogen is fully ionized and forms a plasma. Since the plasma particles are electrically charged, a confinement by magnetic fields is possible. The reaction products n and ^{4}He carry the energy from the fusion reaction. The alpha particles are confined within the magnetic field and sustain the plasma temperature after ignition. The neutrons transport their energy (14.1 MeV) into the blanket, where it is collected by heat exchangers. Also in the blanket neutrons generate the tritium fuel from lithium, since tritium is an isotope with a short half-life of 12.3 years and therefore is not naturally abundant. The tritium breeding reactions are:

$$^6Li + n \longrightarrow {}^4He + T + 4.8\ MeV$$

and

$$^7Li + n \longrightarrow {}^4He + T + n - 2.5\ MeV$$

Therefore, the fusion reaction is based on deuterium and lithium as fuel elements. Deuterium has a natural abundance of 0.0145% and can easily be extracted from water. Lithium occurs in the lithosphere with an average concentration of 50 ppm and can be extracted from abundant minerals. Total resources of both fuel elements for nuclear fusion are therefore essentially unlimited and widely distributed around the globe. The D–T fusion is not a chain reaction and each deviation of one of the required parameters to sustain the reaction terminates it. Nuclear fusion is an intrinsically safe energy source without the risk of a runaway process. During operation, components of a fusion reactor will be activated by the energetic neutrons. By carefully selecting the materials and components used for construction of the reactor vessel, the structural materials and components, the radioactive inventory can be limited to isotopes with short half-lifes. Thus, the activity of the components drops to levels which allow recycling within the first 100 years [4].

The magnetic confinement of the hot plasma is technically realized by two concepts, both based on a toroidal geometry. In a stellarator [5], the magnetic fields confining the plasma are produced by magnetic field coils arranged

around the torus only. The magnetic configuration can be maintained in steady state, however, at the cost of a complex external coil system. The most advanced modular stellarator is currently under construction at the Max-Planck-Institut für Plasmaphysik in Greifswald. The second concept, which is realized in most magnetic confinement fusion experiments around the world, is the tokamak [6]. The magnetic field confining the plasma is composed of a toroidal component, created by external magnetic field coils, and a poloidal component which is generated by a current induced in the plasma torus itself. As a consequence, a tokamak can only operate in a pulsed mode without auxiliary facilities which permanently sustain a toroidal current in the plasma. Nevertheless, the tokamaks TFTR (Tritium Fusion Test Experiment, USA) and JET (Joint European Torus, EU), the largest fusion device built up to now, demonstrated the production of substantial fusion power [7]. In 1997, JET achieved a fusion power of 16 MW, 65% of the power necessary for the external plasma heating (fusion gain Q factor of 0.65). To optimize energy confinement and to improve the fusion gain, a device with larger dimensions is necessary.

The next step in magnetic confinement fusion is the large-scale fusion experiment ITER, built jointly in a partnership between Europe, Japan, Russia, South Korea, China, India, and the USA. The contracts were signed in 2005, since 2007 the construction is going on at Cadarache in southern France. The objective of ITER is “to demonstrate the scientific and technological feasibility of fusion energy for peaceful purposes”. The goal for ITER is to operate with a high fusion gain of $Q \approx 10$, which means that the majority of the heating power will be provided by the alpha particles created in the D–T reaction [8, 9].

1.2 Plasma-wall interactions and “mixed materials”

The confinement of energy and particles in a magnetic confinement fusion device is necessarily limited, since it is the aim to convert the released energy into electricity and the continuous reaction requires the alpha particles to be removed from the plasma. Also any impurities need to be removed from the plasma, because they dilute the fuel and cool the plasma by radiative losses. Therefore, the interactions between the plasma and the first wall of the vacuum vessel influence both, the properties of the materials at the first wall, and the properties of the plasma from the outermost regions to the plasma core. Energy

deposited from the plasma drives an number of processes at the wall. Material is eroded by physical sputtering or, in off-normal events, by sublimation or melting. In the case of multi-element first wall components, energy deposited from the plasma can also initiate chemical reactions. Eroded material from the wall is ionized when entering the plasma and subsequently transported along the field lines. Finally, after re-deposition, the elemental distribution at the first wall is altered by this material transport and deposition. Plasma constituents, among them impurities and helium, and in particular the hydrogen isotopes, are implanted into the first wall materials. During collision cascades, defect sites are created which act as traps for the implanted species. In case of temperature excursions leading to elevated wall temperatures, diffusion of the hydrogen isotopes can take place, leading both to a re-emission and a diffusion of implanted species deep into the bulk of the wall materials. This process is of particular importance with respect to safety issues, since implanted tritium accumulates in the wall materials and can even diffuse into structural materials or into the cooling media. The precise knowledge of the radioactive inventory of a fusion device is of importance for radiation protection licensing. Therefore, all physical and chemical processes which can influence the hydrogen isotope inventory of first wall materials, must be known in order to predict the dynamic hydrogen inventory during operation of a fusion device.

In current fusion experiments, a number of first wall materials and conditioning procedures are used [10]. With the use of light, low Z elements like carbon, boron layers, or beryllium, a low effective Z of the plasma could be achieved, minimizing the radiative losses. The advantages of graphites as first wall materials, however, like no melting in case of high heat loads, are neutralized by its hydrogen chemistry. These chemical reactions between hydrogen and carbon not only open chemical erosion channels even at very low particle impact energies, but also lead to the formation of hydrogen-(tritium-)containing radicals which can deposit in remote areas or gaps where a retrieval of the tritium inventory is impossible [11]. Beryllium not only is a low Z material, but reduces also oxygen concentrations in the plasma due to its reactivity. As a metal is exhibits advantages compared to graphites with respect to thermal conductivity and hydrogen chemistry. In particular in JET beryllium has been extensively used and immediately showed the beneficial behavior of strong oxygen gettering [12]. With increasing control of the kinetic energy (i.e. cooling the edge plasma) of

the large flux of particles reaching the wall materials, in particular in the divertor region of a tokamak, high Z elements like tungsten became favorable as wall materials. These elements exhibit a high threshold energy for sputtering, and eroded from the surface they are promptly redeposited close to their origin due to quick ionization and small gyroradii. The feasibility of operating a modern tokamak with a high Z material like tungsten has been demonstrated in ASDEX Upgrade, which has continuously been converted to a full-W machine without performance degradation [13,14]. The research in plasma-wall interactions over many years finally lead to the choice of beryllium, carbon, and tungsten as the plasma-facing materials for the next-step fusion device ITER [8,9]. This decision is also kept after the ITER design review, which was initiated in 2006 after the decision to build ITER. Beryllium is the material of choice for the cladding of the first wall of the main chamber of ITER. This comprises a total surface area of ≈ 690 m^2. Carbon (as a fiber-reinforced, CFC, material) is the choice for the divertor strike points (≈ 55 m^2). Due to the problems of tritium co-deposition in hydrocarbon layers [15], a replacement of the carbon materials at the strike points by tungsten is under discussion, before the ITER operation enters the D–T phase. Tungsten is the design material for all other divertor surfaces with a total surface area of ≈ 140 m^2 [10].

If multiple materials are used as plasma-facing surfaces in a fusion vessel, during plasma operation erosion, transport, and re-deposition will lead to surface layers of one material on the other, or more general: to the formation of multi-component surfaces (“mixed materials”). Thermally and ion-driven processes (diffusion, reaction, ion beam mixing) initiate the formation of mixtures and/or compounds of the available elements. In addition, plasma impurities (e.g. oxygen from oxidized surfaces or leaks, nitrogen from seeding of the plasma edge) and the hydrogen isotopes from the fuel can additionally take part in surface chemical processes. Long before the deliberate application of multiple elements in fusion devices (like e.g. the application of Be together with carbon in JET [16], the initial tungsten campaign in ASDEX Upgrade [17], the JET ITER-like wall program [18, 19], or the planned application of Be, C and W in ITER [8, 9]), it became clear that the deposits at the first wall of fusion devices are composed of a number of elements, which are eroded at some locations within the vessel and re-deposited at different sites. Both deposition and preferential sputtering processes contribute to the final composition, which was hardly to be predicted

(see e.g. [20–26]). After the application of beryllium as a wall material in JET, the formation of compounds between beryllium and the carbon from graphite tiles was identified as a major process which strongly influences the retention of hydrogen isotopes [27, 28]. In laboratory experiments, the sputtering of multi-component surfaces [29] and their formation and erosion properties, as well as their influence on the inventory of hydrogen was investigated [30–39]. However, the results for hydrogen retention in mixed materials or the formation criteria for compound surface layers were in some cases controversial. This is due to the fact that in some cases the vacuum conditions in the experiments were insufficient to prevent oxidative reactions, in particular for experiments involving beryllium. The experimental conditions were not sufficiently well-defined and the results could not be reproduced in different groups. The modeling of mixed materials formation and erosion, based on the exposure of samples to plasma conditions with multiple species (e.g. in the PISCES-B device [40, 41]), was in the first years limited to purely kinematic interactions between impinging species and the surfaces [42–46]. Nevertheless, the PISCES-B device is one of the few experiments which are able to study multi-component surface effects applying a plasma impinging at surfaces, in particular involving beryllium as one of the species [40, 47–58]. A number of material systems and exposure conditions can be studied under conditions which are relevant to the ITER divertor. Only in recent years another experiment which is capable of simulating surface loads with particles and energy similar to the ITER divertor conditions is under construction: the Magnum-PSI experiment [59].

Despite the fact that these plasma simulators are uniquely suited for simulations of ITER divertor loading conditions, they are less adequate to determine single physical parameters, simply due to the complexity of the plasma-surface interaction processes occurring simultaneously. Throughout the inner surface of a fusion device, the environmental conditions at the first wall vary considerably at different locations[1], due to different functionalities of the first wall, e.g.

[1] For ITER, under normal operation conditions the first wall temperatures in the main chamber are expected to vary between 450 and up to 600 K, whereas the surface temperatures in the divertor are expected between 450 and up to 1300 K [60]. Under certain conditions, the surface temperatures can even exceed these values significantly. Particle energies of species impinging at the first wall range between a few eV into the keV regime, again depending on the location within the vessel. Also the particle fluxes arriving at different parts of the first wall range from $10^{19} - 10^{20}$ m^{-2} s^{-1} in the Be-covered main chamber, and up to 10^{24} m^{-2} s^{-1} at the divertor strike points [10].

in the divertor, at the main chamber wall, or at start-up limiters. It is therefore necessary to determine the fundamental properties governing the processes at the first wall. Only a modeling approach based on these data allows predictions for a complex machine. If the material formation, erosion and hydrogen inventory processes are to be simulated, facilitating predictions for the material behavior in ITER for the very different conditions at the first wall locations, it is necessary to reduce the experimental parameter space to few variables. In singling out specific processes in one study, it is possible to determine the parameters which govern temperature or ion-driven processes. By determining the behavior of materials under well-defined conditions, predictions are possible for more complex scenarios.

In this work, fundamental reaction and diffusion processes are studied for materials which are of importance for current and future fusion experiments. In well-defined experiments, the processes driven by temperature or by ion bombardment are observed by qualitative and quantitative techniques. In section 2, the new experimental setups are summarized which were necessary for the specific measurements. Section 3 describes surface reactions in binary carbon–metal systems. In particular, the reactions of carbon layers with the metals beryllium, tungsten, iron, nickel, silicon, and gold for reference purposes, are described for thermally induced reactions. Moreover, for specific systems also compound formation and erosion processes, induced by noble gas ions or reactive species, are summarized. Section 4 describes experiments which aim at surface reactions induced by atomic oxygen on beryllium, tungsten, and gold. The formation of binary alloys in the Be–W system is discussed in section 5. The topic of surface and interface reactions in ternary systems is treated in section 6, both for thermally induced processes and for reactive molecules as ionic species. Finally, in section 7 fundamental studies on the hydrogen retention in and release from beryllium are described. The original publications are listed and attached on pages 103 ff. and are denoted in the references throughout the text by $^{\otimes}$.

2 Experimental approach

The investigation of the influence of surface compound layers on the hydrogen inventory of materials requires experimental conditions in which suitable samples can be produced, characterized, implanted and analyzed under well-controlled environments. Sample preparation involves in a first step the removal of impurity species from the surface and surface-near bulk and a sufficiently good vacuum to keep the prepared surfaces in a controlled state for the time of an experiment. The topic of mixed wall materials involves in particular beryllium and carbon. Beryllium is highly reactive (in particular with oxygen and water), and carbon is a ubiquitous contamination. Controlled surface science experiments therefore require base pressures in the low 10^{-10}, better in the low 10^{-11} hPa regime. Furthermore, the performed dedicated experiments involve sample preparation steps where species are deposited from the vapor phase, implanted as energetic ions, or, in the case of oxygen, deposited as atomic species (see section 2.2 for a description of a source for atomic oxygen). Some of the experiments involving tungsten surfaces included temperature treatments of the prepared samples ranging from 300 K to 1700 K.

The various applied analytical techniques aim at both qualitative and quantitative assessments of the species present at the surface or at surface-near interfaces, as well as of species desorbing from the samples in the case of hydrogen inventory studies. For chemical state analysis, X-ray photoelectron spectroscopy (XPS), is the technique of choice. This method allows for chemical analysis of the surface and surface-near depths both qualitatively (resolving elements and their chemical states) and quantitatively (taking into account models for the depth distribution). XPS is used both in laboratory experiments and with synchrotron radiation. Laboratory experiments employ non-monochromatic sources (Al and Mg anodes), and monochromatic Al Kα radiation. The latter provides an overall resolution of the spectrometer system of 0.29 eV [61]. XPS measurements carried out with synchrotron radiation not only enable high resolution spectroscopy, but are especially useful for gaining chemical informa-

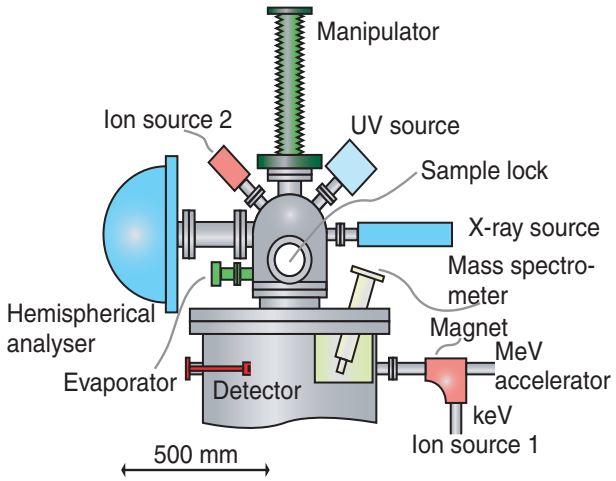

Figure 2.1: Schematic representation of the UHV experiment Artoss, dedicated to studies of the influence of multi-component surface layers on the hydrogen inventory in materials.

tion with tunable information depth. To make use of these specific advantages, experiments at the synchrotron facility HZB-BESSY II in Berlin are performed using a specifically designed sample preparation setup, described in section 2.3.

Experiments aiming at the inventory of hydrogen isotopes require specific analysis techniques for these species. In particular, nuclear reaction analysis (NRA) and temperature-programmed desorption (TPD) are useful for this purpose. Since NRA and other high-energy ion beam analysis techniques require an accelerator, a new UHV setup has been constructed which combines very low vacuum conditions (base pressure in the low 10^{-11} hPa regime), X-ray photoelectron spectroscopy, and low-energy ion sources (eV to keV) for sample preparation and hydrogen implantation, with the availability of high-energy ions (MeV) from a 3 MV tandem accelerator. This setup is described in the following section 2.1.

2.1 *In situ* formation and characterization, hydrogen inventory: The Artoss experiment

The Artoss experiment is dedicated to the preparation and the *in situ* characterization of multi-component surface layers, and in particular the *in situ*

investigation of hydrogen inventories. A schematic view of the apparatus is shown in Fig. 2.1. The experimental setup is described in detail in [62]$^{\otimes}$. Here, the characteristic details are given as a list.

- Base pressure $\leq 3 \cdot 10^{-11}$ hPa
- Sample temperature between approximately 200 K and 1400 K (liquid nitrogen cooling and electron beam heating possibilities)
- Transferable sample holder with integrated heater and thermocouple wiring
- Sample load-lock
- Double cylinder Faraday cup housing the sample, for precise sample current measurements
- Small aperture Faraday cup for ion beam profile characterization
- Pumping system comprising of turbomolecular pumps, titanium sublimator, liquid nitrogen-cooled baffle, ion pump
- Sample preparation:
  - Differentially pumped sputtering source (IQ2)
  - Mass-separated and differentially pumped ion source (IQ1), with optional ion optics to decelerate ions down to ≈100 eV
  - Evaporator for solid materials, e.g. carbon
  - Gas admission via 'gas shower'
- Analysis techniques:
  - X-ray photoelectron spectroscopy (XPS), using non-monochromatic Al and Mg Kα radiation
  - Ultraviolet photoelectron spectroscopy (UPS), He I and He II excitation lines
  - Ion scattering spectroscopy (ISS) in 135° backscattering geometry
  - Hemispherical electrostatic energy analyzer (for XPS, UPS, and ISS) with entrance lens system, allowing for analysis spot sizes down to 70 μm diameter

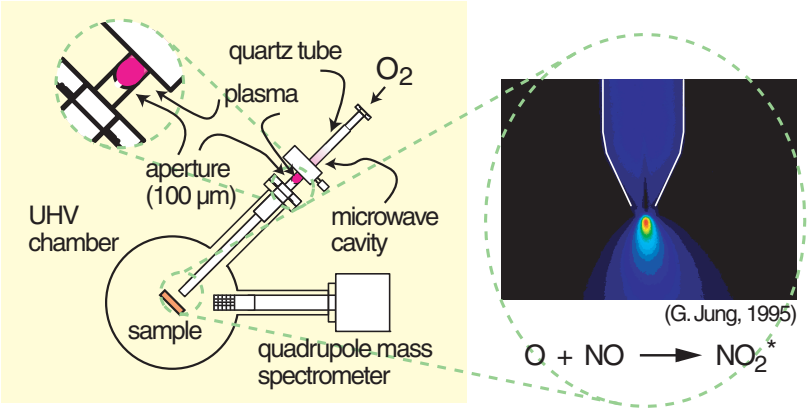

Figure 2.2: Schematic setup of the microwave discharge O atom source. The light emission pattern from the NO_2^* de-excitation was measured in a similar setup by G. Jung [63].

- Temperature-programmed desorption (TPD), using a quadrupole mass spectrometer housed in a differentially pumped stage, in line-of-sight alignment and a tuning-fork chopper
- Accelerator-based ion beam techniques (RBS, NRA, ERD) with implanted silicon barrier detectors at scattering angles of 30°, 135°, 105°, 165°

2.2 Source for atomic oxygen

In order to study the interaction of oxygen atoms with surfaces, molecular oxygen must be dissociated and enabled to reach the surface. A first setup was realized by G. Jung in a diploma study [63] in which the formation of atomic oxygen was demonstrated by light emission from the decay of the metastable NO_2^*, formed in the reaction $O + NO \longrightarrow NO_2^*$. This source was adapted to operate in the UHV preparation chamber of the IPP XPS spectrometer. Essentially, the aperture separating the discharge cavity from the tube extending into the UHV chamber had to be optimized in order to provide a sufficient pressure gradient between the microwave discharge region and the UHV chamber. This was achieved with a 100 μm orifice in the terminal end of the high-pressure quartz tube, which connects to the low-pressure tube extending into the UHV chamber. This orifice diameter allowed a pressure drop by four orders of mag-

nitude between the discharge region and the main chamber. During operation of the atom source, a pressure better than $1 \cdot 10^{-6}$ hPa can be maintained on the UHV side (essentially molecular O_2 over a base pressure in the low 10^{-10} hPa). In the microwave discharge region a pressure of approx. 10^{-2} hPa is necessary to maintain the discharge. During operation, high purity oxygen (99.999%, Linde) is continuously supplied and differentially pumped. The quartz discharge setup is sealed by a quartz/ceramic/stainless steel adaptor flange. Fig. 2.2 schematically shows the setup, as well as the light emission from the NO_2^* de-excitation, as measured in [63]. In this work, the degree of dissociation has been determined to be approximately 30%. Quartz is selected as the material for the discharge region and the guiding tube, since its oxidic surface is expected to be inert towards adsorption and recombination of oxygen atoms.

2.3 Depth-resolved chemical analysis: The LAICA setup for *in situ* sample preparation at HZB-BESSY II

Photoemission measurements using synchrotron radiation enable valence band and core level spectroscopy with strongly improved energy resolution. Moreover, the tunable primary energy of the exciting photons allows the selection of the final kinetic energy of the photoelectrons, thereby providing a means for the investigation of reactive and diffusive processes at the interfaces between layers in multi-component systems. Since the kinetic energy determines the electron mean free path in the solid, tuning the photoelectron kinetic energy allows to select (a) the same information depth for different photoelectron lines from different chemical species and (b) the depth up to which the chemical information is gained [64–70]. This technique has been successfully applied quantitatively for the first time in a 3-component C/Be/W layered system in measurements at the MUSTANG end station at HZB-BESSY II [71]$^{\otimes}$. During these measurements and in a subsequent approach where samples prepared in our Garching laboratory were transported to the SurICat end station at HZB-BESSY II using a UHV transfer chamber, it became clear that sample preparation at HZB-BESSY II and *in vacuo* transfer of the sample into the measurement station without air contact is a prerequisite for a successful application of depth-resolved chemical measurements. Moreover, the sample treatment steps (in particular vapor deposition and annealing procedures) require well-defined environments in case

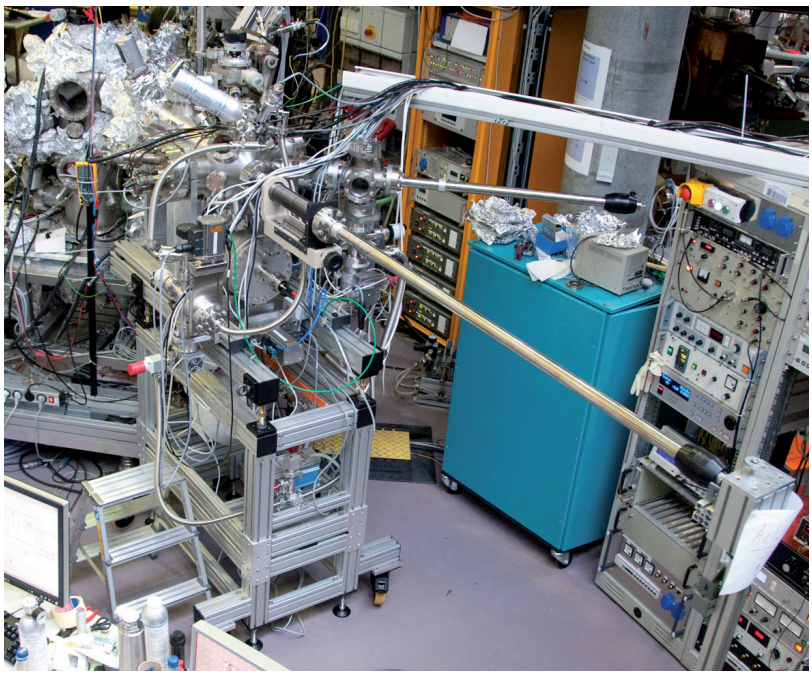

Figure 2.3: The preparation and characterization chamber LAICA, installed at the SurICat end station at the synchrotron HZB-BESSY II.

of beryllium and carbon-containing systems for which the standard equipment at the HZB-BESSY II end stations is not specialized enough.

In order to enable well-defined experiments with depth-resolved chemical analysis in multi-component systems, the preparation chamber LAICA has been designed and constructed. The chamber is equipped to prepare, pre-characterize and store samples which can then be transferred *in vacuo* to a HZB-BESSY II end station. The following list describes the characteristics of the setup:

- Base pressure $\leq 1 \cdot 10^{-10}$ hPa
- Sample transfer system compatible with HZB-BESSY II standard system (Omicron-type sample holders)
- Sample load-lock
- Parking system for samples prepared before the measurement campaign

- Pumping system to bridge power-less chamber transport from HZB-BESSY II laboratory the HZB-BESSY II end station (getter pump)
- Sample heating with electron beam heater up to temperatures of 1370 K
- Ion source for sputter cleaning and ion implantation (keV energy range)
- Capability of measuring sample currents and sample temperatures
- Multiple evaporation sources for layer deposition (currently 3 evaporators possible)
- Characterization of the sample composition and structure, independent from the end station analytical system:
  - Auger electron spectrometer (AES) with cylindrical mirror analyzer and integral electron gun
  - Four-grid low-energy electron diffraction (LEED) system (including back-up AES option)
- Optional integration of atomic oxygen source

The preparation chamber LAICA has been successfully used in a first experimental campaign at the HZB-BESSY II end station SurICat during May 2009. Fig. 2.3 shows the preparation chamber, connected to the SurICat end station at HZB-BESSY II. Preparation of ternary Be/C/W samples and pre-characterization in LAICA, transfer into the SurICat end station, and photoemission measurements using the tunable synchrotron radiation from the HZB-BESSY II synchrotron were successfully performed.

3 Carbon layers on metal

With respect to the investigation of compound formation processes at the surface of first wall materials, the binary carbon-metal systems are of fundamental interest. Carbon is eroded both by physical and chemical processes in a fusion device. The primary species impinging at the first wall from the plasma are atomic carbon species due to the dissociation of molecules in the plasma. Before more complicated processes at the first wall are investigated (like the influence of compound layers on the hydrogen retention and release), the fundamental interaction processes between carbon and metal surfaces leading to the formation of carbon-based compounds need to be understood. The chemical and physical interaction of carbon with elemental surfaces is determined by the energy of the incoming particles and the surface temperature. The possible reactions comprise chemical phase formation and decomposition, and diffusive processes which lead to carbon transport from the surface into the bulk.

Chemical interactions of carbon with elemental surfaces pose a difficult experimental problem due to its ubiquitous occurrence. Therefore, experimental conditions have to be created and maintained where:

- surfaces can be prepared and kept for several hours free of carbon contamination
- carbon can be introduced in a controlled way, either from the vapor phase or as (atomic or molecular) ions
- qualitative and quantitative analysis of carbon and its chemical states can be performed

These requirements are met by performing experiments in UHV, operating electron beam evaporators with increased high voltages, using ion sources with mass-selected beams, and finally combining X-ray photoelectron spectroscopy with ion beam analysis techniques like RBS and NRA. Samples are required to contain low impurity levels, in particular of carbon. Therefore, all experiments are performed either on single crystals or on high purity polycrystals.

The interaction of carbon with beryllium and tungsten is of specific interest due to the application of these elements as first wall materials in ITER. Moreover, iron and nickel as main components in steels are investigated. These metals are of distinguished interest, since the carbide formation reaction for Fe and Ni is endothermic under standard conditions. For comparison, also titanium and silicon are investigated with respect to their carbide formation and carbon diffusion properties. Generally, carbides exhibit different types of chemical bonds in the solid. Beryllium forms an ionic carbide which consists of C^{4-} carbon anions. Carbides from elements with an electronegativity similar to that of C, like silicon, exhibit a more covalent bonding character. Finally the transition metal carbides W, Ti, Fe, Ni are metallic compounds where the carbon is incorporated into the metal lattice at interstitial positions. These positions are predominantly octahedral sites in the metal lattice. This arrangement requires the metal atom radius to be larger than 0.135 nm [72]. In some cases, the carbide exhibits the same metal packing as in the pure metal, in other cases the carbide metal atom lattice is produced by small rearrangements. As a first example for an intercalation carbide (metallic carbide), titanium carbide exhibits the same hcp structure as metallic Ti. In such a structure, the number of octahedral sites is identical to the number of metal atoms. A sequential occupation of these octahedral sites in the Ti lattice forms the titanium subcarbides. In the literature, Ti_8C_5 [73, 74] and Ti_6C_5 [75] are described. In neutron scattering measurements, superlattice lines are found in Ti–C annealing experiments between 1373 and 2273 K [76]. Due to the fact that no distortions in the Ti lattice are necessary to form polytypes, they can easily be formed by mechanical treatments [77]. If all octahedral sites in the lattice are occupied by carbon atoms, the titanium monocarbide, TiC, is formed, which exhibits NaCl structure [78]. The exact 1:1 stoichiometry is not reached in TiC, the maximum stoichiometry is $TiC_{0.95}$ [61, 79]. As a consequence, a TiC crystal always contains vacancies due to missing C atoms in octahedral sites [80]. Tungsten, as a second example for an intercalation carbide, has a bcc structure in the metallic phase. During carbide formation, the octahedral sites are occupied by carbon atoms. Due to the distortions in the metal lattice, the tungsten lattice transforms into a hcp structure, when the W_2C stoichiometry is reached and every second octahedral site is occupied by C [81]. According to the prototype structure CdI_2, empty and occupied octahedral sites are arranged in alternating layers. The tungsten

monocarbide WC forms a special structure, the WC type [82]. The metal atoms are arranged in a hexagonal primitive lattice in which the tungsten atoms form trigonal prisms. The carbon atoms are located in the center of these prisms [83]. Both the Ti and W intercalation compounds are solids with high hardness and melting temperatures due to their structures.

In general, the interaction of elemental carbon with substrates at different temperatures is of concern, since the wall temperature in a fusion device can range from approximately room temperature to well above 1000 K during operation. In specific locations where the particle and energy fluxes ar very high, the surface temperature may even exceed these values. Therefore, the interactions of carbon with metals as a function of the substrate temperature are of primary interest. The results of these investigations are summarized in the following section (chapter 3.1). Reactions between carbon and substrates can also be stimulated by the kinetic energy of particles escaping the plasma and reaching the first wall. These reactions stimulated by ion irradiation of carbon/metal systems, or by implantation of carbon-containing species into the elemental substrates, are addressed in chapter 3.2.

The investigations on binary carbon-metal systems, both for thermally and ion-induced reactions, are summarized with respect to certain aspects and materials in [84]$^{\otimes}$, [85]$^{\otimes}$, [86]$^{\otimes}$, [87]$^{\otimes}$.

3.1 Thermally induced reactions

Carbon layers on Au In contrast to most other metals, gold is inert with respect to carbon diffusion and carbide formation [79]. Therefore, Au substrates are used to study the XPS signals of carbon films deposited by vapor deposition on the substrate at 300 K, and the changes in the carbon layers during annealing. Thus, the elementary carbon states within the C 1*s* BE region are accessible. The C 1*s* signal of vapor-deposited carbon shows two peaks which can be assigned to graphitic carbon with a BE of 284.2 eV, and an additional peak at 285.1 eV [88]$^{\otimes}$. This signal at higher BE is assigned to graphite in a 'disordered' state due to the observation that the intensity of this peak decreases upon annealing [89]$^{\otimes}$. The disordered graphite is comparable to 'non-perfect' sp^2 carbon and the decrease of that intensity during annealing is ascribed to a rearrangement into ordered (sp^2) graphite. The implantation of inert ions, e.g. argon, restores the intensity

at higher BE. A similar broadening at this BE is observed after implantation of Ar^+ at 1 keV into highly-ordered pyrolytic graphite (HOPG) [90]$^{\otimes}$. This precise analysis of the C 1*s* peak is only possible using the monochromatic Al Kα radiation, because a broader primary excitation energy, e.g. using a non-monochromatic Mg or Al Kα source, obscures the shoulder in the C 1*s* peak at the high-BE energy side. Peak fitting of the two C 1*s* peaks using Gauss-Lorentz functions in the software MultiPak [91], gives access to these two peaks. For further analysis of the C 1*s* signals in the different reactive carbon/metal systems, the knowledge of the exact peak positions of the elemental carbon peaks is indispensable.

Carbon layers on Fe and Ni The carbides of Fe and Ni are examples for transition metal carbides with endothermic standard enthalpies of formation. In the experiments described in [88]$^{\otimes}$ the carbon is deposited from the vapor phase on Fe(100) and Ni(111) surfaces at 300 K. The chemical composition is analyzed by XPS at temperatures between 300 K and close to 1000 K, allowing to study the C/metal interface chemistry as a function of carbon coverage and annealing temperature. Although the enthalpies of formation for Ni_3C and Fe_3C are positive, a small carbide intensity is observed in the C 1*s* signals after depositing sub-monolayer carbon amounts on the Fe and Ni substrates at 300 K. The respective binding energies are 283.5 eV for Ni_3C and 283.4 eV for Fe_3C. These values are in agreement with literature data [92–95] and confirm the formation of the carbides by depositing elemental carbon films on the substrates at room temperature. Angle-resolved XPS measurements confirm that at higher C coverage the carbide remains located at the interface between the substrate and the carbon film. Additionally deposited carbon remains in the elemental state and shows both the graphitic and the 'disordered graphitic' peaks.

For thin carbon films (< 1 nm) both on Fe and Ni a partial decomposition of the carbide formed initially at 300 K is observed upon annealing. A minimum in the carbide intensity is reached around 550 K. For thicker carbon deposits, the interfacial carbide is obscured by the overlayers due to the surface sensitivity of XPS. The carbide peak in the C 1*s* region decreases, whereas the overall carbon intensity is almost constant. This is in agreement with the endothermic nature of the carbides. At higher temperatures, carbon diffusion into the bulk sets in, combined with reaction of the remaining carbon in the XPS information depth

to carbides. This leads to a decreasing C 1*s* signal intensity, until the carbon is almost completely lost into the bulk.

The thermal behavior of carbon films on nickel substrates with different surface orientation is compared for Ni(1 1 1) and Ni(1 0 0) after deposition at 300 K [96]$^{\otimes}$. The growth mode of carbon films on Ni is analyzed by examining the inelastic background at the low kinetic energy side of the Ni 3*p* line for a series of carbon layer thicknesses according to Tougaard's model [97–99]. From the comparison of measured and simulated spectra, a layer growth up to ~ 1.3 nm thickness, followed by an island growth mode, can be concluded. A pure island growth mode can be excluded. The formation of an interfacial carbide layer at 300 K upon C deposition is identical on both Ni surfaces. The maximum carbide fraction in the C 1*s* peak (extrapolated to zero coverage) is 65%. At a C layer thickness of 1 nm, still 45% of the C 1*s* intensity is in the carbidic peak. With increasing carbon deposition, the carbide peak shows a binding energy shift. The peak position is close to the bulk BE value at 283.45 eV in the sub-monolayer regime, and decreases in BE up to a C layer thickness of ~ 1.5 ML. Above this coverage, a continuous BE shift to higher values is observed, until the bulk value for Ni_3C of 283.50–283.55 eV is reached at 4 ML. At low C coverages, a surface reconstruction ('clock reconstruction') is described in the literature both for Ni(1 0 0) and Ni(1 1 1) surfaces [100–102]. In all these experiments, the carbon was deposited by hydrocarbon deposition, whereas we deposit C from the vapor phase. We ascribe the observed BE shift to such a surface reconstruction. The increase of the carbide BE between 1.5 and 4 ML is explained by a cluster size effect. The initially formed carbide clusters are embedded and finally covered by a graphite matrix. With increasing temperature, even after the onset of carbon diffusion into the nickel bulk, no additional carbide is formed on both Ni surfaces. For small C coverages, even the Ni_3C decomposition is observed. This behavior agrees well with the metastable, endothermic nature of Ni_3C and is different from the exothermic carbides described below. The detection of carbide intensity after annealing to temperatures where carbon diffusion definitively plays a role is due to carbon segregation back to the surface after cooling down to 300 K. This process was actually used for carbon enrichment experiments [103] and also observed by [104, 105].

The elemental steps of the processes during annealing of carbon films on Ni(1 1 1), Ni(1 0 0), and Fe(1 1 0) are quantitatively analyzed by XPS and kinetic

data are determined [106]$^{\otimes}$. Moreover, the resulting experimental activation barriers for elementary reaction steps during the carbon-metal reactions (carbon subsurface diffusion, carbide formation, and graphite ordering) are compared to DFT simulations, which in addition allow insight into details of the carbon diffusion mechanism during subsurface diffusion. The results allow a quantitative description of the thermally induced processes on the investigated surfaces. Experimentally, the kinetic parameters are determined from measurements where the C/metal systems are held at different elevated temperatures for several hours. In contrast to the measurements described above for the determination of the chemical phases formed during the C–metal reactions ([88]$^{\otimes}$, [96]$^{\otimes}$), the XPS spectra are measured while the samples are at elevated temperatures. The high resolution measurements allow the deconvolution of the C 1*s* signals by peak fitting (Gauss-Lorentz line shapes, Shirley-type background) and thus the determination of the kinetic parameters for the occurring reactions.

The onset of carbon diffusion into the bulk (and therefore out of the analysis depth of XPS) is different for Ni and Fe. The respective onset temperatures correlate with the tendency of the activation barriers for bulk C diffusion in Ni and Fe: 1.5 and 0.8 eV, respectively [107, 108]. Furthermore, the trend in the onset temperatures reflects the surface atom densities, which is smaller for Ni(1 0 0) than for Ni(1 1 1). Consequently, the onset temperatures for the three investigated surfaces Fe(1 1 0), Ni(1 0 0), and Ni(1 1 1) are: 620, 650, and 770 K, respectively. From the experiments where the C films on metals are annealed to increasing temperatures and the chemical composition is analyzed by XPS spectra at 300 K, the temperature regimes for the different elementary reaction steps are identified for the three surfaces. As an example, for Ni(1 1 1), reaction (I), the decomposition of the initially formed carbide, leading to an increase in the elemental carbon, is observed up to 570 K. Reaction (II), the ordering within the elemental carbon (leading to a decrease of the disordered graphitic component), is observed up to 670 K. At this temperature, reaction (III), carbon subsurface diffusion, sets in and leads to a loss of intensity in all components of the C 1*s* signal. Parallel to reaction (III), carbide formation leads to an additional decrease in the elemental carbon intensity and an increase of the carbide intensity. After pronounced carbon diffusion, finally reaction (IV), carbon segregation while cooling down to 300 K, leads to an increase in the total

C 1*s* intensity and to an increase of the carbide signal.

In long-time annealing experiments it is possible to extract kinetic parameters from a set of differential equations which take into account the dependence of the changes of the respective carbon intensities on these elementary reactions. Reaction (I) can be neglected, because all experiments are carried out above 570 K, where the carbide decomposition is already finished. Furthermore, reaction (IV) plays no role while the samples are held at elevated temperatures.

In order to gain insight in the elementary steps for carbon subsurface diffusion, and to confirm the models by comparing experiments to simulations, DFT calculations are performed for the three investigated surfaces. In all cases, the C subsurface diffusion from an adsorbed site above the surface to a site within the substrate proceeds via out-of-plane processes. For Ni(1 1 1), during diffusion carbon pulls one of the neighboring Ni atoms out of the surface plane by almost 0.7 Å. Through this open hole, the C atom migrates to an octahedral subsurface site. The calculated energy barrier for this process of 1.92 eV compares well with the barrier form the experiment of 1.9 eV. After C migration into the subsurface position, the Ni re-assumes its equilibrium position within the surface layer. A very similar process results from the DFT calculations for the Fe(1 1 0) surface. For Ni(1 0 0), where the vertical diffusion is not directly possible due to a second Ni atom below the surface atom, the subsurface diffusion proceeds via a horizontal diffusion step, in which again a Ni atoms is pushed out of the surface plane by 1.1 Å. This is followed by a vertical C diffusion step into a bipyramidal subsurface site. Again, the DFT energy barrier of 1.45 eV for this process is in very good agreement with the 1.4 eV, determined experimentally. Finally, the kinetic parameters determined by this procedure for the elementary reactions can be combined to model the temperature dependent development of the carbon films on the investigated substrates. This simulation reproduces the temperature-induced ordering and diffusion processes quantitatively, confirming the developed model and the respective kinetic parameters.

Carbon layers on W The interaction of carbon films with tungsten surfaces is investigated in detail both for polycrystalline W [89]$^{\otimes}$, [85]$^{\otimes}$ and W(1 1 1) [84]$^{\otimes}$ surfaces. After C deposition from the vapor phase on the W substrates, a WC layer develops at the interface. With continued C deposition, this interfacial carbide is covered by elemental C (both graphitic C and disordered graphitic C),

no additional carbide is formed at 300 K. As a function of annealing temperature, four different regions can be identified. During phase (I), no additional carbide is formed and only the transition of disordered graphitic C into graphitic C is observed, the peak intensity of disordered C (at 284.5 eV in [89]$^{\otimes}$) decreases with annealing temperature. In phase (II), the diffusion of carbon into the W substrate starts. This phase starts on W(1 1 1) around 1000 K, whereas on polycrystalline W the onset is approximately 100 K lower. During phase (II), also the formation of tungsten subcarbide, W_2C, starts. The C 1*s* binding energy for this compound (and also for WC) is determined in separate experiments in which 100 nm tungsten on graphite are annealed to 1070 K and 1370 K. XRD measurements confirm the formation of W_2C and WC at the respective temperatures. In subsequent XPS measurements, the binding energies for W_2C and WC are determined to 283.6 and 283.1 eV, respectively. The corresponding W $4f_{7/2}$ binding energies are 31.8 and 32.2 eV. With these binding energies, a chemical phase analysis of the C 1*s* signal by peak fitting allows the precise quantitative composition analysis. Phase (III) in the temperature diagram is characterized by a constant C amount within the XPS analysis depth. W_2C dominates, although the concentration of WC is slightly increased compared to the phases (I) and (II). In case of polycrystalline W, phase (II) extends approximately between 1000 and 1250 K, whereas on W(1 1 1) the stability phase of W_2C extends up to 1470 K. In phase (IV) at the highest temperatures carbon diffusion into tungsten accelerates again and finally only $\approx$ 10% of the surface within the XPS analysis depth consists of carbon. W_2C decreases and WC becomes the dominating carbide compound at highest temperatures.

Like in the case of the Fe and Ni substrates, the kinetic parameters are determined at several annealing temperatures for carbon on W_{poly} and W(1 1 1) substrates for the formation reaction of W_2C. Grain boundary diffusion influences the activation energy for the subcarbide formation on these substrates: Whereas the activation energy for the W_2C formation on W_{poly} is 0.8 eV, the corresponding value for W(1 1 1) is 1.1 eV. Qualitatively, the influence of the grain boundaries is also visible in the carbon amounts during the phase (III). On the polycrystalline substrate, phase (III) not only exists in a smaller temperature range than on W(1 1 1), but also the amount of carbon is not constant over the whole phase (III) duration.

Carbon layers on Be The initial stages of carbide formation on beryllium and carbon diffusion into the substrate have been investigated in well-defined experiments under UHV conditions with carbon films deposited on Be single crystals [109]$^{\otimes}$, [110]$^{\otimes}$, [84]$^{\otimes}$. The interaction of Be with carbon from ionic species is summarized below in section 3.2. Due to the high reactivity of beryllium, impurities can be avoided only by *in situ* preparation and characterization under UHV conditions. Single crystals as substrate avoid intrinsic contaminations from the substrate. The concentration-dependent diffusion coefficient of Be in graphite and the influence of oxygen at the interface was studied in a combined XPS and RBS depth profile analysis [111]$^{\otimes}$. Although earlier work is available on the C–Be interaction [33–36, 112–114], the system was studied for the first time without any additionally present contaminations (in most cases oxygen or BeO is present in considerable amounts, even exceeding the amount of measured beryllium carbide).

Also in the C–Be system, carbon films deposited at the Be substrate at 300 K form Be_2C for small coverages. The C 1*s* binding energy for C submonolayers is 282.0 eV and reaches the bulk equilibrium value of 282.55 eV after a Be coverage of $1.5 \cdot 10^{16}$ cm^{-2}. Be_2C has a Be 1*s* binding energy of 112.85 eV. Additional carbon is deposited in elemental form. At a total carbon coverage of $9 \cdot 10^{15}$ cm^{-2} the intensities of carbidic end elemental carbon balance in XPS spectra. The Be_2C formed at the interface at 300 K amounts to a maximum carbon coverage of $6 \cdot 10^{15}$ cm^{-2}, therefore more than one monolayer of Be_2C is formed during the 300 K deposition. There are indications that the carbide layer growth is not a true layer-by-layer mode.

Annealing of carbon films on beryllium leads to the formation of additional Be_2C. Already at 473 K, the carbide intensities increase. Depending on the C layer thickness, the carbidization is complete at 673 or 773 K. Up to this temperature, the annealing temperature determines the total amount of Be_2C formed. The Be_2C layers formed on top of the Be substrates are stable at elevated temperature, no dissolution of carbon in the Be bulk is observed. The surface stoichiometry after annealing above 773 K corresponds to the Be_2C stoichiometry. The concentration-dependent diffusion coefficient for Be–C interdiffusion is influenced by a BeO layer at the interface. The interfacial oxide increases the Be–C interdiffusion coefficient approximately by a factor of 2. At low Be concentrations, it is in the order of $1 \cdot 10^{-20}$ m^2 s^{-1}, and $5 \cdot 10^{-20}$ m^2 s^{-1} with

an oxide interface layer. Therefore, an intuitively expected diffusion barrier function of an oxide layer at the C–Be interface is not observed.

Carbon layers on Ti and Si The temperature-dependent reaction and diffusion processes of carbon films on Ti and Si surfaces are studied both since Ti and Si are used in current fusion devices, and as a reference in comparison to the materials above [90]$^{\otimes}$, [84]$^{\otimes}$. Similar to the other metals observed so far, carbon films on titanium show already after deposition at 300 K a well-separated peak of carbide besides the elemental carbon signals. The peak is located at a binding energy of 281.7 eV. The carbide is also detected in the Ti $2p_{3/2}$ signal with a binding energy of 454.6 eV, at 300 K only as a shoulder and as a separate peak after annealing. Upon annealing, the carbide amount increases and above 570 K the total carbon intensity drops. This is similar to the behavior on the other transition metals discussed above. However, in contrast to tungsten, which also forms carbides in an exothermal reaction, the intensity continuously drops with annealing temperature and no plateau is observed for the range in which subcarbides are present. This additional signal in the C 1*s* region is observed above an annealing temperature of 570 K, when an additional peak at 282.4 eV is necessary to reproduce the measured data by peak fitting procedures. As discussed above, this peak is attributed to titanium subcarbides. In the Ti $2p_{3/2}$ signal, the subcarbides cannot be detected due to the close proximity of the metallic and carbidic signals.

Finally, the reactions of carbon films on Si substrates are investigated by depositing monolayer to nm thick carbon films and annealing. After 300 K deposition, also on Si a peak at lower binding energies in the C 1*s* region at 282.8 eV can be detected besides the elemental carbon signals. In the substrate Si 2*p* signal, this carbide cannot be detected, because the Si 2*p* doublet is not resolved in the XPS spectra. Small additional carbide amounts are formed already on annealing to 770 K, whereas the appreciable additional carbide is formed after 970 K annealing and above. At this temperature, a noticeable decrease in the carbon intensity is observed. For thin (0.3 nm) carbon layers, the carbide peak in the Si 2*p* signal is detected at 101.3 eV. Already after 1270 K annealing, the Si:C intensities reach a close to 1:1 ratio. It changes only very little during further annealing steps up to 1683 K.

This stability of the formed carbide layer on Si is comparable to the behavior

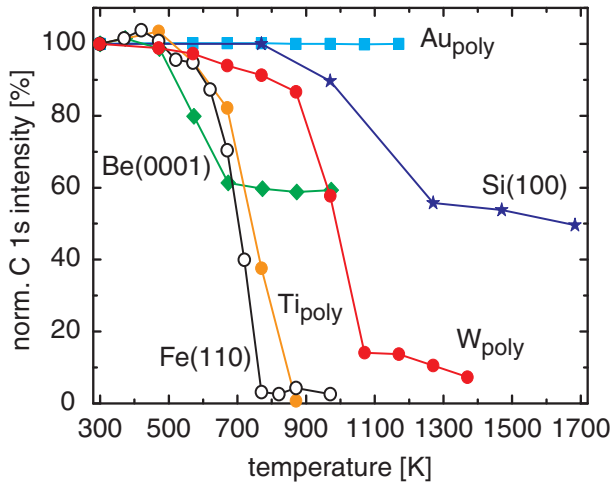

Figure 3.1: Changes in the C 1*s* intensity during annealing of thin C films on various substrates. The initial C 1*s* intensities are normalized to 100%.

of carbide layers on beryllium and different to the carbon dissolution observed on the transition metals. In Fig. 3.1 the total C 1*s* intensities of carbon films in the nm thickness range on various substrates are compared after annealing. The layers are thin enough to initially detect all carbon by XPS. As a comparison with an unreactive substrate, a carbon film on polycrystalline gold is shown. Two processes dominate the interactions of elemental carbon films on substrates: carbide formation and carbon diffusion into the bulk. Besides them, the ordering of disordered graphitic carbon into graphite is observed. Before carbon diffusion sets in, carbide is only present at the interface between carbon layer and the substrate. This interfacial carbide exists even if the carbide formation reaction is endothermic, as in the cases of Fe and Ni. In the cases of Be and Si, the carbon intensity decrease stops after compound formation. This can be understood by the ionic and covalent bond character of the respective carbides. These bonds make an extended bulk diffusion of the carbon atoms impossible, since either the electrostatic forces between the lattice constituents have to be overcome or the direct covalent bonds have to be broken. This is different to the metallic carbides where the carbon atoms are located in different sites within the metal lattice. Depending on the stoichiometry, equivalent sites are unoccupied and no direct bonds have to be broken for carbon migrating from

site to site. In Ti, the octahedral sites within the metal lattice are large enough in order to incorporate carbon. Therefore, it is not necessary to rearrange the metal lattice during carbide formation. This can explain why in the case of Ti no plateau is visible in the temperature range where carbides are present and that carbon is (almost) completely lost from the surface by bulk diffusion. In the case of Ni, Fe, and W, a rearrangement of the metal lattice is necessary upon carbide formation, creating a new phase, although the overall bond character is still metallic. Strong bulk diffusion is also observed. However, in particular in the case of W(1 1 1), the carbide phases show a constant carbon concentration during an extended temperature window.

3.2 Ion-induced reactions

As an alternative to temperature, energy stimulating solid state reactions can be provided to the system by bombardment with kinetic particles. The kinetic energy can be provided by ions which are chemically inert (noble gas ions like He or Ar), and with ions which both provide their kinetic energy to the system and can themselves react with the target elements. The latter is investigated for deuterium ions (chemical reactions with carbon, both as a surface layer or as substrate) and carbon-containing ionic species (C^+, CO^+). Surface chemistry induced by inert ions is investigated for C–Ti systems both for C layers on Ti and vice versa by Ar^+ and He^+ bombardment at several ion energies [115]$^{\otimes}$. The Ar^+ bombardment of C layers on titanium is further compared to C layers on tungsten [87]$^{\otimes}$. The evolution of the surface chemistry of C films on Ti by bombardment with D^+ is investigated by XPS and compared to D^+ bombardment of HOPG [116]$^{\otimes}$. Erosion of thin carbon layers by D^+ at 300 K as a function of the substrate atomic number is studied for the substrate metals Be, Ti, and Ta [117]$^{\otimes}$. Finally, the reactive processes of C-containing ions with beryllium are studied by C^+ and CO^+ implantation ([118]$^{\otimes}$ and [119]$^{\otimes}$).

The influence of ion implantation and sputtering on the chemistry of Ti/C and C/Ti layer systems is demonstrated by XPS measurements during the deposition of the respective layer, and after several ion implantation fluences [115]$^{\otimes}$. Deposition of Ti on a pyrolytic graphite surface at 300 K leads to the formation of a carbide layer at the interface, similar to the reaction when carbon is deposited on Ti. Increased Ti layer thicknesses obscure the TiC peak. A similar interface

reaction has also been observed on diamond [120]. At a Ti layer thickness of 18 nm on pyrolytic graphite, still a small C 1*s* signal can be detected, which is assigned to carbon species in the first layer. This film is bombarded with Ar^+ at 1 keV, sputtering the Ti film. Already after a small Ar^+ fluence of $1 \cdot 10^{16}$ cm^{-2}, a small carbide peak is detected, which is caused by the ion beam. At the interface, a maximum carbide fraction of 23 at% carbide and 32 at% graphite are detected. Further Ar^+ implantation leads to a broadening of the interface due to ion beam mixing and a continuous sputtering of the Ti film. The Ti film, which during the deposition didn't show any carbide except at the Ti–C interface, developed carbidic carbon concentration during the sputter depth profiling. The ion energy influences the amount of carbide formed during the sputtering process. For Ar^+ with 4 keV, the maximum carbide fraction at the interface is 40 at% and only approx. 10 at% elemental carbon. The influence of the ion species on the carbide formation is compared for He^+ and Ar^+ between 500 eV and 4 keV primary energies. For He^+, mean penetration depths are larger, therefore the energy deposited at the interface per incoming ion is lower. However, sputtering yields are lower for He^+ compared to Ar^+, therefore higher fluences are needed for the same erosion. Thus, the energy deposited in the surface layer by nuclear stopping by the two ionic species during sputtering is equal. Since no difference in the carbide/total carbon ratios are observed between He^+ and Ar^+, it can be concluded that the carbide formation due to ion beam mixing is dominated by the nuclear energy loss. Electronic energy loss mechanisms do not play a significant role.

The ion beam influence is also studied in a similar way for carbon deposited on titanium at 300 K. As described above, TiC is formed at the interface. For small coverages, intensity at the TiC binding energy at 281.7 eV is measured. In addition, signal intensity in between the TiC and the elemental C peaks demonstrates that also Ti subcarbides are formed to a small extend. After deposition of 3.7 nm C on Ti, the C 1*s* signal is dominated by elemental carbon, TiC is still visible as a small peak. Already after an Ar^+ fluence of $5 \cdot 10^{15}$ cm^{-2}, the TiC peak dominates the C 1*s* spectrum. Clearly, a second carbide peak develops at 282.4 eV, which is assigned to subcarbides. With increasing Ar^+ fluence, all carbon is converted into TiC and only one peak remains in the C 1*s* spectrum at the TiC binding energy position. A similar energy-dependent effect as for the Ti/C measurements is observed with 4 keV Ar^+. Although ion beam

mixing usually leads to a disordered interface and peaks widths wider than for well-ordered systems, the C 1*s* carbide line width after carbide formation is very small with a FWHM of 0.6 eV. In a similar experiment with C layers on tungsten, much wider carbide line widths are observed. This is attributed to the locally released reaction enthalpy during carbide formation. In the case of TiC, this enthalpy is 1.87 eV per molecule, whereas for W_2C and WC is is 0.23 eV and 0.40 eV, respectively [121]. This locally dissipated energy can lead to an ordering in the solid, counterbalancing the disorder introduced by the ion bombardment.

In a next series of experiments, the ion species is changed from inert noble gas ions to reactive species. Deuterium is selected as an element which not only causes a collision cascade like He^+ or Ar^+, but in addition can undergo chemical reactions with carbon [86]$^{\otimes}$, [87]$^{\otimes}$, [116]$^{\otimes}$. Since the changes in the C 1*s* XPS spectra cannot be resolved unambiguously by peak fitting around the elemental peak, the changes in the spectra with increased implantation fluences are followed by difference spectra between the respective treatment step and the initial spectrum. Thus, even small changes in intensities are visible. Deuterium implantation series into carbon layers on titanium are compared to deuterium as well as Ar^+ implantation into HOPG under identical experimental conditions. For both D^+ and Ar^+ implantation into HOPG, three peaks in the difference spectra are observed. While for Ar^+ the respective binding energy positions are constant during the fluence series, for D^+ only the peaks at 284.2 eV and the weak feature at 284.9 eV stay at constant binding energies. A third peak appears for low fluences at 283.9 eV and shifts during the implantation to 283.7 eV. After a final annealing step, intensity at this binding energy increases, but remains at the same position. Also For D^+ bombardment of C layers on titanium, a shift in the elemental C 1*s* peak is observed at low D^+ fluences. In addition to the elemental carbon signal, the peak associated with TiC at the carbon/metal interface is measured. This peak is fixed in binding energy during the D^+ bombardment. Compared to the changes at the high binding energy side of the elemental signal (above 285 eV) on HOPG, no changes in intensity are observed here for the C films. During D^+ bombardment, the elemental carbon is continuously converted into carbidic C, while also erosion of carbon takes place. The carbon coverage shows an exponential decay until all elemental carbon disappears from the C 1*s* binding energy region. Above this

fluence (which varies with the initial carbon layer thickness) the carbon intensity decreases at a linear rate. The linear decrease is compatible with sputtering yields calculated by the TRIDYN/SDTRIM.SP Monte Carlo codes [122–124]. The higher exponential erosion rate can be interpreted by an erosion mechanism which involves the whole carbon layer simultaneously and can be interpreted with a chemical erosion mechanism, similar to the ion-induced desorption of an adsorbed monolayer [125]. This exponential decrease of the carbon amount is not observed if inert Ar^+ ions are used as projectiles. In this case, a linear decrease of the carbon layer thickness is observed, as expected for a purely physical sputtering process.

Kinematic ion-solid interactions, respectively the collision cascades, are determined by the atomic mass of the atoms in the solid. The enhanced erosion of carbon films on titanium is compared to substrates with clearly higher (tantalum) and a lower (beryllium) atomic masses [117]$^{\otimes}$. Three mechanisms attribute to the reduction of the elemental XPS carbon signal during D^+ bombardment. Ion beam mixing was shown to increase the carbide fraction in the C 1*s* signal by mixing carbon and metal atoms. Physical sputtering leads to erosion of surface atoms by kinematic processes which transfer sufficient energy and momentum to surface atoms that they can overcome the surface binding energy. These two processes can be simulated by Monte Carlo codes based on the binary collision approximation, like TRIDYN/SDTRIM.SP. A third mechanism reducing the elemental carbon layer thickness is a chemical erosion process. Therefore, deviations between TRIDYN simulations and experimental data can be attributed to chemical erosion processes. The analysis of the D^+ implantation experiments on carbon layers on Be, Ti, and Ta allows a detailed characterization of the importance of these three erosion processes as a function of the substrate atomic mass. Ion beam mixing increases from Ta to Be due to the differences in the kinematic collision cascades. Additional carbide formed by ion beam mixing leads to a maximum carbide layer thickness on Ta in the order of one monolayer, whereas in Be this thickness exceeds 5 monolayers. Differences in the chemical erosion of carbon films on the three substrates are influenced by the number of deuterium atoms stopped within the carbon layer. Enhanced carbon erosion by chemical sputtering processes is only observed on Ta and Ti. For Be, this is not the case, because the amount of D stopped within the C layer is not enhanced, and also because forward scattering of carbon into beryllium is very prominent

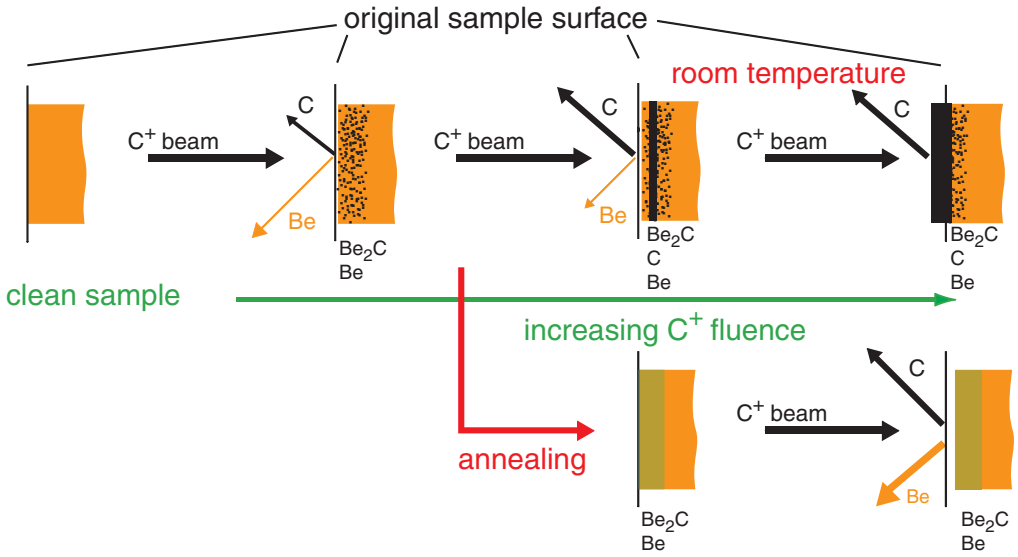

Figure 3.2: Processes during C^+ implantation in Be at 300 K and annealing. The implantation leads to Be_2C formation and buildup of an elemental carbon layer for extended fluences. Annealing of this C layer on Be leads to the formation of a Be_2C surface layer.

for this light substrate.

In a series of experiments, the implantation of carbon-containing ions into beryllium surfaces is studied as an example for reactive systems where one of the reaction components is introduced as ionic species instead of by evaporation and subsequent annealing [87]$^{\otimes}$, [118]$^{\otimes}$, [119]$^{\otimes}$. In contrast to 300 K deposition experiments, ions carry kinetic energy which leads to deposition of the ionic species not at the surface, but (depending on the kinetic energy) in surface-near bulk positions. Moreover, the excess kinetic energy can trigger chemical reactions and initiate compound formation at temperatures much lower than required for reactions of vapor-deposited layers at surfaces. The kinematic interactions of energetic particles with solids can be simulated with Monte Carlo codes like TRIDYN/SDTRIM.SP, as described already above. Chemical phase formations are not included in this simulation, therefore deviations between simulation and experiment can be attributed to reactive processes. The experiments are carried out by preparing C^+ and CO^+ from CO or CO_2 gas in an electron impact ion source and selecting the respective ionic species by their mass in a bending magnet. The experiments involving CO^+ are described in

section 6, here the binary system $C^+ \rightarrow$ Be is summarized. The C^+ implantation is performed with ion energies of 3 and 5 keV. The C^+ implantation leads to carbon accumulation in the beryllium substrate. The carbon amounts measured by RBS are well reproduced by kinematic simulations. Initially, C is deposited at a depth of 20 nm for 5 keV C^+. XPS can therefore detect carbon only above a C fluence of approximately $9 \cdot 10^{16}$ cm^{-2}. All carbon detected up to a C fluence of $4.2 \cdot 10^{17}$ cm^{-2} is in the carbidic state. Above this fluence, the elemental carbon inventory increases. Since the self sputtering yield under the experimental conditions (angle of incidence, implantation energy) is below unity, carbon accumulates further in the sample. As predicted by the TRIDYN simulations, a carbon layer builds up continuously during the C^+ implantation. XPS reveals that finally elemental carbon is the only species in this carbon layer. The Be_2C formed during ion impact at 300 K is restricted to a layer at the former Be surface. This carbon layer, however, can be converted completely into Be_2C upon annealing, as was described in section 3.1 for C films deposited from the vapor phase on Be. The processes are summarized in the schematic diagram shown in Fig. 3.2. The C^+ implantation into beryllium can be simulated well by TRIDYN, because in this binary system, no volatile species are formed. Moreover, also bulk diffusion of C into Be plays no dominant role after completion of a Be_2C layer after annealing. This is different to the ternary Be–C–O system, studied by CO^+ implantation into Be, as described in section 6. There, already at 300 K implantation, a deposition-erosion equilibrium is established which limits the C and O inventory in the Be substrate, leading already at 300 K to a continuous erosion of the material.

4 Atomic oxygen

Due to the high energies of the particles in a fusion plasma, impurity gas molecules are dissociated and reach the wall surfaces as atomic species. Their kinetic energies strongly depend on their origin within the plasma and the position of neutralization. For impurity atoms like oxygen the plasma edge acts as a source. Therefore, low kinetic energies of impurity species are of importance, in addition to particles with keV energies. These low energies occur in particular in regions of high plasma densities like the divertor. For oxygen atoms, their interaction with first wall materials is therefore an important reaction path. For the oxygen surface reactions, a strong difference in reactivity between molecular and atomic species can be expected. Other application fields where atomic oxygen is of importance are space vehicles operating in low-Earth-orbits (LEO) between 200 and 900 km altitude (this is the operational range for the NASA space shuttles, the International Space Station operates at an altitude of approx. 350 km). Here, the atmosphere consists predominantly of oxygen atoms and nitrogen molecules and their interaction with the surface of space vehicles acts as a source of erosion during space missions. Depending on the velocity of the space vehicle, the oxygen atoms impinge at the surface with energies up to a few eV with fluxes between 10^{14} to 10^{15} cm^{-2} s^{-1} [126].

The investigations described in [127]$^{\otimes}$ comprise the first attempt to study the interaction of oxygen atoms with the first wall materials beryllium and tungsten. For the confirmation of oxygen atom production from the microwave discharge, a clean polycrystalline gold surface is used. Molecular oxygen adsorbs at room temperature only if surface impurities like Ca or Si are present [128, 129]. On a clean gold surface, oxygen can only adsorb as atomic species [130]. The sticking coefficient for atomic oxygen on gold is determined from the dissociation degree, the measured pressures and the temperatures. Kinetic gas theory yields the number of impinging atoms on the surface and the oxygen coverage is determined from the attenuation of the XPS Au $4f$ signal intensity. The value for the initial sticking coefficient is $5 \cdot 10^{-3}$. A surprising result from the adsorption

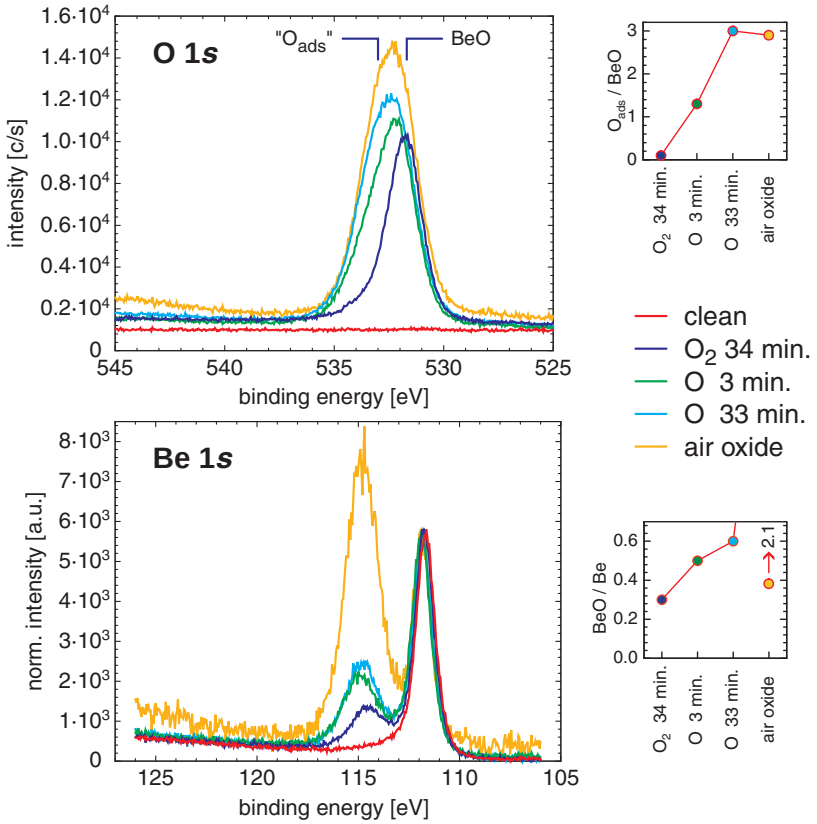

Figure 4.1: XPS spectra in the O 1*s* and Be 1*s* regions for clean beryllium and oxidation experiments with molecular and atomic oxygen, and corresponding intensity ratios.

experiments on gold was the observation that the oxygen atoms adsorbed also on the Au surface in a geometry where it pointed away from the quartz tube. The oxygen atoms have to undergo several collisions with the chamber walls before they can hit the sample surface. This supports the observation of low oxygen atom sticking coefficients qualitatively. Adsorption from other oxygen containing species could be excluded.

The beryllium surface reacts both with atomic and molecular oxygen at room temperature. However, the reactivity of the atomic species is much higher. In Fig. 4.1 the O 1*s* and Be 1*s* photoelectron peaks are compared for the various exposure conditions. In the O 1*s* region, the raw data are plotted after the exposures. The O 1*s* peak after the exposure to molecular oxygen has the smallest

FWHM for all conditions. After exposure to atomic oxygen and also after air-exposure of beryllium, the O 1*s* signals are broader. Using two Gauss-Lorentz peaks at 531.7 and 532.7 eV and deconvoluting the data, the respective widths are 1.88 and 2.54 eV. In Fig. 4.1, the peaks are labeled as BeO and "O_{ads}". The small insert shows the intensity ratios of these deconvolution signals for the experimental conditions. Oxidation of the surface by molecular oxygen (microwave discharge off) results in the narrow O 1*s* peak at the BeO position. Dosing O_{at} for only 3 min results in a more intense O 1*s* peak which can be deconvoluted already in two contributions. An increase of oxidation time to 33 min leads to an only slight increase of overall O 1*s* intensity. The "O_{ads}" to BeO peak ration is similar to that of the air oxide. From these experiments, the two peaks are interpreted as originating from the BeO and an additional species adsorbed at the surface, labeled "O_{ads}". The strongly enhanced oxidation rate of O_{at} compared to O_2 is also visible in the Be 1*s* region, also shown in Fig. 4.1. The spectra are normalized to the metallic Be 1*s* peak. Molecular oxygen dosed for 34 min leads to a BeO/Be intensity ratio of approx. 1/3, whereas only 3 min O_{at} increases it to approx. 1/2. An O_{at} exposure of 33 min only increases this ratio to 0.6, demonstrating a decrease in the oxidation rate with increasing oxide layer thickness. This is in agreement with the results from the Shamir group [131–138] who also find fast oxidation rates for the first 2–3 ML only. Adsorption of water and BeO formation has been studied by DFT [139]. Enhanced oxidation of beryllium has also been observed under simultaneous deuterium ion bombardment with oxygen background gas [140, 141]. Beryllium oxidation under water vapor exposure was studied in several papers, aiming at fusion applications [142–150].

The experiments with tungsten surfaces are carried out at 100 nm films deposited on Si substrates. Before exposure to atomic or molecular oxygen, the surfaces are sputter cleaned and free of oxygen, as demonstrated by XPS measurements. As shown in [127]$^{\otimes}$, the exposure of the cleaned W surfaces to both O_{at} and O_2 at room temperature leads not to a re-appearance of tungsten oxide signals in the W 4*f* binding energy region. However, since the measurements at the W surfaces are performed with monochromatic Al Kα radiation, a broadening of the W $4f_{7/2}$ peak by 0.1 eV is detected, see Fig. 4.2. This broadening occurs both for O_{at} and O_2 dosing and is attributed to the formation of a W–O surface oxide, as observed already for O_2 chemisorption on several W

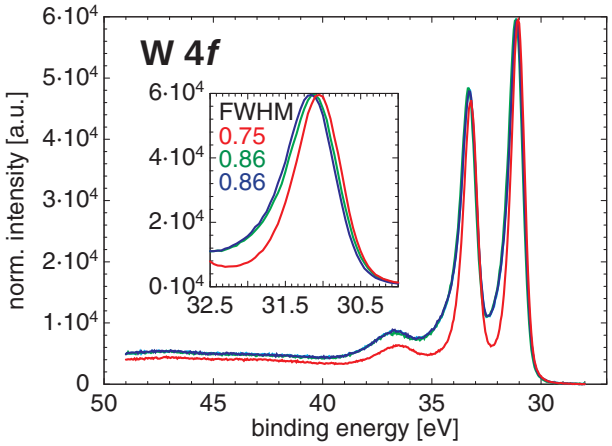

Figure 4.2: XPS spectra in the W 4f region for clean tungsten (red) and after exposure to molecular (green) and atomic (blue) oxygen.

surfaces [151–157].

In summary, both beryllium and tungsten surfaces react with atomic oxygen at room temperature. However, the two metals react very differently. Beryllium oxidizes readily with O_2 and O_{at} and the initial reaction rate for O_{at} is more than an order of magnitude higher than for the molecular species. For tungsten, no oxide layer formation is observed. Oxygen only chemisorbs in the first monolayer and forms a monolayer surface oxide. No difference in the chemisorption behavior between O_{at} and O_2 can be detected on polycrystalline tungsten films.

5 Beryllium–tungsten alloy formation

The surface chemical and physical interactions between beryllium and tungsten are of importance for the performance of the ITER first wall due to anticipated different properties of the formed alloys compared to the pure substances. In the literature, the binary phase diagram of the Be–W system is available, predicting the formation of several alloy phases. Fig. 5.1 shows the bulk phase diagram, adapted from [79], where the three alloy phases Be_2W, $Be_{12}W$, and $Be_{22}W$ are visible. All three compositions show small phase widths and are ordered alloys. If the formation of the intermetallic Be–W compounds occurs during the operation of ITER, the consequence for tungsten parts is a strong reduction of the melting point, depending on the final composition. Early studies of the Be–W system showed the alloy formation from powder precursors [158–160]. The few existing surface science experiments in the Be–W system deal with work function measurements of Be on tungsten [161–163]. Further publications addressed mainly the surface structure of Be adsorbed on tungsten single crystals and desorption processes. Auger electron spectroscopy was used, with the focus on structural properties. Alloy formation as a possible surface process was discussed merely for the highest coverages investigated on the W(211) surface (8 ML) [164, 165].

In several series of experiments [166]$^{\otimes}$, [167]$^{\otimes}$, [168]$^{\otimes}$, [169]$^{\otimes}$ and theoretical approaches [170, 171], Be–W interactions were studied. Both, Be on W, and the reverse system W on Be, were studied by layer deposition and subsequent stepwise annealing. Be is deposited *in situ* from the vapor phase with thicknesses up to a few nm on clean polycrystalline W substrates and sequentially annealed up to 1070 K and investigated by XPS [166]$^{\otimes}$, [167]$^{\otimes}$ and in collaborations with the Doerner group at UCSD [172]. In collaborative activities, the formation of alloys in the Be–W system was also studied by DFT ab initio calculations and compared to experimental results [170, 171].

Due to the increased importance of possible surface alloy formations and their consequences on the reduction of the melting point of tungsten parts at the first

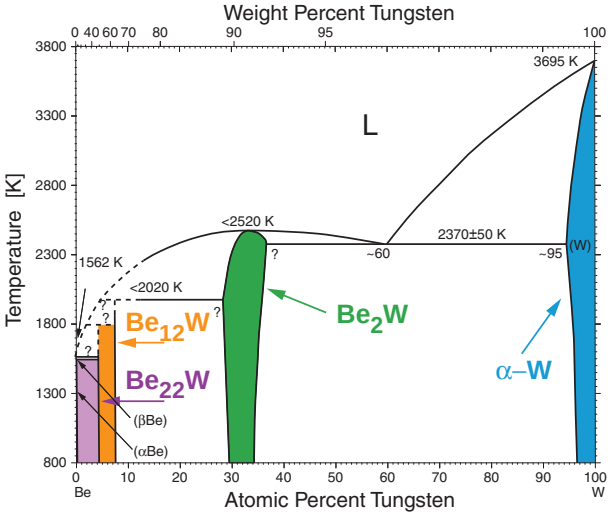

Figure 5.1: Binary phase diagram in the Be–W system, adapted from [79].

wall of ITER, the first dedicated study on the surface alloy focused on Be layers deposited on polycrystalline tungsten substrates at 300 K [166]$^{\otimes}$. Deposition of Be from the vapor phase is critical and a contamination of the vacuum system must be avoided in order not to release BeO dust to the environment after opening the vacuum chambers. Moreover, since Be is very reactive, a very good UHV is necessary. As evaporation material, high-purity (99.999 %) Be (HEK GmbH) is used. A commercial evaporator (EFM3, Omicron) with a water-cooled shroud and a closed volume is suitable to produce Be films on a sample surface area of approx. 10 mm diameter, without contaminating other chamber parts with deposited Be.

The reverse system, W on polycrystalline Be, is studied by tungsten magnetron deposition of a 200 nm layer at 300 K, sequential annealing and XPS up to 1070 K under UHV conditions, and analysis by RBS after transfer through air. After the final annealing step, a sputter depth profile with XPS analysis is performed [168]$^{\otimes}$. Additional structural investigations were performed for both the Be/W and W/Be systems by X-ray diffraction (XRD) [169]$^{\otimes}$, [173].

The formation of Be–W alloys can be directly observed by XPS, e.g. in the shift of the Be 1*s* core level [170]. Both XPS and RBS allow a quantitative analysis of the reactions and are sensitive to different depths: XPS probes the first few nm, whereas RBS probes several 100 nm to a few μm, depending on

the used projectile particle and primary energy. Together with sputtering of the surface by argon ions, XPS enables a chemically resolved depth profiling of the surface. Using these techniques, the behavior of the Be-W system in the different experimental approaches was studied. For the case of thin Be layers deposited on tungsten at 300 K, a surface alloying restricted to the interface monolayers is observed. Additionally deposited Be is in the metallic state. This interface alloy formation is visible in both the core level shift of the Be 1*s* and of the W 4*f* lines. Also the shape of the valence band spectra changes in a characteristic way with alloy formation and exhibits a small intensity shift towards the Fermi edge [167]$^{\otimes}$. Above 670 K, the alloy peak fractions increase, indicating the formation of additional alloy phase. The stoichiometry Be_2W for the alloy is determined from the alloy fractions in the Be 1*s* and the W 4*f* intensities. At the same time, the overall Be intensity decreases with increasing annealing temperature. The diffusion of Be beyond the surface alloy layer deeper into the W substrate is excluded according to sputter depth profiles after the annealing experiments. No Be intensity is detected beyond a depth determined by the ion-beam induced mixing. The Be sputtering depth profile is confirmed by a Monte Carlo simulation using TRIDYN. Long-term ($\sim$ 3 h) annealing experiments of thin Be layers with different initial thicknesses show that, regardless of the initial Be thickness, the final alloy layer always has an equivalent Be thickness of $\sim$ 1.2 nm. Moreover, the loss of the excess Be takes place already during the temperature ramp-up. Only small additional increases in alloy amounts are observed during the annealing at constant temperature [166]$^{\otimes}$, [168]$^{\otimes}$. From this observation, together with the sputter depth profiles, it is concluded that the Be_2W alloy formation competes with Be sublimation from the surface. The Be_2W alloying reaction cannot act as an efficient driving force for keeping the Be in the solid phase.

In the reverse system, W deposited on Be, the formation of a Be–W alloy starts only above 970 K, as determined from RBS spectra. However, this technique is not sensitive enough to exclude the possibility of an interface alloy formation in the order of a monolayer, as observed in the Be/W experiments. The stoichiometry of the alloy observed at $T > 970$ K is $Be_{12}W$. This alloy also exhibits characteristic core level shifts in the Be 1*s* and W 4*f* lines. The formation of a stable $Be_{12}W$ alloy layer on the Be substrate from a W layer, without a typical diffusion tail into he substrate, indicates that the system has

reached an energetically favorable situation. From the temporal evolution of the alloy layer thickness a diffusion coefficient of $1.6 \cdot 10^{-13}$ cm^2 s^{-1} at 1070 K is determined [168]$^{\otimes}$. For 1023 and 1123 K, additional diffusion coefficients for the Be–W interdiffusion are available: $4.3 \cdot 10^{-15}$ cm^2 s^{-1} and $5.8 \cdot 10^{-13}$ cm^2 s^{-1}, respectively [173].

A third class of experiments involves Be impinging continuously at non-thermal energies on W surfaces, as a seeded impurity in a deuterium plasma. Non-thermal interactions of Be as a plasma impurity were performed with polycrystalline W surfaces at elevated temperatures between 1023 and 1260 K [168]$^{\otimes}$, [173]. The kinetic energy of the Be particles from the plasma is $\sim$ 60 eV with an applied bias voltage of -75 V, and $\sim$ 10 eV without bias voltage. The composition of the final surface is investigated by AES, XPS, and WDX. If the kinetic energy of the Be particles is high enough, sputtering of the surface must be considered. For lower Be energies ($\sim$ 10 eV), the formation of Be alloys at the surface is observed for temperatures between 1070 and 1150 K [173]. At a temperature of 1260 K, Be is found in depths well above 1 μm with a concentration of 10%, although the concentration in the deuterium plasma was below 0.5%. As determined by XPS, Be is present both in the metallic and alloyed states. However, the Be 1*s* core level shift allows no decision between Be_2W and $Be_{12}W$. From the experimental conditions, also the question whether the Be is transported into these depths by diffusion or whether a compound surface layer has been deposited by the plasma-surface interaction processes, cannot be decided. Nevertheless, Be is accumulated to a 10% level in the sample from a minor plasma impurity [168]$^{\otimes}$.

As a consequence for the operation of ITER with Be in the main chamber and W in the divertor region, only a very thin nm layer of Be_2W alloy is expected to form during operation. According to the divertor principle, material transport occurs mainly from the main chamber to the divertor and not opposite. Therefore, the formation of W layers on the Be main chamber walls is improbable, whereas Be transport into the divertor is possible. Below $\approx$ 1000 K, Be is deposited and forms a metallic layer. At higher temperatures, Be both sublimates and forms the 1–2 nm Be_2W layer, which can be safely assumed not to change the overall physical properties of the tungsten divertor surface, since no bulk alloy formation is expected under these conditions. However, if a Be deposition on tungsten occurs at high surface temperatures for extended times, an alloying

can be expected.

6 Ternary surface reactions

The next step towards the understanding of surface reactions under the complex situation at the first wall of a fusion device with multiple first wall materials is the extension of the investigations to ternary systems. This comprises also surface reactions involving plasma impurities like oxygen. In this chapter, however, hydrogen as a reactive component is not considered. When the number of reactants is increased to three, not only can additional chemical reactions occur, but also new chemical phases can be formed. In cases where volatile species are produced, the erosion behavior of the mixed material at the first wall is changed dramatically, as is shown in the experiments where CO^+ ions are implanted into beryllium. Overall, the complexity of the systems under investigation increases by addressing a third chemical component. The systems Be–C–O [118]$^{\otimes}$, [119]$^{\otimes}$, C–O–W [174]$^{\otimes}$, Be–C–W [71]$^{\otimes}$, and Be–O–W [175] were addressed in several series of experiments.

The ternary system Be–C–O is investigated in experiments where the C and O species are implanted into Be substrates at 300 K by CO^+ ions at primary energies of 3, 5, and 12 keV. Implantation of CO^+ simulates the simultaneous implantation of C and O, since the molecular ion dissociates readily upon impact at the Be surface. The implantation of CO^+ can be compared to the implantation of C^+ described in section 3.2, since the difference is the increased number of components only. Polycrystalline Be substrates are implanted by CO^+ at all three different energies and the surface composition is analyzed with RBS as a function of the implantation fluence [118]$^{\otimes}$. The overall weight loss due to erosion processes is measured on polycrystalline beryllium for doses up to 0.9 C. Finally, the surface chemical states are characterized using XPS for 3 keV CO^+ implantations in single crystalline Be [119]$^{\otimes}$.

The ternary Be–C–O system is characterized by a constant C and O inventory in the implantation zone after an initial fluence region where all impinging CO^+ are accumulated in the beryllium. The transition from accumulation to a deposition-erosion equilibrium occurs at CO^+ fluences between $1 \cdot 10^{17}$ cm^{-2}

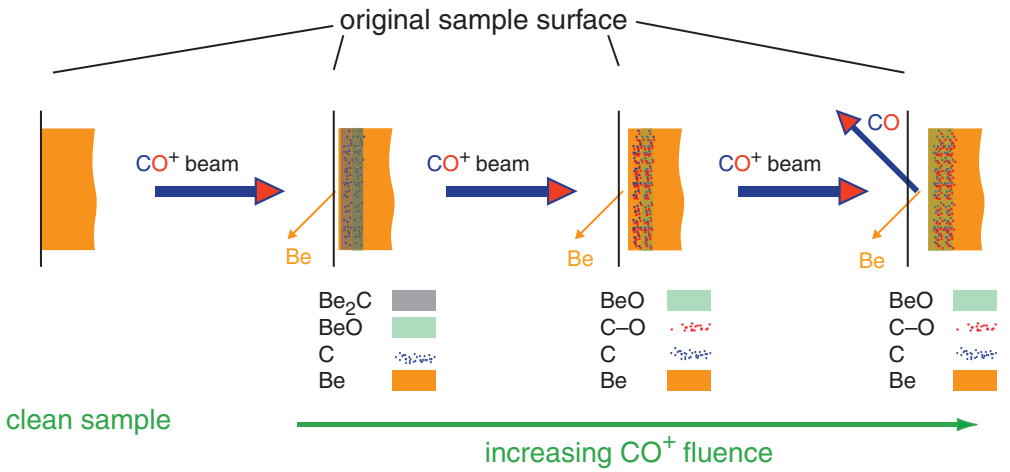

Figure 6.1: Evolution of the surface composition of beryllium at 300 K during CO^+ implantation. The equilibrium is characterized by a continuous Be erosion and a constant C and O inventory.

and $4 \cdot 10^{17}$ cm^{-2} for primary energies between 3 and 12 keV. At higher fluences, the C and O inventories in the beryllium are constant and their absolute amounts are correlated to the CO^+ primary energy: Higher energies result in a deeper and wider implantation profile and therefore to larger C and O amounts at equilibrium. The C/O ratio depends on the ion energy and approaches unity for higher ion energies. This is explained by the vanishing difference in the implantation depth for O and C, calculated by TRIM.SP Monte Carlo calculations. XPS measurements during the 3 keV CO^+ implantation experiment show that beryllium bound in Be_2C is only present during this fluence region. This is detected in both the C 1*s* and Be 1*s* regions, whereas the initial implantation beyond the beryllium surface is proven by the delayed detection of carbon in the fluence series. During the deposition-erosion equilibrium, all Be in the compound layer zone is bound in BeO, whereas oxygen is also chemically bound to carbon. This is shown in the XPS C 1*s* region where intensity at binding energies in the 286–290 eV range is detected. The majority of the carbon (seen in the C 1*s* signal) is present in elementary form. The formation of the Be–C–O mixed layer is summarized graphically in Fig. 6.1.

The ternary system C–O–W is investigated in experiments where carbon films are deposited on tungsten oxides of different stoichiometry [174]$^{\otimes}$. During

annealing steps between 300 K and 1670 K the surface composition is analyzed by XPS. In contrast to small oxygen contaminations present as adsorbate or in the background atmosphere (up to $1 \cdot 10^{-7}$ hPa O_2), under which conditions the reaction and diffusion behavior is equal to that of pure binary W–C systems (see section 3.1), interlayers of W(IV) and W(VI) oxides change the reaction behavior between carbon and tungsten. This is due to the fact that at 300 K oxygen from the gas phase adsorbs or reacts only to two-dimensional chemisorption or monolayer oxides [176–178]. Higher oxygen coverages can only be achieved at elevated temperatures or higher O_2 partial pressures [179].

The tungsten oxide layers are produced under atmospheric pressures in a furnace with different oxygen partial pressures, and are subsequently annealed in the UHV system. More details are given below in the discussion of the Be–O–W ternary system. XPS measurements of the W $4f$ region demonstrate that in principle WO_2 and WO_3 are prepared: The W $4f_{7/2}$ peak positions correspond with the binding energies for the respective oxides in the literature [180]. However, due to the annealing steps in UHV and due to the fact that the metallic tungsten substrates make a quantitative stoichiometry determination difficult, the resulting surface compositions are $WO_{\approx 2.1}$ for the W(VI) oxide and $WO_{<2}$ for the W(IV) oxide. On both oxide layers on the tungsten substrates finally a carbon layer of approx. 1 nm thickness is deposited in UHV.

The W(VI) oxide interlayer is gradually reduced during annealing steps up to 970 K, visible in the appearance and a shift of a W $4f$ doublet. However, the overall composition of the surface is unchanged. After 1170 K, this changes significantly: The carbon signal disappears completely in the photoelectron spectra and the W $4f_{7/2}$ maximum shifts to the position of metallic tungsten at 31.4 eV. During the annealing steps, no indication for formation of tungsten carbides is detected. Between 1170 K and 1670 K, the oxygen amount decreases until a final state is reached which is equivalent to the adsorption state of oxygen on pure tungsten. A two-stage mechanism proposed by Dean et al. [181, 182] for the reduction of higher tungsten oxides with C via WO_2 and W under the formation of CO and CO_2 is partly able to explain these observations. However, the loss of oxygen above 1170 K without the presence of carbon needs an additional explanation. A possible loss path could be the dissolution of oxygen in the W bulk.

The carbon film on the W(IV) oxide interlayer is prepared similarly. No

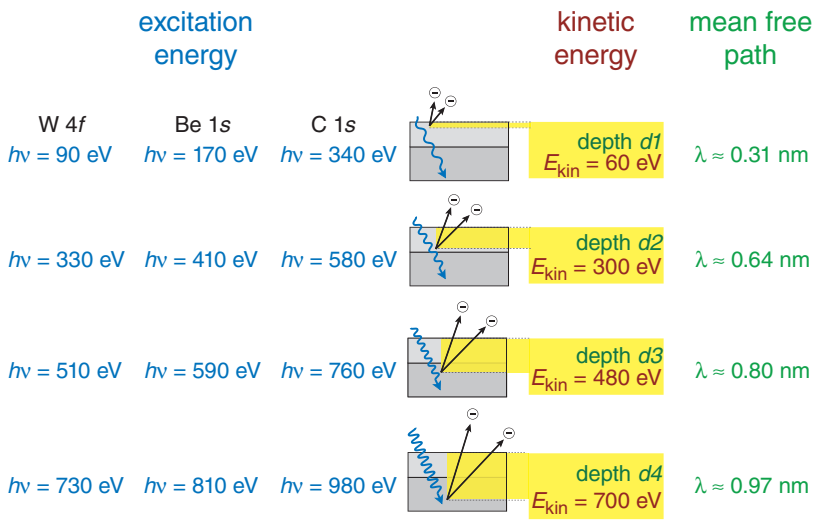

Figure 6.2: Photon energies, related photoelectron kinetic energies, and inelastic electron mean free path lengths according to the Seah-Dench model [185] for the depth-resolved XPS measurements carried out at HZB-BESSY II for the C/Be/W ternary system.

changes are observed in the overall composition, and also the W 4*f* doublet at the W(IV) oxide position at 32.8 eV is unaltered until after the 970 K annealing step. Similar to the W(VI) oxide layer, the carbon amount decreases after annealing to 1170 K, probably also due to CO and CO_2 formation. However, an elemental carbon fraction of 6 at.% remains. The following annealing steps up to 1670 K lead to a decrease of the oxygen concentration, but not to a decease of the remaining carbon. This could be caused by a substitution reaction $WO_2 \longrightarrow WC$ which is observed for the WO_2 reduction with CO [183, 184]. In the spectra, all remaining carbon has reacted to WC, indicated by a shift of the C 1*s* peak to 282.9 eV. Again also in the W(IV) case the final oxygen amount is similar to chemisorbed oxygen on tungsten and to the W(VI) case. The oxidation state of an oxide interlayer between carbon and the tungsten substrate significantly influences the reactions in this ternary system. No tungsten carbides are formed if the oxide interlayer is W(VI) oxide, even in a reduced stoichiometry.

The ternary system Be–C–W constitutes the composition determined by the wall materials foreseen for ITER. A layer system C/Be/W has been selected for first investigations applying depth-resolved chemical analysis at the synchrotron HZB-BESSY II [71]$^{\otimes}$. The carbon layer is applied as top layer, since *in*

situ preparation and sample transfer without air exposure was not possible for this first measurement series. The sample was prepared at IPP Garching, transported to HZB-BESSY II Berlin, and measured in the MUSTANG end station at the RGBL-PGM beam line. Several annealing steps up to 1200 K are applied and the Be 1*s*, C 1*s*, and W 4*f* core levels are measured. The photon energy is selected such that the kinetic energy of the emitted photoelectrons from all three core levels is identical. The inelastic electron mean free path is a function of the electron kinetic energy. This means that electrons from all three core levels originate from the same depth. Four different kinetic energies are selected to cover four information depths [185–192]. Fig. 6.2 summarizes the necessary photon energies for the main Be, C, and W core levels for the four selected photoelectron kinetic energies in order to access four different depth intervals with the respective electron inelastic mean free paths. In order to compare the elemental intensities from the different measurements and to interpret their respective changes for the measured depths and annealing steps, the measured intensities have to be normalized with the respective photoelectron cross section, electron emission angle, primary photon flux, analyzer transmission, asymmetry parameter, and the synchrotron ring current at the time of the specific measurement. After this procedure, the relative signal intensities at different depths can be compared and information on the chemical state in these accessible depth regions is available.

The analysis of the depth-resolved XPS measurements at the C/Be/W system demonstrates that already at 300 K Be diffuses through the carbon layer and forms BeO at the surface with oxygen from the air. Be_2C formation starts at the C/Be interface and the carbide layer expands towards the surface. The Be_2C formation is complete at 850 K. At this temperature, C starts to diffuse into the the bulk and begins to form W_2C. Surface morphology changes (island formation) are observed above 1050 K, even more pronounced at 1200 K. The alloy Be_2W is formed at the Be/W interface already at 300 K, increases at 530 K and decreases again at 850 K. Above this temperature, the amount of W_2C increases up to the last annealing step at 1200 K. The processes at the interfaces and in the bulk of the ternary C/Be/W system during the annealing steps are consistent with the analysis of the respective binary systems [36,89,110,167]. As far as it can be concluded from the first depth-resolved XPS measurements, no new ternary phases in the C–Be–W system are formed during annealing from

300 to 1200 K. Recently, new measurements in this system were performed with samples prepared *in situ* in the LAICA preparation chamber (see chapter 2.3, p. 19) and transferred into the SurICat end station at HZB-BESSY II without air contact [193].

Finally, the **ternary system Be–O–W** has been investigated with respect to temperature-dependent phase formation [175]. Beryllium films are deposited on tungsten oxide-covered tungsten substrates. W(VI) and W(IV) oxides were produced and compared in their reactivity towards beryllium. W(VI) oxide is produced by oxidation of polished tungsten foils at 773 K for 1 hour in air. Both XPS and XRD confirm the formation of a WO_3 layer. The selective formation of WO_2 is not possible by direct oxidation of tungsten. A usual preparation procedure for WO_2 is the reduction of WO_3 in humid hydrogen at temperatures above 973 K. WO_3 is reduced in steps via substoichiometric tungsten oxides ($WO_3 \longrightarrow WO_{2.9} \longrightarrow WO_{2.7} \longrightarrow WO_2 \longrightarrow W$) [181,182,194–198]. However, it is difficult to stop the reduction when all higher oxides have been reduced to WO_2 and before the formation of metallic W. This can be controlled by monitoring the water vapor pressure [194]. In this work, we selected a preparation route via the comproportioning reaction $W + 2\,WO_3 \longrightarrow 3\,WO_2$. The WO_3 films on W are produced by oxidation in air at 673 K for 15 min. The furnace is flushed with pure nitrogen at 1 bar during the reaction to reduce the oxygen partial pressure. The tungsten foil with the formed oxide film is then annealed in UHV for 10 min at 523 K in order to desorb adsorbed impurities. XPS analysis of the precursor film shows only peaks at binding energies of WO_3. Subsequently, an annealing step in UHV at 973 K for 60 min results in an oxide layer on tungsten which, according to XPS analysis, consists of 42% WO_2, 31% WO_{3-x}, 25% WO_3 and 2% W. The XRD measurement is dominated by the peaks of metallic tungsten due to the thin oxide layer. Additional peaks are attributed to WO_2, no diffraction peaks of other tungsten oxides are present. Although the W(IV) oxide film still contains higher oxidation states, experiments can be performed with W(IV) oxide, in particular by comparing the results with experiments carried out using the pure W(VI) oxide films. With the described preparation techniques, W(VI) and W(IV) oxide films are available which allow the application of XPS as a tool to characterize surface chemical reactions. Onto such substrates, beryllium is evaporated under UHV, annealing and XPS analysis steps are carried out *in situ* without additional air transfer.

Table 6.1: Binding energies of the species detected in the W $4f_{7/2}$ region in the Be–O–W ternary systems.

binding energy [eV]	species
31.3	W metal
31.7	Be_xWO_3 (x=0–1)
32.9	WO_2
34.5	WO_{3-x}
35.7	WO_3
36.5	$BeWO_4$

The chemical state of the surfaces is investigated by XPS, measuring the core levels Be 1*s*, O 1*s*, and W 4*f*, after beryllium deposition at 300 K and subsequent annealing steps up to 1273 K. Valence band spectra are interpreted using published experimental [199–208] and theoretical [209] spectra for tungsten oxides and sodium tungsten bronzes. After Be deposition, both oxide surfaces show additional peaks in towards lower binding energies. This is interpreted by the reduction of tungsten oxides. In addition, the comparison of the W 4*f* and the Be 1*s* regions shows that new species are formed, since not all observed peaks can be assigned to oxides or the metals. From the available elements, the ternary compounds beryllium tungstate $BeWO_4$ and beryllium tungsten bronze Be_xWO_3 (x = 0–1) are assigned to the new peaks. Both signals are only detected at samples with Be films and are not present in uncoated oxide films which are annealed to the same temperatures. Since no information on the stoichiometry of the beryllium tungsten bronze is available, the stoichiometry $BeWO_3$ is assumed and used in the quantitative analysis. The binding energies in Table 6.1 are assigned to the species detected in the W 4*f* region and are used for the analysis of the spectra by peak fitting, allowing for the compound peaks generally a variation of ±0.1 eV.

The intensities from these species are determined by peak fitting in the W 4*f* BE region. The Be 1*s* spectra are used for confirmation of the determined reactions, as well as the spectra in the O 1*s* region. The results of the quantitative analysis are plotted in Fig. 6.3 for the W(VI) and W(IV) oxide films. W(VI) oxides are readily reduced by deposited beryllium at 300 K and also the tungstate and the tungsten bronze are formed. The red line marks the begin of the ternary phases in the composition plot.

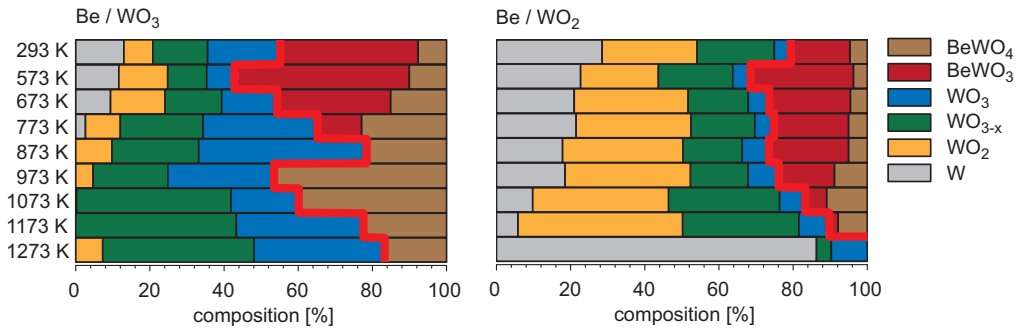

Figure 6.3: Composition of the Be-covered W(VI) and W(IV) oxide layers after annealing to the indicated temperatures, as derived from the analysis of the W $4f$ signals. The red line indicates the formed ternary compounds.

On the W(VI) oxide, the initially 88.1% WO_3 are reduced 19.6% WO_3 and 14.8% WO_{3-x}. Furthermore, 7.8% WO_2 and 13.0% metallic W are detected. During annealing at increased temperatures the initially formed $BeWO_3$ fraction decreases. The $BeWO_4$ fraction increases, has a maximum after 973 K annealing, and is still present after the 1273 K annealing step. At this temperature, most of the tungsten within the XPS information depth is present as WO_3 and WO_{3-x}. Only at the lower annealing temperatures, also metallic W and WO_2 is detected in small fractions. After 1273 K, again for WO_2 a 7.2% share is measured.

The annealing sequence for a Be-coated W(IV) oxide surface leads to a different reaction sequence. Since the W(IV) oxide film is thinner than the W(VI) oxide films and also contains W(VI) oxides, metallic tungsten and the ternary compounds $BeWO_4$ and $BeWO_3$ are present after Be deposition. Other than the W(VI) oxides, the WO_2 does not react with the beryllium and is present throughout the annealing sequence, up to an annealing temperature of 1173 K. After the next annealing step at 1273 K, however, the WO_2 has completely vanished. Metallic W dominates the surface within the XPS analysis depth. This temperature corresponds to the decomposition temperature of WO_2 [72].

The difference in the reactivities of the W(VI) and W(IV) oxides can be discussed in terms of different oxide structures and hence different diffusivities of the beryllium species (Be and BeO) in the oxides. The structure of WO_3 and of WO_{3-x} is determined by coordination octahedrons of O in WO_6 units. These units are linked at the corners, forming the oxide. In WO_3, tungsten

is coordinated by corner-sharing octahedrons. By removing oxygen along the shear planes, the structure of WO_{3-x} is reached. Both structures result in a 3-dimensional network of channels throughout the whole system [72,194]. Within this structure, hexagonal channels are formed which extend throughout the crystallites. The symmetry of this structure determines a three-dimensional network with orthogonal channels. This network of channels allows the diffusion of Be and BeO through the material. Within the oxide, Be^{2+} ions can diffuse in all three space directions. This picture is supported by the structure of the tungsten bronze. The Be^{2+} ions are incorporated in these channels in these compounds [72,204,210]. Therefore, the size of the channels is sufficiently large for Be^{2+} ions. The structure of WO_2 is of the rutile type [211], channels like in the WO_3 species are absent. Therefore, diffusion of Be within the WO_2 is suppressed, an incorporation of Be into the WO_2 grains is not possible and a reaction between WO_2 and Be, as in the case of the WO_3 species, is impossible. However, diffusion of Be into the oxide film is observed. It can take place along the grain boundaries which are visible in AFM pictures of the WO_2 film. Finally, in contrast to the binary system Be–W (see chapter 5), no alloy formation is observed in the ternary Be–O–W systems. The beryllium films on the WO_2 and WO_3 films show a different chemistry than the binary Be–W system.

Based on the XPS analysis of the chemical phases formed during the reactions between the W(VI) and W(IV) oxide films and the beryllium during the annealing steps, a quantitative model has been developed which describes the possible and relevant elementary chemical reactions in each step [175]. The quantitative analysis is based on the intensity changes in the W 4*f* signals during the reaction steps. The Be 1*s* and O 1*s* signals are used only for consistency checks. All relevant chemical species can be identified only in the W 4*f* signals. In addition, it is assumed that the reactions take place in a homogeneous layer and therefore a depth dependence of the W 4*f* signal is irrelevant. This is justified, because the diffusion of the Be^{2+} ions is fast in the tungsten oxides, both due to grain boundary and intra-grain diffusion. Changes in the thickness of the beryllium layer, in particular during the reaction steps at lower temperatures, can also be neglected if only the W 4*f* signal compositions are used for the quantitative analysis. For the beryllium reactions on the oxide films, the chemical reactions can be determined from the single reaction steps. For the chemical processes W(VI) oxide films, the reactions are shown in the following. In an analog way,

also the reactions on the W(IV) oxide films are determined [175].

Temperature step 573 K The sum equations at each temperature step are derived from the difference between this temperature and the preceding temperature step. I.e., the analysis at 573 K is based on the XPS measurements after the 573 K annealing step, and the difference to the measurements after the 300 K step.

$$1.3\,W + 16.3\,WO_3 + 1.2\,BeO + 11.1\,Be \longrightarrow$$
$$5.4\,WO_2 + 9.9\,BeWO_3 + 2.4\,BeWO_4$$

The following single reactions are involved with the given weight factors, determined by solving the reaction equation system:

$$2\,WO_3 + W \longrightarrow 3\,WO_2 \qquad \times 1.4$$
$$WO_3 + Be \longrightarrow WO_2 + BeO \qquad \times 1.2$$
$$WO_3 + BeO \longrightarrow BeWO_4 \qquad \times 2.4$$
$$WO_3 + Be \longrightarrow BeWO_3 \qquad \times 9.9$$

Temperature step 673 K

$$2.2\,W + 16.6\,BeWO_3 + 10.9\,O_2 \longrightarrow$$
$$1.5\,WO_2 + 12.3\,WO_3 + 5.0\,BeWO_4 + 11.6\,BeO$$

The following single reactions and weight factors are involved:

$$WO_3 + BeO \longrightarrow BeWO_4 \qquad \times 5.0$$
$$W + \tfrac{3}{2}O_2 \longrightarrow WO_3 \qquad \times 1.7$$
$$W + 2\,WO_3 \longrightarrow WO_2 \qquad \times 0.5$$
$$BeWO_3 + \tfrac{1}{2}O_2 \longrightarrow BeO + WO_3 \qquad \times 16.6$$

Temperature step 773 K

$$6.8\ W + 5.3\ WO_2 + 18.7\ BeWO_3 + 22.2\ O_2 \longrightarrow$$
$$22.9\ WO_3 + 7.9\ BeWO_4 + 10.8\ BeO$$

The following single reactions and weight factors are involved:

$$WO_3 + BeO \longrightarrow BeWO_4 \qquad \times 7.9$$
$$W + \tfrac{3}{2}O_2 \longrightarrow WO_3 \qquad \times 6.8$$
$$WO_2 + \tfrac{1}{2}O_2 \longrightarrow WO_3 \qquad \times 5.3$$
$$BeWO_3 + \tfrac{1}{2}O_2 \longrightarrow BeO + WO_3 \qquad \times 18.7$$

Temperature step 873 K

$$2.6\ W + 11.9\ BeWO_3 + 1.4\ BeWO_4 + 9.7\ O_2 \longrightarrow$$
$$0.37\ WO_2 + 15.47\ WO_3 + 13.3\ BeO$$

The following single reactions and weight factors are involved:

$$BeWO_4 \longrightarrow BeO + WO_3 \qquad \times 1.4$$
$$BeWO_3 + \tfrac{1}{2}O_2 \longrightarrow BeO + WO_3 \qquad \times 11.9$$
$$W + 2\,WO_3 \longrightarrow 3\,WO_2 \qquad \times 0.13$$
$$W + \tfrac{3}{2}O_2 \longrightarrow WO_3 \qquad \times 2.5$$

Temperature step 973 K

$$5.1\ WO_2 + 19.8\ WO_3 + 24.9\ BeO + 2.6O_2 \longrightarrow 24.9\ BeWO_4$$

The following single reactions and weight factors are involved:

$$WO_2 + \tfrac{1}{2}O_2 \longrightarrow WO_3 \qquad \times 5.1$$
$$BeO + WO_3 \longrightarrow BeWO_4 \qquad \times 24.9$$

Temperature step 1073 K

$$4.4\ WO_2 + 6.6\ BeWO_4 + 2.2\ O_2 \longrightarrow 11.0\ WO_3 + 6.6\ BeO$$

The following single reactions and weight factors are involved:

$$\begin{aligned} BeWO_4 &\longrightarrow WO_3 + BeO && \times 6.6 \\ WO_2 + \tfrac{1}{2}O_2 &\longrightarrow WO_3 && \times 4.4 \end{aligned}$$

Temperature step 1173 K

$$0.2\ WO_2 + 17.5\ BeWO_4 + 0.1\ O_2 \longrightarrow 17.7\ WO_3 + 17.5\ BeO$$

The same single reactions as in the annealing step at 1073 K are involved with different weight factors:

$$\begin{aligned} BeWO_4 &\longrightarrow WO_3 + BeO && \times 17.5 \\ WO_2 + \tfrac{1}{2}O_2 &\longrightarrow WO_3 && \times 0.2 \end{aligned}$$

Temperature step 1273 K

$$5.7\ BeWO_4 + 1.6\ WO_3 \longrightarrow 7.3\ WO_2 + 5.7\ BeO + 3.6\ O_2$$

The following single reactions and weight factors are involved:

$$\begin{aligned} BeWO_4 &\longrightarrow WO_3 + BeO && \times 5.7 \\ WO_3 &\longrightarrow WO_2 + \tfrac{1}{2}O_2 && \times 7.3 \end{aligned}$$

This detailed reaction analysis demonstrates that the chemical processes in the ternary Be–O–W systems can be identified by XPS analysis. A chemically consistent reaction scheme is developed. Although the developed reaction systems are not unique solutions in a mathematical sense, the consideration of the processes visible in the Be 1*s* and survey spectra and the available information in the literature lead to this solution.

7 Hydrogen inventory in beryllium

Since beryllium has been selected as a wall material for some existing fusion devices, and in particular with the decision to use it as the material for the first wall in the main chamber of ITER, the hydrogen isotope inventory in this metal (in the following short: hydrogen inventory, if not a specific isotope is addressed) became a major scientific issue and the topic of numerous studies [30, 32–34, 49, 212–263]. The influence of neutron-induced defects is addressed in specific studies. However, since no neutron source with the typical spectrum from D–T fusion reactions is available, those studies rely on defects created by fission neutrons [264–294]. The fundamental aspects of beryllium surfaces [295–331] and their behavior upon hydrogen adsorption [332–340] with respect to surface structure and reconstruction were studied both experimentally and by ab initio methods.

Nevertheless, due to its toxic nature (more precisely, the carcinogenic property of BeO dust), experimental investigations of the hydrogen inventory in beryllium received far less attention compared to carbon or tungsten. Numerous investigations focus on hydrogen inventories from *post mortem* analysis of Be-containing wall samples from fusion devices, in particular from JET as the largest fusion device using beryllium at the first wall [12, 28, 341–351]. Another experimental device which is able to handle beryllium in a plasma environment is the linear plasma device PISCES-B at UCSD [40, 41]. Here, it is possible to study in particular hydrogen inventories in materials exposed to plasmas containing Be as an impurity species, as well as in bulk Be samples after plasma exposure. *Post mortem* analysis of samples treated in PISCES-B allows to address issues of impurity influence on the hydrogen inventory, e.g. [53, 57, 352].

Despite the large number of investigations, the data on hydrogen retention in beryllium varies strongly for different experiments and in turn also their interpretation [114, 353]. There are several aspects to why the results and their interpretation vary so widely. First, the investigated beryllium materials vary in purity and production technology: High purity single crystals are used as

well as rolled foils with impurity contents in the percent range. These various materials exhibit strong differences in bulk structure, porosity, morphology, and impurity concentration. Second, the experimental conditions of the specific investigation are in many cases not well defined or not well controlled. Beryllium is highly reactive towards oxidation and has the tendency to form an oxide layer even under well-controlled vacuum conditions. This oxide coverage is in most cases not well defined. In the hydrogen release process the desorption from the surface is an important step: The surface properties can strongly influence the release properties of hydrogen from beryllium, and, as a consequence, the specific conditions of the different experiments described in the literature might result in strong retention property variations. Finally, the models applied to evaluate experimental data and to interpret the results in terms of physical and chemical processes also influence the quantitative description of the hydrogen retention and release processes. Therefore, identification of the mechanistic details is important for a complete description and prediction of hydrogen retention and release.

The investigation described below focus on a strict control of the surface composition. UHV conditions with pressures in the low 10^{-11} hPa range are required to keep the surfaces clean for the time of an experiment. The *in situ* available analytical tools comprise the characterization of the surface composition by XPS, the quantification of the implanted hydrogen species by NRA, and the quantification of the desorbing species by TPD. The specific influence of surface morphology and structure is addressed in *ex situ* investigations. Experimental results are interpreted taking into account both available parameters from the experimental literature, and also ab initio DFT calculations [340, 354–358]. The aim of the investigations is a model description of the atomistic retention and release mechanisms for hydrogen in beryllium.

The first experiments on deuterium retention and thermal release from clean metallic surfaces are performed on single crystals with $(1\,1\,\overline{2}\,0)$ surface orientation [359]$^{\otimes}$. The surface is cleaned by repeated argon sputtering and heating cycles, until the residual oxygen coverage is less than 0.2 ML. Due to the low base pressure of $\leq 3 \cdot 10^{-11}$ hPa experiments on a clean Be surface can be carried out for several hours, before a contamination layer of 1 ML is accumulated. Deuterium is implanted into the clean Be$(1\,1\,\overline{2}\,0)$ surface using a mass-separated D_3^+ ion beam at 3 keV, which corresponds to a kinetic energy of 1 keV per D.

The TPD spectra are measured using a quadrupole mass spectrometer (QMS) in line-of-sight geometry to the sample, and heating the sample by electron impact at different linear temperature ramps. The absolute amounts of retained deuterium are determined by NRA using the D(^{3}He, p)^{4}He reaction with 800 keV $^3He^+$ ions [360]. These measurements are also used to calibrate the QMS signal for quantitative analysis. The retention measurements result in a 78% retention rate of deuterium in the clean beryllium up to a fluence of $1.5 \cdot 10^{17}$ cm^{-2}. Above a deuterium fluence of approx. $2 \cdot 10^{17}$ cm^{-2} the sample saturates. This is in good agreement with earlier work, although the surface in those measurements was covered by unknown amounts of BeO [239, 361]. The deuterium desorbs over a wide temperature range and exhibits two desorption features. One release stage occurs around 450 K, is fairly sharp and has a double peak structure. A second desorption stage is observed above 700 K, extends up to 900 K and evidently contains several desorption peaks. Above that temperature, no deuterium is retained in the sample, as is shown both by subsequent TPD runs and by NRA. A more detailed analysis is performed in [362]$^{\otimes}$. Although the desorption feature around 450 K occurs at similar temperatures as the desorption of deuterium adsorbed at a Be(0 0 0 1) surface [334], it is not due to surface desorption in the case of implanted D. Both the different shape of the desorption peak and the amount of deuterium desorbing at this temperature are not compatible with deuterium adsorbed at the surface only, leading to the interpretation of a “supersaturated” zone.

In desorption experiments of implanted deuterium in Be(1 1 $\bar{2}$ 0) with clean and BeO-covered samples [363]$^{\otimes}$ it is discovered that the surface has no rate-limiting effect. All deuterium retained after 1 keV implantation in BeO-covered or clean Be(1 1 $\bar{2}$ 0) is retained in and released from binding states in the bulk which are not affected by the surface oxide compared to the clean Be surface. However, increasing deuterium amounts are released at a temperature of 680 K from the BeO-covered surface. The amount of deuterium released at this temperature depends on the areal density of BeO which hints at deuterium bound on the BeO surface or within the BeO layer.

Implantation of deuterium at elevated temperatures alters the retention behavior. When the sample is implanted at 530 K, the desorption stage around 450 K does not appear in the subsequent TPD measurement. The corresponding states are not occupied during the implantation due to the elevated substrate

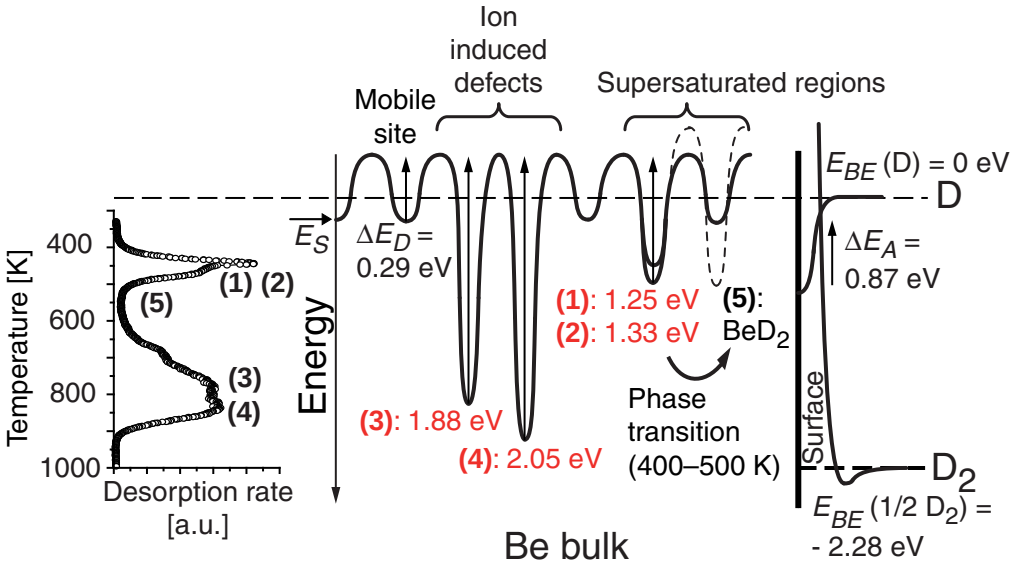

Figure 7.1: Energy diagram showing the activation energies for D in Be. The values (1) to (4) are determined from the TPD experiments (shown as an example at the left side) and modeling. Surface processes are depicted to the right.

temperature. However, the total amount of retained deuterium is not simply reduced by the amount bound in the 450 K desorption states at 300 K implantation, but a new desorption peak appears at 570 K. The release peaks above 700 K are not affected by the elevated implantation temperature. Since the decomposition of BeH_2 starts at 570 K [364, 365], it can be concluded that the endothermic deuteride is formed from the amount which was before bound in the supersaturated zones. A chemical shift in the XPS Be 1*s* signal due to the hydride formation, however, as observed in [261], is not observed here, indicating that the hydride is not present at the sample surface, but beyond the XPS information depth. This is consistent with the fact that supersaturation is expected to occur where the implantation depth profile peaks, i.e. at about 40 nm below the surface. Despite their endothermic character, beryllium hydride molecules were formed in in the gas phase and deposited at substrates at 10 K by laser ablation techniques and subsequentially analyzed by IR spectroscopy [366].

The experimentally observed desorption behavior of implanted deuterium from beryllium is modeled by two approaches for the low and high tempera-

ture release stages. According to the interpretation of the high temperature state as originating from implantation-induced binding states, the hydrogen transport and trapping code TMAP7 [367, 368] is used for this desorption feature. This code is based on the numerical solution of the diffusion equation, taking into account flux equilibria as boundary conditions in the modeled system. Temperature-driven transport, diffusion, surface recombination and trapping in defects are modeled. The required parameters such as diffusivity [212] and surface recombination [334] are taken from the literature. The high temperature desorption stage can be modeled in TMAP7 with two different detrapping energies. The deuterium profile before the onset of the TPD run is calculated by the Monte Carlo code SDTrim.SP [123, 124] and approximated by a Gaussian distribution. The simulated desorption flux is adjusted to the experimental desorption spectrum by manually adjusting the activation energies for detrapping of deuterium from the two modeled binding sites. For the different experimental temperature ramps and measured desorption fluxes, good agreement between TPD spectra and modeling results is found for activation energies of 1.88 eV and 2.05 eV. The desorption stage at low temperatures, however, cannot be modeled by TMAP7, since modifications of the substrate lattice are not contained in the computer code. These structural modifications, however, are the consequence of the supersaturation of Be with deuterium, as is shown in DFT calculations. Therefore, the low temperature release is modeled by a rate equation approach [369]. This approach assumes a first order reaction and a release mechanism involving a single temperature-dependent rate-limiting step (one activation barrier). Again, the activation energies are manually adjusted in order to fit the modeled release rates to the experimental spectra, taking into account the true experimental temperature ramps. The best fit results in activation energies of 1.25 and 1.33 eV for the two peaks in the low temperature release stage. This procedure yields reasonable agreement between experiment and modeling, however, the simulated release peaks are in all cases slightly too broad when compared to the experimental data. This indicates that the parameters of the release mechanism are reasonable, but the model is incomplete. An improved description should incorporate diffusive processes, both for the deuterium and for the defects responsible for the trapping. However, such an approach requires modeling at a more detailed level than the approach described so far. A suitable tool is a Kinetic Monte Carlo (KMC) code under

development, being able to bridge short and long time scales, like trapping and detrapping of hydrogen in defects and diffusion of hydrogen or vacancy clusters. Such a KMC approach also requires as an input fundamental parameters like energy barriers for vacancy formation, annihilation and diffusion, accessible in part by experiment and by ab initio DFT calculations. All activation energies determined from TPD experiments and subsequent modeling are summarized in the energy diagram shown in Fig. 7.1.

For further clarification of the mechanisms of hydrogen retention in beryllium, and in particular of the influence of structural and morphological aspects, experiments are performed comparing implantation and desorption of deuterium in beryllium single crystals and polycrystals [370]$^{\otimes}$, [371]$^{\otimes}$. By implanting deuterium ions with different primary energies into Be(1 1 $\bar{2}$ 0) and Be_{poly}, the depth distributions both of implanted hydrogen and of the traps generated in the collision cascades, as well as the available sinks for mobile defects (surface and grain boundaries) are varied. Modeling of the measured TPD spectra by TMAP7 allows for interpretation and discussion of retention and release mechanisms. The fluence dependence and retention behavior of 1 keV D^+ implantation at 300 K for Be(1 1 $\bar{2}$ 0) and Be_{poly} is similar. Below approx. $1 \cdot 10^{17}$ cm^{-2}, only desorption at the high temperature stage is observed. The desorption at 400–500 K only starts above a threshold deuterium fluence of approx. $1.2 \cdot 10^{17}$ cm^{-2}. This suggests that the proposed retention mechanisms (ion-induced defects as the reason for high temperature desorption with single vacancies and vacancy clusters as binding sites for hydrogen, and supersaturated zones for low temperature desorption) are identical for single and polycrystalline beryllium. Grain boundaries, as detected by EBSD in the Be_{poly}, have no influence on these mechanisms. Moreover, grain boundaries as additional deep trapping sites for hydrogen can be discarded from these measurements. There is, however, a difference in the highest deuterium release temperatures between Be(1 1 $\bar{2}$ 0) and Be_{poly}. For the same implantation conditions, the release from the ion-induced traps in Be_{poly} is complete at 850 K, whereas from Be(1 1 $\bar{2}$ 0) it continues until 920 K. Since grain boundaries can act as annihilation zones for defects, the number of defects is smaller for Be_{poly} than for single crystalline materials [372–375]. As vacancies are mobile, their depth distribution in single crystals may even extend deeper into the crystal in the absence of annihilation at grain boundaries. Both the number of defects

and their depth profile is varied in TMAP7 runs and the results support this interpretation.

A similar shift to higher temperatures of the high temperature desorption edge is observed for deuterium implantation with increased primary ion energy, both for Be_{poly} and Be(1 1 $\bar{2}$ 0). Again, TMAP7 simulations using implantation profiles for the applied D^+ ion energies of 1, 2 and 3 keV, calculated by SDTrim.SP, reproduce the shift of the high temperature edge. The important result is that the same activation energy for detrapping is used in all energy-dependent TMAP7 simulations. Therefore, a model assuming the same trap nature for different implantation energies in polycrystalline and single crystalline beryllium is justified. However, the TMAP7 simulation program cannot take into account alterations in the beryllium structure (amorphization, vacancy mobility and clustering etc.) during implantation and in particular during annealing. These processes most probably change the nature of the traps during the TPD run, which intrinsically is an annealing process. Therefore, it is not surprising that TMAP7, although being able to reproduce the shift of the leading edge as a function of trap depth profile (single/polycrystal, implantation energy), cannot reproduce all features of the TPD spectra. In particular, the shape of the desorption peaks is not reproduced. The simulated desorption peaks are generally too broad. Structural and morphological changes, caused by beryllium atom mobility, are observed experimentally. A polycrystalline surface, which underwent several implantation–desorption cycles, shows differences in surface morphology on grains of different orientation. These changes are characterized by SEM and EBSD on the same surface area. The damage observed on grains oriented with the Be(0 0 0 1) parallel to the surface is much higher than on grains where the basal plane is oriented perpendicular to the surface. This correlates well with the anisotropy of the activation energy for diffusion of Be self interstitials, as calculated by DFT: The barrier for diffusion along the basal planes is roughly a factor of 8 lower than perpendicular to the (0 0 0 1) planes. Simulating these processes is again a field where KMC models are promising. Currently, activities are underway to combine the experimental data and the results from *ab initio* DFT calculations in a lattice KMC approach to test the proposed mechanisms for hydrogen trapping and release from beryllium. First results demonstrate that the width of the desorption peaks is reduced, if annealing, i.e. annihilation of traps, is included in KMC simulations.

8 Summary

The work described in this thesis and the original publications is concerned with the formation and erosion of multi-component surfaces from elements which are of relevance for fusion first wall materials. In addition, the retention and release properties of clean and oxide-covered beryllium for hydrogen isotopes (hydrogen and deuterium) are investigated. The research is motivated by the decision to use three different wall materials in the next-step fusion experiment ITER. Beryllium is planned for the main chamber wall, tungsten for the divertor and baffle, and carbon as a CFC material will, according to the current design, be used in the divertor strike point areas. In addition to these elements, oxygen as a plasma impurity is an important reaction component. Moreover, iron and nickel, the main components of stainless steel, are investigated. Since the reaction conditions at the first wall of a fusion device strongly differ throughout the vessel, the parameter space for surface chemistry is quite large. The first wall will exhibit temperatures from around room temperature up to 1300 K and more in the divertor. The particle fluxes of the various species incident on the wall materials vary by several orders of magnitude, and so do their kinetic energies.

In the presented work, surface chemical and physical processes are studied in well-defined experiments which allow the detailed study of elementary reactions between two or more elements, initiated either by temperature or by kinetic particle impact. Thus, a description of these processes is possible at a fundamental level, leading to a detailed understanding with predictive potential towards the complex system in a real fusion device. In many solid state surface reactions, the availability of the components is determined by diffusion. Interdiffusion of components towards the reaction front is the rate-limiting process. Therefore, the thermal energy is not so much necessary to overcome an activation barrier as in the gas or liquid phases, but is necessary to enable interdiffusion between the reactants. Implantation of species with sufficient kinetic energy leads to the stimulation of chemical reactions, and to the formation of

defects within the collision cascade. These defects then can act as binding sites (traps) for gaseous species like hydrogen. For the re-emission of implanted gaseous species bound in traps, thermal energy is required. The trap nature (mono-, di-vacancies etc.) and the trap depth profile are affected by defect mobilities. In a fusion first wall material, in particular the trapping of hydrogen isotopes is a most crucial process, since it leads to a hydrogen isotope inventory in the wall. This inventory can be released under thermal excursions and needs to be known in the case of tritium for the assessment of the radioactive inventory.

Experimental requirements for the detailed study of single processes of surface chemistry and hydrogen inventories in fusion-related materials require the preparation and characterization of well-defined surfaces. Ultra-high vacuum and pure species deposition (both from the gas phase and as ionic species) are prerequisites. Analysis techniques are necessary which allow the characterization of elemental compositions and the chemical states of the species at the surface and up to depths which are relevant in reaction and implantation experiments. Both qualitative and quantitative analysis is required. The tools addressing these requirements are mainly X-ray photoelectron spectroscopy (both with laboratory sources and with variable photon energies at a synchrotron), temperature-programmed desorption spectroscopy, ion-beam based spectroscopies (low-energy ion scattering, Rutherford backscattering, nuclear reaction analysis). Sample preparation requires ion beams (for reactive species, mass-separated ion beams are required) with precise current measurements, and evaporation sources where monolayer to nm thick layers can be prepared in a controlled way. Preparation and analysis is required in UHV systems without the need to transfer the samples through air. The respective experimental facilities which enable well-defined preparation and analysis *in situ* were designed and constructed specifically for the described investigations. These *in situ* techniques are supplemented by a variety of microscopy methods and techniques for structural characterization (X-ray diffraction, electron back-scatter diffraction) available in dedicated setups *ex situ*.

Interactions in binary systems were investigated in a number of binary carbon–metal combinations, where mostly the metals act as substrates, and in the W–Be system. The reactions are triggered by thermal energy. By annealing the samples to different temperatures or at a constant temperature for

extended periods of time, activation energies and reaction constants for surface processes were determined. Thus, the formation of carbides on tungsten, beryllium, titanium, iron, nickel, and silicon were studied. The carbide phases were characterized with respect to their stoichiometry, their reactivity at 300 K, their onset temperature for carbide formation and the carbon diffusion into the bulk. In the C/Fe and C/Ni systems, the influence of the surface structure on the reaction and diffusion processes was studied in detail, and the experimental results were compared to *ab initio* density functional theory calculations. For tungsten and titanium, the formation of several carbide phases was observed. For all elements forming metallic carbides, an excessive diffusion and dissolution of carbon from the surface into the bulk is observed, which strongly reduces the surface carbon concentration above an element-specific temperature threshold. For ionic and more covalent carbides (Be_2C and SiC), the surface carbide layer is stable up to very high temperatures. In the Be–W intermetallic system, the formation of surface alloys of Be_2W and $Be_{12}W$ stoichiometry was observed, depending on the layer/substrate sequence and the availability of constituents. For Be films on W, a delicate balance between alloy formation and Be sublimation limits the surface alloy to 1–2 nm only. In cooperations, the Be–W system was investigated by density functional theory calculations. The combination of experiment and theory leads to a mechanistic understanding of the various processes.

Surface chemistry can not only be triggered thermally, but also by energetic ions or reactive species like atomic oxygen. Ions in the keV range deposit their energy within the first several 10 nm of a surface, thus influencing the processes in this depth range. Atomic oxygen with thermal energies adsorbs at the surface, but an enhanced reactivity compared to molecular O_2 is expected. Experiments with reactive species were carried out with mass-separated beams of carbon-containing ions (C^+ and CO^+), implanted into the surface of beryllium. Atomic oxygen was prepared in a microwave discharge, compatible to the UHV environment. Furthermore, surface reactions between carbon and tungsten, as well as carbon and titanium, were also studied by triggering them with the kinetic energy provided by beams of noble gas ions. Finally, deuterium ion interactions with carbon layers on several metals were investigated, where both the ion-solid kinematics and C–H chemistry take place and determine the erosion characteristics of several nm-thick carbon films on Be, Ti, and Ta

substrates. Molecular carbon ion species trigger carbide and oxide formation reactions on beryllium within the ion range when implanted at 300 K, which is observed only at elevated temperatures in the case of vapor-deposited C layers on Be. The implantation of C^+ can, at least for larger fluences, be well explained by the kinematic interactions, since the ion energies and impact angles results in a C self-sputtering yield below unity. At 300 K, C layers develop, which react to carbide upon annealing. However, for CO^+ implantation at 300 K, a deposition–erosion equilibrium develops which leads to a constant erosion of the beryllium substrate without additionally necessary thermal energy. The interaction of oxygen atoms at 300 K is investigated on tungsten and beryllium. The formation and sticking behavior of O_{at} is studied on gold for comparison. On tungsten, O_{at} forms surface oxide in the first monolayer, which is identical to the adsorption of O_2. No extended oxide layer formation is observed. On beryllium, however, O_{at} show a much higher reactivity compared to O_2. Moreover, the O 1*s* peak suggests several oxygen species at the surface in the case of O_{at} exposure.

As shown for CO^+ implantation into beryllium, the increase in number of species available at the surface for reactions complicates possible reactions. This is in particular the case when volatile products can be formed. Surface reactions in ternary systems were studied by depositing carbon or beryllium on W(IV) and W(VI) oxide surfaces, prepared on tungsten substrates. In the case of carbon films, the reactions at elevated temperatures lead to a reduction of the oxides. However, on the W(VI) oxide surface, the complete loss of carbon is observed, whereas on W(IV) oxide, a limited carbon concentration remains at elevated temperatures and forms WC. Also for Be layers on W(IV) and W(VI) oxides, different surface reactions are observed. In this ternary system, not only binary reaction products are formed, but also beryllium tungstate and tungsten bronze. The reactivity, however, can only be attributed to the W(VI) oxide, the W(IV) oxide is less reactive. The difference was interpreted in terms of the oxide structures and different diffusivities of the Be species. Ternary systems demonstrate that an additional species increase the complexity of the possible processes. In addition to information on the chemical state of the elements in the surface, diffusion processes can only be addressed in layered systems if a depth resolution is available. This can be achieved by tuning the photon energy in photoemission experiments such that for all elements the same depth inter-

vals are analyzed. Experiments at the synchrotron HZB-BESSY II with samples transferred from IPP Garching to Berlin *in vacuo* showed that this chemically resolved depth profiling can be performed successfully. Due to the reactivity of Be-containing systems, in particular towards oxidation (requiring well-defined UHV conditions in all steps of the sample preparation and dedicated evaporators), a new preparation chamber has been constructed and successfully used at HZB-BESSY II. Future measurements will help to elucidate the importance of diffusion properties, e.g. the formation of diffusion barriers, during surface reactions in ternary systems. The depth-resolved chemical analysis promises a qualitative and even semi-quantitative access to interface reactions in layered sample geometries.

With the established well-defined experimental conditions it was possible to investigate for the first time the hydrogen retention and release from beryllium without surface contamination layers. These experiments not only precisely quantify the hydrogen retention in beryllium, but also allow an assessment of the trapping mechanisms. By a quantitative analysis of the desorption spectra, the activation energies for hydrogen release from beryllium were determined. Further experiments allowed to address the influence of the beryllium structure and the anisotropic diffusion properties in the lattice. These studies are also accompanied with *ab initio* density functional theory calculations in collaborations. It was clarified that thin oxide coverages up to a few monolayers have no influence on the release activation energies, which means that the hydrogen release from beryllium is not rate-limited by surface recombination. With the experimentally determined activation energies for desorption, a model which unifies processes on strongly different time scales, like de-trapping and diffusion of both hydrogen and vacancies, can now be attempted using Kinetic Monte Carlo simulations.

Bibliography

[1] World Energy Outlook 2008, International Energy Agency (OECD/IEA) (2008).

[2] Intergovernmental Panel on Climate Change (IPCC), *Climate Change 2007 – Mitigation of Climate Change: Contribution of Working Group III to the Fourth Assessment Report* (Cambridge University Press, Cambridge, United Kingdom and New York, NY, USA, 2007).

[3] A. Bradshaw, VGB Powertech 86 (2006) 64.

[4] D. Maisonnier, I. Cook, P. Sardain, R. Andreani, L. Di Pace, R. Forrest, L. Giancarli, S. Hermsmeyer, P. Norajitra, N. Taylor, and D. Ward, *A Conceptual Study of Commercial Fusion Power Plants* (EFDA-RP-RE-5.0, 2004).

[5] M. Wakatani, *Stellarator and Heliotron Devices*, volume 95 of *International Series of Monographs on Physics* (Oxford University Press, 1998).

[6] J. Wesson, *Tokamaks*, volume 118 of *International Series of Monographs on Physics* (Oxford University Press, 2004), 3rd edition.

[7] J. Jacquinot and the JET team, Plasma Phys. Controlled Fusion 41 (1999) A13.

[8] ITER Physics Basis Editors et al., Nucl. Fusion 39 (1999) 2137.

[9] K. Ikeda and et al., Nucl. Fusion 47 (2007).

[10] G. Federici, C.H. Skinner, J.N. Brooks, J.P. Coad, C. Grisolia, A.A. Haasz, A. Hassanein, V. Philipps, C.S. Pitcher, J. Roth, W.R. Wampler, and D.G. Whyte, Nucl. Fusion 41 (2001) 1967.

[11] J. Roth, Phys. Scr. T124 (2006) 37.

[12] P.R. Thomas and The JET Team, J. Nucl. Mater. 176-177 (1990) 3.

[13] K. Krieger, H. Maier, and R. Neu, J. Nucl. Mater. 266-269 (1999) 207.

[14] R. Neu et al., Plasma Phys. Controlled Fusion 49 (2007) B59.

[15] W. Jacob, J. Nucl. Mater. 337-339 (2005) 839.

[16] M. Keilhacker and JET team, Phys. Fluids B: Plasma Phys. 2 (1990) 1291.

[17] R. Neu et al., Plasma Phys. Controlled Fusion 38 (1996) A165.

[18] G.F. Matthews, P. Edwards, T. Hirai, M. Kear, A. Lioure, P. Lomas, A. Loving, C. Lungu, H. Maier, P. Mertens, D. Neilson, R. Neu, J. Pamela, V. Philipps, G. Piazza, V. Riccardo, M. Rubel, C. Ruset, E. Villedieu, and M. Way on behalf of the ITER-like Wall Project Team, Phys. Scripta T128 (2007) 137.

[19] H. Maier, T. Hirai, M. Rubel, R. Neu, Ph. Mertens, H. Greuner, Ch. Hopf, G.F. Matthews, O. Neubauer, G. Piazza, E. Gauthier, J. Likonen, R. Mitteau, G. Maddaluno, B. Riccardi, V. Philipps, C. Ruset, C.P. Lungu, I. Uytdenhouwen, and JET EFDA contributors, Nucl. Fusion 47 (2007) 222.

[20] D.L. Smith, J. Nucl. Mater. 75 (1978) 20.

[21] S. Fukuda, S. Kato, M. Mohri, and T. Yamashina, J. Nucl. Mater. 111-112 (1982) 839.

[22] P. Varga and E. Taglauer, J. Nucl. Mater. 111&112 (1982) 726.

[23] A. Virag, W. Jäger, G. Friedbacher, M. Grasserbauer, F. Waelbroek, J. Winter, U. Littmark, H. Nickel, and E. Kny, Surf. Interface Anal. 12 (1988) 357.

[24] Y. Hasebe, K. Kondoh, and K. Morita, J. Nucl. Mater. 162-164 (1989) 945.

[25] E. Taglauer, J. Nucl. Mater. 128-129 (1984) 141.

[26] Y. Hirooka, A. Pospieszcyk, R.W. Conn, B. Mills, R.E. Nygren, and Y. Ra, J. Vac. Sci. Technol. A 7 (1989) 2935.

[27] A.T. Peacock, J.P. Coad, F. Lama, R. Behrisch, A.P. Martinelli, B.E. Mills, M. Pick, J. Partridge, J.C.B. Simpson, and Y.K. Zhu, J. Nucl. Mater. 176&177 (1990) 326.

[28] A.P. Martinelli, R. Behrisch, and A.T. Peacock, J. Nucl. Mater. 212-215 (1994) 1245.

[29] J. Roth, J. Nucl. Mater. 176-177 (1990) 132.

[30] R.G. Macaulay-Newcombe and D.A. Thompson, J. Nucl. Mater. 212-215 (1994) 942.

[31] K. Ashida, M. Matsuyama, K. Watanabe, H. Kawamura, and E. Ishitsuka, J. Nucl. Mater. 210 (1994) 233.

[32] M. Mayer, R. Behrisch, H. Plank, J. Roth, G. Dollinger, and C.M. Frey, J. Nucl. Mater. 230 (1996) 67.

[33] R.A. Anderl, G.R. Longhurst, R.J. Pawelko, and M.A. Oates, J. Fusion Energy 16 (1997) 95.

[34] K. Ashida, K. Watanabe, and T. Okabe, J. Nucl. Mater. 241-243 (1997) 1060.

[35] K. Ashida and K. Watanabe, Fusion Eng. Des. 37 (1997) 307.

[36] J. Roth, W.R. Wampler, and W. Jacob, J. Nucl. Mater. 250 (1997) 23.

[37] K. Ashida, K. Watanabe, I. Kitamura, and S. Ikeno, J. Nucl. Mater. 266-269 (1999) 434.

[38] M.I. Guseva, A.L. Suvorov, S.N. Korshunov, and N.E. Lazarev, J. Nucl. Mater. 266-269 (1999) 222.

[39] K. Ashida, K. Fujino, T. Okabe, M. Matsuyama, and K. Watanabe, J. Nucl. Mater. 290-293 (2001) 42.

[40] R.P. Doerner, M.J. Baldwin, and K. Schmid, Phys. Scr. T111 (2004) 75.

[41] D.G. Whyte, G.R. Tynan, R.P. Doerner, and J.N. Brooks, Nucl. Fusion 41 (2001) 47.

[42] Y. Hirooka, Fus. Technol. 30 (1996) 987.

[43] Y. Hirooka, Phys. Scr. T64 (1996) 84.

[44] Y. Hirooka, Fusion Eng. Design 37 (1997) 299.

[45] Y. Hirooka, J. Nucl. Mater. 258-263 (1998) 1045.

[46] R.P. Doerner, A.A. Grossman, S. Luckhardt, R. Seraydarian, F.C. Sze, and D.G. Whyte, J. Nucl. Mater. 266-269 (1999) 392.

[47] Y. Hirooka, J. Won, S. Keller, S. Boivin, M. Khandagle, and J.N. Brooks, Fus. Technol. 26 (1994) 540.

[48] Y. Hirooka, J. Won, R. Boivin, F.C. Sze, and V. Neumoin, J. Nucl. Mater. 230 (1996) 173.

[49] R.P. Doerner, A. Grossman, S. Luckhardt, R. Seraydarian, F.C. Sze, D.G. Whyte, and R.W. Conn, J. Nucl. Mater. 257 (1998) 51.

[50] R.P. Doerner, S.C. Luckhardt, R. Seraydarian, F.C. Sze, and D.G. Whyte, Phys. Scr. T81 (1999) 35.

[51] K. Schmid, M. Baldwin, R.P. Doerner, and A. Wiltner, Nucl. Fusion 44 (2004) 815.

[52] K. Schmid, M. Baldwin, and R.P. Doerner, J. Appl. Phys. 97 (2005) 064912.

[53] M.J. Baldwin, K. Schmid, R.P. Doerner, A. Wiltner, R. Seraydarian, and Ch. Linsmeier, J. Nucl. Mater. 337-339 (2005) 590.

[54] R.P. Doerner, M.J. Baldwin, and R.A. Causey, J. Nucl. Mater. 342 (2005) 63.

[55] M.J. Baldwin, R.P. Doerner, D. Nishijima, K. Schmid, D.G. Whyte, J.G. Kulpin, and G. Wright, J. Nucl. Mater. 358 (2006) 96.

[56] R.P. Doerner, J. Nucl. Mater. 363-365 (2007) 32.

[57] R. Pugno, K. Schmid, M.J. Baldwin, R.P. Doerner, J. Hanna, D. Nishijima, V. Rohde, and J. Roth, J. Nucl. Mater. 375 (2008) 168.

[58] J. Hanna, M.J. Baldwin, R.P. Doerner, D. Nishijima, and R. Seraydarian, J. Nucl. Mater. 386-388 (2009) 756.

[59] A.W. Kleyn, W. Koppers, and N. Lopes Cardozo, Vacuum 80 (2006) 1098.

[60] H. Bolt, V. Barabash, G. Federici, J. Linke, A. Loarte, J. Roth, and K. Sato, J. Nucl. Mater. 307–311 (2002) 43.

[61] S. Miller, G.L.P. Berning, H. Plank, and J. Roth, J. Vac. Sci. Technol. A 15 (1997) 2029.

[62] Ch. Linsmeier, P. Goldstraß, and K.U. Klages, Phys. Scr. T94 (2001) 28.

[63] G. Jung, Max-Planck-Institut für Quantenoptik MPQ Report 231 (1998).

[64] H. Shimada, N. Matsubayashi, M. Imamura, T. Sato, and A. Nishijima, Appl. Surf. Sci. 100-101 (1996) 56.

[65] F. Esaka, K. Furuya, H. Shimada, M. Imamura, N. Matsubayashi, T. Sato, A. Nishijima, T. Kikuchi, A. Kawana, and H. Ichimura, Surf. Sci. 377-379 (1997) 197.

[66] H. Shimada, K. Sato, N. Matsubayashi, M. Imamura, T. Saito, and K. Furuya, Appl. Surf. Sci. 144-145 (1999) 21.

[67] S.D. Horodetsky and J.I. Kleiman, Phys. Status Solidi A 191 (2002) 195.

[68] N. Matsubayashi, B.P. Singh, M. Imamura, T. Tanaka, Y. Sato, T. Ogiwara, M. Suzuki, and S. Kiyota, Surf. Interface Anal. 36 (2004) 853.

[69] M. Zier, S. Oswald, R. Reiche, and K. Wetzig, Microchim. Acta 156 (2007) 99.

[70] S.V. Merzlikin, N.N. Tolkachev, T. Strunskus, G. Witte, T. Glogowski, C. Wöll, and W. Grünert, Surf. Sci. 602 (2008) 755.

[71] F. Kost, Ch. Linsmeier, M. Oberkofler, M. Reinelt, M. Balden, A. Herrmann, and S. Lindig, J. Nucl. Mater. 390-391 (2009) 975.

[72] A.F. Holleman and E. Wiberg, *Lehrbuch der anorganischen Chemie* (de Gruyter, Berlin, New York, 1995), 101st edition.

[73] B.V. Khaenko, S.Ya. Golub, and M.P. Arbuzov, Sov. Phys. Crystallogr. 25 (1980) 63.

[74] B.V. Khaenko, S.Ya. Golub, and M.P. Arbuzov, Kristallografiya 25 (1980) 112.

[75] N.V. Dzhalabadze, B.G. Eristavi, N.I. Maisuradze, and E.R. Kuteliya, Phys. Metals Metallogr. 86 (1998) 59.

[76] H. Goretzki, Phys. Status Solidi 209 (1967) K141.

[77] N.V. Dzhalabadze, B.G. Eristavi, N.I. Maisuradze, K.K. Tshkovrebashbili, and E.R. Kuteliya, Powder Metall. Metal Ceram. 38 (1999) 292.

[78] A.N. Christensen, Acta Chem. Scand. Ser. A 32 (1978) 89.

[79] T.B. Massalski, H. Okamoto, P.R. Subramanian, and L. Kacprzak, *Binary Alloy Phase Diagrams* (ASM International, Materials Park, Ohio, 1996), 2nd ed., version 1.0 edition.

[80] F.J.J. van Loo and G.F. Bastin, Metallurg. Trans. A 20A (1989) 403.

[81] T. Epicier, J. Dubois, C. Esnouf, G. Fantozzi, and P. Convert, Acta Metallurgica 36 (1988) 1903.

[82] J. Leciejewski, Acta Cryst. 14 (1961) 200.

[83] U. Müller, *Anorganische Strukturchemie* (Teubner, 1992).

[84] Ch. Linsmeier, J. Luthin, and P. Goldstraß, J. Nucl. Mater. 290-293 (2001) 25.

[85] Ch. Linsmeier, J. Roth, and K. Schmid, IAEA Atomic and Plasma-Material Interaction Data for Fusion 12 (2003) 79.

[86] Ch. Linsmeier, J. Luthin, K.U. Klages, A. Wiltner, and P. Goldstraß, Phys. Scr. T111 (2004) 86.

[87] Ch. Linsmeier, AIP Conf. Proc. 740 (2004) 182.

[88] A. Wiltner and Ch. Linsmeier, Phys. Status Solidi A 201 (2004) 881.

[89] J. Luthin and Ch. Linsmeier, Surf. Sci. 454-456 (2000) 78.

[90] J. Luthin and Ch. Linsmeier, Phys. Scr. T91 (2001) 134.

[91] MultiPak, Physical Electronics Corp., Ver. 6–8 (1994–2006).

[92] I.N. Shabanova and V.A. Trapeznikov, J. Electron Spectrosc. Relat. Phenom. 6 (1975) 197.

[93] G. Panzner and W. Diekmann, Surf. Sci. 160 (1985) 253.

[94] S. Sinharoy and L.L. Levenson, Thin Solid Films 53 (1978) 31.

[95] E.O.F. Zdansky, A. Nilsson, and N. Mårtensson, Surf. Sci. 310 (1994) L583.

[96] A. Wiltner and Ch. Linsmeier, Surf. Sci. 602 (2008) 3623 .

[97] S. Tougaard, *QUASES Background Analysis of XPS / AES*, part 1 and 2 (QUASES - Tougaard APS, 1994–1999).

[98] S. Tougaard, J. Vac. Sci. Technol. A 14 (1996) 1415.

[99] S. Tougaard, Surf. Interface Anal. 26 (1998) 249.

[100] C. Klink, I. Stensgaard, F. Besenbacher, and E. Lægsgaard, Surf. Sci. 342 (1995) 250.

[101] C. Klink, L. Olesen, F. Besenbacher, I. Stensgaard, E. Lægsgaard, and N.D. Lang, Phys. Rev. Lett. 71 (1993) 4350.

[102] K.C. Prince, M. Surman, T. Lindner, and A.M. Bradshaw, Solid State Commun. 59 (1986) 71.

[103] M. Eizenberg and J.M. Blakely, J. Chem. Phys. 71 (1979) 3467.

[104] C.M. Whelan, R. Neubauer, D. Borgmann, and R. Denecke, J. Chem. Phys. 115 (2001) 8133.

[105] R. Neubauer, C.M. Whelan, R. Denecke, and H.-P. Steinrück, Surf. Sci. 507-510 (2002) 832.

[106] A. Wiltner, Ch. Linsmeier, and T. Jacob, J. Chem. Phys. 129 (2008) 084704.

[107] H. Bakker, H.P. Bonzel, C.M. Bruff, M.A. Dayananda, W. Gust, J. Horváth, I. Kaur, G.V. Kidson, A.D. Le Claire, H. Mehrer, G.E. Murch, G. Neumann, N. Stolica, and N.A. Stolwijk, *Diffusion in Solid Metals and Alloys*, Landolt-Börnstein Numerical Data and Functional Relationships in Science and Technology, New Series, Group III: Crystal and Solid State Physics, Vol. 26, ed. H. Mehrer (Springer-Verlag, Berlin, 1990).

[108] S. Diamond and C. Wert, Trans. Metall. Soc. AIME 239 (1967) 705.

[109] P. Goldstraß and Ch. Linsmeier, Nucl. Instrum. Methods B 161-163 (2000) 411.

[110] P. Goldstraß, K.U. Klages, and Ch. Linsmeier, J. Nucl. Mater. 290-293 (2001) 76.

[111] K. Schmid, A. Wiltner, and Ch. Linsmeier, Nucl. Instrum. Methods B 219 (2004) 947.

[112] T.G. Nieh, J. Wadsworth, and A. Joshi, Scripta Metallurgica 20 (1986) 87.

[113] C.-T. Tzeng, K.-D. Tsuei, and W.-S. Lo, Phys. Rev. B 58 (1998) 6837.

[114] R.A. Anderl, R.A. Causey, J.W. Davis, R.P. Doerner, G. Federici, A.A. Haasz, G.R. Longhurst, W.R. Wampler, and K.L. Wilson, J. Nucl. Mater. 273 (1999) 1.

[115] J. Luthin, H. Plank, J. Roth, and Ch. Linsmeier, Nucl. Instrum. Methods B 182 (2001) 218.

[116] K.U. Klages, A. Wiltner, J. Luthin, and Ch. Linsmeier, J. Nucl. Mater. 313-316 (2003) 56.

[117] M. Reinelt and Ch. Linsmeier, Nucl. Instrum. Meth. Phys. Res. B 258 (2007) 270.

[118] P. Goldstraß, W. Eckstein, and Ch. Linsmeier, J. Nucl. Mater. 266-269 (1999) 581.

[119] P. Goldstraß and Ch. Linsmeier, J. Nucl. Mater. 290-293 (2001) 71.

[120] T. Tachibana, B.E. Williams, and J.T. Glass, Phys. Rev. B 45 (1992) 11975.

[121] I. Barin, *Thermochemical Data of Pure Substances*, volume 1 & 2 (VCH, Weinheim, 1995), 3rd edition.

[122] W Möller, W. Eckstein, and J.P. Biersack, Comput. Phys. Commun. 51 (1988) 355.

[123] W. Eckstein, *Computer Simulation of Ion-Solid Interactions*, Springer Series in Materials Science, Vol. 10 (Springer, Berlin, 1991).

[124] W. Eckstein, R. Dohmen, A. Mutzke, and R. Schneider, *SDTrimSP: A Monte-Carlo Code for Calculating Collision Phenomena in Randomized Targets* (Max-Planck-Institut für Plasmaphysik, IPP-Report 12/3, 2007).

[125] E. Taglauer, W. Heiland, and J. Onsgaard, Nucl. Instr. Meth. 168 (1980) 571.

[126] J.L. Koontz, K. Albyn, and J.L. Leger, J. Spacecraft 28 (1991) 315.

[127] Ch. Linsmeier and J. Wanner, Surf. Sci. 454-456 (2000) 305.

[128] N. Saliba, D.H. Parker, and B.E. Koel, Surf. Sci. 410 (1998) 270.

[129] M.E. Schrader, Surf. Sci. 78 (1978) L227.

[130] J.J. Pireaux, M. Chtaib, J.P. Delrue, P.A. Thiry, M. Liehr, and R. Caudano, Surf. Sci. 141 (1984) 211.

[131] S. Zalkind, M. Polak, and N. Shamir, Appl. Surf. Sci. 115 (1997) 273.

[132] S. Zalkind, M. Polak, and N. Shamir, Surf. Sci. 385 (1997) 318.

[133] S. Zalkind, M. Polak, and N. Shamir, Surf. Sci. 513 (2002) 501.

[134] S. Zalkind, M. Polak, and N. Shamir, Surf. Sci. 529 (2003) 189.

[135] S. Zalkind, M. Polak, and N. Shamir, Surf. Sci. 539 (2003) 81.

[136] S. Zalkind, M. Polak, and N. Shamir, Israel J. Chem. 45 (2005) 147.

[137] S. Zalkind, M. Polak, and N. Shamir, Phys. Rev. B 71 (2005) 125413.

[138] S. Zalkind, M. Polak, and N. Shamir, Surf. Sci. 601 (2007) 1326.

[139] M.A. Gomez, L.R. Pratt, J.D. Kress, and D. Asthagiri, Surf. Sci. 601 (2007) 1608.

[140] V.Kh. Alimov, R.Kh. Zalavutdinov, and A.P. Zakharov, J. Nucl. Mater. 266-269 (1999) 417.

[141] R.Kh. Zalavutdinov, V.Kh. Alimov, A.E. Gorodetsky, and A.P. Zakharov, Protect. Metals 43 (2007) 432.

[142] K.A. McCarthy, G.R. Smolik, R.A. Anderl, R.J. Pawelko, M.A. Oates, and R.S. Wallace, Fusion Eng. Des. 37 (1997) 543.

[143] R.A. Anderl, R.J. Pawelko, M.A. Oates, G.R. Smolik, and K.A. McCarthy, J. Fusion Energy 16 (1997) 101.

[144] R.A. Anderl, R.J. Pawelko, G.R. Smolik, and RG. Castro, Fusion Technol. 34 (1998) 738.

[145] R.A. Anderl, K.A. McCarthy, M.A. Oates, D.A. Petti, R.J. Pawelko, and G.R. Smolik, J. Nucl. Mater. 258-263 (1998) 750.

[146] D.A. Petti, G.R. Smolik, and R.A. Anderl, J. Nucl. Mater. 283-287 (2000) 1390.

[147] A. Markin, A. Gorodetsky, F. Scaffidi-Argentina, H. Werle, C.H. Wu, and A. Zakharov, Fusion Technol. 38 (2000) 357.

[148] R.A. Anderl, R.J. Pawelko, G.R. Smolik, G. Piazza, F. Scaffidi-Argentina, and L.L. Snead, J. Nucl. Mater. 307-311 (2002) 1375.

[149] S.I. Sorokin and D.A. Davydov, Plasma Devices and Operations 11 (2003) 257.

[150] C. Tomastik, W. Werner, and H. Störi, Nucl. Fusion 45 (2005) 1061.

[151] D.M. Riffe and G.K. Wertheim, Surf. Sci. 399 (1998) 248.

[152] G. Tréglia, M.C. Desjonquères, D. Spanjaard, Y. Lassailly, C. Guillot, Y. Jugnet, Tran Minh Duc, and J. Lecante, J. Phys. C: Solid State Physics 14 (1981) 3463.

[153] J.F. van der Veen, F.J. Himpsel, and D.E. Eastman, Phys. Rev. B 25 (1982) 7388.

[154] G.K. Wertheim, P.H. Citrin, and J.F. van der Veen, Phys. Rev. B 30 (1984) 4343.

[155] P. Alnot, D.J. Auerbach, R.J. Behm, and C.R. Brundle, Surf. Sci. 213 (1989) 1.

[156] C.H.F. Peden and N.D. Shinn, Surf. Sci. 312 (1994) 151.

[157] J.F. Morar, F.J. Himpsel, G. Hughes, J.L. Jordan, F.R. McFeely, and G. Hollinger, J. Vac. Sci. Technol. A 3 (1985) 1477.

[158] F.W. Batchelder and R.F. Raeuchle, Acta Cryst. 10 (1957) 648.

[159] C.R. Watts, Int. J. Powder Metallurg. 4 (1968) 49.

[160] E.A. Vasina and A.S. Panov, Izvestiya Akademii Nauk SSSR, Metally 1 (1974) 197.

[161] Z. Polański, Z. Sidorski, and S. Zuber, Acta Physica Polonia A49 (1976) 299.

[162] S. Zuber, Z. Sidorski, and Z. Polański, Surf. Sci. 87 (1979) 375.

[163] J.J. Czyżewski, W. Grzesiak, and J. Krajniak, Acta Physica Polonica A60 (1981) 249.

[164] W. Schlenk and E. Bauer, Surf. Sci. 94 (1980) 528.

[165] E. Chrzanowski and E. Bauer, Surf. Sci. 173 (1986) 106.

[166] A. Wiltner and Ch. Linsmeier, J. Nucl. Mater. 337-339 (2005) 951.

[167] A. Wiltner and Ch. Linsmeier, New J. Physics 8 (2006) 181.

[168] Ch. Linsmeier, K. Ertl, J. Roth, A. Wiltner, K. Schmid, F. Kost, S.R. Bhattacharyya, M. Baldwin, and R.P. Doerner, J. Nucl. Mater. 363-365 (2007) 1129.

[169] A. Wiltner, F. Kost, S. Lindig, and Ch. Linsmeier, Phys. Scr. 128 (2007) 133.

[170] A. Allouche and Ch. Linsmeier, J. Phys.: Conf. Ser. 117 (2008) 012002.

[171] A. Allouche, A. Wiltner, and Ch. Linsmeier, J. Phys.: Cond. Matter 21 (2009) 355011.

[172] R.P. Doerner, M. Baldwin, J. Hanna, Ch. Linsmeier, D. Nishijima, R. Pugno, J. Roth, K. Schmid, and A. Wiltner, Phys. Scr. 128 (2007) 115.

[173] M.J. Baldwin, R.P. Doerner, D. Nishijima, D. Buchenauer, W.M. Clift, R.A. Causey, and K. Schmid, J. Nucl. Mater. 363–365 (2007) 1179.

[174] J. Luthin and Ch. Linsmeier, J. Nucl. Mater. 290-293 (2001) 121.

[175] M. Köppen and Ch. Linsmeier (2009) to be published.

[176] T. Engel, H. Niehus, and E. Bauer, Surf. Sci. 52 (1975) 237.

[177] E. Bauer and T. Engel, Surf. Sci. 71 (1978) 695.

[178] J. Feydt, A. Elbe, H. Engelhard, G. Meister, and A. Goldmann, Surf. Sci. 440 (1999) 213.

[179] H. Daimon, R. Ynzunza, J. Palomares, H. Takabi, and C.S. Fadley, Surf. Sci. 408 (1998) 260.

[180] J.F. Moulder, W.F. Strickle, P.E. Sobol, and K.D. Bomben, *Handbook of X-ray Photoelectron Spectroscopy* (Ed.: J. Chastain, Perkin-Elmer Corp., Eden Prairie, MN, 1992).

[181] D.A. Venables and M.E. Brown, Thermochim. Acta 282/283 (1996) 251.

[182] D.A. Venables and M.E. Brown, Thermochim. Acta 282/283 (1996) 265.

[183] D.A. Venables and M.E. Brown, Thermochim. Acta 291 (1997) 131.

[184] T. Kodama, H. Ohtake, S. Matsumoto, A. Aoki, T. Shimizu, and Y. Kitayama, Energy 25 (2000) 411.

[185] M.P. Seah and W.A. Dench, Surf. Interface Anal. 1 (1979) 2.

[186] D.E. Fowler, J. Gyulai, and C. Palmstrom, J. Vac. Sci. Technol. A 1 (1983) 1021.

[187] M.P. Seah, Vacuum 36 (1986) 399.

[188] S. Tanuma, C.J. Powell, and D.R. Penn, Surf. Interface Anal. 11 (1988) 577.

[189] S. Tanuma, C.J. Powell, and D.R. Penn, Surf. Interface Anal. 17 (1991) 911.

[190] S. Tanuma, C.J. Powell, and D.R. Penn, Surf. Interface Anal. 17 (1991) 927.

[191] B. Lesiak, A. Jablonski, Z. Prussak, and P. Mrozek, Surf. Sci. 223 (1989) 213.

[192] A. Jablonski and C.J. Powell, Surf. Sci. Reports 47 (2002) 33.

[193] M. Köppen, Ch. Linsmeier, and A. Vollmer (2009) to be published.

[194] E. Lassner and W.-D. Schubert, *Tungsten: Properties, Chemistry, Technology of the Element, Alloys, and Chemical Compounds* (Kluwer Academic/Plenum Publishers, New York, 1999), 1st edition.

[195] T.H. Fleisch and G.J. Mains, J. Chem. Phys. 76 (1982) 780.

[196] J. Haber, J. Stoch, and L. Ungier, J. Solid State Chem. 19 (1976) 113.

[197] J.O. Hougen, R. Reeves, R., and G.G. Mannella, J. Ind. Eng. Chem. 48 (1956) 318.

[198] M.G. Charlton, Nature 174 (1954) 703.

[199] R.D. Bringans, H. Höchst, and H.R. Shanks, Vacuum 31 (1981) 473.

[200] R.D. Bringans, H. Höchst, and H.R. Shanks, Phys. Rev. B 24 (1981) 3481.

[201] F. Bussolotti, L. Lozzi, M. Passacantando, S. La Rosa, S. Santucci, and L. Ottaviano, Surf. Sci. 538 (2003) 113.

[202] R.J. Colton and J.W. Rabalais, Inorg. Chem. 15 (1976) 236.

[203] R. Gehlig, E. Salje, A.F. Carley, and M.W. Roberts, J. Solid State Chem. 49 (1983) 318.

[204] H. Höchst, R.D. Bringans, and H.R. Shanks, Phys. Rev. B 26 (1982) 1702.

[205] A. Katrib, F. Hemming, P. Wehrer, L. Hilaire, and G. Maire, J. Electron Spectrosc. Relat. Phenom. 76 (1995) 195.

[206] O.Yu. Khyzhun, J. Alloys Comp. 305 (1) (2000) 1.

[207] O.Yu. Khyzhun, Yu.M. Solonin, and V.D. Dobrovolsky, J. Alloys Comp. 320 (2001) 1.

[208] S. Santucci, C. Cantalini, M. Crivellari, L. Lozzi, L. Ottaviano, and M. Passacantando, J. Vac. Sci. Technol. A 18 (2000) 1077.

[209] D.W. Bullett, J. Phys. C: Solid State Phys. 16 (1983) 2197.

[210] R.A. Wheeler, M.-H. Whangbo, T. Hughbanks, R. Hoffmann, J.K. Burdett, and T.A. Albright, J. Am. Chem. Soc. 108 (1986) 2222.

[211] F.H. Jones, R.G. Egdell, A. Brown, and F.R. Wondre, Surf. Sci. 374 (1997) 80.

[212] E. Abramov, M.P. Riehm, D.A. Thompson, and W.W. Smeltzer, J. Nucl. Mater. 175 (1990) 90.

[213] R.A. Causey, W.L. Hsu, B.E. Mills, J. Ehrenberg, and V. Phillips, J. Nucl. Mater. 179&177 (1990) 654.

[214] W.L. Hsu, R.A. Causey, B.E. Mills, J. Ehrenberg, and V. Phillips, J. Nucl. Mater. 176&177 (1990) 218.

[215] R.G. Macaulay-Newcombe, D.A. Thompson, and W.W. Smeltzer, Fusion Eng. Design 18 (1991) 419.

[216] R.G. Macaulay-Newcombe, D.A. Thompson, and W.W. Smeltzer, J. Nucl. Mater. 191-194 (1992) 263.

[217] W.R. Wampler, J. Nucl. Mater. 196-198 (1992) 981.

[218] Y.M. Zakaria, R.G. Macaulay-Newcombe, and D.A. Thompson, Workshop on Beryllium for Fusion Applications, KFK 527, Ed. M. Dalle Donne (1993) 331.

[219] R.A. Causey and K.L. Wilson, J. Nucl. Mater. 212-215 (1994) 1436.

[220] F. Schiettekatte, D. Kéroack, G.G. Ross, and B. Terreault, Nucl. Instrum. Meth. B 90 (1994) 401.

[221] D. Kéroack and B. Terreault, J. Nucl. Mater. 212-215 (1994) 1443.

[222] E.A. Denisov, T.N. Kompaniets, A.A. Kurdyumov, S.N. Mazayev, and Yu.G. Prokofiev, J. Nucl. Mater. 212-215 (1994) 1448.

[223] V.Kh. Alimov, R.Kh. Zalavutdinov, A.E. Gorodetsky, and A.P. Zakharov, J. Nucl. Mater. 220-222 (1995) 947.

[224] L. Buisson, P. Bracconi, and X. Claudon, Appl. Surf. Sci. 84 (1995) 211.

[225] E. Ishitsuka, H. Kawamura, Y. Hishinuma, M. Nakamura, and K. Tatenuma, Fusion Technol. 28 (1995) 647.

[226] R.A. Anderl, J.D. Baker, G.L. Bourne, and R.J. Pawelko, Fusion Technol. 28 (1995) 1114.

[227] K. Kizu, K. Miyazaki, and T. Tanabe, Fusion Technol. 28 (1995) 1205.

[228] G.R. Longhurst, R.A. Anderl, T.J. Dolan, and M.J. Mulock, Fusion Technol. 28 (1995) 1217.

[229] A.A. Pisarev, Fusion Technol. 28 (1995) 1262.

[230] B. Terreault, D. Kéroack, G.G. Ross, R.G. Saint-Jacques, F. Schiettekatte, K. Touhouche, and P. Zheng, J. Nucl. Mater. 220-222 (1995) 790.

[231] V.N. Chernikov, V.Kh. Alimov, A.N. Markin, and A.P. Zakharov, J. Nucl. Mater. 228 (1996) 47.

[232] I.P. Chernov, Y.P. Cherdantsev, and V.G. Abdrashitov, J. Nucl. Mater. 233-237 (1996) 857.

[233] A.V. Markin, V.N. Chernikov, S.Yu. Rybakov, and A.P. Zakharov, J. Nucl. Mater. 233-237 (1996) 865.

[234] V.M. Sharapov, L.E. Gavrilov, V.S. Kulikauskas, and A.V. Markin, J. Nucl. Mater. 233-237 (1996) 870.

[235] B. Tsuchiya and K. Morita, J. Nucl. Mater. 233-237 (1996) 898.

[236] A.A. Pisarev and M.L. Grachova, J. Nucl. Mater. 233-237 (1996) 1137.

[237] N. Yoshida, S. Mizusawa, R. Sakamoto, and T. Muroga, Fusion Technol. 30 (1996) 798.

[238] M.I. Guseva, A.Yu. Birukov, V.M. Gureev, L.S. Daneljan, S.N. Korshunov, Yu.V. Martynenko, P.S. Moskovkin, Yu.A. Sokolov, V.G. Stoljarova, V.S. Kulikauskas, and V.V. Zatekin, J. Nucl. Mater. 233-237 (1996) 681 .

[239] V.Kh. Alimov, V.N. Chernikov, and A.P. Zakharov, J. Nucl. Mater. 241-243 (1997) 1047.

[240] A.A. Haasz and J.W. Davis, J. Nucl. Mater. 241-243 (1997) 1076.

[241] K. Morita and B. Tsuchiya, J. Nucl. Mater. 248 (1997) 27.

[242] B. Tsuchiya and K. Morita, J. Nucl. Mater. 248 (1997) 42.

[243] B. Tsuchiya and K. Morita, J. Nucl. Mater. 241-243 (1997) 1065.

[244] J. Won, F.E. Spada, R. Boivin, R.P. Doerner, S. Luckhardt, F.C. Sze, and R.W. Conn, J. Nucl. Mater. 241-243 (1997) 1110.

[245] A.P. Zakharov, A.E. Gorodetsky, V.Kh. Alimov, S.L. Kanashenko, and A.V. Markin, J. Nucl. Mater. 241-243 (1997) 52.

[246] R.A. Causey, G.R. Longhurst, and W. Harbin, J. Nucl. Mater. 241-243 (1997) 1041.

[247] V.M. Sharapov, V.Kh. Alimov, and L.E. Gavrilov, J. Nucl. Mater. 258-263 (1998) 803.

[248] V.M. Sharapov, E. Gavrilov, and V.Kh. Alimov, Plasma Devices and Operations 6 (1998) 89.

[249] A.Yu. Biryukov, D.V. Andreev, S.A. Gavrilov, L.S. Danelian, V.I. Antropovand, and S.N. Mazaev, Plasma Devices and Operations 6 (1998) 259.

[250] G.R. Longhurst, R.A. Anderl, R.A. Causey, F. Gianfranco, A.A. Haasz, and R.J. Pawelko, J. Nucl. Mater. 258-263 (1998) 640.

[251] S.P. Vagin, P.V. Chakrov, B.D. Utkelbayev, L.A. Jacobson, R.D. Field, and H. Kung, J. Nucl. Mater. 258-263 (1998) 719.

[252] R.A. Causey and D.S. Walsh, J. Nucl. Mater. 254 (1998) 84.

[253] G. Federici, R. Anderl, J.N. Brooks, R. Causey, J.P. Coad, D. Cowgill, R.P. Doerner, A.A. Haasz, G. Longhurst, S. Luckhardt, D. Mueller, A. Peacock, M. Pick, C.H. Skinner, W. Wampler, K. Wilson, C. Wong, C. Wu, and D. Youchison, Fusion Eng. Des. 39-40 (1998) 445.

[254] V.Kh. Alimov and V.N. Chernikov, J. Nucl. Mater. 273 (1999) 277.

[255] J. Won, R.P. Doerner, and R.W. Conn, J. Nucl. Mater. 256 (1998) 96.

[256] A.V. Markin, V.P. Dubkov, A.E. Gorodetsky, M.A. Negodaev, N.V. Rozhanskii, F. Scaffidi-Argentina, H. Werle, C.H. Wu, R.Kh. Zalavutdinov, and A.P. Zakharov, J. Nucl. Mater. 283-287 (2000) 1094.

[257] A.P Zakharov, A.E. Gorodetskii, and V.Kh. Alimov, Russ. J. Inorg. Chem. 47 (2002) 552.

[258] A.M. Zimin, M.I. Guseva, N.G. Elistratov, L.S. Danelyan, V.M. Gureev, B.N. Kolbasov, V.S. Kulikauskas, V.G. Stolyarova, N.N. Vasiliev, and V.V. Zatekin, Plasma Devices and Operations 12 (2004) 89.

[259] C.H. Skinner, A.A. Haasz, V.Kh. Alimov, N. Bekris, R.A. Causey, R.E.H. Clark, J.P. Coad, J.W. Davis, R.P. Doerner, M. Mayer, A. Pisarev, J. Roth, and T. Tanabe, Fusion Sci. Technol. 54 (2008) 891.

[260] G. De Temmerman, M.J. Baldwin, R.P. Doerner, D. Nishijima, and K. Schmid, Nucl. Fusion 48 (2008) 075008.

[261] G. De Temmerman and R.P. Doerner, Nucl. Fusion 49 (2009) 042002.

[262] A. Anghel, C. Porosnicu, M. Badulescu, I. Mustata, C.P. Lungu, K. Sugiyama, S. Lindig, K. Krieger, J. Roth, A. Nastuta, G. Rusu, and G. Popa, Nucl. Instrum. Meth. B 267 (2009) 426.

[263] R.P. Doerner, M.J. Baldwin, G. De Temmerman, J. Hanna, D. Nishijima, J. Roth, K. Schmid, G.R. Tynan, and K. Umstadter, Nucl. Fusion 49 (2009) 035002.

[264] J.C. Nicoitd, J. Delaplace, J. Hillairet, D. Schumacher, and Y. Adda, J. Nucl. Mater. 27 (1968) 147.

[265] J. Delaplace, J.C. Nicoitd, D. Schumacher, and G. Vogl, Phys. Status Solidi 29 (1968) 819.

[266] M. Dalle Donne, F. Scaffidi-Argentina, C. Ferrero, and C. Ronchi, J. Nucl. Mater. 212-215 (1994) 954.

[267] D.L. Baldwin and M.C. Billone, J. Nucl. Mater. 212-215 (1994) 948.

[268] F. Scaffidi-Argentina, M. Dalle Donne, C. Ferrero, and C. Ronchi, Fusion Eng. Des. 27 (1995) 275.

[269] S. Cho and M.A. Abdou, Fusion Eng. Des. 28 (1995) 265.

[270] M.A. Lomidze, A.E. Gorodetsky, and A.P. Zakharov, Fusion Technol. 28 (1995) 1211.

[271] S.L. Kanashenko, A.E. Gorodetsky, A.P. Zakharov, and W.R. Wampler, Phys. Scr. T64 (1996) 36.

[272] H. Kwast, H. Werle, and C.H. Wu, Phys. Scr. T64 (1996) 41.

[273] D.V. Andreev, V.N. Bespalov, A.Ju. Birjukov, B.A. Gurovich, and P.A. Platonov, J. Nucl. Mater. 233-237 (1996) 880.

[274] A.Kh. Klepikov, I.L. Tazhibaeva, V.P. Shestakov, O.G. Romanenko, Y.V. Chikhray, E.A. Kenzhin, Yu.S. Cherepnin, and L.N. Tikhomirov, J. Nucl. Mater. 233-237 (1996) 837.

[275] F. Scaffidi-Argentina, M.D. Dalle Donne, C. Ronchi, and C. Ferrero, Fusion Technol. 32 (1997) 179.

[276] A.Kh. Klepikov, I.L. Tazhibaeva, O.G. Romanenko, Y.V. Chikhray, V.P. Shestakov, and E.A. Kenzhin, J. Nucl. Mater. 258-263 (1998) 798.

[277] F. Scaffidi-Argentina, M.D. Dalle Donne, C. Ronchi, and C. Ferrero, Fusion Technol. 33 (1998) 146.

[278] I.L. Tazhibaeva, A.Kh. Klepikov, V.P. Shestakov, O.G. Romanenko, Y.V. Chikhray, E.A. Kenzhin, Yu.S. Cherepninand, and L.N. Tikhomirov, Plasma Devices and Operations 6 (1998) 251.

[279] I.B. Kupriyanov and V.V. Vlasov, Fusion Technol. 38 (2000) 350.

[280] E. Ishitsuka, H. Kawamura, T. Terai, and S. Tanaka, J. Nucl. Mater. 283-287 (2000) 1401.

[281] V. Barabash, G. Federici, M. Rödig, L.L. Snead, and C.H. Wu, J. Nucl. Mater. 283-287 (2000) 138.

[282] F. Scaffidi-Argentina, C. Sand, and C.H. Wu, J. Nucl. Mater. 290-293 (2001) 211.

[283] F. Scaffidi-Argentina, Fusion Eng. Des. 58-59 (2001) 641.

[284] V.P. Chakin, V.A. Kazakov, A.A. Teykovtsev, V.V. Pimenov, G.A. Shimansky, Z.E. Ostrovsky, D.N. Suslov, R.N. Latypov, S.V. Belozerov, and I.B. Kupriyanov, Fusion Eng. Des. 58-59 (2001) 535.

[285] E. Rabaglino, C. Ferrero, J. Reimann, C. Ronchi, and T. Schulenberg, Fusion Eng. Des. 61-62 (2002) 769.

[286] E. Rabaglino, J.P. Hiernaut, C. Ronchi, and F. Scaffidi-Argentina, J. Nucl. Mater. 307-311 (2002) 1424.

[287] M. Uchida, E. Ishitsuka, and H. Kawamura, J. Nucl. Mater. 307-311 (2002) 653.

[288] F. Scaffidi-Argentina, G. Piazza, and R. Rolli, Fusion Eng. Des. 69 (2003) 505.

[289] I.B. Kupriyanov, V.A. Gorokhov, V.V. Vlasov, A.M. Kovalev, and V.P. Chakin, J. Nucl. Mater. 329-333 (2004) 809.

[290] P. Kurinskiy, A. Cardella, M. Klimiankou, A. Möslang, and A.A. Goraieb, Fusion Eng. Des. 75-79 (2005) 709.

[291] I.B. Kupriyanov, G.N. Nikolaev, V.V. Vlasov, A.M. Kovalev, and V.P. Chakin, J. Nucl. Mater. 367-370 (2007) 511.

[292] N. Nankov, T. Troev, L. Petrov, and E. Popov, Nucl. Instrum. Meth. B 266 (2008) 3392.

[293] A. Schmidt, I. Uytdenhouwen, W. Kühnlein, M. Rödig, J. Linke, T. Hirai, and G. Pintsuk, Fusion Eng. Des. 83 (2008) 1108.

[294] A. Möslang, R.A. Pieritz, E. Boller, and C. Ferrero, J. Nucl. Mater. 386-388 (2009) 1052.

[295] R.D. Plummer and W.L. Gordon, Phys. Rev. Lett. 13 (1964) 432.

[296] E. Jensen, R.A. Bartynski, T. Gustafsson, E.W. Plummer, M.Y. Chou, M.L. Cohen, and G.B. Hoflund, Phys. Rev. B 30 (1984) 5500.

[297] E. Jensen, R.A. Bartynski, T. Gustafsson, and E.W. Plummer, Phys. Rev. Lett. 52 (1984) 2172.

[298] R.A. Bartynski, E. Jensen, T. Gustafsson, and E.W. Plummer, Phys. Rev. B 32 (1985) 1921.

[299] E.W. Plummer, Phys. Scr. T17 (1987) 186.

[300] J.B. Hannon, E.W. Plummer, R.M. Wentzcovitch, and P.K. Lam, Surf. Sci. 269-270 (1992) 7.

[301] H.L. Davis, J.B. Hannon, K.B. Ray, and E.W. Plummer, Phys. Rev. Lett. 68 (1992) 2632.

[302] J.B. Hannon and E.W. Plummer, J. Electron Spectrosc. Relat. Phenom. 64-65 (1993) 683.

[303] E.W. Plummer and J.B. Hannon, Progr. Surf. Sci. 46 (1994) 149.

[304] H.I.P. Johansson, L.I. Johansson, E. Lundgren, J.N. Andersen, and R. Nyholm, Phys. Rev. B 49 (1994) 17460.

[305] L.I. Johansson, H.I.P. Johansson, E. Lundgren, J.N. Andersen, and R. Nyholm, Surf. Sci. 321 (1994) L219.

[306] R. Stumpf, J.B. Hannon, P.J. Feibelman, and E.W. Plummer, Proc. 134th Heraeus Seminar World Scientific, Singapore (1995) 151.

[307] L.I. Johansson, Surf. Rev. Lett. 2 (1995) 225.

[308] L.I. Johansson and H.I.P. Johansson, Nucl. Instrum. Meth. B 97 (1995) 430.

[309] P. Hofmann, R. Stumpf, V.M. Silkin, E.V. Chulkov, and E.W. Plummer, Surf. Sci. 355 (1996) L278.

[310] P. Hofmann, K. Pohl, R. Stumpf, and E.W. Plummer, Phys. Rev. B 53 (1996) 13715.

[311] J.B. Hannon, K. Pohl, P.J. Rous, and E.W. Plummer, Surf. Sci. 364 (1996) L617.

[312] J.B. Hannon, E.J. Mele, and E.W. Plummer, Phys. Rev. B 53 (1996) 2090.

[313] B.G. Briner, Ph. Hofmann, M. Doering, H.-P. Rust, E.W. Plummer, and A.M. Bradshaw, Europhys. Lett. 39 (1997) 67.

[314] P.T. Sprunger, L. Petersen, E.W. Plummer, E. Lægsgaard, and F. Besenbacher, Science 275 (1997) 1764.

[315] Ph. Hofmann and E.W. Plummer, Surf. Sci. 377-379 (1997) 330.

[316] P. Hofmann, B.G. Briner, M. Doering, H.-P. Rust, E.W. Plummer, and A.M. Bradshaw, Phys. Rev. Lett. 79 (1997) 265.

[317] L.I. Johansson, P.-A. Glans, and T. Balasubramanian, Phys. Rev. B 58 (1998) 3621.

[318] B.G. Briner, Ph. Hofmann, M. Doering, H.-P. Rust, E.W. Plummer, and A.M. Bradshaw, Phys. Rev. B 58 (1998) 13931.

[319] S. Lizzit, K. Pohl, A. Baraldi, G. Comelli, V. Fritzsche, E.W. Plummer, R. Stumpf, and Ph. Hofmann, Phys. Rev. Lett. 81 (1998) 3271.

[320] K. Pohl, J.-H. Cho, K. Terakura, M. Scheffler, and E.W. Plummer, Phys. Rev. Lett. 80 (1998) 2853.

[321] J.-H. Cho, K. S. Kim, S.-H. Lee, M.-H Kang, and Z. Zhang, Phys. Rev. B 61 (2000) 9975.

[322] Ismail, Ph. Hofmann, A.P. Baddorf, and E.W. Plummer, Phys. Rev. B 66 (2002) 245414.

[323] S.-J. Tang, Ismail, P.T. Sprunger, and E.W. Plummer, Phys. Rev. B 65 (2002) 235428.

[324] A. Baraldi, S. Lizzit, K. Pohl, P. Hofmann, and S. de Gironcoli, Europhys. Lett. 64 (2003) 364.

[325] J. Rundgren, Phys. Rev. B 68 (2003) 125405.

[326] C.Q. Sun, B.K. Tay, Y.Q. Fu, S. Li, T.P. Chen, H.L. Bai, and E.Y. Jiang, J. Phys. Chem. B 107 (2003) 411.

[327] C.Q. Sun, Phys. Rev. B 69 (2004) 045105.

[328] P.-A. Glans, L.I. Johansson, T. Balasubramanian, and R.J. Blake, Phys. Rev. B 70 (2004) 033408.

[329] S.-J. Tang, J. Shi, B. Wu, P.T. Sprunger, W.L. Yang, V. Brouet, X.J. Zhou, Z. Hussain, Z.-X. Shen, Z. Zhang, and E.W. Plummer, Phys. Status Solidi B 241 (2004) 2345.

[330] J. Shi, S.-J. Tang, W. Biao, P.T. Sprunger, W.L. Yang, V. Brouet, X.J. Zhou, Z. Hussain, Z.-X. Shen, Z. Zhenyu, and E.W. Plummer, Phys. Rev. Lett. 92 (2004) 186401.

[331] S.-J. Tang, H.-T. Jeng, C.-S. Hsue, Ismail, P.T. Sprunger, and E.W. Plummer, Phys. Rev. B 77 (2008) 045405.

[332] K.B. Ray, J.B. Hannon, and E.W. Plummer, Chem. Phys. Lett. 171 (1990) 469.

[333] V. Lossev and J. Küppers, J. Nucl. Mater. 196-198 (1992) 953.

[334] V. Lossev and J. Küppers, Surf. Sci. 284 (1993) 175.

[335] K.B. Ray, X. Pan, and E.W. Plummer, Surf. Sci. 285 (1993) 66.

[336] P.J. Feibelman, Phys. Rev. B 48 (1993) 11270.

[337] R. Stumpf and P.J. Feibelman, Phys. Rev. B 51 (1995) 13748.

[338] K. Pohl and E.W. Plummer, Phys. Rev. B 59 (1999) R5324.

[339] K. Pohl, E.W. Plummer, S.V. Hoffmann, and P. Hofmann, Phys. Rev. B 70 (2004) 235424.

[340] A. Allouche, Physical Review B 78 (2008) 085429.

[341] M.J. Rubel, J.P. Coad, and D. Hole, J. Nucl. Mater. 386-388 (2009) 729.

[342] B.N. Kolbasov, P.V. Romanov, M.I. Guseva, B.I. Khripunov, V.G. Stankevich, N.Yu. Svechnikov, and A.M. Zimin, Plasma Devices and Operations 14 (2006) 303.

[343] J. Tiliks, G. Kizane, A. Vitins, E. Kolodinska, V. Tilika, and B. Lescinskis, Fusion Eng. Des. 83 (2008) 1388.

[344] J. Likonen, E. Vainonen-Ahlgren, J.P. Coad, R. Zilliacus, T. Renvall, D.E. Hole, M. Rubel, K. Arstila, G.F. Matthews, and M. Stamp, J. Nucl. Mater. 337-339 (2005) 60.

[345] F. Scaffidi-Argentina, S. Ciattaglia, P. Coad, R.-D. Penzhorn, and V. Philipps, J. Nucl. Mater. 307-311 (2003) 1411.

[346] M. Mayer, V. Philipps, P. Wienhold, H.G. Esser, J. von Seggern, and M. Rubel, J. Nucl. Mater. 290-293 (2001) 381.

[347] A. Rossi, T. Loarer, G. Saibene, R.D. Monk, L.D. Horton, M.L. Apicella, and B. Annaratone, J. Nucl. Mater. 266-269 (1999) 922.

[348] R.G. Macaulay-Newcombe, D.A. Thompson, and J.P. Coad, J. Nucl. Mater. 258-263 (1998) 1114.

[349] J.P. Coad, J. Nucl. Mater. 226 (1995) 156.

[350] P. Andrew and M. Pick, J. Nucl. Mater. 220-222 (1995) 601.

[351] G. Federici, R.A. Causey, P.L. Andrew, and C.H. Wu, Fus. Eng. Des. 28 (1995) 136.

[352] R.P. Doerner, R.W. Conn, S.C. Luckhardt, F.C. Sze, and J. Won, Fusion Eng. Des. 49-50 (2000) 183.

[353] R.A. Causey, J. Nucl. Mater. 300 (2002) 91.

[354] H. Krimmel and M. Fähnle, J. Nucl. Mater. 231 (1996) 159.

[355] H. Krimmel and M. Fähnle, J. Nucl. Mater. 255 (1998) 72.

[356] M.G. Ganchenkova and V.A. Borodin, Phys. Rev. B 75 (2007) 054108.

[357] M.G. Ganchenkova, P.V. Vladimirov, and V.A. Borodin, J. Nucl. Mater. 386-388 (2009) 79.

[358] M.G. Ganchenkova, V.A. Borodin, and R.M. Nieminen, Phys. Rev. B 79 (2009) 134101.

[359] M. Reinelt and Ch. Linsmeier, Phys. Scr. 128 (2007) 111.

[360] V.Kh. Alimov, M. Mayer, and J. Roth, Nucl. Instrum. Meth. B 234 (2005) 169.

[361] W.R. Wampler, J. Nucl. Mater. 122&123 (1984) 1598.

[362] M. Reinelt, A. Allouche, M. Oberkofler, and Ch. Linsmeier, New J. Phys. 11 (2009) 043023.

[363] M. Reinelt and Ch. Linsmeier, J. Nucl. Mater. 390-391 (2009) 568.

[364] P.E. Barry, J.S. Bowers, R.G. Garza, P.C. Souers, J.S. Cantrell, and T. Beiter, J. Nucl. Mater. 173 (1990) 142.

[365] D. Nishijima, R.P. Doerner, M.J. Baldwin, G. De Temmerman, and E.M. Hollmann, Plasma Phys.Contr. Fusion 50 (2008) 125007.

[366] T.J. Tague and L. Andrews, J. Am. Chem. Soc. 115 (1993) 12111.

[367] G.R. Longhurst, Idaho National Engineering and Environmental Laboratory Bechtel BWXT Idaho, LLC, Report INEEL/EXT-04-02352 (2004).

[368] J.A. Ambrosek and G.R. Longhurst, Idaho National Engineering and Environmental Laboratory Bechtel BWXT Idaho, LLC, ReportINEEL/EXT-04-01657 (2004).

[369] A.M. de Jong and J.W. Niemantsverdriet, Surf. Sci. 233 (1990) 355.

[370] M. Oberkofler, M. Reinelt, A. Allouche, S. Lindig, and Ch. Linsmeier, Phys. Scr. T138 (2009) 014036.

[371] M. Oberkofler, M. Reinelt, S. Lindig, and Ch. Linsmeier, Nucl. Instrum. Meth. B 267 (2009) 718.

[372] J.A. Hudson, D.J. Mazey, and R.S. Nelson, J. Nucl. Mater. 41 (1971) 241.

[373] D.I.R. Norris, J. Nucl. Mater. 40 (1971) 66.

[374] S.J. Zinkle and K. Farrell, J. Nucl. Mater. 168 (1989) 262.

[375] B.N. Singh and A.J.E. Foreman, Philos. Mag. 29 (1974) 847.

Acronyms

AES	Auger electron spectroscopy
AFM	Atomic force microscope
bcc	Body-centered cubic
BE	(Photoelectron) binding energy
DFT	Density functional theory
EBSD	Electron back-scatter diffraction
EDX	Energy-dispersive X-ray microanalysis
FWHM	Full-width-at-half-maximum
hcp	Hexagonal close-packed
HOPG	Highly-ordered pyrolytic graphite
IR	Infrared
ISS	Ion scattering spectroscopy (synonymous to LEIS)
ITER	International thermonuclear experimental reactor
LEED	Low-energy electron diffraction
LEIS	Low-energy ion scattering spectroscopy (synonymous to ISS)
ML	Monolayer
NRA	Nuclear reaction analysis
QMS	Quadrupole mass spectrometer
RBS	Rutherford backscattering spectrometry
RT	room temperature, usually 293–300 K
SEM	Scanning electron microscopy
TDS	Thermal desorption spectroscopy
TPD	Temperature-programmed desorption

UHV	Ultra-high vacuum
UPS	Ultraviolet photoelectron spectroscopy
WDX	Wavelenght-dispersive X-ray microanalysis
XPS	X-ray photoelectron spectroscopy
XRD	X-ray diffraction

Acknowledgement

This work would not have been possible without the enthusiasm, the curiosity and the skills of all the PhD, diploma and master students who joined me for research in plasma-wall interactions. Over the years, Dr. Peter Goldstraß, Dr. Jens Luthin, Dr. Konrad Klages, Dr. Almut Wiltner, Dr. Matthias Reinelt, Dr. Florian Kost, Martin Oberkofler, Rainer Piechoczek, and Martin Köppen participated or are still engaged in the investigation of fundamental processes at fusion first wall materials. With each of them it was and still is a pleasure to collaborate!

I am indebted to Prof. H.-J. Freund for generously offering me his support to pursue the Habilitation project. Prof. A. Bradshaw helped me in establishing the contacts to Prof. W. Domcke. Prof. H. Bolt and Dr. J. Roth continuously supported and encouraged my research activities, for which I am particularly grateful. Many discussions with them over the years stimulated my work to an invaluable degree.

Prof. U. Heiz, Prof. H.J. Neusser and Dr. H. Selzle accompanied me through my teaching activities at the Chemistry Department of the Technical University Munich, and made me familiar with these aspects of the academic life. I thank them for the continuous support during the last years.

The stimulating and friendly atmosphere created by the colleagues in the Surface Physics and Materials Research departments at IPP, and the innumerable discussions, make the scientific life at IPP very agreeable. Pars pro toto I would like to mention Dr. Klaus Schmid who is always ready to discuss new ideas, accompany others through the fog around them, and enlighten everyone with a few unconventional passing comments.

The experimental work was made possible by our skilled and cooperative technical staff. During the construction of Artoss, in particular J. Schäftner contributed with ingenious ideas and tremendous dedication to realize the challenging requirements. Over the years, all technical staff members contributed in solving our small and not-so-small technical problems, and they all do this with an utmost degree of proficiency. It is J. Dorner's and M. Fußeder's merit, that operation of the tandem accelerator is always reliable and smooth.

Finally, I would like to thank our cooperation partners outside IPP for many discussions and stimulating new insights. On the experimental part, I would like to mention Dr. R. Doerner and his crew from UCSD, San Diego. On the theory part, I gratefully acknowledge to collaborations with Dr. T. Jacob, now at University Ulm, and Dr. A. Allouche from Université de Provence, Marseille.

Original Publications

Chapter 2 — Experimental approach

1. Ch. Linsmeier, P. Goldstraß, and K.U. Klages
   ARTOSS — A new surface science experiment to study the hydrogen inventory in multi-component materials
   Phys. Scripta T94 (2001) 28.
   (Ref. [62], p. 110)

Chapter 3 — Carbon layers on metal

2. A. Wiltner, Ch. Linsmeier, and T. Jacob
   Carbon reaction and diffusion on Ni(1 1 1), Ni(1 0 0), and Fe(1 1 0): Kinetic parameters from x-ray photoelectron spectroscopy and density functional theory analysis
   J. Chem. Phys. 129 (2008) 084704.
   (Ref. [106], p. 116)

3. A. Wiltner and Ch. Linsmeier
   Thermally induced reaction and diffusion of carbon films on Ni(1 1 1) and Ni(1 0 0)
   Surf. Sci. 602 (2008) 3623.
   (Ref. [96], p. 126)

4. M. Reinelt and Ch. Linsmeier
   Enhanced room temperature erosion of ultra-thin carbon films on beryllium, titanium and tantalum by deuterium ions
   Nucl. Instrum. Methods B 258 (2007) 270.
   (Ref. [117], p. 136)

5. Ch. Linsmeier
   Carbon-containing compounds on fusion-related surfaces: thermal and ion-induced formation and erosion
   AIP Conference Proceedings 740 (2004) 182.
   (Ref. [87], p. 140)

6. A. Wiltner and Ch. Linsmeier
   Formation of endothermic carbides on iron and nickel
   Phys. Status Solidi (a) 201 (2004) 881.
   (Ref. [88], p. 156)

7. Ch. Linsmeier, J. Luthin, K.U. Klages, A. Wiltner, P. Goldstraß
   Formation and erosion of carbon-containing mixed materials on metals
   Phys. Scripta T111 (2004) 86.
   (Ref. [86], p. 164)

8. K. Schmid, A. Wiltner, and Ch. Linsmeier
   Measurement of beryllium depth profiles in carbon
   Nucl. Instrum. Methods B 219–220 (2004) 947.
   (Ref. [111], p. 170)

9. Ch. Linsmeier, J. Roth, and K. Schmid
   Formation and erosion of mixed materials
   IAEA Atomic and Plasma-Material Interaction Data for Fusion, Vol. 12 (2003) 79.
   (Ref. [85], p. 176)

10. K.U. Klages, A. Wiltner, J. Luthin, and Ch. Linsmeier
    Deuterium bombardment of carbon and carbon layers on titanium
    J. Nucl. Mater. 313–316 (2003) 56.
    (Ref. [116], p. 194)

11. J. Luthin, H. Plank, J. Roth, and Ch. Linsmeier
    Ion beam induced carbide formation at the Ti–C interface
    Nucl. Instrum. Methods B 182 (2001) 218.
    (Ref. [115], p. 200)

12. J. Luthin and Ch. Linsmeier
    Characterization of electron beam evaporated carbon films and compound formation on titanium and silicon
    Phys. Scripta T91 (2001) 134.
    (Ref. [90], p. 210)

13. P. Goldstraß, K.U. Klages, and Ch. Linsmeier
    Surface reactions on beryllium after carbon vapor deposition and thermal treatment
    J. Nucl. Mater. 290–293 (2001) 76.
    (Ref. [110], p. 214)

14. P. Goldstraß and Ch. Linsmeier
Formation of mixed layers and compounds on beryllium due to C^+ and CO^+ ion bombardment
J. Nucl. Mater. 290–293 (2001) 71.
(Ref. [119], p. 218)

15. Ch. Linsmeier, J. Luthin, and P. Goldstraß
Mixed material formation and erosion
J. Nucl. Mater. 290–293 (2001) 25.
(Ref. [84], p. 224)

16. J. Luthin and Ch. Linsmeier
Carbon films and carbide formation on tungsten
Surf. Sci. 454–456 (2000) 78.
(Ref. [89], p. 232)

17. P. Goldstraß and Ch. Linsmeier
Combined ion and electron spectroscopy study of the surface reactions of beryllium with carbon
Nucl. Inst. Methods B, 161–163 (2000) 411.
(Ref. [109], p. 238)

Chapter 4 — Atomic oxygen

18. Ch. Linsmeier and J. Wanner
Reactions of oxygen atoms and molecules with Au, Be, and W surfaces
Surf. Sci. 454–456 (2000) 305.
(Ref. [127], p. 242)

Chapter 5 — Beryllium–tungsten alloy formation

19. Ch. Linsmeier, K. Ertl, J. Roth, A. Wiltner, K. Schmid, F. Kost, S.R. Bhattacharyya, M. Baldwin, and R.P. Doerner
Binary beryllium-tungsten mixed materials
J. Nucl. Mater. 363–365 (2007) 1129.
(Ref. [168], p. 248)

20. A. Wiltner, F. Kost, S. Lindig, and Ch. Linsmeier
Structural investigation of the Be–W intermetallic system
Phys. Scripta T128 (2007) 133. (Ref. [169], p. 258)

21. A. Wiltner and Ch. Linsmeier
    Surface alloying of thin beryllium films on tungsten
    New J. Phys. 8 (2006) 181.
    (Ref. [167], p. 262)

22. A. Wiltner and Ch. Linsmeier
    Formation of a surface alloy in the beryllium-tungsten system
    J. Nucl. Mater. 337–339 (2005) 951.
    (Ref. [166], p. 274)

Chapter 6 — Ternary surface reactions

23. F. Kost, Ch. Linsmeier, M. Oberkofler, M. Reinelt, M. Balden, A. Herrmann, and S. Lindig
    Investigation of chemical phase formation in the ternary system beryllium, carbon and tungsten with depth-resolved photoelectron spectroscopy
    J. Nucl. Mater. 390–391 (2009) 975.
    (Ref. [71], p. 280)

24. J. Luthin and Ch. Linsmeier
    Influence of oxygen on the carbide formation on tungsten
    J. Nucl. Mater. 290–293 (2001) 121.
    (Ref. [174], p. 284)

25. P. Goldstraß, W. Eckstein, and Ch. Linsmeier
    Erosion of beryllium and deposition of carbon and oxygen due to the bombardment with C^+ and CO^+ ions
    J. Nucl. Mater. 266–269 (1999) 581.
    (Ref. [118], p. 290)

Chapter 7 — Hydrogen inventory in beryllium

26. M. Oberkofler, M. Reinelt, A. Allouche, S. Lindig, and Ch. Linsmeier
    Towards a detailed understanding of the mechanisms of hydrogen retention in beryllium
    Phys. Scr. (2009) accepted.
    (Ref. [370], p. 296)

27. M. Oberkofler, M. Reinelt, S. Lindig, Ch. Linsmeier
Structure-dependent deuterium release from ion implanted beryllium: comparison between Be(1 1 $\bar{2}$ 0) and Be(poly)
Nucl. Instrum. Methods B 267 (2009) 718.
(Ref. [371], p. 312)

28. M. Reinelt and Ch. Linsmeier
Ion implanted deuterium retention and release from clean and oxidized beryllium
J. Nucl. Mater. 390–391 (2009) 568.
(Ref. [363], p. 318)

29. M. Reinelt, A. Allouche, M. Oberkofler, and Ch. Linsmeier
Retention mechanisms and binding states of deuterium implanted into beryllium
New J. Phys. 11 (2009) 043023.
(Ref. [362], p. 322)

30. M. Reinelt and Ch. Linsmeier
Temperature programmed desorption of 1 keV deuterium implanted into clean beryllium
Phys. Scripta T128 (2007) 111.
(Ref. [359], p. 342)

Physica Scripta. T94, 28–33, 2001

ARTOSS – A New Surface Science Experiment to Study the Hydrogen Inventory in Multi-Component Materials

Christian Linsmeier*, Peter Goldstraß and Konrad U. Klages

Max-Planck-Institut für Plasmaphysik, EURATOM Association, Boltzmannstr. 2, D-85748 Garching bei München, Germany

Received June 26, 2000; accepted February 2, 2001

PACS Ref: 68.35.Fx, 66.30.Ny, 82.65.-i, 82.80.Ms, 82.80.Pv, 82.80.Yc

Abstract

The design of a new instrument is described along with results demonstrating the capabilities of *in situ* preparation and analysis. The purpose of the ARTOSS experiment is the preparation and analysis of multi-component surface layers on materials – in particular those which are well-suited for the first wall of present and future fusion devices – and their behaviour with respect to the hydrogen inventory in such materials. Relevant preparation and analysis techniques are combined to achieve this aim. For preparation, surfaces can be cleaned *in situ* and layer preparation includes vapour deposition, ion beam bombardment at energies between 100 eV and 20 keV as well as admission of gases. Photoelectron spectroscopies analyse the chemical state of elements within the surface layers, ion beam techniques enable quantitative measurements, including hydrogen isotope analysis. For ion beam analysis, low-energy (up to 5 keV) as well as high-energy ions (3 MV tandem accelerator) are available *in situ*. Thermal desorption and re-emission measurements complete the capabilities for hydrogen detection in multi-component materials. Sample transfer into the ultra-high vacuum system is possible via a sample load-lock. Results are presented for carbon layers on beryllium and surface modifications of beryllium by C^+ and CO^+ ion bombardment to demonstrate the capabilities of the new experiment.

1. Introduction

Understanding the mechanisms affecting the hydrogen inventory in first wall materials in fusion experiments is crucial for plasma control and safety issues. In future fusion devices, plasma density control relies on precise knowledge of the factors affecting the pumping and release of hydrogen in the first wall materials. An understanding of the processes governing the accumulation of tritium in first wall materials is also essential for radiation protection and control purposes. As a consequence of a multi-material first wall in fusion devices, mixed surface layers are formed due to erosion and re-deposition [1]. The accumulation and release behaviour of hydrogen is modified by these surface layers. In particular, diffusion, recombination and desorption processes are affected. The design of ARTOSS allows the preparation of samples as well as analysis with well-suited techniques of surface science in one chamber under ultra-high vacuum (UHV) conditions.

While the Fast Transfer System in JET [2], equipped with ion beam analysis as well as photoelectron spectroscopy techniques, allowed the *in vacuo* analysis of exposed tiles in JET, ARTOSS is designed to not only analyse but also prepare mixed materials under well defined conditions.

2. Apparatus

The apparatus consists of three chambers and a load lock. Chamber I holds a low energy ion source for implantation, chamber II contains a bending magnet for mass separation of the low energy ion beam. The ultra-high vacuum chamber III, the main target chamber, is equipped with the facilities to prepare and analyse samples.

2.1. *Chamber I: Ion source 1*

The ion source (IS 1) is used to generate an ion beam from gaseous precursor materials for implantation and sputter cleaning of samples in chamber III. Ionisation is achieved by electron impact from an incandescent filament. Ion energies are between 1 keV and 20 keV with an energy width of about 3 eV [3]. Chamber I can be isolated from chamber II by a mechanical valve. Ion lenses and steering plates allow to form the ion beam and to steer it into the bending magnet. A special steering plate allows to blank the beam by applying an appropriate voltage. In conjunction with a detector system fitted to the main chamber III, this allows time-of-flight ion beam analysis [3].

2.2. *Chamber II: Bending magnet*

In chamber II the ion beam from IS 1 is deflected through 80° by a bending magnet into the main target chamber III. Thus, a mass separated monoenergetic beam is available. The chamber is equipped with an ion pump (PHI Captorr 640 l/s) and a turbomolecular pump. The ion beam of the 3 MV tandem accelerator is guided through chamber II, with the bending magnet switched off. The chamber also acts as a differential pumping stage between the accelerator beam line (typical pressure 10^{-6} Pa), the ion source chamber I and the UHV target chamber III. The magnet current is controlled by a Hall probe and field controller (Bruker B-H 15) outside the vacuum chamber in the centre of the magnet.

2.3. *Chamber III: Main target chamber*

A schematic side view of the main target chamber is shown in Fig. 1. It is equipped with a turbomolecular pump to maintain a base pressure of below $1 \cdot 10^{-8}$ Pa after baking. With a Ti sublimator and a liquid nitrogen cooling trap the base pressure can be reduced to below $5 \cdot 10^{-9}$ Pa during experimental operations.

The keV (from IS 1) and MeV (from the tandem accelerator) ion beams are guided towards the sample in the centre of chamber III through an ion optical system. It has two operational modes: It is used to focus the keV ion beams by electrostatic lenses and to decelerate the keV ion beam from IS 1 down to energies below 100 eV. The lens system is based on [4] and is optimised for the ARTOSS geometry by SIMION [5]. The keV or decelerated ion beams may be scanned across the sample with two pairs

*Corresponding author: e-mail: linsmeier@ipp.mpg.de

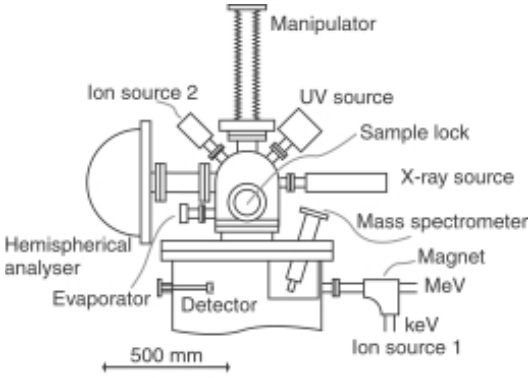

Fig. 1. Schematic side view of the main target chamber. The components are drawn in one plane for the purpose of demonstration.

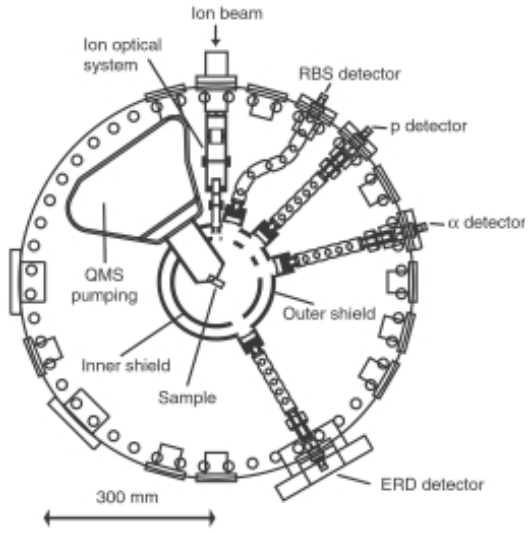

Fig. 2. Installations in the ion beam analysis plane. Shown are the double cylinder Faraday cup, the QMS differential pumping stage, the ion optical lens and the four surface barrier detectors.

of deflection plates at the exit of the lens system. In addition to prepare multi-component materials by ion implantation, the chamber can be backfilled with gases through a leak valve. For vapour deposition of solid materials an electron evaporation source (Omicron EFM3, with external Fug power supply) is available.

In the plane of the beam lines from IS 1 and the 3 MV tandem accelerator four bakeable silicon surface barrier detectors (Eurisys Measurements) are installed at scattering angles of 165°, 135°, 105° and 30° for Rutherford backscattering (RBS), nuclear reaction analysis (NRA) and elastic recoil detection (ERD), respectively. The layout of these detectors is shown in Fig. 2. In particular the 135°, 105° and 30° detectors are well-suited for hydrogen isotope analysis. ERD detects target atoms recoiled by MeV ions (e.g. 2.7 MeV ^{4}He or 24 MeV ^{28}Si), while NRA allows depth profiling of deuterium by the ^{3}He(d,p)^{4}He reaction. For precise sample current measurements, the sample is shielded by a double cylinder Faraday cup with dimensions large compared to the sample size. The outer cylinder is at ground potential. During ion beam analysis and implantation, the inner cylinder is biased with respect to the sample to collect secondary electrons and reflected charged particles. Therefore, the inner cylinder is included in the sample current measurement (Keithley 6517A electrometer or Ortec 439 digital current integrator).

Further techniques to study the hydrogen isotope inventory and interaction with multi-component materials are available with a line-of-sight quadrupole mass spectrometer (adapted version of Balzers QMG 422). The ioniser is coplanar with the ion beam plane. The mass spectrometer is housed in a differential pumping stage within the main chamber III, pumped by two sequential turbomolecular pumps to increase the compression for light particles. A movable cone with an entrance aperture of the size of the sample diameter (12 mm) is placed directly in front of the sample during thermal desorption spectroscopy (TDS) or direct re-emission measurements. The differential pumping stage lowers the background pressure around the mass spectrometer, which is particularly important during direct re-emission measurements. In these experiments, the sample is implanted by an ion beam through the ion optical lens system through a channel in the collector cone, while the mass spectrometer detects particles emitted from the sample. To discriminate directly emitted particles from background particles, a tuning-fork chopper interrupts the particle flux from the sample periodically (about 10 Hz) and the mass spectrometer signal is detected by a lock-in amplifier. For TDS measurements, the chopper does not obscure the line-of-sight between sample and quadrupole ioniser. When not in use, the bottom plate of the differential pumping stage with the collector cone is opened and the cone does not obstruct the ion beam analysis equipment.

Above the ion beam analysis plane surface analysis and preparation equipment is installed in a second plane. For sample cleaning by sputtering and for sputter depth profiling, a second ion source (IS 2, Specs IQ 12/38) is available. Up to four different gases are available simultaneously and are dosed by means of a leak valve. The chamber is equipped with two photon sources: An ultraviolet source (VSI/Specs UVS 300) for valence band spectroscopy (ultraviolet photoelectron spectroscopy, UPS) employing He I and He II radiation and an X-ray gun (PHI, model 04-548) with Al and Mg anodes for core level spectroscopy (X-ray photoelectron spectroscopy, XPS). All ion and photon sources are confocal with the entrance lens system (PHI Omni Focus III) of the hemispherical electrostatic analyser (PHI, model 10-360). The analyser is equipped with a multi-channel detector for fast data acquisition. Both positive ions and electrons can be analysed. Thus, low-energy ion scattering spectroscopy (ISS) with monolayer surface sensitivity is possible.

The sample may be positioned through the computer-controlled manipulator in all three dimensions, as well as rotated about the vertical axis. On the lower end of the manipulator a Faraday cup (aperture 0.5 mm) is available to enable the determination of the intensity, the precise pos-

ition as well as the profiles of the ion beams. Three permanently mounted reference materials (gold, silver, highly oriented pyrolytic graphite) are used for energy calibration. Samples can be heated by a filament which is mounted on the sample holder as well as cooled through a liquid nitrogen reservoir which is mounted to the manipulator.

The samples are mounted on a transferable support which also contains a filament for electron bombardment heating, contacts for thermocouples (chromel-alumel) and a separate connection for sample current measurements. The whole unit can be transferred from the load lock to the central manipulator. Therefore, filament exchanges or broken thermocouples can be repaired without breaking the vacuum in the main chamber. Sample temperatures between below 200 K and above 1000 K are easily accessible. The cooling system is particularly useful during TDS experiments to bring the sample back to low temperatures after a desorption run.

The sample transfer into the main vacuum chamber passes through a differentially pumped load lock. Up to three samples can be stored in parking positions where they may already be annealed before transfer into the main chamber. The base pressure in the load lock after extended pumping is below $5 \cdot 10^{-7}$ Pa.

3. Preparation of multi-component surface layers

Samples may be cleaned by noble gas sputtering from IS 2 at keV ion energies, also during sample annealing. In a beryllium single crystal it was possible to reduce the oxygen impurity to below 10^{14} cm^{-2} by Ar^+ and He^+ ion bombardment. Multi-component surface layers can be created through vapour deposition with the electron beam evaporation source as well as by implantation of ions with energies ranging from below 100 eV (operating the electron optical system in deceleration mode) to 20 keV using IS 1. During deposition of carbon from a high-purity (99.999%) source the pressure does not exceed $5 \cdot 10^{-8}$ Pa.

The ion implantation experiments on beryllium described below employed CO_2 (Linde 4.5) as source gas both for C^+ and CO^+ ions. CO as source gas leads to larger beam currents, however, the CO in the residual gas leads to adsorbed C and O (both up to 4%) on the Be surface. On the sample, beam currents of 50 nA are reached for a C^+ beam, whereas for CO^+ currents up to 400 nA are possible. Figure 3 shows a contour plot of the C^+ implantation spot after 5 mC implantation, measured by scanning XPS analysis spots over the implantation zone. The circular shape of the implantation spot can be observed. The shape can be interpreted as a convolution of a homogeneous circular implantation spot with the XPS analysis spot. This agreement confirms the design of the ion optical lens for beam formation without using an aperture close to the sample surface. During ion implantation, the pressure in the main chamber stays below $2 \cdot 10^{-8}$ Pa.

4. Analysis

The set-up of ARTOSS allows *in situ* analysis with a variety of techniques which have been chosen to investigate various properties of multi-component surface layers. Analysis

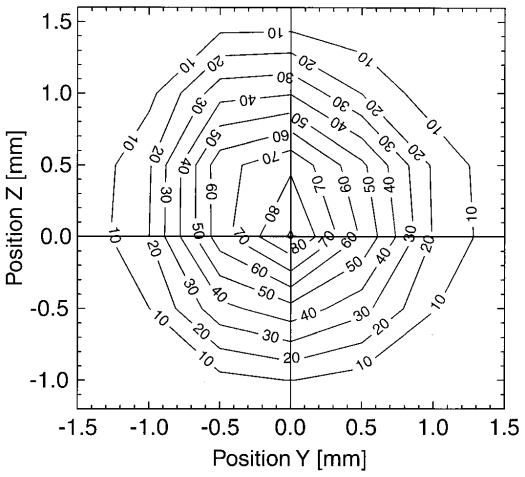

Fig. 3. Contour plot of the implantation spot after 5 keV C^+ ion bombardment. Data points are scanned XPS measurements with an analysis spot size of 0.8 mm. The numbers in the contour lines indicate relative C 1s intensities.

has so far concentrated on X-ray and ultraviolet photoemission spectroscopy (XPS, UPS) as well as ion beam techniques.

Photoemission spectroscopy yields information on the composition and on the chemical state of the constituents of the multi-component surface layers. For the photoemission experiments an X-ray source and a UV source are available. The emitted photoelectrons are detected and analysed in the electrostatic hemispherical analyser with an electrostatic deflection of 180°. Both constant pass energy (FAT, fixed analyser transmission) and fixed retarding ratio (FRR) modes are employed.

Ion beam techniques allow the determination of depth profiles of deposited and implanted ions. These techniques yield absolute quantities of the composition of surface layers. The standard ion beam analysis used in ARTOSS so far is Rutherford backscattering (RBS) at a scattering angle of 165°.

While XPS is very sensitive in the top several monolayers, the range of RBS is considerably deeper (several hundred nm to some μm, depending on ion species and primary energy). It is, however, not possible to obtain information on very thin surface layers which XPS can detect. Therefore, XPS and RBS not only complement each other in elemental and chemical state information, but also with respect to quantitative analysis. XPS is sensitive at very low coverages down to small fractions of a monolayer. Up to several monolayers, both methods provide quantitative information with similar accuracy and this coverage region allows a comparison of both methods. At surface layers with thicknesses well above the inelastic mean free path of the photoelectrons RBS is still able to probe the layer thickness with large accuracy. Figure 4 shows a comparison of both methods for carbon films deposited on beryllium. Below the inelastic mean free path of the photoelectrons (depicted in Fig. 4 as horizontal lines for Be 1s and C 1s photoelectrons) both RBS and XPS results agree well. For thicker carbon layers,

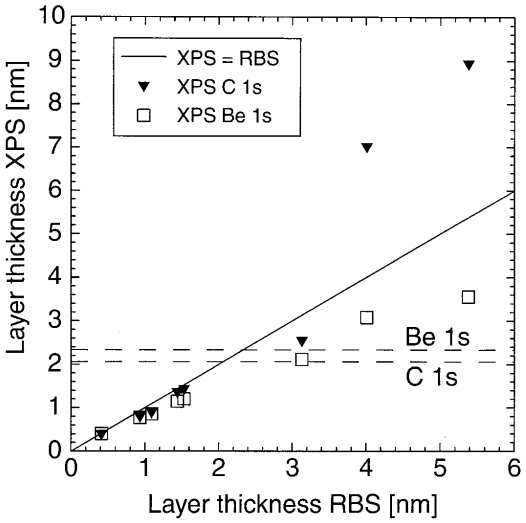

Fig. 4. Carbon layer thickness obtained from the XPS C 1s and Be 1s signals versus the thickness from the RBS signal. The broken lines indicate the inelastic mean free paths of C 1s and Be 1s photoelectrons in carbon.

RBS is the method of choice, since for XPS not only inelastic mean free paths limit the information depth, but also the layer morphology is crucial for quantification of thick layers. The combination of XPS and RBS has been applied successfully to characterise mixed carbidic and oxidic surface layers on beryllium. It is, however, not possible to detect hydrogen with these techniques.

To study the effect of these layers on the hydrogen inventory in metals with mixed material surface layers the apparatus is therefore equipped with three further surface barrier detectors for elastic recoil detection (ERD, scattering angle 30°) and nuclear reaction analysis (NRA, 135° and 105°) as well as the line-of-sight quadrupole mass spectrometer (QMS). This QMS makes it possible to apply thermal desorption spectroscopy (TDS) by heating the sample with a constant temperature gradient. Furthermore, re-emission of hydrogen may be investigated. The desorbed and re-emitted particles can be modulated with a chopper operating at around 10 Hz and a lock-in amplifier. This set-up will make it possible to quantify and eliminate the background from the signal. A similar set-up has been used at KFA Jülich previously to study the hydrogen inventory in carbon-based materials [6,7].

Due to its low mass, hydrogen cannot be detected by RBS under backscattering geometries. It is, however, possible to detect recoiling hydrogen in the forward direction. The set-up of ARTOSS therefore includes an ERD counter at 30° scattering angle. For ERD, the sample is bombarded with projectiles (e.g. 2.7 MeV ^{4}He or 24 MeV ^{28}Si) in a geometry where incoming and outgoing trajectories are 75° to the surface normal. The detector is designed to detect recoiling H isotopes while scattered He ions are not detected. This can be achieved by covering the counter with a thin foil (e.g. 15 μm stainless steel) which may only be penetrated by the recoiling H isotopes. This set-up makes it possible to obtain depth profiles of hydrogen without background signals.

For NRA, the nuclear reaction

$$D + {}^3He \rightarrow p + {}^4He + 18.352\ MeV$$

is used to determine depth profiles of deuterium in a sample. The reaction has a broad resonance at an energy around 640 keV for the incoming ^{3}He ions. Detectors are mounted at scattering angle of 135° and 105°. The 135° detector is covered by a 0.1 mm stainless steel foil such that only the high-energy protons from the nuclear reaction are detected, while the 105° detector is located such that it detects ^{4}He at a shallow exit angle. The solid angle of the 105° detector is $3 \cdot 10^{-3}$sr. While the large area 135° proton detector quickly yields quantitative information on the amount of deuterium in the surface of the sample, a depth profile of the deuterium may be obtained through analysis of the ^{4}He detected at 105° due to the shallower exit angle and thus a longer path through the sample [8]. Using a 800 keV ^{3}He beam, the accessible depth in graphite is about 1500 μm [9].

5. Results: carbon/beryllium and C^+ and CO^+ bombardment of beryllium

So far, the experiments in ARTOSS have been performed on Be single crystals with (0001) orientation. The formation of multi-component surface layers has been studied for carbon vapour deposition and ion bombardment with monoenergetic C^+ and CO^+ ions at energies ranging from 3 keV to 12 keV. The interaction between ions, deposited carbon and the substrate material is studied by means of RBS, XPS and UPS.

Vapour-deposited carbon layers on beryllium were subject to annealing experiments up to 773 K. The carbide formation at the interface was studied for different carbon layer thicknesses by XPS, UPS and RBS. Results are presented in detail elsewhere [10]. For very thin carbon amounts below $3.7 \cdot 10^{15}$ C atoms/cm^2 RBS is unable to detect carbon while XPS can already detect a signal. Up to a layer thickness of 1–3 nm, XPS and RBS agree quantitatively. Above, RBS is used to measure the carbon amount. It is found that deposited carbon reacts with beryllium to form carbide (Be_2C) readily at room temperature. The carbide layer, however, is restricted to the interface between carbon and beryllium. At 300 K, the carbide formation is limited to a carbon amount of $6 \cdot 10^{15}$ C atoms/cm^2, which corresponds to about 6 monolayers. Larger amounts of carbon are deposited as elementary carbon (graphite). The formation of the carbide at elevated temperatures is seen both in XPS and UPS. Figure 5 shows valence band spectra of a clean Be surface and after deposition of $1.042 \cdot 10^{17}$ C atoms/cm^2. The spectra are excited by He I radiation, the analyser is operated in the FRR mode. The clean spectrum shows the Fermi edge of the clean metallic substrate and small intensity maximum between 5 and 10 eV binding energy which may be due to a very small O contamination, also detectable by XPS. After C evaporation a peak develops around 7 eV. This is attributed to σ bonds in carbon [11] and indicates graphitic carbon at the surface. This is due to the high surface sensitivity of UPS, induced by the attenuation

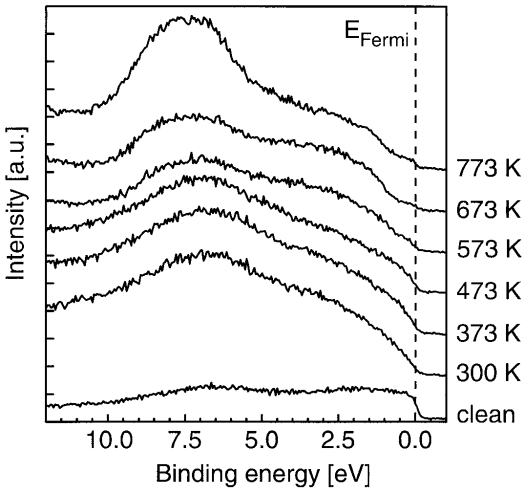

Fig. 5. Valence band spectra measured with He I excitation of carbon films evaporated on a Be (0001) single crystal. The spectra are recorded after annealing the sample to the indicated temperatures.

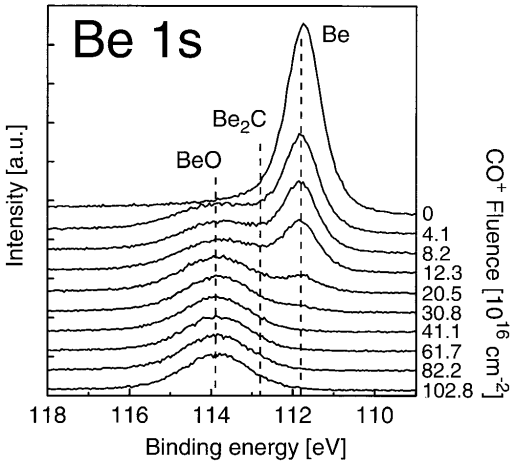

Fig. 6. Series of XPS spectra in the Be 1s region of a Be (0001) sample, implanted with the CO^+ fluence indicated to the right. Plotted are raw data, without background subtraction. The lines indicate the binding energies for metallic Be, BeO and Be_2C.

of the low-energetic photoelectrons from the valence band. At 573 K intensity around 2 eV develops which indicates Be_2C at the surface [12,13]. XPS measurements after 673 K annealing indicate that all C has reacted to carbide. This is confirmed by UPS by the intensity decrease at the Fermi edge. The spectrum exhibits a band gap of about 1.2 eV, which is consistent with Be_2C (001) single crystal experiments [12,13]. The increasing oxygen contamination at the surface for higher annealing temperatures leads to the intensity maximum in the UPS spectra between 5 and 10 eV. In summary, the carbon deposited on beryllium forms a limited carbide layer at the C-Be interface at 300 K. Upon annealing, the elementary carbon successively reacts with the Be substrate under Be_2C formation. The annealing temperature determines the amount of formed carbide, provided that there is sufficient elementary carbon available. RBS measurements after annealing up to 973 K prove that no carbon is lost into the bulk beryllium. Further details are discussed in [10].

The bombardment of a beryllium surface with CO^+ ions simulates the co-bombardment of the first wall of a fusion experiment with carbon and oxygen particles from the plasma. Whereas for pure C^+ bombardment a carbon surface layer on the beryllium is formed and therefore Be erosion terminates, CO^+ bombardment establishes a deposition/erosion equilibrium. This leads to a continuous erosion of the beryllium [14]. The chemical interaction of the ions with Be and therefore the reason for the deviation from a mere kinematic particle-solid interaction is studied by XPS and UPS in addition to RBS measurements. A Be (0001) single crystal is bombarded with 5 keV CO^+ ions under normal incidence. By RBS the total amounts of C and O in the surface after certain implantation fluences are quantified and the formation of a Be-C-O mixed surface layer is confirmed. The XPS spectra in the Be 1s regime are shown in Fig. 6 after the implantation steps. Mg Kα radiation is employed, the analyser is operated in FAT mode with a pass energy of 23.5 eV. The spectrum before ion bombardment only shows a peak at 111.8 eV which is metallic Be. All subsequent spectra have intensity at higher binding energies indicating a chemical reaction of metallic beryllium. From reference experiments we determined the Be 1s binding energies for BeO and Be_2C to be 113.9 eV and 112.8 eV, respectively. Using this information, the Be 1s spectra can be fitted unambiguously with these three contributions. An example for a CO^+ implantation fluence of $8.2 \cdot 10^{16}$ cm^{-2} is shown in Fig. 7. The experimental data points are connected by a dashed line which is the sum of the Shirley background and the three peaks, drawn as solid lines. The fine line around the background curve indicates the difference between data points and fit. All XPS spectra in Fig. 6 were fitted similarly. From these fits it can be concluded that Be_2C is only present in the initial phase of the ion bombardment. The Be_2C concentration has a maximum at approximately $1 \cdot 10^{17}$ cm^{-2} and is no more detectable after $4 \cdot 10^{17}$ cm^{-2}. After this fluence, all Be detectable by XPS is chemically bound to oxygen forming BeO. This fluence corresponds to the transition from the C, O inventory build-up to the deposition/erosion equilibrium observed earlier [14]. The conclusion from the photoelectron spectroscopy measurements is that the formed mixed Be-C-O surface layer consists of BeO, elementary carbon and some additional C-O compounds like carbonates, which cannot be discriminated further. All Be in the surface layer is BeO and Be_2C only exists as long as not enough oxygen is available to react with the available beryllium. Further details of this investigation are presented elsewhere [15].

6. Summary and outlook

The new experiment ARTOSS combines all relevant techniques to prepare and study multi-component materials rel-

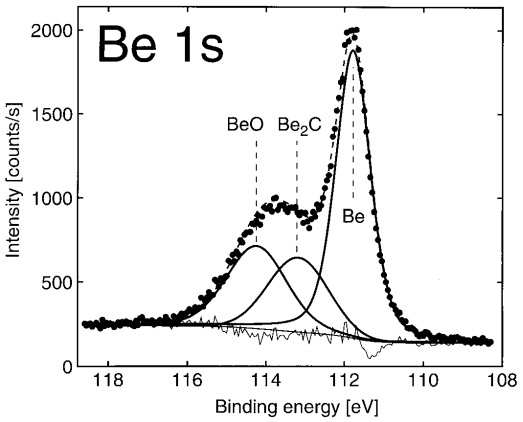

Fig. 7. XPS spectrum of a Be (0001) surface after CO^+ implantation of $8.2 \cdot 10^{16}$ cm^{-2}. The points are the raw data. The binding energies for Be in different chemical states are indicated. The fit results for these three states are plotted as solid lines and their sum is represented by the dashed line beneath the data points. The Shirley background and the deviation between measured data and fit are also given.

evant for the first wall of present and future fusion devices. The main target chamber facilitates sample preparation and analysis under UHV conditions. Sample transfer into UHV is possible by means of a sample load-lock. Preparation options include gas admission, sample heating and cooling, vapour deposition by evaporating materials and sample bombardment with mass-analysed ion beams at energies between 100 eV and 20 keV. Analysis techniques comprise of photoelectron spectroscopies (UPS and XPS), ion beam spectroscopies (both low-energy ions up to 5 keV and ions from a 3 MV tandem accelerator) and particle desorption and re-emission analysis by means of a line-of-sight mass spectrometer in a differentially pumped stage. Experiments have been conducted to study the surface chemistry of beryllium with carbon and oxygen. Carbon layers on beryllium have been produced by vapour deposition and carbidisation processes were studied at different substrate temperatures. The deposition and erosion behaviour of beryllium under C^+ and CO^+ ion bombardment has been investigated. Further studies will focus on the influence of carbidic and oxidic surface layers on beryllium on the hydrogen inventory in this material. This will be done by implantation of hydrogen at various energies into beryllium substrates with well-defined surface layers. The inventory, re-emission and erosion/deposition processes during these treatments will be studied by photoelectron and ion beam spectroscopies as well as by thermal desorption measurements. All measurements are carried out in situ and some can be performed simultaneously during the sample treatments.

Acknowledgements

It is a pleasure to acknowledge the excellent engineering and technical skills of S. Bassen, J. Schäftner and A. Holzer without whom the design and construction of this complex experimental set-up would not have been possible. In the design of the line-of-sight QMS installation the discussions with E. Vietzke were of great help.

References

1. Linsmeier, Ch., Luthin, J. and Goldstraß, P., J. Nucl. Mater. **290–293**, 25 (2001).
2. Coad, J. P., *et al*. J. Nucl. Mater. **176&177**, 145 (1990).
3. Aratari, R. and Eckstein, W., Nucl. Instr. Meth. Phys. Res. B **42**, 11 (1989).
4. Liebl, H., Bohdansky, J., Roth, J. and Dose, V., Rev. Sci. Instrum. **58**, 1830 (1987).
5. Dahl, D., SIMION 3D V. 6.0, 43rd ASMS Conf. Mass Spectrometry and Allied Topics, Atlanta (1995).
6. Vietzke, E., Flaskamp, K. and Philipps, V., J. Nucl. Mater. **111&112**, 763 (1982).
7. Franzen, P., Vietzke, E., Haasz, A. A., Davies, J. W. and Philipps, V., J. Nucl. Mater. **196–198**, 967 (1992).
8. Roth, J. and Scherzer, B. M. U., J. Nucl. Mater. **93&94**, 601 (1980).
9. Franconi, E., Rubel, M. and Emmoth, B., Nucl. Fusion **29**, 787 (1989).
10. Goldstraß, P., Klages, K. U. and Linsmeier, Ch., J. Nucl. Mater. **290–293**, 76 (2001).
11. Schelz, S., Richmond, T., Kania, P., Oelhafen, P. and Güntherrodt, H., Surf. Sci. **359**, 227 (1996).
12. Tzeng, C., Tsuei, K. and Lo, W., Phys. Rev. B **58**, 6837 (1998).
13. Tzeng, C., Yuh, J., Lo, W., Chu, R. and Tsuei, K., Surf. Sci. **423**, 232 (1999).
14. Goldstraß, P., Eckstein, W. and Linsmeier, Ch., J. Nucl. Mater. **266–269**, 581 (1999).
15. Goldstraß, P. and Linsmeier, Ch., J. Nucl. Mater. **290–293**, 71 (2001).

THE JOURNAL OF CHEMICAL PHYSICS **129**, 084704 (2008)

Carbon reaction and diffusion on Ni(111), Ni(100), and Fe(110): Kinetic parameters from x-ray photoelectron spectroscopy and density functional theory analysis

A. Wiltner,[1] Ch. Linsmeier,[1,a)] and T. Jacob[2]
[1]*Max-Planck-Institut für Plasmaphysik, EURATOM Association, Boltzmannstrasse 2, D-85748 Garching b. München, Germany*
[2]*Fritz-Haber-Institut der Max-Planck-Gesellschaft, Faradayweg 4-6, D-14195 Berlin, Germany*

(Received 20 February 2008; accepted 22 July 2008; published online 25 August 2008)

This paper investigates the reactivity of elemental carbon films deposited from the vapor phase with Fe and Ni substrates at room temperature. X-ray photoelectron spectroscopy (XPS) measurements are presented as a method for evaluating kinetic reaction data. Carbon films are deposited on different surface orientations representing geometries from a dense atom packing as in fcc (111) to an open surface structure as in fcc (100). During annealing experiments several reactions are observed (carbon subsurface diffusion, carbide formation, carbide decomposition, and graphite ordering). These reactions and the respective kinetic parameters are analyzed and quantified by XPS measurements performed while annealing at elevated temperatures (620–820 K). The resulting activation barriers for carbon subsurface diffusion are compared with calculated values using the density functional theory. The determined kinetic parameters are used to reproduce the thermal behavior of carbon films on nickel surfaces. © *2008 American Institute of Physics*.
[DOI: 10.1063/1.2971177]

I. INTRODUCTION

The investigation of diffusion and segregation as well as the determination of kinetic parameters of carbon in Fe and Ni are reported in literature by several authors. The resulting activation barriers differ strongly. Most diffusion barriers given in the literature are determined as bulk values. A summary about diffusion barriers and diffusivity of carbon in Fe and Ni is given in Ref. 1. Diamond and Wert[2] analyzed the carbon diffusion by the anelastic behavior of C dissolved in Ni and determined an activation barrier of 1.5 eV between 370 and 800 K. Massaro and Petersen[3] investigated ^{14}C films after ethylene decomposition on polycrystalline Ni samples and determined a smaller diffusion barrier of 0.87 eV between 620 and 970 K. In a short comment Berry[4] confronted this value with 1.73 eV, determined above 970 K, and suggested one activation barrier applicable at all temperatures. This assumption is in agreement with density functional theory (DFT) calculations by Siegel and Hamilton.[5] The authors calculated the bulk diffusion barrier for carbon migration along octahedral sites (1.75 eV) and along octahedral via tetrahedral sites (1.62 eV). The latter value seemed to be more favorable. In addition, they determined different heats of solution for carbon in paramagnetic and ferromagnetic nickel (Curie temperature T_C=627 K). Diamond and Wert[2] observed in their first measurements a negligible effect of the magnetic state on the diffusion barrier. The values given above represent activation barriers for carbon diffusion in bulk material. Schouten *et al.*[6,7] investigated the carbon dissolution through different Ni planes by Auger electron spectroscopy (AES) measurements. They determined diffusion barriers of 1.54 eV (370–770 K) on Ni(110) and 1.21 eV (474–563 K) on Ni(100). The carbon films were deposited by methane decomposition in the given temperature ranges. On Ni(111) the authors could not deposit carbon films by this procedure. Sau and Hudson[8] deposited carbidic and graphitic carbon films on Ni(110) by ethylene decomposition at temperatures between 575 K (carbidic carbon films) and 775 K (graphitic carbon films) and analyzed them by AES measurements. For graphitic carbon films they determined a diffusion barrier of 3.9 eV above 883 K. At lower temperatures the dissolution process did not follow a first order reaction and an activation barrier was not determined. Moreover, they did not determine a diffusion barrier for the carbidic carbon layer due to slow carbon dissolution. DFT calculations of carbon films on different Ni planes are not reported by now. As mentioned above, the diffusion barriers for carbon dissolution into Ni through different surface planes were determined after hydrocarbon decomposition reactions. In this work we deposit elemental carbon films from the vapor phase while keeping the substrates at room temperature (RT). This facilitates the analysis of carbon diffusion from the surface to subsurface positions (initial step for carbon bulk diffusion) without the need of any additional decomposition reaction.

Carbon diffusion in Fe was reported in the literature by several authors. Due to the rearrangement of the Fe lattice from α-Fe [body-centered cubic (bcc)] to γ-Fe [face-centered cubic (fcc)] at temperatures above 1010 K, different activation barriers are expected.[9] Between 500 and 890 K the diffusion barrier (0.8 eV) follows an Arrhenius behavior, whereas at higher temperatures the linear dependence is no longer observed.[1] McLellan and Wacz[10] summarized the

a)Electronic mail: linsmeier@ipp.mpg.de.

TABLE I. Free energy of formation at 300 K (Ref. 18) for carbides described in Refs. 14–17—Fe_3C and Ni_3C—Refs. 21 and 28.

Carbide	ΔG_f^0 (eV)
TiC	−1.87
Be_2C	−1.19
SiC	−0.73
WC	−0.40
W_2C	−0.23
Fe_3C	+0.21
Ni_3C	+0.66

available experimental values for carbon diffusion in α- and γ-Fe. The average diffusion barrier in α-Fe is determined to 0.84 eV. DFT calculations for carbon bulk diffusion in both lattice structures are in good agreement with these experimental values (0.86 eV for α-Fe).[11] The diffusion barriers given in literature are again bulk values, whereas this work focuses on the surface-subsurface diffusion as the elementary step in C dissolution. Dissolution measurements of carbon films on different Fe planes and a determination of diffusion barriers are not reported to our knowledge. Moreover, DFT calculations considering the Fe surface orientation are not available in the literature.

Carbon films deposited by thermal hydrocarbon or carbon monoxide decomposition on Fe and Ni surfaces are investigated with respect to their use as catalysts (e.g., Ref. 12). A recent review by Hwu *et al.*[13] provided a comprehensive overview of the chemical reactions between transition metal carbide surfaces and a variety of inorganic and organic molecules. In this work we investigate the interaction of elemental carbon films deposited on Fe and Ni surfaces with different surface structures. The formation reaction of the respective carbides (Fe_3C and Ni_3C) are endothermic, in contrast to almost all other carbides. We already studied the thermal behavior of elemental carbon films on W, Ti, Si, and Be.[14–17] These elements form carbides in an exothermic formation reaction. For Ni_3C and Fe_3C, however, the enthalpies of formation are positive, and the formation reaction is therefore endothermic.[18] The respective values of the carbide formation reactions (free energy of formation and Gibbs function ΔG_f^0) are given in Table I. In addition to the reactivities of Fe and Ni with C, the metal and carbide structures have to be taken into account in the discussion of mobilities of species during solid state reactions. Si and Be form carbides with a prominent ionic bond character.[19] In agreement with this, we do not observe a dissolution of the carbon layers into the bulk at high temperatures.[14,17] The carbides, once formed, are stable in their carbon-metal stoichiometries up to 900 K (Be_2C) and 1100 K (SiC), respectively. All other substrates investigated up to now and discussed in this work form metallic (intercalation) carbides with carbon atoms in different sites within the metal lattices. The Ti lattice with a hexagonal close packing (hcp) possesses octahedral sites large enough for carbon atom incorporation. TiC is formed if all octahedral sites are filled by carbon atoms.[20] However, not all available sites are occupied by carbon atoms and therefore stoichiometric TiC (Ti:C=1:1) is not observed in real crystals. The maximum stoichiometric ratio reported in literature is $TiC_{0.95}$.[9] A successive filling of octahedral sites by carbon atoms leads to subcarbides (Ti_xC_y, $y<x$). Both species (TiC and subcarbides) are observed in our experiments.[17] Metallic W has a bulk bcc structure. The octahedral sites within this metal lattice are too small for carbon atom incorporation.[19] Therefore, the metal lattice rearranges during carbide formation. W_2C, tungsten subcarbide, is observed after W rearrangement into a hcp structure with carbon atoms in $\frac{1}{2}$ of octahedral sites.[20] The tungsten carbide, WC, is created by a rearrangement of W into a hexagonal primitive packing with carbon atoms in trigonal prismatic sites.[20] In previous experiments performed in our group, both carbides are observed.[17] W_2C is stable between 1100 and 1300 K, whereas WC is formed above 1300 K. Both in Ti and W binary systems with carbon, the carbide formation starting with layers on the metals is accompanied by carbon diffusion. The incorporation of carbon atoms in sites within the metal lattice requires carbon migration in agreement with this observation. Moreover, the amount of formed carbide agrees with the tendency of the Gibbs free energy for the carbide formation reaction (see Table I). Furthermore, the onset in carbon diffusion complies with the tendency of the respective diffusion barriers (bulk values) for these metals. Ti (1.3 eV) shows the lowest onset temperature, followed by W (1.8 eV).[1]

In the temperature region investigated in this work, Fe has a bcc structure (α-Fe).[9] The octahedral sites are again too small for carbon atom incorporation.[19] During carbide formation, the metal lattice has to rearrange into a orthorhombic structure, in which the carbon atoms occupy trigonal prismaticlike sites.[20,21] In the case of Ni_3C formation, the metal lattice (fcc) rearranges into a hcp structure (similar to W_2C) with carbon atoms in octahedral sites.[20,21] From these structure data, we expect a similar thermal behavior of carbon films on W, Ti, Fe, and Ni. The endothermic carbide formation reactions of Fe_3C and Ni_3C should lead to different carbide amounts after RT deposition and in annealing experiments.

Experimentally, we select x-ray photoelectron spectroscopy (XPS) analysis using monochromatic Al $K\alpha$ radiation and carry out carbon deposition with thicknesses from submonolayer to several nanometers. The high surface sensitivity of XPS with information depths of several nanometers allows us to perform chemical state analysis from the film surface, the film-substrate interface, to the first substrate layers. Therefore, XPS promises a detailed examination of the surface reaction steps and analysis of the influence of the surface orientation on them.

II. METHODS

A. Surface preparation and analysis

The measurements are performed in a PHI ESCA 5600 XPS system equipped with an additional preparation chamber. Both vacuum systems are connected via an UHV valve to allow for sample transfer without air contact. The analysis chamber has both a standard (Mg and Al $K\alpha$) and a monochromatic (Al $K\alpha$, $h\nu$=1486.6 eV) x-ray source. It is equipped with an ion gun (Specs IQE 12/38) and provides a

base pressure better than 2×10^{-8} Pa. Using the monochromatic x-ray source a resolution of 0.26 eV is achieved in XPS spectra. The analysis spot is 0.8 mm in diameter. We calibrate the binding energy by measuring gold (Au $4f_{7/2}$: 84.00 eV), silver (Ag $3d_{5/2}$: 368.3 eV), and copper (Cu $2p_{3/2}$: 932.7 eV) peaks.[22] All binding energies given in this paper are referenced to the Au $4f_{7/2}$ peak position.

The preparation chamber (base pressure better than 2×10^{-8} Pa) contains a commercial evaporation source (Omicron EFM3) operated with additional power supplies for carbon deposition. The carbon layers are deposited from the vapor phase by electron beam evaporation from a graphite rod (Goodfellow, 99.999%). During the deposition procedure the substrates are held at RT (pressure better than 3×10^{-7} Pa). A quadrupole mass spectrometer is used for residual gas analysis.

Carbon films are deposited on Ni and Fe single crystal substrates. The Ni (1 cm in diameter) and Fe crystals (0.5 cm in diameter) are used after mirror-finish polishing. We use the Ni(111), Ni(100), and Fe(110) surface orientations as examples for surface atom densities from dense to open surface atom packings [surface atom density: Ni(111)>Fe(110)>Ni(100)]. The substrates are cleaned by sputtering (3 kV Ar^+) and annealing (970 K) cycles until no impurities are detected in the XPS spectra. After surface preparation the carbon films are deposited with film thicknesses up to several nanometers followed by XPS analysis. The pass energy of the XPS system is set to 93.90 eV for survey scans and 2.95 eV for high resolution spectra in order to deconvolute components in the C 1*s* binding energy regions. X-ray source and analyzer entrance axis are arranged at an angle of 90°. To achieve highest signal intensity with best information rate originating from the interface region, we orient the sample to a takeoff angle of 22° with respect to the surface normal. After the carbon film characterization at RT (~300 K) the samples are annealed in two experimental procedures (denoted as A and B in this paper). During procedure A, the samples are annealed in steps of 50–100 K up to 970 K by holding the sample at each temperature for 30 min. After cooling down to RT the samples are analyzed again with survey and high resolution scans. This procedure A allows us to analyze the chemical phases that are accessed by the respective annealing temperatures. Details are given in a separate publication.[28] In order to determine kinetic parameters we use procedure B. In this experimental strategy samples are held at different elevated temperatures for several hours. The samples are analyzed while annealing using survey and high resolution scans (only C 1*s* signal) alternatingly. The survey scans are used for thickness (carbon amount) evaluation, while the high resolution scans enable the deconvolution of the C 1*s* signals and from this a determination of kinetic parameters for the occurring reactions. The determination of carbon film thicknesses uses both the carbon and substrate signals and is described elsewhere in detail.[28] The C 1*s* signals are analyzed using a commercial software package [MULTIPAK (Ref. 23)]. For the fit procedure of the components within the C 1*s* signal, we apply Gauss–Lorentz lineshapes and use a Shirley-type background. The metal signals are not analyzed in detail.

B. DFT calculations

The calculations on carbon diffusion were performed with SEQQUEST,[24,25] a periodic DFT program with localized basis sets. As exchange-correlation functional we used the PBE generalized gradient approximation.[26] While the core electrons of each metal atom were replaced by an optimized, norm-conserving pseudopotential,[27] the remaining valence electrons were treated explicitly with a contracted double zeta plus polarization basis set of Gaussian functions, which had been optimized for the atom and solid. Throughout the studies we used a Brillouin zone sampling of 10×10 k points for the corresponding 1×1 surface unit cells, which had been carefully checked for convergence.

All calculations were performed with a six-layer slab, where the last two layers were fixed to their calculated bulk crystal structures, while the remaining four layers plus the carbon atom (except the direction of diffusion) were fully optimized (to <0.01 eV/Å). Due to the dipole correction employed in SEQQUEST, the diffusion was explored on one side of the slab only. The process itself was studied with a 2×2 surface unit cell, resulting in 0.25 ML coverage, by successively pushing the carbon atoms into the surface and reoptimizing the system in each step. Due to the low number of degrees of freedom, we found this procedure to be more appropriate than using transition state finding methods.

III. RESULTS AND DISCUSSION

A. Carbon films after RT deposition and annealing experiments, applying procedure A

A detailed characterization of carbon films on Ni(111), Ni(100), and Fe(110), both after RT deposition and after annealing applying procedure A (including the description of their interactions with the substrates), is presented elsewhere.[21,28] Here, we give a brief summary. Although the Ni_3C and Fe_3C formation reactions from the elements are endothermic, a small carbide intensity after RT deposition on the metal substrates (Fe and Ni) is observed. The RT reactivity is higher on Fe(110) compared to the two Ni substrates, Ni(111) and Ni(100), which show similar reactivities. The carbide intensity is restricted to the carbon-metal interface and amounts to 1 ML at maximum. Signatures of the carbide formation are found in the layer (C 1*s*) and substrate (Ni $2p_{3/2}$, Fe $2p_{3/2}$) signals, respectively, as well as the valence band region. The carbide intensity is observed in the C 1*s* signal as binding energy shifts of −0.7 eV (Ni_3C) and −0.8 eV (Fe_3C), compared to the graphite peak position at 284.2 eV. Both metal signals, as well as the intensity maximum in the valence band region, show a small shift toward higher values (ΔBE=+0.2 eV). The C 1*s* signals are dominated by the elemental signals, besides which a small carbide peak is observed. This elemental (not reacted) carbon consists of a graphitic and a disordered graphitic fraction. The latter component is observed at 285.1 eV (ΔBE=+0.9 eV). This peak component is assigned to a disordered graphitic structure since its intensity increases with ion bombardment (e.g., Ar^+) and decreases during annealing treatments. For a detailed description we refer to Ref. 17.

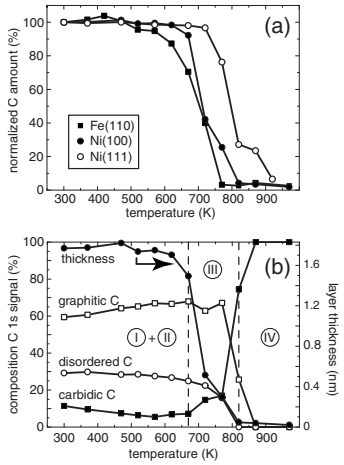

FIG. 1. Normalized carbon amount of carbon films on Fe(110) (■), Ni(100) (●), and Ni(111) (◯) in (a) after annealing steps according to experimental procedure A (see text). The carbon diffusion sets in at 620, 670, and 770 K, respectively. Within a temperature range of 150 K the carbon is almost completely lost into the metal bulk on all three surfaces. The C 1*s* signal composition of a 1.8 nm carbon layer on Ni(100) with increasing annealing temperature is plotted in (b). Up to 570 K carbide decomposition [reaction (I)] is visible. The ordering reaction [reaction (II)] is observed up to 670 K. The carbon diffusion [reaction (III)] sets in at 670 K, accompanied by carbon loss into bulk material and increasing carbide intensity (carbide formation reaction). After the pronounced carbon diffusion the remaining carbon signal is caused by carbon segregation [reaction (IV)].

The thermal behavior applying procedure A is illustrated in Fig. 1. In panel (a) carbon films on all three metal surfaces investigated in this study are compared. The carbon amounts are normalized to the value after RT deposition (300 K). In Fig. 1(a) the onset of carbon diffusion is visible as a loss of carbon from the near-surface region into the metal bulk and therefore out of the XPS information depth (the amount drops below 94% of the initial value). On Fe(110) the carbon diffusion sets in at 620 K, followed by Ni(100) at 670 K and Ni(111) at 770 K. The onset temperature corresponds to the tendency of the activation barriers for carbon bulk diffusion given in literature, as summarized in Table II.[1] Furthermore, the trend in the onset temperature reflects the surface atom densities in the series (100)<(111) for the two nickel surfaces. In Fig. 1(b) the details of the temperature evolution in the carbon layer thickness and the C 1*s* details are shown for a carbon film on Ni(100) with an initial thickness of 1.8 nm. The evolution of the carbon layer thickness is equivalent to the normalized curve in Fig. 1(a). As described above, carbidic and elemental carbon species are identified within the C 1*s* signal. The latter carbon component consists of the graphitic and disordered graphitic fractions. The evolution with annealing temperature of the carbon species in the different chemical environments indicates three regions of different chemical reactions. These temperature regions and the reactions within are labeled by (I)–(IV). Reaction (I) describes the decomposition of carbide, indicated by the carbide signal intensity decrease up to 570 K. Since the carbon layer thickness is unaffected and therefore carbon subsurface or bulk diffusion can be excluded in this temperature region, we refer this behavior to a carbide decomposition reaction. The carbide decomposition is also observed on Fe(110) and Ni(111) and is explained by the metastable character of the respective surface carbides, which are created during the carbon layer deposition at RT. Parallel to the carbide decomposition reaction (I), we identify an ordering reaction (II) within the elemental carbon signals. This reaction is observed on all substrates investigated by now (Au, W, Ti, Si, Be, Fe, and Ni).[14–16,21] The ordering reaction leads to a decrease of the disordered graphitic carbon intensity and is observed until carbon diffusion through the interface into the bulk substrate (reaction III) sets in. While the total carbon signal decreases (due to carbon bulk diffusion), the relative intensity of the carbide signal increases. We assign this relative increase to the carbide formation reaction, producing additional carbide in the surface zone. As mentioned above, the respective carbides are intercalation compounds with carbon atoms in sites within the metal lattice. Therefore, carbon diffusion is required for carbide formation. The relative increase in carbide signal intensity depends on the substrate surface. On Fe(110) and Ni(100) we observe after pronounced carbon diffusion only signal intensity originating from carbidic carbon, while on Ni(111) elemental carbon is still detected up to 920 K. Above the onset temperature of the carbon bulk diffusion, the C 1*s* signal intensity is almost completely lost. The remaining carbon amounts to less than 1 ML and is explained by carbon segregation [reaction (IV)] while cooling down to RT from the respective annealing temperature. The remaining C 1*s* signal after the last annealing step at 970 K exhibits only carbidic carbon on Fe and

TABLE II. Activation energies resulting from experimental data (E^{expt}) and DFT calculations (E^{DFT}), as determined in this work, or given in literature (E^{lit}) for carbon diffusion in the bulk metals (E_D), carbide formation (E_C), and graphite ordering reactions (E_O). The precision of E_O is estimated to ±0.2 eV by calculating the model with several energies. For all other experimental energy values the statistical uncertainty is given.

Substrate	E_D^{expt} (eV)	E_D^{DFT} (eV)	$E_{D,bulk}^{lit}$ (eV)	$E_{D,bulk}^{DFT,lit}$ (eV)	E_C^{expt} (eV)	E_O^{expt} (eV)
Ni(111)	1.9 ± 0.1	1.92	1.5[a,b]	1.62/1.75[c]	1.1 ± 0.4	0.9
Ni(100)	1.4 ± 0.1	1.45	1.5[a,b]	1.62/1.75[c]	1.3 ± 0.2	0.9
Fe(110)	1.3 ± 0.2	1.44	0.8[a]	0.86[d]	1.1 ± 0.2	0.9

[a]Reference 1.
[b]Reference 2.
[c]Reference 5.
[d]Reference 11.

both Ni surfaces. In all experiments carried out according to procedure A, the thermal behavior (i.e., the characteristic onset temperature for the identified reactions) of the thin carbon films depends only on the substrate species and surface structure, and not on the initially deposited carbon layer thickness (investigated up to several nanometers).

From the annealing experiments according to procedure A, we conclude the identification of reactions (I)–(IV). The carbide formation reaction and the carbon diffusion take place in the same temperature regime. Therefore, they can only barely be discerned in this experimental strategy (procedure A). Since we are interested in the respective kinetic parameters for these reactions, we continue with annealing experiments according to procedure B.

B. Determination of kinetic parameters, applying procedure B

Carbon films with initial layer thicknesses of several nanometers are deposited on Fe(110), Ni(100), and Ni(111). These samples are then annealed at several elevated temperatures, which are selected according to the results of procedure A experiments. During the long-term annealing the samples are analyzed at the respective elevated temperatures by XPS. As described in Sec. III A, the different reactions are identified within the changes in the C $1s$ signals, whereas the substrate signals (Fe $2p$ and Ni $2p$) provide no additional information on the change of chemical nature. The first analysis step is the determination of the carbon layer thickness after RT deposition, while annealing, and again at RT after each thermal treatment. It is determined from survey spectra (acquisition time ~5 min), using both substrate and layer signal intensities from the same spectrum. We determine the mean free paths for C $1s$ (λ_C^C) and metal photoelectrons (λ_M^C) passing through the carbon layer by using the empirical fit given in Ref. 29. The respective values are $\lambda^C_{C\ 1s}=1.494$ nm, $\lambda^C_{Fe\ 2p_{3/2}}=1.201$ nm, and $\lambda^C_{Ni\ 2p_{3/2}}=1.082$ nm. For a detailed description of the carbon layer thickness determination, we refer to Ref. 28.

Since the carbon signal decrease depends on the carbon loss into the bulk, i.e., the carbon diffusion through the film-bulk interface, we can use the carbon layer thicknesses (determined from survey spectra) for a quantification of this reaction. The evolution of the carbon layer thickness at elevated temperatures provides the kinetic parameter k_D for reaction (III), which is the carbon subsurface diffusion. The correlation between $d_{C\ 1s}$ (total thickness in nanometers) and k_D (in s^{-1}) is given by

$$-\frac{d[d_{C\ 1s}]}{dt}=k_D(T)d_{C\ 1s}\rightarrow \ln\frac{d_{C\ 1s}}{d_{C\ 1s,0}}=-k_D(T)t. \qquad (1)$$

The respective initial conditions are as follows: $d_{C\ 1s}$ is the carbon layer thickness at each time t at temperature T and $d_{C\ 1s,0}$ is the carbon layer thickness at $t=0$ and temperature T. Thereby we assume a first order reaction for carbon diffusion. In Fig. 2 the evolution of $\ln(d_{C\ 1s}/d_{C\ 1s,0})$ with annealing time is plotted for Ni(111), Ni(100), and Fe(110) in (a), (b), and (c), respectively. For the highest temperatures in panels (b) and (c) the assumption of a first order reaction is

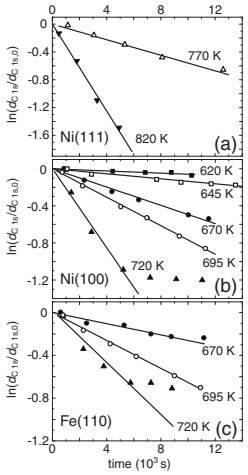

FIG. 2. Determination of $k_D(T)$ using the time-dependent evolution of the carbon layer thickness at different temperatures on Ni(111) in (a), Ni(100) in (b), and Fe(110) in (c). The decrease of the layer thickness is plotted under an assumption of a first order reaction ($\ln[d_{C\ 1s}/d_{C\ 1s,0}]$ vs t).

valid only up to an annealing time of ~6000 s. Above, a deviation from the linear fit is observed. All other values comply with the linear behavior in the logarithmic plot, justifying the first order assumption. Under the assumption of an Arrhenius behavior of $k_D(T)$, we can determine the respective activation barrier for carbon subsurface diffusion (E_D) as given by

$$k_D(T)=k_0\exp\left(-\frac{E_D}{k_BT}\right). \qquad (2)$$

Here, k_0 (in s^{-1}) is the pre-exponential factor, k_B is the Boltzmann constant, and T is the temperature (in Kelvin). The Arrhenius plots in Fig. 3 show the linear behavior of $\ln k(T)$ with T^{-1} for Ni(100) and Fe(110). In the case of Ni(100) and Fe(110), we use for the highest temperatures the data up to 6000 s with a clearly linear relationship between $\ln(d_{C\ 1s}/d_{C\ 1s,0})$ and t (Fig. 2). For Ni(111) only two measurements are available at 770 and 820 K and are used for the determination of E_D. The resulting experimentally determined activation barriers E_D^{expt} for all three surfaces are given in Table II.

During the experiments according to procedure B, alternatingly spectra in survey and high resolution modes are measured. The C $1s$ spectra in high resolution mode (acquisition time 7–10 min) are measured several times consecutively, followed by one survey spectrum for the determination of the carbon layer thickness. For the total C $1s$ signal intensity we use the time evolution of carbon layer thicknesses, which result from the $k_D(T)$ time dependence [Eq. (1)]. As mentioned above, we deconvolute the C $1s$ signal with an elemental (not reacted) and a carbidic carbon fraction. The elemental carbon consists of graphitic and disordered graphitic C. We determine the thicknesses of these fractions within the total C $1s$ signal under the assumption

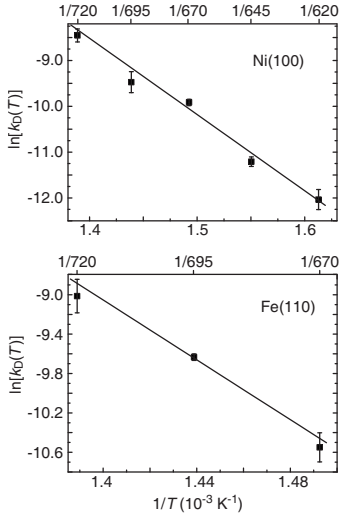

FIG. 3. Determination of the diffusion barrier (E_D) under the assumption of an Arrhenius behavior for Ni(100) and Fe(110) [see Eq. (2)]. The resulting activation barriers are given in Table II.

of equally distributed components in the carbon layer and relate the fraction intensities to the respective thicknesses.

Figure 4 shows a schematic overview of the reactions identified within annealing procedure A, as described above in Sec. III A. These reactions are analyzed in detail with annealing experiments according to procedure B. The determination of the kinetic parameters for reaction (III) (k_D and E_D) are given above. The other reactions are analyzed with the following assumptions and correlations.

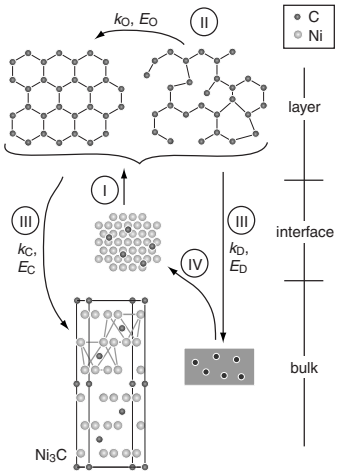

FIG. 4. Illustration of the reactions identified within annealing experiments according to procedure A (see Fig. 1), as an example shown for carbon layers on Ni(111). The respective kinetic parameters for reactions (II), ordering reaction, and (III), carbon subsurface diffusion and carbide formation, are determined by experiments according to annealing procedure B.

- Decomposition of the initially formed carbide [reaction (I)] leads to an increase in elemental carbon, in particular, to an increase of the graphitic component.
- The ordering reaction (II) within the elemental carbon leads to a decrease in disordered graphitic C.
- Carbon subsurface diffusion [reaction (III)] leads to loss in signal intensity of all components of the C 1s signal.
- Carbide formation [parallel to reaction (III)] leads to an additional decrease in the elemental carbon intensity.
- Carbon segregation [reaction (IV)] while cooling down to RT leads to an increase in total C 1s signal intensity and to an increase of the carbidic signal.

The last process [reaction (IV), carbon segregation] can be neglected because the XPS spectra are measured at elevated temperatures and carbon segregation is only observed while cooling down to RT. Since carbon films are analyzed at elevated temperatures higher than 570 K, also the carbide decomposition reaction (I) can be neglected because it occurs only at temperatures below 570 K. The other reactions (ordering reaction and carbide formation) can be analyzed by XPS measurements using procedure B.

The carbide formation reaction is quantified by analyzing the decrease of elemental carbon and the total C 1s signal intensities. Since the carbide formation is accompanied by carbon diffusion, these reactions are correlated as given by

$$\frac{d[d_{\mathrm{carb}}]}{dt} = \frac{d[d_{\mathrm{C\ 1}s}]}{dt} - \frac{d[d_e]}{dt} = k_{\mathrm{C}}(d_{\mathrm{C\ 1}s} - d_e). \tag{3}$$

Here, d_{carb} is the thickness of the carbidic fraction, $d_{\mathrm{C\ 1}s}$ is the total carbon layer thickness, and d_e is the respective elemental carbon layer thickness (all thicknesses are given in nanometers). From this equation k_{C} is determined, which describes the loss of elemental carbon due to carbide formation. Both thicknesses ($d_{\mathrm{C\ 1}s}$ and d_e) are additionally affected by carbon diffusion (k_D). Solving Eq. (3) under consideration of the carbon layer thickness [Eq. (1)] leads to

$$d_e(t) = e^{(k_{\mathrm{C}}t)}[d_{e,0} + d_{\mathrm{C\ 1}s,0}(-1 + e^{-(k_{\mathrm{C}}+k_D)t})]. \tag{4}$$

Using the time-dependent evolution of d_e with the initial conditions ($d_{\mathrm{C\ 1}s}|_{t=0} = d_{\mathrm{C\ 1}s,0}$ and $d_e|_{t=0} = d_{e,0}$), the k_{C} values at the annealing temperatures T are determined. Figure 5 shows the decrease of normalized d_e with annealing time t on Ni(111) in (a), Ni(100) in (b), and Fe(110) in (c). The lines in the plots result from Eq. (4), using the determined $k_{\mathrm{C}}(T)$ and $k_D(T)$ values. Assuming again an Arrhenius behavior, E_{C} is determined as described in Eq. (2). The resulting values are given in Table II.

Similar to the approach described before, the ordering reaction is analyzed using the respective interdependent car-

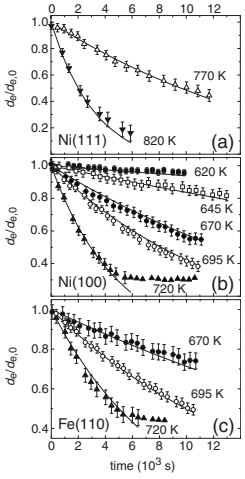

FIG. 5. Determination of $k_C(T)$ using the decrease of elemental carbon at different temperatures on Ni(111) in (a), Ni(100) in (b), and Fe(110) in (c). The lines given in the panels are evaluated using Eq. (4). The resulting activation barriers (E_C) are given in Table II.

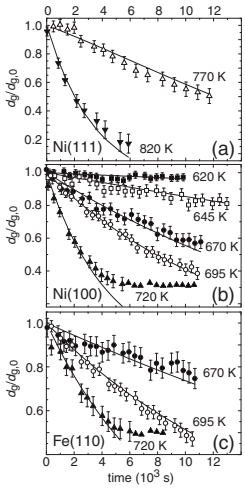

FIG. 6. Decrease of graphitic carbon at different temperatures on Ni(111) in (a), Ni(100) in (b), and Fe(110) in (c). The lines result from Eq. (6) using the described assumptions for the ordering reaction within the elemental carbon. The activation barriers (E_O) are given in Table II.

bon fractions and k values. In a first step the evolution of the disordered graphitic fraction within the elemental carbon signal d_{dis} is defined, as given by

$$\frac{d[d_{\mathrm{dis}}]}{dt} = \frac{d[d_e]}{dt} - \frac{d[d_g]}{dt} = -k_O(d_e - d_g). \tag{5}$$

The respective parameters are the thicknesses of graphitic carbon (d_g), total elemental carbon (d_e), and k_O, the kinetic parameter for the ordering reaction. Moreover, the correlation between d_e and $d_{\mathrm{C}\ 1s}$ has to be accounted for. Both the graphitic carbon and the disordered fraction are affected by carbon subsurface diffusion (k_D) and carbide formation (k_{C}). Therefore, the graphitic fraction increases by the ordering reaction but decreases with carbon diffusion and carbide formation. Solving Eq. (5) by using these conditions leads to

$$d_g(t) = e^{-(k_O t)}[d_{g,0} + d_{e,0}(-1 + e^{(k_{\mathrm{C}}+k_O)t}) + d_{\mathrm{C}\ 1s,0}(-e^{(k_{\mathrm{C}}+k_O)t} + e^{(-k_D+k_O)t})]. \tag{6}$$

The initial conditions are as mentioned above: $d_{\mathrm{C}\ 1s}|_{t=0} = d_{\mathrm{C}\ 1s,0}$, $d_e|_{t=0} = d_{e,0}$, and $d_g|_{t=0} = d_{g,0}$. This equation includes all kinetic parameters (k_D, k_{C}, and k_O). Figure 6 shows the decrease in graphitic carbon ($d_g/d_{g,0}$) with annealing time t of carbon films on Ni(111) in (a), Ni(100) in (b), and Fe(110) in (c). The lines represent the values resulting from Eq. (6), which lead, again under an assumption of an Arrhenius behavior [Eq. (2)], to the respective E_O values. Since the ordering reaction is a process within the carbon layer, it should be independent of the substrate and should give the same E_O values for all substrates. As summarized in Table II, the activation barriers are identical within the experimental precision for the three substrate surfaces, confirming the confinement of the ordering reaction to the carbon layer.

The carbide decomposition reaction and carbon segregation are not determined by XPS measurements using procedure B. All other reactions are analyzed with the described assumptions. Section III C presents calculations using the DFT in order to verify the resulting kinetic parameters.

C. DFT calculations

In order to simulate the process of carbon diffusion from the surface into the material on the three surfaces of this work, each study is started with initially optimizing a carbon adsorbate layer. After this preoptimization the adsorbates are successively pushed into the surface and the energy is mapped. Since diffusion into the surface induces certain strain to the surface atoms, a coverage of 0.25 ML (2×2 surface unit cell) is assumed, giving enough freedom to the surface atoms. To ensure that the system is (almost) not constrained by the simultaneous diffusion of the periodic images, we also performed similar calculations with finite clusters, finding the same behavior.

First, the diffusion of carbon into Ni surfaces is studied, which have either (111) or (100) orientation. Starting with the hexagonal close packed (111) surface plane, where carbon preferentially adsorbs on fcc sites and forms three equivalent C–Ni bonds with $a(\mathrm{C-Ni}) = 1.83$ Å, we observe that during the diffusion carbon pulls one of the nearby Ni atoms (see Ni_1 in Fig. 7) out of the surface plane by almost 0.7 Å. Through the thus opened "hole", the carbon atom migrates to octahedral subsurface sites, with an effective energy barrier of 1.92 eV, which nicely compares to the experimentally determined E_D of 1.9 eV. Since the vacant octahedron offers enough space for the carbon, after this *out-of-plane* process Ni_1 equilibrates back to the surface layer. By diffusing into the surface the system gains an overall energy

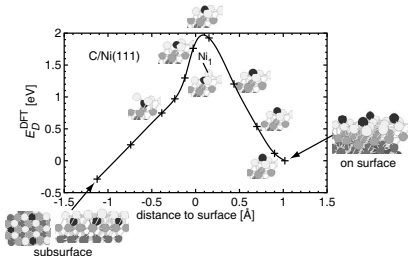

FIG. 7. Theoretical activation energy E_D^{DFT} as a function of the distance of carbon to the surface layer for Ni(111) (referenced to the adsorbed system). The curve is obtained by overlapping the curves for diffusion into the surface and afterward diffusion back onto the surface. While for the initial (surface) and final (subsurface) structures an extended system is shown, the process itself is sketched with figures of various intermediate structures with a 2×2 unit cell only. The process shown here is comparable to the C diffusion into Fe(110). (Lines to guide the eyes.)

of 0.29 eV per C atom. In order to further manifest the transition state, the process and energy barrier are afterward verified by calculations modeling the reverse diffusion back to the surface.

Carbon diffusion into the Ni(100) plane was investigated in an analogous way (see Fig. 8). In contrast to Ni(111), where at the fcc site there is no Ni atom below in the second layer, in the case of Ni(100) the direct vertical diffusion is hindered by a second Ni atom below. Consequently, the vertical migration is accompanied by a horizontal diffusion, by which again one Ni atom (Ni_1 in Fig. 8) is pushed out of the surface layer by 1.1 Å, finally allowing carbon to occupy a nearby bipyramidal subsurface site. The energetic barrier is calculated to be 1.45 eV, which is in very good agreement with the measured value of 1.4 eV. This value is again verified by checking the reverse process. Since Ni(100) is a relatively open surface compared to Ni(111), the calculated and measured diffusion barriers are in much better correspondence to the energetic barrier for bulk diffusion. Similar to Ni(111) it is found that having carbon in subsurface positions is 0.31 eV per carbon more stable than adsorbed on the surface.

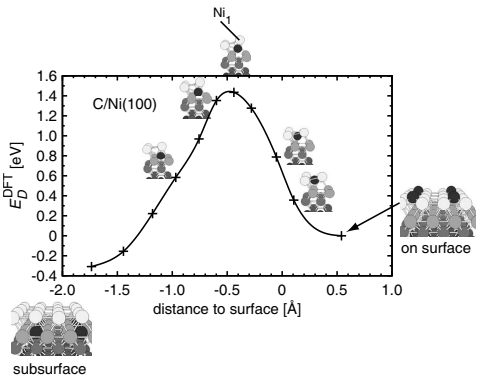

FIG. 8. Theoretical activation energy E_D^{DFT} as a function of the distance of carbon to the surface layer for Ni(100) (referenced to the adsorbed system). The curve is obtained by overlapping the curves for diffusion into the surface and afterward diffusion back onto the surface. While for the initial (surface) and final (subsurface) structures an extended system is shown, the process itself is sketched with figures of various intermediate structures with a 2×2 unit cell only. (Lines to guide the eyes.)

Finally, the carbon subsurface diffusion step into Fe(110) is studied and a similar out-of-plane process is discovered, as already described for Ni(111). Therefore, only the obtained diffusion barrier of $E_D^{DFT}=1.44$ eV is reported. Motivated by the experiment, further studies will aim at investigating the carbide formation process.

D. Discussion

The reactions identified within the experimental procedure A are analyzed in detail by annealing carbon films at elevated temperatures for several hours (procedure B). The C 1*s* signal intensity corresponds to the total carbon layer thickness. Analyzing the evolution of this intensity with annealing time at different temperatures provides the quantification of carbon diffusion into the metal substrate. A first, more qualitative assumption concerning carbon diffusion results from the onset temperature in procedure A (see Sec. III A). In accordance with the tendency of the respective literature bulk diffusion values, an earlier onset on Fe(110) compared to Ni is observed. The two Ni surfaces also differ in their onset temperature for carbon diffusion. As expected, the more open surface structure of Ni(100) shows a lower diffusion onset temperature compared to Ni(111), representing the most dense surface atom packing.

As shown in Sec. III B, the determination of the subsurface diffusion barriers using procedure B for these three surfaces is successful. The decrease of surface carbon amounts corresponds to a first order reaction and the evolution of layer thicknesses with annealing time complies with this. In the case of Ni(100) and Fe(110) we observe a deviation from a first order reaction kinetics only for the highest temperature investigated here (720 K). This observation is explained by the experimental procedure. We deposit thin films on the substrate and lose the carbon through diffusion into the bulk. However, the solubility of carbon atoms in Ni and Fe is small. This is observed in our experiments as carbon segregation while cooling down to RT, already also known from literature.[9,19] The small solubility of C in Fe and Ni was already used for surface enrichment experiments and the measurement of bulk to surface diffusion and segregation, respectively, applying AES and low-energy electron diffraction (LEED) analyses.[30–33] Furthermore, this behavior indicates a diffusion reaction comprising of multiple elemental processes that, however, cannot be observed separately in our experiments. For carbon diffusing from the surface into the bulk metal (i.e., reaching an interstitial site in the metal lattice), in a first step the surface barrier has to be overcome in order to occupy subsurface positions. These interstitial positions within the metal lattice are energetically separated by an energy barrier that describes the diffusion of carbon atoms within the bulk. A carbon atom in a subsurface (first "bulk" position below the surface) interstitial site can diffuse

through the lattice if the diffusion barrier energy is available. In our analysis we do not distinguish between these two activation barriers and describe the carbon diffusion from the surface layer into the bulk as one process. The qualitative justification for this description lies in the argument that the activation barrier for surface-subsurface diffusion is larger than for the bulk diffusion. Therefore, if at a given temperature subsurface diffusion is possible, this is also the case for the bulk diffusion steps. The results for the energy barriers for subsurface diffusion from the experimental analysis are in very good agreement with the values determined by DFT analysis describing, in particular, the surface-subsurface diffusion step. This supports the assumption that the energy barrier for subsurface diffusion is larger than the energy barrier for carbon diffusion within the equivalent bulk sites. Comparing the two nickel surfaces, the activation energies determined in this work (both experimentally and calculated by DFT) are larger for the close-packed Ni(111) surface than for the more open Ni(100) surface. For Ni(100), subsurface diffusion and diffusion within the bulk have very similar values (1.4 eV in our experiment, 1.45 eV in our calculation, and 1.5 eV in literature[2]). For Ni(111), the subsurface diffusion activation barriers are (both experimentally determined and from DFT) 1.9 eV, compared to the bulk literature value of 1.5 eV.[2] This demonstrates that the open surface structure minimizes the additional energy barrier for the subsurface diffusion. Finally, migration of carbon through a carbide and a carbon-rich region with proceeding reactions, respectively, might also influence the activation barriers for diffusion. The latter point could also cause a deviation from a first order reaction.

The components within the C 1*s* signal, which represent the different carbon phases present, are affected by several reactions. These reactions are interdependent and the respective kinetic parameters are determined considering these interdependencies. The carbon diffusion is observed as a decrease of the overall C 1*s* signal intensity. All other reactions observed during the annealing procedure are accompanied by the carbon diffusion and the respective kinetic parameter, k_D, has to be taken into account for the determination of all other parameters. The changes in the elemental carbon intensity is, e.g., affected by the carbon diffusion and by the carbide formation reaction. If carbide formation takes place, we expect a stronger decrease in the total carbon intensity than if caused exclusively by carbon diffusion. Indeed, the decrease proceeds faster than reproduced only by the kinetic parameter k_D. This additional decrease is described by k_C, the kinetic parameter for the carbide formation reaction. As mentioned above, the carbide structures for both nickel and iron are different than a pure carbon intercalation in the metal host lattice. Both metal lattices rearrange for carbon atom incorporation upon carbide formation. The carbon migration into the metal lattices is described by carbon diffusion (k_D). The carbon incorporation in sites within the rearranged metal lattice is characterized by carbide formation (k_C). Since the bulk structure of the carbides is independent of the surface under investigation, we expect similar E_C values for Ni(111) and Ni(100). These values (1.1 and 1.3 eV) agree fairly well within the experimental resolution and confirm the assumptions given above. Furthermore, we expect a similar value for Fe(110) and the Fe_3C formation reaction due to comparable processes within the metal lattice and the carbide structure. The estimated activation barrier for carbide formation in Fe (1.1 eV) is identical to the Ni(111) value. DFT calculations for the carbide formation reaction are not available by now.

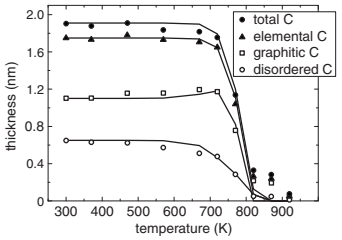

FIG. 9. Experimental results (data points) and simulation (lines) of the thermally induced processes for an initially 1.9 nm carbon film on a Ni(111) surface. The simulation is based on the kinetic parameters for the elemental reactions determined in this work. The experiment is conducted according to procedure A.

The next process that is quantified is the ordering reaction observed within the elemental carbon signal. As mentioned above, the sum intensity decreases due to carbon diffusion. The disordered graphitic fraction decreases further due to the ordering reaction. The carbide formation reaction leads to a decrease of both graphitic and disordered graphitic carbon intensities. Since the ordering reaction is not affected by the substrate, we expect identical parameters for these three surfaces. The resulting activation barriers confirm this. Carbon films on all surfaces investigated here show the same activation barrier (0.9 eV). Literature data or calculated values are not available. The determined kinetic parameters for the elemental reaction steps can finally be used to model the temperature dependent development of carbon films on the investigated substrates. The results of such a model calculation are shown in Fig. 9. The data points represent the experimentally determined carbon species applying procedure A. After each temperature step the sample reaches RT for surface analysis using XPS survey scans (for film thickness determination) and high resolution scans of the C 1*s* core level. Since each temperature step is reached after a short ramp-up time and the sample is cooled down to RT without active cooling, the kinetic values ($k(T)$) and the annealing time have to be corrected by a pre-exponential factor c. Its value, $c=3.5$, scales the annealing time (t) and $k(T)$, as shown by

$$d_x(T_i) = d_x(T_{i-1})\exp^{-ck(T_i)t}. \quad (7)$$

The lines given in Fig. 9 are the results from a simulation using the kinetic parameters for the elemental reactions such as carbon subsurface diffusion (k_D), carbide formation (k_C), and ordering of disordered carbon (k_O). The simulation reproduces the temperature-induced ordering and diffusion processes quantitatively, confirming the model and the respective kinetic parameters developed in this work.

IV. SUMMARY

We present XPS measurements of thin carbon films on Fe(110) and Ni(100) and (111) surfaces for a quantitative deconvolution of different reactions observed during annealing experiments. We determine the kinetic parameters for these reactions, which are interdependent. The substrate element as well as the surface structure affect the carbon diffusion and we determine different activation barriers for these metal surfaces. The calculated values of activation energies for the elemental reaction steps using the DFT approach are in very good agreement with our experimental results. Both experimental and theoretical results confirm the influence of the surface structure, and the resulting values differ from bulk data given in literature. Isothermal annealing experiments allow the determination of kinetic parameters for the observed interdependent reactions (carbide formation and ordering reaction), which facilitate a quantitative description of the thermally induced reactions of carbon films on the investigated surfaces.

ACKNOWLEDGMENTS

T.J. gratefully acknowledges support by the "Fonds der Chemischen Industrie" (FCI) and the "Deutsche Forschungsgemeinschaft" (DFG) within the Emmy-Noether-Program.

[1] H. Bakker, H. P. Bonzel, C. M. Bruff, M. A. Dayananda, W. Gust, J. Horváth, I. Kaur, G. V. Kidson, A. D. Le Claire, H. Mehrer, G. E. Murch, G. Neumann, N. Stolica, and N. A. Stolwijk, in *Diffusion in Solid Metals and Alloys*, Landolt-Börnstein Numerical Data and Functional Relationships in Science and Technology, New Series, Group III: Crystal and Solid State Physics, Vol. 26, edited by H. Mehrer (Springer-Verlag, Berlin, 1990).
[2] S. Diamond and C. Wert, Trans. Metall. Soc. AIME **239**, 705 (1967).
[3] T. A. Massaro and E. E. Petersen, J. Appl. Phys. **42**, 5534 (1971).
[4] B. S. Berry, J. Appl. Phys. **44**, 3792 (1973).
[5] D. J. Siegel and J. C. Hamilton, Phys. Rev. B **68**, 094105 (2003).
[6] F. C. Schouten, E. T. E. Brake, O. L. J. Gijzeman, and G. A. Bootsma, Surf. Sci. **74**, 1 (1978).
[7] F. C. Schouten, O. L. J. Gijzeman, and G. A. Bootsma, Surf. Sci. **87**, 1 (1979).
[8] R. Sau and J. B. Hudson, J. Vac. Sci. Technol. **16**, 1554 (1979).
[9] T. B. Massalski, H. Okamoto, P. R. Subramanian, and L. Kacprzak, *Binary Alloy Phase Diagrams, Version 1.0*, 2nd ed., (ASM International, Materials Park, OH, 1996).
[10] R. B. McLellan and M. L. Wacz, J. Phys. Chem. Solids **54**, 583 (1993).
[11] D. E. Jiang and E. A. Carter, Phys. Rev. B **67**, 214103 (2003).
[12] H. H. Hwu, B. Fruhberger, and J. G. Chen, J. Catal. **221**, 170 (2004).
[13] H. H. Hwu and J. G. Chen, Chem. Rev. (Washington, D.C.) **105**, 185 (2005).
[14] P. Goldstrass, K. U. Klages, and Ch. Linsmeier, J. Nucl. Mater. **290–293**, 76 (2001).
[15] J. Luthin and Ch. Linsmeier, Surf. Sci. **454–456**, 78 (2000).
[16] Ch. Linsmeier, J. Luthin, and P. Goldstrass, J. Nucl. Mater. **290–293**, 25 (2001).
[17] J. Luthin and Ch. Linsmeier, Phys. Scr. **T91**, T134 (2001).
[18] I. Barin, *Thermochemical Data of Pure Substances*, 3rd ed. (VCH, Weinheim, 1995), Vols. 1 and 2.
[19] A. F. Holleman, and E. Wiberg, *Lehrbuch der Anorganischen Chemie* (Walter de Gruyter, Berlin, 1995), 101st ed.
[20] Inorganic Crystal Structure Database, Version 1.2.0, 2003.
[21] A. Wiltner and Ch. Linsmeier, Phys. Status Solidi A **201**, 881 (2004).
[22] M. P. Seah, I. S. Gilmore, and G. Beamson, Surf. Interface Anal. **26**, 642 (1998).
[23] MULTIPAK, Version 6.1A, Physical Electronics, 1999.
[24] P. A. Schultz (unpublished); A description of the method is in P. J. Feibelman, Phys. Rev. B **35**, 2626 (1987).
[25] C. Verdozzi, P. A. Schultz, R. Wu, A. H. Edwards, and N. Kioussis, Phys. Rev. B **66**, 125408 (2002).
[26] J. P. Perdew, K. Burke, and M. Ernzerhof, Phys. Rev. Lett. **77**, 3865 (1996).
[27] D. R. Hamann, Phys. Rev. B **40**, 2980 (1989).
[28] A. Wiltner and Ch. Linsmeier, "Thermally induced reaction and diffusion of carbon files on Ni(111) and Ni(100)," Surf. Sci. (submitted).
[29] M. P. Seah and W. A. Dench, Surf. Interface Anal. **1**, 2 (1979).
[30] M. Eizenberg and J. M. Blakely, Surf. Sci. **82**, 228 (1979).
[31] J. F. Mojica and L. L. Levenson, Surf. Sci. **59**, 447 (1976).
[32] H. J. Grabke, W. Paulitschke, G. Tauber, and H. Viefhaus, Surf. Sci. **63**, 377 (1977).
[33] W. Arabczyk and U. Narkiewicz, Surf. Sci. **352–354**, 223 (1996).

Surface Science 602 (2008) 3623–3631

Contents lists available at ScienceDirect

Surface Science

journal homepage: www.elsevier.com/locate/susc

Thermally induced reaction and diffusion of carbon films on Ni(1 1 1) and Ni(1 0 0)

A. Wiltner, Ch. Linsmeier *

Max-Planck-Institut für Plasmaphysik, EURATOM Association, Boltzmannstrasse 2, D-85748 Garching b. München, Germany

ARTICLE INFO

Article history:
Received 6 May 2008
Accepted for publication 2 October 2008
Available online 10 October 2008

Keywords:
Carbon
Nickel
Carbides
Surface chemical reaction
X-ray photoelectron spectroscopy

ABSTRACT

Thin carbon films on Ni(1 1 1) and Ni(1 0 0) and the reactive and diffusive interactions between film and substrate are investigated using X-ray photoelectron spectroscopy (XPS). The carbon films are deposited from the vapor phase with the substrates at room temperature. After deposition the films contain mainly elemental carbon. Restricted only to the carbon–nickel interface carbidic carbon is observed. Carbon films of various thicknesses between 0.4 and 3.2 nm are investigated after thermal treatments up to 970 K. The C 1*s* signal intensities are used for chemical analysis, both in a qualitative and quantitative way. The initially formed carbide partially decomposes between 400 and 570 K. Additional carbide formation sets in again, combined with incipient carbon diffusion, at higher temperatures. Carbon diffusion into the bulk leads to a decreasing C 1*s* signal intensity until the carbon is almost completely lost into the bulk.

1. Introduction

The binary system carbon/nickel is studied by various authors with respect to the application of Ni as a catalyst [1–19]. Eizenberg et al. [1,2] doped different Ni crystal planes with carbon by holding the sample in a quartz capsule filled with graphite powder at high temperatures. The authors reported a decreasing carbon signal with increasing annealing temperature measured by Auger electron spectroscopy (AES). Depending on the surface orientation they observed a graphite monolayer condensation in a temperature range of 100 K until the carbon was completely lost into the bulk. Other authors prepared carbon films by thermal decomposition of hydrocarbons or carbon monoxide [3–11,14–16]. Various measurement techniques and crystal planes, respectively, were used. McCarthy [3] found a carbide layer after decomposition of ethene on Ni(1 0 0), and measured the thermal behavior with AES and low energy electron diffraction (LEED). Schouten et al. [4] decomposed methane on Ni(110) and analyzed the solution of carbon into Ni using AES. Zdansky et al. deposited carbon by decomposition of ethene followed by CO adsorption on the C precovered Ni(1 0 0) surface [5]. They reported a surface-to-bulk carbide transformation induced by CO adsorption. Rosei et al. measured the structure of graphitic C on Ni(1 1 1) by surface extended energy loss fine structure (SEELFS) [6]. The graphite layer was deposited by thermal decomposition of CO at 570 K. Steinrück et al. observed the adsorption and temperature dependent decomposition of hydrocarbons (propene, methanol) on Ni(1 0 0) by fast X-ray photoelectron spectroscopy (XPS) studies [7,8]. Several investigations dealt with a surface reconstruction called 'clock reconstruction', observed on Ni(1 0 0) and Ni(1 1 1) measured by scanning tunneling microscopy (STM), LEED and photoemission techniques [9–13]. This reconstruction was explained by carbide formation. Both crystallographic orientations show this surface process after C deposition of 0.2–0.6 ML. Carbon deposited above these coverages leads to graphite formation. Nakamura et al. observed the growth of carbon and carbide formation on Ni depending on crystal plane and carbon source (CO and C_2H_4) by STM, AES and LEED [14–16]. On the Ni(9 7 7) surface they observed the carbidic C up to a coverage of 1.8 ML. Levenson et al. [17–19] prepared 'the inverse system' by depositing thin Ni films on graphite. They found Ni_3C at room temperature followed by carbide decomposition at temperatures below 470 K using XPS and AES. The carbide was completely decomposed at temperatures above 670 K.

Another topic of interest described in the literature is the observation of binding energy shifts due to varying cluster sizes. Egelhoff et al. [20,21] deposited transition metals (Cu, Ni and Pd) on carbon substrates and measured the binding energy shift in the metal valence band regions using ultraviolet photoelectron spectroscopy (UPS) and in the core level regions by XPS. The authors reported continuous binding energy shifts with increasing metal cluster sizes. No shift in the binding energy of the carbon signal was observed. In particular, no carbide formation on Ni, potentially visible as binding energy shifts, was observed.

In this work carbon films are deposited from the vapor phase produced by an electron beam evaporation source. The film deposition is performed by holding the substrate at room temperature, any decomposition reaction of molecular precursors, common to all

* Corresponding author. Tel.: +49 89 3299 2285; fax: +49 89 3299 962285.
E-mail address: linsmeier@ipp.mpg.de (Ch. Linsmeier).

0039-6028/$ - see front matter © 2008 Elsevier B.V. All rights reserved.
doi:10.1016/j.susc.2008.10.003

Table 1
Free energy of formation (Gibbs function) at 300 K [27] for carbides described in [22–25] and Ni_3C.

Carbide	ΔG_f^0 (eV)
TiC	−1.87
Be_2C	−1.19
SiC	−0.73
WC	−0.40
W_2C	−0.23
Ni_3C	+0.66

previously conducted studies described in the literature above, is not necessary. The surface composition and chemistry is monitored in situ by XPS analysis. Films prepared under these conditions show a thin carbide layer at the adsorbate–metal interface and additionally elemental (not reacted) carbon. Such behavior was observed also on various other substrates [22–26]. Carbon film thicknesses range from the sub-monolayer region up to several nanometers. The maximum initial film thickness in our experiments is only limited by the information depth of the applied analysis method, XPS. Since we are interested in the interfacial properties between carbon layer and Ni, the maximum film thicknesses applied here are in the range of a few nanometers. The deposition of elemental carbon at room temperature allows a detailed study of processes like growth mode and binding energy shifts immediately after film deposition. In addition, the dependence of different processes (carbon diffusion, growth mode, binding energy shifts) on the substrate temperature and film thickness can be investigated in detail.

The chosen analysis technique, XPS, provides information on the near-surface region due to the limited escape depth of the photoelectrons and is a sensitive tool to study chemical reactions. The binding energies of electrons in the core levels are affected by the chemical state of the respective element. Therefore, core level shifts provide both an identification of elements involved in chemical surface reactions and the changes in the chemical binding states. In addition, binding energy shifts are caused by processes like cluster size effects or surface rearrangements.

In addition to Ni we investigate carbon films on W, Be, Ti and Si, as reported earlier [22–25]. The reactivity of carbon films depends on thermodynamic properties of the respective carbides. In all substrate cases investigated by our group up to now, the reactivity of carbon films correlates with the thermodynamic properties of the respective carbides. The enthalpies of formation for carbides of W, Si, Be, and Ti are all exothermic. However, Ni_3C exhibits endothermic behavior at temperatures up to 800 K [27]. The free energies of formation (Gibbs functions, ΔG_f^0) for the discussed carbides are shown in Table 1. Keeping the thermodynamic properties in mind a comparison of the thermal behavior of these binary systems is interesting.

In this work we investigate the carbide formation on Ni crystal planes (1 1 1) and (1 0 0), and we will compare their chemical reactivity with the other substrates.

2. Experimental

The XPS experimental setup consists of analysis and preparation chambers connected by a UHV valve with base pressures better than 1×10^{-8} Pa. The preparation chamber is equipped with an Omicron EFM3 electron beam evaporation source and a quadrupole mass spectrometer (QMS). The analysis chamber consists of a PHI 5600 XPS system and an ion gun (Specs IQE 12/38). To achieve highest resolution monochromatic Al Kα radiation is used. The hemispherical analyzer is driven at pass energies of 2.95 eV for high resolution scans and at 93.90 eV for survey scans. The binding energies are calibrated with respect to the Au $4f_{7/2}$ peak at 84.00 eV. The linearity of the binding energy scale is calibrated using the Cu $2p_{3/2}$ (932.7 eV), Ag $3d_{5/2}$ (368.3 eV) and Au $4f_{7/2}$ lines [28]. The analyzer entrance lens is set to an analysis spot size of 0.8 mm in diameter.

The polished Ni(1 1 1) and Ni(1 0 0) crystals (diameter 1 cm) are cleaned using Ar^+ sputtering (3 keV) and annealing (up to 970 K) cycles until no impurities are observed in the survey spectra. Next to the respective Ni crystal a gold foil is fixed on the sample holder for periodic checks of the Au $4f_{7/2}$ peak position. Carbon deposition is performed from a high purity graphite rod (99.999%, Goodfellow) with the Ni crystals at room temperature (300 K). During the carbon deposition the pressure is better than 1×10^{-7} Pa.

3. Data analysis

For the analysis of the XPS signal intensities and peak fitting the PHI MultiPak [29] software package is used. A Shirley background is subtracted from the spectra shown in this paper. In the peak fitting procedures for the C 1*s* signals symmetric Gauss–Lorentz functions are used. For the Ni 2*p* peaks we do not apply a peak fitting procedure. Photoelectron intensities are determined by integrating the spectra and subtraction of a Shirley background. For intensities of the different contributions to the C 1*s* signals the integrals of the fitted functions are used.

The carbon layer thickness is evaluated using an electron attenuation length of 1.082 nm (λ_{Ni}^C) for Ni $2p_{3/2}$ and 1.494 nm (λ_C^C) for C 1*s* photoelectrons, calculated with the 'universal' Seah–Dench equation (1), as reported in [30].

$$\lambda(E_S^F) = \frac{538}{E_S^2}a + 0.41a^{3/2}E_S^{1/2} \tag{1}$$

The parameters are the kinetic energy of the photoelectrons (E_S in eV) and the atom diameter (a in nm). We use a density of 1.8 g/cm^3 for the carbon layers [22,31]. From this a thickness of 0.22 nm for 1 ML of carbon is calculated. For the determination of the layer thickness we use both substrate (I_S) and layer intensities (I_C) as well as the sensitivity factors S_{Ni} and S_C for our XPS system [32]. The measured intensities I_{Ni} and I_C are usually correlated to the layer thickness d_C by the following equations.

$$I_{Ni} = I_{Ni}^{\infty}\exp\left(-\frac{d_C}{\lambda_{Ni}^C\cos\theta}\right)$$
$$I_C = I_C^{\infty}\left[1-\exp\left(-\frac{d_C}{\lambda_C^C\cos\theta}\right)\right] \tag{2}$$

Thereby θ is the angle between the sample surface normal and the analyzer. The intensities I_{Ni}^{∞}, I_C^{∞} corresponding to the pure metal and an extended carbon layer are not known for each specific measurement, because the sample is moved for carbon layer deposition from the analysis to the preparation chamber leading to different sample positions in front of the analyzer. Moreover, the photon fluxes differ for separate measurement runs. These uncertainties in the intensity measurements are avoided by using the ratio of the substrate (I_{Ni}) and layer intensities (I_C) from the same XPS spectrum. The ratio of the sensitivity factors corresponds to the ratio of the intensities of pure elemental Ni (I_{Ni}^{∞}) and carbon (I_C^{∞}) samples (Eq. (3)).

$$\frac{I_{Ni}^{\infty}}{I_C^{\infty}} = \frac{S_{Ni}}{S_C} \tag{3}$$

From these equations results the relation between intensities and carbon layer thickness d_C which is given in Eq. (4).

$$\underbrace{\frac{I_C}{I_{Ni}}\cdot\frac{S_{Ni}}{S_C}}_{r} = \underbrace{\left[\exp\left(\frac{1}{\lambda^C_{Ni}\cos\theta}\right)\right]^{d_C}}_{m} - \underbrace{\left[\exp\left(\frac{1}{\lambda^C_{Ni}\cos\theta}-\frac{1}{\lambda^C_{C}\cos\theta}\right)\right]^{d_C}}_{n} \quad (4)$$

The carbon layer thickness d_C is evaluated by numerical analysis of Eq. (5) using the Mathcad software package.

$$m^{d_C} - n^{d_C} - r = 0 \rightarrow d_C \quad (5)$$

4. Results

4.1. Carbon films at room temperature

We deposit carbon films from sub-monolayer coverages up to several nanometers. Performing the film deposition from the vapor phase at room temperature allows a determination of the growth mode and a detailed deconvolution of the C 1*s* signals into chemical states. The growth mode can be determined either by a determination of layer and substrate intensity ratios or by a detailed investigation of the inelastic background at the low kinetic energy region of a XPS line (Tougaard's model). The ratio of intensities was already used for the layer thickness estimation under an assumption of a layer growth mode. Since a direct measurement of the layer morphology by other analysis techniques than XPS is not available, we use Tougaard's model as an independent method for the determination of the growth mode. In Fig. 1 the Ni 3*p* signal region of carbon layers on Ni and calculated survey spectra are plotted. The calculated spectra are obtained by using the software package Quases which includes Tougaard's model [33–35]. This model describes the influence of the film morphology on the inelastic background at the lower kinetic electron energy side of a photoelectron peak. It is sensitively affected by the growth mode. According to Tougaard's model, we examine the inelastic background in the survey scans at the low kinetic energy side of the Ni 3*p* peak at 66 eV, since no additional signal intensity from other elements is observed in this binding energy region. A comparison of carbon films with increasing thickness indicates a layer growth mode up to ~1.3 nm. For thicker carbon films the examination of the background region concludes a layer followed by island growth mode. In particular, the island growth mode can be excluded from this comparison, since the respective distinct background increase, as calculated according to Tougaard's model (uppermost curve in Fig. 1) is not observed in the measured spectra.

In the following we will focus on the XPS analysis of the carbon layers after room temperature deposition. For the separation of chemically different carbon binding states in the C 1*s* signal we use peak fitting routines of the MultiPak software package. During the fit procedure, we use known binding energies of graphitic and disordered graphitic carbon at 284.2 (FWHM = 1.0 eV) and 285.1 eV (FWHM = 1.4 eV), respectively. These binding energies are identified by measuring carbon films on Au. In this system, no reaction or diffusion phenomena are observed up to annealing temperatures of 1200 K [23]. In the case of carbon films on Ni an additional peak at 283.5 eV is necessary to reproduce the measured C 1*s* spectra in the fit procedure. The peak separation of 0.9 eV between both graphitic species and the peak position of the graphitic carbon at 284.2 eV were kept constant during the fitting procedure, only the third component was allowed to shift in its position. This third signal component is assigned to the nickel carbide. The binding energy value is in good agreement with Ni_3C data reported in literature [5,18,36]. The C 1*s* spectra of two carbon films of different thicknesses on Ni(1 1 1) and their deconvolution results are shown in Fig. 2. In Fig. 2a, the results of a thin film (0.2 nm, ~1 ML) clearly show an additional peak at the lower binding energy side of the two elemental peaks, indicating the carbide. Larger amounts of carbon deposited on the Ni surface lead to a smaller carbide signal. Fig. 2b shows the C 1*s* region for a total carbon film thickness of 1.9 nm after RT deposition. The elemental carbon consists of the graphitic modification leading to a photoelectron peak at 284.2 eV, and a disordered graphitic modification with a signal at higher binding energy. This peak is visible as a shoulder already in Fig. 2a of the 1 ML C film and becomes more pronounced for the greater film thickness (Fig. 2b). A detailed quantification of the C 1*s* signal on Ni(1 1 1) and Ni(1 0 0) using graphitic, disordered graphitic and carbidic carbon, as described above, is shown in Fig. 3. This figure contains the results from both the Ni(1 1 1) (grey symbols) and Ni(1 0 0) (black and open symbols). Both substrates exhibit a similar C 1*s* signal composition with increasing carbon layer thickness. Neither in the development of the elemental fractions, nor in the carbide fraction, differences are visible for the two Ni surfaces.

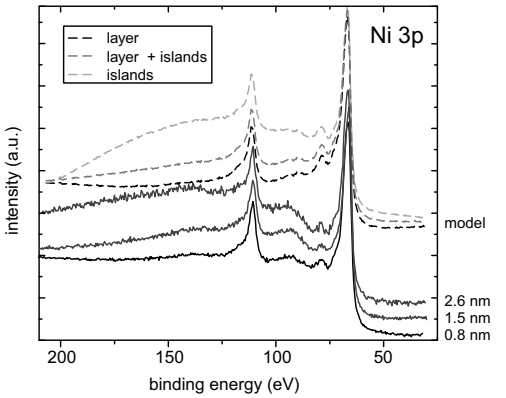

Fig. 1. Comparison of measured (lower part) and calculated survey spectra (upper part) of the Ni 3*p* region applying Tougaard's model for layer, layer plus island and island growth modes.

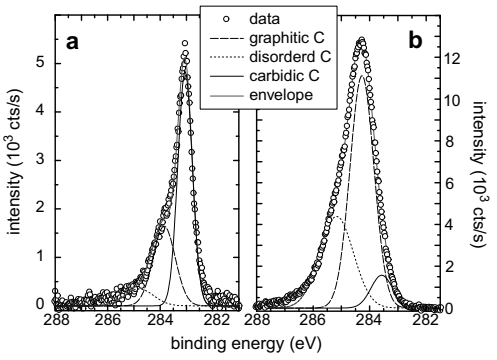

Fig. 2. C 1*s* signals and the components identified using the MultiPak fit routines. The signals show elemental carbon consisting of graphitic (- -) at 284.2 eV and disordered graphitic (···) carbon at 285.1 eV. The best result is obtained using carbidic carbon (—) at 283.0 eV (a) and 283.5 eV (b). The data (○) after Shirley background subtraction and the sum of all components (grey line) are shown. The thicknesses of the carbon layers on Ni(1 1 1) are 0.2 nm (a) and 1.9 nm (b), respectively.

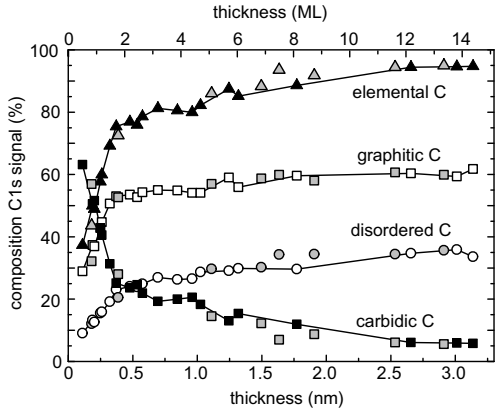

Fig. 3. Evolution of the C 1*s* signal components with increasing carbon film thickness on Ni(100) and Ni(111). The C 1*s* signals show graphitic (□), disordered graphitic (○), elemental (▲) and carbidic (■) carbon. Grey symbols represent the data on Ni(111), all others on Ni(100). Only the Ni(100) data points are connected by lines. Within the experimental scatter there is no deviation between Ni(100) and Ni(111) data points.

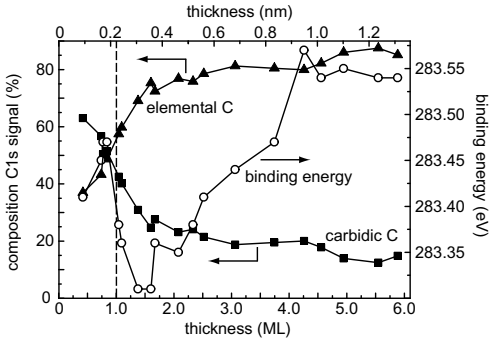

Fig. 4. Elemental (▲) and carbidic C intensity fractions (■), compared with the binding energy shift (○) of the carbidic component from the sub-monolayer region up to 6 ML after carbon deposition on Ni(111) and Ni(100). The carbide peak binding energy is referred to the peak position of graphitic C at 284.2 eV. The carbide BE has a minimum at a C layer thickness of 1.5 ML and reaches the bulk value at 4 ML coverage.

Although nickel carbide is an endothermic compound, a nickel carbide peak is measured directly after depositing C on substrates at RT. The carbide amount is small and the respective peak intensity at 283.5 eV decreases rapidly on deposition of additional carbon. The maximum fraction of carbide in the carbon peak is 65%. After carbon deposition of 1 ML we identify 45% carbide within the C 1*s* signal. Additional deposited carbon is in the elemental state leading to smaller carbide intensities. The elemental carbon attenuates the photoelectrons coming from the film–substrate interface. This observation can be explained by a carbide layer restricted to the interface, increasingly covered by elemental carbon. As mentioned above, the elemental carbon shows graphitic and disordered graphitic carbon. The ratio of disordered/graphitic C starts at 0.3 and reaches 0.6 in maximum after deposition of ~8 ML. As described by Mason in [37] and for measurements of transition metals on C by Egelhoff et al. [20,21], a continuous binding energy shift of the respective core levels to lower or higher values is observed upon increasing deposition. This binding energy shift was explained by a cluster size effect. Following this interpretation, isolated particles exhibit different peak positions as larger clusters or completed layers. We also find a binding energy shift for the carbidic C peak position compared to the graphite fraction at 284.2 eV. The graphite peak position is constant in the observed coverage region from sub-monolayer up to 3.2 nm carbon layers. As already mentioned above, we kept the BE separation between the graphitic and disordered graphitic C 1*s* components fixed. Only the carbidic peak position was allowed to shift in its position. Fig. 4 shows the carbidic and elemental carbon amount and the binding energy shift of the carbide fraction as a function of the deposited layer thickness. The BE shift of the carbide peak is observed on both Ni surfaces. Within the first monolayer the binding energy is close to the bulk value at 283.45 eV, immediately after additional C deposition this value decreases (283.30 eV) and reaches the bulk value (283.55 ± 0.05 eV in average) again after ~4 ML. The Ni $2p_{3/2}$ peak shows a small change in the position towards higher binding energy (ΔBE = 0.2 eV) after sub-monolayer deposition. A continuous shift like in the C 1*s* peak region is not observed. Within the Ni 2*p* signal we cannot identify an additional component, only the peak position shifts slightly. Therefore, the substrate signal is not further analyzed. The valence band region exhibits a similar peak shift (ΔBE = 0.2 eV) as the Ni 2*p* region. A comparison of core level binding energies measured in our work with values given in the literature is listed in Table 2.

4.2. Thermally induced processes

In order to investigate possible reaction or diffusion processes at elevated temperatures, the carbon films are annealed in steps of 50 or 100 K between room temperature and 970 K. The sample is kept at each temperature for 30 min. The XPS measurements are performed after cooling down to room temperature. Parameters which can influence possible reaction and diffusion processes are the carbon layer thickness, annealing time and Ni surface, respectively.

The carbon diffusion is analyzed by observing the carbon layer thickness. To compare the diffusion from surface to the bulk, carbon films of similar thicknesses are deposited on the Ni(111) and Ni(100) surfaces. Fig. 5 shows these two comparable carbon layers (1.8 and 1.9 nm) on Ni(100) and Ni(111). In addition we show the thermal evolution of a thin carbon film on Ni(111) (0.4 nm) and one further carbon layer on Ni(100) (1.5 nm). The carbon diffusion sets in at 650 K on the more open surface structure (100) and at 750 K on Ni(111), indicated by the dashed lines in Fig. 5. The carbon is almost completely lost into the bulk within a temperature window of 150 K above the onset of surface-to-bulk diffusion. Compared to other metals, on Ni(111) and Ni(100) a changed decrease rate of the carbon signal is observed before the carbon is fully lost into the bulk. This small step in the layer thickness is observed in particular for layers above several monolayers, and leads to a less strong decrease for thin layers (as shown for the 0.4 nm film on Ni(111)). This thin carbon layer was annealed for only 20 min at each temperature step. A pronounced carbon diffusion at 750 K is not observed. After the carbon diffusion a residual carbon layer thickness of less than 1 ML is observed on both Ni surfaces. At 970 K the C 1*s* intensity is almost completely lost on both Ni surfaces. For the layer thickness estimation we use inelastic mean free paths for C 1*s* and Ni 2p photoelectrons passing a graphite layer. During the thermal treatment the carbon layer is modified and the inelastic mean free path could change due to altered layer densities and composition (e.g. Ni_3C formation). A pure carbide layer would change the inelastic mean free paths by a factor

Table 2
Peak positions determined in this work (BE^{exp}) compared to literature data (BE^{lit}).

C 1*s*	BE^{exp} (eV)	BE^{lit} (eV)	References	Ni $2p_{3/2}$	BE^{exp} (eV)	BE^{lit} (eV)	References
Graphitic	284.2	284.2	[23]	Ni	852.8	852.7	[32]
		284.3–284.5	[32]			852.9	[36]
Disordered	285.1	285.2	[23]	Ni_3C	853.0	853.8	[36]
		285.1	[48]				
Carbidic	283.5	283.6[a]	[5,18]				

[a] The literature value is shifted with respect to the graphite peak position, measured in our work at 284.2 eV.

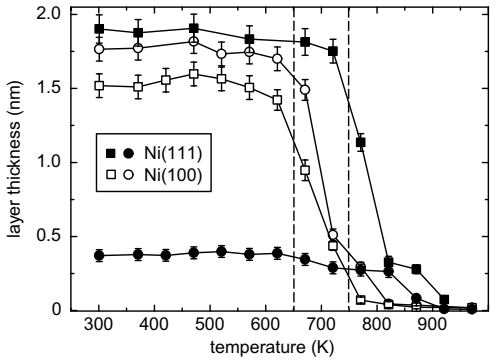

Fig. 5. Thermal behavior of carbon films with different initial layer thicknesses on Ni(100) and Ni(111). The Ni(100) surface (open symbols) shows an onset temperature of carbon diffusion at ~650 K, the Ni(111) surface (filled symbols) at ~750 K (marked by dashed lines). The error bars represent statistical errors from both measured intensities.

of 1.6 applying the Seah–Dench equation for inorganic compounds. However, as we will show in the next section, the carbide intensity is small and the elemental carbon dominates the C 1*s* signal up to high temperatures.

As described above in Section 4.1, the inelastic background in the spectra is evaluated on the high-BE side of the Ni 3*p* signal for determination of the growth mode after room temperature deposition (see Fig. 1). Comparing the spectra in this BE region with increasing annealing temperature, island formation during the annealing experiments can be excluded. Therefore, the carbon layer thickness determination by assuming a model which is based on a layer growth mode is justified.

In Fig. 6 the binding energy regions of the C 1*s* and substrate signals for a 1.8 nm thick film on Ni(100) (panel a and b) are shown. In panel (c) the C 1*s* signals for the 0.4 nm carbon film on Ni(111) are plotted, together with the fit results for graphitic and carbidic carbon. Since the disordered fraction is small for very thin films, this peak is omitted for clarity. Different temperature regions and signal shifts due to reactions are observed and analyzed in detail in the following.

The results of the quantitative analysis of the C 1*s* signals with increasing temperature by applying the MultiPak peak fitting routine is shown in Fig. 7. We now focus on a carbon film (1.8 nm, Figs. 5, 6a and b) deposited on Ni(100) for which the changes of the carbon chemical states are plotted in Fig. 7a. The fraction of carbidic carbon shows an initial decrease with increasing annealing temperatures up to ~500 K while the total carbon amount at the surface is unchanged. The carbide intensity starts to increase from this lower intensity level for temperatures above the minimum around 600 K. At 650 K the carbon diffusion sets in, accompanied by an increase of the carbide fraction. The carbon is almost completely lost from the surface (accessible by XPS) into the bulk within a temperature window of 150 K. The C 1*s* signal shows only carbide intensity above 870 K, the elemental carbon vanishes completely. For comparison, the 1.9 nm thick film on Ni(111), shown in Fig. 7b, exhibits only a small variation in the carbide amount, still going through a minimum in the temperature range of 400–570 K. In a similar experiment on Ni(111), starting however with a thinner carbon layer of 0.4 nm (Figs. 6c, 7b), also a minimum in the same temperature range is observed. This carbide decomposition is visible as a loss of carbide intensity whereas the total C 1*s* signal intensity is almost constant. Compared to Ni(100), the diffusion sets in at 750 K. The carbon is lost into the bulk at a temperature above 920 K. The C 1*s* signal exhibits elemental as well as carbidic carbon still at 920 K. Also the thin carbon film (0.4 nm) shows an incomplete reaction, visible as elemental and carbidic C 1*s* signal components at 920 K. At 970 K again only carbidic carbon is observed for the thin film (see Figs. 6c and 7b).

The carbide decomposition (temperature region where the carbide fraction passes through a minimum) is visible in the substrate signal (Fig. 6b). Above RT, the Ni 2*p* signal shows a binding energy shift towards the metal value ($\Delta BE = -0.2$ eV). The C 1*s* binding energy region shows no overall shift during the carbide decomposition reaction (470–670 K) (panels a and c). Accompanied with the onset of carbon diffusion at 750 K the C 1*s* signal shifts towards higher binding energy values while the substrate signal position is not modified. The graphite peak position (labeled 'graph.' in Fig. 6c) is at 284.6 eV ($\Delta BE = 0.4$ eV) and the carbide intensity (labeled 'carb.' in Fig. 6c) is determined at 283.9 eV ($\Delta BE = 0.3$ eV). After the majority of carbon is lost into the bulk (above 870 K), only a small C 1*s* peak remains at the carbide peak position. The binding energy of 283.0 eV for this peak is comparable (although somewhat smaller) to the low coverage value given in Fig. 4. An identical behavior is observed for carbon films on Ni(111). The substrate signal shifts towards the metal value with beginning carbide decomposition (carbide minimum region) and stays constant up to 970 K. In the C 1*s* signal a shift towards higher values with the onset of carbon diffusion is measured. The residual carbide intensity after the annealing steps at 920 K is again observed at lower BE values compared to the bulk carbide position (Fig. 6c).

On both nickel surfaces an ordering reaction within the elemental carbon is observed which leads to an increase in graphitic carbon (peak at a BE of 284.2 eV), while the disordered fraction decreases (peak intensity at 285.1 eV). The ratio of disordered and ordered graphitic C decreases from 0.6 at maximum after room temperature deposition to 0.2 at minimum, before the carbon is lost into the bulk. This ordering reaction is also observed in annealing experiments of carbon films on Au, W, Si, Ti, W, and in case of HOPG (highly oriented pyrolytic graphite) after ion bombardment [22–25]. This is visible in Fig. 7 for both Ni surfaces, in particular in the temperature regime from RT to the onset of carbon diffusion from the surface into the bulk (650 K on Ni(100), 750 K on Ni(111)).

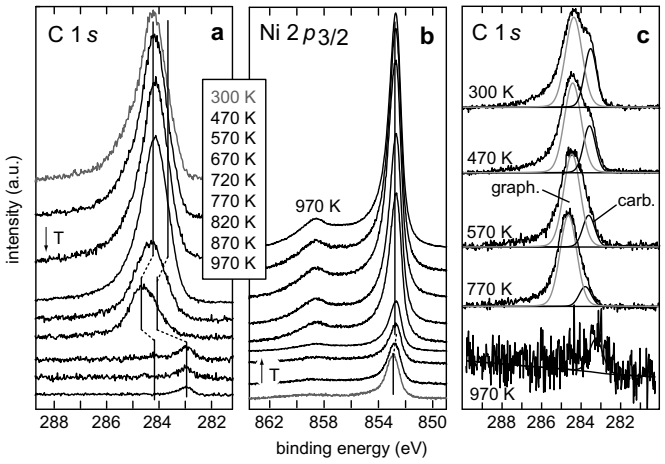

Fig. 6. C 1*s* and Ni $2p_{3/2}$ signal regions from a 1.8 nm C film on Ni(1 0 0) (a and b), plotted with increasing annealing temperatures (see arrow directions). In panel (c) the C 1*s* signals for a 0.4 nm thin carbon film on Ni(1 1 1) are shown. The carbide decomposition reaction is visible as a loss of the carbide intensity. The Ni 2*p* peak (b) shifts with beginning carbide decomposition from the carbide position towards the metal value ($\Delta BE = -0.2$ eV). With incipient carbon diffusion a total C 1*s* peak shift towards higher values is observed (a and c). The peak positions of carbidic and graphitic carbon are labeled. The residual carbide signal observed at temperatures above 850 K shifts to lower values, compared to the respective peaks in the signals at lower annealing temperatures.

5. Discussion

The first part of this section discusses the information gained on surface structure and layer growth modes, which is deduced from the observed binding energies and their respective shifts during the deposition of carbon on the nickel surfaces. Bäumer et al. deposited Ni on the basal plane of graphite at low (90 K) and room temperature (300 K) and characterized the system with LEED and XPS [38]. The authors report cluster growth at these temperatures. In our work the inverse system (carbon on Ni) at room temperature is investigated. An analysis of substrate and layer signals with increasing carbon layer thicknesses indicate initially a layer growth mode. In particular, an island growth mode is excluded from a comparison of the evolution of the inelastic background with increasing layer thickness. As the simulated spectra show, the island growth mode would appear as a distinct increase of the inelastic background while a layer growth mode leads to a smooth background beside the XPS line. For thicker carbon films (> 1.3 nm) our analysis of survey spectra an initial layer-by-layer growth, followed by island growth, is concluded (see Fig. 1). The inelastic background beside the Ni 3*p* signal increases only slightly with increasing layer thickness. However, for detailed and more direct studies of the growth mode of elemental carbon deposited on nickel other UHV techniques like STM are required.

XPS measurements after room temperature deposition with increasing carbon layer thicknesses show a clearly visible shift in the carbide binding energy. Two different characteristics are identified. In the sub-monolayer region the carbide peak is close to the bulk BE value at 283.45 eV, followed by a decrease in BE. The carbide peak position is determined at 283.3 eV at minimum for a layer thickness of 1.5 ML. Above this coverage the carbide peak shifts again continuously towards higher values, until the bulk value for Ni_3C of 283.50–283.55 eV is reached at 4 ML. The BE shift detected at sub-monolayer coverages can be related to the surface reconstruction ('clock reconstruction') described in literature for this coverage regime [9,10,12]. This surface reconstruction is observed for carbon films both on Ni(1 1 1) and Ni(1 0 0) between a coverage of 0.2 ML and 0.6 ML. Carbon deposition (by hydrocarbon decomposition) above this coverage leads to graphite formation in these studies. Due to the carbide signal position and the carbide amount of less than 100% in that coverage region we assume a similar surface reconstruction in our case after carbon deposition from the vapor phase. However, in all previous investigations of the C/Ni system by other groups carbon was never deposited elemental from the vapor phase and with substrates at RT. The interpretation of a surface reconstruction is deduced in our case from the shift of the carbide peaks. The continuous shift from 283.3 eV to again higher BEs (283.5–283.55 eV) between 1.5 ML and 4 ML is explained by a size effect, as discussed in [39] (the author gives there an extensive survey on core level shifts). The carbide peak position is then affected by the increasing graphite matrix. Based on the interpretation of the BE shift due to this size effect, this BE shift can be quantitatively estimated using the thermodynamic approach described by Mårtensson et al. [40]. In this model the BE shift is calculated by the '$Z + 1$' approach. This approach is also known as the equivalent–core–approximation (ECA) and is used for the determination of surface core level shifts and binding energy shifts in binary compounds like alloys (see also [39]). In this approach the overall enthalpy can be written as a sum of the enthalpies of all reaction sequences. This is also known in literature as the 'Born–Haber cycle', which can be written in terms of the enthalpy of solution (ΔH_{Sol}) for the binary system $Z;Z + 1$ (Eq. (6)).

$$\Delta E_B = \Delta H_{Sol}^{Z \to Z+1} + \Delta H_{Sol}^{Z+1 \to Z} \tag{6}$$

This equation has to be improved for binary compounds (A_xB_y) where A is equivalent to Z and A + 1 represents $Z + 1$, respectively, and B is the matrix [40,41]. The BE shift (ΔE_B) is then correlated to the energies of solution (E(A; B), E(A + 1; B), E(A + 1; A)). The essential thermodynamic values are determined using the semi-empirical equation given in [42]. For this equation physical values like atomic volume and work function as well as empirical scaling values are essential. It should be noted, that the semi-empirical equation is only valid for a concentration of 5% A in B at maximum. Cluster size effects represent this concentration limit and the

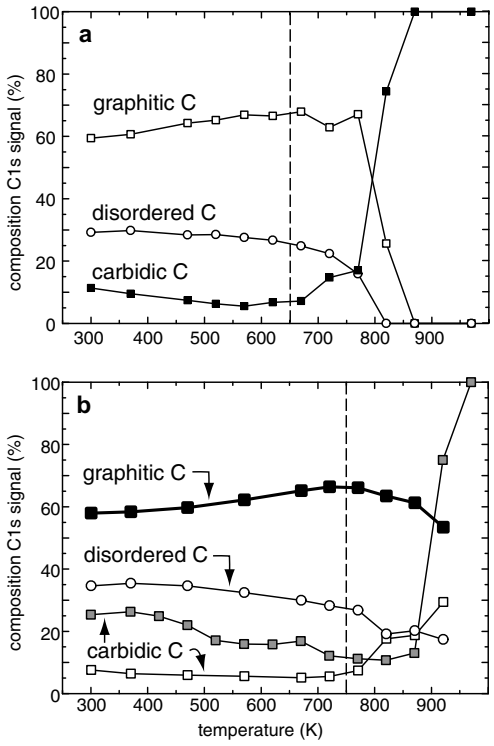

Fig. 7. Changes in the components of the C 1*s* signal with annealing temperature for carbon films on Ni(100) (a) and on Ni(111) (b). The initially deposited carbon layer on Ni(100) is 1.8 nm. On Ni(111) the initial carbon layer thickness amounts to 1.9 nm. In addition, the thermal evolution of the carbidic carbon for a 0.4 nm thin film is shown in (b) by the grey symbols). The temperatures of incipient carbon diffusion from Fig. 5 are marked by dashed lines. The carbon film on Ni(100) shows a pronounced minimum in the carbide component (■). For the 1.9 nm film on Ni(111) only a small minimum in the carbide fraction is visible, whereas the 0.4 nm thin film clearly shows the carbide decomposition reaction. The graphitic carbon fraction (□) increases due to rearrangement of disordered (○) into ordered C. Additional carbide is formed upon incipient carbon diffusion. Above 850 K the remaining carbon signal on Ni(100) shows only carbide intensity, whereas on Ni(111) at 920 K the carbide formation is still incomplete.

determined values can be used for the estimation of a BE shift applying the '$Z+1$' approach as given in literature. Applying this '$Z+1$' approach to our system we expect a BE shift for the carbide peak position in the C 1*s* signal of −0.61 eV, compared to the experimentally determined value of −0.89 eV (283.3 eV) in maximum in the 1–2 ML coverage region. For the Ni 2*p* signal a binding energy shift of +0.8 eV is expected from this model. We observe a shift of +0.2 eV in maximum in our experiments. A continuous BE shift with increasing carbon layer thickness is not observed. For comparison, Gibbs et al. measured a BE shift of +0.9 eV for the Ni 2*p* signal after Ni implantation in carbon [36], which is within the conditions of the '$Z+1$' approach (low concentration of Ni in C). These experiments and model calculations, however, are not directly comparable to our measurements due to different concentrations of Ni and C. The given model values and measurements by Gibbs et al. represent the 'low concentration' range of Ni in C, while our measurements are performed at the reverse concentration limit (large amount of Ni). An investigation of core level shifts on binary metal systems which form random alloys (A_xB_y) shows a linear dependence on the stoichiometric ratio of A and B [41]. Therefore, the core level shift of a binary system (A_xB_y) can be estimated by an evaluation of the 'low concentration' value (5% A in B and vice versa) applying the '$Z+1$' approach. This value represents the BE shift for element A and B, respectively, for the binary system in maximum. The second point is a core level shift of $\Delta BE = 0$ eV representing the bulk values for A (100% A) and B (100% B). Under assumption of a linear dependence from the 'low concentration' to the '100%' side the core level shift of A_xB_y can be determined for the respective *x* and *y* values. The expected BE values according to such a linear interpolation for Ni_3C (25% B in A) are: +0.2 eV for Ni 2*p* and −0.5 eV for carbide in C 1*s*. These values are in good agreement with our experimentally determined BE shifts of +0.2 eV (Ni 2*p*) and −0.7 eV (carbidic C 1*s*). To summarize these observations, we assume a surface reconstruction in the carbon sub-monolayer region, followed by a size effect between 1.5 ML and 4 ML. The additional carbon deposition above 1.5 ML is not leading to a further surface reconstruction and the carbide particles are embedded and finally covered by a graphite matrix with a contribution of defects in the graphite lattice.

The second part of the discussion is devoted to reaction and diffusion processes of elemental carbon on nickel, particularly taking into account the endothermic nature of Ni_3C. In the quantitative XPS analysis of the C 1*s* signal composition we find a maximum carbide amount while the first carbon monolayer is deposited. 65% of the C 1*s* signal intensity corresponds to the carbide. Although the formation reaction of Ni_3C is endothermic, the carbide is detected after depositing carbon from the vapor phase on nickel at room temperature. We deposit carbon films on different materials (W, Be, Ti and Si) with respect to the thermodynamic properties of their carbides. On these substrates the corresponding carbides show exothermic carbide formation reactions. Accordingly, the carbon films exhibit a larger carbide fraction after room temperature deposition compared to Ni. In the case of carbon films on Be, for example, we find an increase in carbide intensity while depositing carbon layers up to 3 ML [22].

In [43] we give a survey about all binary systems measured in our group by now. A comparison of carbon films on various substrates (Be, Si, W, Ti and Ni) shows a dependence of the thermal behavior on thermodynamic properties (diffusion and carbide formation processes). The onset temperature of carbon diffusion on those substrates which show carbides with comparable carbide structures (intercalation compounds) corresponds to the tendency of the respective activation barriers for carbon diffusion in the bulk metals. These values are given in literature [44]. Ni(100) shows the lowest onset temperature, followed by Ti (1.3 eV), Ni(111) and W (1.8 eV). The activation barrier for carbon diffusion in bulk Ni is 1.5 eV [44]. The difference between Ni(100) and Ni(111) observed in this work (Fig. 5) is explained by the more open surface structure of Ni(100). For a detailed explanation of the reaction and diffusion kinetics we refer to [45]. Another aspect of interest is the carbide formation reaction and their thermodynamic properties. The carbides of both Ti and W are formed in an exothermic formation ($\Delta G_f^0 < 0$) reaction, whereas the respective Ni carbide is formed in an endothermic reaction ($\Delta G_f^0 > 0$). Carbon films on Ti and W show a noticeable carbide formation after annealing experiments at higher temperatures, which agrees with the exothermic reaction behavior. On Ni, however, we cannot observe a clearly visible increase in carbide intensity (Fig. 7). With the onset of carbon diffusion (T_{Diff} is given as a line in Fig. 7) the carbide amount increases only barely. Another difference to the carbides formed in an exothermic reaction is the temperature window in which a minimum in the carbide fraction is observed. The decrease of initially present carbide is attributed to the metastable character of Ni_3C. With increasing annealing temperature the carbide formed upon initial C deposition at RT decomposes, leading to an increasing

intensity of elemental carbon. The carbide decomposition was already observed by Levenson et al. [17–19]. They reported a beginning decrease in carbide amount at 420 K and a complete decomposition at 670 K. However, we observe carbide intensity up to 970 K. Levenson et al. investigated Ni implanted into carbon substrates. Therefore, small amounts of remaining carbide might be obscured by the dominating signal of the elemental carbon in the substrate. Since in our measurements the C 1*s* signal intensity is constant in that temperature region, the carbide decomposition is explained by a surface process and a reconstruction, respectively.

We now focus on the BE shifts of the carbon core level peaks. During the peak fits we set the peak separation of graphitic and disordered graphitic carbon within the C 1*s* signal constant. Only the carbidic carbon peak is allowed to shift in its position. Firstly we will focus on the total C 1*s* signal, followed by the discussion of the detailed deconvolution. Independent on the surface structure (Ni(1 1 1) and Ni(1 0 0)) the total C 1*s* signal shifts towards higher values while carbon diffusion sets in. In contrast, the valence band and Ni 2*p* regions shift to lower BEs already at lower temperatures, with the onset of carbide decomposition, and show no further change in peak position during the following thermal treatments. Therefore, the shifts of Ni 2*p*, valence band and C 1*s* regions cannot be explained by changed experimental properties. In that case, the regions would show a position change at the same temperature and, moreover, in the same direction. The Ni 2*p* as well as the valence band region shift due to the carbide decomposition and the peak energies then correspond with the respective metal values. The changes in the C 1*s* signal, however, occur while the carbon is lost into the bulk and after carbon diffusion. In that temperature region the carbon migrates into the bulk and the Ni surface and bulk atoms have to rearrange for carbide formation and carbon diffusion. Consequently, the BE shifts occurring upon carbon diffusion are attributed to a rearrangement of surface atoms. In addition, there is no evidence for other carbon species than elemental and carbidic carbon. Since direct measurements of the surface atoms (like STM) of our reactive binary system are not done by now we conclude this rearrangement of surface atoms from the already described BE shift for carbon films after room temperature deposition ('clock reconstruction'). The carbide peak position of the residual C 1*s* signal is at lower values compared to the Ni_3C bulk position. This observation is due to the already described size effect (see C deposition on Ni at RT) and isolated carbide particles.

Continuing with the composition of the C 1*s* signal. Independent from the substrate (C on Be, Si, W, Ti and Ni) we find elemental carbon with a similar ratio of graphitic and disordered graphitic carbon. Upon continuing carbon deposition the disordered carbon fraction increases with carbon layer thickness up to a maximum ratio of disordered to graphitic C of 0.6. The disordered fraction is comparable to 'non-perfect' sp^2 C and the decrease of that intensity during annealing is ascribed to a rearrangement into ordered (sp^2) graphite. In earlier experiments we deposited carbon films on gold, which is an inert substrate with respect to both carbide formation and carbon bulk diffusion. Therefore, carbon diffusion or any other reaction can be excluded. The deposited carbon films show a clearly visible ordering after thermal treatment. This ordering reaction in the deposited carbon films also occurs on reactive substrates during annealing experiments ([22–25]). The resulting chemical state of the carbon after the onset of diffusion into the Ni bulk at temperatures up to 970 K depends on the surface orientation. After deposition of comparable layer thicknesses and equal annealing times we find elemental as well as carbidic C on Ni(1 1 1) and only carbidic C on Ni(1 0 0). This again is due to the more open surface structure of Ni(1 0 0) and the onset of carbon diffusion at lower temperatures, compared to Ni(1 1 1). The detection of carbide intensity even after the onset of carbon diffusion and the decreasing C 1*s* signal is explained by carbon segregation. The solubility of carbon in Ni is small, increases with temperature and amounts to 2.7% in Ni at 1600 K [46,47]. The C 1*s* signal intensity during the annealing procedure at 970 K is almost completely lost due to the higher solubility compared to 300 K. During cooling down to room temperature, however, the C 1*s* signal intensity appears again due to carbon atoms migrating back to the Ni surface. Carbon segregation on Ni was also observed by [7,8] and was actually applied for carbon enrichment experiments described in [1].

6. Summary

This paper comprehensively describes for the first time the interaction of carbon deposited elementally at room temperature on nickel surfaces, followed by annealing steps up to 970 K. To this, carbon films of different thicknesses from sub- to several monolayers are deposited on Ni(1 0 0) and Ni(1 1 1). The carbon–metal reaction and diffusion processes at RT and at elevated temperatures are compared with other binary C/metal systems. Ni_3C, although being formed in an endothermic reaction, is detected after room temperature deposition of carbon. An analysis of the C 1*s* signals shows carbide intensity restricted to the film–substrate interface. The initially formed carbide decomposes during annealing up to 570 K (temperature window of minimum carbide intensity), demonstrating the metastable character of Ni_3C. After heating to higher temperatures, carbide intensity is observed, accompanied by carbon diffusion into the bulk. The onset temperatures of both carbon diffusion from surface into bulk and carbide formation depend on the surface structure. Ni(1 0 0) shows an onset around 650 K, whereas the diffusion and reaction on Ni(1 1 1) set in at 750 K. The different characteristics in BE shift for the C 1*s* signal are explained by surface reconstruction in the carbon sub-monolayer region and carbon diffusion, respectively. The carbide peak position is detected close to the carbide bulk value while elemental carbon is deposited in the sub-monolayer region. This observation is explained by the 'clock reconstruction' of the Ni surface, described in the literature. Deposition of elemental carbon from 1.5 ML up to 4 ML leads to a continuous carbide peak shift from a distinct BE minimum to the carbide bulk value. The BE shift in this coverage region is explained by a cluster size effect. The C 1*s* signal position shifts again during annealing experiments. The first BE shift to higher values is measured when the carbon diffusion is observed, followed by a second BE shift to lower values when the carbon atoms segregate back to the surface. While the first BE shift is explained by the diffusion process where the Ni surface and bulk atoms have to rearrange for carbon diffusion, the additional BE shift after the final thermal treatment is explained by the cluster size effect.

References

[1] M. Eizenberg, J.M. Blakely, J. Chem. Phys. 71 (1979) 3467.
[2] M. Eizenberg, J.M. Blakely, Surf. Sci. 82 (1979) 228.
[3] J.G. McCarthy, R.J. Madix, Surf. Sci. 54 (1979) 121.
[4] F.C. Schouten, E. Te Brake, O.L.J. Gijzeman, G.A. Bootsma, Surf. Sci. 74 (1978) 1.
[5] E.O.F. Zdansky, A. Nilsson, N. Mårtensson, Surf. Sci. 310 (1994) L583.
[6] R. Rosei, M. De Crescebzi, F. Sette, C. Quereima, A. Savoia, P. Perfetti, Phys. Rev. B 28 (1983) 1161.
[7] C.M. Whelan, R. Neubauer, D. Borgmann, R. Denecke, H.-P. Steinrück, J. Chem. Phys. 115 (2001) 8133.
[8] R. Neubauer, C.M. Whelan, R. Denecke, H.-P. Steinrück, Surf. Sci. 507–510 (2002) 832.
[9] C. Klink, I. Stensgaard, F. Besenbacher, E. Lægsgaard, Surf. Sci. 342 (1995) 250.
[10] C. Klink, L. Olesen, F. Besenbacher, I. Stensgaard, E. Lægsgaard, N.D. Lang, Phys. Rev. Lett. 71 (1993) 4350.
[11] J.H. Onuferko, D.P. Woodruff, B.W. Holland, Surf. Sci. 87 (1979) 357.
[12] K.C. Prince, M. Surman, T. Lindner, A.M. Bradshaw, Solid State Commun. 59 (1986) 71.
[13] R. Terborg, J.T. Hoeft, M. Polcik, R. Lindsay, O. Schaff, A.M. Bradshaw, R.L. Toomes, N.A. Booth, D.P. Woodruff, E. Rotenberg, J. Denlinger, Surf. Sci. 446 (2000) 301.

[14] H. Nakano, J. Nakamura, Surf. Sci. 482–485 (2001) 341.
[15] H. Nakano, S. Kawakami, T. Fujitani, J. Nakamura, Surf. Sci. 454–456 (2000) 295.
[16] H. Nakano, J. Ogawa, J. Nakamura, Surf. Sci. 514 (2002) 256.
[17] S. Sinharoy, M.A. Smith, L.L. Levenson, Surf. Sci. 72 (1978) 710.
[18] S. Sinharoy, L.L. Levenson, Thin Solid Films 53 (1978) 31.
[19] M.A. Smith, S. Sinharoy, L.L. Levenson, J. Vac. Sci. Technol. A 16 (1979) 462.
[20] W.F. Egelhoff Jr., G.G. Tibbetts, Solid State Commun. 29 (1978) 53.
[21] W.F. Egelhoff Jr., G.G. Tibbetts, Phys. Rev. B 19 (1979) 5028.
[22] P. Goldstrass, K.U. Klages, Ch. Linsmeier, J. Nucl. Mater. 290–293 (2001) 76.
[23] J. Luthin, Ch. Linsmeier, Surf. Sci. 454–456 (2000) 78.
[24] Ch. Linsmeier, J. Luthin, P. Goldstrass, J. Nucl. Mater. 290–293 (2001) 25.
[25] J. Luthin, Ch. Linsmeier, Phys. Scripta T91 (2001) 134.
[26] P. Reinke, P. Oelhafen, Surf. Sci. 468 (2000) 203.
[27] I. Barin, Thermochemical Data of Pure Substances, third ed., vols. 1 & 2, VCH, Weinheim, 1995.
[28] M.P. Seah, I.S. Gilmore, G. Beamson, Surf. Interface Anal. 26 (1998) 642.
[29] MultiPak Ver. 8.2B, Phys. Electron. (2006) (This code uses a sum of Gauss and Lorentz functions to approximate the Voigt function).
[30] M.P. Seah, W.A. Dench, Surf. Interface Anal. 1 (1979) 2.
[31] B. Lesiak, A. Jablonski, Z. Prussak, P. Mrozek, Surf. Sci. 223 (1989) 213.
[32] J.F. Moulder, W.F. Stickle, P.E. Sobol, K.E. Bomben, Handbook of X-ray Photoelectron Spectroscopy, in: J. Chastain (Ed.), Perkin Elmer Corp., Eden Prairie, 1992.
[33] S. Tougaard, QUASES Background Analysis of XPS/AES, Part 1 and 2, 1994 – 1999, QUASES – Tougaard APS.
[34] S. Tougaard, J. Vac. Sci. Technol. A 14 (1996) 1415.
[35] S. Tougaard, Surf. Interface Anal. 26 (1998) 249.
[36] R.A. Gibbs, N. Winograd, V.Y. Young, J. Chem. Phys. 72 (1980) 4799.
[37] M.G. Mason, Phys. Rev. B 27 (1983) 748.
[38] M. Bäumer, J. Libuda, H.J. Freund, Surf. Sci. 327 (1995) 321.
[39] W.F. Egelhoff Jr., Surf. Sci. Rep. 6 (1987) 253.
[40] P. Steiner, S. Hüfner, N. Mårtensson, B. Johansson, Solid State Commun. 37 (1981) 73.
[41] N. Mårtensson, R. Nyholm, H. Calén, J. Hedman, B. Johansson, Phys. Rev. B 24 (1981) 1725.
[42] A.R. Miedema, P.F. de Châtel, F.R. de Boer, Physica 100B+C (1980) 1.
[43] Ch. Linsmeier, AIP Conf. Proc. 740 (2004) 182.
[44] Landolt-Börnstein, Numerical Data and Functional Relationships in Science and Technology New Series, in: O. Madelung (Ed.), Group III "Crystal and Solid State Physics", Diffusion in Solid Metals and Alloys, vol. 26, Berlin, 1990.
[45] A. Wiltner, Ch. Linsmeier, T. Jacob, J. Chem. Phys. 129 (2008) 084704.
[46] A.F. Holleman, E. Wiberg, Lehrbuch der Anorganischen Chemie, 101st ed., Berlin, 1995.
[47] T.B. Massalski, H. Okamoto, P.R. Subramanian, L. Kacprzak, Binary Alloy Phase Diagrams, Version 1.0, second ed., ASM International, Materials Park, Ohio, 1996.
[48] R. Haerle, E. Riedo, A. Pasquarello, A. Baldereschi, Phys. Rev. B 65 (2001) 5101.

Available online at www.sciencedirect.com
ScienceDirect
Nuclear Instruments and Methods in Physics Research B 258 (2007) 270–273
NIM B Beam Interactions with Materials & Atoms
www.elsevier.com/locate/nimb

Enhanced room temperature erosion of ultra-thin carbon films on beryllium, titanium and tantalum by deuterium ions

M. Reinelt, Ch. Linsmeier *

Max-Planck-Institut für Plasmaphysik, EURATOM Association, Boltzmannstraße 2, 85748 Garching b. München, Germany

Available online 29 December 2006

Abstract

Most present fusion devices use carbon at least partially as a first wall material. Due to high particle loads, especially hydrogen isotopes from the plasma, wall material is eroded and redeposited at different positions. This leads to the formation of surface layers, which are themselves subject to erosion. It is known that carbon exhibits chemically enhanced erosion by low energy hydrogen ions or elevated temperatures. However, room temperature erosion of carbon by keV ions is considered to be governed by a purely kinematic sputtering process. We found that this is not necessarily the case for carbon surface layers with thicknesses of a few nanometers. To investigate the basic mechanisms governing the erosion of carbon, carbon layers in the range of several nm thickness are evaporated on clean metal substrates. The films are irradiated with 1 or 1.3 keV deuterium ions and the surface layer thickness and composition are analysed by X-ray photoelectron spectroscopy (XPS). For our studies we choose carbon films on tantalum, titanium and beryllium to compare the influence of a wide range of substrate atomic masses. Our experimental data is compared to Monte Carlo calculations using the SDTRIM code which takes into account kinematic interactions and adjusts the sample composition dynamically. We discuss the results with respect to the kinematic collision interaction and the ion-induced chemical phase formations.

PACS: 68.55.Jk; 79.60.Dp; 79.20.Rf; 82.80.Pv

Keywords: Carbon; Carbide; Thin film; XPS; Erosion; Deuterium

1. Introduction

Mixed material surface layers are formed in fusion devices with different plasma facing materials. The complexity of the behaviour of those layers with respect to hydrogen bombardment grows rapidly with each element introduced into the system. In order to get a better understanding of the basic mechanisms that govern the erosion and substrate-modifying processes, we investigate the erosion of carbon films deposited on titanium, beryllium and tantalum substrates by keV deuterium ions as models for ternary systems metal/carbon/deuterium. Both chemical (by carbon–hydrogen reactions) [1] and physical mechanisms (by collision cascades) [2,3] contribute to the erosion process of thin carbon films on metals. The kinematic process is influenced by substrates of different atomic mass. XPS is successfully applied for the investigation of the erosion process as it gives quantitative information on the chemical composition of the surface layers.

2. Experimental

The metallic substrates under investigation are polished poly-crystalline titanium and tantalum and polished single-crystalline beryllium disks. The surfaces are cleaned by 3 keV Ar^+ sputtering under 45° incidence. Carbon is deposited up to several nm thickness by a Omicron EFM-3 UHV evaporator loaded with Goodfellow high purity carbon rods (99.999%). The carbon film on titanium is irradiated with a 4 keV D ion beam under 45° incidence

* Corresponding author. Tel.: +49 89 3299 2285; fax: +49 89 3299 962285.
E-mail address: linsmeier@ipp.mpg.de (Ch. Linsmeier).

0168-583X/$ - see front matter © 2007 Elsevier B.V. All rights reserved.
doi:10.1016/j.nimb.2006.12.111

from a Specs IQ 12/38 ion source without mass selection. It is assumed that the main species in the ion beam are D_3^+ ions. The carbon films on tantalum and beryllium are irradiated with a monoenergetic and mass separated 3 keV D_3^+ ion beam (80° bending magnet) under normal incidence. The energies per deuterium ion are therefore 1 keV for Ta and Be and 1.33 keV for Ti, respectively. The substrates are at room temperature during carbon deposition and deuterium bombardment. Before each fluence step, the 2D Gaussian shaped ion beam profile is scanned using a Faraday cup with a 0.5 mm opening mounted on the sample manipulator. The sample centre is placed in the maximum of the ion beam. Additionally, the beam is scanned several millimeters over the sample to provide a flattened and thus more stable beam profile. The applied deuterium fluence is calculated from the ion current in the Faraday cup scanning the beam for several minutes before bombardment of the target. XP spectra are recorded after each fluence step in the irradiation spot centre with a diameter of the analysis spot of 0.8 mm. All experiments are performed in situ under ultra high vacuum (UHV) conditions with a base pressure better than 10^{-8} Pa.

3. Results

After deposition of the carbon film, the XP spectra show a decrease of the metal substrate intensity, while a peak around 284.5 eV appears. This peak is assigned to C 1s core level photoelectrons and can be deconvoluted into several compounds using peak fitting routines provided by the software Multipak [4]. Details of the fitting procedure are given in [5]. Three carbon binding energies are necessary to provide a reasonable fit (Fig. 1). The dominating peak at a binding energy of 284.2 eV can be assigned to graphitic carbon. A broadening of the peak at the high binding energy side indicates a disordered graphitic carbon state at 285.2 eV which is characteristic for evaporated carbon and is interpreted as stable point defects in the graphite lattice i.e. carbon with dangling bonds [6]. In the following these two states are referred to as elemental carbon. At lower binding energies, a third carbon state can be detected originating initially from a metal–carbon interface of about one monolayer thickness with binding energies typical for metal carbides (282.7 eV for TaC, 281.8 eV for TiC and 282.5 eV for Be_2C) [7]. Bombardment of the samples with

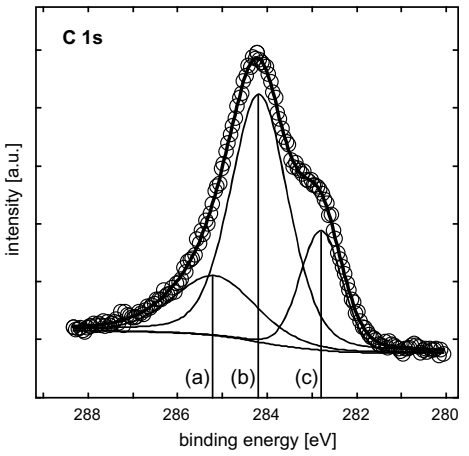

Fig. 1. Deconvolution of the C 1s binding energy region of carbon on tantalum: graphitic (a) and disordered graphitic (b) states (elemental carbon) and carbidic state (c).

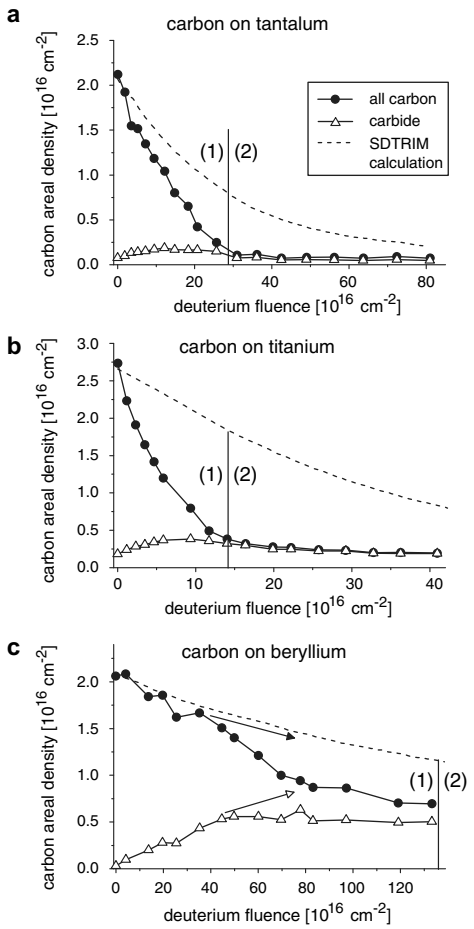

Fig. 2. Erosion of carbon layers on (a) tantalum, (b) titanium and (c) beryllium by keV deuterium ions at room temperature in stages (1) and (2). Comparison of carbon areal densities from dynamic SDTRIM calculations with experimental overall carbon and metal carbide areal densities.

deuterium ions leads to a decrease of the amount of elemental carbon by three possible mechanisms. These are a kinetic sputtering process, carbide formation via ion beam mixing and chemical erosion, which results from the formation of volatile hydrocarbon species. Two stages can be recognised in the experimental data (Fig. 2) by different slopes of the carbon areal density curves. During the first stage, elemental carbon is removed while the carbide amount increases. This stage lasts as long as there is elemental carbon left on the surface. At the beginning of the second stage, elemental carbon is completely removed and the uncovered carbide layer is sputtered. Directly after deposition of the carbon films a quantification of the carbon amount is possible from XPS data by assuming a layered structure and comparing substrate and surface layer intensities. With increasing deuterium fluence, the carbide formation introduces an error into the quantification, as the measured substrate intensity is not only attenuated by elemental carbon, but also by the formed carbide layer with unknown thickness and different inelastic mean free path (IMFP) of the photoelectrons compared to the elemental carbon. To compensate this error, the IMFP of the sample surface layer containing both elemental carbon and metal carbide is changed with increasing deuterium fluence. At the beginning of the first stage, the surface layer is assumed to be mainly elemental carbon. At the end of the first stage, the surface layer consists of metal carbide. The change of the IMFP with deuterium fluence is determined experimentally from the ratio of the deconvoluted XPS peak areas. This yields the corrected amount of carbon in both chemical states in the surface layer. The areal density of carbide is calculated from this corrected overall carbon areal density using again the XPS peak area ratios. The IMFP values for elemental carbon and carbide are determined by a semi-empirical formula for inorganic compounds [8] applying an experimentally determined material density of 1.8 g/cm^3 for the deposited carbon films [9].

4. Discussion

In the following, the contribution of the three possible mechanisms for carbon erosion during the first phase will be discussed. Photoelectrons from elemental carbon that is displaced from the layer into the metal substrate by ion beam mixing exhibit a shift in their binding energy, as the chemical surrounding of these carbon atoms changes from carbon to metal. Elemental carbon that is lost due to ion beam mixing is hence detected as carbide. Starting from an initial carbide amount representing about one monolayer at the carbon/metal interface, the amount increases before it reaches the surface and is removed by sputtering. The influence of the substrate on this process can be seen from the different maximum carbide areal densities, as shown in Figs. 2(a)–(c). Ion-induced carbide formation has the smallest contribution on tantalum with a maximum carbide layer thickness of 1 monolayer and dominates the loss of elemental carbon on beryllium (>5 monolayers). To determine the contribution of the chemical erosion, the experimental data is compared to the remaining carbon amount calculated by SDTRIM [2,3] (Fig. 2) as a function of fluence. This comparison shows a deviation between SDTRIM calculations and experimentally determined carbon amounts both for Ti and Ta substrates. This is due to the fact that SDTRIM considers only kinematic processes and neglects chemical interactions. Therefore we conclude that the difference between experimental data and simulation can be attributed to a loss channel by chemical sputtering. Two requirements have to be met to allow chemical sputtering. First, volatile species have to be formed by reaction of hydrogen with carbon dangling bonds. Second, the volatile species have to escape the sample surface. This implies either carbon temperatures above 400 K or low ion energies (~eV) [10,11], both of which are not realized in this experiment. Nevertheless, deuterium is stopped within the carbon surface layer in an amount which depends on the collision cascades. The deuterium implantation profiles calculated by SDTRIM for the surface regions of the three samples are shown in Fig. 3. Most deuterium is stopped in the carbon layer on tantalum because the collision cascade and the deuterium implantation profile are shifted towards the surface on substrates with higher atomic masses. The disordered graphitic state observed by XPS provides the necessary carbon dangling bonds for the initial formation of hydrocarbon groups. During ion bombardment, additional dangling bonds (defects in the graphite lattice) are created in the collision cascade. This is supported by the observation that the ratio between disordered and graphitic state is constant for deuterium ion bombardment while the amount of disordered state is increased by argon bombardment [12]. Because the hydrocarbons are already formed at the surface or a few monolayers below, a high substrate temperature is not necessary to allow the escape of volatile

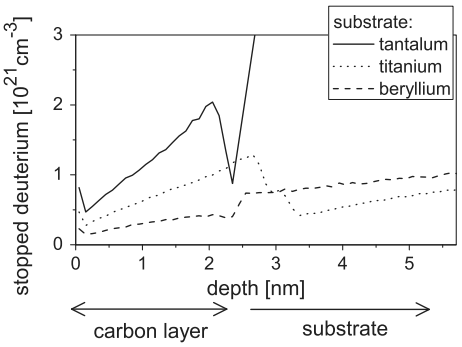

Fig. 3. Deuterium implantation profiles in the near surface region from SDTRIM calculations for a deuterium fluence of 10^{16} cm^{-2}. The maximum amount of deuterium in this comparison is stopped in the carbon layer on tantalum. This fraction can lead to a chemically enhanced erosion of carbon.

species. Thus, the amount of stopped deuterium in the carbon layer can contribute as a carbon loss channel allowing chemical sputtering and explaining quantitatively the measured enhanced erosion on tantalum (Fig. 2(a)) by formation of volatile species of an average formal stochiometry of $CD_{1\text{-}2}$.

As can be seen in Fig. 2(c), there is no deviation between SDTRIM and experimental data during the first fluence steps for deuterium bombardment of carbon on beryllium. The erosion is therefore governed by kinematic processes only. This is in agreement with the calculations of the deuterium implantation profile as only a small amount is stopped in the carbon layer on Be (Fig. 3). The difference between the experimentally determined carbon areal density and the SDTRIM calculation on Be at fluences above 5×10^{17} D cm^{-2} is caused by loss of carbon due to forward scattering beyond the XPS detection depth, not observed on the Ti and Ta samples with higher atomic masses. This is confirmed by in situ Rutherford backscattering spectroscopy (RBS) and angle-resolved XPS (ARXPS). From 5×10^{17} to 1.3×10^{18} D cm^{-2}, RBS shows almost no decrease of the overall carbon amount, while the XPS measurements suggest 50% carbon loss. ARXPS still shows a layered structure at 5×10^{17} D cm^{-2} and a homogeneous carbon distribution of Be_2C stochiometry throughout the XPS information depth at 1.3×10^{18} D cm^{-2}. This means that the deeper parts of the carbon depth profile are not detected in the measurements. The real trends of the XPS areal densities for the total carbon amount and the carbide fraction are indicated by the arrows in Fig. 2(c).

In the case of titanium substrate (Fig. 2(b)), the angle of incidence of the D ions is 45°. This is taken into account in the SDTRIM calculation. Also, the ion beam is not mass selected, which results in an unknown mixture of different possible ion species (D^+, D_2^+ and D_3^+). The main ion species is assumed to be D_3^+, resulting accordingly in a kinetic energy of 1.3 keV per D and the highest deuterium fluence of the three possible D ion species. This assumption yields the smallest deviation between SDTRIM calculation and experiment. Nevertheless, the difference between measured and calculated sputter yields (Fig. 2(b)) is greater than could be explained by stopped deuterium at the end of the collision cascades or forward scattering of carbon beyond the detection range. However, chemical sputtering is also possible for carbon on titanium. In addition to the deuterium available due to stopping within the carbo layer range, additional deuterium implanted deeper into the Ti metal can reach the carbon layer by diffusion from the substrate to the interface. This can provide the deuterium amount necessary to further increase chemical sputtering. It is also possible that structural modifications due to titanium hydride formation contribute by increasing one of the loss channels for carbon. This, however, can apply to both titanium and tantalum, since both metals can form hydrides. This hypothesis is subject to further investigations using tungsten as substrate. Tungsten is of similar atomic mass as tantalum, also forms intercalations carbides, but does not form hydrides.

5. Conclusions

Depending on the substrate atomic mass, ultra-thin carbon films show different erosion characteristics during keV deuterium ion bombardment at room temperature. Contributions to the overall loss of elemental carbon from the surface are kinematic sputtering, carbide formation by ion beam mixing and chemical sputtering. The contribution of ion beam mixing is determined by quantification of the carbidisation measured by XPS and increases from tantalum to beryllium. By comparing the experimental results with SDTRIM calculations we deduce a contribution of chemical sputtering depending on the substrate atomic mass. Tantalum shows enhanced erosion due to chemical sputtering caused by stopped deuterium at the end of the collision cascades in the carbon layer. Carbon erosion on beryllium is not enhanced and well described by kinematic sputtering and ion beam mixing processes only. Titanium shows enhanced erosion which is not quantitatively explained by mere stopped deuterium and might be influenced by an additional mechanism providing deuterium to the interface, as enhanced deuterium diffusion.

References

[1] M. Balden, J. Roth, J. Nucl. Mater. 280 (2000) 39.
[2] W. Eckstein, Computer Simulation of Ion–Solid Interactions, Springer Series in Materials Science, Vol. 10, Springer, Berlin, 1991.
[3] W. Eckstein, R. Dohmen, A. Mutzke, R. Schneider, Rep. IPP 12/3, Max-Planck-Institut für Plasmaphysik, Garching, 2007.
[4] MultiPak, Ver. 7.0.1, Physical Electronics, 2004.
[5] A. Wiltner, Ch. Linsmeier, Phys. Status Solidi A 201 (2004) 881.
[6] J. Luthin, Ch. Linsmeier, Surf. Sci. 454–456 (2000) 78.
[7] Ch. Linsmeier, J. Luthin, P. Goldstrass, J. Nucl. Mater. 290–293 (2001) 25.
[8] W. Gries, Surf. Interface Anal. 24 (1996) 38.
[9] P. Goldstrass, K.U. Klages, Ch. Linsmeier, J. Nucl. Mater. 290–293 (2001) 76.
[10] J. Küppers, Surf. Sci. Rep. 22 (1995) 249.
[11] C. Hopf, W. Jacob, J. Nucl. Mater. 342 (2005) 141.
[12] K.U. Klages, A. Wiltner, J. Luthin, Ch. Linsmeier, J. Nucl. Mater. 313–316 (2003) 56.

Carbon-containing compounds on fusion-related surfaces: Thermal and ion-induced formation and erosion

Christian Linsmeier

Max-Planck-Institut für Plasmaphysik, EURATOM Association,
Boltzmannstr. 2, D-85748 Garching, Germany
Email: linsmeier@ipp.mpg.de

Abstract. The deposition of carbon on metals is the unavoidable consequence of the application of different wall materials in present and future fusion experiments like ITER. Presently used and prospected materials besides carbon (CFC materials in high heat load areas) are tungsten and beryllium. The simultaneous application of different materials leads to the formation of surface compounds due to the erosion, transport and re-deposition of material during plasma operations. The formation and erosion processes are governed by widely varying surface temperatures and kinetic energies as well as the spectrum of impinging particles from the plasma. The knowledge of the dependence on these parameters is crucial for the understanding and prediction of the compound formation on wall materials. The formation of surface layers is of great importance, since they not only determine erosion rates, but also influence the ability of the first wall for hydrogen isotope inventory accumulation and release. Surface compound formation, diffusion and erosion phenomena are studied under well-controlled ultra-high vacuum conditions using in-situ X-ray photoelectron spectroscopy (XPS) and ion beam analysis techniques available at a 3 MV tandem accelerator. XPS provides chemical information and allows distinguishing elemental and carbidic phases with high surface sensitivity. Accelerator-based spectroscopies provide quantitative compositional analysis and sensitivity for deuterium in the surface layers. Using these techniques, the formation of carbidic layers on metals is studied from room temperature up to 1700 K. The formation of an interfacial carbide of several monolayers thickness is not only observed for metals with exothermic carbide formation enthalpies, but also in the cases of Ni and Fe which form endothermic carbides. Additional carbon deposited at 300 K remains elemental. Depending on the substrate, carbon diffusion into the bulk starts at elevated temperatures together with additional carbide formation. Depending on the bond nature in the carbide (metallic in the transition metal carbides, ionic e.g. in Be_2C), the surface carbide layer is dissolved upon further increased temperatures or remains stable. Carbide formation can also be initiated by ion bombardment, both of chemically inert noble gas ions or C^+ or CO^+ ions. In the latter case, a deposition-erosion equilibrium develops which leads to a ternary surface layer of constant thickness. A chemical erosion channel is also discussed for the enhanced erosion of thin carbon films on metals by deuterium ions.

INTRODUCTION

Formation and erosion of compound layers at the first wall of fusion devices are a consequence of the application of different materials in fusion devices. Different particle and energy loads in the various regions of the vessel require first wall materials with physical and chemical properties able to cope with the specific local conditions. In current and future fusion devices, the main candidates for wall materials are beryllium, tungsten and carbon [1]. Other materials like titanium or stainless steel (iron, nickel) are also used in

CP740, *The Physics of Ionized Gases: 22nd Summer School and International Symposium*,
edited by L. Hadžievski, T. Grozdanov, and N. Bibić

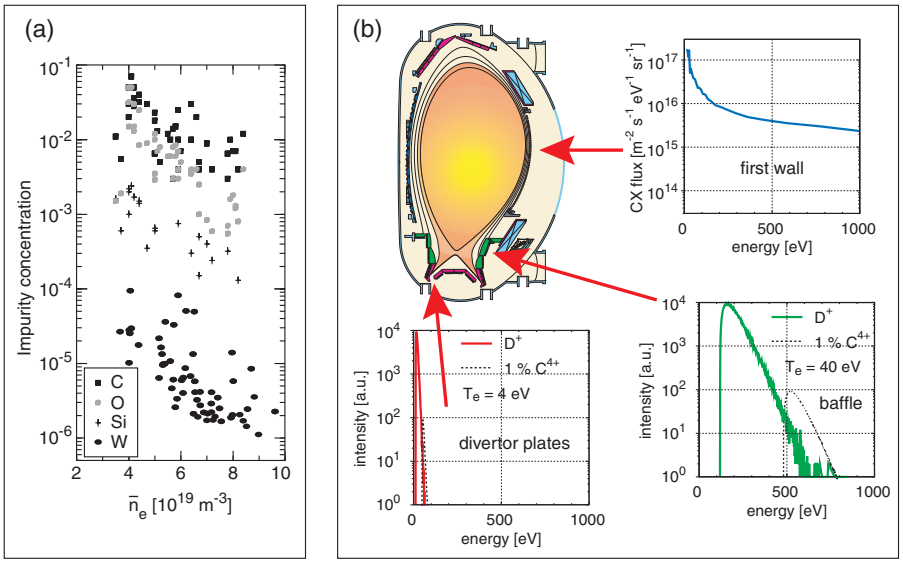

Figure 1. Impurity concentrations during ASDEX Upgrade discharges [4] with different plasma densities (a) and measured (first wall) and calculated (divertor and baffle) impurity particle energies impinging on the wall materials in ASDEX Upgrade.

current machines. Beryllium is used in JET and foreseen to be used as the material lining the main plasma chamber. Tungsten is applied in current tokamaks, e.g. in ASDEX Upgrade [2], and will be used in the ITER divertor, except for the plasma strike zones. Here, ITER intends to rely on CFC (carbon fiber composite) materials due to the highest particle and energy fluxes in these areas. For pure materials, a large data base is available on their physical and chemical properties regarding erosion, hydrogen inventory and anticipated performance in a next-step fusion device [3]. However, the continued erosion of wall materials, transport along magnetic field lines, and re-deposition of material at different areas within the vessel will lead to the formation of surface and near-surface compound layers. These ”mixed materials” are of great interest, since their erosion and hydrogen retention properties can differ largely from the pure materials due to altered physical, chemical and adsorption properties.

The light elements carbon and oxygen are of special importance, since these elements form volatile or gaseous compounds together with the metals used as wall materials. As a consequence, even small concentrations of these elements lead to wall erosion due to the recycling behavior. Figure 1a shows plasma impurity concentrations measured at ASDEX Upgrade, determined spectroscopically for plasma discharges with different densities [4]. The impurity concentrations for all elements plotted here decrease for increasing plasma density. The increased number of particles due to higher densities is over-compensated by the smaller particle energies, leading to a smaller erosion at higher plasma densities. Therefore, impurity concentrations decrease at higher plasma densi-

ties. The concentrations of both carbon and oxygen lie in the percent range, although only carbon is used as a wall material. Source of oxygen are oxidized metal surfaces and the presence of oxygen as impurity demonstrates the recycling behavior. Although the source for oxygen is limited under operational conditions, oxygen is still present in the plasma after extended operations. Tungsten is present only in small concentrations in the $10^{-5} - 10^{-4}$ range, although this material was present in the high-flux region within the divertor of ASDEX Upgrade during the relevant measurements. In Fig. 1a also silicon is visible, since during the experimental campaigns when these spectroscopic data were acquired experiments with siliconized walls were performed. Silicon, however, is otherwise not present without this pre-treatment. The energies of the particles impinging at the wall differ strongly on the position within the vessel. Figure 1b shows experimental and simulation results of charge exchange (CX) particle energies in ASDEX Upgrade. These neutrals originate from kinetic ions coming from the plasma center which get neutralized in collisions with other plasma constituents and therefore are no longer confined by the magnetic field. The spectrum for the first wall is measured with a low-energy neutral particle analyzer in the mid-plane of the device. Plotted is a spectrum for a neutral-beam heated discharge. Absolute numbers differ depending on heating power, plasma density, hydrogen isotope, etc. [5]. However, it is clear from the spectrum that particle energies extend from 20 eV (lower detection limit) into the keV regime. Typical fluxes are in the 10^{16} $cm^{-2}s^{-1}$ regime for neutrals, ions play only a minor role at the outer main wall. This situation may be very different at the inner wall, as recent results suggest [6]. The data plotted in the panels for the baffle (which is the entry part from the main chamber into the divertor) and the divertor plates are results from Monte Carlo simulations. At these positions, no experimental data on the particle energy distributions are available. The calculations are based on experimental electron temperatures and consider a Maxwellian energy distribution. They are carried out with the TRIM.SP code [7, 23] to simulate the particle spectrum at the given energies. At the baffle, particle energies are in the several 100 eV range for pure deuterium plasmas. Small amounts of impurities increase the energies easily by some 100 eV, as the calculation for a 1% C^{4+} impurity concentration shows. In the baffle, CX neutrals arrive at the wall with fluxes in the 10^{17} $cm^{-2}s^{-1}$ regime, whereas the ion fluxes are already in the 10^{19} $cm^{-2}s^{-1}$ range. Finally, at the divertor plates particle energies are below 100 eV for detached plasmas with electron temperatures of 4 eV. However, both CX neutral and ion fluxes are in the 10^{19} $cm^{-2}s^{-1}$ ranges. These results illustrate the parameter range for species and particle energies which have to be considered for the formation and erosion processes of wall materials. Another set of parameters is the wall temperature. It also depends strongly on the position and the respective energy deposition. It ranges from room temperature or slightly above to 1000 K and above at positions of heavy energy impact, for example at limiters.

This paper focuses on the formation and erosion of surface compound layers with respect to carbon. As outlined above, carbon is a dominating impurity in all fusion plasmas if carbon is used as one of the first wall materials. This is due to its tendency to form volatile compounds with hydrogen (hydrocarbons) and oxygen (CO, CO_2) and consequently the high recycling behavior. The Results section is structured in order to address different parameter sets. First, reaction and diffusion properties are discussed by analyzing thin elemental carbon films on various substrates at 300 K and at elevated

temperatures. Second, implantation of carbon species (C^+, CO^+) into beryllium at keV energies is investigated. Finally, investigations of interfacial reactions between elemental carbon layers on metals induced by noble gas ions and the erosion of carbon layers by D^+ ions are shown.

EXPERIMENTAL

The task to determine the fundamental properties of the interaction of potential wall materials with impurities from the plasma requires very well-defined conditions. Parameters like surface composition and sample temperature must be controlled thoroughly. It is also necessary to have control over the energy and composition of the interacting species. Therefore, all our experiments are carried out under ultra-high vacuum (UHV) conditions. Main tools for the characterization of the mixed materials are photoelectron and ion spectroscopies. X-ray photoelectron spectroscopy (XPS) probes core-level transitions yielding information on the specific element, including its chemical environment. Ion spectroscopies are accelerator techniques like Rutherford backscattering spectroscopy (RBS). They provide e.g. quantitative compositional data along with depth distributions. Our experimental setup 'Artoss' [8] combines both surface sensitive tools and ion beam techniques available through a 3 MV tandem accelerator in one chamber. Also *in situ* available are different ion sources for sample bombardment at energies between 100 eV and 20 keV, gas admission facilities and an electron beam evaporator, used here to deposit carbon thin films. For high resolution XPS measurements, a second UHV system ('XPS') is available [9], equipped with a monochromatic Al X-ray source and an ion source for sample preparation. This analysis chamber is connected to a preparation chamber where thin films can be prepared by electron beam evaporation from several sources. Annealing of samples is possible in both experimental set-ups.

All data described in this paper are collected under UHV conditions (base pressures of low 10^{-9} Pa in 'Artoss' and low 10^{-8} Pa in the 'XPS' system). The carbon films are deposited with an Omicron EFM3 electron beam evaporation source using high-purity graphite rods (99.999%, Goodfellow). During carbon deposition the pressure is less than 1×10^{-7} Pa. Non-monochromatic Mg Kα and monochromatic Al Kα radiation are used in 'Artoss' and 'XPS' experiments, respectively. The photoelectron binding energies (BEs) are measured with hemispherical analyzers (PHI) driven at pass energies of 2.95 or 23.5 eV for high-resolution spectra and at 93.5 eV for survey scans. The binding energy scale is calibrated with respect to the Au $4f_{7/2}$ peak at 84.0 eV and for the linearity calibration additionally the Cu $2p_{3/2}$ and Ag $3d_{5/2}$ peaks are used. Peak fitting is performed with a commercial software package [10]. A Shirley background and Gauss-Lorentz fit functions are applied. Quantitative XPS analysis of layer thicknesses is carried out taking into account both the intensities from layer and substrate. Details are given elsewhere [22]. The metal samples used here exhibit polished surfaces and are cleaned *in situ* by Ar^+ sputtering and heating cycles until no contamination can be detected by XPS. We used polycrystalline samples of Au, Be and Ti, as well as single crystals of W(111), Be(0001) and Fe(110). Ar^+ and D^+ are produced from Linde gases (5.0 purity, $D_2 \geq 99.8\%$) in a non-mass separated ion source (Specs IQE 12/38) in the

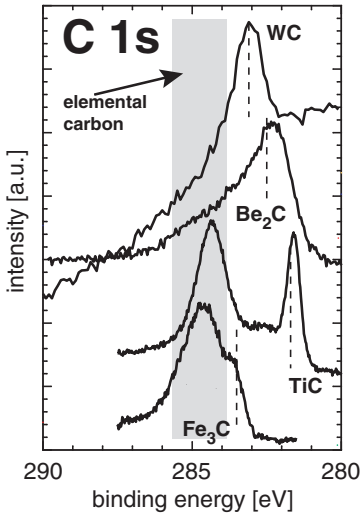

compound	ΔG^0_f [eV]
Ni_3C	0.67
Fe_3C	0.21
W_2C	-0.23
WC	-0.40
SiC	-0.74
Be_2C	-1.19
TiC	-1.88

Figure 2. XPS spectra in the C 1s region of thin carbon films (thickness approx. one monolayer and above) on metal surfaces after deposition at 300 K. The lines indicate the binding energy position of the indicated carbides. Peaks in the highlighted area represent elemental carbon. The Gibbs energies of formation (ΔG^0_f) are taken from [11].

'XPS' system. C^+ and CO^+ are produced both from CO (Linde, 3.7) and CO_2 (Linde, 4.5) gases and the ions are mass-separated in a 80° bending magnet.

RESULTS AND DISCUSSION

Carbon films on metals

The reactivity of several materials with elemental carbon is studied at room temperature (300 K) and elevated temperatures by depositing carbon from the vapor phase on polished high-purity samples by XPS. Starting from sub-monolayer coverages, the chemical state of both carbon and metal substrates can be observed with high sensitivity. At 300 K, all materials investigated so far [12, 13, 14, 15, 16] react with carbon readily under formation of a surface carbide. Figure 2 shows C 1s XPS spectra of thin carbon layers (monolayer range) on Ti, W, Fe and Be substrates. All spectra are plotted without background subtraction. Generally, the carbide layer formed during 300 K deposition is limited to the carbon-substrate interface. Carbon deposited in excess remains in the elemental state. In the cases of Fe, Ti, and also Be substrates shown here carbon clearly is present both as carbide (BE position indicated by the dashed lines) and as graphitic carbon. This is intuitively not surprising for the exothermic carbides of Be and Ti. However, even for the endothermic reaction between Fe and C, Fe_3C formation

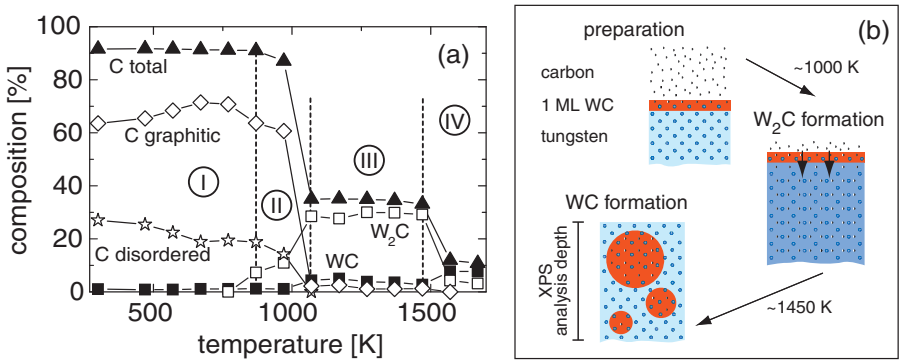

Figure 3. Composition of a 3.9 nm C film on W(111) during annealing, determined by XPS from the C 1s signal (a). W_2C and WC formation processes are accompanied by C diffusion into the W bulk (b).

is observed after 300 K deposition. The table given in Fig. 2 shows the Gibbs free energies of formation of several carbides relevant for fusion materials [11]. Stoichiometric carbides are observed in all four cases shown here. For Ti, which exhibits the narrowest carbide peak at 281.8 eV in this series, additional intensity around 282.6 eV is observed. This indicates the formation of subcarbides like Ti_8C_5 or Ti_6C_5 [17, 18]. Since a narrow photoelectron peak indicates not only exact stoichiometry but also a well-ordered local atomic environment, the narrow TiC peak demonstrates the formation of stoichiometric, locally well-ordered TiC besides the substoichiometric phases.

The interaction of carbon films on metallic surfaces at elevated temperatures is illustrated with the example of a 3.9 nm carbon film on a W(111) single crystal surface. The film is deposited at 300 K and heated up to 1670 K in 100 K steps. The sample is held at the elevated temperatures for 30 min and cooled to 300 K before XPS measurements. A single crystal was chosen in this series to exclude effects from grain boundary diffusion. Figure 3a shows carbon phase evolution with temperature. The analysis is performed by deconvolution of the C 1s signal into several components. These components are elemental carbon (which itself is composed of a graphitic and disordered graphitic part), tungsten subcarbide (W_2C) and tungsten carbide (WC) [19]. The behavior over the whole temperature range can be divided into four phases. Phase 1 shows a constant carbon amount up to 970 K. The disordered graphitic part in the C 1s signal decreases while in parallel the ordered graphitic fraction increases. Due to the gentle annealing, defects created during the carbon deposition can react and the graphitic structural order is improved. The initially present carbide at the interface (see Fig. 2 for thin C layers) remains unchanged. Around 1000 K, phase 2 is characterized by a beginning diffusion of carbon into the substrate, accompanied by the formation of a subcarbide phase (W_2C).

Phase 3 between 1070 and 1470 K shows a constant carbon amount within the XPS analysis region and also no changes in the carbide phases. W_2C dominates although the concentration of WC has slightly increased compared to phases 1 and 2. Above 1470 K, carbon diffusion into the substrate accelerates and finally only approx. 10% of the surface within the XPS analysis depth consists of carbon. W_2C decreases at the cost of

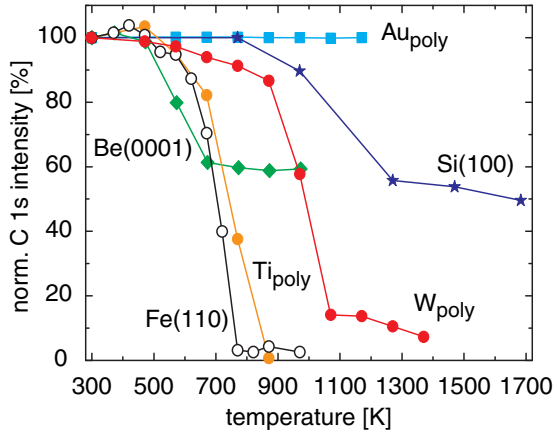

Figure 4. Comparison of the temperature-dependent reaction and diffusion behavior of carbon films on several substrates. The initial C 1s intensities are normalized to 100%.

WC, which becomes the dominating carbide compound. The whole process is illustrated in Fig 3b. These four phases are observed similarly on other substrates. However, not all metals form well-distinguished carbide phases like it is the case here with tungsten. E.g. titanium has a broad range of substoichiometric carbide phases with smaller C fractions than in TiC [20, 17, 18, 21]. A marked difference is observed for metals which form endothermic carbides: Ni and Fe (see table in Fig. 2). Here, during phase 1 not only ordering in the elemental carbon is observed. A decrease in the respective carbide concentration also shows the decomposition of the initially formed carbides due to their endothermic nature. With two Ni surfaces, the temperature onset for carbon diffusion into the Ni was examined with respect to the surface orientation. On Ni(110), which is more open surface, diffusion sets in at 670 K. On the dense Ni(111) surface, however, no C diffusion is observed below 770 K. This demonstrates that the surface atom density is a crucial parameter for carbon diffusion in the case of thin surface films [22].

Two processes dominate the interactions of elemental carbon film on substrates: carbide formation and carbon diffusion into the bulk. Besides them, the ordering of disordered graphitic carbon into graphite is observed. Before carbon diffusion sets in, carbide is only present at the interface between carbon layer and substrate. This interfacial carbide even exists if the carbide formation reaction is endothermic, as in the cases of Fe and Ni. Figure 4 compares the carbon-substrate interactions for carbon layers of a few nm thickness on several elements. The layers are thin enough to detect all carbon by XPS. Shown are the total C 1s intensities, normalized to 100% after the carbon deposition at 300 K. As a comparison with an unreactive substrate, a carbon film on polycrystalline gold is shown. Au neither forms a carbide, nor is carbon soluble in Au. The results demonstrate that the initial carbon intensity stays constant up to 88% of the melting temperature of gold. No carbon loss is observed. This is different for all other elements examined here which form carbides. In the cases of Be(0001) and Si(100) substrates, a final carbon intensity is reached which reflects approximately the stoichiometry

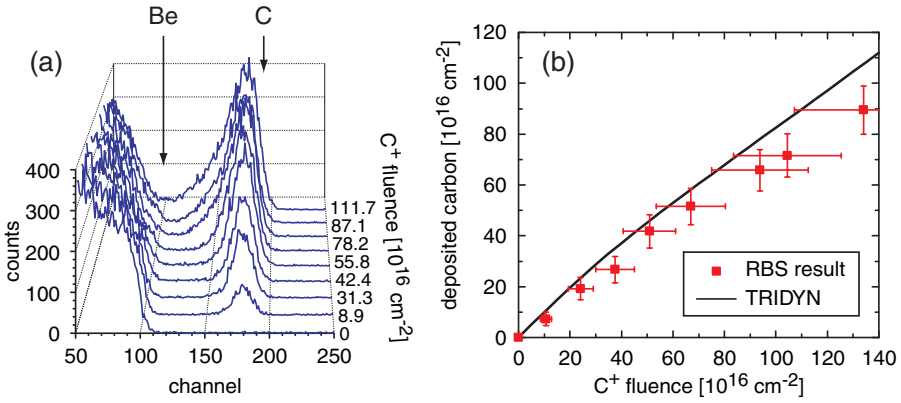

Figure 5. RBS spectra (a) and quantitative analysis (b) a of bombardment of a Be substrate by 5 keV C^+. Carbon is accumulated in Be and forms an overlayer. The experiment is well reproduced by a TRIDYN simulation.

of the respective carbides (Be_2C and SiC). Deviations from the stoichiometric ratio of the compounds are due to different relative substrate sensitivities before and after compound formation because of the exponential escape depths of electrons. No extended carbon loss into the bulk is observed, the inter-diffusion of substrate and carbon stops after compound formation. This can be understood with the ionic bond character in these compounds. The charged nature of the lattice constituents prevents diffusion of carbon out of the formed compound layer. This is very different in case of the metallic carbides which form e.g. on Fe, Ti, and W. Here, carbon occupies different sites within the metal host lattices. Since neither the metal atoms nor carbon carry electrical charges, diffusion between similar sites is facilitated compared to an ionic solid. In the Fe and W cases, formed carbide phases stabilize the carbon concentration in certain temperature regimes. This is not the case for Ti, since here no rearrangements in the metal lattice are necessary upon carbide formation. The influence of grain boundary diffusion can be seen in the comparison of Fig. 3a and the W curve in Fig. 4. In contrast to the W(111) substrate, in case of W_{poly} more gradual changes between the carbon phases are observed. In the polycrystalline solid, grain boundary diffusion is a second path besides carbon diffusion through the metal lattice. The difference of W(111) and W_{poly} is also reflected in the different activation energies for the subcarbide formation process (phase 2 in Fig. 3a). For C/W(111) the activation barrier for this process is 1.1 eV, whereas for C/W_{poly} the activation energy is reduced to 0.8 eV.

Carbon ion implantation

Interactions of metal surfaces with energetic particles of keV energies which are present mainly in the main chamber of fusion devices (Fig. 1b), are investigated in ion implantation experiments. The difference to the interactions described in the last section

is that such ions carry kinetic energy which leads to the deposition of the respective species not at the surface, but in deeper areas of the substrate. Moreover, the excess kinetic energy can trigger chemical reactions and thereby initiate compound formation at much lower temperatures than necessary for reactions of vapor-deposited layers with surfaces. Kinetic interactions between keV particles and solid surfaces can be simulated using Monte Carlo codes like TRIM.SP or TRIDYN [7, 23]. These programs calculate collisional processes in the target by tracing each particle and all generated secondary particles in an amorphous solid, calculating energy and momentum transfer according to binary elastic collisions and electronic stopping processes, until the particles' kinetic energies are below a threshold energy. TRIDYN additionally takes into account compositional changes in the target with respect to the depth from the surface. This is done by dividing the target in thin layers and dynamically adapting their respective composition. However, no chemical (e.g. compound formation) and diffusional effects are included in the simulation. Therefore, chemical processes can be deduced by comparing experimental results with TRIDYN simulations.

Figure 5 shows the modifications of a Be surface by implantation of 5 keV C^+. In Fig. 5a RBS spectra measured after increasing C^+ fluences are plotted. For small C^+ fluences the carbon signal is shifted to lower channels compared to the C surface position which is indicated by the arrow. Complementary, the Be edge shifts to lower channels during increased implantation. Additionally, carbon intensity builds up between the C and Be edges. These observations demonstrate the formation of a carbon layer at the surface. After an initial phase where C^+ is deposited below the Be surface and Be is sputtered by C^+ ions, carbon accumulates also at the outermost surface. Since the impact angle and ion energy lead to a carbon self-sputtering yield below 1, continued C^+ implantation leads to a buildup of a carbon surface layer, as soon as enough carbon has accumulated at the surface. In Fig. 5b the carbon amounts determined from the RBS spectra are plotted against the implanted C^+ fluence together with a TRIDYN simulation. The trend of the experimental curve is reproduced perfectly by the Monte Carlo simulation. Even quantitatively, the agreements is well within the experimental errors. The errors shown with the data points account for the quantification of the deposited carbon by RBS and the error in the implantation current measurement. The error in the RBS amounts is calculated as the square root of the RBS intensity. For the implantation current measurement an error of 20% is assumed. The observed agreement between TRIDYN and experimentally determined carbon after ion implantation leads to the conclusion that, even though there are chemical reactions taking place (formation of Be_2C [24]), the kinematic simulation is sufficient to describe the experimental results. This is due to the fact that no volatile species are produced and not diffusion phenomena are present under these conditions.

The situation changes completely for a system which contains oxygen as third element. Figure 6 shows the results for an experiment in which a Be surface is bombarded with CO^+. This experiment mimics the simultaneous bombardment by C and O, since CO^+ splits up upon impact at the surface. The kinetic energy of the molecular ion is distributed according to the atomic mass ratio, therefore O taking a slightly larger part than C. In Fig. 6a the amounts of carbon and oxygen collected in the sample during implantation of 3, 5 and 12 keV CO^+, measured by RBS, are shown, together with a TRIDYN simulation for the 5 keV case. For low fluences, the CO^+ are implanted into the Be and

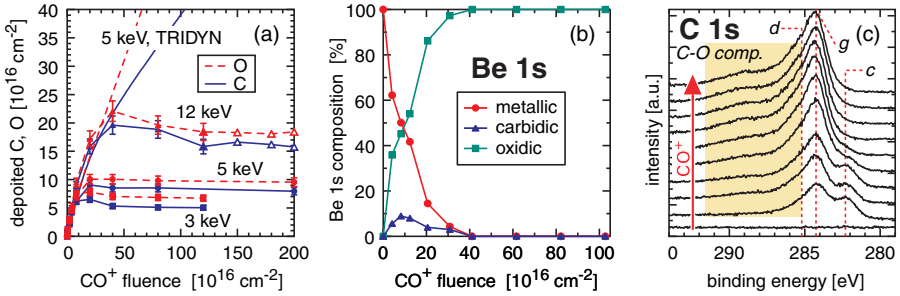

Figure 6. CO^+ implantation into beryllium at three different primary energies. The accumulated amounts of C and O are measured by RBS and compared to a TRIDYN simulation (a). The Be 1s XPS analysis of a 5 keV CO^+ bombardment shows a transient formation of Be_2C. For larger fluences Be is completely bound in BeO (b). Carbon is present initially in *c*arbidic and elemental form (*g*raphitic and *d*isordered graphitic), later also C-O compounds appear in the highlighted BE area (c).

the measured data points follow well the TRIDYN simulation. After a transition fluence which depends on the ion energy the C and O amounts in the Be sample level off and stay constant for larger CO^+ fluences. In all cases, the amount of O is slightly larger than of C. However, the ratio C/O approaches 1 for increasing energies (0.75, 0.85 and 0.90 for the respective CO^+ energies of 3, 5, and 12 keV). Calculations by TRIM.SP show that the different implantation depths of C and O into Be adjust for increasing kinetic energies. Therefore, the reason for different C and O amounts is the asymmetric splitting of the CO^+ kinetic energy. The O implantation zone is dynamically slightly broader than that for C. XPS analysis reveals the chemical species formed during the CO^+ implantation process. In Fig. 6b the result of the Be 1s signal deconvolution and plotted against the fluence. The initially metallic Be reacts readily both with C (forming Be_2C) and O (forming BeO). The Be_2C phase, however, is only present in a transient low-fluence regime. BeO as the more exothermic compound is the only Be compound in the steady-state regime at higher fluences. For C, the chemical composition is more complicated. Figure 6c shows the C 1s regions with increasing CO^+ fluence, indicated by the arrow. At low fluences, again the carbidic species is visible (labelled *c*) and vanishes again for prolonged ion bombardment. Right from the beginning, elemental carbon can be found (graphitic, *g*, and disordered carbon, *d*). Continued CO^+ bombardment additionally leads to intensity in the highlighted area, labelled *C-O comp*. Here, several carbon-oxygen compounds appear (carbonates, adsorbed CO and CO_2 [25, 26]. The appearance of constant C and O inventories in the Be substrate despite the continued CO^+ bombardment can only be explained by a chemical erosion channel which releases C and O at the same rate as it is deposited by the ion beam. Due to the complicated chemical surface composition, further experiments are necessary to clarify the mechanism. For Be at the first wall of a fusion device under these conditions, a continuous erosion is the consequence from these observations, since the continuously eroded mixed surface layer always also contains beryllium.

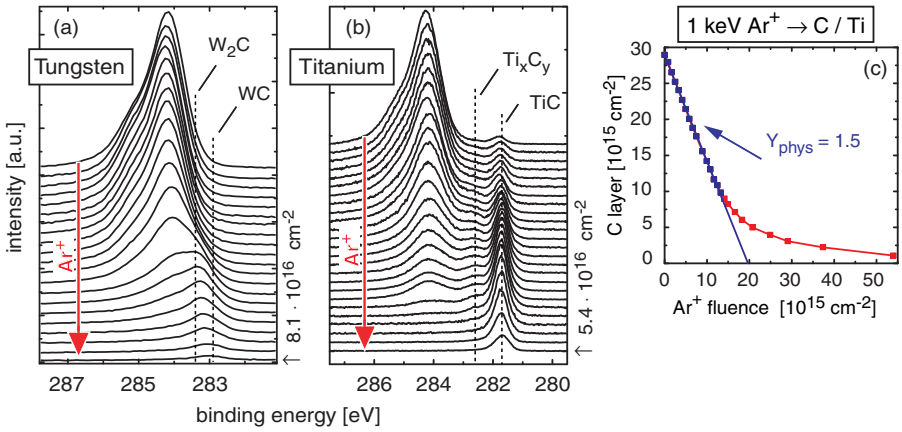

Figure 7. Bombardment of carbon layers on W (a) and Ti (b) by 1 keV Ar^+. The initially linear decrease of the carbon amount on a Ti substrate (c) is typical for a physical sputtering mechanism.

Ion-induced surface reactions

An alternative energy contribution to the system compared to annealing in order to initiate chemical reactions between surface layers and substrate is bombardment at 300 K by kinetic ions. If noble gas ions are used, the dispersed kinetic energy can be used for ion beam mixing processes, whereas the projectile cannot participate in chemical reactions. If, on the other hand, e.g. D^+ ions are used, they can additionally undergo chemical reactions with the solid themselves. These two alternatives are discussed for Ar^+ and D^+ bombardments of carbon layers on titanium. In addition, Ar^+ bombardment of a C layer on tungsten is discussed.

Figure 7 demonstrates the formation of stoichiometric and substoichiometric carbides for carbon layers on W (7a) and Ti (7b) by Ar^+implantation. After C deposition and at low fluences, the C 1s spectra are dominated by elemental carbon (graphitic and disordered, which is visible as a shoulder at higher BEs around 285.2 eV [19]). On Ti, TiC at the layer-substrate interface is visible. Upon Ar^+ bombardment (increasing Ar^+ fluences are indicated by arrows), several processes can be observed. First, the total amount of carbon decreases due to sputtering. Second, since the high-BE shoulder in the elementary peak vanishes faster than the total decrease of elemental carbon intensity, the disordered fraction seems to erode quicker than the graphitic part. Third, the intensity in the BE regions of the carbides increases during bombardment and passes through a maximum. Finally, it also decreases, as erosion by sputtering continues. Intermediately, on both metals subcarbides (W_2C, Ti_xC_y) are formed. Fourth, quantitative examinations of the carbide peak widths show that on Ti, the TiC peak widths correspond to the experimental resolution. However, on W, the widths are wider than this resolution. This implies that the carbon atoms in the formed TiC are all in an identical, well-ordered local atomic environment. The formed WC, however, must be present less well

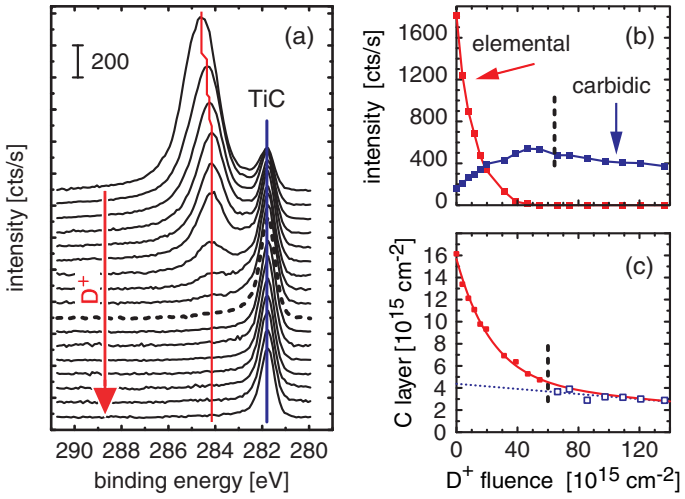

Figure 8. C 1s XPS spectra (a) during 4 keV D^+ bombardment of a C layer on Ti. With increasing fluence (indicated by the arrow), elemental C is eroded and initially TiC is formed, before at large fluences also TiC is sputtered (b). The total erosion of C is plotted in (c). The dashed spectrum and lines indicate the fluence where elemental C has vanished.

locally ordered. This interpretation yet awaits a direct confirmation, e.g. by EXAFS measurements. A quantitative analysis of the changes in the carbon amount on Ti during the Ar^+ bombardment is plotted in Fig. 7c. The first part of the erosion curve shows a linear decrease. This is a strong indication for physical sputtering of an adlayer of more than one monolayer in thickness. From the slope results a sputtering yield of $Y_{phys} = 1.5$. Since Ar is a noble gas for which no chemical interaction of Ar^+ with the substrate elements is expected, this linear behavior confirms these expectations.

However, if deuterium ions are used instead of unreactive Ar^+, an additional chemical erosion channel opens up. Figure 8 shows an experiment where a C layer on Ti is bombarded by 4 keV D^+ ions. The C 1s spectrum series (Fig. 8a) shows the erosion of the elemental C and the evolution of carbidic C. Again, the increasing D^+ fluence is indicated by an arrow and corresponds to the scale in Fig. 8c. XPS allows for quantitative analysis of the interaction process by separating the carbon phases. These results are plotted in Fig. 8b and show that the elemental carbon is eroded quickly, while TiC is formed in a parallel process. After the removal of elemental C, erosion of TiC starts as well. The vertical dashed lines in Figs. 8b+c indicate this fluence which corresponds to the dashed spectrum in Fig. 8a. The conversion of the C 1s intensity in a carbon coverage reveals two separate processes responsible for the C erosion. The data points in Fig. 8c are fitted by the sum of an exponential decay (solid line) and a linear function (dotted lined). For a mere physical sputtering process, only a linear function is expected for layers larger than a monolayer [27]. This behavior is indeed observed here for fluences above 6×10^{16} cm^{-2} with a sputtering yield $Y_{phys} = 0.01$, in reasonable agreement with

TRIDYN calculations. However, the first part at lower fluences fits to an exponential function. This can only be explained if the entire carbon layer reacts simultaneously. This supports a model in which the penetrating D^+ interact chemically with the entire carbon layer under hydrocarbon formation. These products then need to diffuse to the surface and desorb. The erosion yield for such a process, calculated from the exponential function, is $Y_{chem} = 0.09$ and almost one order of magnitude larger than the physical sputtering yield. To proof this mechanism, experiments with detection of desorbing species are under way.

CONCLUSIONS

The presence of carbon materials in a fusion device is justified by beneficial physical properties of carbon with respect to thermal stability and conductivity. During operation, carbon is eroded, transported along magnetic field lines, and re-deposited at different locations than originally designed. Therefore, carbon becomes a reaction parter to the additionally employed materials at the first walls, which are predominantly metals. The reactivity of carbon present in thin layers ranging from sub-monolayers to nm films is studied with respect to carbon-substrate and carbon-plasma particle interactions. Particle species coming from the plasma are to the large part hydrogen isotopes, but also plasma impurities like carbon itself and oxygen. Particle energies range from close to thermal to several keV which trigger different particle-surface interaction processes. At low kinetic energies, adsorption/desorption phenomena as well as chemical interactions dominate. They not only depend on the availability of reactive material, but also on the substrate temperature which controls diffusion in the reactive solid-solid systems. At kinetic energies in the keV regime, in addition to chemical processes kinematic ion-solid interactions occur. This comprises erosion by physical sputtering and also chemical reactions activated by ion-beam mixing effects and the accompanied energy entry into the surface layers.

In this paper the carbide formation at 300 K and elevated substrate temperatures is discussed for exo- and endothermic metals which form ionic as well as metallic carbides. In all cases, carbide formation occurs already at 300 K. At this temperature, it is limited to monolayers at the very interface between carbon and substrate. Carbide formation in excess to this thin interface sets in at substrate-specific temperatures. In parallel, carbon-substrate inter-diffusion occurs. In case of the ionic carbides, no dissolution of the carbon in the bulk of the substrates is observed. The formed carbide layers are thermally stable. If the carbide type is metallic, as it is the case for many transition metals, surface carbide layers are only stable in a limited temperature range. Above this, dissolution of carbon in the metal bulk dominates. Whether thin a carbon layer remains at the surface or not seems to be determined by bulk restructuring effects. If the metal atoms have similar structures in metal and carbides, dissolution of carbon is almost quantitative (this is the case for Ti). If carbide structures differ significantly from the bulk metal structure, even at very high temperatures, carbides are still present at the surface (e.g. for Fe and W).

Carbide formation reactions can also be initiated by ion impact. This is not only of importance for fusion first wall materials, but should also kept in mind when sputter

depth profiling a sample for chemical analysis! Carbide formation by ion impact is a consequence of ion beam mixing. For metals forming several carbide phases, initially subcarbides are observed (Ti and W). At extended fluences, the stoichiometric carbide phases TiC and WC are formed. Narrow carbide peak widths indicate a high local order around C atoms in TiC, whereas in WC lower structural ordering seems to be the result of Ar^+-induced carbide formation. This correlates with the higher formation enthalpies in TiC which initiate local ordering processes. Reactive ion bombardment also leads to chemical reactions in addition to kinematic processes. This is especially the case for element combinations which potentially can form volatile molecules. In the ternary systems Be–C–O and Ti–C–D, enhanced erosion rates compared to mere kinematic sputtering processes are observed. This observation points out the importance of studies of complex systems for the prediction of first wall processes in fusion devices.

ACKNOWLEDGEMENTS

The author gratefully acknowledges the continued discussions with J. Roth. The results presented here are parts of the PhD theses by P. Goldstraß, J. Luthin, A. Wiltner and K.U. Klages.

REFERENCES

1. R.R. Parker, Nucl. Fusion 40 (2000) 473.
2. R. Neu, K. Asmussen, K. Krieger et al., Plasma Phys. Control. Fusion 38 (1996) A165.
3. G. Federici, C.H. Skinner, J.N. Brooks, J.P. Coad, C. Grisolia, A.A. Haasz, A. Hassanein, V. Philipps, C.S. Pitcher, J. Roth, W.R. Wampler, and D.C. Whyte, Nucl. Fusion 41 (2001) 1967.
4. R. Neu, K. Krieger, private communication.
5. H. Verbeek, J. Stober, D.P. Coster, W. Eckstein, R. Schneider, Nucl. Fusion 38 (1998) 1789.
6. K. Krieger, A. Geier, X. Gong, H. Maier, R. Neu, V. Rhode, ASDEX Upgrade Team, J. Nucl. Mater. 313–316 (2003) 327.
7. J.P. Biersack, W. Eckstein, Appl. Phys. 34 (1984) 73.
8. Ch. Linsmeier, P. Goldstraß, K.U. Klages, Physica Scipta T94 (2001) 28.
9. S. Miller, G. Berning, H. Plank, and J. Roth, J. Vac. Sci. Technol. A 15 (1997) 2029.
10. MultiPak Ver. 6.1A, Physical Electronics, 1999.
11. I. Barin, Thermochemical Data of Pure Substances, 3rd ed., Vol. 1&2, Weinheim (1995).
12. P. Goldstraß, Ch. Linsmeier, Nucl. Instrum. and Meth. B 161–163 (2000) 411.
13. P. Reinke and P. Oelhafen, Diamond Relat. Mater. 8 (1999) 155.
14. J. Luthin, H. Plank, J. Roth, and Ch. Linsmeier, Nucl. Instr. and Meth. B 182 (2001) 218.
15. J. Luthin and Ch. Linsmeier, Physica Scripta T91 (2001) 134.
16. A. Wiltner and Ch. Linsmeier, Phys. Stat. Sol. (a) 201 (2004) 881.
17. B.V. Khaenko, S.Ya. Golub, and M.P. Arbuzov, Sov. Phys. Crystallogr. 25 (1980) 63.
18. N.V. Dzhalabadze, B.G. Eristavi, N.I. Maisuradze, and E.R. Kuteliya, Phys. Met. Metallogr., 86 (1998) 59.
19. J. Luthin and Ch. Linsmeier, Surf. Sci. 454–456 (2000) 78.
20. T.B. Massalski, H. Okamoto, P.R. Subramanian, L. Kacprzak, *Binary Alloy Phase Diagrams*, 2nd Ed., Version 1.0, ASM International, Materials Park, Ohio (1996).
21. H. Goretzki, Phys. Status Solidi 20 (1967) K141.
22. A. Wiltner and Ch. Linsmeier, to be published.
23. W. Eckstein, *Computer Simulation of Ion-Solid Interactions*, Springer Series in Materials Science, Vol. 10, Springer, Berlin (1991).

24. P. Goldstraß, and Ch. Linsmeier, J. Nucl. Mater. 290–293 (2001) 71.
25. E. Meyer, D. Reinhart, D. Borgmann, G. Wedler, Surf. Sci. 320 (1994) 110.
26. J.F. Moulder, W.F. Stickle, P.E. Sobol, K.E. Bomben, *Handbook of X-Ray Photoelectron Spectroscopy*, Ed. J. Chastain, Perkin-Elmer Corp. Eden Prairie (1992).
27. E. Taglauer, W. Heiland and J. Onsgaard, Nucl. Instr. and Meth. 168 (1980) 571.

phys. stat. sol. (a) **201**, No. 5, 881–887 (2004) / **DOI** 10.1002/pssa.200304362

Formation of endothermic carbides on iron and nickel

A. Wiltner and **Ch. Linsmeier***

Max-Planck-Institut für Plasmaphysik, EURATOM Association, Boltzmannstrasse 2, 85748 Garching b. München, Germany

Received 30 October 2003, accepted 31 January 2004
Published online 18 March 2004

PACS 68.35.Fx, 68.55.Jk, 68.60.Du, 79.60.Dp

The formation of endothermic carbides on Fe and Ni is studied using X-ray photoelectron spectroscopy (XPS) by deposition of carbon films from the vapor phase and subsequent annealing steps. The reaction between carbon and metal substrates is measured by shifts in the C 1s photoelectron peaks. By comparison with two elementary carbon photoelectron energies determined from carbon films on unreactive Au substrates, a carbide peak in the C 1s spectra on reactive Fe and Ni substrates is identified. The carbides formed after deposition of carbon films at room temperature are located at the interface between carbon film and metal substrate. We report on the behavior of elementary carbon films with respect to film thickness and thermal treatment leading to carbide formation and carbon diffusion into the bulk.

1 Introduction Various authors reported on the interaction of C with Fe or Ni. We focus on photoelectron spectroscopy measurements concerning the carbides. Shabanova et al. [1] measured the Fe 2p, C 1s and valence band energy region of Fe_3C at 510 K by XPS. Panzner et al. [2] reported on iron carbide measured with XPS, UPS, AES and EELS. They prepared the carbide (Fe_3C) on iron-chromium (Cr: 3%) and iron-manganese (Mn: 20%) alloys. Other authors confirm the binding energies given in this report. Sinharoy et al. [3–5] reported on Ni films on graphite. They observed a decomposition of carbide between 420 and 670 K. Zdansky et al. [6] formed a carbon layer on Ni by thermal decomposition of C_2H_4 or CO. Nickel carbide was observed in XPS measurements. Other authors [7, 8] found carbide after carbon segregation. In those experiments the carbon films on Ni were prepared by thermal decomposition of hydrocarbons or precipitation at high temperatures. We deposit the carbon films from the vapor phase with substrates at room temperature thereby making accessible investigations of the reactivity between metal and carbon during thermal treatments.

In earlier work we studied carbon films on W, Ti, Si and Be [9–12]. These substrates all show exothermic carbide formation and we find increased carbide fractions at elevated annealing temperatures. The onset of carbide formation and the amount of carbide detected at the interface (within the XPS information depth) depends both on thermodynamic properties as well as on the structures of the respective elements and carbides.

Iron and nickel form endothermic carbides under standard conditions. The respective Gibbs free energies of formation (ΔG_f^0) are given in Table 1. Carbon films on Ti, Si, Be and W upon heating behave according to the thermodynamic properties of the respective carbides. Ti with the most negative value of ΔG_f^0 shows the most pronounced carbide formation at the lowest temperature compared to the other substrates. Furthermore, the carbide formation depends on the substrate and carbide struc-

* Corresponding author: e-mail: linsmeier@ipp.mpg.de, Tel.: +49-89-3299 2285, Fax.: +49-89-3299 1149

Table 1 Free enthalpy of formation at 300 K [18] for Ni_3C and Fe_3C and carbides measured before and reported in [9–12].

carbide	ΔG_f^0 (eV)
TiC	−1.87
Be_2C	−1.19
SiC	−0.73
WC	−0.40
W_2C	−0.23
Fe_3C	+0.21
Ni_3C	+0.66

tures. The carbides of Ti and W are intercalation compounds. Ti with a hexagonal close packing provides octahedral sites within the metal lattice. These sites are consecutively filled by carbon leading to subcarbides and – if all sites are filled – the stoichiometric TiC (in fact "TiC" is always slightly understoichiometric: $TiC_{0.95}$ [13]). In the case of W, the metal atoms are arranged in a body centered cubic packing. The octahedral sites within this lattice are too small to accommodate carbon. There are two carbides known for W: W_2C and WC. In the case of WC the metal has to rearrange into a hexagonal primitive structure with trigonal prismatic sites. WC is formed if 1/2 of these sites are occupied by C. In the case of W_2C the metal rearranges into a hexagonal close packing in which the octahedral sites are occupied by C. To conclude the structure description, the formation of intercalated carbides (TiC, WC and W_2C) requires a migration of C into the metal lattice. This behavior is visible as carbon diffusion together with an increasing carbide intensity. Si and Be are examples for carbides with ionic bonding (SiC, Be_2C). The thermal behavior of carbon films on these two substrates is comparable. Once the carbide is formed in the respective stoichiometric ratio, the compound layer is stable during further annealing. Corresponding to the more negative value of ΔG_f^0 for Be_2C, the carbide formation sets in at lower temperatures than for SiC. To summarize the observations about carbide formation from carbon on elemental substrates, we find a clearly visible trend in carbide formation depending on the thermodynamic properties. Furthermore, the carbide formation is governed both by carbon diffusion and metal lattice structure.

Keeping the thermodynamic properties in mind, we deposit carbon films on Ni and Fe. These metals show endothermic carbides (see Table 1) with similar carbide structure [14]. Both carbides are intercalation compounds and the metal substrates have to rearrange during the carbide formation. Such a behavior is comparable to WC and W_2C. The bulk structure models for Fe, Ni and their respective carbides are shown in Fig. 1. In the case of Fe the metal has to rearrange from a body centered cubic packing into a complex orthorhombic structure with carbon in trigonal prismatic like sites. Nickel on

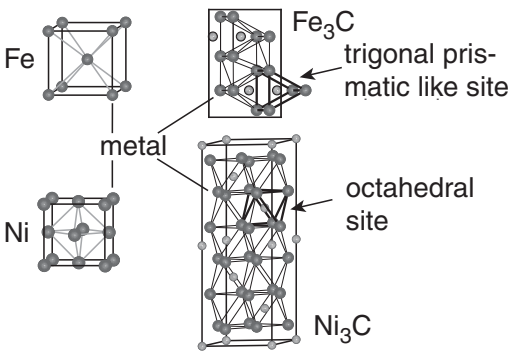

Fig. 1 Lattice structures of the metals (dark gray circles) and the carbides. Carbon (light gray circles) occupies trigonal prismatic sites in Fe_3C and octahedral sites in Ni_3C. In both structures the metal has to rearrange during the carbide formation.

the other hand has to rearrange from a cubic close lattice into a trigonal structure with a hexagonal close packing of Ni and C in octahedral sites.

This work describes our studies of carbon films on Ni and Fe and their carbide formation with respect to their thermodynamic properties. We compare these endothermic reactions with earlier studied carbides on W, Ti, Si and Be.

2 Experimental The XPS measurements are performed in a commercial XPS system (PHI 5600 ESCA, base pressure $<3 \cdot 10^{-8}$ Pa) with monochromatic Al Kα radiation. The hemispherical analyzer is driven at a pass energy of 2.95 eV for high resolution measurements and at 93.90 eV for survey scans. The binding energy scale is calibrated with respect to the Au $4f_{7/2}$ (84.0 eV) peak. For linearity calibration, additionally the Ag $3d_{5/2}$ (368.3 eV) and Cu $2p_{3/2}$ (932.7 eV) signals are used [15]. Measuring with a pass energy of 2.95 eV leads to a full-width-at-half-maximum (FWHM) of 0.6 eV for the Au $4f_{7/2}$ peak. The angle between X-ray source and the analyzer is 90°. The sample can be rotated leading to different take-off angles. For the measurements an analysis angle of 68° between analyzer and surface (22° take-off angle) is used. Under this angle the information depth is maximized since we are interested in chemical information from the carbon-substrate interface. The samples are cleaned in situ by repeated sputtering (3 kV Ar^+) and annealing (up to 970 K) cycles until no impurities are observed in the spectra. Fe(100) (diameter 0.5 cm) and a Ni(111) (diameter 1 cm) crystals are used as substrates. A polycrystalline Au foil on the sample holder in addition to the Fe and Ni crystals is used for monitoring of the Au 4f peak position. Carbon films are deposited in a preparation chamber (pressure during deposition $<3 \cdot 10^{-7}$ Pa) which is connected with the XPS chamber via a UHV valve. The carbon source is an Omicron EFM3 electron beam evaporator filled with a graphite rod (99.999%, Goodfellow). XPS data is analyzed using the MultiPak [19] program. A Shirley background and Gauss–Lorentz functions are fitted to the experimental data. For the figures in this paper, the Shirley background is subtracted before plotting experimental data and fitted peaks.

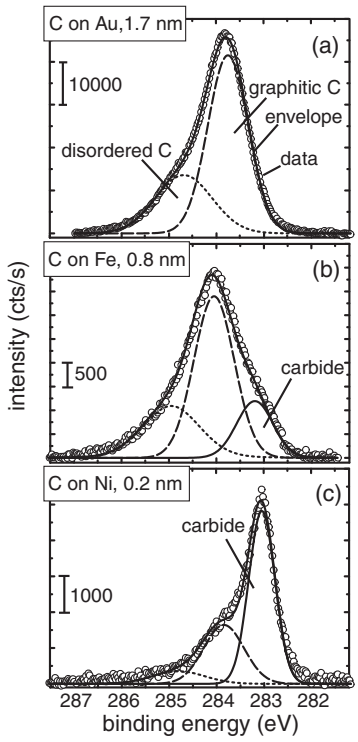

Fig. 2 Photoelectron spectra of carbon films deposited on Au (a), Fe (b) and Ni (c). The elemental state in the C 1s signal (measured data: open circles) consists of graphitic C (- -) at 284.2 eV and disordered C (···) at 285.1 eV. On reactive substrates an additional component in the carbidic state (solid line) is found. The envelope (solid line) represents the sum of all components and matches with the measured C 1s signal.

3 Results

3.1 Carbon films at room temperature In contrast to all other substrates we reported in [9–12], carbon on Au shows no reaction or diffusion into the bulk. We use unreactive carbon films on Au in order to characterize the elementary carbon states within the C 1s binding energy region. The C 1s signal (Fig. 2a) exhibits graphitic carbon at 284.2 eV and an additional state at higher binding energy (285.1 eV) which we assign to disordered graphitic C. This carbon fraction is clearly visible as a shoulder in the C 1s signal in

case of thicker films. XPS measurements of a HOPG (highly oriented pyrolytic graphite) sample show graphitic C. After Ar^+ bombardment of HOPG an additional state at higher binding energy is created, denoted as disordered graphitic C. The amount of this disordered fraction can be modified by ion bombardment as well as by annealing. Ion bombardment leads to an increase in disordered C, but this fraction can be reordered again during annealing. Thermal treatment of deposited films on Au without irradiation leads to a shift of intensity from disordered to ordered graphitic C.

Reactive carbon films on already described substrates [9–12] show a thin carbide layer at the interface, but the carbide amount differs. Even being endothermic, we find a small carbide intensity on Ni and Fe after 300 K deposition. Figure 2 shows carbon films on Fe (b) and Ni (c) and compares them to the already described films on Au (a). The binding energies of the carbides are at 283.5 eV for Ni_3C and 283.4 eV for Fe_3C, respectively. Both signals have a FWHM of 1.0 eV. These values are in good agreement with literature data [1, 2, 4, 6]. The carbide intensity mentioned above is very small on iron and nickel (corresponding to less than 1 ML), whereas we find a larger carbide fraction on the other substrates. This carbide layer is located at the interface between deposited carbon layer and metal substrate. This restriction of the carbide to the interface is clearly visible in XPS measurements under different take-off angles. Figure 3 illustrates the angle dependence of the C 1s signal composition. The more surface sensitive the measurements are (60° take-off angle), the higher is the carbide intensity. In this example we deposit a carbon film (1.6 nm) on Ni. In the case of 22° take-off angle we find 5% carbide intensity, whereas under 60° the fraction amounts to 18%. In addition to the angle dependence of the carbide intensity we find a maximum carbide amount in thin films (∼1 ML). Additionally deposited C is in the elementary state.

The carbon film thickness is evaluated under assumption of a layer growth with inelastic mean free paths (IMFP) of 1.082 nm (Ni $2p_{3/2}$), 1.494 nm (C 1s) and 1.201 nm (Fe $2p_{3/2}$). We use the "universal" Seah-Dench equation (Eq. (1)) as reported in [16].

$$\lambda(E_S) = \frac{538}{E_S^2}\, a + 0.41 a^{3/2} E_S^{1/2} \qquad (1)$$

E_S (in eV) represents the energy of the photoelectrons, a is the atom diameter (in nm). For the calculation of a a density of 1.8 g/cm^3 for the deposited carbon films is applied [9, 17].

3.2 Thermal behavior of carbon films Carbon films on Ni and Fe are annealed in steps of 50 or 100 K for 10 or 30 min. XPS measurements are performed at room temperature

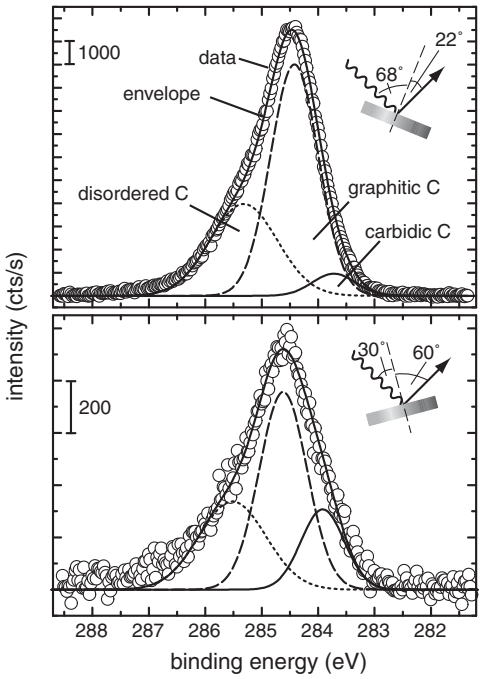

Fig. 3 C 1s signal composition under different take-off angles. The example shows a 1.6 nm carbon film on Ni. Spectrum (a) is measured under 22° take-off angle with respect to the surface normal whereas spectrum (b) is measured under 60° take-off angle. The measurement under 22° has a larger information depth and shows smaller intensity resulting from interfacial carbide.

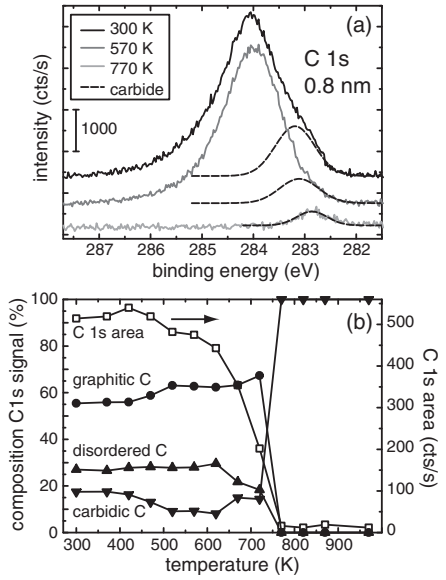

Fig. 4 Thermal behavior of a 0.8 nm carbon film on Fe. Exemplary C 1s signals are shown in (a), demonstrating the carbidic state (- -) within the spectra. The quantitative analysis of the C 1s signals by peak fitting and the resulting composition of the carbon peak is shown in (b). The C 1s area represents the total carbon amount present within the XPS analysis depth.

between the treatment steps. On both substrates the carbide formed initially after carbon deposition decomposes at relatively low temperatures, while the total C 1s intensity remains constant. In Fig. 4 the C 1s signals and the surface composition of a carbon film (0.8 nm) on Fe resulting from the fit procedure are shown. The thermal behavior of a thin 0.4 nm carbon film on Ni is similar (not shown). The C 1s signal of thin films (<1 nm) shows a shoulder at lower binding energies assigned to carbide (Fig. 2). After annealing the carbide intensity decreases and reaches its minimum at 520 K. The overall C 1s area is nearly constant in this temperature region and the decrease in carbide is explained by decomposition of the initially formed carbide. This observation complies with the endothermic enthalpy of formation of the Fe and Ni carbides and is therefore expected from their metastable character. A decomposition of Ni_3C is also reported in [3–5]. The authors observe a beginning decomposition at 420 K and a complete loss of carbide above 670 K, as measured by AES. We find a clear decrease in carbide intensity of carbon films on Fe and Ni only for thin films (∼1 nm) and attribute this to the surface sensitivity of XPS measurements. In the case of thicker films the elementary carbon covering the interfacial carbide attenuates the photoelectrons coming from the carbide and the small variation in the carbide fraction is only barely detectable. The results for a thicker carbon film (1.9 nm) on Ni are shown in Fig. 5. The carbide intensity is nearly constant until the total C 1s intensity decreases, only a very small decrease between 300 and 800 K is visible. The ordering of the elementary state is clearly visible by a decrease in the disordered C fraction. Starting around 800 K we observe additional carbide formation. This increase in carbide intensity is accompanied by an onset of carbon diffusion into the bulk leading to a smaller total C 1s signal intensity.

On Fe the carbon diffusion sets in at 670 K. The carbon remaining in the surface region contributing to the XPS signal is in the carbidic state, whereas the elementary carbon vanishes. The diffusion and reaction of carbon on Fe is independent on the carbon film thickness on the time scale accessible in our experiments. For short annealing cycles of 10 min, the same behavior is observed for thin (<1 nm) and thick (a maximum thickness of 9 nm is examined) carbon films. Diffusion sets in at 670 K, the total carbon intensity decreases rapidly and the carbon remaining at the surface is in the carbidic state.

C diffusion and reaction on Ni are different. The onset of carbon diffusion depends on the film thickness. In the case of a thin film (0.4 nm, not shown) we find an incipient diffusion at 720 K followed by a small plateau, and a pronounced diffusion at 870 K. The thicker film (1.9 nm, Fig. 5) shows a plateau, too, but only in the temperature range between 820 and 870 K. A similar behavior is observed for carbon films on W [10, 11]. Here, the plateau is caused by the formation and stability of the W_2C subcarbide phase. It is present on W(111) within a wide temperature range between 1000

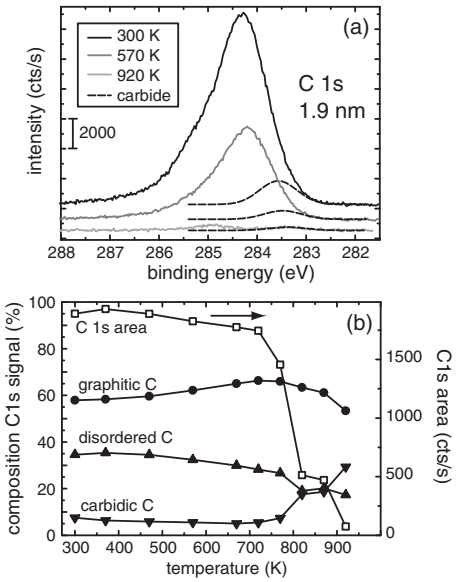

Fig. 5 Thermal behavior of a 1.9 nm carbon film on Ni. In (a) some exemplary C 1s signals and the carbide peak (- -) within them are shown. In (b) the components of the C 1s signal are plotted, together with the temperature variation of the total C 1s integral.

and 1500 K. In analogy to the C/W(111) case, the small plateau for carbon films on Ni between 820 and 870 K is explained by additional carbide formation. Measurements at elevated temperatures where the sample is not cooled to 300 K for XPS analysis confirm this interpretation. Above the plateau region (>870 K) both elementary as well as carbidic C is observed on the thick film (1.9 nm). The thin carbon film (0.4 nm) shows only carbide intensity and elementary carbon vanishes completely. This demonstrates a time dependence of diffusion and reaction of carbon films on Ni. For larger carbon amounts deposited on Ni longer annealing times are necessary to reach the same surface composition. On a 1.6 nm film we observe an incomplete reaction and diffusion for 50 K temperature steps, held for 10 min, respectively. Subsequent repeated annealing steps at 970 K lead to additional carbon diffusion.

The data presented above are measured using heating-cooling-cycles. The sample temperature is held for 10 or 30 min (after ramping up of several minutes) and XPS analysis is performed after cooling the sample down to 300 K. During the annealing and the following analysis the sample is at the same position. Therefore we can compare the results over the whole measurement campaign.

After strong carbon diffusion over a temperature range of 150 K we find a almost constant carbon signal of <1 ML, which is completely carbdic (Fig. 4). We ascribe this to carbon segregation during the cooling-down phase. Carbon films on Ni also show segregation leading to a small carbide intensity (<1 ML) at the surface. It is well known from literature [7, 8, 20] that carbon segregates on Ni and Fe. Both metals show a small solubility of carbon, it amounts to 0.018% in α-Fe at 1011 K and 2.7% in Ni at 1600 K [21, 13].

4 Summary The thermal behavior of carbon films on Fe and Ni is measured using XPS as an excellent chemically resolving surface sensitive method. Even though the enthalpies of formation for carbides of Ni and Fe are endothermic, we find a thin carbide layer at the interface after C deposition from the vapor phase at room temperature. The amount of interfacial carbide is smaller than on substrates with exothermic carbides (W, Si, Ti, Be). Thermal treatments at elevated temperatures lead in the first phase to carbide decomposition and to ordering of the elementary carbon. In a second phase, parallel to the onset of pronounced carbon diffusion additional carbide is formed. The carbon segregates after annealing and cooling to room temperature, leading to a small carbide intensity at 300 K.

References

[1] I. N. Shabanova and V. A. Trapeznikov, J. Electr. Spectr. Relat. Phenom. **6**(4), 297 (1975).
[2] G. Panzner and W. Diekmann, Surf. Sci. **160**, 253 (1985).
[3] S. Sinharoy, M. A. Smith, and L. L. Levenson, Surf. Sci. **72**, 710 (1978).

[4] S. Sinharoy and L. L. Levenson, Thin Solid Films **53**, 31 (1978).
[5] M. A. Smith, S. Sinharoy, and L. L. Levenson, J. Vac. Sci. Technol. A **16**(2), 462 (1979).
[6] E. O. F. Zdansky, A. Nilsson, and N. Mårtensson, Surf. Sci. **310**, L583 (1994).
[7] C. M. Whelan, R. Neubauer, D. Borgmann, R. Denecke, and H. P. Steinrück, J. Chem. Phys. **115**(17), 8133 (2001).
[8] R. Neubauer, C. M. Whelan, R. Denecke, and H. P. Steinrück, Surf. Sci. **507–510**, 832 (2002).
[9] P. Goldstrass, K. U. Klages, and Ch. Linsmeier, J. Nucl. Mat. **290–293**, 76 (2001).
[10] J. Luthin and Ch. Linsmeier, Surf. Sci. **454–456**, 78 (2000).
[11] Ch. Linsmeier, J. Luthin, and P. Goldstrass, J. Nucl. Mat. **290–293**, 25 (2001).
[12] J. Luthin and Ch. Linsmeier, Physica Scripta T **91**, 134 (2001).
[13] T. B. Massalski, H. Okamoto, P. R. Subramanian, and L. Kacprzak, Binary Alloy Phase Diagrams, 2nd Ed., Version 1.0, ASM International, Materials Park, Ohio (1996).
[14] Inorganic Crystal Structure Database, Version 1.2.0 (2003).
[15] J. F. Moulder, W. F. Stickle, P. E. Sobol, and K. E. Bomben, in: Handbook of X-ray photoelectron spectroscopy, edited by J. Chastain, Perkin Elmer Corp. Eden Prairie (1992).
[16] M. P. Seah and W. A. Dench, Surf. Interf. Anal. **1**, 2 (1979).
[17] B. Lesiak, A. Jablonski, Z. Prussak, and P. Mrozek, Surf. Sci. **223**, 213 (1989).
[18] I. Barin, Thermochemical Data of Pure Substances, V.1 2, VCH, Weinheim, 3rd Ed. (1995).
[19] MultiPak, Version 6.1A, Physical Electronics (1999).
[20] W. Arabczyk, F. Storbeck and H. J. Müssig, Appl. Surf. Sci. **65/66**, 94 (1993).
[21] A. F. Holleman and E. Wiberg, Lehrbuch der Anorganischen Chemie, V. 101 (1995).

Physica Scripta. Vol. T111, 86–91, 2004

Formation and Erosion of Carbon-Containing Mixed Materials on Metals

Ch. Linsmeier*, J. Luthin, K. U. Klages, A. Wiltner and P. Goldstraß

Max-Planck-Institut für Plasmaphysik, EURATOM Association, Boltzmannstraße 2, D-85748 Garching b. München, Germany

Received September 17, 2003; accepted November 20, 2003

PACS ref: 68.35, 82.65, 28.52.F, 81.05.J, 82.80.P

Abstract

In this paper we discuss the formation and erosion of multi-component materials ('mixed materials') on metals with respect to carbon deposition from the vapor phase. The carbide formation and carbon accumulation at the surface are governed both by chemical reactions and by carbon diffusion into the bulk metal. Carbide formation at room temperature is restricted to several monolayers at the interface between carbon and supporting metal. Additional energy entry into the system either by ion bombardment or by annealing enhances the carbide formation. The carbon amount present at the surface decreases after a material-dependent temperature threshold for diffusion in the case of metallic carbides of transition metals. Taking into account oxygen as a reactive plasma impurity, e.g. by starting with an oxidized surface before carbon deposition, new erosion channels open up in these ternary systems due to chemical interactions, rendering interaction simulations by kinematic Monte Carlo models insufficient. Chemical erosion mechanisms additional to mere kinematic processes are also responsible for carbon erosion by deuterium ion impact, shown for film thicknesses smaller than the ion range. They lead to enhanced carbon film erosion rates compared to erosion by sputtering.

1. Introduction

Materials under consideration for the first wall in modern fusion experiments and for ITER comprise different elements. Under discussion are the metals beryllium and tungsten as well as carbon for areas exposed to high particle and energy loads [1,2]. In addition to these elements, reactive plasma impurities like oxygen will be unavoidable. Together with the hydrogen fuel material, this spectrum of elements spans the field for the formation of compounds at the surface of first wall materials and the species responsible for their erosion. Formation and erosion processes of mixed materials will also determine the ability of the first wall for hydrogen isotope inventory accumulation and release.

Chemical and physical interactions of impurity species from the plasma are determined by particle energies, species, substrate temperatures and components interacting at the surface simultaneously. Those parameters trigger different processes like chemical reaction, diffusion, desorption. In this paper we show examples for binary and ternary systems under various conditions of additional energy entry into the systems: by annealing or by ion impact. Diffusion and chemical reactions play a crucial role in the formation and erosion of compounds at surfaces. The mutual dependency of processes complicates general predictions for first wall behavior patterns. This is of eminent concern if chemical interactions are expected, as it is the case if one of the species in the system under investigation is carbon. Carbon undergoes solid state chemical reactions, diffuses through several solids of relevance as first wall material, and can form volatile species like hydrocarbons, or carbon monoxide and carbon dioxide in the presence of oxygen.

2. Experimental

All data described in this paper are collected in the experiments 'Artoss' [3] and 'XPS' [4] under UHV conditions (low 10^{-9} and low 10^{-8} Pa base pressures, respectively). The carbon films are deposited with an Omicron EFM3 electron beam evaporation source using high-purity graphite rods (99.999%, Goodfellow). During carbon deposition the pressure is less than 1×10^{-7} Pa. Non-monochromatic Mg Kα and monochromatic Al Kα radiation are used in 'Artoss' and 'XPS' experiments, respectively. The photoelectron binding energies (BEs) are measured with hemispherical analyzers (PHI) driven at a pass energy of 2.95 or 23.5 eV for high-resolution spectra and at 93.5 eV for survey scans. The binding energy scale is calibrated with respect to the Au $4f_{7/2}$ peak at 84.0 eV and for the linearity calibration additionally the Cu $2p_{3/2}$ and Ag $3d_{5/2}$ peaks are used. Quantitative analysis and peak fitting are performed with a commercial software package [5]. A Shirley background and Gauss–Lorentz fit functions are applied. The metal samples used here exhibit polished surfaces and are cleaned *in situ* by Ar^+ sputtering and heating cycles until no contamination can be detected by XPS. We used polycrystalline samples of Au, Be and Ti, as well as single crystals of W(111), Be(0001) and Fe(110). Ar^+ and D^+ were produced from Linde gases (5.0 purity, $D_2 \geq 99.8\%$) in a non-mass separated ion source (Specs IQE 12/38).

3. Results and discussion

3.1. *Thermal reactivity*

The reactivity of carbon with metallic substrates is investigated by depositing increasing amounts of carbon from the vapor phase on polished surfaces of tungsten, beryllium, iron, and titanium. The reaction progress is measured after deposition at room temperature (300 K) and after each subsequent annealing step. Since elementary carbon and carbides show different C 1s electron binding energies (BE), the reaction between carbon and the respective substrates is monitored by the photoelectron intensities at the characteristic energies. Figure 1 shows the C 1s spectra of approximately 1 ML (monolayer) of carbon after deposition on W, Be, Fe and Ti. The substrates are at

* e-mail: linsmeier@ipp.mpg.de

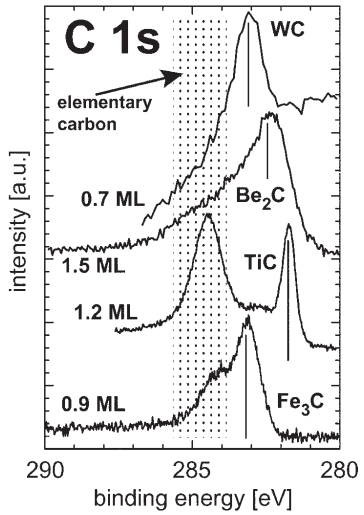

Fig. 1. XPS spectra in the C 1s region of thin carbon layers on W, Be, Ti and Fe. The carbon layer thicknesses are given in monolayers. The respective carbide peak positions are indicated by vertical lines. The hatched area marks the binding energy where elementary carbon signals appear.

300 K during the deposition. The spectra are plotted without background subtraction and the binding energy of the respective carbide is marked by a line. Binding energy values are taken from the literature for W, Ti [6] and Fe [7,8] and determined in separate experiments for Be [9] and also for Fe [10]. The region in which elementary carbon lines occur is hatched. In all four cases carbide formation is obsereved already after 300 K deposition. In particular this is interesting for the endothermic compound Fe_3C with a Gibbs free energy of formation of +0.2 eV [11]. The other carbides plotted here are all exothermic. The formed carbide, however, is restricted to the interface between deposited carbon and substrate surface. Excess carbon does not react and is visible in the spectra at 284.2 eV and above, characteristic for carbon in ordered and disordered graphitic states [12]. The binding energies observed for small carbon amounts demonstrate that stoichiometric carbides are formed. In the case of Ti, the TiC peak at 281.8 eV is very narrow and its width corresponds to the experimental resolution for this measurement. Therefore, the TiC giving rise to this peak is not only stoichiometric, but also well ordered. In the case of Ti, additional intensity besides the elementary carbon peaks and the TiC signal is recorded between those peaks around 282.6 eV. Here, peaks of substoichiometric carbides like Ti_8C_5 or Ti_6C_5 occur [13,14]. However, also in the case of Ti the majority of the formed carbide is TiC. It is obvious from the different C 1s spectra in Fig. 1 and the annotated carbon layer thicknesses that the ratio between carbidic and elementary intensity depends both on the initially deposited amount of carbon and on the specific reactivity of the substrate. For Fe where the carbide formation is endothermic, 0.9 monolayers (ML) of carbon do not react quantitatively. However, 1.5 ML carbon on Be react almost completely during 300 K deposition. Also in the case of tungsten, 0.7 ML carbon deposition leads to practically no intensity in the elementary carbon region, although the Gibbs free energy for WC is only −0.4 eV. The strong slope in the background on which the C 1s signal is superimposed in this case is due to the neighboring W $4d_{3/2}$ peak. The Ti reactivity is intermediate despite the large Gibbs free energy of −1.9 eV : 1.2 ML deposited carbon react to approximately half, forming both stoichiometric TiC and substoichiometric carbides.

Upon annealing, additional carbide is formed in all cases studied so far [15,16]. The diffusion behavior, however, depends strongly on the type of carbide. Figure 2 compares two examples: Be and W substrates. Be_2C is an ionic solid where the lattice constituents are Be^{2+} and C^{4-} ions, respectively. Tungsten carbides (WC and W_2C (subcarbide) phases are known), are metallic carbides where the carbon atoms are localized at different sites within a tungsten packing (hcp in W_2C, hexagonal primitive in WC). These different types of solids influence the diffusion. The open symbols in Fig. 2 show the relative C 1s intensity after increased annealing temperatures. The initial carbon intensities are set to 100%. In the case of Be, the C 1s intensity increases slightly after soft annealing, probably caused by a smoothing of the carbon surface layer. Above 450 K annealing, the intensity starts to decrease and levels off around 60% of the initial intensity. This indicates the formation of Be_2C which is stable up to the finally applied annealing temperature of 873 K. After carbide formation, no diffusion or dissolution of the surface carbon (bound in Be_2C) into the Be bulk is observed [17]. Since both the Be and the W samples in these experiments are single crystals (Be(0001) and W(111), respectively), grain boundary diffusion can be excluded here. However, the diffusion behavior is very different in the case of tungsten, which forms a metallic carbide. Here, carbon diffusion into deeper layers already starts around 570 K, where no additional carbide formation is observed for this 3.9 nm layer. Further diffusion sets in above 1000 K. The C 1s intensity drops to approx. 20% of the initial value. The region between 1000 and 1500 K, where the relative C intensity stays constant, is characterized by the presence of tungsten subcarbide (W_2C). Above this temperature, another strong loss of carbon from the surface-near region

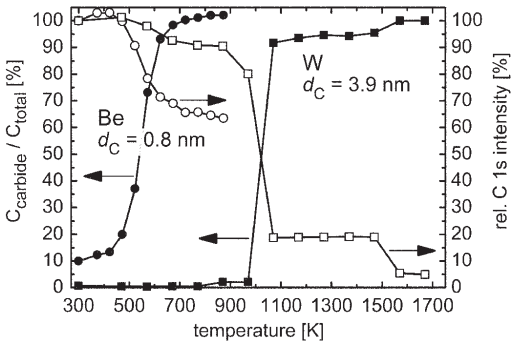

Fig. 2. Annealing of carbon layers on Be and W. The full symbols indicate the fraction of carbide in the total carbon intensity. The open symbols show the relative C 1s intensity after each annealing step (the C 1s after carbon deposition is set to 100%).

accessible by XPS into the bulk is measured. The remaining carbon in the surface region is completely bound in carbide, whereas above 1500 K, in contrast to the former regime, WC dominates. The carbide fraction of the total carbon intensity is plotted as full symbols in Fig. 2. In the case of Be, the carbide intensity drop is complemented by the increase of the carbide concentration. This can be understood as the interdiffusion and reaction of Be with C under Be_2C formation. When this reaction is complete and no further elementary carbon is available, the interdiffusion stops. The formed Be_2C layer is thermally stable. This is plausible, since no diffusion of lattice constituents is expected due to the ionic nature of Be_2C. For tungsten and its carbides the picture is different. Carbon can easily diffuse between energetically similar lattice sites and penetrates from the surface into deeper layers upon thermal activation. Strong diffusion sets in above 1000 K and leads to interdiffusion of carbon and tungsten and the formation of carbides. The first carbide phase formed is W_2C and at temperatures above 1500 K the WC contribution is increased. In contrast to the Be case, however, the final total C concentration in the surface region is very small (resulting at 1673 K in only approx. 5% of the initial carbon intensity). The final picture of the reaction scheme between a carbon layer on tungsten is the presence of distributed WC islands within a W metal matrix.

The formation of compounds between a surface layer and the substrate material requires that the reactant species come into proximity. This is facilitated by diffusion which sets in at a characteristic temperature for each substrate. In Fig. 3 the metals Be, Fe, Ti, W and Au are compared during annealing experiments. The plot shows the integral C 1s intensities for each carbon layer/metal couple which are normalized to 100% for the layer intensity after 300 K deposition. The Au experiment serves as a reference, since Au is inert with respect to carbide formation and carbon is insoluble in gold [18]. No intensity change due to carbon diffusion or compound formation is expected, which is confirmed by the experiment. For each of the reactive elements, a characteristic temperature is found where the carbon intensity drops significantly. This temperature is coincident with the onset of carbide formation, as can be observed in C 1s detail spectra (not shown here). For Be, the final carbon intensity stays at a high level due to the thermal stability of the formed Be_2C layer. In the other cases, which all represent examples for metallic carbides, strong diffusive carbon losses are observed. On Ti, the diffusion into the bulk metal is so strong that finally only traces of carbon, bound in TiC, are detectable at the surface. The structures of metallic Ti, Ti subcarbides (Ti_xC_y) and TiC are characterized by the fact that they all have a hcp Ti structure. Carbon successively occupies octahedral sites in this lattice, until they are all filled by C in stoichiometric TiC. Actually, TiC is slightly understoichiometric ($TiC_{0.95}$ [18]) and a TiC crystal always contains vacancies due to missing C atoms [19]. The missing structural transition in the titanium lattice from metal to carbides and the availability of unoccupied C lattice sites explains the strong loss of carbon from the surface region by diffusion. Carbidization in Fe also proceeds in a narrow temperature interval. However, after Fe_3C formation the carbon intensity stays constant at a low level. In contrast to the Ti case, the small amount of carbide is stable at the surface. Tungsten behaves somewhat similar to Be in such that the W_2C phase which is formed between approx. 1000 and 1500 K, leads to a constant carbon amount in the surface region. Only after increased annealing temperatures, the WC phase formation starts and carbon is lost into the bulk.

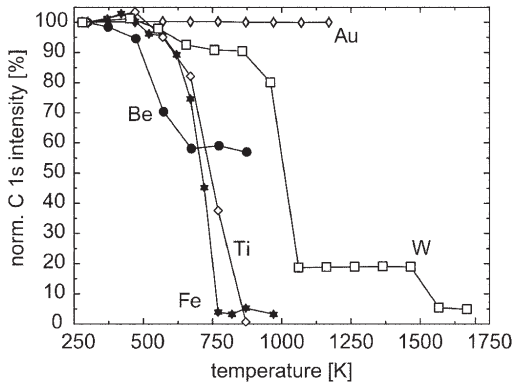

Fig. 3. Relative carbon XPS intensities (amount after deposition is set to 100%) on Au, Be, Fe, Ti and W after annealing.

3.2. *Ion induced reactivity*

The formation of carbides beyond a thin interface film between deposited elementary carbon and metal substrate can also be promoted by energy impact through ion beams. Figure 4 shows the composition of a 3.2 nm carbon film on titanium, measured by XPS, during the bombardment with 1 keV Ar^+. It is known from previous work [20] that also in the case of C on Ti the carbide formation at 300 K is limited to the layer–substrate interface. Therefore, the increase of the TiC intensity during the Ar^+ bombardment is due to additional carbide formed during the ion impact. Sputtering of the carbon layer leads to a total carbon intensity decrease with increasing Ar^+ fluence, as seen in Fig. 4. Synchronously with the decrease of the C fraction in

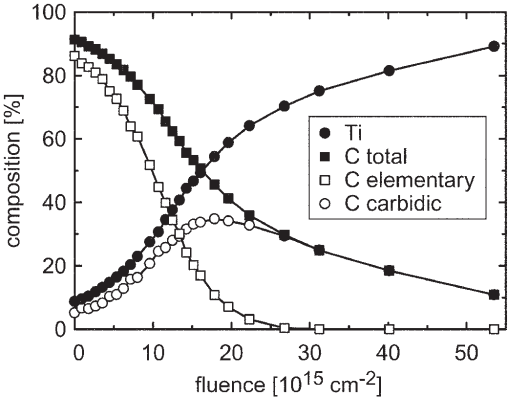

Fig. 4. Composition of a 3.2 nm C film on Ti during ion bombardment with 1 keV Ar^+. Angle of incidence is 45°. The open symbols show the elementary and carbidic components in the total C signal.

the composition the Ti part increases. The contributions to the carbon fraction, however, change from predominantly elementary to purely carbidic. Initially, the majority of the carbon signal stems from the elementary layer. Only a small part is carbidic. The carbide is located at the interface with the Ti substrate. The photoelectrons from this region are therefore attenuated during the transmission through the graphite layer. With increasing Ar^+ fluence, the fraction of elementary carbon decreases much faster than the total carbon part. At the same time, the carbide part increases. Elementary carbon reacts with Ti substrate material under carbide formation. Around a fluence of $1.3 \times 10^{16}\,cm^{-2}$, equal amounts of carbon are present elementarily and bound to Ti in carbides. Above that fluence, carbides dominate the C 1s signal. Above $2.7 \times 10^{16}\,cm^{-2}$, no more elementary carbon is detected. The total C 1s signal is only composed of carbide intensity. Further ion bombardment leads to continued sputtering of carbides. The fact that the carbide part increases while the total carbon amount decreases (up to $1.8 \times 10^{16}\,cm^{-2}$) is a clear sign for the ion-induced reaction between elementary carbon and titanium, forming titanium carbides (TiC and subcarbides, not discriminated in this plot).

During the interaction of Ar^+ ions with a solid, chemical reactions between the projectile and the elements in the surface are excluded due to the inert nature of argon. However, for the interaction of hydrogen isotopes with carbon-containing materials chemical reactions involving the projectile species cannot be excluded. We address this topic by bombarding a 1.4 nm carbon layer on titanium by D^+ ions of 4 keV kinetic energy. The carbon layer is analyzed by XPS after each fluence step. The results are plotted in Fig. 5. Initially, the carbon layer consists of a carbide interface between carbon and titanium with an overlying elementary carbon film. The composition of the carbon layer during ion implantation is plotted in Fig. 5(a). The ordered graphitic and disordered components are added and plotted as the elementary fraction. Also the carbide and subcarbide intensities are summarized and plotted as the carbidic fraction. During the ion bombardment, the elementary carbon is continuously converted into carbidic compounds. This reaction terminates after a fluence of $5 \times 10^{16}\,cm^{-2}$, after which all carbon detected by XPS is in a carbidic state. Parallel to this graphite–carbide conversion the carbon layer on the Ti substrate is continually eroded. This is visible in Fig. 5(b) where the carbon coverage is shown as a function of the D^+ ion fluence. The amount of carbon detected at the surface decreases exponentially after a small initial increase (first data point at zero D^+ fluence is not included in the exponential fit to the data points). Above $6 \times 10^{16}\,cm^{-2}$ the exponential trend of the carbon loss converts into a linear decrease. The data points are fitted by a sum of an exponential function and a straight line, as is shown by the solid and broken lines in Fig. 5(b), respectively. The different functions suggest different erosion mechanisms. Moreover, the change from exponential to linear carbon loss coincides with the complete erosion or conversion of the elementary carbon species. The initial exponential decay shows that the whole carbon layer reacts simultaneously with the incoming D^+ ions. This is similar to an ion-induced desorption process of an adsorbed monolayer

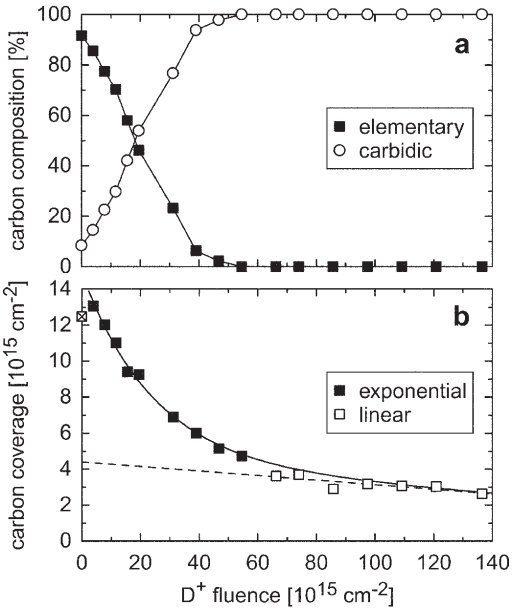

Fig. 5. Bombardment of a 1.4 nm carbon film on Ti by 4 keV D^+ under 45° incidence. The decomposition of the carbon signal in elementary and carbidic carbon is shown in (a). The amount of carbon on the surface during ion impact is given in (b). The full symbols are fitted by an exponential function (solid line), the open symbols are fitted by a linear function (dashed line).

[21]. A plausible mechanism is a chemical erosion process between the deuterium and the elementary carbon involving the whole carbon layer simultaneously. From the exponential fit, a reaction cross-section for this process is calculated to $\sigma_{chem} = 4.2 \times 10^{-17}\,cm^2$, which can be converted into a chemical erosion yield of $Y_{chem} = 0.08$ carbon atoms per deuterium ion. For the subsequent linear erosion regime, a physical sputtering process is assumed. This seems reasonable, since the initial coverage for this process is still approx. 2 ML and even at the end of the studied fluence regime approx. 1.3 ML. The sputtering yield from the linear fit is $Y_{phys} = 0.01$ carbon atoms per deuterium ion, which agrees reasonably well with a TRIDYN calculation for 4 keV D^+ impinging on a carbon layer supported on titanium.

3.3. *Structure-dependent reactivity*

The reactivity of a carbon containing surface depends strongly on its structure. An example was already the different erosion behavior of the C/Ti system by deuterium ions after complete transformation of the elementary carbon into TiC, as shown in Fig. 5. Carbon erosion proceeds exponentially with applied fluence only as long as elementary carbon is present. When only carbide is present at the surface, a linear decrease of the carbon amount is observed. Another example will be discussed here in detail: reactivity of carbon layers deposited on tungsten oxides with different stoichiometry and bulk structure. Before discussing the ternary system W–C–O, a brief summary about the binary systems W–C and W–O is required. In the case of C layers on

W, upon annealing two carbide phases are observed together with carbon diffusion into the W bulk. This is already discussed in Section 3.1 and the carbide formation with increasing annealing temperature is shown in Fig. 2. The carbon diffusion into the W bulk leads to an almost complete loss of carbon in the surface zone accessible by XPS. However, even after 1670 K annealing procedures, the C concentration remains at a 6% level. In the binary W–O system, reaction progress leading to oxygen chemisorption on tungsten, two-dimensional oxidation or bulk oxidation depends on the oxygen coverage (partial pressure) and temperature. Adsorption of oxygen on tungsten at 300 K in vacuum leads to the formation of a surface oxide with 0.5 ML O coverage. This is independent on whether the oxygen species reaching the tungsten surface are molecular or atomic [22]. According to the literature, elevated temperatures, higher oxygen pressures or longer times are necessary to achieve higher coverages [23]. We examined a polycrystalline tungsten sample exposed to molecular oxygen at 1×10^{-5} Pa O_2 partial pressure at 300 K for 60 min. Annealing up to 970 K does not change the tungsten/oxygen ratio. Above this temperature, the oxygen amount decreases. After the highest annealing temperature of 1670 K during this series, still an oxygen fraction of 10 at.% is detected in the XPS signal. For submonolayer coverages, oxygen atoms are the only desorption product [24]. For higher oxygen coverages, a substantial part can desorb as tungsten oxide [25].

The ternary W–C–O system is studied by depositing carbon on two different tungsten oxide films. These oxide layers are produced on polycrystalline tungsten samples by oxidation in a furnace under atmospheric conditions. Two different nominal WO_x stoichiometries are examined: WO_3 and WO_2. Figure 6 shows XPS spectra in the W 4f, O 1s and C 1s regions as well as the elemental surface compositions at high annealing temperatures between 950 and 1700 K. Panel (a) shows the data for the W(VI) oxide (WO_3), panel (b) for the W(IV) oxide (WO_2), respectively. Cleaning in the UHV system by sputtering was avoided in order not to influence the stoichiometry by preferential sputtering and not to destroy the oxide structure. To desorb possibly adsorbed contamination, the W(VI) sample was annealed to 470 K in UHV, the W(IV) sample to 970 K prior to carbon deposition. Before annealing, the W(VI) oxide shows the W $4f_{7/2}$ binding energy of 35.7 eV, characteristic for WO_3. After the 970 K annealing (already with deposited carbon adlayer), the W 4f region shows a second doublet at lower binding energy (W $4f_{7/2}$ at 34.0 eV) indicating the reduction of a part of the oxide. The spectra are plotted in Fig. 6(a). However, the binding energy is not as low as in the W(IV) oxide film, where the W $4f_{7/2}$ peak is located at 32.8 eV before and after cleaning (heating to 870 K in UHV in this case). Figure 6(b) shows the W(IV) oxide film after C deposition and annealing to 970 K. Again, no significant peak shift is measured. The BEs of the untreated W(VI) and W(IV) oxide films agree with values in the literature [6], and therefore confirming our assumption of WO_3 and WO_2 phases in our oxide films.

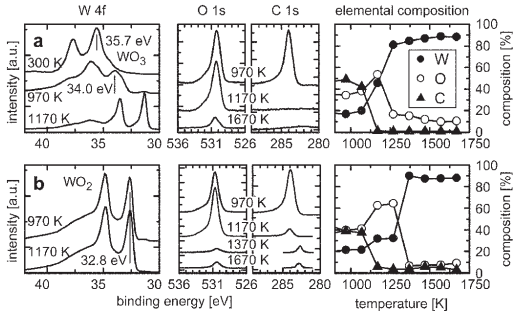

Fig. 6. Erosion of carbon layers on different tungsten oxides. Panels (a) show the W 4f, O 1s and C 1s XPS spectra for carbon on a W(VI) oxide film as well as the elemental composition determined by XPS after annealing between 950 and 1700 K. Panel (b) gives the same information for a carbon layer on a W(IV) oxide film. The oxide films are supported on polycrystalline tungsten.

The overall behavior of the two oxide species is different at high temperatures. Whereas the carbon is lost completely from the W(VI) oxide surface above 1100 K (Fig. 6(a)), the W(IV) oxide (Fig. 6(b)) retains an approximately 6 at.% carbon concentration. However, this is not the only difference during the annealing treatment. The panels showing the W 4f peaks demonstrate the stability of the WO_2 up to 1170 K. Above this temperature, the peak position shifts to the tungsten metal BE (not shown). This shift is earlier observed in the WO_3 case: here the metal positions are already present after 1170 K annealing. However, the W/O ratios are constant up to this annealing step in both cases. Also very similar are the O 1s peaks. The peak maximum is constant at 530.5 eV and all O 1s signals up to 1170 K exhibit a small shoulder on the high-BE side. Annealing to higher temperatures leads to a loss in oxygen, similar to the behavior of the binary W–O system. The final O 1s spectra after 1670 K annealing are identical to those of a binary adsorption experiment of oxygen on clean tungsten. In contrast to the O 1s signals, the evolution of the C 1s spectra during the annealing series is different for W(VI) and W(IV). Not only is the carbon eroded completely on the W(VI) surface, but also the C 1s binding energies are different. The carbon film on the W(VI)-oxide surface is completely gone after the 1170 K treatment. The spectrum in the C 1s region is flat for all temperature steps from 1170 K up to 1670 K. As long as carbon is detected on the W(VI) oxide, it has the BE of elementary carbon. No intensity at the carbide position is measured throughout the whole treatment series. Venables and Brown proposed a two-stage mechanism for the reduction of higher tungsten oxides with carbon to WO_2 and finally W under CO and CO_2 formation in bulk material experiments [26,27]. After carbon erosion, the continued loss of oxygen can be explained by dissolution of oxygen into the W bulk. On the W(IV) surface, the carbon intensity also drops during 970 K annealing. However, in contrast to the observations on the W(VI) surface, after 1170 K carbon is still present on W(IV) and is found at the elementary peak position. After subsequent annealing steps at higher temperatures, the oxygen intensity starts to drop, but the C 1s intensity does not change significantly. Also, the C 1s peak has shifted to the carbide peak position. The interpretation of this behavior is that oxygen does not desorb as CO or CO_2 from a surface where carbon is chemically bound as carbide. This is similar to the erosion of carbon by deuterium (Section 3.2) where the chemical

erosion channel stops after carbon is only present in titanium carbide. The WC formation could proceed by a substitution mechanism $WO_2 \rightarrow WC$ which has been described for bulk WO_2 reduction with CO [28,29]. The reaction is complete after the 1370 K annealing step. Higher temperatures provide no significant further changes. Again, the final O concentration in this experiment is comparable to the coverage in the W(VI) case and in O/W experiments. The last panels in Fig. 6 show the elemental surface compositions for the W(VI) and W(IV) oxide samples, respectively. The discussed intensity changes during the annealing procedures are represented by the compositions. The total loss of C from the W(VI) oxide above 1100 K is clearly visible. The O concentration after 1670 K annealing is identical in both surfaces and also to a O/W adsorption experiment. Obviously, the small final oxygen coverage is independent of the presence of carbon at the surface. Up to 1670 K, carbon residuals present as WC cannot be removed by oxygen from the formerly W(IV) oxide surface. The complete carbon removal by oxygen is only possible from the W(VI) oxide surface. Once carbon has reacted with tungsten to form WC, erosion by co-adsorbed oxygen does not take place.

4. Summary

In this paper we discussed formation and erosion of carbon-containing compounds at the surface of metals in two- and three-component systems by means of X-ray photoelectron spectroscopy. Driving forces for reactions are thermal annealing and ion bombardment with reactive (D^+) and inert (Ar^+) species. For carbon layers on metals deposited at 300 K substrate temperatures from the vapor phase, the formation of a carbide layer at the carbon–metal interface is observed. Carbon in excess of a monolayer-thick carbide interface is deposited elementarily. Carbide is formed regardless whether the the Gibbs free energy of formation is exothermic (as in the case of W, Be and Ti) or endothermic (Fe). The carbide formation can proceed if elementary carbon comes into proximity of metal atoms, either by diffusion or ion beam mixing. In the case of metallic carbides thermal annealing leads to almost complete loss of carbon from the surface region by dissolution into the metal bulk. In ionic Be_2C, interdiffusion stops after the carbide formation is complete and the formed compound is stable. Intermixing of carbon and metal atoms can also be facilitated by ion beam mixing, as is shown in the case of C/Ti. Ion bombardment leads to an increase of the relative carbide concentration and finally to erosion of the carbon-containing layer. If the ion species can react chemically with carbon like deuterium, in addition to the physical sputtering process enhanced erosion of elementary carbon is observed. After complete carbidization, the erosion rate drops back to the physical sputtering yield. In the ternary system W–C–O is shown that the structure of the oxide film on metallic tungsten, onto which carbon is deposited, determines the erosion path. Above 1100 K, carbon reacts with oxygen from the tungsten oxide film and desorbs. However, complete removal of carbon is only observed if the oxide film was W(VI) oxide (WO_3). In the case of W(IV) oxide (WO_2), a small carbon amount remains. Independent on the carbon concentration, the tungsten surface keeps a small amount of oxygen up to 1670 K annealing. These examples demonstrate that the chemical and physical processes governing formation and erosion of carbon-containing surface layers depend on a number of parameters like composition, temperature, reactivity and structure. To predict the behavior of a fusion first wall considering multiple materials in the presence of carbon, detailed knowledge about these parameters is necessary.

References

1. Federici, G. *et al.*, Nucl. Fusion **41**, 1967 (2001).
2. ITER Groups, Nucl. Fusion **39**, 2391 (1999).
3. Linsmeier, Ch., Goldstraß, P. and Klages, K. U., Physica Scipta **T94**, 28 (2001).
4. Miller, S., Berning, G., Plank, H. and Roth, J., J. Vac. Sci. Technol. A **15**, 2029 (1997).
5. MultiPak, Physical Electronics.
6. Moulder, J. F., Stickle, W. F., Sobol, P. E. and Bomben, K. E., "Handbook of X-Ray Photoelectron Spectroscopy," (Edited by J. Chastain), (Perkin-Elmer Corp. Eden Prairie 1992).
7. Shabanova, I. N. and Trapeznikov, V. A., J. Electr. Spectr. Relat. Phenom. **6**, 297 (1975).
8. Panzner, G. and Diekmann, W., Surf. Sci. **160**, 253 (1985).
9. Goldstraß, P. and Linsmeier, Ch., Nucl. Instrum. Meth. B **161–163**, 411 (2000).
10. Wiltner, A. and Linsmeier, Ch., in preparation for Physica Scripta.
11. Barin, I., "Thermochemical Data of Pure Substances," 3rd ed., Vol. 1 & 2, (Weinheim 1995).
12. Luthin, J. and Linsmeier, Ch., Surf. Sci. **454–456**, 78 (2000).
13. Khaenko, B. V., Golub, S. Ya. and Arbuzov, M. P., Kristallografiya **25**, 112 (1980).
14. Dzahalabadze, N. V., Eristavi, B. G., Maisuradze, N. I. and Kuteliya, E. R., Phys. Metals Metall. **86**, 59 (1998).
15. Linsmeier, Ch., Luthin, J. and Goldstraß, P., J. Nucl. Mater. **290–293**, 25 (2001).
16. Reinke, P. and Oelhafen, P., Diamond Relat. Mater. **8**, 155 (1999).
17. Goldstraß, P., Klages, K. U. and Linsmeier, Ch., J. Nucl. Mater. **290–293**, 76 (2001).
18. Massalski, T. B., Okamoto, H., Subramanian, P. R. and Kacprzak, L., "Binary Alloy Phase Diagrams," 2nd Ed., Version 1.0, (ASM International, Materials Park, Ohio 1996).
19. van Loo, F. J. J. and Bastin, G. F., Metallurg. Trans. A **20**, 403 (1989).
20. Luthin, J., Plank, H., Roth, J. and Linsmeier, Ch., Nucl. Instr. Meth. B **182**, 218 (2001).
21. Taglauer, E., Heiland, W. and Onsgaard, J., Nucl. Instr. Meth. **168**, 571 (1980).
22. Linsmeier, Ch. and Wanner, J., Surf. Sci. **454–456**, 305 (2000).
23. Daimon, H., Ynzunza, R., Palomares, J., Takabi, H. and Fadley, C. S., Surf. Sci. **408**, 260 (1998).
24. Engel, T., von dem Hagen, T. and Bauer, E., Surf. Sci. **62**, 361 (1977).
25. Menzel, D., "Desorption Phenomena," in: "Topics in Applied Physics," Vol. 4, Interactions on Metal Surfaces, (Edited R. Gomer), (Springer, Berlin 1975) 101.
26. Venables, D. S. and Brown, M. E., Thermochimica Acta **282/283**, 251 (1996).
27. Venables, D. S. and Brown, M. E., Thermochimica Acta **282/283**, 265 (1996).
28. Venables, D. S. and Brown, M. E., Thermochimica Acta **291**, 131 (1997).
29. Kodama, T. *et al.*, Energy **25**, 411 (2000).

Available online at www.sciencedirect.com
SCIENCE DIRECT®
ELSEVIER
Nuclear Instruments and Methods in Physics Research B 219–220 (2004) 947–952
NIM B
Beam Interactions with Materials & Atoms
www.elsevier.com/locate/nimb

Measurement of beryllium depth profiles in carbon

K. Schmid *, A. Wiltner, Ch. Linsmeier

Max-Planck-Institut für Plasmaphysik, Boltzmannstraße 2, D-85748 Garching b., München, Germany

Abstract

This paper is concerned with the measurement of Be diffusion profiles in C by combining RBS and XPS sputter depth profiling. The total Be content in the samples was measured by RBS (2 MeV $^4He^+$) at a scattering angle of 102° in order to increase depth resolution and sensitivity for Be. To apply a depth scale to the XPS sputter profiles measured using 3 keV Ar^+ at 45° angle of incidence, the Monte-Carlo code TRIDYN was used to calculate the surface recession as a function of surface composition. The so obtained high resolution depth profiles were then scaled in such a way that their integrals would correspond to the total amount of Be as measured by RBS. From these diffusion profiles of Be in C the concentration-dependent inter-diffusion coefficient $D(c)$ was determined by applying Boltzmann–Matano analysis. We found that O impurities have an appreciable influence on the diffusion of Be into C namely the diffusion is increased by a factor of ~2 when O is present at the Be/C interface.

PACS: 66.30.Ny; 79.20.A; 81.05.T; 81.40.E; 81.70.Jb

1. Introduction

In modern fusion devices the surfaces of the first plasma facing wall consists of a mixture of various materials. For instance in the current ITER design [1] the divertor will be made from C and W whereas the rest of the first wall will be made from Be. The C tiles in the divertor will be subject to a high heat load and due to erosion of Be from the first wall to a high Be impurity flux. The possible formation of a shielding Be layer on these C surfaces will be governed by Be re-erosion and Be diffusion into the C bulk. Diffusion data for Be in C is sparse and limited to tracer diffusion coefficients [2] which cannot be applied to the diffusion of high Be concentrations in C. For concentrations above ≈10% the concentration dependence of diffusion cannot be neglected. It is therefore the aim of this work to measure Be diffusion profiles in C in order to extract the concentration-dependent inter-diffusion coefficient $D(c)$ for Be in C by applying Boltzmann–Matano analysis [3]. An earlier work showed that no dissolution of carbon in the Be substrate material occurs up to annealing temperatures of 873 K [4].

Measuring accurate depth profiles in these samples by conventional RBS is difficult due to the overlap of the Be with the C substrate spectra. Therefore we applied a combined approach of different techniques. We used RBS to quantitatively measure the Be content in these samples and used the broadening of the Be peak after annealing to extract a crude depth profile by simulating the

* Corresponding author. Tel.: +49-89-3299-2285/1387; fax: +49-89-3299-2279.
E-mail addresses: klaus.schmid@ipp.mpg.de, kschmid@ferp.ucsd.edu (K. Schmid).

0168-583X/$ - see front matter © 2004 Elsevier B.V. All rights reserved.
doi:10.1016/j.nimb.2004.01.194

spectra with appropriate depth distributions. XPS sputter depth profiling was used to obtain Be concentration profiles in C. The sputter technique features higher sensitivity and depth resolution than RBS but has the disadvantage that depth information is only available indirectly through the fluence [$m^{-2}\,s^{-1}$] and sputter time. Another downside of sputter profiling is that due to ion beam mixing the concentration profiles are broadened and that preferential sputtering yields surface concentrations different from the true bulk values.

To apply a depth scale to the raw XPS sputter profile we used the Monte-Carlo code TRIDYN [5] to calculate the surface recession as a function of surface composition and fluence. These calculations also suggested that ion beam induced mixing could be approximated analytically as the convolution of the true depth profile with a Gaussian. After determining the width of this Gaussian from a series of TRIDYN calculations the XPS sputter profiles could be deconvoluted to extract the Be diffusion profiles. The determined profiles where then scaled in such a way that their integrals would give the same total amount of Be as measured by RBS.

2. Experimental

2.1. Sample preparation

All the samples used in this work are comprised of a polished pyrolytic graphite substrate with evaporated Be layers with varying thicknesses in the range of several 10 nm. Two sets of samples were created, differing in the evaporation conditions which resulted in different O impurity distributions. In both cases before Be deposition the graphite substrates were degassed at 1073 K for 12 h in a vacuum oven with a base pressure of 10^{-4} Pa and showed no O at the C surface in subsequent XPS measurements.

The first set (≡type A) of Be films was evaporated in a UHV preparation chamber connected to the XPS spectrometer and showed only minor O impurities. After transport through air the O concentration on the surface as measured by XPS reached ~50%.

The second set (≡type B) of Be films was evaporated in a chamber with a base pressure of 10^{-6} Pa, carried through air afterwards, and showed O impurities both at the Be–C interface (~20% O) and at the Be surface (~50% O). These different O impurity distributions should allow to determine if and how O impurities qualitatively influence the inter-diffusion of Be and C.

2.2. RBS measurements

Rutherford backscattering spectra were taken under two scattering angles: 102° and 165°. $^4He^+$ ions at 2 MeV were used as projectiles with perpendicular impact on the samples. An ion charge of 40 μC was acquired for each spectrum of the Be films. Due to the small masses of C and Be, however, the signal-to-noise ratio in the 165° backscattering direction is bad. Moreover, these spectra have no depth profile information for the Be films. Therefore the depth profiles were determined based on the spectra from the 102° detector. This lower scattering angle leads to pile up at small channel numbers due to the increased count rate and to a strong deviation between measured and simulated spectra. Especially in this case of a light substrate (carbon) and an even lighter film (beryllium) a large fraction of the whole spectrum is influenced by this process. To nevertheless compare measured and simulated spectra, a polynomial background was fitted to the edge around the Be peak and subtracted from the measured data. The (small) background in the O peak region was taken care of by subtracting a linear function. The such produced spectra of "pure" Be and O signals were then compared to simulated spectra. Simulations were carried out using the program SimNRA [6,7] (V. 5.40). Composition and number of layers were manually modified until the agreement between background-subtracted measured and simulated Be and O peaks was satisfactory. Then the carbon contents of the layers was modified to optimize the agreement between the simulated carbon edge and the measured data.

2.3. XPS sputter profiling

The measurements were carried out in a UHV chamber (base pressure: mid-10^{-9} Pa) consisting of

a XPS system and a preparation chamber. Both parts are connected via an UHV valve. In the preparation chamber the Be films were deposited using an Omicron EFM3 electron beam evaporation source with a BeO crucible filled with Be pieces (HEK GmbH, 99.999%).The constant evaporation flux was monitored using mass spectrometry of Be and BeO masses. During the evaporation process the pressure in the preparation chamber was less than 8×10^{-8} Pa. The XPS system consists of a commercial XPS system (PHI 5600 ESCA) and an ion gun (Specs IQE 12/38). For the depth profiles monochromatic Al Kα radiation was used and the hemispherical analyzer was driven at a pass energy of 29.35 eV. The depth profiles were performed with a rastered 3 keV Ar^+ at an incidence angle of 45° and a spot size of 0.43 or 0.37 cm^2. The ion current was held constant at 0.5 μA. The XPS analysis spot was 0.8 mm in diameter. For analysis of the XPS data a commercial software package (MultiPak) was used.

To apply a depth scale to the raw XPS sputter data (concentration versus Ar^+ fluence [$m^{-2}\,s^{-1}$]) the surface recession rate due to 3 keV Ar^+ bombardment of a Be and C containing target was calculated using TRIDYN [5]. In the simulation the Be concentration was varied linearly from 0 to 1 in order to obtain the surface recession rate ξ [Å/$m^{-2}\,s^{-1}$] as a function of sample composition and Be concentration, respectively. By comparing the sputter yields for Be and C obtained from these calculations also the preferential sputtering coefficient r could be determined. Thus the depth x_k corresponding to kth data point in the raw XPS sputter data can be calculated from Eq. (1):

$$x_k = \sum_{i=1}^{k} \xi(c_{\mathrm{Be}_i}) * \Delta\Phi_i, \tag{1}$$

with c_{Be_i} = Be surface concentration at data point i; $\Delta\Phi_i$ = fluence step since data point $i-1$; $\xi(c_{\mathrm{Be}_i})$ = surface recession rate at concentration c_{Be_i}.

To investigate the broadening of the depth profile due to ion-induced mixing, the erosion of a Be layer with a sharp interface towards the C bulk was simulated using TRIDYN. By comparing the input depth profile with the calculated surface concentration versus eroded depth ($\Longleftrightarrow$ simulation of an XPS sputter profile) we found that the broadening of the Be/C interface could be described approximately as the convolution of the input depth profile and a Gaussian with $2\sigma = 45$ Å. The width of 45 Å depends on the species and energy of the incident particle and the elements in the system.

Using these simulation results the XPS sputter profile $c_{\mathrm{XPS}}(x)$ expected from a given input depth profile $c_{\mathrm{INP}}(x)$ can be analytically calculated according to Eq. (2):

$$c_{\mathrm{XPS}}(x) = \int_{-\infty}^{\infty} \delta(r, c_{\mathrm{INP}}(\bar{x})) * \rho(x-\bar{x})\mathrm{d}\bar{x}, \tag{2}$$

with $\delta(r, c_{\mathrm{INP}}(x))$ = surface concentration due to preferential sputtering; $\rho(x)$ = Gaussian with $2\sigma = 45$Å.

For a binary system $\delta(r, c_{\mathrm{INP}}(x))$ can be written as

$$\delta(r, c_{\mathrm{INP}}(x)) = \frac{c_{\mathrm{INP}}(x)}{c_{\mathrm{INP}}(x) + r - c_{\mathrm{INP}}(x) * r}, \tag{3}$$

with r = preferential sputtering factor.

Eq. (3) can also be used in a ternary system separately for each element. One only has to adjust r accordingly. This can be achieved by calculating an average r for each element from the results of a TRIDYN calculation.

The Be diffusion profiles were obtained by iteratively adjusting $c_{\mathrm{INP}}(x)$ in Eq. (2) until the calculated $c_{\mathrm{XPS}}(x)$ reproduced the raw XPS sputter data. To verify the depth profiles obtained obtained by this procedure they were used as input depth profiles in a TRIDYN calculation and the simulated sputter profile resulting from that calculation was then compared to the experimental XPS sputter data. A comparison between the raw XPS sputter data (with a calculated depth scale) of a type A sample, the deconvoluted depth profiles ($\equiv c_{\mathrm{INP}}(x)$) and the analytical and TRIDYN sputter profile simulation is given in Fig. 1. A summary of all the deconvoluted Be, C and O depth profiles obtained from XPS sputter data is depicted in Fig. 3. As an example the low resolution RBS profiles of a type B sample are compared to the deconvoluted profiles obtained from the corresponding XPS sputter data in Fig. 2.

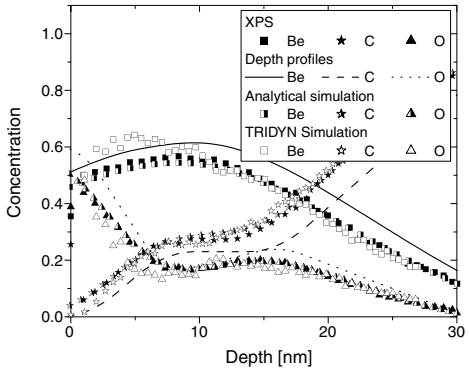

Fig. 1. A comparison between the raw XPS sputter data (with a calculated depth scale) of a type A sample (4 h at 973 K), the deconvoluted depth profiles and the analytical and TRIDYN sputter profile simulation.

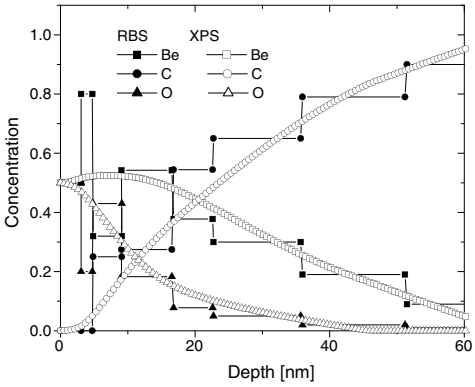

Fig. 2. Comparison of RBS and deconvoluted XPS depth profiles of Be, C and O of a type B sample after annealing for 4 h at 973 K.

2.4. Boltzmann–Matano analysis

The diffusion coefficient in a concentration gradient depends on the local concentration of the elements [8]. To extract this concentration-dependent inter-diffusion coefficient $D(c)$ for Be and C, Boltzmann–Matano analysis (BM analysis) was applied to the measured Be depth profiles. As described in more detail in [3] $D(c)$ can be calculated from the diffusion profile according to Eq. (4):

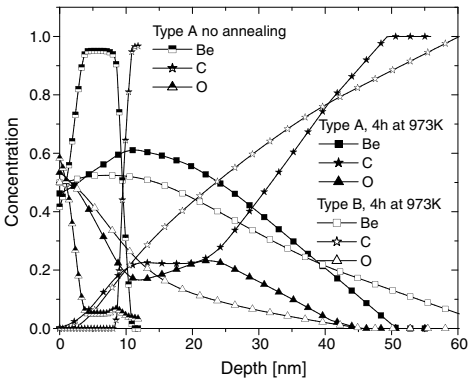

Fig. 3. Summary of the deconvoluted Be, C and O depth profiles obtained from the XPS sputter data for type A and B samples after annealing for 4 h at 973 K. Also shown is the depth profile of a type A sample prior to annealing.

$$D(\bar{c}) = \frac{1}{2t\left.\frac{\mathrm{d}c}{\mathrm{d}x}\right|_{\bar{c}}} \int_{\bar{c}}^{1} x(c)\mathrm{d}c, \qquad (4)$$

$c(x)$ = measured depth profile,

t = diffusion time,

provided that the boundary conditions in Eq. (5) are met prior to diffusion

$$\begin{aligned} c &= c_0 \quad \text{for } x < 0,\ t = 0, \\ c &= 0 \quad \text{for } x > 0,\ t = 0. \end{aligned} \qquad (5)$$

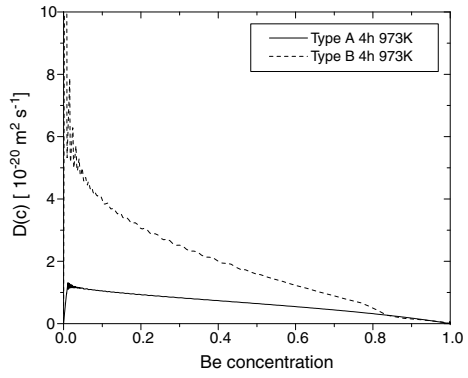

Fig. 4. Comparison of the concentration-dependent diffusion coefficient $D(c)$ for a type A and B sample, each annealed for 4 h at 973 K.

This means that the diffusion couple used should have a sharp interface in order to fulfill these conditions. In addition to Eq. (5) the sample must be infinite in both $+x$ and $-x$ directions. For a real world Be/C diffusion couple this means that the C must not completely penetrate through the Be layer.

To investigate the influence of O on the diffusion of Be in C the O depth profile was initially ignored and the Be and C depth profiles were scaled that the two concentrations would add up to 100% without changing the ratio of Be to C. The results for $D(c)$ as obtained from Eq. (4) using these pure Be/C profiles are depicted in Fig. 4.

3. Discussion

Using the total amounts of Be from an RBS measurement and with the aid of a Monte-Carlo code like TRIDYN, raw XPS sputter profiles (surface concentration versus fluence) can be converted into an approximate depth profile (concentration versus depth). This is shown in Fig. 1 for a type A sample after annealing (4 h, 973 K) as full symbols. The total amount of beryllium in this case is $(183 \pm 8) \times 10^{15}$ cm^{-2}, corresponding to a pure Be layer thickness of 15 nm.

This approximate depth profile information consists of the true elemental depth distribution convoluted with the broadening due to ion beam mixing from the sputtering ions. Taking this into account, the analytical XPS depth profile is calculated and plotted as half-open symbols in Fig. 1. As can be seen from the plot, the agreement between raw XPS depth profile with applied depth scale and the analytical profile convoluted with the broadening is good. This calculation is now iterated under variation of the true elemental depth profile until the resulting profile is identical to the raw XPS data. The resulting deconvoluted depth profiles for the elements in this sample are plotted as lines in Fig. 1.

To prove the validity of this result, the resulting depth profile is used as input for a TRIDYN calculation. The simulated TRIDYN depth profile should reproduce the initial raw XPS depth profile. This is the case, as can be seen in Fig. 1, where the final TRIDYN profile simulation is plotted as open symbols. By applying this iterative procedure a true depth profile accounting for all physical effects can be produced. There is also a good fit between the low resolution RBS depth profiles and the profiles derived form the XPS sputter data as exemplified in Fig. 2 comparing depth profiles of a type A sample. In Fig. 3 the depth profiles of a type A sample before annealing and of annealed types A and B samples are shown. Not shown is a depth profile for a type B sample before annealing which has a large BeO contribution both at the sample surface and at the metal layer–carbon substrate interface. Because the profiling process is destructive the plots in Fig. 3 result from different samples, they differ in the absolute thickness of the Be layer, but not in the general layer structure.

Prior to annealing the samples show sharp ad-layer–carbon interface. After annealing of both sample types (A and B) a strong broadening of the interface is observed but no C has reached the surface as required for BM-analysis. The depth profiles after annealing for 4 h at 973 K differ for types A and B samples. As visible in Fig. 3, the Be depth profiles of the type B samples, which prior to annealing showed O impurities both at the surface and at the Be–C interface, are flatter and extend deeper into the C bulk. This indicates stronger diffusion in the case of a BeO layer at the Be–C interface. This observation is confirmed by the results from the BM analysis. Concentration-dependent diffusion coefficients $D(c)$ are calculated from smoothed RBS depth profiles for types A and B samples after 4 h annealing at 973 K. The $D(c)$ results are plotted in Fig. 4. The diffusion rates for the type B samples are higher by roughly a factor of two. The oscillations at very small Be concentrations are mathematical artifacts. The diffusion coefficient at low Be concentrations in the order of 1×10^{-20} m^2 s^{-1} for type A samples and 5×10^{-20} m^2 s^{-1} for type B samples. The stronger inter-diffusion for a layer with a BeO interface is unexpected since intuitively an oxidic layer is anticipated to act as a diffusion barrier.

4. Conclusions

Inter-diffusion between beryllium layers and carbon substrates at 973 K was investigated using

a combination of RBS and XPS sputter depth profiling. XPS sputter depth profiles show a very good depth resolution, but suffer from ion beam mixing and preferential sputtering effects. By combining quantitative Be amounts from RBS measurements with TRIDYN simulations, high-resolution depth profiles can be extracted from the XPS sputter profiles which agree well with the crude step-like profiles from the RBS evaluations.

Two different types of samples were investigated. Type A contains no interfacial oxide between the Be and C substrate, whereas type B which is produced under worse vacuum conditions has an interfacial oxide layer.

From the measured depth profiles, concentration-dependent diffusion coefficients were determined for both sample types. For type B samples containing an interfacial oxide film, the $D(c)$ is larger by approximately a factor of 2. More data is needed to draw decisive conclusions about the influence of oxygen on the diffusion of beryllium in carbon.

Acknowledgements

We thank J. Roth for discussions and J. Dorner for technical support during measurements at the 3 MV Tandem accelerator.

References

[1] ITER Physics Basis, Nuclear Fusion 39 (1999) 2391.
[2] V.P Gladkov, V.S. Zozov, D.M. Skorov, At. Eng. 34 (4) (1973) 290.
[3] K. Schmid, J. Roth, J. Nucl. Mater. 302 (2002) 96.
[4] P. Goldstraß, K.U. Klages, Ch. Linsmeier, J. Nucl. Mater. 290–293 (2001) 76.
[5] W. Möller, W. Eckstein, J.P. Biersack, Comput. Phys. Commun. 51 (8) (1988) 355.
[6] M. Mayer, SIMNRA User's Guide, Report IPP 9/113, Max-Planck-Institut für Plasmaphysik, Garching, Germany, 1997.
[7] www.rzg.mpg.de/~mam/, matej.mayer@ipp.mpg.de.
[8] R.J. Borg, G.J. Dienes, An Introduction to Solid State Diffusion, Academic Press, 1988.

FORMATION AND EROSION OF MIXED MATERIALS

Ch. LINSMEIER, J. ROTH, K. SCHMID
Max-Planck-Institut für Plasmaphysik, EURATOM Association,
Garching bei München, Germany

Abstract

The formation of compounds between wall materials and plasma impurities at the first wall of fusion devices involves a broad spectrum of species and interaction parameters such as ion energies, surface temperatures, impurity concentrations. Most of these parameters are hardly controllable in fusion experiments. To elucidate formation and erosion mechanisms, well-controlled laboratory experiments are described. In the first part of this review, carbide formation for the elements Be, Si, Ti and W is reported for thin carbon films on pure substrates. At room temperature, carbide formation is found in all systems up to a monolayer carbide coverage. For larger carbon amounts, elementary carbon films are formed. At elevated temperatures, the carbide formation is determined by thermochemistry and carbon transport by diffusion. For metallic carbides (W, Ti), strong carbon diffusion into the bulk substrate takes place at high temperatures. Several carbide phases are observed as a function of temperature. For ionic (Be) and covalent (Si) carbides, stable and stoichiometric carbide layers up to temperatures close to the respective melting points are formed. The second part of this review describes phase formation and erosion processes by impurity ion bombardment. For carbon ion impact, layer deposition, carbide formation and carbon diffusion processes depend on the parameters substrate temperature, angle of ion incidence and ion energy. This is shown in detail for carbon ion impact on tungsten. A reproduction of experimental results is possible after the determination of the concentration-dependent diffusion coefficient of carbon in tungsten. Finally, simultaneous bombardment of surfaces by multiple species is discussed for the combinations carbon-hydrogen and carbon-oxygen, experimentally carried out by CH_3^+ and CO^+ bombardments of tungsten and beryllium, respectively. Complex dynamic processes are observed as a function of particle fluence and substrate temperature.

Introduction

The formation of mixed materials relevant to fusion first walls is a complex process involving a broad spectrum of particle species, particle energies, material temperatures, just to mention some. Under real conditions during plasma discharges in a fusion experiment these parameters are hardly controllable. Moreover, analytical methods are limited, especially those which probe the chemical composition and state of the surface as well as depth profiles. Nevertheless, at JET an attempt was started a decade ago with the Fast Transfer System to employ ion and photoelectron spectroscopies *in vacuo* [1]. The fundamental properties of the interaction of potential wall materials and impurities from the plasma, however, can only be studied under full control of all experimental parameters. Therefore, studies have to be carried out under well-defined conditions which are achieved in ultra-high vacuum (UHV) environments. The goal of those studies is both the full control of all experimental parameters and their limitation to only a few parameter variations during specific experimental series. Through this approach we aim at gaining full understanding of the behavior of systems consisting of two to several elements under variation of incoming particle energies, sample temperatures, surface morphologies or chemical reaction conditions.

In the first part of this paper we summarize studies carried out recently concerning the formation of carbides in binary systems of carbon and several elements relevant for nuclear fusion. Specifically, we investigate materials used or under consideration for plasma facing components or wall conditioning procedures. In particular, we will discuss the formation of carbides of the elements beryllium, silicon, titanium and tungsten. In the second part, the influence of the intermixing and compound formation during carbon bombardment on the erosion properties of potential plasma facing materials is presented. Multi-species ion bombardment is simulated by using CH_3^+ or CO^+ ions.

I. Formation of mixed materials

Since carbon is an ubiquitous contamination at all surfaces, experiments to study the chemical interaction of surfaces with carbon require the thorough cleaning of the samples and experimental procedures fully under UHV conditions. Experimental details are given in ref. [2,3] and are only shortly described here. Carbon is provided as a surface layer at thicknesses between submonolayer coverage and several nm [2]. The analysis of the chemical and physical processes during the carbide formation at the surfaces is carried out mainly by photoelectron and ion spectroscopies. Main tool is X ray photoelectron spectroscopy (XPS) which probes core-level photoelectron binding energies and therefore yielding elemental identification of the electron-emitting atom, including its chemical environment. Ion spectroscopies comprise of techniques available from a 3 MV tandem accelerator, e.g. Rutherford backscattering spectrometry (RBS). In the experimental setup ARTOSS we combine both electron and ion spectroscopies together with sample cleaning and preparation facilities [3]. High-resolution XPS measurements are possible in a second UHV system, equipped with both a dual anode (Mg/Al) X ray source and a monochromatic Al X ray source [4]. This chamber is connected to a preparation chamber where films can be evaporated onto the samples and thermal treatments are carried out under UHV conditions. The samples used for the carbide formation studies are a beryllium (0001) single crystal, a silicon (100) waver, and polycrystalline foils of titanium and tungsten.

1. Room temperature reactivity

The C 1s peaks deposited at room temperature on the four elements Be, Si, Ti and W are plotted in Fig. 1 without background subtraction. The shaded area marks the binding energy regime where elementary carbon binding energies appear. The carbide binding energies (taken from the literature for Ti, Si, and W [5] and from a separate experiment for Be [6]) are shown in Fig. 1 by vertical lines. In all four cases a stoichiometric carbide is formed at the surface at room temperature. In the Ti case intensity is detected between the narrow TiC peak at 281.8 eV and the broadened elementary carbon signal at 284.2 eV. Photoelectron intensity at this binding energy around 282.6 eV between TiC and elementary carbon originates from substoichiometric Ti carbides like Ti_8C_5 or Ti_6C_5 [7,8]. The width of the peak originating from stoichiometric TiC equals the experimental resolution for this measurement and is considerably smaller than both the elementary and the substoichiometric carbide signals. A sharp XPS signal can only be observed for a phase which not only possesses exact stoichiometry but also exhibits a well-ordered and uniform local environment of the atoms giving rise to a photoelectron peak of identical energy. In this case of a carbon layer on Ti a well-ordered and stoichiometric TiC layer develops. In addition, substoichiometric carbides are present, however, only producing a broad range photoelectron intensity of smaller magnitude than for the TiC phase.

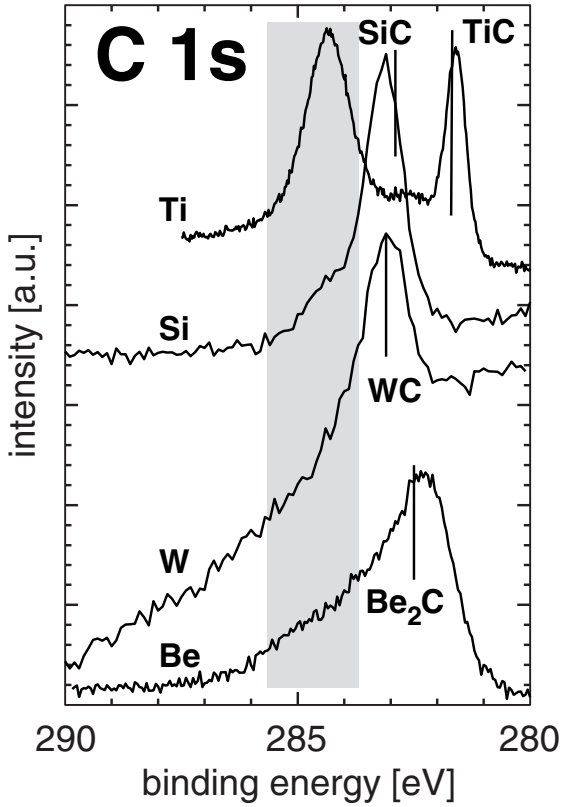

Fig. 1. Carbide formation at 300 K at the interface between elementary carbon layers and Ti, Si, W, and Be substrates. The C coverages are: approximately 2 ML C on Ti_{poly} and Be (0001); below 1 ML C on Si (100) and W_{poly}.

The formation of carbides is also observed for the three other elements (Si, W and Be) under study here. In all cases we find that for sub-monolayer carbon amounts the deposited carbon leads to a photoelectron peak at carbide binding energies. When the amount of carbon on the surface is increased, intensity in the elementary binding energy range appears. We conclude that impinging carbon atoms readily react with elementary surfaces. As soon as a monolayer of carbide has formed, this chemical interaction stops and further carbon deposited on the surface retains its elementary character. The carbon directly at the interface between substrate and adsorbed layer exhibits a charge density distribution which is characteristic for the respective carbide. A similar behavior is also observed for molybdenum [9].

The variation of the chemical state of deposited carbon with increasing carbon amounts on a Be surface is shown in Fig. 2. Plotted is the integrated intensity of the total C 1s binding energy range and the respective elementary and carbidic carbon intensities after depositing increasing amounts of carbon from an electron beam evaporation source. The carbon coverage is determined by RBS using ^{4}He at 600 keV. At the smallest carbon coverage, almost all C 1s intensity is localized at the carbide binding energy. With increasing carbon deposition, the

carbide amount increases up to a coverage of 1.2 ML. Further increase of the total carbon at the surface does not lead to the formation of further Be_2C. However, the carbon remains in the elementary chemical state. Therefore it can be concluded that at room temperature no diffusion through the adlayer takes place. Neither diffuses beryllium from the substrate through the formed carbide layer and reacts with freshly deposited carbon, nor is the elementary carbon at the surface able to diffuse through the formed Be_2C monolayer and reach metallic beryllium. Therefore, the carbide formation reaction stops after roughly one monolayer for Be_2C has been formed at the C–Be interface.

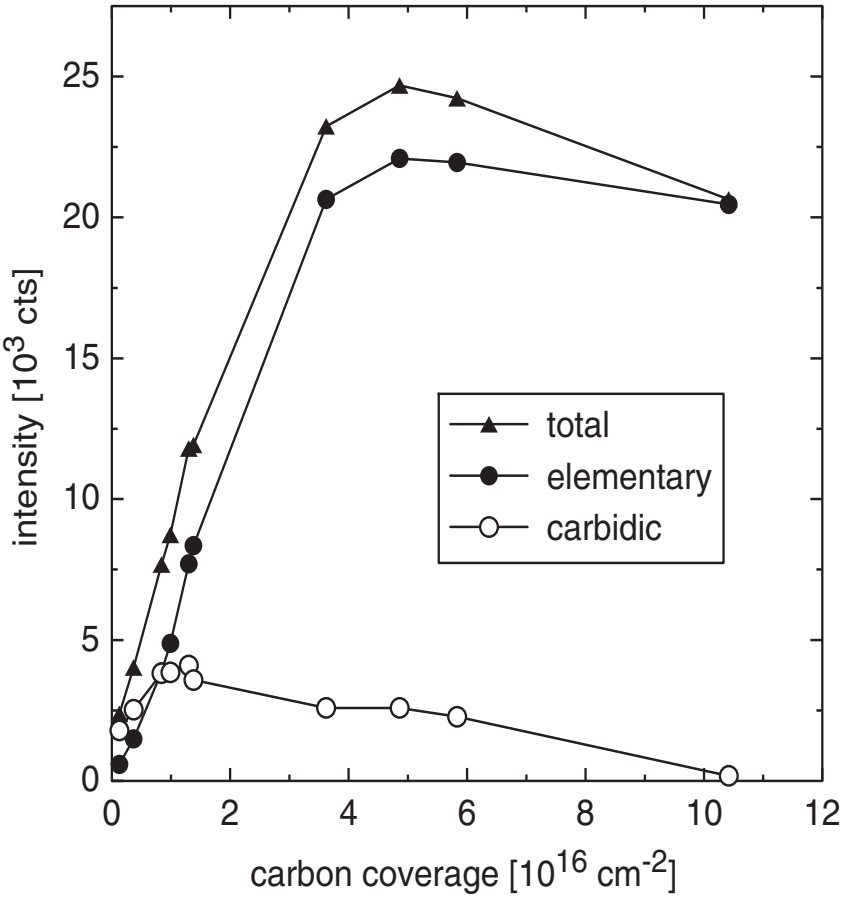

Fig. 2. XPS intensity in the C 1s region for a C/Be sample, plotted as a function of deposited carbon amount. The total C intensity can be separated in carbide and elementary C fractions.

With further increasing carbon coverage the carbide intensity actually decreases after the Be_2C monolayer has formed. This indicates that the carbide is situated at the very interface between the Be surface and the deposited carbon layer. The carbide photoelectrons from the C–Be interface are therefore attenuated on their way to the spectrometer through the elementary carbon overlayer. The attenuation of the photoelectrons is also visible in the

elementary and total C 1s intensities. With increasing carbon coverage the total carbon intensity rises almost linearly up to $3x10^{16}$ cm^{-2}. Above a carbon coverage of $4x10^{16}$ cm^{-2} the intensity levels off since the total depth of information for XPS (limited by the inelastic mean free path of photoelectrons) is reached. The maximum in the carbon intensity at a carbon coverage around $5x10^{16}$ cm^{-2} indicates a change in the surface morphology during the carbon deposition. The growing carbon layer initially exhibits a rough surface. Due to the roughness more carbon atoms are exposed compared to a flat surface. The decreasing carbon intensity above $5x10^{16}$ cm^{-2} suggests a flattening of the carbon layer around this fluence.

2. Carbide formation at elevated temperatures

The limited mobility of carbon or beryllium at room temperature limiting the carbide amount formed during these experiments to approximately one monolayer is also visible in Fig. 3. This figure shows the amount of carbon which has reacted to Be_2C as a function of the total carbon amount deposited at the surface, for sample temperatures between 300 K and 673 K. The bisecting line in this diagram thus indicates the quantitative formation of Be_2C. The intensity from the XPS measurements is calibrated against the RBS data thus giving absolute numbers for the carbon areal density. The measurements at 300 K and 373 K in Fig. 3 are very similar in initial slope and final carbide amount.

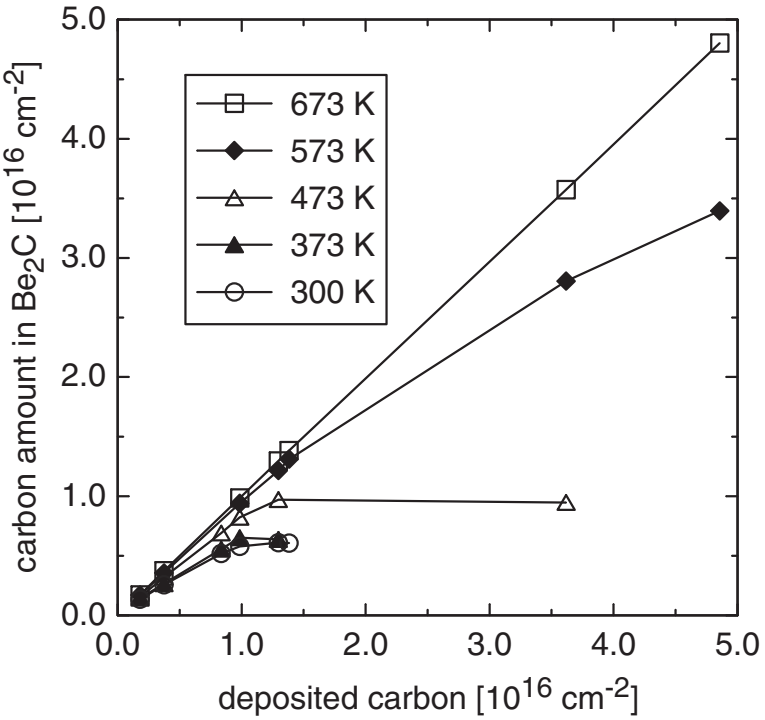

Fig. 3. Total amount of carbon bound in Be_2C at each temperature step as a function of the initially deposited carbon amount at 300 K. The data points at equal temperatures (but different samples) are connected to guide the eye.

The initial slope at these temperatures deviates notably from the bisecting line. This indicates that from the deposition start on the carbide formation is incomplete. There is always carbon deposited elementarily at the surface. The final amount of carbide indicated by the leveling of the curves is reached after carbon deposition of $1x10^{16}$ cm^{-2}. The carbidic carbon amount of $6x10^{15}$ cm^{-2} corresponds to 5.6 ML of Be_2C, calculated with a Be_2C bulk density of 1.90 g cm^{-3}. The reaction between carbon and beryllium at 473 K is still not quantitative from the start on. However, more carbon reacts with beryllium at this temperature and the final amount of carbide reached after the deposition of $1.3x10^{16}$ cm^{-2} corresponds to 12.2 ML Be_2C. Already at the substrate temperature of 573 K almost all deposited carbon reacts with beryllium initially. The curve starts to bend from the 45° line after a carbon amount of approx. $1.5x10^{16}$ cm^{-2}. Within these measurements no constant Be_2C amount is reached. This is also true for the experiment at a Be substrate temperature of 673 K. The amount of carbon converted to Be_2C corresponds in the whole range examined to the total amount deposited at the surface. All data points lie well on the bisecting line. These measurements demonstrate that the amount of carbide is characteristic for a given temperature, provided that sufficient elementary carbon is available. A similar behavior was described by Miller for titanium layers on carbon [10].

RBS measurements which probe the total amount of carbon on beryllium substrates show that the carbide layer formed at the metal surface is stable up to temperatures of 900 K [11]. Neither diffusion of carbon into the Be bulk nor diffusion of Be metal through the carbide surface layer is observed. The stability of the carbide layer on Be is explained by the nature of the chemical bond in Be_2C. This compound is of ionic nature where the solid constituents are Be^{2+} and C^{4-} ions, respectively. Diffusion of one lattice species through the solid requires to overcome the Coulomb barrier between ionic species.

A different diffusion behavior of carbon can be expected for transition metals (e.g. W, Ti) which form metallic carbides. These carbides are characterized by a lattice structure defined by metal atom packings. Carbon atoms are positioned at sites defined by the metal atom structure, e.g. octahedral sites ion the case of TiC or trigonal prismatic sites in WC. Since there are equal amounts of those sites and metal atoms, a complete occupation of all sites in the metal lattice by carbon atoms defines the composition *M*C (e.g. WC, TiC). In subcarbides (e.g. W_2C), half of the octahedral sites of a W hcp (hexagonal close packed) structure are occupied by carbon, usually in an ordered way. However, since there is a number of energetically equivalent sites within arrangements defined by spheres packing, diffusion between these equivalent sites is easily possible. The small energy barriers between the sites are also the reason why some transition metals not only form compounds of exact stoichiometry. Phases with varying stoichiometry exist. This is the case for Ti, where the TiC phase has a compositional range of 32 to 48.8 at.% C [12].

The composition changes and carbon diffusion for a carbon film on tungsten at different temperatures are shown in Fig. 4. Fig. 4a shows the composition of the surface layer accessible by XPS, calculated from the C 1s and W $4f_{7/2}$ photoelectron peaks. The result of the C 1s deconvolution is shown in detail for the temperature range 873 K to 1373 K in Fig. 4b. Beginning at room temperature, the chemical state of carbon is elementary with a very small contribution of WC which stems from the carbide layer at the C–W interface. The elementary carbon itself shows two states: most of the carbon (roughly 2/3) features an ordered graphitic configuration, whereas a minor part (1/3) is also graphitic, but with a locally disordered structure [13]. This disordered graphite converts into an ordered phase during temperatures up to 870 K. The total amount of carbon in the surface layer stays constant. The carbide fraction

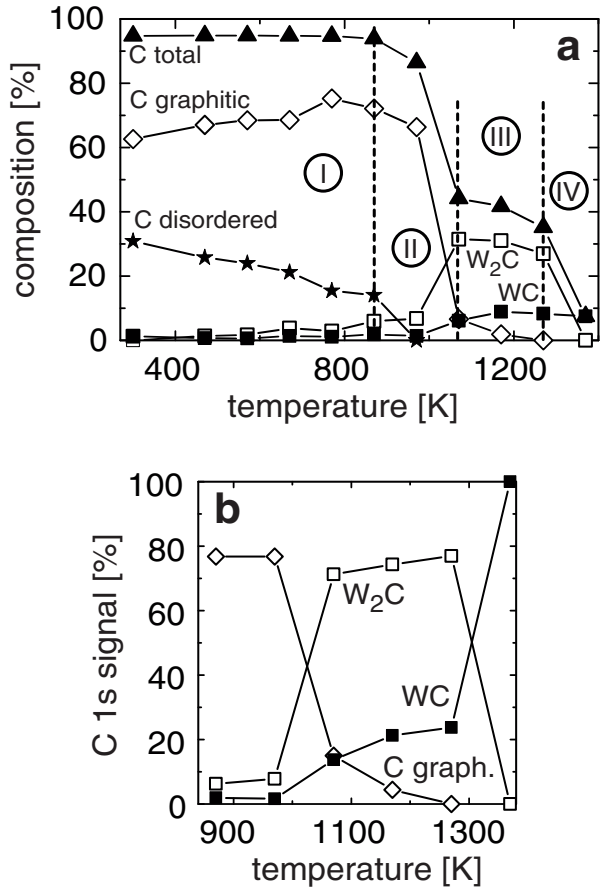

Fig. 4. (a) Surface composition of a 1.5 nm carbon film deposited on tungsten, as a function of annealing temperature. The dashed lines indicated the four phases during the carbidization process on tungsten. (b) Relative fractions of the C 1s intensity within the temperature range where major carbide amounts are formed.

increases only slightly up to this temperature. At 970 K a chemical reaction between elementary carbon and metallic tungsten sets in. In the C 1s spectrum a new binding state is necessary to fit the experimental data and the W $4f_{7/2}$ peak shifts to higher binding energies, indicating carbide formation. The total carbon intensity starts to decrease. Between 1070 K and 1270 K the carbon is predominantly bound in W_2C with decreasingly smaller fractions of elementary carbon and an increasing part of carbon in bound WC. In this temperature regime the loss of carbon from the surface layer is reduced after the strong drop around 1000 K. The surface layer still contains around 40 at.% of carbon. Another significant change in the carbon content is observed after heating the sample to 1370 K. The total C 1s intensity decreases and the W $4f_{7/2}$ signal is dominated by metallic tungsten. Carbon is diffused into the tungsten bulk to a substantial degree.

As indicated in Fig. 4a the temperature range can be divided into four regions. In phase (I) only carbide formed during the sample preparation exists. Disordered parts of carbon in the elementary carbon layer order with increasing temperature. Phase (II) starts between 870 K and 970 K. A part of elementary carbon reacts with tungsten under W_2C formation. The total amount of carbon within the XPS analysis depth significantly decreases. At 1070 K a transition from phase (II) to phase (III) occurs. In this phase W_2C dominates which is particularly obvious in Fig. 4b which shows the relative parts of the carbon chemical states in the C 1s integral. W_2C is formed by carbon atoms located at the octahedral sites in a hcp W arrangement. To form W_2C from W and C from the deposited layer, transport of C atoms to these sites is necessary. This explains the strong decrease of the C 1s signal upon W_2C formation. Besides W_2C also WC develops where carbon is located in trigonal prismatic sites in a hexagonal primitive W packing. After the W_2C formation further decrease of the carbon amount is slowed down until the transition from phase (III) to phase (IV) at 1270 K. In phase (IV) all carbon exists as WC. The total carbon amount within the XPS analysis region has further decreased strongly.

The strong decrease of the carbon intensity during the thermal treatments of a 1.0 nm carbon layer on polycrystalline Ti is shown in Fig. 5. After deposition, the carbon is predominantly elementary, only at the C–Ti interface TiC is present. The carbide fraction rises from 2 at.% at 300 K to 18 at.% after heating the sample to 670 K. At higher temperatures the total carbon intensity significantly decreases. In the spectrum after 770 K only 38 at.% of the initial C 1s intensity are present. The peak is shifted completely to the binding energy of TiC at 281.8 eV and the part of subcarbide (denoted by Ti_xC_y) rises to 18 at.%. The C 1s intensity after the 870 K treatment has almost vanished, it remains only 0.7 at.% of the initial value at 300 K. The total intensity after the 870 K treatment is located at

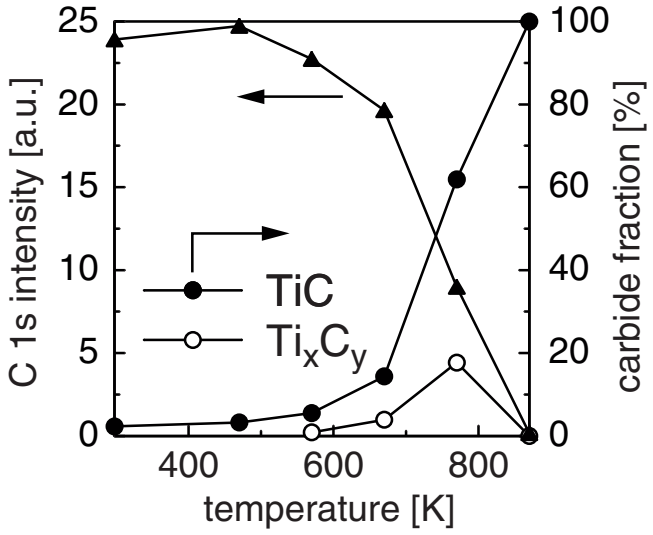

Fig. 5. XPS temperature profile from a 1.0 nm C layer on polycrystalline Ti. Plotted are the carbide and subcarbide contributions to the total C 1s intensity (circles) and the decrease of the total C 1s intensity (triangles).

the TiC binding energy, no elementary carbon or carbon in Ti subcarbides are present. TiC is a metallic carbide, similar to WC. However, during the phase transition from metallic Ti over subcarbides with varying stoichiometry, the host atoms remain in their hcp structure and the carbide stoichiometry is determined by the degree of occupation of the octahedral sites by carbon atoms. This explains the broad phase range of the subcarbides and also the truly substoichiometric nature of TiC where always carbon vacancies exist.

The interaction of carbon with elemental surfaces of Be, Ti and W is determined both by the chemical reaction between carbon and the metals and by the diffusion of carbon in the substrate material. All carbides discussed here have negative enthalpies of formation, listed in Table 1. The formation of carbides from the elements releases energy and therefore takes place spontaneously if carbon and metal atoms are both available. The availability in the layered samples under study here is in turn governed by the diffusion of carbon towards the metal (or metal diffusion into the carbon layer). Besides chemical driving forces for atom mobility the structure of the solid and types of chemical bonds are crucial. As soon as a carbide has formed at the interface (which takes place spontaneously upon deposition of carbon on the clean metal surfaces) the atoms must diffuse through a growing carbide layer. This diffusion is easily possible in case of the transition metals Ti and W, which form metallic carbides. Here, carbon atoms occupy void lattice sites in the metals' host structure which is best described in both cases by packings of spheres. Many energetically equivalent sites are present in the host lattice. Therefore, only a small activation barrier has to be overcome for carbon atoms changing sites. Since we start with a layered structure, both entropic and chemical driving forces lead to the dilution of carbon atoms in the bulk metals at elevated temperatures. In the case of tungsten structural rearrangements are necessary during the transition from metallic tungsten (body centered cubic, bcc) to W_2C (hexagonal close packing, hcp) and WC (hexagonal primitive). The two carbide phases can be well distinguished in the experiment during the temperature increase. Such a restructuring is not necessary in the Ti system, since metal and carbides all have hcp structures. Since no restructuring is necessary during the metal-carbide transition, this may be the reason that the subcarbide phase is not specifically visible during the carbide formation reaction. In contrast to the metallic carbides of Ti and W, Be_2C is an ionic solid. Diffusion of species here means that ions must travel through the lattice whereby Coulomb forces have to be overcome. The experiments show that the carbide layers on Be substrates are stable up to 900 K. This observation correlates well with this picture. In Fig. 6 the elements Be, Ti and W are compared during the carbide formation. Plotted are the C 1s intensities (normalized to the value after carbon deposition at 300 K) for increased sample temperatures. Also plotted as a reference are the results of a similar experiment using Au as substrate. Gold is inert towards carbide formation and carbon is insoluble in gold [12]. Therefore, no intensity drop due to compound formation or carbon diffusion into the Au bulk is expected. For the reactive metals an initial phase can be identified starting at room temperature in which only small carbon losses take place. They can be interpreted by some intermixing between carbon and substrate material. After this initial phase all three metals exhibit a characteristic temperature where the carbon intensity drops significantly. We identify this phase with quantitative carbide formation. At the end of this temperature region all available carbon is chemically in the carbidic state. For Be and W a final phase can be identified where the C 1s intensity drop stops or at least strongly slows down. In case of Be the carbon intensity stays at a high level indicating the stability of the formed carbide. No diffusive losses to the bulk take place for this ionic carbide. For W, only a small amount of carbide is present at the surface. The majority of the carbon has been lost by diffusion into the bulk substrate. In the case of Ti, this final phase lacks completely. Diffusion of carbon in Ti is so strong that finally only traces for TiC remain detectable in the surface layer.

Table 1. Free enthalpies of formation (ΔG_f) for binary carbides of Ti, Be and W [14].

Compound	**ΔG_f [eV]**
TiC	-1.88
Be_2C	-1.19
WC	-0.40
W_2C	-0.23

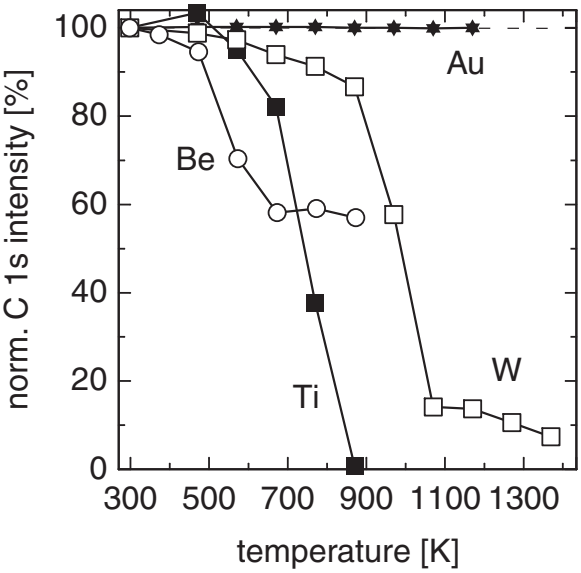

Fig. 6. Changes in the XPS C 1s intensities during annealing of thin carbon films deposited at 300 K on the indicated materials. The curves are normalized to the initial carbon intensity (100 %).

II: Erosion behavior of mixed materials

In fusion devices the deposition of non-recycling impurity atoms will always be in the form of energetic ions. Therefore implantation and phase formation will proceed simultaneously with ion induced erosion. In the following this situation will be discussed for the bombardment of typical plasma facing materials, such as W, Be, Ti and Si, with carbon ions.

1. Estimates from kinetic Monte Carlo code simulations

First investigations [15] on the dependence of the erosion yield of W under carbon ion bombardment have been performed previously at room temperature and interpreted using the Monte-Carlo Code TRIDYN [16]. The erosion and deposition processes occurring during C bombardment were investigated by *in situ* monitoring of the samples weight change as a

function of the applied C fluence. Fig. 7a shows the weight change of a W sample due to carbon bombardment at different angles of incidence. The typical shape of the weight change observed in these experiments can be seen in the 0° or 35° graphs in Fig. 7a. Initially the sample's weight decreases due to W erosion, moves through a transition point and then starts to increase again. The occurrence of the transition point an the proximate increase of the samples weight is due the deposition of C. This formation of a C layer is dominated by the carbon self sputtering yield . At normal incidence, carbon self sputtering is always below unity and protective layers build up. At grazing angles of incidence the self sputtering yield increases above unity, leaving the substrate surface open for continuous erosion as can be seen in the 70° graph in Fig. 7a [15]. The limits for W erosion and C deposition in the parameters space of energy and angle of incidence is shown in Fig. 7b. The agreement of the transition from deposition to erosion with calculations of the energy and angle of incidence where the sum of self sputtering yield and reflection coefficient is equal to unity [17] underlines the importance of the self sputtering yield of carbon. These code calculations cannot take into account effects of enhanced surface temperatures, such as the diffusion of carbon in the bulk W, carbide phase formations or the radiation enhanced sublimation (RES) of carbon, which dominates the self sputtering at enhanced temperatures.

These processes lead to a temperature dependence of erosion by carbon. Diffusion and RES introduce additional C loss channels from the surface thereby hindering the formation of a protective C layer. They can inhibit layer formation above a certain temperature threshold and lead to continuos erosion of the substrate material. For all materials under examination here carbon will accumulate at the surface at room temperature, thus forming a protection layer for erosion and the steady state erosion yield of the substrate material will be zero. However, the surface will no longer be that of the substrate material originally intended, but a carbon surface! With increasing temperature the formation of carbides can change the erosion behavior of the substrate material by increasing the surface binding energy of the atoms which governs sputtering at a given energy and angle of incidence. This is especially true for carbides with a high energy of formation like Be_2C and SiC.

From the results presented in section I estimates for the influence of diffusion and phase formation can be obtained The sputtering yield of Be and Si, which form stable carbides at 500 K and 1100 K, respectively, is expected to be reduced compared to the clean material. In the case of Ti and W diffusion becomes fast enough to leave the surface almost unchanged by the implanted carbon atoms at temperatures above 800 K and 1000 K, respectively. For Au no phase formation or inward diffusion could be found up to 1500 K and the deposition of carbon layers should prevent erosion at all temperatures.

2. Temperature dependence of W erosion due to carbon ion bombardment

The temperature dependence of erosion / deposition due to carbon ion bombardment has been investigated in detail for W, Ta, Pt and Au [18] and examples will be given here for the C^+/W system. Fig. 8 shows the fluence dependence of the weight change of a W sample bombarded at normal angle of incidence with 2.4 keV C^+ ions at different temperatures.

While at room temperature the data agree well with the behavior shown in Fig. 7a, already at 773 K a slower weight increase is observed at high fluences. This is an indication of an enhanced self sputtering yield after the deposition of a carbon layer on the W surface and must be interpreted in terms of RES of carbon [18,19]. With further increasing temperature

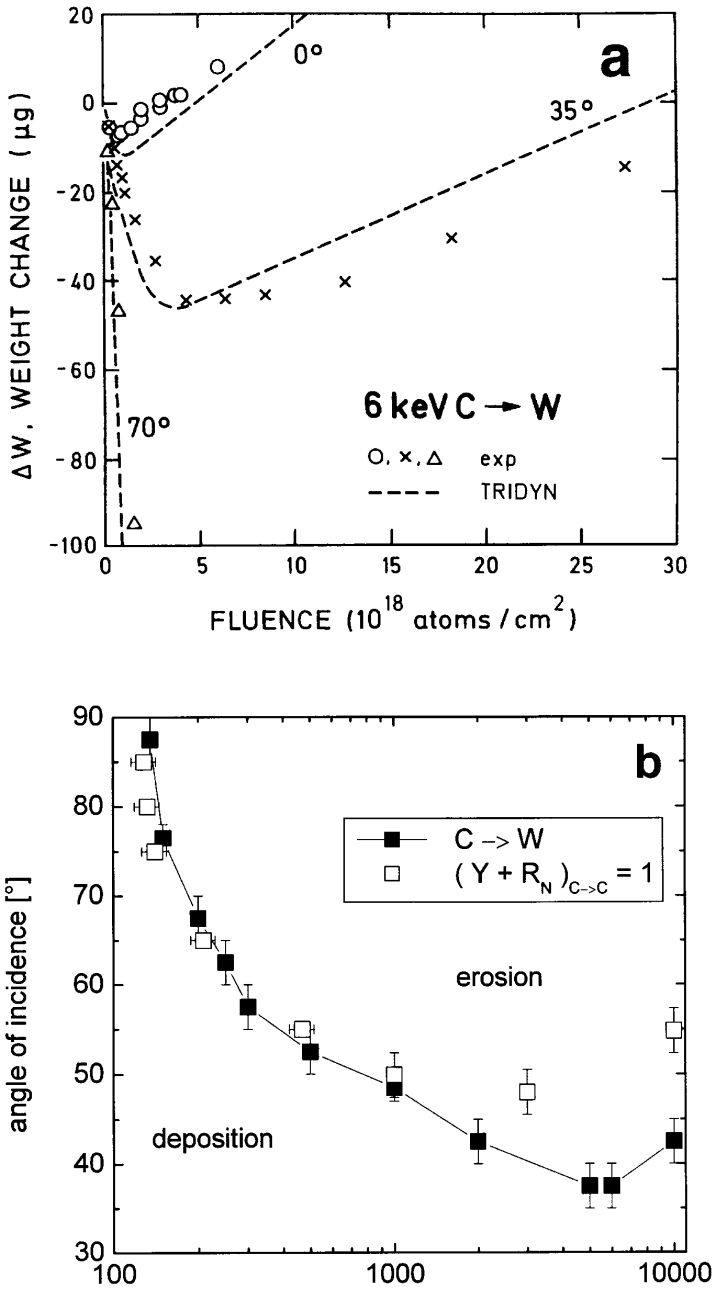

Fig. 7. C^+ ion bombardment of tungsten. a) weight change as a function of applied carbon fluence for 0°, 35° and 70° angles of incidence (with respect to surface normal) b) angular and energy dependence of the transition from erosion to deposition.

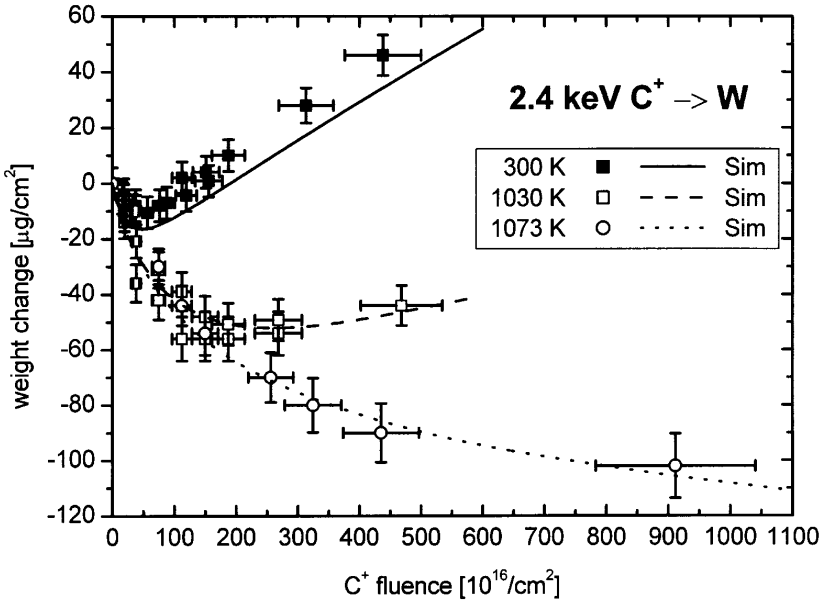

Fig. 8. Comparison of experimental and simulated weight change data of 2.4 keV C^{+} → W in the temperature range from 300 K to 1073 K.

the initial weight loss extends to higher fluences. This can be interpreted as the manifestation of carbon diffusion into W in competition with carbon implantation, thus leaving the surface exposed to erosion to higher carbon fluences. The final weight increase has again a smaller slope due to the RES increase with temperature [19,20]. In order to simulate the observed behavior in separate experiments the RES erosion yields and the diffusion coefficient of carbon in W are determined from the interdiffusion of carbon layers on W samples at elevated temperatures. Measurements of the carbon self sputtering yield demonstrate that the effect of RES extends down to room temperature and must be taken into account for all elevated temperatures [18]. The data is collected in Fig. 9 and agrees well with literature data for the RES yield at higher temperatures [19,20]. The diffusion coefficients are found to be strongly depended on carbon concentration, decreasing more than an order of magnitude for carbon concentrations above 30 at.% in the investigated temperature range up to 1173 K [21]. In Fig. 10 the concentration dependent diffusion coefficient D(C) for low C concentrations [21] is compared with literature data [22]. Literature data are quite scattered and the low concentration values of D(C) from [21] lie between literature data for diffusion of C in W and in WC. At temperatures above 1200 K the diffusion of carbon is so fast that a carbon ion flux of 1.5×10^{14} $cm^{-2}s^{-1}$ is insufficient to result in complete surface coverage. The surface remains uncovered by carbon at high fluences and continuous weight loss occurs. The lines shown in Fig. 8 were obtained by computer calculations that took into account the simultaneous erosion/deposition and diffusion processes by coupling the Monte-Carlo code TRIDYN [16] with the new diffusion code DIFFUSEDC [18]. In this coupled approach the application of a certain fluence Φ is approximated by discrete fluence steps $\Delta\Phi$ and time steps Δt. Each step starts with a TRIDYN calculation during which the implantation of a fluence

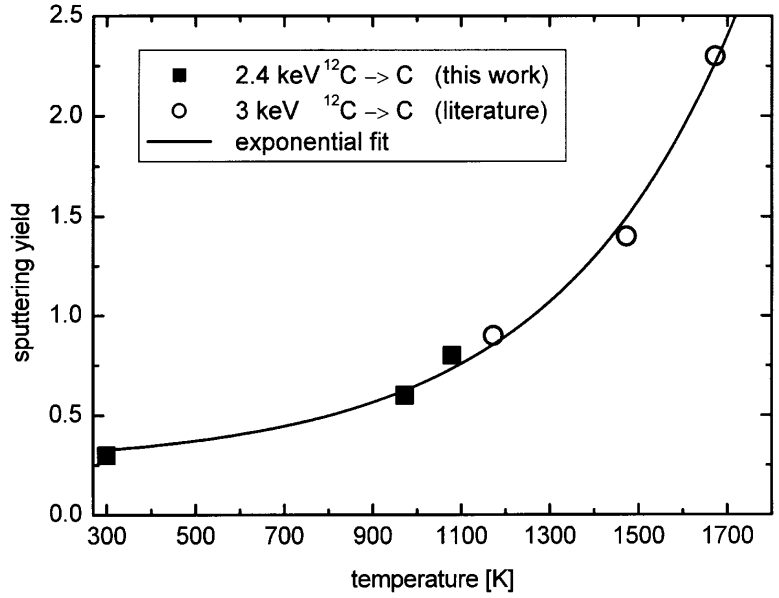

Fig. 9. Temperature dependence of the C self sputtering yield together with an exponential fit to the available data.

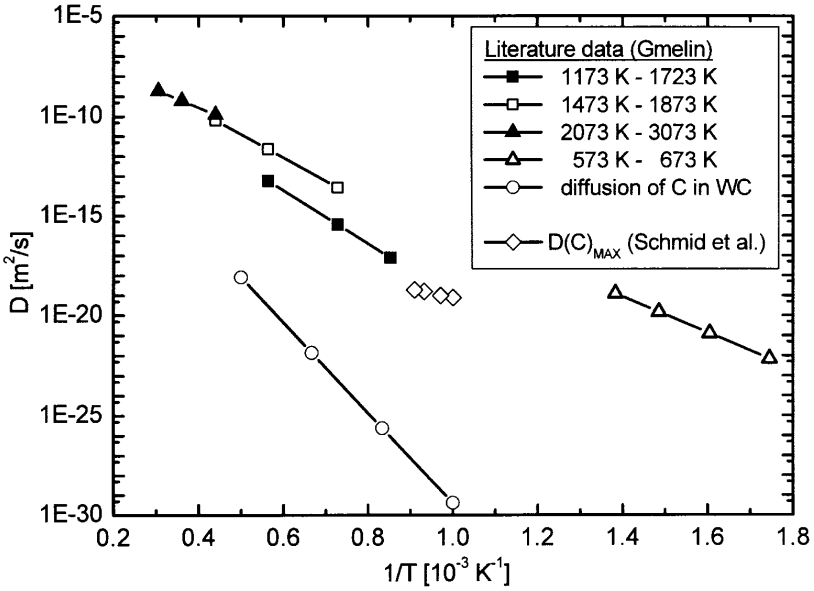

Fig. 10. Summary of available data on diffusion of C in W and C in WC.

$\Delta\Phi$ is simulated, thereby taking the enhanced carbon erosion due RES into account by reducing the surface binding energy. The resulting carbon depth profile then serves as the input into a DIFFUSEDC calculation during which the evolution of the implanted carbon due to diffusion during a time period Δt is simulated. The result of this calculation in turn serves a input in the next TRIDYN run. This cycle is repeated N times with $N = \Phi/\Delta\Phi$. In this calculations the discretization parameters $\Delta\Phi$ and Δt were chosen small enough that the implantation and diffusion processes can be considered to occur simultaneously. The agreement of the curves and the experimental data without additional free fitting parameters indicates the diffusion and RES are the responsible processes for the temperature dependence of erosion/deposition.

Other high-Z target materials yield qualitatively similar results but are different in details. For Ta, carbon diffusion coefficients are known to be about two orders of magnitude smaller than for W, thus making diffusion negligible in the temperature range up to 1200 K. The experimental data show a strongly reduced erosion phase at small fluences and a deposition phase in agreement with the temperature dependent RES yields. Bombardment of Au results in a carbon layer deposition at any temperature up to 1073 K, which starts to flake off at high fluences [18].

3. Multi-species ion bombardment

In fusion devices, typically, the plasma facing components are bombarded simultaneously by different ion species. Together with the flux of impurity ions, such as carbon, oxygen or atoms from wall materials, a much larger flux of fuel ions, i.e. hydrogen isotopes, impinges onto the surface. In order to simulate the simultaneous impact of carbon and hydrogen ions, CH_3^+ ions were used in comparison with C^+ ions [19]. The CH_3^+ energy was chosen at 3 keV such that the carbon ions obtain the same energy as in the case of single C^+ bombardment at 2.4 keV. The equivalent energy for hydrogen is 200 eV. In Fig. 11 the fluence dependence of erosion by CH_3^+ is compared to C^+ ions. Already at 300 K an increased erosion yield for CH_3^+ is found. CH_3^+ at 1000 K leads to continuos weight loss of the sample. In simulations of the erosion/deposition due to CH_3^+ the additional erosion (physical + chemical) due to the incident 200 eV hydrogen atoms must be taken into account. In this case TRIDYN may simulate the physical sputtering yield, while additional chemical erosion effects [23] must be taken into account separately. Chemical erosion is therefore added as an additional step (YCHEM) in the TRIDYN + DIFFUSEDC coupling cycle described above. In YCHEM the carbon depth profile calculated by TRIDYN is modified according to a given chemical sputtering yield analogous to the dynamic surface relaxation performed by TRIDYN. In order to simulate the results of CH_3^+ bombardment on W depicted in Fig. 10, two types of calculations were performed. At 300 K where diffusion is negligible only TRIDYN+YCHEM is used with chemical erosion yield of 4%. The high temperature bombardment at 1000 K is simulated using the full sequence TRIDYN+DIFFUSEDC+YCHEM. The agreement with the experimental data in excellent. The resulting code package now allows the simulation of erosion/deposition in divertor or first wall conditions under fusion experiments which cannot be reproduced directly in ion beam experiments.

The simultaneous impact of different impurity ions, such as C^+ and O^+, is simulated by bombardment with CO^+ ions. As substrate in this case Be was chosen [24,25] and the CO^+ ion energy was 3 keV.

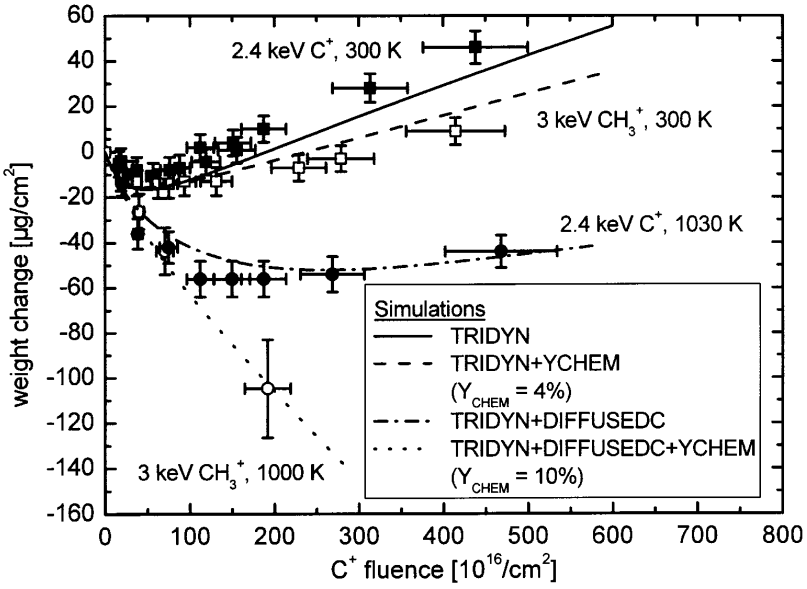

Fig. 11. Comparison of the temperature dependence of the W samples weight change during C^+ and CH_3^+ bombardment.

While at room temperature a carbon layer is deposited, as in the case of W, CO^+ bombardment results in a saturation of the deposited amount of both C^+ and O^+. The erosion of carbon by oxygen ions is higher than unity [26] such that a surface concentration less than 100 at.% C results in an eroded carbon flux equal to the incident CO^+ ion flux. Such a high erosion yield must be due to chemical re-erosion of deposited carbon by oxygen atoms, where CO and CO_2 formation is found [26,27]. Chemical phase analysis shows a surface layer of BeO intermixed with amorphous carbon [28]. The coverage does not protect the Be substrate from erosion. At room temperature continuous weight loss of the Be sample prevails (Fig. 12).

The erosion yield of Be increases with increasing surface temperature up to 473 K, indicating a reduced Be coverage by carbon. This may be due to enhanced C erosion or by diffusion of Be to the surface. At further elevated temperatures initially a weight increase occurs, turning into erosion at high fluences. Depth profiling of C and O after reaching steady state erosion reveals the increasing interdiffusion of Be with C and O which results in the initial weight increase.

Conclusions

Under bombardment with non-recycling impurities the surfaces of pure materials used as plasma-facing component will be modified. This modification has been investigated for the case of bombardment by carbon ions or CO^+ and CH_3^+ molecules. Substrates investigated are Be, Si, Ti, and W.

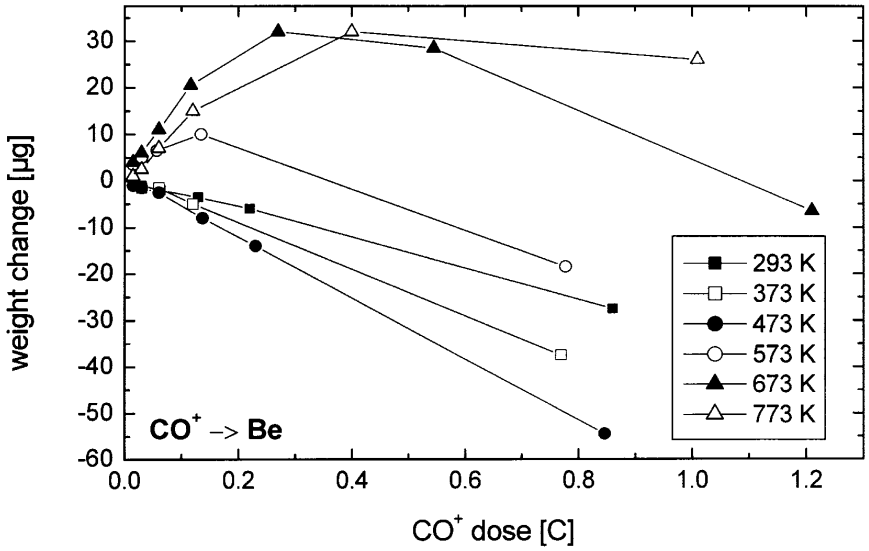

Fig. 12. Weight change of a Be target during 3 keV CO^+ bombardment in the temperature range from 293 K to 773 K.

The chemical interaction of carbon with these materials is investigated by deposition of elementary carbon layers and subsequent thermal treatment. The processes of chemical phase formation (carbidization) and diffusion have been analyzed by X ray photoelectron spectroscopy. Carbide formation was observed in all cases. Carbon diffusion into the bulk at elevated temperatures is observed for the transition metals Ti and W. For Be and Si, however, which are forming ionic and covalent carbide compounds, respectively, no carbon diffusion into the bulk takes place. For W and Ti, both subcarbides and carbides with different stoichiometries are identified.

At room temperature and normal angle of incidence on all elements a carbon layer is deposited by C^+ ion bombardment, protecting the underlying substrate from erosion. At elevated temperatures the formation of compounds and carbide phases occur. The temperatures where carbide formation sets in correlates with the heat of formation of the different carbides. Simultaneously, interdiffusion of implanted carbon atoms and substrate atoms occur.

These modifications at elevated temperatures have strong influence on the erosion behavior of the substrate. Transitions from deposition to erosion occur at elevated temperatures and a detailed investigation is presented for the case of C^+ and CH_3^+ bombardment of W. The transition temperature depends on the diffusion coefficient for carbon into W and on the temperature dependent self sputtering yield of carbon. Using these data the erosion behavior can be simulated in a modified TRIDYN code and extrapolated to the conditions in future fusion reactors.

Multi-species ion bombardment were simulated using CO^+ and CH_3^+ ions and show additional complications due to the chemical interaction of the incident species. In order to simulate multi-species bombardment as expected in fusion plasma conditions dual beam

experiments will have to be performed where ion fluxes can be varied independently. Additionally, drastic differences are expected with respect to hydrogen retention and diffusion in mixed material surfaces and needs to be investigated.

REFERENCES

[1] J.P. Coad, H. Bergsåker, S. Burch, G. Kaveney, F. Lama, G.F. Neill, J. Partridge, J.C.B. Simpson, and J. Vince, J. Nucl. Mater. 176&177 (1990) 145.
[2] Ch. Linsmeier, J. Luthin, and P. Goldstraß, J. Nucl. Mater. 290-293 (2001) 25.
[3] Ch. Linsmeier, P. Goldstraß, and K.U. Klages, Physica Scipta T 94 (2001) 28.
[4] S. Miller, G. Berning, H. Plank, and J. Roth, J. Vac. Sci. Technol. A 15 (1997) 2029.
[5] J.F. Moulder, W.F. Stickle, P.E. Sobol, and K.E. Bomben, *Handbook of X ray Photoelectron Spectroscopy*, Ed. J. Chastain, Perkin-Elmer Corp., Eden Prairie (1992).
[6] P. Goldstraß and Ch. Linsmeier, Nucl. Instrum. and Meth. B 161-163 (2000) 411.
[7] B.V. Khaneko, S.Ya. Golub, and M.P. Arbuzov, Kristallografiya (1980) 112.
[8] N.V. Dzhalabadze, B.G. Eristavi, N.I. Maisuradze, and E.R. Kuteliya, The Physics of Metals and Metallurgy 86 (1998) 59.
[9] P. Reinke and P. Oelhafen, Diamond Relat. Mater. 8 (1999) 155.
[10] S. Miller, PhD thesis, Universität Bayreuth (1997).
[11] P. Goldstraß, K.U. Klages, and Ch. Linsmeier, J. Nucl. Mater. 290-293 (2001) 76.
[12] T.B. Massalski, H. Okamoto, P.R. Subramanian, L. Kacprzak, *Binary Alloy Phase Diagrams*, 2nd Ed., Version 1.0, ASM International, Materials Park, Ohio (1996).
[13] J. Luthin and Ch. Linsmeier, Surf. Sci. 454–456 (2000) 78.
[14] I. Bahrin, *Thermochemical Data of Pure Substances*, 3rd Ed., Vol. 1&2, Weinheim (1995).
[15] J. Roth, W. Eckstein, J. Bohdansky J. Nucl. Mater. 165 (1989) 193.
[16] W. Möller, W. Eckstein, Computer Physics Communications 51 (1988) 355-368.
[17] W. Eckstein, J. Nucl. Mater. 281 (2000) 195.
[18] K. Schmid, PhD Thesis, Universität Bayreuth (2002).
[19] K. Krieger, J. Roth, J. Nucl. Mater. 290-293 (2001) 107.
[20] J. Roth, J. Bohdansky, W. Ottenberger, J. Nucl. Mater. 165 (1989) 193.
[21] K. Schmid and J. Roth, J. Nucl. Mater. 302 (2002) 96.
[22] Gmelin Handbook, W, Suppl. Vol. A 5b (1993).
[23] J. Roth, J. Nucl. Mater. 266-269 (1999) 51.
[24] P. Goldstraß, PhD thesis, Universität Bayreuth (2000) and IPP-Report 9/126 (2000).
[25] P. Goldstraß, W. Eckstein, and Ch. Linsmeier, J. Nucl. Mater. 266-269 (1999) 581.
[26] E. Hechtl, J. Bohdansky, J. Roth J. Nucl. Mater. 103&104 (1981) 333.
[27] E. Vietzke, A.A. Haasz, in: "Physical Processes of the Interaction of Fusion Plasmas with Solids" Eds: W.O. Hofer, J. Roth (Academic Press London 1996) p. 135.
[28] P. Goldstraß, Ch. Linsmeier, J. Nucl. Mater. 290-293 (2001) 71.

ELSEVIER

Journal of Nuclear Materials 313–316 (2003) 56–61

journal of nuclear materials

www.elsevier.com/locate/jnucmat

Deuterium bombardment of carbon and carbon layers on titanium

K.U. Klages, A. Wiltner, J. Luthin, Ch. Linsmeier *

Max-Planck-Institut für Plasmaphysik, EURATOM Association, Boltzmannstrasse 2, D-85748 Garching b. München, Germany

Abstract

Interaction of deuterium ions with highly oriented pyrolytic graphite and thin carbon layers on titanium are studied by X-ray photoelectron spectroscopy (XPS) measurements. The effects induced by the deuterium beam are compared to bombardment with chemically inert argon ions. XPS allows the identification of several carbon states: graphitic carbon, disordered graphitic carbon, ion-induced radiation defects in carbon, and carbidic carbon in the carbon films on titanium. Erosion of the carbon film by deuterium proceeds through two paths: first a chemical erosion with a cross-section of 4.7×10^{-17} cm^2 removes elementary carbon. At the same time, carbidic carbon is eroded with a linear yield of 0.003 within the fluence range between 8×10^{16} and 1.4×10^{17} cm^{-2}.

PACS: 68.35.Dv; 79.20.Rf; 82.20.Pm; 82.80.Pv
Keywords: Carbon; Titanium; Carbide; Erosion; Surface effects; XPS

1. Introduction

The application of different materials for use as plasma-facing components (PFCs) at the first wall of modern fusion experiments [1] and in the design of ITER [2,3] leads to the formation of multi-component materials due to erosion, material transport through the plasma and redeposition of materials at different locations [4,5]. Elevated wall temperatures and energetic particles allow compound formation at the surfaces as well as diffusion of surface species into the bulk material [6,7]. Compound surface layers influence the hydrogen inventory in the PFCs by modifying the hydrogen isotope diffusion through these layers, the chemical erosion behavior of the PFC surface towards hydrogen, and the hydrogen adsorption and desorption properties of the surfaces.

In order to understand and consequently predict hydrogen isotope interactions with multi-component PFC materials it is necessary to comprehend the principal interaction mechanisms of hydrogen with pure and mixed PFC materials. In previous work we studied the surface interaction of carbon with several materials, leading to carbide formation and carbon diffusion at elevated temperatures [6,8–10]. We also demonstrated that the bombardment of carbon layers on Ti and W with chemically inert noble gas ions leads both to sputtering and formation of a carbide phase at the surface [11]. In this work, the interaction of deuterium ions in the keV energy regime with pure carbon, as well as with carbon films on titanium is studied by X-ray photoelectron spectroscopy (XPS). The results of the XPS measurements are compared to kinematic simulations of the ion–solid interactions using the Monte Carlo code TRIDYN [12] which describes dynamic compositional changes due to ion bombardment.

2. Experimental

Samples for this investigation are highly oriented pyrolytic graphite (HOPG ZYA, Advanced Ceramics), and a polycrystalline titanium foil (Goodfellow). Sample areas are approx. 1 cm^2 and thicknesses 1 mm. The

* Corresponding author. Tel.: +49-89 3299 2285; fax: +49-89 3299 2279.
E-mail address: linsmeier@ipp.mpg.de (Ch. Linsmeier).

0022-3115/03/$ - see front matter
PII: S0022-3115(02)01332-6

HOPG surface is stripped by adhesive tape before insertion into the ultra-high vacuum system (UHV, base pressure in the low 10^{-8} Pa range). XPS measurements performed directly after sample insertion show only signals originating from carbon; no further cleaning of the HOPG surface in UHV is applied prior to ion bombardment.

Titanium is mechanically polished to mirror-like finish. Cleaning under vacuum involves heating/sputtering cycles (970 K, 5 keV Ar^+) until only metal signals are detected by XPS. Carbon films on Ti are deposited from an Omicron EFM3 source using high-purity carbon (99.999%, Goodfellow). The chemical state of the sample surfaces is characterized using XPS with monochromatic AlKα radiation (PHI ESCA 5600). This technique is very suitable to distinguish carbon in its graphitic and carbidic phases [9]. Additional details regarding the analysis and sample preparation system can be found elsewhere [13].

The binding energies in the XPS spectra are referenced to the graphitic C 1s signal at 284.2 eV from the respective spectra. The analyzer work function is referenced to the Au $4f_{7/2}$ signal at 84.0 eV. Spectra are accumulated with a pass energy of 2.95 eV at an electron exit angle of 22° with respect to the surface normal. Ion bombardment is carried out using a non-mass separated ion source (Specs IQ 12/38). Ion fluences are calculated with known implantation areas at the sample surface and sample current measurements. For deuterium bombardment, fluences are calculated assuming D^+ ions, although D_2^+ and D_3^+ may as well be present.

3. Results

3.1. Graphite

An HOPG sample is bombarded with 1 keV D^+ ions up to fluences of 2.3×10^{16} cm^{-2}. Between ion bombardment cycles, XPS spectra are taken in survey and high resolution modes. Survey spectra prove no contamination accumulation at the sample surface during all treatment steps, since only peaks attributable to carbon are observed. Already after a D^+ fluence of 1×10^{15} cm^{-2} the C 1s peak shows a shift in its overall maximum of 0.1 eV to lower binding energies (from 284.2 to 284.1 eV). After 2.3×10^{16} cm^2, the shift amounts to 0.15 eV and after annealing at 700 K the peak maximum is at 284.0 eV. In contrast to Ar^+ bombardment measurements of thin carbon layers on gold [9] where the disorder introduced by the ion beam and the remaining graphitic peak can be separated unambiguously by peak fitting, this procedure is not successful here. Nonetheless, to gain information on the additionally introduced binding states of carbon under D^+ irradiation, the C 1s spectrum from clean, unirradiated HOPG is subtracted from the respective spectra after ion impact after Shirley background removal. The difference spectra are plotted in Fig. 1 in two groups for better visibility. The upper group consists of the first six implantation steps between 1.0 and 4.7×10^{15} cm^{-2}. The lower group comprises the following five implantation steps from 6.6 to 23×10^{15} cm^{-2} together with the final annealing experiment at 700 K for 30 min. Solid and broken lines alternate with increasing fluences, the first and last curves in the groups are marked in the plot. Positive intensity differences (values above the 0 lines) in these spectra denote additional intensity compared to clean HOPG, whereas negative values show decreased intensity at the respective energy.

The difference spectra immediately indicate intensity variations during the treatment cycles at three distinct binding energies. The intensity changes (height at maximum/minimum in Fig. 1) of the three peaks in the difference spectra are plotted with increasing deuterium fluence in Fig. 2(a). The largest changes take place at a binding energy (BE) of 284.2 eV, which we attribute to graphitic carbon. The position of this peak does not change throughout the whole treatment series. However, intensity in this position continuously decreases compared to the clean HOPG. After the final 700 K heating, a slight increase in intensity at this position is again observed. The peak at the higher BE of 284.9 eV is very weak, but also stable in position. Intensity at this BE

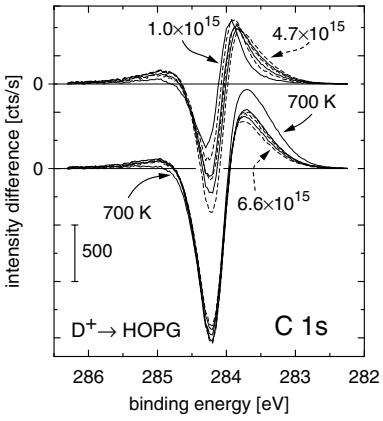

Fig. 1. XPS difference spectra in the C 1s region of HOPG bombarded with 1 keV D^+ ions. The consecutive fluence steps are separated into two groups. Successive spectra are marked with solid and broken lines, respectively. Some fluences are indicated, the intermediate fluences correspond to the values of the data points in Fig. 2. The final spectrum is measured after annealing at 700 K for 30 min.

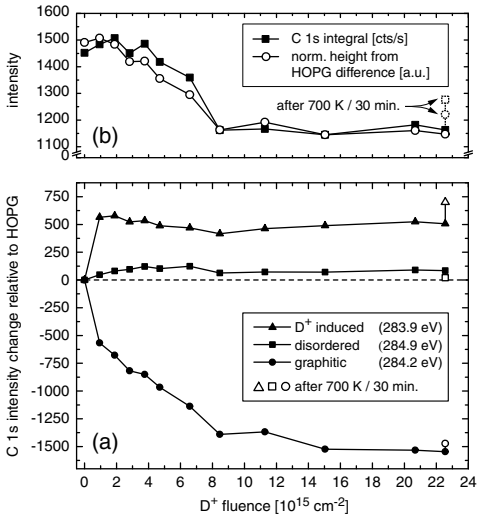

Fig. 2. Panel (a) shows the intensity changes of the three peaks identified in Fig. 1. Positive values indicate an increase in intensity compared to HOPG at the respective BE, negative values a decrease. Panel (b) compares the total C 1s intensity from the raw spectra (after subtraction of a Shirley background) with the sum of the heights from panel (a) at each fluence. The height curve is normalized to compare with the intensity curve. Values after 700 K heating are indicated in the plots.

increases during the first implantation steps up to approx. 7×10^{15} cm^{-2}. At higher fluences, first a small decrease is noticed and the intensity is then constant up to the final implantation step. After heating at 700 K, the intensity around 284.9 eV almost drops back to the level at the clean HOPG surface. The third peak component appears around 283.9 eV and shifts during the implantation to 283.7 eV. This component appears immediately after the first ion implantation step and maintains the initial maximum intensity throughout the subsequent ion treatments. It is only after the 700 K heating that the intensity of this component increases again and reaches a new maximum, while remaining constant at 283.7 eV BE.

A justification for this method of spectrum evaluation by differences is the overall development of the sum of the three difference peaks. In Fig. 2(b) the sum of the three peaks is plotted together with the total C 1s peak integral from the XPS spectra (after Shirley background subtraction). For comparison, the sum is normalized to the amplitude of the C 1s curve. Both lines show the same overall behavior: after a small initial intensity increase during the start of ion bombardment the curves decrease until a fluence of approx. 8×10^{15} cm^{-2} is

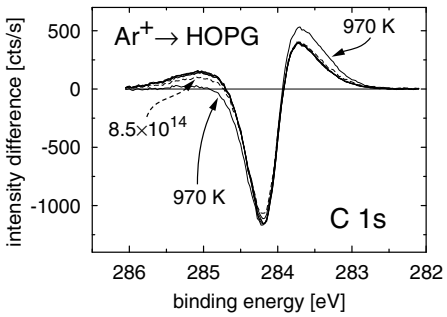

Fig. 3. XPS difference spectra in the C 1s region of HOPG bombarded with 1 keV Ar$^+$. Sample treatments are indicated. The overlapping spectra correspond to fluences from 2.1 to 8.5×10^{15} cm^{-2}, respectively.

reached. At higher fluences, no changes are observed. The intensity increase seen for the C 1s peak after sample heating to 700 K is also reproduced by the sum of the difference peaks.

The variations in the difference spectra of the HOPG bombarded with deuterium is compared to HOPG bombarded with argon. Fig. 3 shows an analogous experiment to Fig. 1 for 1 keV Ar$^+$ up to a fluence of 8.5×10^{15} cm^{-2} and final annealing to 970 K for 60 min. As in the difference spectra from the D$^+$ experiment, three peaks are observed. However, the peak positions after Ar$^+$ bombardment do not vary with fluence. The peak around 285 eV appears under Ar$^+$ bombardment and develops with fluence. The dashed line corresponds to 8.5×10^{14} cm^{-2}, the subsequent implantation steps (fluence of 2.1–8.5×10^{15} cm^{-2}) already show saturation at this BE. After annealing to 970 K this peak almost completely vanishes again, as in the deuterium case. The gradual changes with fluence are also visible in the intensity at 284.2 eV. At this position, however, no influence of the annealing step is recognized. The peak around 283.7 eV exhibits the most pronounced alteration after annealing. While Ar$^+$ bombardment creates this peak already after the first fluence step and subsequent implantation cycles do not modify it, annealing strongly increases the intensity at this BE. The peak position, however, remains unaffected.

3.2. Carbon films on titanium

A 2.9 nm carbon film on titanium is bombarded with 4 keV D$^+$ ions up to a fluence of 1.4×10^{17} cm^{-2}. Depending on the applied model for electron attenuation lengths is solids [14], it is several nm for our experimental parameters. The XPS information depth therefore is larger than the carbon layer thickness. Fig. 4 shows the C 1s range after the indicated fluences. The

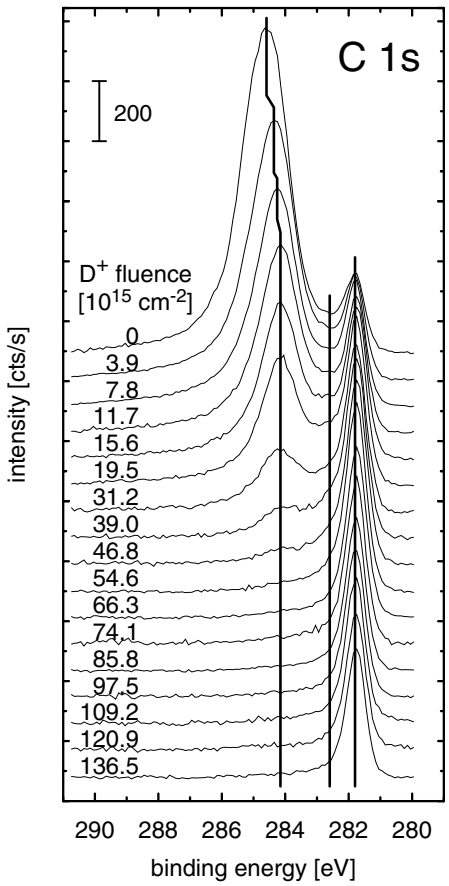

Fig. 4. XPS spectra in the C 1s region of a 2.9 nm carbon film on titanium before and after D^+ ion bombardment at 4 keV. The curves are labeled with the applied D^+ fluences. The vertical lines indicate binding energies of graphitic carbon (284.2 eV), titanium subcarbides (282.6 eV), and TiC (281.8 eV), respectively.

spectrum without ion bombardment shows a broad peak (compared to HOPG) located at 284.6 eV, originating from graphitic carbon. A second peak at 281.8 eV originates from TiC, formed at the interface between deposited carbon and titanium metal. Between these peaks, intensity is recorded around 282.6 eV, where titanium subcarbides are located. The graphitic peak shifts already after a fluence of 3.9×10^{15} cm^{-2} by 0.11 eV to lower binding energies and reaches a fixed position at 1.2×10^{16} cm^{-2} after a total shift of 0.22 eV. At the same time, no shift is observed in the position of the TiC signal. The total intensity of the C 1s signal decreases.

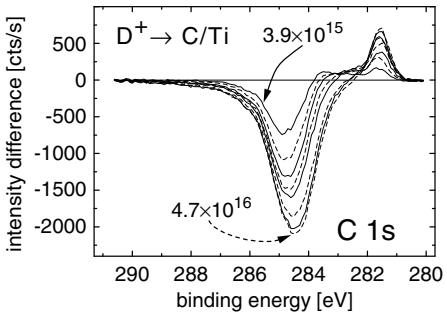

Fig. 5. XPS difference spectra after D^+ implantation in 2.9 nm carbon on Ti, in the fluence range between 3.9×10^{15} and 4.7×10^{16} cm^{-2} (difference spectra at higher fluences in Fig. 4 are omitted for clarity, since they exhibit only minor further changes). Consecutive spectra are marked with solid and broken lines, respectively. The intermediate fluence values can be taken from Fig. 4.

The graphitic peak vanishes after a D^+ fluence of 5.5×10^{16} cm^{-2}, up to where the TiC signal continually increases. Within the fluence range applied here, no complete erosion of formed TiC is observed. Compared to the spectra of the bombarded HOPG samples, no increased intensity around 285.2 eV due to ion-beam-induced effects is visible.

These observed changes in the C 1s signals are more clearly visible in the difference spectra (plotted in Fig. 5). Shown is the difference of the unirradiated spectrum from the spectra observed after fluences of 3.9×10^{15}–4.7×10^{16} cm^{-2}. Compared to HOPG in Figs. 1 and 3 where a peak in the differences around 285 eV is observed, here only an intensity decrease is visible. No additional intensity is produced by the D^+ ion beam. In contrast to Ar^+ bombardment experiments of carbon films on Ti (not shown here) where the disordered graphitic carbon (peak at 285.2 eV), produced during the carbon vapor deposition, is eroded during the first ion implantation steps, no peak is formed at this BE under D^+ bombardment.

The peak around 283.8 eV, well developed in the HOPG experiments, is also identified on the C film. However, the maximum is only distinct at the 3.9×10^{15} cm^{-2} fluence; at higher ion fluences it vanishes. The 281.8 eV peak originating from carbon in a TiC environment is clearly observed and remains fixed for all fluences. The carbide intensity continues to increase with fluence, while the total carbon intensity decreases. Intensity pointing to the existence of titanium subcarbides (around 282.6 eV) is visible at the initial stages of D^+ bombardment. After 1.6×10^{16} cm^{-2} the subcarbides are hardly discernible in the difference spectra. However, in the raw spectra (Fig. 4) there is still intensity around this

BE. The existence of subcarbides therefore cannot be excluded.

4. Discussion

During deuterium and argon ion bombardment of HOPG a shift in BE and a broadening of the C 1s peak are observed. The shift of the C 1s peak to lower BE for both ion species is caused by a decrease in intensity at the graphitic carbon position (284.2 eV) and an increase of intensity at lower BE. The difference spectra reveal a peak 0.35–0.53 eV below the graphitic signal. In contrast to the existing literature the difference spectra allow to distinguish components in the C 1s signal rather than to characterize spectral changes through mere peak shifts. Compared to results from earlier work we are able to attribute the main peak and the high-BE signal to graphitic carbon and carbon in a disordered graphitic environment [9]. The fact that the high-BE component (285.2 eV) also disappears in the HOPG experiments under annealing corroborates the assignment to a disordered graphite state. The new peak at lower BE is assigned to states induced by the ion beams. A shift to lower BE has previously been observed in the literature [15,16] without separating components in the C 1s signal. In our measurements we do not observe a shift towards higher BEs after extended ion implantation. On the contrary, after annealing of the implanted samples the C 1s signal shifts even further to lower BE.

The intensity decrease in the C 1s signal during ion implantation into HOPG is explained by the dilution of the carbon in the XPS information depth by hydrogen or argon. In contrast to what has been reported in the literature [15–17] we do not observe a peak shift to higher BEs at prolonged D^+ implantation; this shift has been attributed to the formation of C–H bonds [16,17]. BEs above 285.0 eV could also be attributed to sp^3-hybridized carbon [18] which, however, is unlikely to be produced within a collision cascade at low fluences. Not compatible with the argument of C–H bond formation for a signal at any new BE is the fact that all shifts/contributions observed here appear under both D^+ and inert Ar^+ bombardment. An interpretation of the shift to lower BEs by C–H bond formation of unsaturated hydrocarbons would be the BE values for sp and sp^2 carbon from [18]. HREELS measurements also indicate the formation of sp^2 and sp^3 carbon [19]. However, the identical observations for Ar^+ implantation rule out this interpretation at least as far as being the only explanation. Similar shifts were also observed under He^+ implantation [20]. We therefore attribute the C 1s intensity below 284.0 eV to defects in the graphite lattice, produced by the collision cascades, and therefore different from the disordered graphitic carbon with a BE of 285.2 eV. The reason for the smaller changes at below 284 eV in the case of the carbon film compared to the HOPG is the lower degree of structural order in the film. The film C 1s peak is initially already much wider than from HOPG and changes due to the ion-beam-induced effects are harder to detect.

The C 1s spectra and also the respective difference spectra of the carbon film on titanium do not allow a similar distinction between the elementary carbon binding states as in the case of HOPG. Initially, the disordered graphite phase has a high weight within the whole peak. The D^+ bombardment leads to an erosion, preferentially of the disordered graphite, and finally also of the graphitic carbon. The preferential erosion of the disordered phase is concluded from the decrease of the full-width-at half-maximum of the high-BE peak (1.63 eV initially and 1.04 eV after 3.9×10^{16} cm^{-2}), the total shift of the peak to lower BEs, as well as from the asymmetric development of the peak in the difference spectrum. As in the HOPG experiments, the D^+ bombardment leads to the formation of a small amount of radiation-induced defects, visible by the small peak around 283.6 eV in the difference spectra. In contrast to the HOPG samples, these defects in the film are only visible initially and are obscured by the decrease of the subcarbide phases during D^+ implantation. Carbon bound directly to titanium in TiC is initially present at the interface between the carbon layer and the substrate [6], and becomes more accessible to XPS with progressing layer erosion and even increases by ion-beam mixing. Ion-beam-induced carbide formation was already observed for noble gas ions [11]. After a maximum of the TiC signal (at 281.8 eV) at 5.5×10^{16} cm^{-2} this intensity decreases because of TiC erosion.

The total C 1s intensity decreases exponentially up to a fluence of 8×10^{16} cm^{-2}. Above, the intensity decrease follows a linear shape. The threshold between the two parts is characterized by the complete disappearance of carbon intensity other than from TiC (peak at 281.8 eV). The different slopes suggest different erosion mechanisms. Below the threshold, elementary carbon is eroded chemically by deuterium ions. The exponential shape is caused by an erosion mechanism which involves the entire carbon layer, similar to the ion-induced desorption of an adsorbed monolayer [21]. This is plausible since the implantation range of 4 keV D^+ in C on Ti extends to more than 100 nm, as calculated by TRIDYN. Therefore, the whole carbon layer of 2.9 nm is irradiated and chemical erosion takes place simultaneously throughout the entire layer. From the exponential curve, a reaction cross-section for carbon by D^+ of $\sigma_{chem} = 4.7 \times 10^{-17}$ cm^{-2} is calculated. Above the threshold fluence, an erosion yield of 0.003 results from a linear fit to the data. This number is in the range of the physical sputtering yield: TRIDYN calculations [22] for 4 keV D^+ on graphite give a yield of 0.0074. Taking into account that TiC has a 1:1

stoichiometry, the result of this work agrees well with this TRIDYN calculation.

5. Summary

In summary, different binding states of carbon on HOPG and carbon films on titanium during the interaction with deuterium ions are identified. The difference spectra enable one to identify contributions from disordered graphitic carbon as well as from radiation-induced defects besides the graphitic carbon state. The C 1s peak shift to lower binding energies due to ion implantation is caused by an increase of the radiation-induced defects on HOPG. In carbon films, the disordered graphitic fraction is eroded preferentially, before the remaining elementary carbon reacts. An erosion cross-section for thin carbon films is determined. Carbon bound in TiC at the interface erodes by a different mechanism with a linear rate within the applied fluences. No formation of hydrocarbons by D^+ bombardment, especially with sp^3-hybridized carbon, is observed.

References

[1] G. Federici, C.H. Skinner, J.N. Brooks, J.P. Coad, C. Grisolia, A.A. Haasz, A. Hassanein, V. Philipps, C.S. Pitcher, J. Roth, W.R. Wampler, D.C. Whyte, Nucl. Fusion 41 (2001) 1967.
[2] ITER Project, Detailed Design Document, IdoMS# G 16 DDD 2 96-11-27 W.
[3] R.A. Anderl, R.A. Causey, J.W. Davis, R.P. Doerner, G. Federici, A.A. Haasz, G.R. Longhurst, W.R. Wampler, K.L. Wilson, J. Nucl. Mater. 273 (1999) 1.
[4] H. Maier, K. Krieger, M. Balden, J. Roth, ASDEX Upgrade-Team, J. Nucl. Mater. 266–269 (1999) 1003.
[5] V. Rohde, R. Neu, R. Dux, T. Härtl, H. Maier, J. Luthin, H.G. Esser, V. Philipps, ASDEX Upgrade-Team, ECA 23J (1999) 1513.
[6] Ch. Linsmeier, J. Luthin, P. Goldstraß, J. Nucl. Mater. 290–293 (2001) 25.
[7] Ch. Linsmeier, J. Roth, K. Schmid, IAEA APID Series vol. 10, in press.
[8] P. Goldstraß, K.U. Klages, Ch. Linsmeier, J. Nucl. Mater. 290–293 (2001) 76.
[9] J. Luthin, Ch. Linsmeier, Surf. Sci. 454–456 (2000) 78.
[10] J. Luthin, Ch. Linsmeier, Physica Scripta T 91 (2001) 134.
[11] J. Luthin, H. Plank, J. Roth, Ch. Linsmeier, Nucl. Instrum. and Meth. B 182 (2001) 218.
[12] W. Eckstein, Computer Simulation of Ion–Solid Interactions, Springer Series in Materials Science, vol. 10, Springer, Berlin, 1991.
[13] S. Miller, G. Berning, H. Plank, J. Roth, J. Vac. Sci. Technol. A 15 (1997) 2029.
[14] A. Jablonski, C.J. Powell, Surf. Sci. Rep. 47 (2002) 33.
[15] H. Gotoh, Fusion Technol. 6 (1984) 424.
[16] K. Ashida, K. Kanamori, K. Ichimura, M. Matsuyama, K. Watanabe, J. Nucl. Mater. 137 (1986) 288.
[17] D. Ugolini, J. Eitle, P. Oelhafen, Appl. Phys. A 54 (1992) 57.
[18] A. Fink, W. Widdra, W. Wurth, C. Keller, M. Stichler, A. Achleitner, G. Comelli, S. Lizzit, A. Baraldi, D. Menzel, Phys. Rev. B 64 (2001) 045308.
[19] M. Portail, I. Forbeaux, N. Papapeorgiou, M. Carrère, D. Roy, J.-M. Layet, Surf. Sci. 454–456 (2000) 384.
[20] K. Ashida, K. Ichimura, M. Matsuyama, K. Watanabe, J. Nucl. Mater. 128&129 (1984) 792.
[21] E. Taglauer, W. Heiland, J. Onsgaard, Nucl. Instrum. and Meth. 168 (1980) 571.
[22] W. Eckstein, C. García-Rosales, J. Roth, W. Ottenberger, Max-Planck-Institut für Plasmaphysik, Garching, IPP-Report 9/82, 1993.

ELSEVIER Nuclear Instruments and Methods in Physics Research B 182 (2001) 218–226

NIM B Beam Interactions with Materials & Atoms

www.elsevier.com/locate/nimb

Ion beam-induced carbide formation at the titanium–carbon interface

J. Luthin, H. Plank, J. Roth, Ch. Linsmeier *

Max-Planck-Institut für Plasmaphysik, EURATOM Association, Boltzmannstr. 2, D-85748 Garching, Germany

Abstract

In this paper we report on the carbidization of thin Ti films on graphite (Ti/C) and carbon films on Ti substrates (C/Ti) due to bombardment with noble gas ions (Ar^+ and He^+) at room temperature. The chemical state of the films is investigated by X-ray photoelectron spectroscopy (XPS). Directly after evaporation of the Ti (and C films, respectively) on the substrates about one monolayer of TiC is detected. Subsequent ion bombardment can lead to a complete conversion of elementary carbon into carbide. Spectra recorded during Ar^+ and He^+ depth profiling of Ti/C films with ion energies in the range between 0.5 and 4 keV clearly show the existence of TiC at the interface. The total amount of TiC formed increases with ion energy indicating a more effective ion beam mixing at higher energies. At 4 keV Ar^+ ion energy all Ti at the interface is detected as carbide resulting in a composition of stoichiometric TiC. The C/Ti samples show in addition to TiC a distribution of titanium subcarbides.

1. Introduction

Transition metal carbides, commonly referred to as refractory carbides, possess an unusual combination of physical and chemical properties [1] which make them attractive both from a fundamental and technological point of view [2]. Titanium carbide as a model substance of the d-metal carbides has received great attention in the literature to study the peculiarities of the electronic structure and interatomic interactions due to the simplicity of the crystal structure (NaCl type) [3]. Especially titanium carbide coatings are widely used in a variety of applications owing to their excellent qualities, such as high thermal stability, high hardness and good corrosion resistance [4]. Therefore TiC coatings have also been considered as protective layers in plasma-facing parts of nuclear fusion devices [5] and were already used as limiter material [6,7] and wall coating [8,9]. Although the first results were not too convincing [10] the usefulness of TiC as a first wall material in fusion plasma experiments is still an open question. To predict the processes that can occur applying carbides and carbide-forming materials in nuclear fusion research we are performing systematic investigations of the fundamental interactions between carbon and various elements [11–17]. Apart from the understanding of the basic

* Corresponding author. Tel.: +49-89-3299-2285; fax: +49-89-3299-2279.

E-mail address: linsmeier@ipp.mpg.de (Ch. Linsmeier).

0168-583X/01/$ - see front matter
PII: S0168-583X(01)00679-6

compound formation mechanisms in metallic carbides and the insight into the atomic arrangement of titanium and carbon after ion bombardment, these investigations show the consequences of the observed reactions for the utilization of TiC coatings at the inner wall of fusion experiments. The thermally induced carbide formation of titanium and carbon has already been reported [18,19]. The work presented here focus on the irradiation-induced carbide formation at the titanium/carbon interface due to He^+ and Ar^+ noble gas bombardment. Furthermore the obtained results are of special interest for XPS sputter depth profiling which is a powerful method to follow the depth-resolved composition of unknown samples [20,21].

2. Experimental

Ti films are evaporated from a Ti rod (Goodfellow, 99.99%) and carbon films are evaporated from a graphite rod (Goodfellow, 99.999%) at room temperature (RT, ~300 K) under ultra-high vacuum (UHV) conditions ($<1.5 \times 10^{-7}$ Pa). The substrates were polycrystalline pyrolytic graphite cut parallel to the basal planes and polycrystalline titanium. The chemical state of the films is characterized using X-ray photoelectron spectroscopy (XPS) with monochromatic Al K_α radiation (PHI ESCA 5600) which is a very suitable technique for distinction between carbon in its graphitic and carbidic phases [14]. The evaporation chamber is connected to the XPS system. Thus, samples can be transferred for XPS analysis without leaving UHV. All spectra are shown after Shirley background subtraction [22] and all peaks are normalized to the same height for comparison. The composition of the investigated surfaces are calculated from the photoelectron spectra using curve fitting procedures and sensitivity factors provided by the manufacturer [23]. The XPS system is equipped with a differentially pumped ion gun allowing sample bombardment with inert gases in the energy range between 0.5 and 5 keV. Additional details regarding the analysis system can be found elsewhere [18].

3. Results and discussion

3.1. Titanium on graphite

Titanium layers on graphite were produced by depositing Ti, evaporated from a metal wire. The initial carbon surface was free of any contamination, as measured by XPS. Ti deposition was interrupted and the surface was analyzed by XPS to investigate the properties of the Ti–C interface. The intensities of the Ti and C photoelectron signals provide information about the Ti layer thickness. The peak position of the C 1s signal indicates the chemical state of the carbon at the surface. Carbon in its graphitic modification is characterized by a C 1s binding energy of 284.4 eV. Carbon in a carbidic chemical state is shifted by 2.7 eV towards lower binding energies [18,24]. By applying curve fitting techniques [23] the carbon signal can be separated into elementary (graphitic) and carbidic contributions [15]. Fig. 1 shows the composition of the surface during the Ti deposition. The Ti layer thickness is calculated from the initial Ti signal increase and assuming a constant deposition rate for Ti. The latter is justified by a constant flux from the evaporator,

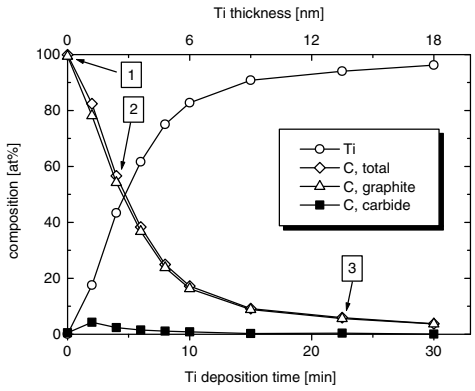

Fig. 1. Surface composition, measured by XPS, of a titanium film on graphite. The Ti deposition was interrupted periodically for XPS analysis. Carbide is formed only initially at the Ti–C interface. XPS spectra at points indicated by labels are plotted in Fig. 2(a).

measured by a flux monitor. The indicated composition is an average over the XPS information depth, calculated from the peak intensities (C 1s and Ti 2p) and the tabulated sensitivity factors [25].

During the deposition of Ti on the graphite substrate the C 1s intensity decreases due to the attenuation of the photoelectrons by the Ti overlayer. Simultaneously, the Ti 2p intensity increases. Until a layer thickness of approx. 5 nm the intensities change almost linearly, as depicted in Fig. 1. After evaporation times of 2 and 4 min, respectively, the carbon signal consists of two peaks at binding energies of 284.2 and 281.7 eV. The peak at higher binding energy is assigned to graphite, the small contribution at 281.7 eV originates from a small carbide layer. After 4 min Ti deposition, the total carbon signal amounts to a 57 at.% carbon composition. The graphite fraction is 55 at.% and the remaining 2 at.% stem from TiC. The corresponding spectrum to the labeled data points in Fig. 1 are plotted in Fig. 2 at data point (2). Clearly a small TiC peak is visible, which is not present at the virgin graphite surface (spectrum (1)). This peak shows that at RT TiC is formed at the interface between the carbon substrate and the deposited Ti layer. This reaction only takes place for small Ti coverages, since the carbide signal disappears upon further Ti deposition. This interface reaction was also observed for Ti layers on a diamond substrate [26] and for thin carbon films on a titanium substrate [15]. Moreover, other materials show a similar behavior of RT reactivity, limited to the interface between substrate and carbon adlayer [11]. During the preceding Ti deposition the carbon signal decreases continuously. However, even at the final layer thickness of 18 nm a small carbon signal is measured, as plotted in Fig. 1. The C 1s spectrum corresponding to a layer thickness of approx. 13.5 nm is plotted in Fig. 2(a), labeled (3). This peak clearly shows only a contribution of graphitic carbon, no carbide signal is measured. Since the layer thickness is about 7 times larger that the attenuation length of C 1s photoelectrons in titanium (calculated to 2.7 nm for 1200 eV kinetic energy of the electrons, according to [27]), a signal from the carbon substrate can be excluded. Experimental evidence for C at the surface is obtained by XPS measurements under different exit angles with respect to the sample surface. Low exit angles lead to an increased C 1s intensity due to the higher surface sensitivity. Therefore, the carbon peak is assigned to carbon on top of the deposited titanium layer. Two possible reasons for this carbon adlayer can be discussed. First, titanium deposited from the vapor phase on a substrate exhibits grain growth [28]. Along the grain boundaries carbon segregation to the surface would be possible. An indirect confirmation for this process is the absence of a surface carbon signal in experiments with silicon as a substrate material instead of graphite [29]. However, since the carbon detected at the sample surface is in direct contact with metallic titanium, the formation of TiC is expected. Since the C 1s signal only has a peak at 284.2 eV characteristic for graphite or adsorbed CO species, TiC formation can be excluded. Therefore, the second reason, namely CO adsorption from the residual gas, is more likely to cause this carbon intensity. This is also supported by the observation of a constant carbon fraction throughout the whole titanium film, as will be shown by depth profiling the sample by 1 keV Ar^+ ions (Fig. 3(a)).

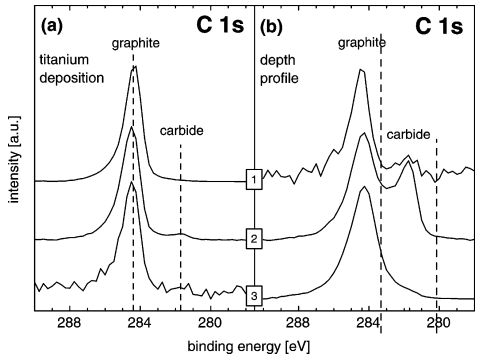

Fig. 2. XPS spectra in the C 1s energy regime during (a) Ti deposition on graphite and (b) during depth profiling with 1 keV Ar^+. The spectrum labels correspond to the, respectively, tagged points during deposition (see Fig. 1) and depth profiling (see Fig. 3(a)).

From the sequential deposition of Ti on graphite and the XPS analysis described above, a

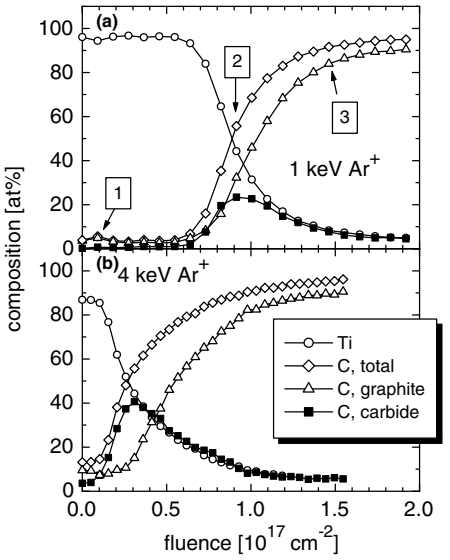

Fig. 3. Depth profiles of (a) an 18 nm Ti film on graphite by 1 keV Ar^+ and (b) a 5 nm Ti film on graphite by 4 keV Ar^+. The marked points in (a) correspond to the respective XPS spectra in Fig. 2(b).

conclusive picture of the layer growth and chemical interaction of titanium on graphite can be drawn. At initial stages of metal deposition with nominal Ti layer thicknesses up to 5 nm the metal partially reacts with the substrate under TiC formation at RT. The C 1s signal is dominated by the graphite substrate signal, but an additional carbide peak is measured. Due to the asymmetric shape of the Ti 2p signals and the small shift during the carbidization it is impossible to discern a small fraction of TiC from a predominantly metallic Ti signal. Upon further Ti deposition, the carbide signal vanishes and the C 1s peak only consists of a graphite peak. This supports the interpretation that carbide formation is limited to the very interface (direct contact between titanium and carbon) and further titanium is deposited metallic. Even for titanium layers thick enough to attenuate the carbon substrate signal completely, a C 1s peak remains detectable. This is due to a thin carbon layer at the sample surface. The final layer morphology is therefore a thin adsorbed carbon-containing layer at the surface, a metallic titanium layer below with a thickness determined by the evaporated amount of Ti, a shallow TiC layer at the Ti–C interface, and all supported by the graphite substrate.

Subsequent to the Ti deposition the 18 nm Ti film on graphite was bombarded by 1 keV Ar^+ ions at an incident angle of 45°. By repeatedly measuring XPS spectra a depth profile of the layer composition is recorded. This depth profile is shown in Fig. 3(a). Up to an Ar^+ fluence of 0.6×10^{17} cm^{-2} the composition is almost constant. A carbon concentration of 3 at.% is determined in the Ti film. The XPS spectrum after an Ar^+ fluence of 0.1×10^{17} cm^{-2} corresponding to the composition labeled (1) is shown in Fig. 2(b). In contrast to the C 1s signal observed before ion bombardment (spectrum (3) in Fig. 2(a)), now a small carbide peak is detected. This small amount of carbide is formed by the ion beam. The increasing fluence leads to a continuous erosion of the Ti film and to an increase of the carbon intensity measured by XPS. A C 1s spectrum taken at the interface between the Ti film and the graphite substrate is shown in Fig. 2(b), labeled (2). The two peaks at 284.4 and 281.7 eV correspond to graphite and carbidic C, respectively. The total carbon concentration at this fluence is 55 at.% and is composed of 32 at.% of graphite and 23 at.% of TiC. This fraction represents the maximum carbide fraction throughout the depth profile (Fig. 3(a)). Further Ar^+ bombardment results in broadening of the interface due to ion beam mixing. The concentration of graphite increases while Ti and carbidic C decreases. A C 1s spectrum taken at an Ar^+ fluence of 1.5×10^{17} cm^{-2} (see Fig. 2(b), spectrum 3) shows a strong graphite signal. With respect to a spectrum taken from clean unbombarded graphite (see Fig. 2(a), spectrum 1), the C 1s peak is broadened due to ion-induced radiation damage as reported in the literature [17,30] and confirmed at a highly oriented pyrolytic graphite (HOPG) surface [15]. Additionally, a small shoulder at the binding energy of carbidic C is seen. The concentrations of Ti and carbidic C are very similar indicating the existence of stoichiometric TiC. This is confirmed

by a binding energy shift of Ti 2p electrons from 453.6 eV for metallic Ti to 454.9 eV for Ti in TiC [18,31]. Clearly, the film which did not contain any detectable carbidic carbon concentration after deposition has developed a carbidic interface during subsequent sputter depth profiling. Both the surface carbon overlayer and carbon at the interface were reacted to carbide during ion bombardment.

In order to investigate the influence of ion energy on irradiation-induced carbidization, in Fig. 3(b) a depth profile of a 5 nm Ti film on graphite is shown using 4 keV Ar^+ ions at an incident angle of 45°. About 10 at.% C are measured at the surface (fluence 0). Besides CO adsorbed at the surface during Ti evaporation also a signal from the substrate contributes to the intensity, since this Ti film is much thinner than the one discussed before. Again, very small carbide concentrations are measured up to an Ar^+ fluence of 0.1×10^{17} cm^{-2}. The film thickness of about 5 nm is of the same order as the penetration depth of 4.5 nm for 4 keV Ar^+ in Ti, as calculated by the Monte-Carlo code TRIM.SP [32]. Although ions penetrate the interface, no ion beam mixing and no carbidization is seen at the surface. An explanation for this observation is the small diffusivity of Ti and C in TiC [33,34]. TiC formed at the interface in the mean projected range of the ions acts as a barrier preventing further carbon to reach Ti metal [35]. Increasing the fluence, the Ti film is eroded and the interface is reached. In contrast to the depth profile using 1 keV Ar^+ (Fig. 3(a)), in the interface region carbon is found here mainly as carbide with a maximum concentration of about 40 at.% at an Ar^+ fluence of 0.3×10^{17} cm^{-2}. Thus, ion beam mixing and carbidization is more effective at 4 keV Ar^+ ion energy yielding also a stronger interface broadening (Ar^+ fluence region up to 1×10^{17} cm^{-2}). The interface is defined as the region between a Ti (resp. C) concentration of 16 and 84 at.% (corresponding to 2σ width of an error function) [36]. As observed for 1 keV Ar^+ depth profiling, concentrations of Ti and carbidic C indicate the existence of stoichiometric TiC formed due to irradiation.

The influence of the ion species on the carbide formation at the interface is studied by profiling Ti layers on graphite by He^+ and Ar^+ ions. In Fig. 4, the ratio of carbidic to total carbon at the interface is plotted against ion energy of bombarding species, i.e. He^+ and Ar^+, in the energy range between 0.5 and 4 keV. This ratio is calculated from areas under the respective curves in a depth profile (see e.g. Fig. 3). The interface width is approximated from the composition profile as defined above (2σ width) and represents the depth interval in which the primary ions can influence the interaction between the deposited film and the substrate material. At 0.5 keV ion energy, about one third of total C is found in a carbidic phase, both for bombardment with He^+ and Ar^+. The amount of reacted carbon increases with ion energy. At 4 keV about half of the carbon present in the interaction zone has reacted to TiC, regardless of the ion species. With respect to carbidization, no significant difference is observed between He^+ and Ar^+ irradiation. The carbide amount is determined by the nuclear energy deposited within the interface region during the depth profile. The number of ions necessary for sputtering through the interfacial layer is inversely proportional to the sputtering yield of the ions, which is proportional to the nuclear energy loss. Comparing He^+ and Ar^+ irradiation, mean penetration depths are larger for He^+ and, therefore, the energy deposited in the interface per incoming ion is lower [32]. On the

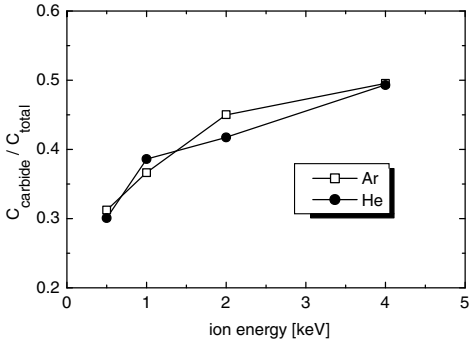

Fig. 4. Comparison of the carbide fraction in the total C 1s signal during depth profiling by He^+ and Ar^+ of Ti films on graphite, as a function of ion energy. The carbon intensities are integrated over a fluence regime in the depth profiles where the Ti signal reaches from 16% to 84%, respectively.

other hand, sputtering yields are lower for He^+ bombardment [37,38] and for eroding the Ti film and reaching the interface more He^+ ions are needed, i.e. higher fluences. Therefore, both ion species deposit an equal amount of nuclear energy into the layer while sputtering through it. This demonstrates that for the effects observed here (carbide formation due to ion beam mixing at the interface) electronic energy loss mechanisms of the projectile during its path through the solid do not play a significant role. Ion beam mixing is a consequence of the nuclear energy loss and therefore takes place at the end of the collision cascade.

3.2. Carbon on titanium

To understand the carbidization process in detail and to avoid the influence of the carbon-containing overlayer found for the Ti/C samples, measurements of the system C/Ti are performed. For the investigation of the deposition profile of carbon on titanium, carbon films with different thicknesses are prepared after sputter/annealing cycles (5.0 keV Ar^+, 970 K) of the Ti substrate (Fig. 5). Before evaporation the XPS analysis reveals clean Ti. Because of the difficulties of carbon electron beam evaporation the maximum film thickness is about 5 nm [14,39]. In this work the thickness of the films is estimated using the attenuation of the Ti $2p_{3/2}$ signal as described in [40,41]. As a consequence of the relatively low carbon coverage the XPS analysis of the Ti 2p photoelectrons shows substrate photoelectrons passing through the carbon films even after deposition. Because of the relatively low shifts in Ti 2p binding energy it is difficult to separate the elementary from the carbidic Ti signal. Therefore most of the interpretation is based on the C 1s spectra. In Fig. 6(a) C 1s spectra are shown after 5, 20 and 50 min of evaporation (spectra labeled 1–3). It has to be noticed that the investigation of C/Ti could be performed with improved XPS energy resolution [14] compared to the Ti/C measurements. The C 1s spectrum 1 shows about 2 nm carbon. Beside the peak of elementary carbon at 284.2 eV we find a second peak at 281.7 eV which indicates the formation of titanium carbide (TiC) in the interfacial region during the preparation process. Furthermore, the signal intensity between the two peaks shows clearly the existence of non-stoichiometric carbide which can be expected from the Ti–C phase diagram [42]. Carbide formation in early stages of carbon film growth has been found also for other systems like C/Be or C/Mo [12,43].

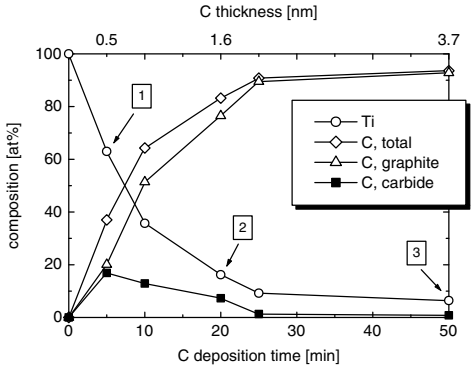

Fig. 5. Surface composition of a carbon film on titanium during film deposition, measured by XPS. The composition is averaged over the XPS information depth. The carbon layer thickness is calculated from the attenuation of the Ti 2p signal by the carbon adlayer for the three indicated measurements. The corresponding XPS spectra are shown in Fig. 6(a).

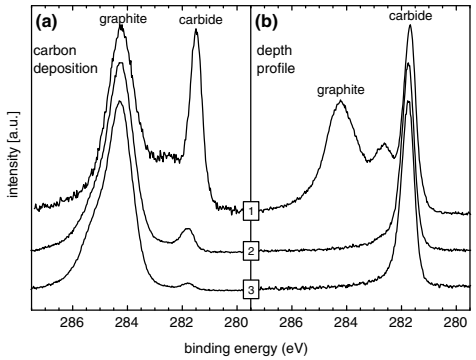

Fig. 6. XPS spectra in the C 1s regime during (a) carbon deposition on Ti and (b) during depth profiling with 4 keV Ar^+. The spectra correspond to the tagged data points in Fig. 5 for C deposition (panel a) and Fig. 7(b) for depth profiling (panel b).

Titanium belongs to the group of metallic carbides where the C atoms occupy the octahedral sites of the close packing in the Ti hcp lattice. The monocarbide TiC is formed when all octahedral sites are occupied by C atoms. It has to be noted, however, that stoichiometric "TiC" always includes a small fraction of vacancies in the lattice. Therefore, the true stoichiometry of titanium carbide is $TiC_{0.95}$ [44]. Higher concentrations of vacancies in the carbon sublattice identify non-stoichiometric titanium carbides and subcarbides. It seems to be sure that a complete TiC layer is formed directly at the interface. Spectra 2 and 3 of Fig. 6(a) show the increasing C 1s signal of elementary carbon with increasing evaporation time where the carbidic signal is attenuated by the covering layers. Continued carbon evaporation leads to a coverage of the carbide layer with elementary carbon, as shown in Fig. 5. From the spectra (2) and (3) in Fig. 6(a) the carbide layer thickness is calculated. It is assumed that the carbide is located at the interface between Ti substrate and the carbon layer of graphitic structure. For the graphite overlayer, a density of 1.8 g/cm^3 [45] is used to calculate the electron inelastic mean free path (2.2 nm for Ti 2p photoelectrons). The calculations result in a TiC layer thickness of 0.2–0.3 nm in both spectra, which corresponds to approx. one monolayer of TiC. This confirms that the TiC formation is limited to the interface between carbon and titanium at RT.

The asymmetric C 1s peak shape of the elementary carbon shows the formation of disordered and graphite-like carbon [14]. In Fig. 6(b) XPS spectra after different fluences of 4.0 keV Ar^+ ion bombardment (incident angle 45°) are shown. The spectrum labeled 1 reveals the drastic changes that occur after a fluence of $\sim 0.6 \times 10^{15} Ar^+/cm^2$. The Ti signal increases to 7 at.% and a second peak at 282.4 eV binding energy is detected which might originate from Ti_8C_5 or Ti_6C_5 [46,47]. In addition to this a broad distribution of non-stoichiometric carbide can be seen in the spectrum. The spectra labeled 2 and 3 reveal that with increasing Ar^+ fluence all carbon is converted into TiC. Following the atomic interpretation the carbidization occurs by ion beam mixing of the C atoms into the titanium lattice and radiation damage of the Ti lattice have to be taken into account. As long as unreacted carbon is present a stepwise filling of the octahedral Ti lattice sites leads to the formation of non-stoichiometric titanium carbide in addition to TiC. After occupation of all possible lattice sites the TiC formation is complete. From this state on only the erosion of the carbide film is visible. Depth profiles for 1.0 and 4.0 keV Ar^+ are presented in Fig. 7. Again one observes the energy-dependent behavior already discussed for Ti/C. With 4.0 keV Ar^+ ions a lower fluence is necessary to achieve complete carbidization of the evaporated film.

The line width of the C 1s peak for carbide formed during Ar^+ bombardment is unusually small for an ion-bombarded surface. Fig. 6(b) shows the spectra during the ion bombardment. Spectra (2) and (3) exhibit a FWHM of 0.6 eV and determined mostly by the experimental resolution. This line width is also measured at TiC films

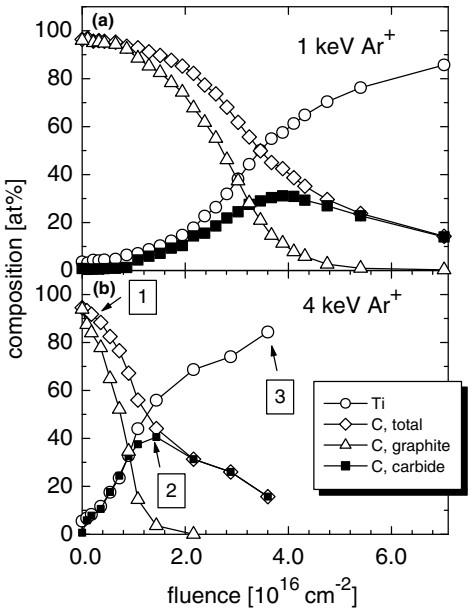

Fig. 7. Depth profiles for (a) 4.1 nm C on Ti by 1 keV Ar^+ and (b) 3.7 nm C on Ti by 4 keV Ar^+. The marks in panel b correspond to the respective spectra in Fig. 6(b).

produced thermally. A typical line width for an ion-bombarded surface is shown in Fig. 2(b), spectrum (3), for graphite, clearly being wider. The line widths observed in the Ti–C system are also narrower than in a similar experiment carried out with carbon layers on tungsten [48]. Ion bombardment in the C/W system also leads to carbide formation [49] . However, in this case the carbide C 1s line widths are broader and the transition from elementary C to carbide is blurred. In the C/Ti system under study here this transition is well-defined, showing two well-separated peaks in the C 1s region (see Fig. 6(a)). We interpret this behavior by a driving force leading to local ordering in the C/Ti system, but not in the case of C/W. The driving force for this process is the free enthalpy of formation (ΔG_f) for the carbide formation from the elements. For the $C + Ti \rightarrow TiC$ reaction an enthalpy of −1.87 eV is released per molecule. For the corresponding reaction $C + W \rightarrow WC$, however, only −0.40 eV are released [50]. This energy is dissipated at the location of carbide formation and can lead to an increased order in the solid, counterbalancing the disorder introduced by the ion beam bombardment.

4. Summary

Titanium carbide formation at the solid interface between these two elements is already observed at room temperature after vapor deposition of one species on a substrate comprising of the second. This compound layer is restricted, however, to the direct interface and leads to approximately one monolayer of titanium carbide. It is observed both for carbon layers on titanium and vice versa. This was demonstrated in experiments where consecutive deposition steps were interrupted by XPS measurements. Noble gas ion bombardment (using He^+ and Ar^+) at ion energies between 0.5 and 4 keV strongly increases the amount of formed carbide. Depth profiles measured by ion bombardment and intermediate XPS analysis reveal that carbidization is a consequence of ion beam mixing. The maximum carbide concentration depends on the primary ion energy, since ion beam mixing is more effective at higher ion energies. During erosion of the surface layer the portion of carbidic carbon increases until all carbon is found as carbide at the surface layer/substrate interface. At this stage stoichiometric TiC is formed. This is different at the beginning of the carbidization process: subcarbides are detected at the initial stage of carbon deposition on clean titanium and also at incipient ion bombardment of carbon films on Ti.

In consequence, for depth profiles, often showing an interfacial reaction between film and substrate, the interpretation has to consider that compounds detected at the interface may be the result of ion irradiation as shown for the system titanium and carbon at room temperature. The carbidization process in a solid can be understood by mere mixing of the compound constituents. As soon as the elements Ti and C are in direct contact with each other, a reaction to carbide takes place. This is the case at the interface between an evaporated layer on a substrate, leading to carbide formation in the order of one monolayer. During ion beam bombardment, the collision cascades lead to intermixing of the materials at the interface. The carbidization reaction then releases the enthalpy of formation which can lead to a local ordering, determined by the narrow C 1s peaks in the XPS spectra.

References

[1] L.E. Toth, Transitition Metal Carbides and Nitrides, Academic Press, New York, 1971.
[2] L.I. Johansson, Surf. Sci. Rep. 21 (1995) 177.
[3] V.A. Gubanov, A.L. Ivanovsky, V.P. Zhukov, Electronic Structure of Refractory Carbides and Nitrides, Cambridge University Press, Cambridge, 1994.
[4] R. Bertoncello, A. Casagrande, M. Casarin, A. Gilesenti, E. Lanzoni, L. Mirenghi, E. Tondello, Surf. Interface Anal. 18 (1992) 525.
[5] H. Bolt, Fusion Eng. Des. 22 (1985) 85.
[6] Y. Hirohata, S. Adachi, S. Fukuola, M. Mohri, T. Yamashina, N. Noda, S. Tanahashi, J. Fujita, J. Nucl. Mater. 122/123 (1984) 1160.
[7] J.L. Cecchi, TFTR Group, J. Nucl. Mater. 128/129 (1984) 1.
[8] Y. Shimomura, K. Shimizu, T. Hirayama, M. Azumi, H. Ninomiya, J. Nucl. Mater. 128/129 (1984) 19.
[9] E. Taglauer, P. Varga, K. Ertl, Vacuum 36 (1986) 23.
[10] P. Grigul, et al., J. Nucl. Mater. 196–198 (1992) 101.

[11] Ch. Linsmeier, J. Luthin, P. Goldstraß, J. Nucl. Mater. 290–293 (2001) 25.
[12] P. Goldstraß, Ch. Linsmeier, Nucl. Instr. and Meth. B 161–163 (2000) 411.
[13] P. Goldstraß, Ch. Linsmeier, J. Nucl. Mater. 290–293 (2001) 71.
[14] J. Luthin, Ch. Linsmeier, Surf. Sci. 454–456 (2000) 78.
[15] J. Luthin, Ch. Linsmeier, J. Nucl. Mater. 290–293 (2001) 121.
[16] S. Miller, R. Fischer, H. Plank, J. Roth, V. Dose, J. Appl. Phys. 82 (1997) 3314.
[17] J. Roth, H. Graupner, S.P. Withrow, D. Zehner, R.A. Zuhr, J. Appl. Phys. 79 (1996) 7695.
[18] S. Miller, G. Berning, H. Plank, J. Roth, J. Vac. Sci. Technol. A 15 (1997) 2029.
[19] J. Luthin, C. Linsmeier, Phys. Scr. T91 (2001) 134.
[20] V. Rohde, R. Neu, R. Dux, T. Härtel, H. Maier, J. Luthin, H.G. Eser, V. Philipps and ASDEX Upgrade Team, in: B. Schweer (Ed.), Proceedings of the International Congress Plasma Physics and 26th EPS Conference Control Fusion and Plasma Physics, Maastricht 1999, ECA 23, J. Europ. Phys. Soc., Mulhouse, 1999, p. 1513.
[21] H. Maier, J. Luthin, M. Balden, M. Rehm, F. Koch, H. Bolt, Surf. Coat. Technol. (2001), in print.
[22] D. Shirley, Phys. Rev. B 5 (1972) 4709.
[23] MultiPak Ver. 2.2, Phys. Electron., 1996.
[24] J.I. Johansson, A.L. Hagström, B.E. Jacobson, S.B.M. Hagström, J. Electron Spectrosc. 10 (1977) 259.
[25] J.F. Moulder, W.F. Stickle, P.E. Sobol, K.E. Bomben, in: J. Chastain (Ed.), Handbook of X-Ray Photoelectron Spectroscopy, Perkin Elmer, Eden Prairie, 1992.
[26] T. Tachibana, B.E. Williams, J.T. Glass, Phys. Rev. B 45 (1992) 11,975.
[27] S. Tanuma, C.J. Powell, D.R. Penn, Surf. Interface Anal. 17 (1991) 911.
[28] I.J.M.M. Raajimakers, Thesis, Eindhoven, 1988.
[29] S. Miller, Thesis, Bayreuth, 1997.
[30] W.M. Lau, L.J. Huang, I. Belloand, Y.M. Yiu, S.T. Lee, J. Appl. Phys. 75 (1994) 3385.
[31] L. Ramquist, K. Hamrin, G. Johansson, A. Fahlmann, C. Nordling, J. Phys. Chem. Solids 30 (1969) 1835.
[32] W. Eckstein, Computer Simulation of Ion–Solid Interactions, Springer Series in Materials Science, Vol. 10, Springer, Berlin, 1991.
[33] S. Sarian, J. Appl. Phys. 40 (1969) 3515.
[34] S. Sarian, J. Appl. Phys. 39 (1968) 5036.
[35] J.P. Hirvonen, M. Nastasi, J.W. Mayer, Nucl. Instr. and Meth. B 13 (1986) 479.
[36] M. Neubauer, Hyperfein-Untersuchungen an ionenbestrahlten Ag/Fe und In/Fe-Schichten, Cuvillier Verlag, Göttingen, 1997.
[37] W. Eckstein, C. García-Rosales, J. Roth, W. Ottenberger, Max-Planck-Institut für Plasmaphysik, Garching, IPP-Report 9/82, 1993.
[38] H.H. Andersen, H.L. Bay, in: R. Behrisch (Ed.), Sputtering by Particle Bombardement, Vol. 1, Springer, Berlin, 1981.
[39] S. Schelz, T. Richmond, P. Kania, P. Oelhafen, H.-J. Güntherrodt, Surf. Sci. 359 (1996) 227.
[40] M. Seah, in: Practical Surface Analysis, Wiley, Norwich, 1985.
[41] Ch. Linsmeier, Vacuum 6/7 (1994) 673.
[42] Binary Alloy Phase Diagrams, second ed., American Society for Metals, Metals Park, OH, 1996.
[43] P. Reinke, P. Oelhafen, Diam. Relat. Mater. 8 (1999) 155.
[44] F.J.J. van Loo, G.F. Bastin, Metall. Trans. A 20A (1989) 403.
[45] B. Lesiak, A. Jablonski, Z. Prussak, P. Mrozek, Surf. Sci. 223 (1989) 213.
[46] N.V. Dzahalabadze, B.G. Eristavi, N.I. Maisuradze, E.R. Kuteliya, Phys. Met. Metall. 86 (1998) 59.
[47] B.V. Khaenko, S.Ya. Golub, M.P. Arbuzov, Kristallografiya 25 (1980) 112.
[48] J. Luthin, Thesis, Bayreuth, 2001, and IPP-report 9/129, 2001.
[49] J. Luthin, K. Schmid, Ch. Linsmeier, J. Roth, to be published.
[50] I. Bahrin, Thermochemical Data of Pure Substances, third ed., Vol. 1&2, VCH, Weinheim, 1995.

Physica Scripta. T91, 134–137, 2001

Characterization of Electron Beam Evaporated Carbon Films and Compound Formation on Titanium and Silicon

J. Luthin and Ch. Linsmeier

Max-Planck-Institut für Plasmaphysik, EURATOM Association, Boltzmannstraße 2, D-85748 Garching b. München, Germany

Received September 18, 2000; accepted December 11, 2000

PACS ref: 82.65.-i, 82.80.Pv

Abstract

The formation of carbon-based mixed materials is unavoidable on the plasma-facing components (e.g. first wall and divertor) of fusion devices when carbon is used together with other materials. On the surfaces of these components very different conditions with respect to particle and energy impact occur. To predict the mixed material formation under these conditions the precise knowledge of the fundamental mechanisms governing these interactions is essential. In this paper we present the results of carbon interaction with titanium and silicon, as model substances for metallic and covalent carbides, during thermal treatment. To perform basic studies of the reactions of carbon with different elements, thin carbon films are produced by electron beam evaporation on the different substrates under UHV conditions. All measurements for chemical analysis are performed using X-ray photoelectron spectroscopy (XPS). We discuss first the properties of the deposited carbon films. The carbon films are characterized on inert gold surfaces and are compared to bulk graphite. Annealing of the carbon films up to 970 K leads to a transition from a disordered carbon network into a graphitic structure. Preparation of carbon films at room temperature on titanium or silicon leads to a limited carbide formation at the carbon/substrate interface. Carbon deposited in excess of several monolayers is present in elementary form. Annealing of the samples leads to complete carbidization consuming the available carbon in both cases. Titanium reacts to TiC and additional substoichiometric carbide, silicon forms SiC with exact stoichiometry.

1. Introduction

Thermal treatment of carbon covered surfaces can lead to the formation of carbon-mixed materials namely carbides. With regard to the plasma-facing parts of fusion experiments elements like beryllium, silicon, tungsten and titanium are of special interest [1]. In previous studies the interactions of carbon on beryllium and carbon on tungsten were investigated in detail [2,3], because Be and W are the favorite materials for the ITER design [4,5]. The work presented here deals with the temperature dependent interaction of carbon with silicon which is currently used in some of the existing tokamaks as a wall conditioning material [6,7], and titanium, which was used as limiter material [8]. These four elements present examples for the different classes of carbides which are: ionic carbides, e.g. Be_2C, covalent carbides, e.g. SiC and metallic carbides, e.g. TiC, W_2C and WC [9,10]. The understanding of the fundamental chemical surface reactions between carbon and different elements is necessary before further investigations can show possible implications on plasma surface interaction effects expected in a fusion device e.g. erosion/redeposition, H-recycling, H-uptake and release. Our previous work [3] showed that the complete and detailed characterization of the deposited carbon films is necessary in order to distinguish the chemical interaction of carbon with the substrate materials from the modifications within the carbon layer. Therefore carbon layers on inert gold substrates are investigated and compared to well-defined surfaces of highly oriented pyrolytic graphite (HOPG).

2. Experimental

The XPS measurements are carried out using a PHI 5600 ESCA system with a monochromatic Al Kα source and a hemispherical energy analyzer. All XPS spectra are presented after Shirley background subtraction [11]. Energy calibration is performed using the Au $4f_{7/2}$ peak at 84.0 eV. The analysis system is connected to a preparation chamber and samples can be transferred without leaving UHV. To anneal the samples a radiation heating source and an electron beam heater are available. For sample cleaning and studies of ion beam induced reactions the XPS system is equipped with an ion gun (0.5–5.0 keV). The base pressure in both vessels is in the low 10^{-8} Pa range. The Si, Ti and Au substrates are cleaned by repeated sputter/annealing cycles (5.0 keV Ar^+/970 K). Carbon films are supplied by UHV electron beam evaporation of graphite [12], which provides contamination free deposition within the XPS detection accuracy. Deposition rates between 0.01 and 0.04 nm/min are used. Further details of the experimental setup are described elsewhere [13].

3. Results and discussion

3.1. *Carbon film characterization*

A 3.7 nm thick carbon film is prepared on an inert polycrystalline gold substrate. The film thickness is calculated using the attenuation of the Au $4f_{7/2}$ signal [14] considering a density of 1.8 g/cm^3 for the deposited carbon film [15,16]. In Fig. 1(a) the C 1s core level spectrum of the carbon film is shown after deposition at 300 K. The XPS signal shows a strongly asymmetric shape, the maximum is located at 284.2 eV and a shoulder is formed at a higher binding energy. Two Gauß-Lorentz peaks are necessary to fit the data [17], the position of the additional peak is at 285.2 eV. Annealing of the carbon film at 970 K leads to a reduction of the full-width-at-half-maximum (FWHM) in the XPS signal which continues at higher temperatures [3]. Due to annealing the fraction of the peak at 285.2 eV decreases. Structural investigations of electron beam evaporated carbon films have shown the existence of small graphitic clusters and disordered carbon [12,18]. After thermal treatment we would expect an increased graphitic order. We propose that the XPS peak at 284.2 eV originates from carbon atoms with graphitic configuration and the broader peak at 285.2 eV

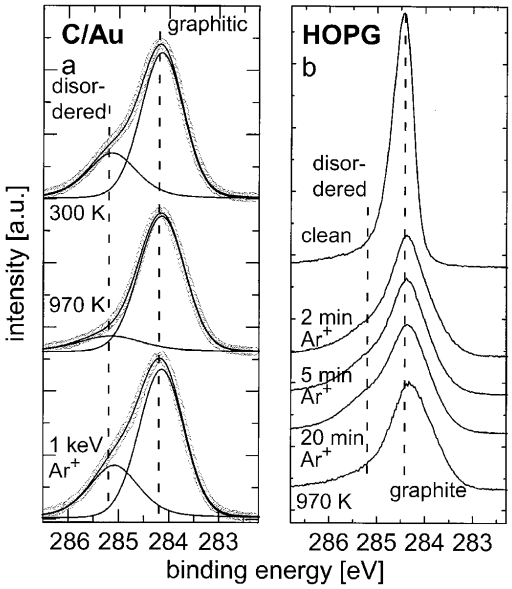

Fig. 1. Photoelectron spectra of the C 1s peak of (a) a 3.7 nm carbon film on a gold substrate and of (b) highly oriented pyrolytic graphite (HOPG). The spectra of the carbon film (circles) are shown together with the deconvoluted peaks and the sum. Indicated are the respective sample treatments before the spectrum acquisition.

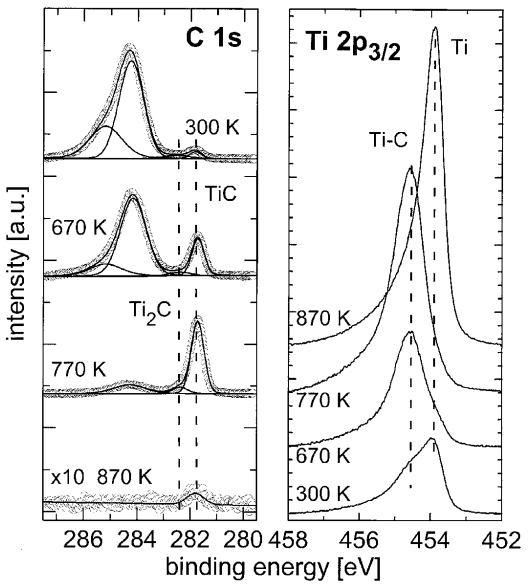

Fig. 2. Photoelectron spectra of the C 1s and Ti $2p_{3/2}$ core level transitions of a 1.0 nm carbon film on titanium. The annealing temperatures are indicated at the spectra. The C 1s data (circles) are fitted with peaks at the positions for elementary and carbidic carbon. The lines represent the peaks and the sum of the deconvoluted signals. The carbide lines are indicated, the elementary carbon peaks are identified as demonstrated in Fig. 1(a).

results from disordered carbon. This interpretation is supported by the spectrum taken at an annealed film after 1.0 keV Ar^+ ion bombardment, shown at the bottom part of Fig. 1(a). The deconvolution results in an increased fraction arising from disordered carbon. C 1s spectra of an HOPG sample are shown in Fig. 1(b) for comparison with the behavior of the carbon film. The maximum of the graphite peak is at 284.5 eV, the FWHM of 0.4 eV is very small compared to the evaporated carbon (FWHM: 0.9 eV). After 1.0 keV Ar^+ ion bombardment the peak broadens and a shoulder develops at higher binding energy. This shoulder becomes more pronounced with increasing bombardment time, as demonstrated in Fig. 1(b) for 2, 5 and 20 min Ar^+ bombardment. Therefore we conclude that the intensity at 285.2 eV arises from the disordering of the graphitic network. The shape of the XPS signal measured at the bombarded HOPG resembles the signal of the evaporated carbon film. To complete the comparison between evaporated carbon and HOPG the sample is also annealed at 970 K which again causes a narrowing of the peak, but the resulting FWHM is still much larger than in the virgin HOPG spectrum. As reported in the literature the annealing temperature of 970 K can only effect an early stage of the graphitization process [19].

From the measurements presented here we conclude that evaporated carbon can be found in two different binding states: One is attributed to a graphitic arrangement of the carbon atoms and in the second binding state carbon atoms are found in a disordered environment.

3.2. *Carbide formation on titanium*

To investigate the carbide formation of carbon on titanium, a 1.0 nm carbon layer is prepared on a polished polycrystalline titanium sample. Fig. 2 shows the XPS spectra in the C 1s and Ti $2p_{3/2}$ binding energy ranges. The C 1s spectrum displays a large elementary carbon signal composed of graphitic and disordered contributions, as discussed in Section 3.1. At a binding energy of 281.7 eV an additional well-separated peak is visible. The growth of carbon adlayers with the formation of a chemical compound limited to the carbon/substrate interface at room temperature (RT, around 300 K) is observed for several elements [1,20]. The RT reactivity is possible if the formation enthalpy of the carbidization reaction is negative which is the case for TiC [21]. In agreement with binding energy values taken from the literature [13,22] we conclude that the peak at 281.7 eV originates from TiC. The Ti $2p_{3/2}$ signal reveals a metallic contribution at 453.9 eV and a second fraction arising from TiC at 454.6 eV. Due to annealing, carbon reacts with titanium forming further amounts of carbide. Up to 670 K annealing temperature the carbide intensity in the C 1s signal increases only slightly to 15%. A further peak has to be introduced at 282.4 eV between the C 1s binding energy of elementary carbon and TiC to achieve a good fit. At higher temperatures the total carbon intensity decreases significantly. It is reduced to 38% of the initial value after annealing at 770 K. In the C 1s spectrum the intensity maximum is shifted to the binding energy value of TiC. Also the additional peak

at 282.4 eV grows. We attribute this peak to titanium subcarbide. This is supported by observations in the literature where neutron diffraction experiments of Ti-C alloys and other structural investigations on Ti-C thin films were performed [23]. Stoichiometries like Ti_6C_5 [24] and Ti_8C_5 [25] are reported. In the Ti-C phase diagram Ti_2C is recorded as an additional phase [26]. The Ti 2p signals of the different titanium states are too close to gain additional information from this binding energy regime within the available spectrometer resolution. Annealing at 870 K leads to an almost complete dissolution of the carbide. The Ti $2p_{3/2}$ signal is fitted with one peak at 453.9 eV indicating that no carbide remains. Above annealing temperatures of 670 K a large oxygen contamination accumulates and finally 20% of oxygen are present in the surface layer accessible by XPS. As already mentioned, titanium carbide belongs to the class of metallic carbides. These are characterized by carbon atoms located in octahedral sites in a metal atom spheres packing. In the case of TiC all octahedral sites are occupied and in the case of substoichiometric carbides unoccupied sites are present. In Ti_2C half of the octahedral sites would be occupied by C atoms. Diffusion of carbon between different equivalent sites explains the loss of carbon from the XPS detection zone into the bulk of the sample. Auxiliary investigations of the system Ti/C [13] show that an evaporated titanium layer on graphite is fully carbidized at 970 K and a constant carbon concentration is observed above this temperature. This can be understood only by carbon atoms travelling from the graphite substrate into the Ti layer to form carbide. From this study and our experiment presented here it is evident that the mobility of carbon within the Ti lattice determines the carbidization process.

3.3. *Carbide formation on silicon*

The temperature dependence of the carbide formation of carbon on silicon is investigated with a 1.6 nm thick carbon film evaporated onto a clean Si(111) substrate at RT. C 1s core-level spectra from RT to 1070 K are shown in Fig. 3. The C 1s spectrum after deposition (300 K) can be fitted with three binding states, two belonging to the different elementary carbon states (see Section 3.1). The additional peak is at a binding energy of 282.8 eV which is the value for SiC reported in the literature [27,28]. Again the formation enthalpy for carbidization is negative [21] and the third C 1s peak indicates the chemical reaction between carbon and silicon, forming silicon carbide at RT. Curve fitting estimates the carbidic fraction at this temperature region to be 3% of the C 1s signal. The Si 2p substrate signal in Fig. 3 consists of a doublet which is not resolved in our measurement. The binding energy of the Si $2p_{3/2}$ state determined here is 99.4 eV and is attributed to elementary silicon [27]. Because of the small thickness of the carbon film, the elementary Si 2p substrate signal dominates and the carbidic contribution is not distinguishable here. Annealing steps below 970 K, only reveal a reduction in the FWHM of the C 1s signal due to the merging of the two initially observed elementary carbon states. The carbidic fraction rises to 6% at 770 K. In the Si 2p signal no significant changes are visible. At 970 K the carbide amount increases to 11% of the C 1s Signal. In the Si 2p binding energy region the XPS signal is broadened significantly. The spectra recorded at 1070 K show drastic changes. The peak maximum of the

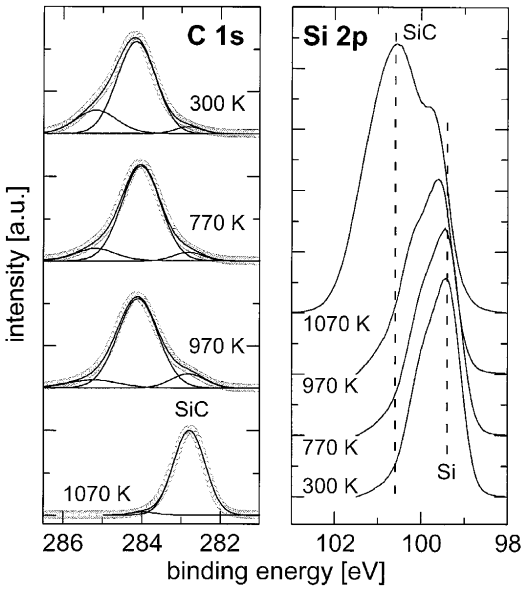

Fig. 3. Photoelectron spectra of the C 1s and Si 2p core level transitions of a 1.6 nm carbon film on silicon. The annealing temperatures are indicated at the spectra. The C 1s data (circles) is shown together with the deonvoluted contributions. The SiC peak is indicated, the elementary carbon peaks are identified as demonstrated in Fig. 1(a).

C 1s signal is shifted to 282.8 eV and only a small amount of less than 3% of unreacted elementary carbon is left. Also the maximum of the Si peak is shifted 1.2 eV towards higher binding energies. The intensity of the carbon signal is decreasing by 50% of its initial value after annealing at 1070 K. Compared with the carbon/titanium system diffusion of carbon into the silicon substrate plays a much smaller role here. This circumstance is a consequence of the binding state in the solid. SiC represents the class of covalent carbides where the Si–C bond is of covalent character. A diffusion of carbon into the silicon bulk would require the rupture of a direct covalent bond. This is different to the mechanism in metallic carbides (see the Ti sample above, Section 3.2) where carbon may occupy energetically identical sites in the metal lattice. Therefore, we conclude that the covalent structure of SiC is responsible for the stability of the carbide layer on the Si substrate.

4. Summary

Carbon layers on metal substrates are studied by XPS. The structure of the deposited films is compared to HOPG and the influence of ion bombardment on the graphitic order of HOPG and carbon films on gold is demonstrated. XPS investigations reveal the chemical interaction of carbide formation at the interface between carbon films and silicon and titanium substrates. Carbon films deposited by electron beam evaporation of high-purity carbon show two peaks in the C 1s binding energy regime. A peak at 284.2 eV originates from graphitic carbon, a second peak at 285.2 eV from disordered carbon networks. Annealing leads to an

ordering of the carbon layers, indicated by a decrease of the 285.2 eV component. Ar^+ ion bombardment introduces disorder in the carbon film which leads to the reappearance of the 285.2 eV signal. This is also observed for HOPG where the peak from a disordered phase increases with extended Ar^+ bombardment time. An annealing of the disordered HOPG surface does not restore the initial order completely, but restores the graphite structure partially. It also leads to a C 1s signal component at lower binding energies than the graphite peak at 284.5 eV.

The disorder in the graphite network observable in HOPG and in carbon on gold is also observed for films deposited on silicon and titanium. In addition to this peak, C 1s photoelectrons at lower binding energies indicate the formation of a chemical compound between the substrates (Ti, Si) and carbon. Carbide formation already takes place at room temperature (around 300 K) for both elements. The amount of carbide increases with increasing annealing temperature. In the case of titanium two carbide phases (TiC and another substoichiometric carbide, probably titanium subcarbides) are identified at C 1s binding energies of 281.7 eV and 282.4 eV, respectively. Strong diffusion sets in above 770 K which leads to an almost quantitative loss of carbon from the surface layer accessible by XPS. The strong diffusion is explained by the metallic structure of the titanium carbides. Silicon reacts with carbon to SiC with a C 1s carbide peak at 282.8 eV. The reaction is almost quantitative at 1070 K. No carbon loss into the Si bulk can be noticed up to this temperature. This is again attributed to the structure of the SiC solid with covalent bonds between carbon and silicon.

References

1. Linsmeier, Ch., Luthin, J. and Goldstraß, P., J. Nucl. Mater. **290–293**, 25 (2001).
2. Goldstraß, P. and Linsmeier, Ch., Nucl. Instr. Meth. B **161–163**, 411 (2000).
3. Luthin, J. and Linsmeier, Ch., Surf. Sci. **454–456**, 78 (2000).
4. Anderl, R. A. *et al*., J. Nucl. Mater. **273** 1 (1999).
5. Barabash, V., Federici, G., Matera, R., Raffray, A. R. and ITER Home Teams, Physica Scripta **T81**, 74 (1999).
6. Winter, J. *et al.*, Phys. Rev. Lett. **71**, 1549 (1999).
7. Rohde, V. *et al.*, ECA Vol. **23J**, 1513 (1999).
8. Grigull, P. *et al.*, J. Nucl. Mater. **196–198**, 101 (1992).
9. Müller, U., ''Anorganische Strukturchemie'', (Teubner Verlag, Stuttgart, 1992).
10. Holleman, A. F., ''Lehrbuch der Anorganischen Chemie'', (Walter de Gruyter, Berlin, 1985).
11. Shirley, D., Phys. Rev. B **5**, 4709 (1972).
12. Schelz, S., Richmond, T., Kania, P., Oelhafen, P. and Güntherrodt, H.-J., Surf. Sci. **359**, 227 (1996).
13. Miller, S., Berning, G., Plank, H. and Roth, J., J. Vac. Sci. Technol. A **15**, 2029 (1997).
14. Seah, M., In: ''Practical Surface Analysis'', (John Wiley and Sons, Norwich, 1985).
15. Goldstraß, P., Klages, K. U. and Linsmeier, Ch., J. Nucl. Mater. **290–293**, 76 (2001).
16. Lesiak, B., Jablonski, A., Prussak, Z. and Mrozek, P., Surf. Sci. **223**, 213 (1989).
17. MultiPak Ver. 2.2, Physical Electronics (1996).
18. Besold, J. *et al.*, Thin Solid Films **293**, 96 (1997).
19. Lespade, P., Al-Jishi, R. and Dresselhaus, M. S., Carbon **2** 427 (1982).
20. Reinke, P. and Oelhafen, P., Diam. Relat. Mater. **290–291**, 148 (1996).
21. Bahrin, I., ''Thermochemical Data of Pure Substances'', 3rd Ed., Vol. 1&2, (Weinheim, 1995).
22. Ramqvist, L., Hamrin, K., Johansson, G., Fahlman, A. and Nordling, C., J. Phys. Chem. Solids **30** 1835 (1969).
23. Goretzki, H., Phys. Status Solidi **20**, K141 (1967).
24. Dzhalabadze, N. V., Eristavi, B. G., Maisuradze, N. I. and Kuteliya, E. R., Phys. Met. Metallogr. **86**, 59 (1998).
25. Khaenko, B. V., Golub, S.Ya. and Arbuzov, M. P., Kristallografiya **25**, 112 (1980).
26. Massalski, T. B., Okamoto, H., Subramanian, P. R. and Kacprzak, L., ''Binary Alloy Phase Diagrams'', 2nd Ed., Version 1.0, (Materials Park, Ohio, 1996).
27. Kusunoki, I. and Igari, Y., Appl. Surf. Sci. **59**, 95 (1992).
28. Contarini, S., Howlett, S. P., Rizzo, C. and De Angelis, B. A., Appl. Surf. Sci. **51**, 177 (1991).

ELSEVIER

Journal of Nuclear Materials 290–293 (2001) 76–79

journal of nuclear materials

www.elsevier.nl/locate/jnucmat

Surface reactions on beryllium after carbon vapour deposition and thermal treatment

P. Goldstrass, K.U. Klages, Ch. Linsmeier *

Max-Planck-Institut für Plasmaphysik, EURATOM Association, Boltzmannstr. 2, D-85748 Garching, Germany

Abstract

Surface reactions and carbon layer formation on clean metallic beryllium are investigated in situ by X-ray photoelectron spectroscopy (XPS) and Rutherford backscattering spectroscopy (RBS). The carbon is supplied by an electron beam evaporation device. The deposited films are successively heated to temperatures between 373 and 873 K in steps of 100 K and analysed after each step. After deposition at room temperature an amount of Be_2C up to 6×10^{15} cm^{-2} is present at the beryllium/carbon interface with elementary carbon on top. A first additional carbide formation takes place after heating to 473 K. For deposited amounts below 5×10^{16} cm^{-2} almost all carbon has reacted to carbide after the 673 K step. The carbidisation is complete at 773 K. Applying annealing times between 10 and 30 min characteristic Be_2C amounts build up for each temperature. Carbon diffusion into the bulk beryllium does not take place for temperatures below 773 K.

Keywords: Beryllium; Carbon; Beryllium carbide; Material mixing

1. Introduction

A consequence of a multi-elemental first wall in fusion devices is the formation of mixed layers and compounds at the plasma facing components due to erosion and (re-)deposition processes. Beryllium has been used in JET and led to a significant improvement of the plasma performance and a substantial change of the first wall hydrogen inventory [1–4]. It is considered as a candidate first wall material for ITER along with tungsten and carbon [5]. Mixed beryllium/carbon materials exhibit altered properties regarding erosion and hydrogen retention with respect to the pure materials. Therefore, it is important to understand the surface reactions and the compound formation of carbon with beryllium at both room temperature and elevated temperatures. To minimise the influence of impurities (e.g., oxygen) sample preparation and in situ analysis has to be performed under ultra-high vacuum conditions. As we recently reported [6] vapour deposited carbon forms Be_2C at the beryllium/carbon interface at room temperature similarly to molybdenum [7] and tungsten [8]. We observed the first additional Be_2C formation at a lower temperature (473 K) than reported earlier (673–773 K [9–12]). In this paper we study the reaction of carbon layers with metallic beryllium after deposition and thermal treatment. We quantify the absolute carbide amounts at the different temperatures by combining the results of in situ X-ray photoelectron spectroscopy (XPS) and in situ Rutherford backscattering spectroscopy (RBS).

2. Experiment

A beryllium single crystal (0 0 0 1) was cleaned using 1 keV Ar^+ bombardment. The only detectable impurities after the cleaning process were oxygen (XPS: $<10^{14}$ cm^{-2}) and argon (RBS: $<10^{15}$ cm^{-2}). Carbon amounts between 0.18 and 10.42×10^{16} cm^{-2} (0.20 and 11.55 nm, assuming a density of 1.8 g cm^{-3}) were deposited on the substrate at room temperature using an electron beam evaporation device (Omicron EFM 3) and graphite (Goodfellow, 99.999%) as evaporant. Each film was heated in steps of 100 K from 373 to 873 K and

* Corresponding author. Tel.: +49-89 3299 2285; fax: +49-89 3299 2279.

E-mail addresses: peter.goldstrass@ipp.mpg.de (P. Goldstrass), linsmeier@ipp.mpg.de (C. Linsmeier).

0022-3115/01/$ - see front matter
PII: S0022-3115(00)00617-6

kept at each temperature for 10 min. To investigate the influence of the heating duration, the sample remained at each temperature for 30 min in one series of measurements. After each step the sample was allowed to cool down for XPS (Mg K_α, 1253.6 eV) and RBS ($^4He^+$, 1 MeV, normal incidence, 165° scattering angle) analysis. The oxygen contamination of all films remained below 10^{15} cm^{-2} after the temperature treatment. For XPS an electrostatic hemispherical analyser (Physical Electronics, Ø 279.4 mm) was used. It is equipped with an entrance lens system and operated at a constant pass energy of 23.5 eV. The photoelectrons were detected at 90° relative to the sample surface and the Au $4f_{7/2}$ core level line (84.0 eV) of a clean gold sample was used for energy calibration. XPS C 1s spectra were fitted, using the MultiPak V 5.0 A code (Physical Electronics). For this fitting procedure (least-squares fit) each of the contributions has been approximated by a symmetric Gaussian/Lorentzian function centered at its characteristic binding energy. A Shirley-type background subtraction was applied to the spectra prior to the actual fitting procedure.

The base pressure in the new UHV chamber ARTOSS [13] and the pressure during RBS and XPS analysis was below 10^{-8} Pa. The pressure during carbon evaporation did not exceed 5×10^{-8} Pa. During the heating process the pressure stayed below 1.5×10^{-7} Pa for all temperatures.

3. Results and discussion

3.1. Carbon layer composition

As previously reported, C 1s XPS spectra measured after carbon vapour deposition on clean metallic beryllium showed three different components of the C 1s signal [6]: graphitic and disordered carbon (binding energies 284.2 and 285.2 eV, respectively [8]) and Be_2C (binding energy 282.1–282.6 eV).

The carbon signal composition as a function of the deposited carbon amount is shown in Fig. 1. For small coverages the majority of the carbon is bound in carbide. However, this Be_2C contribution decreases with an increasing deposited amount while the percentages of graphitic and disordered carbon increase to values of about 60% and 30%, respectively. This behaviour is explained by a limited carbide formation at the beryllium/carbon interface and the deposition of elementary carbon on top of the carbide. Assuming this model the measured carbide percentage decreases due to the limited information depth of the XPS technique. This limitation is due to the Lambert–Beer law which gives an exponentially decreasing probability for the emitted photoelectrons to escape from a certain sample depth according to their inelastic mean free path. The exponential-like behaviour of the Be_2 C percentage thus is a further confirmation of our model. The absolute carbide amounts after deposition at 300 K as a function of the total deposited carbon amount are shown in Fig. 4 by the 300 K curve. If the deposited carbon amount is large enough, then the carbide amount reaches a coverage-independent maximum of 6×10^{15} cm^{-2}. This amount is larger than a monolayer (about 10^{15} cm^{-2}) which may at least in part be due to an increased net surface caused by a considerable surface roughness. Also a deviation from the layer model that is applied to derive Fig. 4 (see Section 3.2) may lead to an error in the calculated amount. Because elementary carbon is present in the sample before the maximum amount of carbide is observed, the film is unlikely to grow layer by layer. That an island growth mode has to be preferred is also confirmed by the fact that during sublimation carbon clusters are formed which are unlikely to split and be mobile on the beryllium surface [14,15].

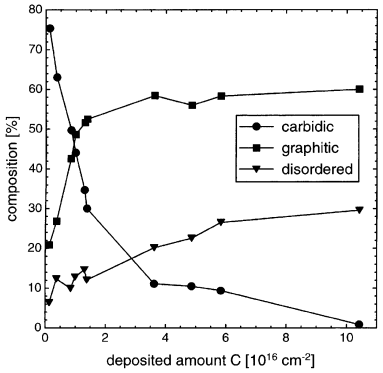

Fig. 1. Composition of the C 1s XPS signal as a function of the total deposited carbon amount after deposition at room temperature. Three different contributions can be distinguished: beryllium carbide (Be_2C), graphitic and disordered carbon.

Fig. 2 shows the results of XPS C 1s spectra fitting for a deposited carbon amount of 4.86×10^{16} cm^{-2} at each temperature step. The first additional carbide formation takes place after heating to 473 K. The XPS spectra show that a homogeneous carbide layer is present on top of the beryllium after the carbidisation is complete [6]. Thus a pure carbide layer on top of the beryllium substrate, growing in thickness with increasing temperature, can be assumed. Therefore, the first small additional carbide formation at 473 K may be due to two processes. The thickness of the carbide layer may simply grow. However, the deposited film is unlikely to grow layer by layer and thus the as-deposited interface is unlikely to consist of homogeneous carbide. Therefore, the formation of a homogeneous carbide layer at the interface would also explain a growing intensity of carbide.

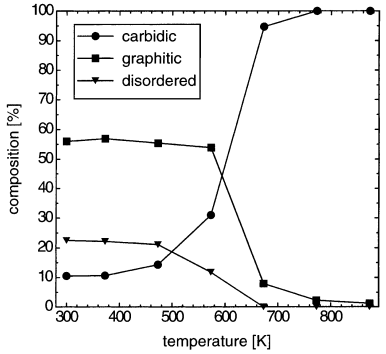

Fig. 2. Composition of the C 1s XPS signal after heating to the different temperatures for a deposited carbon amount of 4.86×10^{16} cm^{-2}. The three contributions are the same as in Fig. 1.

A more significant additional carbide formation takes place during heating to 573 K. These temperatures are lower than those reported in the literature, where a similar carbidisation of carbon on beryllium (diffusion of beryllium into carbon, respectively) is reported not to take place below temperatures varying from 673 to 773 K [9–12]. Because in the reported experiments either a different carbon modification was deposited (fullerenes [9]) or the samples were known to have a high oxygen contamination (at least 20% [10–12]), the lower temperature observed here can be explained by the very low contamination level of the samples. Moreover, all the carbon films studied in the cited publications have been too thick to allow a detailed investigation of the interface with the applied analysis techniques. This may also explain why the carbide formation during deposition at room temperature and the quantitatively small reaction after 473 K have not been observed before.

Above 473 K, the carbide percentage increases with increasing temperature. In the case of the smaller deposited carbon amounts (below approximately 2×10^{16} cm^{-2}) the carbidisation of the film is completed after heating to 673 K. For the bigger amounts (e.g., Fig. 2) the carbidisation is nearly complete at 673 K and at 773 K the entire deposited carbon has reacted.

Fig. 2 also shows that the percentage of graphitic carbon remains constant up to 573 K for a deposited carbon amount of 4.86×10^{16} cm^{-2}. However, the lowest deposited amount partly consists of graphitic carbon and has completely reacted to carbide at 573 K. This shows that there is no significant difference in the activation energies of disordered and graphitic carbon for carbide formation or carbon diffusion, respectively. Therefore, the observed temperature-dependent carbide formation is not due to different properties of these two carbon modifications.

3.2. Be_2C quantification

XPS results show an increase of the beryllium amount during the temperature treatment. This is due to the limited escape depth of the photoelectrons (and thus limited range of the analysis method) and to the beryllium diffusion into this analysis region during carbide formation [6]. The RBS measurements (Fig. 3) clearly show that the total carbon amount present on the sample remains constant. Each connected series of data points in Fig. 3 represents a different initial amount of deposited carbon and shows that this remains constant during the temperature treatment. Although a slight decrease of the carbon amount above 700 K is indicated by three of the series, there is no clear common trend. Besides these quantitative RBS results, the shapes of the carbon signals in the RBS spectra do not indicate a diffusion into the beryllium bulk either (symmetric shape remains, no low energy tail which would appear due to diffusion). This proves that the entire deposited carbon forms a Be_2C layer on top of the beryllium substrate. The stoichiometric composition of this layer has been reported in a previous publication [6].

Using XPS and assuming a layer structure (elementary carbon on top of Be_2C on top of beryllium), it is possible to determine the remaining amount of elementary carbon after each temperature step, if its thickness is in the order of the inelastic mean free path length of the emitted photoelectrons [6]. Subtraction from the respective total carbon amounts present (measured by RBS, see Fig. 3) gives the total amount of carbon bound

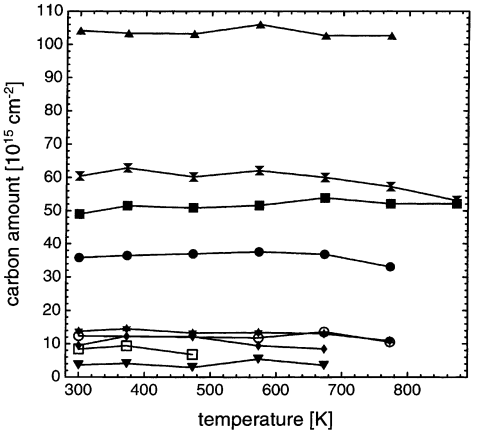

Fig. 3. Carbon amount, measured by RBS, present on the sample after deposition at 300 K and heating to the indicated temperatures. Each series of connected points (identical symbols) shows the development with temperature for a different deposited carbon amount.

in Be_2C after each temperature step. The results of this calculation are shown in Fig. 4. It shows that characteristic carbide amounts are formed for the following annealing temperatures: 300 K (after deposition), 373 K (no difference to 300 K) and 473 K. Although the 573 K curve does not reach saturation within the investigated region of deposited carbon amounts, it clearly shows a tendency to do so. For 673 K, the deviation from a complete reaction of the carbon is only very small but present for the higher deposited amounts.

Increasing the annealing time for each temperature to 30 min (instead of 10 min) does not change the limited carbide amounts observed for the different temperatures. This legitimates the assumption that either the reaction stops after the respective carbide amount has been formed or its time dependence is of a kind that does not lead to a significant change of the formed carbide amount within the annealing time difference applied here. In the literature a time-dependent diffusion of beryllium into the carbon film on a comparable time scale has been observed [10] and a nucleation process has been proposed to explain the rather rapid carbidisation of the films starting at temperatures above 673 K [12]. Because of the difference between the reported and observed temperatures the results are difficult to compare and it is difficult to assess at which temperature the first additional carbide formation takes place. Additionally, the deposited carbon amounts in these reported cases are much higher and the samples have a high oxygen contamination level, which may well be due to a BeO interface. If this is true, then the BeO interface may act as a diffusion barrier and thus influence the carbidisation process. Therefore, the understanding of the temperature and time dependence of the carbidisation process of thick carbon layers with a low contamination level on a clean beryllium substrate will be subject to further investigations.

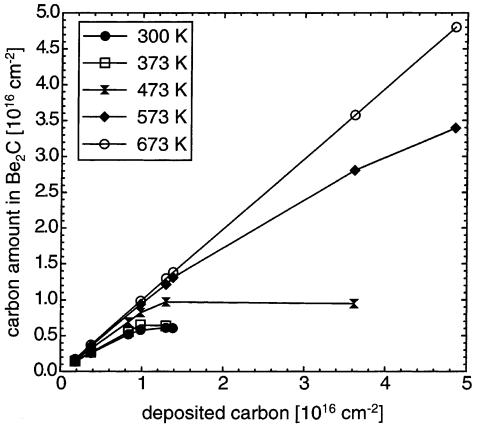

Fig. 4. Total amount of carbon bound in Be_2C at each temperature step as a function on the initially deposited carbon amount at room temperature. The data points measured at equal temperatures (but different samples) are connected to guide the eye.

4. Conclusions

It has been shown that during vapour deposition of carbon on clean metallic beryllium carbide is formed at the beryllium/carbon interface. The carbide amount is somewhat more than a monolayer. When exposing the deposited films to elevated temperatures the first additional carbide formation takes place during heating to 473 K, well below the temperatures so far known in the literature. For annealing times from 10 to 30 min the formation of limited carbide amounts, characteristic for each annealing temperature, is observed. The diffusion/reaction mechanism giving rise to this behaviour is not yet clear and needs further investigation. For deposited carbon amounts up to 5×10^{16} cm^{-2}, the carbidisation is complete after heating to 773 K and the entire deposited carbon amount is used to form a stoichiometric Be_2C layer on top of the beryllium substrate. No carbon is lost by diffusion into the bulk beryllium.

References

[1] The JET Team: presented by P.R. Thomas, J. Nucl. Mater. 176&177 (1990) 3.
[2] R. Satori, G. Saibene, D. Goodall, E. Usselmann, P. Coad, D. Holland, J. Nucl. Mater. 176&177 (1990) 624.
[3] P. Rebut, M. Hugon, S. Booth, J. Dean, K. Dietz, K. Sonnenberg, M. Watkins, JET-R(85)03. JET Joint Undertaking, Abingdon, 1985.
[4] E. Bertolini, Fus. Eng. Des. 27 (1995) 27.
[5] ITER Project, Detailed Design Document, IdoMS#G 16 DDD 2 96-11-27 W 0.2, 1996.
[6] P. Goldstrass, Ch. Linsmeier, Nucl. Instrum. and Meth. B 161–163 (2000) 411.
[7] P. Reinke, P. Oelhafen, Diamond Rel. Mater. 8 (1999) 155.
[8] J. Luthin, Ch. Linsmeier, Surf. Sci. 454–456 (2000) 78.
[9] C. Tzeng, K. Tsuei, W. Lo, Phys. Rev. B 58 (1998) 6837.
[10] R. Anderl, R. Causey, J. Davis, R. Doerner, G. Federici, A. Haasz, G. Longhurst, W. Wampler, K. Wilson, J. Nucl. Mater. 273 (1999) 1.
[11] T. Nieh, J. Wadsworth, A. Joshi, Scripta Metall. (1986) 87.
[12] K. Ashida, K. Watanabe, T. Okabe, J. Nucl. Mater. 241–243 (1997) 1060.
[13] Ch. Linsmeier, P. Goldstrass, K.U. Klages, Physica Scripta (submitted).
[14] R. Hultgren, Selected Values of the Thermodynamic Properties of the Elements, American Society for Metals, Metals Park, Ohio, 1973.
[15] C. Wu, U. Maszanowski, J. Martin, J. Nucl. Mater. 258–263 (1998) 782.

ELSEVIER

Journal of Nuclear Materials 290–293 (2001) 71–75

journal of nuclear materials

www.elsevier.nl/locate/jnucmat

Formation of mixed layers and compounds on beryllium due to C^+ and CO^+ bombardment

P. Goldstrass [1], Ch. Linsmeier *

Max-Planck-Institut für Plasmaphysik, EURATOM Association, Boltzmannstr. 2, Garching D-85748, Germany

Abstract

Compound formation on a clean beryllium single crystal (0 0 0 1) during bombardment with 5 keV C^+ and 3 and 5 keV CO^+ ions is studied by means of in situ X-ray photoelectron spectroscopy (XPS). In combination with in situ Rutherford backscattering analysis (RBS), TRIDYN computer simulation, and measurements of the weight change of the sample due to the bombardment, models for the sample composition changes and erosion mechanisms are derived for both ion species. In the case of C^+ bombardment a carbon layer builds up on top of the beryllium. The transition region from pure beryllium to pure carbon consists partly of Be_2C and the beryllium erosion stops as the covering carbon layer develops. During CO^+ bombardment a deposition/erosion equilibrium is established. After initial C and O accumulation, the beryllium substrate is covered by a ternary mixture layer of about 10 nm thickness containing BeO, elementary carbon and C–O compounds. Be_2C is present only at low fluences and before the equilibrium is established. The erosion of beryllium proceeds and a chemical erosion process limits the deposited amounts of carbon and oxygen via emission of CO.

Keywords: Beryllium; Carbon; Beryllium carbide; Erosion; Ion irradiation

1. Introduction

In present experiments and in the design of future fusion plasma devices like ITER, several elements are being considered as first wall materials [1]. This use of multiple materials and the presence of impurities in the plasma (e.g., oxygen) will result in the formation of mixed materials at the first wall because of erosion and (re-) deposition during the discharges. The use of multiple materials in JET has led to a considerable improvement of the plasma performance and the hydrogen inventory of the first wall [2–5]. Carbon has been used in most fusion machines and both carbon and beryllium are candidate first wall materials for ITER [1].

Earlier investigations showed that in the case of C^+ bombardment of beryllium, a carbon adlayer builds up on top of the substrate and protects the beryllium from further erosion. In the case of CO^+ bombardment (simulating an oxygen and carbon co-bombardment) a deposition/erosion equilibrium is established. This cannot be explained assuming physical sputtering to be the only erosion mechanism [6]. In this paper the chemical interactions between the different elements in these mixed materials are studied to develop deposition/erosion models for both ion species.

2. Experiment

A polished beryllium single crystal (0 0 0 1) was cleaned by 1 keV Ar^+ sputtering and bombarded with 5 keV C^+ and 5 keV CO^+ at normal incidence in the new UHV experiment ARTOSS [7]. After the cleaning process the only detectable impurity was oxygen (X-ray photoelectron spectroscopy (XPS) measurement:

* Corresponding author. Tel.: +49-89 3299 2285; fax: +49-89 3299 2279.

E-mail addresses: peter.goldstrass@ipp.mpg.de (P. Goldstrass), linsmeier@ipp.mpg.de (C. Linsmeier).

[1] Tel.: +49-89 3299 1497; fax: +49-89 3299 1149.

0022-3115/01/$ - see front matter
PII: S0022-3115(00)00618-8

$<10^{14}$ cm^{-2}). The oxygen contamination did not exceed this value during the implantation experiments. Both ion species were supplied by a Colutron type ion source using CO_2 as a precursor gas. The ion beam emitted by this source had an energy width of 3 eV [8] and was mass separated by an 80° deflection magnet before entering the main UHV chamber. The position of the ion beam ($\phi \sim 3$ mm) on the sample surface was monitored using a Faraday cup (ϕ 0.5 mm). The integrated image of the ion beam intensity profile on the sample was measured by spatially resolved XPS (analysis spot ϕ 0.8 mm) and used to calculate the ion fluence as a function of the measured ion implantation dose. The implantation was interrupted after certain fluences for in situ XPS (Mg K_α, 1253.6 eV) and Rutherford backscattering analysis (RBS) ($^4He^+$, 1 MeV, 165° scattering angle) analysis. The electrostatic analyser for XPS was operated at a constant pass energy of 23.5 eV. The photoelectrons were detected at 90° relative to the sample surface and the Au $4f_{7/2}$ core level line (84.0 eV) of a clean gold sample was used for energy calibration. The base pressure in the ARTOSS main UHV chamber and the pressure during analysis and ion bombardment stayed below 10^{-8} Pa.

In a separate experiment the weight change of a polished polycrystalline beryllium target during 3 keV CO^+ ion bombardment at normal incidence was measured using the high-current ion source described in [9]. The remaining carbon and oxygen impurity concentrations after polishing were in the range of $(5–10) \times 10^{16}$ cm^{-2}. The weight of the target was determined after certain ion doses using a Mettler 22 vacuum microbalance with a sensitivity <1 μg. The weight change was calculated in relation to the original sample weight measured before the ion bombardment in the same vacuum chamber. The base pressure in the target chamber was about 10^{-7} Pa, the pressure during ion bombardment about 10^{-4} Pa.

The Monte Carlo program TRIDYN (version 40.3) [10,11] was used to calculate the ion ranges and sputtering yields. This program takes into account all collisional effects such as implantation, reflection, and sputtering. Ions and collisional cascades are tracked until the respective particle energy falls below the surface binding energy of this particle in the target. These energies are based on the elemental heats of sublimation and are interpolated to take into account the surface composition of the target [12]. Chemical erosion, diffusion and segregation are not considered. Though the program is able to take changes in target composition due to the ion beam into account, this option was not used here because we wanted to obtain physical sputtering yields for a fixed target composition under simultaneous bombardment with two ion species.

3. Results and discussion

3.1. C^+ bombardment

The RBS analysis after the implantation steps shows a continuous increase of the deposited carbon amount with increasing fluence and this behaviour is well reproduced by TRIDYN computer simulations, as we recently reported elsewhere [6]. Depth profiles given by TRIDYN suggest that a carbon layer builds up on top of the beryllium substrate [6]. This adlayer formation is also confirmed by weight change measurements which show a continuous increase of the sample weight with increasing ion fluence [13]. This is also consistent with a carbon self sputtering yield below unity at normal incidence [14].

The fluence dependence of the surface composition, derived from the XPS measurements using the intensity ratios and the characteristic sensitivity factors of the different elements [15], confirms this model. The carbon share of the surface composition increases with fluence until it reaches almost 100% at a C^+ fluence of 111.7×10^{16} cm^{-2}. This means that a pure carbon adlayer builds up on the beryllium substrate because the probability for a photoelectron emitted at a certain depth to leave the sample decreases exponentially with depth (it can be estimated that $<5\%$ of the overall intensity comes from a depth >6 nm).

In addition to the elementary composition of the surface layer, XPS analysis gives information about the chemical composition of the growing adlayer. Fig. 1 shows the XPS spectra of the C 1s binding energy region after the denoted C^+ implantation fluences. For a fluence of 8.9×10^{16} cm^{-2} there is almost no carbon signal visible. This is due to the mean implantation depth of the carbon ions in beryllium (TRIDYN: 20 nm) which is beyond the reach of XPS. The increase of fluence then leads to a broadening of the implantation profile and simultaneously to erosion of beryllium at the surface. Because of these effects the implanted carbon is not visible for XPS until a fluence of 20.1×10^{16} cm^{-2}.

At this and at the next higher fluence the carbon signal is almost entirely located at a C 1s binding energy which is characteristic of Be_2C [16]. A second peak, originating from elementary carbon [17] is not observed until the C^+ fluence reaches a value of 42.4×10^{16} cm^{-2}. For higher fluences the elementary signal increases and dominates the spectrum more and more until only a small carbide signal is left at a fluence of 111.7×10^{16} cm^{-2}.

The observed behaviour can be explained by the following model: Directly after implantation of carbon into clean beryllium Be_2C is formed. With increasing deposited carbon amount and simultaneous beryllium sputtering the carbon fraction in the surface layer accessible by XPS exceeds the stoichiometric value of 33%

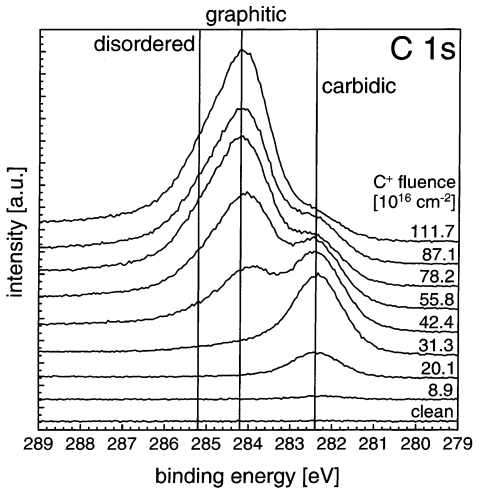

Fig. 1. XPS spectra of the C 1s binding energy region at the denoted C^+ fluences. The vertical lines indicate the peak positions for graphitic and disordered carbon and beryllium carbide.

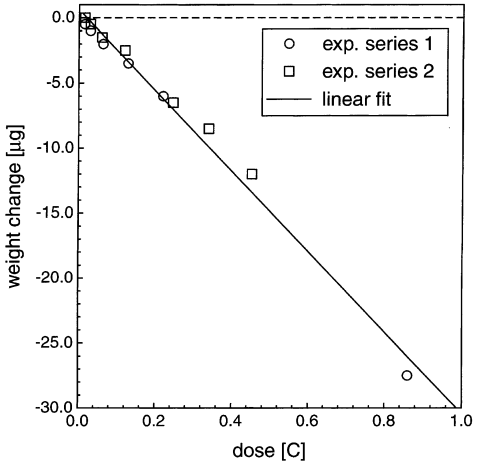

Fig. 2. Weight change of a polycrystalline beryllium target with 3 keV CO^+ dose. The solid line is the result of a linear fit including the two separate experimental series shown.

(41% at 42.4×10^{16} cm^{-2}). Therefore the carbon cannot completely be bound in Be_2C anymore. Eventually this leads to the sample structure of elementary carbon on top and Be_2C in the transition region between pure carbon and pure beryllium.

3.2. CO^+ bombardment

In the case of CO^+ bombardment the molecular ions split upon impact on the sample surface and the ion energy is divided between carbon and oxygen corresponding to their mass ratio of 3:4, thus simulating a co-bombardment of the sample with carbon and oxygen. We recently showed that in contrast to the C^+ bombardment the deposited amounts of carbon and oxygen are limited and a deposition/erosion equilibrium is established after a certain fluence.

Fig. 2 shows the weight change of a polycrystalline beryllium target during 3 keV CO^+ bombardment. Because the equilibrium is already established at the lowest dose shown in the graph (15 mC, RBS shows equilibrium after 0.5 mC) a linear fit is used to obtain a beryllium sputtering yield (see Table 1). Taking into account the fact that the total deposited amounts of carbon and oxygen do not change any more after equilibrium is reached (i.e., unity erosion yield for both elements) the whole weight loss must be due to a continuing beryllium erosion.

Table 1
Experimental and calculated (TRIDYN) erosion yields of beryllium, carbon and oxygen due to 5 keV CO^+ bombardment[a]

	Be	C	O
TRIDYN	0.36	0.24	0.29
Experimental	0.33	1.00	1.00

[a] In the calculations a homogeneous target containing 40% O, 32% C and 28% Be is assumed.

The chemical composition of the ternary surface layer can be derived from the XPS binding energy spectra of the Be 1s and C 1s regions. Fig. 3 shows the XPS spectra of the C 1s region after the denoted CO^+ fluences. Besides the contributions from disordered and graphitic carbon, Be_2C and a broad intensity band at values above the energy characteristic for disordered carbon are observed. These last signals cannot be attributed to a single compound but can be generally assigned to C–O compounds like CO, CO_2 or carbonates whose binding energies are known to lie in the marked region [18,19]. While the beryllium carbide signal decreases and eventually vanishes with increasing fluence, the C–O compound intensity increases and reaches a saturation level after equilibrium is reached. This means that inside the ternary mixture layer after implantation carbon is bound to a certain extent in C–O compounds directly after implantation.

While it is not possible to fit the C 1s signal due to the contribution of the C–O compounds, the Be 1s XPS spectra were fitted using the MultiPak V 5.0 A code (Physical Electronics). For this fitting procedure (least

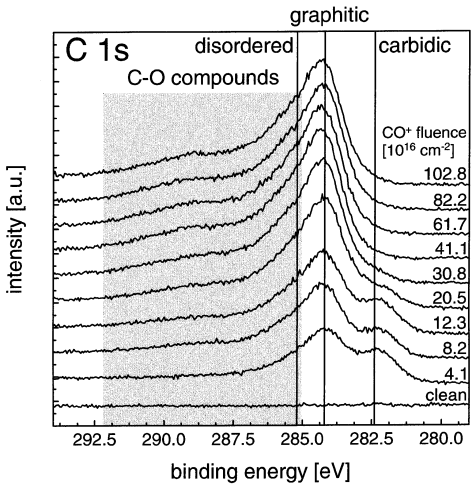

Fig. 3. XPS spectra of the C 1s binding energy region at the denoted CO^+ fluences. The vertical lines indicate the peak positions for graphitic and disordered carbon and beryllium carbide. The grey rectangle marks the known energy region for a number of simple C–O compounds.

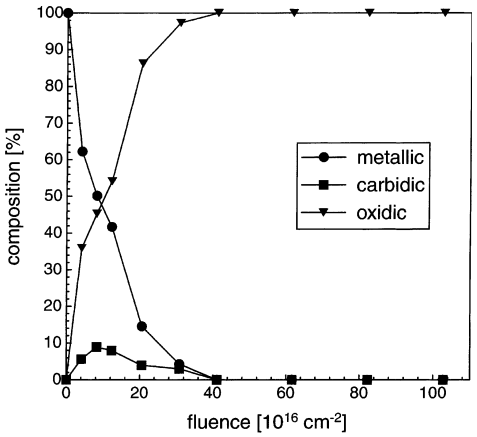

Fig. 4. Composition of the Be 1s XPS signal at the different CO^+ implantation fluences. For the fitting procedure binding energies of metallic beryllium, BeO and Be_2C according to [16,19] have been used.

square fit) each contribution is approximated by a combined, symmetric Gaussian/Lorentzian function centered at its characteristic binding energy. A Shirley-type background subtraction was applied to the spectra before the actual fitting procedure. The results of these fits are shown in Fig. 4. Again there is a Be_2C signal only before the equilibrium is established. After the equilibrium is reached the beryllium in the ternary layer is completely bound in beryllium oxide. At equilibrium the ternary surface layer is composed of BeO, elementary carbon and C–O compounds, no beryllium carbide is detected (enthalpy of formation: BeO:- 612.5 kJ/mol, Be_2C:- 117.0 kJ/mol [20]).

The equilibrium surface composition of the sample can be calculated from XPS spectra in the same way as described in Section 3.1. It results in 40% oxygen, 32% carbon and 28% beryllium. Because of the mentioned photoelectron attenuation, this composition would be valid for a homogeneous surface layer only. However, this composition can be used as an approximation together with the total difference in the deposited carbon and oxygen equilibrium amounts measured by RBS (oxygen: 9×10^{16} cm^{-2}, carbon: 8×10^{16} cm^{-2}). Assuming furthermore densities of 2 g cm^{-3} for carbon and 3 g cm^{-3} for BeO, an estimated homogeneous layer of the quoted composition must be 12 nm thick to agree with both the XPS and RBS results. Because the calculated mean implantation depths (TRIDYN: 8 nm) and implantation profiles for both elements are almost identical and because only the first 6 nm are relevant for XPS, the difference in the total amounts must be explained by an inhomogeneous layer composition near the sample surface. Thus it can be concluded that the ternary surface layer is not homogeneous and that the uppermost surface is rich in oxygen compared to carbon (BeO at the surface, C chemically eroded). The concentrations of carbon and oxygen decrease and become almost equal as the sample depth increases.

However, using the composition measured by XPS as an approximation the physical sputtering yields of carbon, beryllium and oxygen due to 5 keV CO^+ bombardment can be calculated by TRIDYN for equilibrium conditions (see Table 1). Beryllium is bound in BeO only and the BeO enthalpy of sublimation has been used for the TRIDYN calculations. Therefore the particle energy below which TRIDYN stops to calculate the further particle path is correct in the case of beryllium. Comparing the experimental and the calculated beryllium value, they are almost identical. Thus it can be concluded that beryllium is eroded by physical sputtering only. For carbon and oxygen the experimental and the TRIDYN values are clearly different. Here the presence of C–O compounds in the sample must be considered. While a crystal lattice usually has a binding energy of several eV, molecules like CO or CO_2 do not form such a lattice and they have adsorption energies on surfaces which are generally below 1 eV. The assumption of a BeO lattice with stored and adsorbed C–O compounds thus explains a much easier and thus higher erosion of oxygen and carbon which cannot be calculated by TRIDYN because of the too low surface

binding energies compared to the mentioned interpolation. Additionally, the impinging ions can break existing bonds and enable the formation of molecules like CO directly at the surface. In this case even the enthalpy of formation supplies enough energy for desorption ($C + O \rightarrow CO$: $\sim$1.1 eV). Taking into account that the physical sputtering yields of oxygen and carbon are quite similar (see Table 1) and that the overall erosion yield is one for both elements it is probable that the observed chemical erosion is due to the desorption of carbon monoxide molecules.

4. Conclusions

Models have been constructed for the build-up of mixed layers on a beryllium substrate and the erosion of the target during 5 keV C^+ and 5 keV CO^+ bombardment, respectively.

In the case of C^+ implantation an elementary carbon layer builds up on top of a transition region containing beryllium carbide between pure carbon and pure beryllium. Beryllium erosion stops after the development of a shielding carbon layer.

In the case of CO^+ bombardment an erosion/deposition equilibrium is established and an approximately 8 nm thick ternary mixture layer containing beryllium, carbon and oxygen forms on top of the substrate. The composition of this layer is not homogeneous. While the surface is relatively rich in oxygen compared to carbon, the concentration of these two elements approaches a similar value with increasing sample depth. In the ternary mixture layer beryllium is entirely bound in beryllium oxide. Carbon is present as a mixture of elementary carbon and C–O compounds. There is no Be_2C. Beryllium erosion does not stop and is due to physical sputtering by the impinging CO^+ ions with a sputtering yield of 0.33. For carbon and oxygen we suggest a chemical erosion process which takes place via the desorption of carbon monoxide molecules.

References

[1] ITER Project, Detailed Design Document, IdoMS#G 16 DDD 2 96-11-27 W 0.2, 1996.
[2] The JET Team: presented by P.R. Thomas, J. Nucl. Mater. 176&177 (1990) 3.
[3] R. Satori, G. Saibene, D. Goodall, E. Usselmann, P. Coad, D. Holland, J. Nucl. Mater. 176&177 (1990) 624.
[4] P. Rebut, M. Hugon, S. Booth, J. Dean, K. Dietz, K. Sonnenberg, M. Watkins, JET-R(85)03, JET Joint Undertaking, Abingdon, 1985.
[5] E. Bertolini, Fus. Eng. Des. 27 (1995) 27.
[6] P. Goldstrass, W. Eckstein, Ch. Linsmeier, J. Nucl. Mater. 266–269 (1999) 581.
[7] Ch. Linsmeier, K.U. Klages, P. Goldstrass, Physica Scripta, submitted.
[8] R. Aratari, W. Eckstein, Nucl. Instrum. and Meth. B 42 (1989) 11.
[9] W. Eckstein, C. Carcia-Rosales, J. Roth, W. Ottenberger, Sputtering Data, IPP-Report 9/82, 1993.
[10] W. Eckstein, Computer Simulation of Ion–Solid Interaction, Springer, Berlin, 1991.
[11] W. Möller, W. Eckstein, J. Biersack, Comput. Phys. Commun. 51 (1988) 355.
[12] W. Eckstein, M. Hou, V.I. Shulga, Nucl. Instrum. and Meth. B 119 (1996) 477.
[13] E. Gauthier, W. Eckstein, J. Laszlo, J. Roth, J. Nucl. Mater. 176&177 (1990) 438.
[14] J. Roth, J. Bohdansky, W. Ottenberger, J. Nucl. Mater. 165 (1989) 193.
[15] D. Briggs, M. Seah, Practical Surface Analysis by Auger and X-ray Photoelectron Spectroscopy, Wiley, Chichester, 1983.
[16] P. Goldstrass, Ch. Linsmeier, Nucl. Instrum. and Meth. B 161–163 (2000) 411.
[17] J. Luthin, Ch. Linsmeier, Surf. Sci. 454–456 (2000) 78.
[18] Meyer, E. Reinhart, D. Borgmann, G. Wedler, Surf. Sci. 320 (1994) 110.
[19] Moulder, et al., Handbook of X-ray Photoelectron Spectroscopy, Physical Electronics Inc, Eden Prairie Minnesota, 1995.
[20] I. Barin, Thermochemical Data of Pure Substances, vol. 1, third ed., VCH, Weinheim, 1995.

ELSEVIER

Journal of Nuclear Materials 290–293 (2001) 25–32

journal of nuclear materials

www.elsevier.nl/locate/jnucmat

Mixed material formation and erosion

Ch. Linsmeier *, J. Luthin, P. Goldstraß

Max-Planck-Institut für Plasmaphysik, EURATOM-Association, Boltzmannstr. 2, D-85748 Garching, Germany

Abstract

The formation of mixed phases on materials relevant for first wall components of fusion devices is studied under well-defined conditions in ultra-high vacuum (UHV). This is necessary in order to determine fundamental parameters governing the basic processes of chemical reaction, material mixing and erosion. We examined the binary systems comprising of the wall materials beryllium, silicon, tungsten and titanium and carbon, the latter being both a wall material and a plasma impurity. Experiments were carried out to study the interaction of carbon in the form of a vapor-deposited component on clean, well-defined elemental surfaces. The chemical composition and the binding state are measured by X-ray photoelectron spectroscopy (XPS) after annealing treatments. For all materials, a limited carbide formation is found at room temperature. Annealing carbon films on elemental substrate leads to a complete carbidization of the carbon layer. The carbide layers on Be and Si are stable even at very high temperatures, whereas the carbides of Ti and W dissolve. The erosion of these two metals by sputtering is then identical to the pure metals, whereas for Be and Si a protective carbide layer can reduce the sputtering yields.

Keywords: Beryllium; Carbide; Carbon; Carbon deposition; Chemical erosion; Composite materials; Deposition; Diffusion; Erosion; First wall materials; High-*Z* material; Material mixing; Silicon; Titanium; Tungsten; XPS

1. Introduction

The design of modern fusion devices relies heavily on the selection of different materials for the plasma-facing wall parts which are exposed to different particle and heat loads. Besides the elements beryllium, tungsten and carbon, which are the favorite materials in the ITER design [1,2], silicon is currently used for wall conditioning [3,4]. Beryllium was very successfully used in JET as a first wall material and improved the impurity levels and plasma performance significantly [5–8]. Other designs involved titanium as limiter material [9]. Due to particle and heat loads, the wall material is eroded and migrates as plasma impurity to other parts of the vacuum vessel. In addition to the bulk wall materials recycling impurities like oxygen which are highly reactive are of concern. These impurities are deposited with particle energies ranging from thermal energy to several keV, depending on the ionization history and location of redeposition. Implantation and deposition of impurities lead to the formation of multi-elemental layers (e.g., [10]). The altered surfaces exhibit different qualities regarding the physical and chemical behavior compared to the originally designed first wall material. In particular, the physical and chemical erosion, thermal conductivity, hydrogen inventory properties are determined by stoichiometry, composition and chemical state of the surface of first wall materials.

Mixed phases have been addressed in the PSI literature. However, models proposed to describe the behavior of wall materials under plasma-exposed conditions in a fusion vessel are based solely on kinematic interactions, e.g., [11,12]. To predict the behavior of first wall materials for the strongly varying conditions within a real fusion experiment, the fundamental properties of the particle-surface interactions, surface chemistry and diffusion phenomena must be known. We therefore venture on projects which reduce interactions to few, well-controllable parameters to gain an insight into these processes.

* Corresponding author. Tel.: +49-89 3299 2285; fax: +49-89 3299 2279.

E-mail address: linsmeier@ipp.mpg.de (Ch. Linsmeier).

0022-3115/01/$ - see front matter
PII: S0022-3115(00)00428-1

2. Experimental

The task to determine the fundamental properties of the interaction of potential wall materials with impurities from the plasma requires very well-defined conditions. Parameters like surface composition and sample temperature must be controlled thoroughly. It is also necessary to have influence on the energy and composition of the interacting species. Therefore, all our experiments are carried out under ultra-high vacuum (UHV) conditions. Main tools for the characterization of mixed materials are photoelectron and ion spectroscopies. X-ray photoelectron spectroscopy (XPS) probes core-level transitions giving information on the specific element, including its chemical environment. Ion spectroscopies are accelerator techniques like the Rutherford backscattering spectroscopy (RBS). Our experimental setup ARTOSS [13] combines both surface sensitive tools and ion beam techniques available through a 3 MV tandem accelerator in one chamber. Also available in situ are the different ion sources for sample bombardment at energies between 100 eV and 20 keV, gas admission facilities and an electron beam evaporator, used to deposit carbon. For high-resolution XPS measurements, a second UHV system is available [14], equipped with a monochromatic Al X-ray source. This analysis chamber is connected to a preparation chamber where thin films can be prepared by electron beam evaporation from several sources. Gas admission is possible along with the formation of atomic species by means of a microwave discharge source [15]. The samples used in theses studies were polycrystalline foils of titanium and tungsten, a Si(1 0 0) wafer and a beryllium single crystal with (0 0 0 1) orientation. All samples are about 1 mm thick and have a surface area of approx. 1 cm^2. The surfaces are cleaned before carbon deposition by Ar^+ sputtering and/or heating. Carbon is deposited from an Omicron EFM3 evaporation source using high-purity (99.999%) carbon. The binding energies in the XPS spectra are referenced to the Au $4f_{7/2}$ signal at 84.0 eV determined on a clean gold surface.

3. Binary systems

3.1. Room temperature reactivity

Reactivity of the materials tungsten, titanium, silicon and beryllium at room temperature (~300 K) is studied at thermal carbon particle energies deposited from an electron beam evaporation source. XPS is used to determine the carbon amount on the W, Ti, and Si surfaces. In the Be experiments, the carbon layer thickness is additionally determined by RBS. To decide whether the deposited carbon is elementary or has reacted with the substrate material, the C 1s photoelectron peak is measured by XPS. Fig. 1 shows the C 1s spectra after depositing about two monolayers (ML) of carbon on Ti and Be and less than one ML on Si and W, respectively. The data are presented without background subtraction. In all four cases the C 1s intensity exhibits a peak at the binding energy characteristic for the respective carbide. The peak positions for the carbides are taken from the literature (Ti, Si, W [16]) or measured in a separate experiment (Be [18]). The hatched area in Fig. 1 indicates the binding energy range of elementary carbon. For the very thin carbon layers in the case of tungsten and silicon, almost all the C 1s intensity is in the carbide peak. For Si, a shoulder in the elementary carbon area is observed. The strong background in the W signal is due to a neighboring photoelectron peak (W $4d_{3/2}$) and not related to the C 1s signal. For greater coverages in the case of Ti and Be, the intensity in the elementary carbon area is larger. In the Ti spectrum, a distinct second peak is observed. The larger elementary signal in the case of

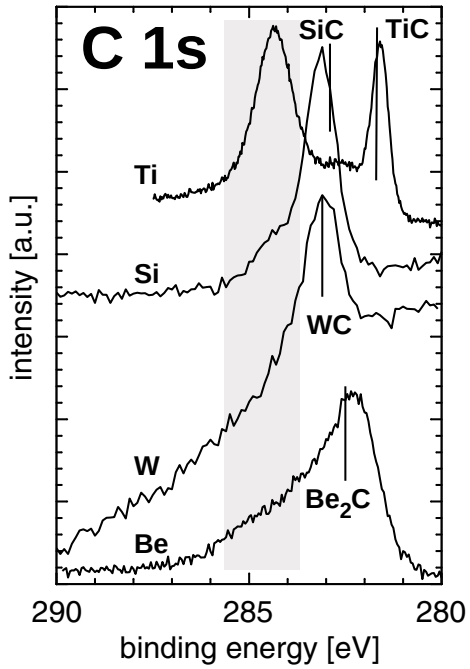

Fig. 1. XPS spectra in the C 1s energy range of thin carbon layers, deposited on the substrates at room temperature. The coverages for Si and W are below one monolayer, for Ti and Be about two monolayers. The vertical lines indicate the binding energies for the respective carbides, taken from the literature [16,18]. Peaks originating from elementary carbon appear in the shaded area.

Ti may be due to a larger carbon amount, since quantification is based in this case on the inelastic mean free path of the photoelectrons, whereas in the case of Be it is carried out by RBS measurement. Therefore, uncertainty in the Ti quantification is much larger than in the case of Be. Nevertheless, both elements exhibit a strong carbidic peak besides the intensity at higher binding energies.

The carbide formation starts at very low coverages and continues as long as there is a direct contact between carbon and the supporting element. Fig. 2 shows the development of the C 1s contributions of carbidic and elementary carbon (the latter separated into graphitic and disordered carbon) for the beryllium substrate. The carbon amounts are deposited sequentially on the clean Be substrate. RBS measurements are used to quantify the carbon coverage. The carbon modifications are distinguished by fitting three Gauss–Lorentz functions to the C 1s signal, each centered at the known peak positions [17,18]. As can be seen in Fig. 2, for low carbon coverage the reaction to Be_2C dominates over the elementary carbon deposition. This is true up to a carbon coverage of 9×10^{15} cm^{-2} where the intensities of carbidic and elementary carbon balance. From this coverage on the carbide amount saturates and further deposited carbon is accumulated in elementary form. The total carbon intensity increases linearly with coverage up to $\sim 2 \times 10^{16}$ cm^{-2}. For larger carbon surface densities, attenuation of the C 1s photoelectrons in the carbon layer on beryllium leads to a change in the slope of the curves. Since the carbide signal intensity starts to decrease, it can be concluded that the carbide is located at the carbon–substrate interface only and further carbon deposition leads to an increase in the elementary carbon coverage, but not to a further carbide formation.

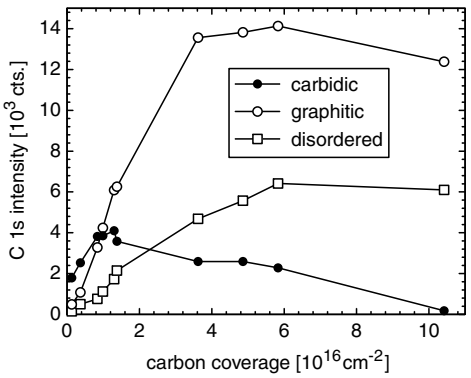

Fig. 2. Different states of carbon in deposited layers on beryllium, measured by XPS at room temperature. Plotted are the integrals of the components in the C 1s signal, determined by curve fitting, as a function of the carbon amount. The carbon coverage is determined by RBS.

3.2. Carbidization

The carbidization process of the elements W, Ti, Si and Be is studied by heating a carbon layer deposited on the samples at room temperature (thickness: several monolayers) to elevated temperatures and measuring the XPS spectra after each step. The corresponding spectra and the temperature profiles are shown in Fig. 3–8.

We begin the discussion of the carbidization process with beryllium. Fig. 3 shows the Be 1s and C 1s binding energy ranges of a carbon film on Be after evaporation (300 K) and after subsequent annealing steps. The Be 1s intensity is strongly attenuated by the overlying carbon film. From the Be 1s and C 1s intensities, a carbon layer thickness of 1.1 nm is calculated (assuming a carbon density of 1.8 g cm^{-3}). The C 1s peak indicates that the majority of the carbon is elementary, the shoulder at higher binding energies is due to a disordered graphite contribution [17]. A small contribution at 282.6 eV originates from the carbide at the carbon/metal interface. This thin carbidic layer is also seen in the Be 1s spectra. At the high energy side of the attenuated metallic Be peak a shoulder appears. Up to an annealing temperature of 473 K only small changes in the

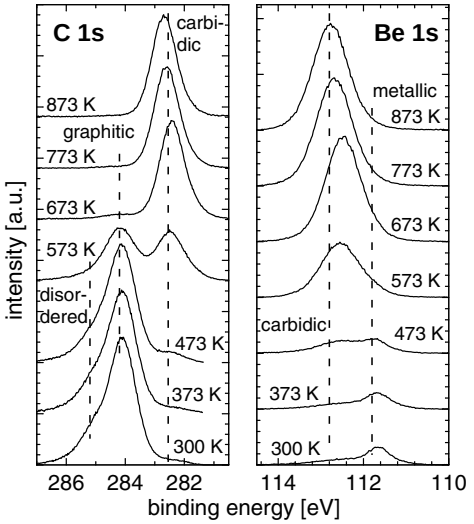

Fig. 3. Series of XPS spectra after deposition and annealing of a carbon layer on a Be (0 0 0 1) substrate. The annealing temperatures are indicated at the respective spectra. The broken lines indicate peak positions for metallic, carbidic and disordered species, respectively.

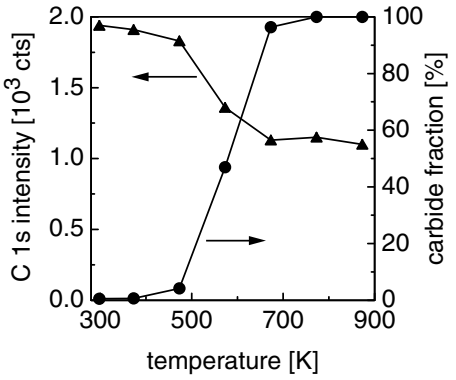

Fig. 4. Carbon intensity and carbide fraction in the total C 1s intensity, measured by XPS at a thin carbon film on Be (0 0 0 1).

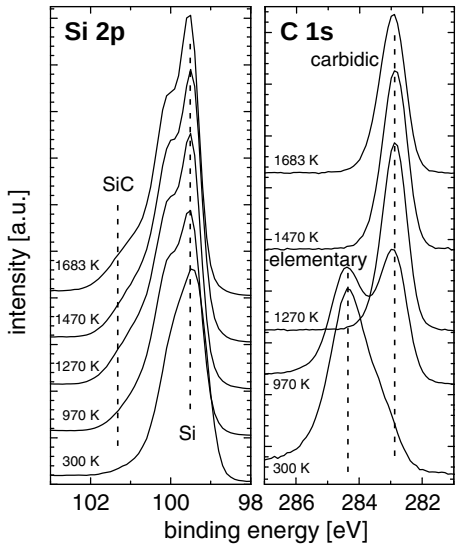

Fig. 5. Series of XPS spectra after deposition and annealing of a carbon layer on a Si (1 0 0) substrate. The annealing temperatures are indicated at the respective spectra. The broken lines indicate peak positions for elementary and carbidic species, respectively.

intensities are observed. In the C 1s region the disordered fraction of graphite decreases slightly and a small peak develops at the carbide position. These changes are also observed in the Be 1s spectra. Fig. 4 shows that up to 473 K the C 1s intensity and the carbide fraction of the C 1s signal change only to a small extent. A strong interaction between carbon and beryllium sets in above

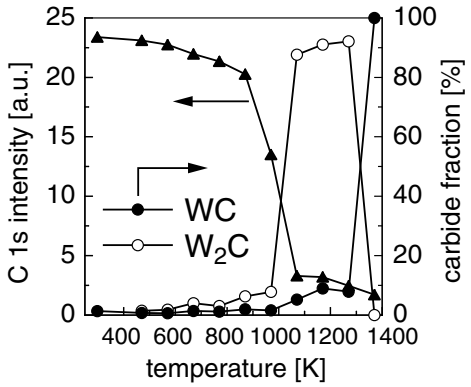

Fig. 6. Temperature profile measured by XPS from a thin carbon layer on polycrystalline tungsten. The circles indicate the carbide and subcarbide contributions to the total C 1s intensity, determined by peak fitting. The triangles show the decrease of the C 1s intensity with annealing temperature.

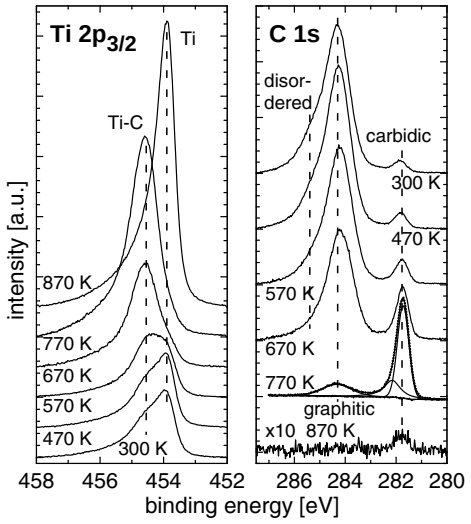

Fig. 7. Series of XPS spectra after deposition and annealing of a carbon layer on a polycrystalline Ti substrate. The annealing temperatures are indicated at the respective spectra. Please note that the Ti series runs bottom-up, whereas the C series starts with the top spectrum. The broken lines indicate peak positions for elementary and carbidic species, respectively. The 770 K spectrum shows the decomposition of the data by peak fitting in an elementary carbon peak and two carbidic peaks. The 870 K C 1s spectrum is enlarged by a factor of 10 compared to all other spectra.

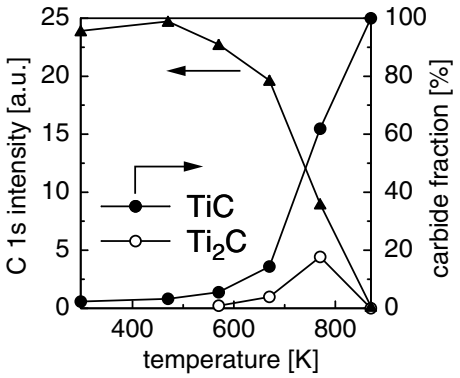

Fig. 8. Temperature profile measured by XPS from a thin carbon layer on polycrystalline titanium. The circles indicate the carbide and subcarbide contributions to the total C 1s intensity, determined by peak fitting. The triangles show the decrease of the C 1s intensity with annealing temperature.

473 K, the spectra after the 573 K step reveal more beryllium at the surface (intensity in the Be 1s region increases). The carbon binding energies indicate that both carbidic and elementary carbon are present in the surface layer, after 573 K approximately half of the carbon has reacted to carbide. The Be signal is already dominated by a peak at the binding energy of Be_2C at 112.8 eV with small intensity at the metallic Be position. The carbidization process proceeds as the annealing temperature is further increased and is almost complete already after annealing to 673 K. The carbide fraction in the C 1s signal reaches 100% and between 673 and 873 K no change in the carbon intensity is observed, as shown in Fig. 4. This demonstrates that carbon does not diffuse into the beryllium bulk upon further annealing once the carbidization is complete. At least up to this temperature the formed Be_2C layer on the beryllium substrate is stable. The interaction of a carbon layer with beryllium is discussed in greater depth in a separate contribution within this volume [19].

The carbidization of silicon is studied at a Si(1 0 0) surface with a carbon adlayer of approx. 0.3 nm thickness. Fig. 5 shows the XPS C 1s and Si 2p spectra for the annealing experiments up to 1683 K. Due to the small carbon coverage the Si 2p spectra are dominated by the elementary Si signal. It consists of a doublet which is not resolved in our spectra but leads to the asymmetric peak shape. Binding energies of the Si $2p_{3/2}$ peak for elementary (99.5 eV) and carbidic (101.3 eV) Si are indicated by broken lines. The C 1s spectrum taken directly after carbon evaporation exhibits a peak of elementary carbon and a small shoulder at the binding energy of SiC. This interfacial carbide is formed during carbon evaporation. Further reaction takes place at elevated temperatures. Almost half of the carbon (41%) has reacted after the 970 K annealing step which causes a more prominent asymmetry in the Si 2p peak and a second peak due to SiC in the C 1s region at 282.95 eV. All the carbon has reacted to SiC after annealing to 1470 K and no further changes are observable after 1683 K. SiC formed at the surface is stable up to this temperature. After 1270 K annealing step the C 1s intensity decreases only very little from 55.7% to 49.5% of its initial value.

The interaction of carbon with tungsten was described earlier [17] and partly also in a separate contribution in this volume [20] and therefore is only summarized here. Fig. 6 shows the carbidization behavior of polycrystalline tungsten between room temperature and 1370 K. Carbide is formed initially during the carbon evaporation at room temperature at the interface and the reaction proceeds with increasing substrate temperature. Between room temperature and 970 K the C 1s intensity decreases only slightly. In this temperature regime also only little additional subcarbide (W_2C) is formed. The C 1s intensity decrease therefore indicates an intermixing of carbon and tungsten in the surface layer to which XPS is sensitive. Above 970 K W_2C becomes the dominating phase. Above 1270 K the subcarbide is converted into tungsten carbide (WC). Unlike the carbide phases on beryllium and silicon, the tungsten carbides do not inhibit diffusion of carbon from the surface into the bulk. At the onset of W_2C formation where the carbon intensity is still 58% of its initial value the carbon concentration in the surface layer decreases to 14%. However, for higher temperatures the carbon amount does not change so rapidly any more. After the 1270 K treatment the intensity decreases only to 11%. The 1370 K annealing step then results in a further decrease to 7% of the room temperature intensity.

The carbidization of titanium proceeds very similar to the process on tungsten. Fig. 7 shows the XPS spectra in the Ti 2p and C 1s binding energy ranges taken after deposition of ca. 1 nm carbon on a polycrystalline titanium substrate and after the indicated annealing steps. The Ti peak consists of a metallic signal at 453.9 eV and a second signal from titanium carbide giving rise to the shoulder at 454.6 eV. The corresponding C 1s spectrum shows a large elementary carbon signal composed of graphitic and disordered contributions. The carbide peak is well separated at a binding energy of 281.8 eV. Upon annealing the carbon reacts with titanium under carbide formation. The processes of carbidization and carbon loss are depicted in Fig. 8. Up to a substrate temperature of 570 K the carbide intensity increases only slightly, the TiC fraction in the total C 1s intensity increases from initially 2.5% to 6.1%. The total carbon intensity does not change significantly. However, after this annealing temperature the data points can only be

fitted by introducing a further peak at a binding energy of 282.4 eV between the TiC and the elementary carbon. This is shown for the 770 K C 1s spectrum in Fig. 7. The peak integrals determined during the fit procedures are shown in Fig. 8. The total carbon intensity starts to drop above 570 K. This continues after the annealing steps at 670 and 770 K after which the carbon intensity remains only 38% of the initial value. The TiC peak intensity increases and becomes the dominating peak in the C 1s region after 770 K. Parallel to the TiC peak also the peak at 282.4 eV grows. In analogy to the tungsten system we attribute this peak to titanium subcarbides (Ti_8C_5, Ti_6C_5) [26,27] with a C 1s binding energy of around 282.4 eV. This is supported by observations in the literature where superlattice lines were found in neutron diffraction experiments of Ti–C alloys annealed between 1373 and 2273 K [21]. These results were recorded as tentative phases in the Ti–C phase diagram [22]. Unfortunately, the Ti 2p signals of metallic Ti and carbides are too close to shed light on the carbide phases. The intensity in this energy region is dominated by the carbide peak at a binding energy of 454.6 eV. The initially larger metallic contribution at 453.9 eV (82% of the peak area after carbon deposition) has decreased to a 16% fraction after annealing to 770 K. These values are estimates determined by fitting two asymmetric Doniach–Šunjić functions [23] to the Ti 2p peaks at the energies for titanium in metallic and carbidic chemical states. The next annealing step at 870 K leads to a complete dissolution of the carbide on the Ti surface. This is very different from the other elements under consideration so far. The Ti 2p region changes both in intensity and in the shape of the peak. The Ti $2p_{3/2}$ peak is fitted perfectly with only one Doniach–Šunjić function at a binding energy of 453.9 eV indicating that no carbide contributes to the signal. The intensity of this peak is the largest of the whole series of spectra. Correspondingly, the C 1s region shows hardly any peak. The signal depicted in Fig. 7 is enlarged by a factor of 10 compared to the other spectra and its integral is only 11 counts. The calculated carbon amount giving rise to this signal is 2% of a monolayer. It has to be noted, however, that the titanium surface becomes more and more reactive during the loss of carbon from the surface. During the last annealing steps at 770 and 870 K the surface accumulates oxygen which becomes the dominating signal after these temperatures. At present it is not clear whether this oxygen has any influence on the behavior described above.

3.3. Carbidization vs diffusion

From the last paragraph it becomes clear that two processes dominate the interaction of carbon with elemental surfaces: carbide formation and carbon diffusion. The chemical reaction between the carbon and the substrate starts in all cases already at room temperature and leads to a carbide layer at the interface between the deposited carbon and the substrate. However, in all cases studied so far the reactions come to a halt after one to several monolayers of carbide have been formed. The driving force of the carbidization reaction is the formation enthalpy of the carbides. All Gibbs energies (free enthalpies) for the materials under study here [24] are exergonic and therefore energy is released during the formation of carbides at room temperature. These negative enthalpies are the reason for the room temperature reactivity. The carbidization reaction can be written as the generic reaction equation:

$$\nu_M M + \nu_C C \rightleftharpoons \nu_{MC} MC + \Delta G_f \quad (1)$$

The law of mass action associated with this formation equation

$$[MC]^{\nu_{MC}} = [M]^{\nu_M}[C]^{\nu_C} e^{-(\Delta G_f/RT)} \quad (2)$$

illustrates that a more negative value of ΔG_f will increase the concentration of the carbide [MC]. Therefore, TiC is the most stable carbide in this selection, followed by Be_2C, SiC and the tungsten carbides (WC and W_2C). From Eq. (2) we can also see that the concentration of carbide depends on the concentration of both the element [M] and that of carbon [C], i.e., the availability of components for the reaction. At this point the diffusion of carbon into the respective substrate material becomes important. Fig. 9 summarizes the surface carbon concentration in the experiments described in Section 3.2. The curves are normalized to the initial carbon intensity after deposition at room temperature. In all cases the carbon layer thickness is thin enough that all carbon can be detected by XPS. The carbon intensity reflects the

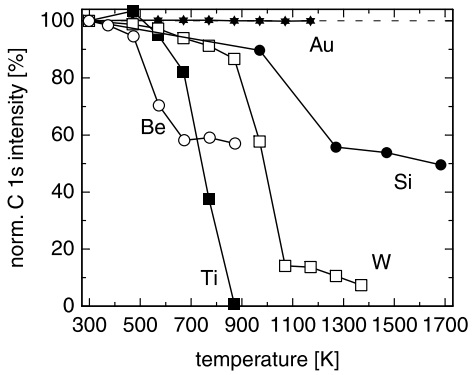

Fig. 9. Changes in the C 1s intensity measured by XPS during annealing of thin carbon films deposited on the indicated materials. The curves are normalized to the initial carbon intensity at room temperature (100%).

amount of carbon available in the surface layer. In addition to the elements Be, Si, Ti and W where carbide formation takes place, a reference experiment with a thin carbon layer on gold is plotted. Gold is inert and does not react with carbon under carbide formation. Moreover, carbon is insoluble in gold [22] and therefore no diffusive losses are expected. This is shown by the measured data points which stay constant at 100% level for all examined temperatures. It is observed that for all reactive elements the interaction can be divided into three phases. Phase I starts at room temperature and continues up to a temperature where the carbon intensity starts to drop. This phase is characterized by small carbon losses. We interpret this phase by an intermixing of the carbon layer with the substrate material which leads to substrate material in the analysis range of XPS. In Phase II the carbon intensity starts to decrease very fast. The start temperatures of this phase are also the temperatures where quantitative carbide formation sets in. Phase III finally is defined as the temperature range where the decrease of carbon intensity stops. This phase is only present in the cases of Be, Si and W. However, for W and, to a smaller extent for Si also, the carbon intensity decreases further even in phase III, but much slower than in phase II. For Ti no phase III is observed, the C intensity drops to zero at the end of phase II. In the cases of Be and Si the carbon intensity remains at a high level which indicates a stable carbide layer on top of the elemental substrate. The tungsten carbide, however, is not stable and dissolves into the substrate bulk. Other than in the case of titanium, there is a small amount of W_2C/WC remaining at the surface. The TiC is dissolved completely and at the final temperature only a trace of carbon can still be detected.

The different behavior of the carbon layers, the carbide formation and the dissolution of carbon in the substrate for the four elements Be, Si, W and Ti can be understood in terms of the structure of their respective carbides. Generally, solid carbides can be divided into three classes. Be_2C is an example of an ionic solid. The lattice constituents are ions and the interaction between them is electrostatic. Therefore, a diffusion of one lattice constituent involves the transport of charged particles in the field of the other ions. It can be qualitatively understood that transport of ions through the ionic lattice is difficult since the Coulomb barriers have to be overcome. The ionic compound Be_2C therefore remains stable even at much higher temperatures than the onset of the Be_2C formation. SiC represents the class of covalent solids. These solids are characterized by direct covalent bonds between the lattice constituents. In this picture it also becomes clear that diffusion of one component into a covalent solid needs directed bonds to be broken. Therefore, diffusion of carbon out of a SiC layer into the Si substrate is not favorable. From the covalent structure of SiC the stability of the carbide layer on the Si substrate can be understood. The situation for the transition metal carbides is different. Both Ti and W form metallic carbides where the carbon sits in the octahedral or trigonal prismatic sites in a metal atom spheres packing. Structure of the carbide is determined by the packing of metal atoms. In the case of the carbides WC and TiC carbon atoms occupy all octahedral sites. In W_2C and possibly also Ti subcarbides carbon fills half of the octahedral sites. Since there is no direct bond between metal and carbon atoms, a diffusion of carbon between different equivalent sites can explain the loss of carbon into the bulk substrate. In the case of tungsten a small concentration of WC remains stable even at high temperatures. In Ti, the diffusion of carbon is so high that the formed TiC layer is dissolved completely at elevated temperatures.

The final composition of the surface layer after an annealing treatment has profound influence on the erosion behavior of the material. With regard to sputtering, the amount of substrate material eroded by this process is proportional to the surface concentration of this constituent. If, as is the case for the elements Be and Si, a stoichiometric carbide layer is formed on the substrate and this layer remains stable at elevated temperatures, erosion by sputtering is only possible at the fraction of this element present in the carbide. In the case of Be_2C, the sputtering yield for Be is reduced by 1/3 compared to pure Be (without taking into account any surface binding energy effects). This reduction of the sputtering yield does not take place for materials like Ti and W where the formed surface carbide is not stable at elevated temperatures. After the carbide layer has been dissolved in these cases, the surface is dominated by the metal. Therefore, the sputtering yield of the pure metal is not reduced due to the dilution of the surface layer by carbon.

4. Summary and conclusions

All elements under study here (Be, Si, W, Ti) react with carbon already at room temperature. The thickness of the carbide layer is limited to the very interface between the carbon layer and the substrate, thus from one to several monolayers. Upon annealing to higher temperatures, the carbon layer reacts with the substrate material under carbide formation. The carbide layers on beryllium and silicon are stable up to very high temperatures, whereas on titanium and tungsten carbon diffusion into the bulk metal is important. This diffusion dissolves the carbide layer completely in the case of titanium and on tungsten only a small carbide amount is stable up to 1683 K. The different behavior of the elements can be understood in terms of the reaction enthalpy of carbide formation and of diffusion. The diffusion of the carbon in the host material is determined by the

structure of the respective carbide. Ionic (Be_2C) and covalent (SiC) carbides exhibit a strong bonding between the element and carbon and therefore no or only very small diffusion is observed. TiC and WC both are metallic carbides where the metal atom packing determines the structural properties. This is the reason why with both metal carbides a high diffusion of carbon is observed. The concentration of metal carbide present at a certain temperature therefore is determined by the reaction enthalpy (which is negative in all cases here and therefore favors carbidization over decomposition) and the availability of carbon for the carbide formation. If carbon is removed from the equilibrium, the carbide at the surface is decomposed. This has a large impact on the sputtering yield: the yield of the element under consideration in a mixed material is determined first of all by the stoichiometry at the surface. If the element fraction is reduced by compound formation, less of this element will be sputtered. If the carbide layer, however, is removed by carbon diffusion into the bulk, the surface concentration and also the sputtering yield of this element are similar to the pure elemental surface.

In extension to the binary systems discussed in this paper ternary mixtures between a wall material, carbon and oxygen as an impurity in fusion plasmas are of great importance. Several new phenomena regarding the surface reactivity and erosion properties are observed. Due to limited space, the ternary systems Be–C–O and W–C–O cannot be discussed here. We direct the reader to the respective contributions in these proceedings [20,25].

References

[1] ITER Project, Detailed Design Document, IdoMS# G 16 DDD 2 96-11-27 W.

[2] R.A. Anderl, R.A. Causey, J.W. Davis, R.P. Doerner, G. Federici, A.A. Haasz, G.R. Longhurst, W.R. Wampler, K.L. Wilson, J. Nucl. Mater. 273 (1999) 1.

[3] J. Winter, H.G. Esser, G.L. Jackson, L. Könen, A. Messiaen, J. Ongena, V. Philipps, A. Pospieszczyk, U. Samm, B. Schweer, B. Unterberg, the TEXTOR Team, Phys. Rev. Lett. 71 (1993) 1549.

[4] V. Rohde, R. Neu, R. Dux, T. Härtl, H. Maier, J. Luthin, H.G. Esser, V. Philipps, the ASDEX Upgrade Team, ECA vol. 23J (1999) 1513.

[5] J.T. Thomas, the JET team, J. Nucl. Mater. 176&177 (1990) 3.

[6] R. Satori, G. Saibene, D. Goodall, E. Usselmann, P. Coad, D. Holland, J. Nucl. Mater. 176&177 (1990) 624.

[7] P. Rebut, M. Hugon, S. Booth, J. Dean, K. Dietz, K. Sonnenberg, M. Watkins, JET-R(85)03, JET Joint Undertaking, Abington, 1985.

[8] E. Bertolini, Fus. Eng. Design 27 (1995) 27.

[9] P. Grigull et al., W7-AS Team, NBI Team, ECRH Group, J. Nucl. Mater. 196–198 (1992) 101.

[10] R. Behrisch, M. Mayer, C. García-Rosales, J. Nucl. Mater. 233–237 (1996) 637.

[11] D. Naujoks, R. Behrisch, In: Proceedings of the International Conference on Plasma Physics, Innsbruck, vol. 16C, part II, 1992, p. 843.

[12] Y. Hirooka, Fus. Eng. Design 37 (1997) 299.

[13] Ch. Linsmeier, P. Goldstraß, K.U. Klages, Phys. Scr. (submitted).

[14] S. Miller, G. Berning, H. Plank, J. Roth, J. Vac. Sci. Technol. A 15 (1997) 2029.

[15] Ch. Linsmeier, J. Wanner, Surf. Sci. 454–456 (2000) 305.

[16] J.F. Moulder, W.F. Stickle, P.E. Sobol, K.E. Bomben, in: J. Chastain (Ed.), Handbook of X-Ray Photoelectron Spectroscopy, Perkin–Elmer, Eden Prairie, MN, 1992.

[17] J. Luthin, Ch. Linsmeier, Surf. Sci. 454–456 (2000) 78.

[18] P. Goldstraß, Ch. Linsmeier, Nucl. Instrum. and Meth. B 161–163 (2000) 411.

[19] P. Goldstraß, K.U. Klages, Ch. Linsmeier, J. Nucl. Mater. this volume.

[20] J. Luthin, Ch. Linsmeier, these Proceedings.

[21] H. Goretzki, Phys. Status Solidi 20 (1967) K141.

[22] T.B. Massalski, H. Okamoto, P.R. Subramanian, L. Kacprzak, Binary Alloy Phase Diagrams, 2nd Ed., Version 1.0, ASM International, Materials Park, OH, 1996.

[23] S. Doniach, M. Šunjić, J. Phys. C: Solid St. Phys. 3 (1970) 285.

[24] I. Bahrin, Thermochemical Data of Pure Substances, 3rd Ed., Vol. 1&2, Weinheim, 1995.

[25] P. Goldstraß, Ch. Linsmeier, these Proceedings.

[26] N.V. Dzahalabadze, B.G. Eristavi, N.I. Maisuradze, E.R. Kuteliya, Phys. Metals Metall. 86 (1998) 59.

[27] B.V. Khaenko, S.Ya. Golub, M.P. Arbuzov, Kristallografiya 25 (1980) 112.

ELSEVIER

Surface Science 454–456 (2000) 78–82

surface science

www.elsevier.nl/locate/susc

Carbon films and carbide formation on tungsten

J. Luthin, Ch. Linsmeier *

Max-Planck-Institut für Plasmaphysik, EURATOM Association, Boltzmannstrasse 2, D-85748 Garching b. München, Germany

Abstract

The reaction of carbon films on tungsten substrates has been investigated using X-ray photoelectron spectroscopy (XPS). Thin C films were evaporated at room temperature on polycrystalline tungsten. For comparison with a non-reactive metal, gold substrates were used. After deposition, XPS analysis showed two different chemical states of unreacted carbon. A quantitative analysis of the deposited carbon amount was performed using the XPS intensities. The gold surface did not react with C after all annealing steps up to 1170 K, and no changes in the integral C 1s intensity were observed. The two C 1s states initially observed in the spectra converged into one peak with increased annealing temperatures. The tungsten samples were annealed up to temperatures of 1270 K. XPS analysis showed the stepwise formation of two different carbide phases. At temperatures below 870 K, the XPS spectra did not reveal any significant changes. At 970 K, the C 1s photoelectron peak was shifted towards lower binding energies. After annealing at 1270 K, a second shift occurred, indicating WC and W_2C formation. Above 870 K, the C concentration of the surface decreased distinctly with increasing annealing temperatures.

Keywords: Carbides; Carbon; Gold; Surface chemical reaction; Tungsten; X-ray photoelectron spectroscopy

1. Introduction

Tungsten is one of the candidate materials for the plasma facing components of the International thermonuclear experimental reactor (ITER) [1]. As long as both elements, tungsten and carbon, are introduced in the main chamber of a fusion experiment or reactor, the carbidization process is of great importance. Until now, there has been no systematic investigation of the interaction of carbon on tungsten substrates, which is necessary prior to the usage of tungsten or tungsten carbide as a first wall, blanket or divertor material in a fusion reactor [2,3].

To produce thin carbon films, a number of different methods have been made available, such as magnetron sputtering [4], mixing W and C plasma streams [5] or evaporation [6]. In particular, the evaporation technique provides well-controlled deposition and very clean carbon films in order to investigate the formation of carbide in the interfacial region [7].

2. Experimental

The thin carbon films investigated in this study were prepared by evaporating carbon from a 1.5 mm diameter graphite rod (Goodfellow, 99.999%) with an Omicron EFM3 electron beam evaporation source. To improve the performance of the Omicron device, an external HV power supply was used. During evaporation, the pressure in the preparation chamber was better than 3.0

* Corresponding author. Fax: +49-89-3299-2279.
E-mail address: linsmeier@ipp.mpg.de (Ch. Linsmeier)

0039-6028/00/$ - see front matter
PII: S0039-6028(00)00181-3

$\times 10^{-7}$ Pa, and the substrate was at room temperature (RT). Deposition rates between 0.01 and 0.04 nm/min were used. The substrates were polished polycrystalline tungsten and gold. To achieve a clean tungsten surface, repeated sputter/annealing (2 keV Ar^+/970 K) cycles were necessary. Prior to evaporation, the gold substrates were sputtered by Ar^+ to remove oxygen contamination. The evaporation chamber was connected by a UHV valve to a commercial XPS system (PHI 5600 ESCA). The experimental set-up is described in detail elsewhere [8]. To achieve the highest energy resolution, the hemispherical energy analyzer was driven at 2.95 eV pass energy, and monochromatic Al Kα radiation was used. The binding energies were calibrated with the Au $4f_{7/2}$ peak at 84.0 eV, where the full-width-at-half-maximum (FWHM) was smaller than 0.6 eV.

Annealing steps up to 970 K could be carried out in the analysis chamber. For higher temperatures, the samples had to be transferred into the preparation chamber, in which, using an electron beam heater, temperatures up to 1270 K could be achieved. In all cases, the desired temperature was reached within 10 min and held for 30 min.

To determine the binding energies and different fractions of binding states in the acquired XPS spectra, curve-fitting procedures were carried out using the MultiPak software package [9]. For the non-linear least-squares optimization procedure, a Gaussian–Lorentzian line shape was applied [10]. All the spectra presented in this paper are shown after a Shirley background subtraction [11].

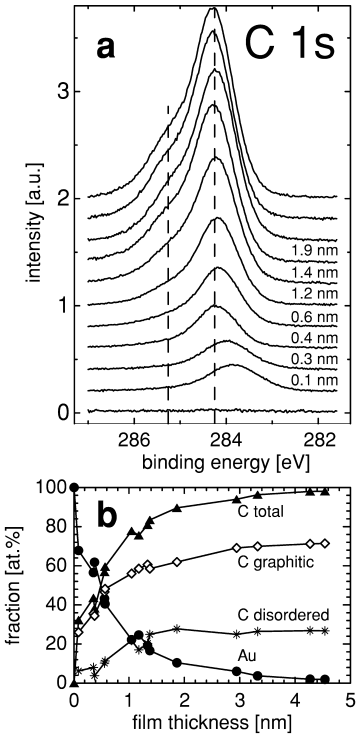

Fig. 1. C 1s core-level spectra of carbon films on gold (a) and composition of the samples within the XPS analysis depth (b).

3. Results and discussion

3.1. Characterization of deposited carbon films

After evaporating carbon onto tungsten at RT, the C 1s binding energy region in the XPS spectra consists of several peaks. To distinguish carbidic phases from adsorbed carbon, gold was used as a non-reactive metal. The carbon amount was quantified using the XPS intensities [12]. Film thicknesses were calculated from the C 1s intensities or the attenuated substrate intensities under the assumption of a layer growth and attenuation of the photoelectrons traveling through the material. A brief description of the calculation procedure is given in Ref. [13]. The thickness values are determined under the assumption of a layer growth, which is confirmed by both the carbon and substrate intensity development. However, the growth behavior has not yet been investigated in detail. The validity of the XPS quantification procedure was verified experimentally in the experiment ARTOSS at the IPP, in which in-situ XPS and Rutherford backscattering (RBS) measurements were performed for the Be–C system [14].

Carbon modifications after evaporation were studied on a gold substrate. C 1s core-level spectra of films with different thicknesses are shown in Fig. 1a. At a very low carbon coverage of 0.1 nm,

we obtain a C 1s peak with a binding energy of 283.9 eV. This peak shifts gradually to a value of 284.2 eV for the sample with the 0.4 nm carbon film, and the peak maximum remains at that value for all samples with higher carbon coverages. In the C 1s signal of the layers thicker than 0.4 nm, a second peak is detected at a binding energy of 285.2 eV, originating from a different binding state of the C atoms. The electronic and atomic structure of evaporated carbon films has already been investigated on Si(100) substrates [6,15]. Two carbon modifications were identified. A graphite-like state leads to a C 1s binding energy signal at 284.0 eV. A peak at 284.8 eV is associated with a lightly disordered carbon modification [16]. These results agree with our observations for the Au–C system.

The composition of the samples within the XPS analysis depth is shown in Fig. 1b. With increasing carbon film thickness up to 1.9 nm, the Au XPS intensity decreased. The two C 1s peak intensities increased. In this range, the fraction of the graphite-like coordinated carbon grows faster than the amount of disordered carbon. Above 1.9 nm, a thickness estimation from the XPS intensities is no longer reliable because the inelastic mean free path of the photoelectrons limits the analysis depth. For larger thicknesses, the flux meter of the evaporator is used as a measure of carbon layer thickness.

To investigate the temperature-dependent behavior of the evaporated carbon films, a sample with 3.0 nm carbon coverage was heated up to 1170 K in steps of 100 K (Fig. 2a). No changes in the integral C 1s intensity were observed, which means that the carbon did not diffuse into the bulk of the substrate material. The shape and intensity of the Au $4f_{7/2}$ peak remained constant after all annealing steps. The gold surface therefore did not react with C under these conditions. Fig. 2b shows the fractions of the different C 1s binding states. The disordered carbon converted into the thermodynamically stable graphitic phase with increasing annealing temperature [17]. This transition of the C 1s signal from two peaks into one signal on the inert gold surfaces, due to the ordering of the graphite structure in the evaporated films, will subsequently be used to distinguish carbon binding states on a reactive tungsten substrate.

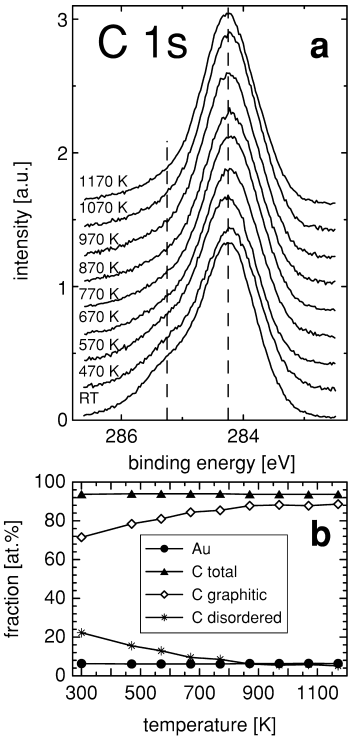

Fig. 2. C 1s core-level spectra of a carbon film on gold as a function of annealing temperature (a) and fractions of the different binding states (b).

3.2. Carbide formation on tungsten

The temperature dependence of the carbide formation was investigated with a 1.0 nm thick carbon film evaporated onto a clean tungsten substrate at RT. The residual oxygen contamination of the cleaned surfaces was less than 3 at.% in all cases. C 1s core-level spectra are shown in Fig. 3a from RT up to 1270 K. The RT spectrum can be fitted with three binding states, two belonging to the different elementary carbon states (graphitic and disordered) and one additional peak at a binding energy of 283.1 eV. The growth of carbon adlayers on tungsten without the formation of a chemical compound (carbides) is similar for

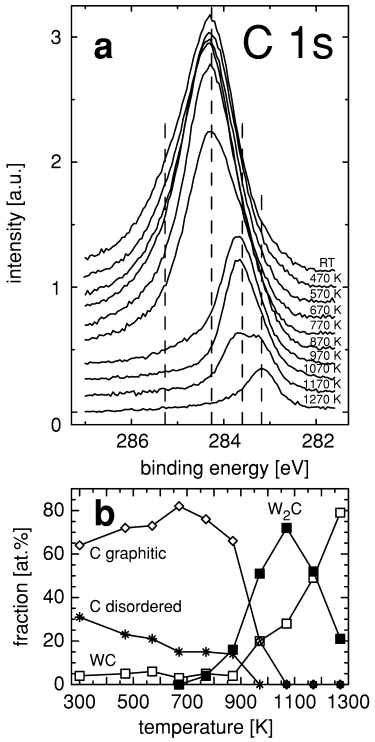

Fig. 3. C 1s core-level spectra of a 1.0 nm thick carbon film on tungsten as a function of annealing temperature (a) and fractions of the different binding states (b).

several metals. For an inert gold surface, this is demonstrated above. For beryllium and silicon as other reactive surfaces, this was shown recently in our laboratory [18]. The third C 1s peak indicates a chemical reaction between carbon and tungsten, forming tungsten carbide. The nature of the tungsten carbide will be elucidated in the following section.

Annealing steps below 870 K did not reveal any significant changes in the C 1s region, but a reduction in the peak FWHM was observed. This resulted from the conversion of the two initially observed elementary C 1s states into a graphitic modification, as demonstrated on the gold substrate. A small amount of approx. 5 at.% WC was present in all spectra up to that temperature. To fit the spectrum recorded at 770 K, we had to include a fourth peak located at 283.6 eV, which we assigned to ditungsten carbide, W_2C. All C 1s and W $4f_{7/2}$ binding energies determined in this work are summarized in Table 1. The assignment of ditungsten carbide (W_2C) and tungsten monocarbide (WC) was deduced from the W–C phase diagram [19]. After annealing at 970 K, the C 1s signal maximum had shifted to that value, indicating that this second carbide phase was dominant at this temperature. Further annealing steps led to a further shift in the peak maximum of 0.5 eV towards lower binding energies, where we had already located the WC carbide phase at 283.1 eV in the spectra of the thin carbon adlayers on tungsten.

Table 1
Binding energies for C 1s and W $4f_{7/2}$ in evaporated carbon films and in tungsten carbides

Substance	C 1s [eV]	W $4f_{7/2}$ [eV]
Graphitic carbon	284.2	
Disordered carbon	285.2	
WC	283.1	32.2
W_2C	283.6	31.8
W		31.4

In Fig. 3b, the fractions of the different C 1s binding states are plotted against the annealing temperature. Up to about 770 K, the two different elementary carbon phases showed the same behavior as described for carbon on gold substrates. The initially disordered carbon layer formed by impinging carbon atoms and clusters from the evaporation source anneal and order to a graphitic carbon modification. Additionally, an almost constant WC concentration of 5% was present. Starting at 770 K, carbide formation set in, initially with the formation of W_2C. Above 870 K this phase and all residual carbon was converted into WC. After heating to 1270 K, most of the carbon had reacted with tungsten under WC formation. From the trend of the curve, a complete reaction to WC at higher temperatures (not yet accessible in our experiment) can be expected. This stepwise formation of W_2C and WC has been reported in the literature for the reaction of W–C powder

mixtures heated in H_2 [20,21]. In contrast to our results, the reactions set in at higher temperatures. The reason for this discrepancy could be the analysis technique. The reaction of the powder mixtures was followed by X-ray diffraction (XRD), where a minimum crystallite size was necessary to detect compound formation. XPS, however, is already sensitive to small amounts of reacted species that do not even have to be crystalline and detects fractions of a monolayer.

The carbide formation in surface layers was confirmed by XRD for a 100 nm tungsten film on polycrystalline graphite. This sample was heated to 1270 K for 30 min, and the XRD measurement was accomplished at a grazing incidence of 2°. The diffraction pattern consists of the graphite substrate signals and a number of weaker diffraction peaks that all originate from WC. Only a very weak signal at the W_2C main diffraction angle indicates a minor amount of this species. The XPS spectrum of this sample is almost completely identical to the spectrum recorded for the carbon film on tungsten annealed at 1270 K. It is particularly notable that the composition of 20% W_2C and 80% WC is the same in both layers, and this is obviously determined by the reaction temperature.

4. Summary

The evaporation of carbon onto polycrystalline tungsten at RT leads to the formation of a thin reacted carbide layer (WC stoichiometry) and carbon in two modifications, as observed from C 1s XPS spectra. The carbon phases were determined by using gold as an inert substrate. High-resolution XPS spectra reveal that most of the carbon has a graphitic structure, and a minor fraction is disordered. The graphitic/disordered ratio depends on the film thickness. Annealing leads to a single carbon peak, indicating complete graphitization of the adlayer. Carbon does not dissolve in gold up to 1170 K. Tungsten reacts with carbon under stepwise carbide formation upon annealing. The formation of W_2C starts at 770 K. The conversion of W_2C and the residual carbon to WC sets in at 970 K. At the same temperature, noticeable diffusion begins, which decreases the overall carbon concentration in the information depth for XPS. This leads to a decrease in the C 1s photoelectron signal. At 1270 K, most of the carbon has reacted to WC, and only a fraction of 20% of W_2C can be detected in the C 1s signal. No other carbon species are present at the surface. Further measurements and simulations of depth distribution and diffusion processes are in progress to help understand the carbidization process in detail.

References

[1] J. Davis, V. Barabash, A. Makhankov, L. Plöchel, K. Slattery, J. Nucl. Mater. 258–263 (1998) 308.
[2] I. Kirillov, I. Danilov, S. Sidorenkov, Y. Strebkov, R. Mattas, Y. Gohar, T. Hua, D. Smith, Fusion Eng. Des. 39/40 (1998) 669.
[3] H. Maier, S. Kötterl, K. Krieger, R. Neu, M. Balden, ASDEX Upgrade Team, J. Nucl. Mater. 258–263 (1998) 921.
[4] P. Srivastava, T.V. Rao, V.D. Vankar, K.L. Chopra, J. Vac. Sci. Technol. A 2 (3) (1984) 1261.
[5] O.R. Monteiro, M.-P. Delplancke-Ogletree, R. Yu Lo, R. Winand, I. Brown, Surf. Coat. Technol. 94–95 (1997) 220.
[6] S. Schelz, T. Richmond, P. Kania, P. Oelhafen, H.-J. Güntherrodt, Surf. Sci. 359 (1996) 227.
[7] P. Reinke, P. Oelhafen, Diamond Relat. Mater. 8 (1999) 155.
[8] S. Miller, G. Berning, H. Planck, J. Roth, J. Vac. Sci. Technol. A 15 (1997) 2029.
[9] MultiPak, Ver. 2.2, Physical Electronics, Eden Prairie, USA, 1996.
[10] R. Jenrich, P. Sampson, Technometrics 10 (1968) 1.
[11] D. Shirley, Phys. Rev. B 5 (1972) 4709.
[12] M. Seah, In: Practical Surface Analysis, Wiley, Norwich, UK, 1985..
[13] Ch. Linsmeier, Vacuum 6/7 (1994) 673.
[14] P. Goldstraß, Ch. Linsmeier, Nucl. Instrum. Meth. B 161–163 (2000) 411.
[15] P. Reinke, G. Francz, P. Oelhafen, J. Ullmann, Phys. Rev. B 54 (1996) 7067.
[16] P. Reinke, G. Francz, P. Oelhafen, Thin Solid Films 290–291 (1996) 148.
[17] P. Reinke, P. Oelhafen, J. Appl. Phys. 81 (1997) 5.
[18] Ch. Linsmeier, P. Goldstraß, J. Luthin, to be published.
[19] Binary Alloy Phase Diagrams, second ed., American Society for Metals, Metals Park, OH, 1996.
[20] L. McCarty, R. Donelson, R. Hehemann, Metall. Trans. A 18 (1987) 969.
[21] N. Vaskevich, V. Senchikin, V. Tretyakov, Poroshk. Metall. 6 (1985) 69.

ELSEVIER Nuclear Instruments and Methods in Physics Research B 161–163 (2000) 411–414

NIM B
Beam Interactions with Materials & Atoms

www.elsevier.nl/locate/nimb

Combined ion and electron spectroscopy study of the surface reactions of beryllium with carbon

P. Goldstraß, Ch. Linsmeier *

Max-Planck-Institut für Plasmaphysik, EURATOM Association, Boltzmannstr. 2, D-85748 Garching, Germany

Abstract

Surface reactions of evaporated carbon on a clean metallic beryllium single crystal (0 0 0 1) are investigated in situ by means of X-ray photoelectron spectroscopy and Rutherford backscattering spectrometry. The carbon is deposited at room temperature. The resulting films are successively heated to temperatures between 473 and 873 K in steps of 100 K and analyzed after each step. The as-deposited films consist of Be_2C at the beryllium/carbon interface, and of a mixture of graphitic and disordered carbon on top. At elevated temperatures carbidization takes place between 473 and 673 K and leads to a homogeneous layer of Be_2C on top of the beryllium. The Be_2C bulk photoelectron energies are found to be 282.7 eV for C 1s and 113.0 eV for Be 1s, respectivley.

PACS: 28.52.Fa; 68.35.-p
Keywords: Beryllium; Carbon; Carbide; Vapour deposition

1. Introduction

Several materials are regarded as candidate first wall materials for current and future fusion devices. Both low-Z elements such as beryllium and carbon, and heavy elements, like molybdenum and tungsten, are under discussion. Additional elements like oxygen, boron and silicon are present in the plasma as impurities [1]. Because of erosion and deposition processes, all these elements will form multi-component materials at the first wall surface and thus lead to a change of its properties. Of the low-Z elements Be has been used in JET [2] and is considered as a future first wall material for ITER [3,4]. Carbon has been extensively used in most fusion machines. Besides other methods for the deposition of thin carbon films, evaporation [5] proves to be a well-controlled technique to form very clean carbon layers. It can be found in the relevant literature that carbidization of the interface takes place after carbon deposition for both molybdenum [6] and tungsten [7]. For carbon layers of 10 nm thickness on beryllium the formation of Be_2C at the sample surface has been reported to appear for temperatures above 873 K [8]. In this paper we study the reaction of a carbon layer with metallic beryllium after deposition and thermal treatment in situ by both X-ray

* Corresponding author. Tel.: +49-89-3299-2285; fax: +49-89-3299-2279.
E-mail address: linsmeier@ipp.mpg.de (Ch. Linsmeier).

0168-583X/00/$ - see front matter
PII: S0168-583X(99)00685-0

photoelectron spectroscopy (XPS) and Rutherford backscattering spectrometry (RBS).

2. Experiment

A beryllium single crystal (0 0 0 1) was cleaned by periodic 1 keV Ar^+ bombardment and heating to 673 K. After the cleaning procedure, the only detectable impurities by XPS and RBS were oxygen (<0.1%) and argon (<2%). Carbon films with thicknesses between 0.1 and 3.7 nm were deposited on the sample by electron beam evaporation of graphite (Goodfellow, 99.999%) using an electron beam evaporation source (Omicron EFM3). During deposition, the sample was kept at room temperature (RT). Each film was heated in steps of 100 K from 373 up to 873 K. The sample was left at each temperature for 10 min and was allowed to cool down below 373 K for XPS and RBS analysis. After the thermal treatment the oxygen contamination did not exceed 2.5%. RBS analysis was performed using 1.0 MeV $^4He^+$ ions at normal incidence. The XPS probe was Mg K_α (1253.6 eV). The photoelectrons were detected at 90° relative to the sample surface. The electrostatic hemispherical analyzer (PHI, ∅ 279.4 mm), equipped with an entrance lens system, is operated at a constant pass energy of 23.5 eV. The Au $4f_{7/2}$ core level line (84.0 eV) of a clean gold sample is used for energy calibration.

The base pressure in the new UHV chamber ARTOSS and during in situ RBS and XPS analysis was in the 8×10^{-11} hPa range. The pressure during evaporation did not exceed 5×10^{-10} hPa. The maximum pressure during the heating process was 1.5×10^{-9} hPa at 873 K.

3. Results and discussion

3.1. Carbon film thickness

To determine the amount of deposited carbon, either the photoelectron signals from the C 1s or Be 1s core levels, or the RBS measurement can be used. Fig. 1 shows a comparison of the results. The layer thicknesses (assuming a graphite density of 2.26 g/cm^3) are in good agreement for values below the attenuation length of the Be 1s (1.3 nm) and C 1s (1.2 nm) photoelectrons in carbon [9]. For layers thicker than the attenuation lengths the equation used for the evaluation of the XPS results [10] fails and leads to the shown deviation from the RBS results. For determining small amounts of light elements at the sample surface XPS is, in comparison to RBS, better suited because of its higher sensitivity.

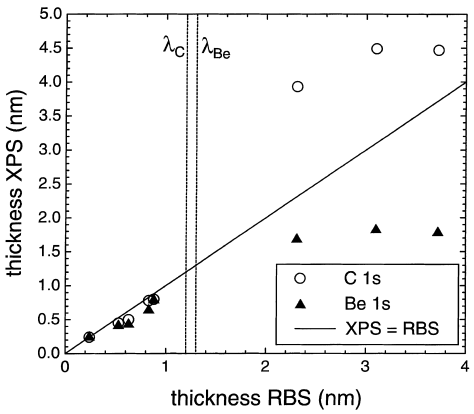

Fig. 1. Carbon layer thickness obtained from the XPS C 1s and Be 1s signals versus the corresponding thickness from the RBS signal. λ_C and λ_{Be} are the attenuation lengths in a carbon layer for Be 1s and C 1s photoelectrons, respectively.

3.2. As-deposited films

Fig. 2 shows the C 1s XPS signal for the different amounts of carbon deposited on clean Be at RT. For the smallest amount only one peak at a binding energy of 282.0 eV is observed. With rising coverage, another peak starts to appear. The signal around 284.2 eV starts to dominate above a carbon coverage of 0.6 nm. A similar behaviour has been observed for carbon films on molybdenum [6] and tungsten [7]. This second peak can be attributed to an overlap of the peaks for graphitic and disordered carbon. The positions of these two peaks were determined on the inert gold surface to be 284.2 eV for graphitic carbon and 285.2 eV for

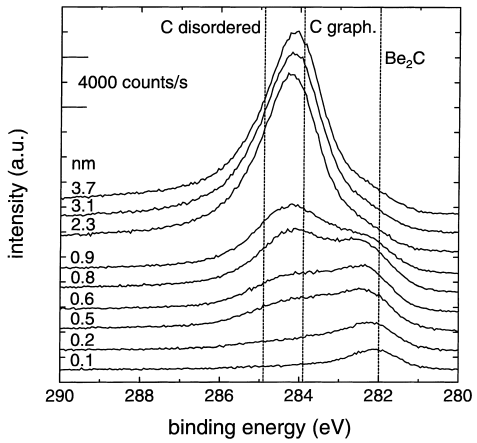

Fig. 2. XPS spectra of the C 1s region for different coverages. The thickness of each layer is given in nm above each spectrum. The dotted lines show the peak positions for graphitic and disordered carbon for the carbon/gold system [7] and the measured Be_2C position for the lowest coverage.

disordered carbon [7]. The investigations of thin carbon films on silicon gave similar results [5,11,12]. The first peak is present at all coverages and it shifts 0.5–0.7 eV to higher energies with rising coverage. The energies of this peak are well within the metal carbide range [13]. Therefore we assign it to the only stable compound of beryllium and carbon [14]: Be_2C. The amount of Be_2C obtained from the XPS measurements first increases with rising coverage, reaches saturation at a thickness equivalent around two monolayers of carbon and decreases for the three highest coverages. This implies a carbidization at the interface. The amount increases until the interface formation is complete and starts to decrease with rising coverage because of the attenuation of the interface signal in the carbon layer on top.

3.3. Thermal treatment

During the thermal treatment a complete carbidization takes place. The coverage-dependent Be_2C peak shift reported in Section 3.1 is still observed after exposure to elevated temperatures. We believe that this is probably due to the incomplete interface formation and/or to beryllium surface effects not yet fully understood.

Fig. 3(a) shows C 1s signals for a carbon amount of 4.2×10^{16} cm^{-2} (3.7 nm) after each heating cycle. Up to 473 K almost no change is noticed in the spectra. Between 473 and 673 K carbide formation takes place and proceeds with increasing substrate temperature until the carbon layer has completely reacted to Be_2C. At 573 K the amounts of carbon and carbide are almost balanced. Above 673 K there is again no major change in the C 1s signal. The Be 1s signal shows a similar but smaller shift due to this reaction compared to the C 1s signal. The difference to the Be_2C

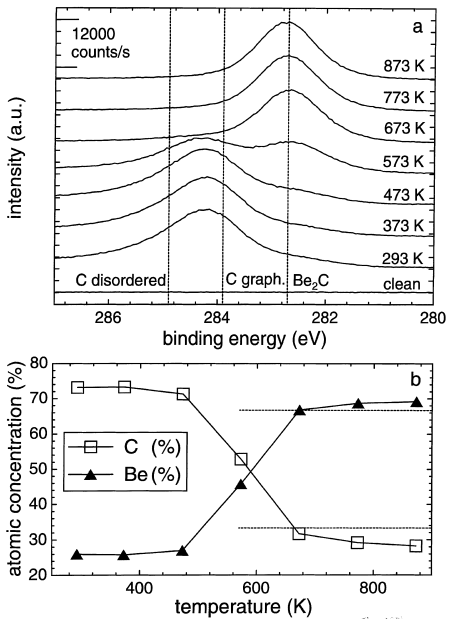

Fig. 3. (a) XPS spectra of the C 1s region for 4.2×10^{16} cm^{-2} carbon (3.7 nm). The given temperatures describe the successive treatment applied in addition to the previous stage. The dotted lines show the peak positions of graphitic and disordered carbon for the carbon/gold system [7] and the measured Be_2C peak position. (b) XPS atomic composition of this sample versus temperature during the thermal treatment. The dotted lines show the Be_2C stoichiometry.

formation temperature of 873 K reported by Ashida et al. may be due to a high impurity contamination (about 20% Zn and 35% O as-deposited) of this layer [8].

Fig. 3(b) shows the change in the surface atomic composition of the same sample with temperature according to the XPS analysis, calculated using the MultiPak software package [15]. After the carbidization of the layer the atomic composition Be:C is 7:3, in good agreement with the theoretical 67:33 for Be_2C.

During the exposure to elevated temperatures up to 873 K carbon neither desorbs from the surface nor diffuses to a large extend into the bulk beryllium. RBS analysis shows that the total amount of carbon decreases only slightly (from 4.7×10^{16} cm^{-2} at 673 K to 4.0×10^{16} cm^{-2} at 873 K). The RBS carbon peak does not show the significant broadening one would expect in case of a carbon diffusion into the bulk. We conclude from the absence of carbon and metal beryllium peaks in the XPS spectra that a homogenous Be_2C layer forms on top of the beryllium substrate. Therefore, the XPS photoelectron energies observed after the temperature treatment for coverages above 1 nm are the Be_2C bulk energies. They are 282.7 eV for C 1s and 113.0 eV for Be 1s, respectively. The difference to the reported bulk peak energy of 282.0 eV for Be_2C reported by Ashida et al. [8] may be explained again by the high impurity contamination of their sample used to determine this energy.

The complete carbidization and formation of a homogeneous Be_2C layer between 473 and 673 K and the formation of Be_2C at the beryllium/carbon interface at RT (as shown in Section 3.1) suggest a temperature-dependent diffusion mechanism for the Be_2C. This will be subject to further studies.

References

[1] K. Krieger, H. Maier, R. Neu, ASDEX Upgrade Team, J. Nucl. Mater. 266–269 (1999) 207.
[2] The JET team: presented by P.R. Thomas, J. Nucl. Mater. 176–177 (1990) 3.
[3] ITER Joint Central Team, J. Nucl. Mater. 3 (1994) 212.
[4] G. Janeschitz, K. Borrass, G. Federici, Y. Igitkhanov, A. Kukushkin, H.D. Pacher, G.W. Pacher, M. Sugihara, J. Nucl. Mater. 220–222 (1995) 73.
[5] S. Schelz, T. Richmond, P. Kania, P. Oelhafen, H.-J. Güntherrodt, Surf. Sci. 359 (1996) 227.
[6] P. Reinke, P. Oelhafen, Diamond and Related Mater. 8 (1999) 155.
[7] J. Luthin, Ch. Linsmeier, Surf. Sci., in: Proc. ECOSS-18, in print.
[8] K. Ashida, K. Watanabe, Fusion Engrg. Design 37 (1997) 307.
[9] M.P. Seah, W.A. Dench, Surf. Interface Anal. 1 (1979) 2.
[10] D. Briggs, M.P. Seah, Practical Surface Analysis, Second ed., Vol. 1, Wiley, Chichester, 1990, p. 245.
[11] P. Reinke, G. Francz, P. Oelhafen, J. Ullmann, Phys. Rev. B 54 (1996) 7067.
[12] P. Reinke, G. Francz, P. Oelhafen, Thin Solid Films 290–291 (1996) 148.
[13] J.K. Moulder, W.F. Strickle, P.E. Sobol, K.D. Bomben, Handbook of X-ray Photoelectron Spectroscopy, Perkin Elmer Co., Physical Electronics Co., Physical Electronics Division, Minnesota 1992.
[14] Gmelin, Handbook of Inorganic and Organometalic Chemistry, eighth ed., Be, Sup. Vol. B4, Springer, Berlin, 1996.
[15] MultiPak Ver. 2.2, Physical Electronics, 1996.

ELSEVIER

Surface Science 454–456 (2000) 305–309

surface science

www.elsevier.nl/locate/susc

Reactions of oxygen atoms and molecules with Au, Be, and W surfaces

Ch. Linsmeier [a,*], J. Wanner [b]

[a] *Max-Planck-Institut für Plasmaphysik, EURATOM Association, Boltzmannstr. 2, D-85748 Garching, Germany*
[b] *Max-Planck-Institut für Quantenoptik, Hans-Kopfermann-Str 1, D-85748 Garching, Germany*

Abstract

In this study, the adsorption of atomic oxygen on polycrystalline gold, tungsten and single crystalline beryllium (0001) surfaces is investigated at room temperature and compared with molecular oxygen. The O atoms are produced by microwave discharge in pure O_2. The gaseous reactants effuse into a UHV chamber. The adsorption or chemical reaction of the oxygen atoms and molecules impinging on the metal surfaces is monitored by X-ray photoelectron spectroscopy (XPS). The main observations of this study are summarized as follows. The gold surface is inert to molecular oxygen but adsorbs O atoms up to a coverage of one monolayer. Beryllium adsorbs both molecular and atomic oxygen and is also oxidized by both species. The rate of oxide formation is significantly larger for O atoms. In the case of tungsten, there is no difference between atoms and molecules in the amount of oxygen adsorbed. Neither species, however, forms any phase of tungsten oxide. Only tungsten binding energies characteristic of the pure metal and for oxygen adsorbed within the first atomic layer are detected.

Keywords: Chemisorption; Compound formation; Gold; Oxidation; Sticking; Surface chemical reaction; Tungsten; X-ray photoelectron spectroscopy

1. Introduction

In the field of gas–surface interactions, rather little is known about the different reactivities of O atoms and oxygen molecules. In this paper, this topic is addressed for reactions with three metal surfaces (Au, Be, W). To our knowledge, interactions of oxygen atoms with Be and W surfaces are reported for the first time. The experiment is described here only very briefly. Details will be given elsewhere [1]. Oxygen atoms are provided by microwave dissociation in pure molecular oxygen in a UHV-compatible discharge source. It is designed for surface chemistry investigations and operates at a degree of dissociation of approx. 30% [2]. The gaseous reactants effuse into a UHV chamber, which houses the clean samples, viz. a polycrystalline gold foil, a polished beryllium single crystal with (0001) orientation, and a 100 nm tungsten film on a silicon substrate evaporated under UHV conditions. The Be single crystal was chosen for reasons of increased purity compared with a polycrystalline sample. For the Au and W samples, we assume that their polycrystalline nature does not have any influence on the reactive behavior towards atomic oxygen. During exposures, the samples are kept at room temperature (RT). The adsorption or chemical reaction of the

* Corresponding author. Fax: +49-89-3299-2279.
E-mail address: linsmeier@ipp.mpg.de (Ch. Linsmeier)

0039-6028/00/$ - see front matter
PII: S0039-6028(00)00215-6

oxygen atoms and molecules impinging on the metal surfaces is monitored by X-ray photoelectron spectroscopy (XPS). All binding energies are referenced to the Au $4f_{7/2}$ peak at 84.0 eV, measured at a clean gold surface. The pressure during the XPS measurements was in the low 10^{-9} hPa range or better.

2. Gold

Oxygen chemisorption on gold from molecular oxygen, as reported in the earlier literature, could be traced back to calcium and silicon impurities [3,4]. It has since been established, however, that oxygen molecules do not adsorb on gold surfaces, whereas oxygen atoms do [5]. Concerning the results of the present study, Fig. 1 compares the O 1s region of XPS spectra under different experimental conditions. The spectra shown are raw data, without subtraction of any background or satellites. The slope of the signal intensity towards higher binding energies is due to the neighboring

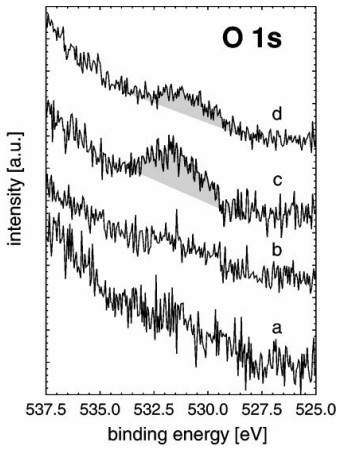

Fig. 1. XPS spectra of a gold surface in the O 1s region, recorded after cleaning (a), after O_2 dosing for 35 min (b), and after dosing O atoms for 32 min (c). Spectrum d shows the adsorption on the gold surface after exposure to atomic oxygen for 30 min, where the sample surface is turned away from the discharge tube. In this case, only atoms that were reflected from vacuum vessel surfaces were able to impinge on the gold sample.

Au $4p_{3/2}$ signal at a binding energy of 547 eV. Spectrum a is taken after cleaning the gold sample by heating (first to 673 K, later to 473 K) and Ar^+ (3 keV) bombardment cycles. No oxygen or other contamination signals are observed after the cleaning procedure.

This is also the case after 35 min exposure to molecular oxygen (spectrum b). The gas was admitted through the discharge tube, the pressure being kept constant at the same value as maintained during the plasma discharge. Only the background signal can be detected. With the discharge on, an oxygen photoelectron signal is already observed after a short 3 min exposure to O atoms. It increases with the exposure time and reaches the intensity depicted in spectrum c after 32 min.

Spectrum d is taken after exposure to O atoms for 30 min. In contrast to the other spectra, the gold surface in these experiments points away from the discharge tube. Oxygen atoms impinging on the gold surface therefore must have hit the sample holder and the chamber walls several times already. The measured O 1s intensity can only be explained by a low sticking coefficient for O atoms on the chamber walls. This seems surprising since the reactivity for oxygen atoms is expected to be much higher than for molecules. However, similar behavior has also been observed for hydrogen atoms [6].

According to Fig. 1, the binding energy for adsorbed O atoms varies between 531.0 and 531.5 eV, which can be taken as constant in view of the low signal-to-noise ratio in the O 1s region. This value is somewhat higher than 529.6 eV, as reported by Evans et al. [7] for atomic oxygen on gold. The peaks are rather broad at full-width-at-half-maximum (FWHM); ranging from 2.10 to 2.70 eV. Broad peaks were also observed by Evans et al. They reported FWHMs of around 2.5 eV. The gold photoelectron signal (Au 4f, not shown in Fig. 1) does not change between clean and oxygen-exposed surfaces. The binding energy is 84.0 eV for the Au $4f_{7/2}$ peak in all cases. The FWHM of the Au $4f_{7/2}$ peak remains constant at 1.2 eV after all the different exposures.

The O 1s signal increases with increasing exposure to atomic oxygen, but slows down with prolonged exposure. However, this signal is too small

to be used for quantification of the adsorbed oxygen, since the low signal-to-noise ratio does not lead to reliable peak integrals. The decrease in gold intensity (Au 4f signal) due to the oxygen adlayer is therefore used to calculate the amount of adsorbed oxygen. To determine the sticking coefficient of oxygen atoms on gold, the number of impinging atoms on the surface is calculated by applying kinetic gas theory. The number of gas particles passing through the aperture hole in the source region depends on the pressure and temperature. The pressure is measured, and the temperature is assumed to be 300 K. The degree of O_2 dissociation is also taken into account. The calculation results in an initial sticking coefficient of 5×10^{-3}, which decreases to 1.5×10^{-3} after adsorption of $1.6 \times 10^{15}\,cm^{-2}$ oxygen atoms. Although gold can be regarded as an especially inert material, a similar low sticking coefficient can account for the high survival probability of oxygen atoms that hit the vacuum chamber walls. This explains the oxygen coverage in the experiment where the gold surface points away from the discharge tube.

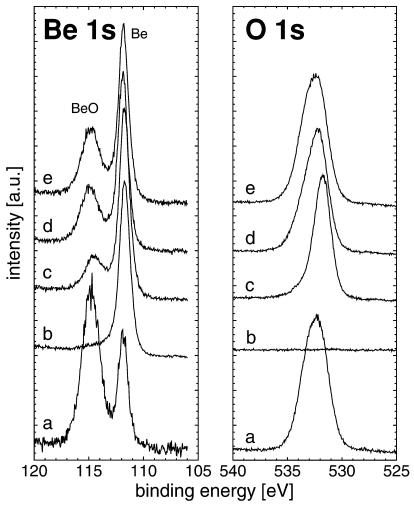

Fig. 2. XPS spectra in the Be 1s and O 1s energy regions from a Be (0001) surface. The spectra were recorded after introduction of the sample into the UHV system (a), after cleaning (b), after dosing with O_2 for 34 min (c), after dosing atomic oxygen for 3 min (d), and for 33 min (e).

3. Beryllium

Initial cleaning to remove the natural oxide layer and contaminants from the Be (0001) single crystal was performed by 2 keV Ar^+ ion bombardment and by heating first to 673 K, later to 473 K. After this initial cleaning procedure, sputtering with 1 keV Ar^+ is sufficient to remove all adsorbed or reacted surface layers. Beryllium reacts with both molecular [8,9] and atomic oxygen. Fig. 2 shows Be 1s and O 1s signals from the Be (0001) surface after several treatments. Spectrum a at the bottom of the panels is recorded after introducing the crystal into the vessel before any cleaning has been carried out. The Be region shows two peaks, originating from Be in the metal state at 111.9 eV and from BeO at 114.8 eV. The oxide is the natural oxide film formed on the beryllium surface in air.

The corresponding O 1s signal can be deconvoluted into a narrow peak with a FWHM of 1.88 eV at 531.7 eV and a broader contribution with a FWHM of 2.54 eV at 532.7 eV. After cleaning (spectra b), the Be 1s signal consists only of the metal contribution, and the oxidic Be signal has vanished. In the corresponding O 1s region, no signal can be detected.

This state of the surface is reproduced again before each of the subsequent sample treatments. Spectrum c is recorded after exposing the clean beryllium surface to molecular oxygen for 34 min at RT. The Be 1s region shows a large metal signal and a small peak at 114.4 eV, which indicates the formation of BeO on the metal surface. The corresponding oxygen 1s peak is sharp in relation to the signal of the air oxide as well as compared to the oxygen signals above (d, e). It can be deconvoluted into a strong signal at 531.8 eV (FWHM 1.8 eV) and a small peak at 533.4 eV (FWHM 2.2 eV).

Spectra d and e in Fig. 2 are taken after exposing the clean Be surface to oxygen atoms. The BeO signal changes significantly in both cases, in comparison with spectrum c after dosing molecular oxygen. Even after interaction with oxygen atoms for only 3 min (spectrum e), the BeO signal is larger than for exposure to O_2 molecules only

(spectrum c). For an 11-fold exposure time (33 min), a further increase in BeO signal intensity is observed (spectrum d). The difference in the spectra after exposure to the molecular and atomic species is explained by the greater reactivity of oxygen atoms with clean beryllium metal. This is also reflected in the photoelectron signals of the O 1s regime, depicted in the right panel of Fig. 2. Molecular oxygen only leads to a narrow O 1s signal, as shown in spectrum c. In the presence of oxygen atoms, broadening is observed. Deconvolution of the signal into two peaks shows that the atomic species leads to development of a second peak at a binding energy of around 533 eV. This signal is always broader than that around 532 eV, which indicates that several chemically or structurally different oxygen environments contribute to this signal. The differences in reactivity are reflected in the ratio of the total O 1s/Be 1s peak areas: For the O_2 treatment, this ratio is 2.7. For 3 min of oxygen atom treatment, it is already 4.7, whereas for 34 min of oxygen atom exposure, it is 6.4. The increased reactivity also leads to evolution of the BeO peak in the Be 1s region. After exposing the clean surface to O_2 for 34 min, the BeO/Be ratio is 0.3. The oxide/metal ratio after only 3 min O atom dosing is already 0.5 and increases to 0.6 after an 11-fold atom-exposure time. This can be explained by a decrease in the reaction rate due to the growth of the oxide layer. For oxide formation, oxygen needs to be present at the interface to the Be metal. With a growing oxide layer, the oxygen must be transported from the surface through the formed oxide to the oxide–metal interface, or the Be to the very surface where it reacts with oxygen from the gas phase. The increasing oxide layer thickness, and hence increased diffusion length, leads to a lower reaction rate.

4. Tungsten

Originally, the tungsten films are covered by a thin WO_3 film formed by oxidation in air. Unlike for the Au and Be spectra, a monochromatic Al X-ray source is used for the W measurements. The W 4f signal of the as-introduced sample consists of two doublets originating from tungsten metal and tungsten in the +6 oxidation state (WO_3), as shown in spectrum a of Fig. 3. This film is thin enough for photoelectrons originating from the metal substrate to penetrate through the oxide overlayer (approx. 5–10 monolayers). The metal signal appears besides the relatively broad W $4f_{7/2}$ peak of the +6 oxidation state at 35.6 eV with a FWHM of 1.49 eV. The large width of the W +6 peak indicates an inhomogeneous structure of the oxide film. The broadened metal peak suggests a continuous transition from the metal to the WO_3 stoichiometry.

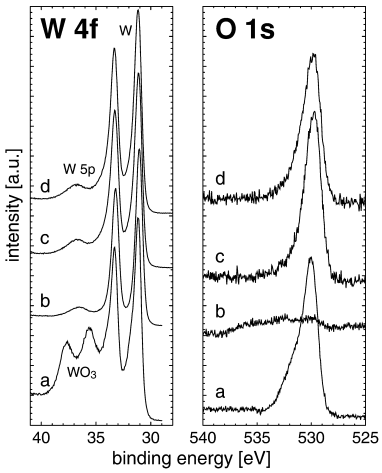

Fig. 3. XPS spectra in the W 4f and O 1s energy regions from a 100 nm tungsten film on silicon. The spectra are taken after introduction of the sample into the UHV system (a), after cleaning (b), after dosing O_2 for 83 min (c), and after dosing atomic oxygen for 62 min (d).

For cleaning, the sample is sputtered with Ar^+ at 3 keV until only tungsten metal signals are measured. Spectrum b in Fig. 3 shows the W 4f region of a clean sample. It consists of the W 4f doublet at the energy position for metallic tungsten and of the W $5p_{3/2}$ signal. These signals can be fitted by a doublet (W 4f) and a single peak (W $5p_{3/2}$) only, indicating that no oxidized tungsten species are present on the surface. The clean surface is exposed to molecular oxygen for 83 min and subsequently, after being cleaned again, to atomic oxygen for 45 and 62 min, respectively.

Unlike the beryllium experiments, there is no

apparent oxidation on the polycrystalline tungsten surface at room temperature. However, the tungsten surface adsorbs oxygen and does not show any difference between exposure to molecular or to atomic oxygen. In the spectra taken after the exposures, only three peaks are observed in the W 4f region: the W 4f doublet at energies indicating tungsten in the metal state (W $4f_{7/2}$ at 31.1 eV) and the W $5p_{3/2}$ peak around 36.9 eV. The absence of a shifted W 4f doublet or shoulders in the metal signal after oxygen exposure indicates that oxygen has not reacted chemically with the tungsten. Since there is photoelectron intensity in the O 1s energy region of the spectrum (right panel of Fig. 3), oxygen is present on the tungsten surface. However, it only adsorbs on the surface, without undergoing any chemical interaction by forming tungsten oxides. This has already been observed for O_2 chemisorption on W(110), W(100) and polycrystalline surfaces [10–16]. The adsorbed oxygen leads to a small broadening of the metallic W $4f_{7/2}$ peak by about 0.1 eV. The width of this peak on the clean surface is 0.76 eV, whereas after oxygen dosing, it rises to 0.86 eV. These values compare to a FWHM of 0.91 eV of the W $4f_{7/2}$ peak at 31.1 eV from the metal supporting a thin air oxide film. The W $5p_{3/2}$ binding energy is also not influenced by the oxygen adsorption, confirming that no chemical interaction takes place between oxygen and tungsten.

The area ratio of the O 1s and W 4f peaks for the air oxide is 0.36. For the clean surface, a value of 0.04 is derived, demonstrating that practically all oxygen is removed. After the oxygen exposure experiments, the intensity ratio rises to a constant value of about 0.12, regardless of the nature of the oxygen species applied. This indicates complete dissociative adsorption of the O_2 molecules. Since 45 min is the minimum exposure time in these experiments, the surface is already saturated with oxygen earlier.

5. Conclusions

Besides mass spectrometric analysis, the production of atomic oxygen in a UHV-compatible microwave discharge of molecular oxygen is proven by adsorption on polycrystalline gold. The initial sticking coefficient of oxygen atoms on gold is found to be 5×10^{-3}. Furthermore, this paper reports the first experimental results on the reaction of beryllium and tungsten with atomic oxygen. Monocrystalline beryllium reacts with both molecular and atomic oxygen, whereas the reactivity is higher for atoms. In addition to the formation of BeO, oxygen atoms adsorb on the surface. Molecular oxygen only leads to BeO formation without an adsorbed adlayer. Polycrystalline tungsten shows no difference in the interaction between molecular and atomic oxygen. Both species adsorb. Comparison with literature results suggests O adsorption within the first atomic tungsten layer. No formation of tungsten oxide films is observed.

References

[1] Ch. Linsmeier, J. Wanner, in preparation.
[2] G. Jung, Max-Planck-Institut für Quantenoptik, MPQ Report 231, (1998)
[3] N. Saliba, D.H. Parker, B.E. Koel, Surf. Sci. 310 (1998) 270.
[4] M.E. Schrader, Surf. Sci. 78 (1978) L227.
[5] J.J. Pireaux, M. Chtaib, J.P. Delrue, P.A. Thiry, M. Liehr, R. Caudano, Surf. Sci. 141 (1984) 211.
[6] K. Flaskamp, H.R. Ihle, G. Stöcklin, E. Vietzke, K. Vogelbruch, C.H. Wu, In: Proc. Int. Symp. Plasma Wall Interaction, Jülich (1976) 285.
[7] S. Evans, E.L. Evans, D.E. Parry, M.J. Tricker, M.J. Walters, J.M. Thomas, Faraday Discuss. Chem. Soc. 58 (1974) 97.
[8] D.E. Fowler, J.M. Blakely, J. Vac. Sci. Technol. 20 (1982) 930.
[9] D.E. Fowler, J.M. Blakely, Surf. Sci. 148 (1984) 265.
[10] D.M. Riffe, G.K. Wertheim, Surf. Sci. 399 (1998) 248.
[11] G. Tréglia, M.C. Desjonquères, D. Spanjaard, Y. Lassaily, C. Guillot, Y. Jugnet, Tran Minh Duc, J. Lecante, J. Phys. C: Solid State Phys. 14 (1981) 3463.
[12] J.F. van der Veen, F.J. Himpsel, D.E. Eastman, Phys. Rev. B 25 (1982) 7388.
[13] G.K. Wertheim, P.H. Citrin, J.F. van der Veen, Phys. Rev. B 30 (1984) 4343.
[14] P. Alnot, D.J. Auerbach, J. Behm, C.R. Brundle, A. Viescas, Surf. Sci. 213 (1989) 1.
[15] C.H.F. Peden, N.D. Shinn, Surf. Sci. 312 (1994) 151.
[16] J.F. Morar, F.J. Himpsel, G. Hughes, J.L Jordan, F.R. McFeely, G. Hollinger, J. Vac. Sci. Technol. A 3 (1985) 1477.

Available online at www.sciencedirect.com
ScienceDirect
Journal of Nuclear Materials 363–365 (2007) 1129–1137
journal of nuclear materials
www.elsevier.com/locate/jnucmat

Binary beryllium–tungsten mixed materials

Ch. Linsmeier [a,*], K. Ertl [a], J. Roth [a], A. Wiltner [a], K. Schmid [a], F. Kost [a], S.R. Bhattacharyya [a,1], M. Baldwin [b], R.P. Doerner [b]

[a] *Max-Planck-Institut für Plasmaphysik, EURATOM Association, Boltzmannstr. 2, 85748 Garching b. München, Germany*
[b] *Center for Energy Research, University of California – San Diego, MC 0417, 9500 Gilman Dr., La Jolla, CA 92093-0417, USA*

Abstract

Both Be and W are planned as wall materials for ITER. Although these materials will dominate the ITER first wall, and despite the fact that their interaction during operation will be dominated by surface processes, mostly bulk material data on the Be–W binary system are available. This article describes investigations of thin films of Be deposited on W, the inverse system (W films on Be), as well as experiments where W surfaces are exposed to a Be-seeded deuterium plasma. The formed alloy phases Be_2W and $Be_{12}W$ are identified by X-ray photoelectron spectroscopy (XPS) and depth profile data both from sputter-XPS and MeV ion beam analysis are presented.

PACS: 68.55.Nq; 79.60.Dp; 79.60.Jv; 82.80.Pv

Keywords: Beryllium; Diffusion; First wall; Surface analysis; Tungsten

1. Introduction

The planned application of both metals beryllium and tungsten together as first wall materials of the next step fusion device ITER is based on the foreseen advantageous properties of these metals for the respective locations in the plasma vessel [1]. Erosion, transport, and redeposition of both materials during operation will lead to transport of elements onto surfaces of different materials. Due to kinetic energy of impinging particles and elevated wall temperatures, alloys and compounds consisting of the present elements will be formed. These 'mixed materials' exhibit strongly altered physical and chemical properties compared to the intended properties of the pure elements which were originally installed. Of all binary systems considered in previous studies, beryllium–tungsten received least attention although Be–W alloys bear the potential of drastically reduced melting temperatures compared to pure W. For the formation of a binary Be–W alloy, two possible scenarios can be envisaged in a fusion device: deposition of tungsten on beryllium surface or vice versa. In this paper we investigate both Be films deposited on W substrates and the reverse system (W films on Be substrates), as well as the interaction of a Be-seeded deuterium plasma with W substrates. The interaction of the depositing

* Corresponding author. Tel.: +49 89 32992285; fax: +49 89 3299962285.
E-mail address: linsmeier@ipp.mpg.de (Ch. Linsmeier).
[1] Permanent address: Surface Physics Division, Saha Institute of Nuclear Physics, 1/AF Bidhan Nagar, Kolkata 700 064, India.

0022-3115/$ - see front matter © 2007 Elsevier B.V. All rights reserved.
doi:10.1016/j.jnucmat.2007.01.224

species with the substrate is determined by the kinetic energy of the incoming particle and by the substrate temperature. Therefore, in the experiments with thin surface layers (Be/W and W/Be), thermal treatments are carried out in vacuum. Subsequently, the surface is investigated by ion beam accelerator-based techniques (Rutherford backscattering spectroscopy, RBS, and nuclear reaction analysis, NRA) and X-ray photoelectron spectroscopy (XPS). By XPS analysis, additional chemical information on the formed Be phases is gained. The W layers which were exposed to Be-seeded D plasmas are also analyzed in their chemical and elemental composition by NRA and XPS. The observations are discussed in order to assess the risks and consequences of the Be–W alloy formation in a fusion device which employs both metals as first wall materials.

This paper reviews the current knowledge on surface reactions in the Be–W system. A bulk phase diagram is available in the literature [2].

2. Experiments

The interaction of beryllium and tungsten is investigated in two different layered systems where both tungsten and beryllium are used as surface layer, respectively (W/Be: tungsten layer on beryllium; Be/W: beryllium layer on tungsten). The first series of experiments uses mechanically and electrochemically polished Be metal substrates (polycrystalline). Tungsten is deposited in a magnetron sputter device (base pressure: 2×10^{-5} Pa) with a layer thickness of 200 nm. Before starting the Be deposition, the surface is etched in a pure Ar plasma. The Be films on polycrystalline tungsten are deposited in a UHV chamber connected directly to the XPS analysis chamber to avoid air transfer of the reactive Be films. The base pressure in the preparation chamber is below 2×10^{-8} Pa, during the Be deposition the pressure is below 4×10^{-8} Pa. The substrates are cleaned using alternating sputter (3 kV, Ar^+) annealing (up to 970 K) cycles until no impurities are detected in XPS survey scans. During deposition of the surface layers, the substrates are kept at room temperature (300 K). The alloying of the two components is studied by annealing the samples to different temperatures in the XPS analysis chamber (base pressure better than 2×10^{-8}), whereby the pressure rises up to 5×10^{-8}. The samples are analyzed after annealing steps by XPS and RBS. XPS is performed in situ for the Be/W experiments. In case of the W/Be samples, for the RBS analysis air transfers were unavoidable.

XPS analysis is carried out in a PHI ESCA 5600 spectrometer using the monochromatic X-ray source (Al Kα, 1486.6 eV). The best spectral resolution in this mode is 0.26 eV. The analyzed area is 0.8 mm in diameter. XPS measurements are performed under a take-off angle of 22° with respect to the surface normal, depth profiles at 45°. The binding energy (BE) scale is referred to the Au $4f_{7/2}$ signal at 84.0 eV and calibrate additionally with the Cu $2p_{3/2}$ and Ag $3d_{5/2}$ signals [3]. High resolution spectra (pass energy 2.95 eV) are used to determine chemical binding states, in particular the chemical shift due to alloying. For quantitative measurements, survey scans with a pass energy of 93.90 eV are used. Chemical data analysis is carried out by fitting Gauss–Lorentz functions to the data, taking into account the background in the Be 1s region by a Shirley background [4]. Ion beam analysis was carried out at the Garching 3 MV tandem accelerator. Standard ion beam analysis techniques (RBS with ^{1}H, ^{3}He, and ^{4}He, scattering angle 165°) were applied. Reliable depth profiles from the RBS spectra are obtained using 'backward' and 'forward' calculations in combination, the 'IBA Data Furnace NDF' program [5] for solving the inverse RBS problem and the 'SIMNRA' program [6] for simulation of the spectra. In these calculations advantage is taken from the fact that for each experimental condition spectra measured with two different ion species and energies are available which entered the fit procedures simultaneously. As a constraint the total amount of W was kept constant. Cross sections for the ^{9}Be(p,α)^{6}Li and the ^{9}Be(p,d)^{8}Be reactions are extrapolated for the scattering angle of 165° from 138° data by Thomas et al. [7].

3. Results and discussion

3.1. Tungsten films on beryllium (W/Be)

The 200 nm W layer on beryllium which is discussed here is prepared and analyzed as described in Section 2, with an unavoidable air transport between annealing and RBS analysis steps. The final sputter XPS depth profile comprises both survey spectra for quantitative analysis and high-resolution spectra to determine the chemical binding states.

The changes of the W layer during the annealing sequence can be followed in the RBS spectra with

^{1}H and ^{4}He, respectively. Using protons has the advantage to make changes in the Be profile visible. The cross section for protons scattered from beryllium is non-Rutherford for the applied energies and yields an enhanced signal for Be. Fig. 1(a) shows the series of RBS spectra measured with protons at 1 MeV primary energy. The spectra are plotted on a semi-logarithmic scale to demonstrate the changes both in the Be and the W signals. Clearly two temperature regimes can be distinguished. Below 1000 K, only very small changes in the spectra are visible. The signal corresponding to the W layer (the W surface edge is located at channel 276) shows only small changes, both in position and intensity. The shift of about 1 channel between 300 K and 970 K is not above experimental uncertainties. At 1070 K, however, shifting of the W edge continues and supports the trend visible at lower temperatures. This shift indicates that tungsten is not any more present at the surface of the sample, but is continually replaced by another surface layer. The solution which element is present at the surface can be found in the Be signal. The Be edge is located at channel 166 in the spectra measured between 300 K and the run at 970 K. No significant difference is visible between these spectra. The Be edge after the first run at 1070 K is still at channel 166, but already intensity appears at channel 181. The Be surface edge is located at this position, therefore Be must be present at the sample surface after the first 1070 K annealing step. During the extended annealing at 1070 K, the Be edge continuously shifts from the 300 K position to the surface edge. The Be surface peak is still visible for annealing times up to 300 min (fine blue lines in Fig. 1(a)). After 360 min annealing, the Be edge lost the surface peak and exhibits the continuous characteristics for a smooth Be depth distribution.

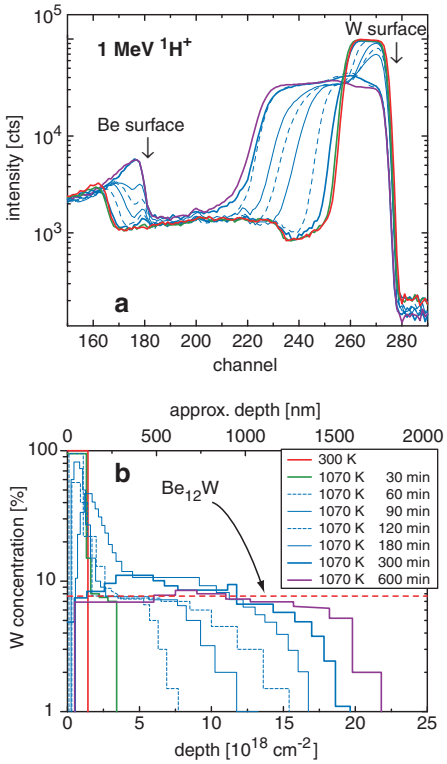

Fig. 1. RBS spectra (a) and depth profiles (b) measured with 1 MeV ^{1}H at a scattering angle of $\theta = 165°$, after annealing of a 200 nm W film on Be to the indicated temperatures/times.

The evolution of a smooth depth distribution is also observed in the tungsten signal. As discussed above, no significant deviations from the 300 K signal are observed up to 970 K. At 1070 K, the W surface signal changes. After 30 min, the leading edge still is at the surface position (within the experimental accuracy), but the trailing edge shifts by three channels to greater depths. This indicates the begin of the interdiffusion of Be and W at the layer-substrate interface. With continued annealing at 1070 K, the intermixing proceeds and also a decrease of the maximum W intensity is observed. During the time evolution and proceeding intermixing, however, the W from the surface layer is not lost into the Be bulk by diffusion. After the maximum time at 1070 K (600 min), there still exists a steep W trailing edge. This indicates that a well-defined intermixed W–Be layer has been formed. A diffusive loss of W into the Be bulk can therefore be excluded. During the annealing, also the leading edge of the W signal shifts to a final position in channel 274.

The observations from the ^{1}H RBS spectra are corroborated in the ^{4}He RBS spectra (not shown). From both series the depth profiles after the respective annealing steps can be calculated, shown in Fig. 1(b). In the semi-logarithmic diagram the tungsten concentration profile is plotted against the particle areal density. This areal density is converted into an approximate depth scale (given in the upper axis) by using the beryllium bulk density (1.85 g cm^{-3}, therefore 10^{15} Be per cm^{2} correspond

to 8.09×10^{-11} m). The initially rectangular W profile of the deposited tungsten layer continually broadens during the annealing steps at 1070 K. The dashed line corresponds to the $Be_{12}W$ composition. During the continued intermixing between tungsten and beryllium, the composition converges to $Be_{12}W$. Deviations from this composition are only observed at the intermixing front. However, the majority of the intermixed layer keeps this composition. After 600 min at 1070 K the profile is almost rectangular. In particular, the W concentration gradient is not exponentially extending into greatest depths, but has a fairly well-defined cut-off. This depth distribution leads to the conclusion that the formed $Be_{12}W$ layer has high stability and is not the result of a dissolution process of tungsten into the Be bulk.

From the front of the $Be_{12}W$ depth distribution a diffusion coefficient D can be estimated. Assuming a two-dimensional diffusion of the W layer into the Be bulk driven by the concentration gradient, the diffusion length x is defined by: $x = \sqrt{4Dt}$. This definition is derived from Fick's two laws and considers net diffusion towards the region of lower concentration due to random-walk motion. Since it neglects any driving forces due to gradients in the chemical potential, this value is only an estimation of D. Fitting the depth of the diffusion front with the above equation results in a diffusion coefficient D of 1.6×10^{-13} cm^2 s^{-1}. The fitted function reproduces well the data points. Therefore, the assumption of a diffusive intermixing is justified.

The question of the formed phase is addressed in XPS measurements at different depths. These depths are accessed by sputter profiling with 3 keV Ar^+. Between the sputtering cycles, XPS spectra in survey resolution are measured to detect impurities and perform elemental quantification. High-resolution spectra of the Be 1s region allow the identification of chemical binding states. The survey spectra demonstrate the purity of the deposited layers. Only signals from the elements W, Be, O, and C are detected, besides Ar from the sputtering process. The depth profiles for the elements Be, W, C, and O are plotted in Fig. 2. The logarithmic fluence scale makes the changes in the surface-near region visible together with the composition in greater depths. Please note that the intermixed layer dominates the total depth under investigation: This layer extends from Ar^+ fluences of 3.5×10^{17} cm^{-2} to 7.5×10^{18} cm^{-2}, corresponding to an estimated depth of 3 μm. The average composition in this

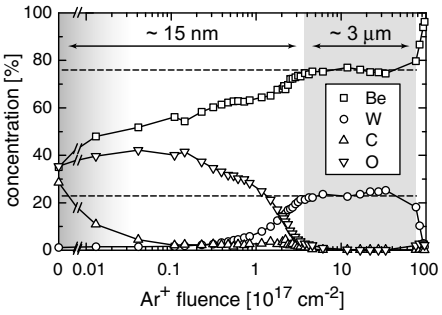

Fig. 2. Depth profile of the formed Be–W layer on a Be substrate after annealing at 1070 K for 600 min. The composition of the intermixed layer is practically constant between Ar^+ fluences of 3.5×10^{17} cm^{-2} and 7.5×10^{18} cm^{-2}.

depth interval from the XPS analysis is 75.7% W and 22.9% Be. This nominal stoichiometry of $Be_{3.3}W$, however, is not the true stoichiometry of the intermixed layer, as determined in the RBS analysis. Since Ar^+ bombardment leads to a strong preferential sputtering (see e.g. [10]), the composition determined here deviates from the true stoichiometry. To compare the XPS results with the RBS data, we calculate the partial sputtering yields of a $Be_{12}W$ alloy for the present Ar^+ bombardment conditions using the Monte Carlo code SDTRIM.SP [11]. Taking into account the resulting yields of $Y_W = 0.21$ and $Y_{Be} = 3.34$, the calculated stoichiometry is Be_9W, close to the stoichiometry $Be_{12}W$, determined by ion beam analysis. Therefore it can be concluded that the deviation of the XPS composition from the IBA compositions is caused mostly by preferential sputtering effects. In contrast to the intermixed $Be_{12}W$ zone, the surface layer does not contain tungsten: the tungsten concentration at small fluences is in the 1–3% range. However, this surface zone (detected up to an Ar^+ fluence of approximately 1×10^{17} cm^{-2}, corresponding to a depth of ≈15 nm) contains oxygen in reasonable amounts. From the XPS quantitative data, a surface layer of BeO can be concluded. Carbon is only present at the very surface of the sample and is easily removed by sputtering with a fluence of 4×10^{15} cm^{-2}. This is the typical signal from an adsorbed contamination layer caused by sample transport through the air. These results corroborate the interpretation of the RBS data where small shifts in the tungsten surface edge were observed (see Fig. 1(a)). Indeed, the Ar^+ depth profile proves the existence of a Be-containing surface layer. Since

oxygen is of no importance at greater depths of the sample, this element must be introduced during the annealing/measurement steps. As shown in the legends in the Figures of the RBS spectra and the IBA depth profile (Fig. 1), several annealing and analysis cycles were carried out. The XPS depth profile is measured after the final annealing step at 1070 K. As discussed above, the W edge shifts to lower channels during the annealing at 1070 K. Therefore, at this temperature a Be surface layer is formed. Initially, this layer must be metallic, since no oxygen reservoir is present in the sample. After air transfer, however, Be reacts with the air to BeO, finally forming the layer observed in Fig. 2. It remains an open question here whether this Be accumulation at the surface is a result of the adsorbed air (oxygen, water) at the surface and the oxide formation with these species as driving force, or whether the Be surface accumulation would also take place without oxide-forming species.

The depth profile is continued until the W signal is only small compared to the Be signal. Even without taking into account any preferential sputtering, it can be concluded that at this fluence the deposited tungsten is almost completely removed. The slight increase in the oxygen concentration at the interface between surface layer (tungsten at deposition time) and bulk (beryllium) can be attributed to a BeO layer at the original Be sample surface. Although a cleaning step in the magnetron device is applied before W deposition (sputtering by pure Ar plasma for 60 s), no evidence is available that the natural oxide layer at the Be surface is removed completely.

The analysis of the sample surface after each sputtering step during the depth profile with high-resolution spectra enables the assignment of chemical states to the Be signals. The Be 1s photoelectron region is deconvoluted using MultiPak [4]. Three Gauss–Lorentz functions are fitted to the data in the Be 1s region. In particular within the binding energy region where both the metallic and alloy signals appear, it is necessary to restrict the fit. Therefore, a fixed difference between the oxidic and metallic Be 1s peak positions of 3.0 eV is used. For the third component in the Be 1s signal all parameters are kept free. In Fig. 3 the composition of the Be 1s signal with respect to the chemical bond state of beryllium is shown. In the near-surface region, the oxidic species dominate. This is expected from the elemental composition shown in Fig. 2 where oxygen is detected in the near-surface region.

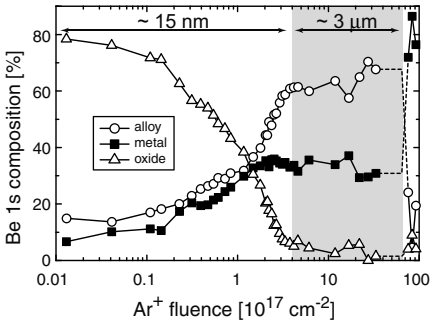

Fig. 3. Composition of the XPS Be 1s signal during the Ar^+ depth profiling. The hatched area between Ar^+ fluences of $4\times10^{17}\,cm^{-2}$ and $7.5\times10^{18}\,cm^{-2}$ represents the alloy zone. At the end of this zone, the trends are extrapolated (dashed lines), since at this fluence no high-resolution spectrum is available.

In this zone also only a few percent tungsten are present. The small oxygen fraction within the hatched alloy zone and also the at the end of the depth profile above $7.5\times10^{18}\,cm^{-2}$ shows a large scatter due to the small intensity in this region. The Be 1s intensity between approximately 113 and 118 eV is fitted by two peaks, labelled 'metallic' and 'alloy'. The resulting intensities and the difference in binding energy between these two peaks are plotted in Fig. 3. Up to a fluence of $2\times10^{17}\,cm^{-2}$, the metallic and alloy peak are approximately of the same intensity, with a slightly larger value for the alloy. At this fluence, the alloy peak gains intensity and reaches more than twice the strength in the shaded area where the $Be_{12}W$ is identified. At the interface to the Be bulk a sharp drop of alloy intensity is observed and finally the Be 1s signal is dominated by the metallic peak. The binding energy difference between metallic and alloy peak is practically constant in the alloy region and is 0.51 eV. Since the stoichiometry of this alloy layer is known from the RBS results, the BE of the Be 1s peak in the $Be_{12}W$ alloy is determined to 111.3 eV.

3.2. Beryllium films on tungsten (Be/W)

In this section, the interaction of thin Be films on a tungsten substrate, the inverse system compared to the W/Be films described in Section 3.1, are discussed. This situation is envisaged for Be being deposited on a W surface.

The Be films are deposited on polycrystalline tungsten at 300 K in a UHV preparation chamber

which is connected to an XPS analysis chamber, as described in Section 2. Sample preparation and analysis are carried out without transfer through the air. Despite the well-controlled vacuum conditions (see above) the deposited metal films are contaminated by oxygen with a maximum concentration of approximately 10% due to the high reactivity of Be. A detailed analysis is published in [8,9].

The deposited beryllium reacts already with the tungsten substrate at 300 K. Both in the Be 1s and W 4f signals a new component at lower BEs is necessary to fit the experimental data. The results for a 1.9 nm Be layer are shown in Fig. 4(a). The Be signal shows a peak at 114.8 eV for BeO and a large signal at lower BEs. This peak can only be fitted if two Gauss–Lorentz functions are used. During the fit procedure, the BE difference between the oxidic and metallic signal is kept constant at 3.0 eV. The additional Be 1s peak is located at 111.1 eV. This peak position results also from fits to Be layers with thicknesses from 0.5 nm to 4.8 nm. Below four monolayers a small variation in peak position towards smaller BEs is observed. However, since the Be signal is very weak due to the small photoelectron cross section, thin Be layers of a few monolayers have a bad signal-to-noise ratio and therefore a larger uncertainty in the fitting results. The corresponding W 4f signals are shown in Fig. 4(b). Here, no oxidic peak is observed, although the W $4f_{7/2}$ signal shows a small broadening after Be deposition (from 0.45 to 0.50 eV). The formation of a W–O surface oxide, however, would lead to a broadening of this peak by 0.11 eV. The W 4f signals are fitted by asymmetric Gauss–Lorentz functions. During the fit procedure, the W $5p_{3/2}$ signal is taken as a reference at 37.0 eV. In addition, the peak positions of the W $4f_{7/2}$ and $4f_{3/2}$ peaks are fixed at the positions from literature [12] and measurements at the clean tungsten surface ($4f_{7/2}$ at 31.4, splitting 2.17 eV). Further, the peak area ratio due to the spin-orbit splitting is kept constant at 0.77 (determined also at the clean W surface, theory would require 0.75). These restraints to the fit procedure result in an additional W 4f doublet located at 31.0 eV (W $4f_{7/2}$). Other than the Be 1s signals, the W 4f peaks remain constant in BE for deposited layers with thicknesses between 0.5 and 4.8 nm, especially for Be layers in the monolayer range. From experiments with increasing deposited Be amounts it becomes evident that only the Be directly at the layer–substrate interface shows the additional peak in the Be 1s spectrum. At 300 K, all additional Be increases the metallic signal only.

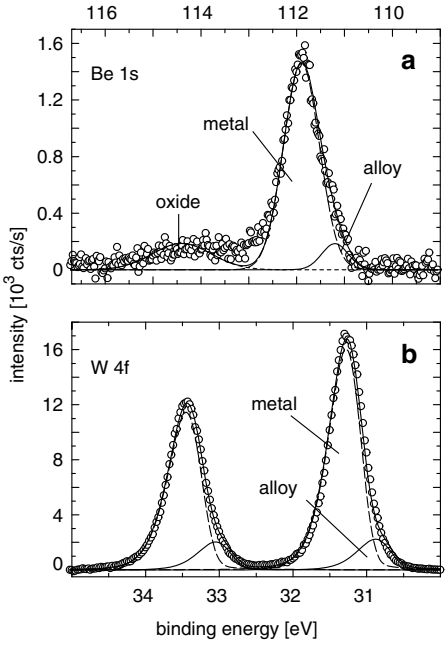

Fig. 4. Be 1s and W 4f signals measured at a 1.9 nm thick Be film on polycrystalline tungsten, deposited in UHV at 300 K. Both Be and W signals afford signals at lower BEs to fit the experimental data.

The situation changes at elevated temperatures. The metallic Be is deposited at 300 K. Two different annealing procedures are compared for Be layers between 1.2 nm and 3.3 nm initial thicknesses. In the first procedure Be layers are annealed for 30 min to increasing temperatures up to 1070 K. After each annealing step, the Be intensity is determined and a remaining thickness is calculated. For the Be layer thickness calculation, both the substrate and the layer signals are used [13]. In addition, the Be 1s region in high-resolution spectra allows the observation of a proceeding reaction between Be and W. In the second series Be layers in the same thickness regime are annealed at constant temperatures for up to 30 h. The composition and layer thickness are measured at the respective elevated temperature. In all cases, the Be intensity decreases above an annealing temperature of 570 K. The decrease in Be intensity goes parallel with a decrease in Be layer thickness. Depending on the initial thickness, the final Be layer amounts

to 1.1–1.4 nm after 1070 K. In all cases examined here, no complete loss of Be in the surface zone accessible by XPS is observed. In case of the long-term annealing experiments, the decrease in Be thickness takes place already during the ramp-up to the respective annealing temperature. During the remaining time, no significant further decrease is observed. A sputter depth profile (using Ar^+ at 3 keV) of an untreated and an annealed Be layer demonstrates that the Be loss cannot be explained by a diffusion of Be into the W bulk [9]. The Be intensity drops to zero after a sputtering fluence of 6×10^{15} cm^{-2} applied to a remaining Be-containing layer of 1.2 nm. The only solution to explain the loss of Be from the surface is sublimation. The remaining Be at the surface starts to react with W at the same temperature at which the layer thickness decreases.

In Fig. 5 the spectra of three Be layers are plotted before and after annealing to 770, 870, and 970 K. The initial Be layers were 1.3, 1.5, and 2.1 nm, respectively. After annealing, all three layers have a thickness between 1.0 and 1.2 nm. These thicknesses are reached already after the comparatively short temperature ramp-up. Therefore, the excess Be is lost very quickly in the initial annealing phase. The spectra shown compare the initial status after room temperature deposition (marked r.t.) with the final state after the annealing to the indicated temperatures. Already after 770 K annealing not only a reduction in Be layer thickness, but also the onset of the alloying reaction is visible. Both W and Be signals shift to lower BEs. At 970 K the formation of a Be–W alloy leads even in the W 4f signal to a second peak which is already visible by eye. Peak fitting to all signals yields Be:W ratios for the three temperatures of 5:1 (770 K), 3:1 (870 K), and 2:1 (970 K). This stoichiometry was also reached in the short-term annealing sequences discussed above. The final stoichiometry Be_2W is reached in the annealing of Be layers on W, but quantitatively only after annealing to at least 970 K. For this stoichiometry, the binding energies for Be 1s and W $4f_{7/2}$ are determined to 111.1 eV and 31.0 eV, respectively. The corresponding peak shifts with respect to the metal are 0.7 eV (Be 1s) and 0.4 eV (W 4f).

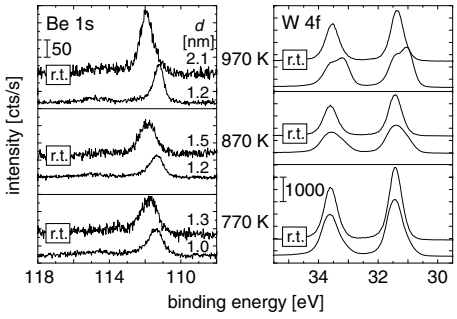

Fig. 5. Changes in the Be 1s and W 4f regions before and after long-term annealing to three different temperatures.

3.3. Interaction of Be-seeded deuterium plasmas with tungsten

In the PISCES-B device Be-seeded deuterium plasmas with variable Be fractions (0.001–0.01) can be produced [14] which are comparable in flux to the target surface to the expected fluxes for the ITER divertor (approximately 10^{19} cm^{-2} s^{-1}) [15]. During exposure, the target can be held at elevated temperatures under controlled conditions. Here we show the results of a tungsten sample which was exposed to a deuterium plasma at a sample temperature of 1260 K. The total flux at the sample was 8.0×10^{21} cm^{-2} s^{-1}. The Be concentration in the plasma was 0.4%, corresponding to a Be flux to the sample of 3.2×10^{19} cm^{-2} s^{-1}. The ion beam analysis of the sample by nuclear reaction analysis with 1 MeV ^{3}He yields a total amount of beryllium in the surface-near region accessible by NRA of 1.4×10^{17} cm^{-2}. No deuterium is measured in this sample due to the high exposition temperature. In the XPS survey spectra the elements W, Be, O, C, and La are detected. Lanthanum is present throughout the whole analyzed depth of ≈1.3 μm. Because of the large photoionization cross section, the La signals are quite prominent in the spectra. However, the total concentration (assuming a homogeneous distribution) is only around 1% and shows the maximum intensity near the surface. The origin of the La is probably eroded material from the LaB_6 cathode. For the quantitative assessment of the composition La is ignored. However, it should be noted that the Be 1s signal is close to a La 4d signal. Boron is not detected in XPS measurements due to its low photoionization cross sections, but it is traceable by NRA.

The compositional depth profile of the W samples exposed to the deuterium plasma seeded with 0.4% Be is shown in Fig. 6(a). The arrows indicate

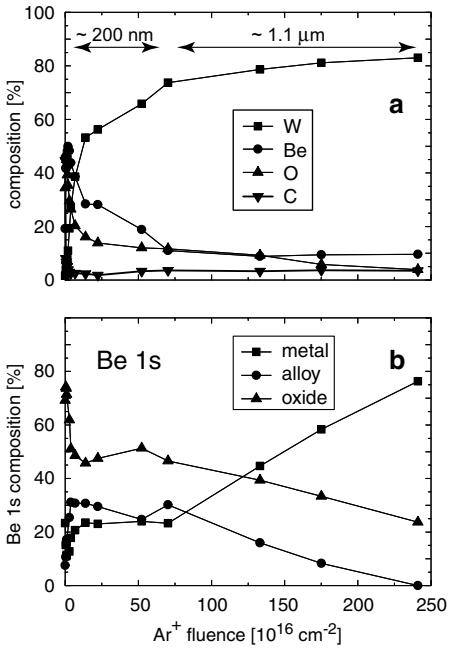

Fig. 6. Sputter depth profile of a W sample exposed to a Be-seeded deuterium plasma. Part (a) shows the elemental composition with depth. Part (b) shows the chemical composition of the Be 1s signal, determined by peak fitting.

the approximate depth, estimated by SDTRIM.SP using the composition from the XPS data. Besides the usual contamination of the first monolayers by air transport, the carbon concentration is almost constant around 3%. Oxygen is present throughout the analyzed depth, initially between 30% and 40%. At greater depths, the oxygen signal drops to 10% and below. The initially higher amounts can be related to the Be concentration. If both elements are present, BeO is the thermodynamically most stable compound. The origin of the oxygen can be either surface contamination or plasma impurities. Since the oxygen is present in greater depths, the latter explanation seems plausible. Due to the high exposure temperature, also oxygen diffusion into the bulk is possible. Up to an Ar^+ fluence of $2\times10^{16}\,cm^{-2}$ the tungsten concentration is small and reaches only around this fluence the 10% level. Therefore, the W substrate is covered by a layer consisting mainly of Be, C, and O. Above that fluence and within the first ≈200 nm, the W concentration increases in parallel to the decrease mainly of the Be component. Except in the very surface-near zone, Be and W show an opposite behavior: As much as W increases, the Be concentration decreases. Above an Ar^+ fluence of approximately $7\times10^{17}\,cm^{-2}$ W dominates the composition around 80% and above. However, during the whole analyzed depth of approximately 1.3 µm Be is present at a 10% level, whereas C and O are still at the 3–5% levels. Since also La is detected up to this depth (not shown), it seems plausible that the mixed material surface layer is produced by deposition of material from the plasma rather than by diffusive processes. However, a clear decision is not possible on the present data.

The analysis of the Be 1s BE region, shown in Fig. 6(b), allows the assessment of the Be chemistry in the deposited layer. The analyzed depth can be clearly separated in two regions, as indicated by the depth arrows in Fig. 6(a). In addition, the very surface is dominated by BeO with a concentration between 70% and 80%. This demonstrates that Be is enriched at the surface at elevated temperatures, as was shown in the case of a W layer on Be (Section 3.1). The driving force for this diffusional process can be the large enthalpy of formation of BeO and requires oxygen present at the surface (either as a plasma impurity or adsorbed by repeated air transports, as in Section 3.1). This BeO layer is reduced to below 50% above 3×10^{16} $Ar^+\,cm^{-2}$ and stays at this level up to 7×10^{17} $Ar^+\,cm^{-2}$. Within thin zone of approximately 200 nm thickness also the fractions of metallic Be and Be bound in a Be–W alloy are constant. The alloy component has around 30%, the metallic phase around 23%. The chemical shift between the metallic and alloy Be 1s signals in this depth zone is 0.6 eV. This shift is in between the shifts determined for Be_2W (0.7 eV) and $Be_{12}W$ (0.5 eV). Therefore, no clear assignment of the Be–W alloy stoichiometry is possible in this case. The large fraction of W in the surface zone, however, points towards a dominating Be_2W phase. Beyond the ≈200 nm surface zone, both alloy and oxide peaks decrease. The alloy peak is no more detectable at the end of the depth profile is fluence, at 2.4×10^{18} $Ar^+\,cm^{-2}$. At this fluence, still 24% of Be is chemically bound in BeO.

4. Conclusions

In this paper we compare three different scenarios for the interaction of Be with W and analyze the

resulting mixed material layers and compounds. The two fundamental cases are discussed first: the formation of Be–W alloy phases starting with a pure layer of one component on a bulk substrate of the respective other. The third case treats the interaction of a deuterium plasma (which is seeded with a small Be concentration) and a hot W substrate. In both cases of the layered systems, an alloy surface layer is formed. However, a strong difference in the thickness of this alloy layer is observed. In the case of a W layer on Be, the final surface layer after annealing to above 1000 K has a thickness of several μm (depending on the initially deposited amount of W). During alloying the whole available tungsten is used to form a $Be_{12}W$ alloy which is stable at the surface of the Be bulk. As a consequence, the properties of this alloy layer determine the physical properties of the material, in particular its melting point. Comparing the alloy layer with the pure metals Be and W, its melting point is approximately that of the pure Be (from the phase diagram only a marginally higher melting temperature for $Be_{12}W$ than for pure Be can be deduced). The deposited W surface layer ($T_m = 3695$ K), however, looses the property of a very high melting point completely. For the opposite system of a pure Be layer on W substrates so far only experiments with layers up to a few nm are carried out. These experiments, however, demonstrate a subtle balance between alloying (the final alloy phase above 970 K is Be_2W in this case) and sublimation of Be. In all cases of initial Be layers between 1 and 4 nm the finally formed Be_2W alloy layers have thicknesses around 1.2 nm. The excess Be is not found in greater depths, as shown in sputter depth profiles. The conclusion to this is that Be sublimates and is no longer available for alloy formation. The balance between Be sublimation and alloy formation by interdiffusion of Be and W determines the formed surface layer in this case. For the application of both Be and W in e.g. ITER, the second scenario seems more probable than the case of W layers deposited on Be. For Be layers on W, eroded Be from the main chamber needs to be transported into the baffle/divertor regions. This is the transport path for light impurities and actually a design feature. The opposite process, transport of eroded W from the baffle into the main chamber and deposition of W on the Be walls, seems very improbable due to the plasma transport properties. However, also W layers on Be might be of importance locally where W and Be surfaces are in close vicinity. Be deposited on W at elevated temperatures would lead to an alloy layer. Due to the limited thickness found in our experiments the detrimental effects of the alloy layer on W seem small, however. Finally, the exposure of W samples to a Be-seeded plasma in PISCES-B demonstrate that even under conditions of small Be concentrations in the plasma Be-containing surface layers are formed. These layers may contain even 10% of Be which is not only found in Be–W alloy phases, but also in BeO. The oxide is the Be compound with the largest enthalpy of formation and is formed together with oxygen as an impurity in the plasma. From the presently available data, measured at high substrate temperatures, the formation of thick Be-containing layers cannot be excluded even for very low Be plasma concentrations. This could be due to Be diffusion caused by the constant influx of Be to the surface. More experiments of this kind are necessary to asses the temperature influence on the composition of the formed Be-containing mixed materials under plasma exposure.

References

[1] R.R. Parker, Nucl. Fusion 40 (2000) 473.
[2] T.B. Massalski, H. Okamoto, P.R. Subramanian, L. Kacprzak, Binary Alloy Phase Diagrams, 2nd Ed., ASM International, Materials Park, Ohio, 1996, Version 1.0.
[3] M.P. Seah, I.S. Gilmore, G. Beamson, Surf. Interface Anal. 26 (1998) 642.
[4] MultiPak, Ver. 7.0.1, Physical Electronics, 2004.
[5] N.P. Barradas, C. Jeynes, R.P. Webb, Appl. Phys. Lett. 71 (1997) 291.
[6] M. Mayer, SIMNRA User's Guide, Report IPP 9/113, Max-Planck-Institut für Plasmaphysik, Garching, Germany, 1997. <http://www.rzg.mpg.de/~mam/, mailto:matej.mayer@ipp.mpg.de>.
[7] R.G. Thomas et al., Phys. Rev. 75 (1949) 1612.
[8] A. Wiltner, Ch. Linsmeier, J. Nucl. Mater. 337–339 (2005) 951.
[9] A. Wiltner, Ch. Linsmeier, New J. Phys. 8 (2006) 181.
[10] E. Taglauer, W. Heiland, in: P. Varga, G. Betz, F.P. Viehböck (Eds.), Proceedings of the International Symposium on Sputtering, Inst. Allg. Phys. TU Wien, 1980, p. 423.
[11] W. Eckstein, Computer Simulation of Ion–Solid Interactions, Springer Series in Materials Science, vol. 10, Springer, Berlin, 1991.
[12] J.F. Moulder, W.F. Stickle, P.E. Sobol, K.E. Bomben, in: J. Chastain (Ed.), Handbook of X-ray Photoelectron Spectroscopy, Perkin–Elmer Corp. Eden Prairie, 1992.
[13] A. Wiltner, Ch. Linsmeier, Phys. Status Solidi A 201 (2004) 881.
[14] R. Doerner, M. Baldwin, K. Schmid, Phys. Scr. T111 (2004) 71.
[15] A.S. Kukushkin, H.D. Pacher, D.P. Coster, et al., J. Nucl. Mater. 337–330 (2005) 50.

IOP Publishing Physica Scripta
Phys. Scr. **T128** (2007) 133–136 doi:10.1088/0031-8949/2007/T128/026

Structural investigation of the Be–W intermetallic system

A Wiltner, F Kost, S Lindig and Ch Linsmeier

Max-Planck-Institut für Plasmaphysik, EURATOM Association, Boltzmannstrasse 2, D-85748 Garching b, München, Germany

E-mail: linsmeier@ipp.mpg.de

Received 26 October 2006
Accepted for publication 27 November 2006
Published 8 March 2007
Online at stacks.iop.org/PhysScr/T128/133

Abstract
The intermetallic Be–W system is investigated by analysing both a W film on polycrystalline Be and the inverse system, Be films on polycrystalline W. The films are annealed up to 1070 K and the alloy formation is investigated by a combination of Rutherford backscattering spectroscopy (RBS) and x-ray photoelectron spectroscopy (XPS). For the structure analysis and identification of the formed alloys, x-ray diffraction (XRD) measurements are used. In the case of W films on Be, we identify $Be_{12}W$ within the diffusion depth, whereas Be films on W show alloy formation restricted to the film–substrate interface. Both XPS and XRD measurements indicate the formation of Be_2W.

PACS numbers: 61.10.Nz, 68.35.Fx, 79.60.-i

1. Introduction

For the international tokamak experiment (ITER), carbon (C), tungsten (W) and beryllium (Be) are planned to be the first wall materials. Therefore, the interactions between these components are of fundamental importance. The Be–W intermetallic system shows three different alloys, namely Be_2W, $Be_{12}W$ and $Be_{22}W$ [1]. Having different physical properties, it is important to know under which conditions the different alloys are formed. Since W is used in the divertor region due to the high melting point ($T_m = 3695$ K), the lower melting point of all known alloys is detrimental to the stability of these parts. In particular $Be_{22}W$ ($T_m <$ 1800 K) and $Be_{12}W$ ($T_m < 2000$ K) have significantly lower melting points. Little is known about the reactivity of Be and W in the literature. Most data reported up to now are measured as bulk data. We are interested in surface and near-surface processes, since two cases can be distinguished concerning processes in a fusion device. Namely, tungsten can be deposited on to a beryllium surface or vice versa. Thus, two approaches have been chosen in our investigations. A tungsten film has been prepared on a beryllium substrate as well as an inverse system. By this means, we can investigate diffusion or desorption processes and alloy formation. After preparation, the samples are heated up by progressive steps and investigated with Rutherford backscattering spectroscopy (RBS), x-ray photoelectron spectroscopy (XPS) and x-ray diffraction (XRD). Whereas RBS and XPS measurements provide information on elemental composition and chemical states, the XRD powder patterns allow the identification of crystallographic phases.

2. Experimental

RBS is performed at the Garching 3 MV tandem accelerator (RBS with ^{1}H, ^{3}He and ^{4}He, scattering angle 165°). XPS analysis is performed in a PHI ESCA 5600 spectrometer. For these measurements, we use a monochromatic Al Kα source ($h\nu = 1486.6$ eV) and an analysed area of 0.8 mm in diameter. The sputter depth profiles are measured in this UHV chamber under an ion impact angle of 45°. For experimental details concerning both techniques and their combination, we refer to [2].

The diffraction patterns are obtained by $\Theta/2\Theta$ scans using an x-ray diffractometer XRD 3003 PTS from Seifert equipped with a Cu anode. The samples are illuminated by an x-ray beam of about 3 mm diameter with the energy of the Cu K$\alpha 1/\alpha 2$ lines ($\lambda = 1.541$ Å). For the Be film on W, we use a fixed incident angle of 1° with respect to the surface. This geometry is used for a low Z (Be) material with a low cross-section for x-rays on a high Z (W) material leading to a higher surface sensitivity.

Two different systems are investigated in the experiments. For the first case, W on Be, a polycrystalline Be substrate

($1 \times 1\,cm^2$) is used. The W film (thickness 200 nm) is deposited in a magnetron sputter device (base pressure 2×10^{-5} Pa). The Be substrate is etched in a pure Ar plasma before the layer deposition is started. The sample is then analysed by RBS and XPS after applying thermal treatments. For the second case, Be on W, we use a polycrystalline W substrate ($1 \times 1\,cm^2$). These measurements are performed in a UHV chamber where surface analysis (using XPS) and sample preparation (cleaning and layer deposition) are possible without transfer through air. The W sample is cleaned using alternating sputter (3 keV Ar^+) and heating cycles (970 K) until no impurities are detected in the XPS spectra. The Be layers are deposited from a commercial evaporator (Omicron EFM3) using a BeO crucible filled with Be pieces (HEK GmbH, 99.999%). The base pressure in the UHV chamber is better than 2×10^{-8} Pa. During the deposition procedure, the pressure is below 4×10^{-8} Pa.

From the RBS spectra measured for the first system (W on Be), we get information about sample composition and depth distribution, whereas XPS analysis provides further information about sample composition in the near-surface region (several nanometres). Moreover, the chemical states of Be and W are determined from chemical shifts. After the final annealing step (1070 K, several hours), the sample is analysed with a sputter depth profile (3 keV Ar^+) in the XPS chamber. From XRD measurements, we get information about both the structures of the layer and the substrate after the final annealing step. For the second system (Be on W), thermal treatment and XPS analysis are performed in the same UHV chamber without any transport through air. RBS measurements are not applied. Immediately after layer deposition, the sample is analysed using XPS spectra in survey and high resolution modus. From the survey scans, the sample composition is estimated. From spectra obtained in the high resolution mode, information on the chemical states is gained from the shifts in the Be 1s and W 4f signals. The samples are annealed in steps of 100 K up to 1070 K and analysed at room temperature. For the XRD analysis, we deposit Be on W ($\gtrsim$50 nm) in a separate preparation sequence and anneal the sample up to 970 K for 90 min in UHV before the XRD measurements are performed.

3. Results and discussion

3.1. W film on Be substrate

The results of RBS and XPS measurements were presented in detail at the PSI-17 conference in 2006 [2]. Here, we present a short summary. After each annealing step (up to 1070 K), the sample is analysed with RBS. Spectra obtained with ^{1}H and ^{4}He give information about changes in the W layer. Below 1000 K, the W layer is barely affected. At 1070 K, a beginning Be–W intermixing at the layer–substrate interface is observed. While the annealing time increases, the W intensity decreases, but the W is not completely lost into the Be bulk. The Be edge is also unaffected up to 970 K. After the first annealing step at 1070 K, an intermixing of W and Be is concluded from the position of the Be edge and an additional Be surface peak. W in the surface layer is replaced by Be. After the final annealing step at 1070 K, the Be surface signal vanishes and the RBS spectrum indicates a smooth Be depth distribution. From the ^{1}H and ^{4}He RBS measurements, the depth profiles are calculated. As is observed in the RBS measurements, the Be–W intermixing begins above 1000 K and leads to a stable phase after 600 min at 1070 K. The stoichiometric ratio indicates the formation of $Be_{12}W$. The sample is then analysed by a sputter depth profile in combination with XPS. After the removal of surface contaminations (C and O), we observe a constant sample composition (75.7% Be, 22.9% W and O) representing the Be–W intermetallic phase. XPS measurements in combination with sputter depth profiling do not represent the true stoichiometry of a compound due to preferential sputtering effects. In the high resolution spectra, we observe an alloy component (111.3 eV) besides the metallic state (111.8 eV) within the Be 1s signal. The binding energy shift between these components reaches −0.5 eV. At the outermost surface, intensity from BeO (114.8 eV) dominates the Be 1s signal. After removal of this BeO surface layer, the whole Be–W layer shows a constant composition within the Be 1s signal (65–70% alloy, 30% metal and <5% BeO).

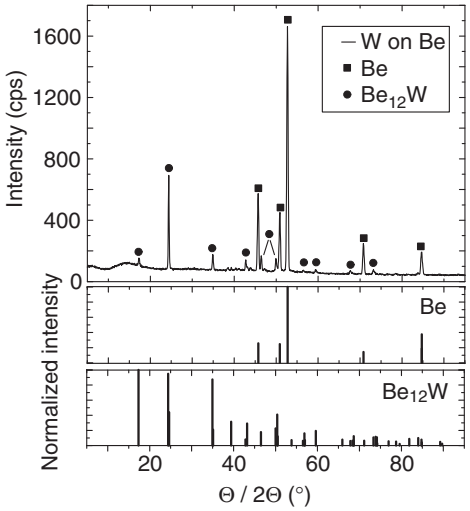

Figure 1. XRD analysis of a 200 nm thick W film on polycrystalline Be after the final annealing step at 1070 K. Reference data are given in the lower panels. Reflexes from Be substrate (■) and $Be_{12}W$ (●) are marked.

For the structural analysis of the Be–W layer, XRD measurements are performed. The diffraction diagram after the final annealing step at 1070 K is shown in the upper panel of figure 1. The reference data for Be and $Be_{12}W$ in the lower panels are taken from the JCPDS–ICDD database [3]. The same reference patterns are estimated from the software package Diamond [4], taking into account the crystal structure of Be and $Be_{12}W$ [5]. The structure parameters are as follows. Be is a metal with a hexagonal lattice structure ($P6_3/mmc$, $a = 2.286$ Å, $c = 3.584$ Å) and $Be_{12}W$ shows a tetragonal unit cell ($I4/mmm$, $a = 7.220$ Å, $c = 4.220$ Å).

From a comparison of measured and reference data, we conclude the formation of $Be_{12}W$. The respective references of $Be_{12}W$ in the measured diffraction pattern are marked by ●. Additional peaks are from the Be substrate (■). In particular, no diffraction patterns originating from W, BeO and Be_2W are measured. Since we observe only Be and $Be_{12}W$ signals, we conclude the formation of this alloy within the Be–W intermixing depth range. The Be pattern originates from the substrate. The diffusion of W and Be leads to the formation of an ordered alloy ($Be_{12}W$) in the Be–W layer, as is also determined by RBS analysis and measured by XPS sputter depth profiling.

From the combination of RBS, XPS and XRD measurements, we conclude a Be–W intermixing above 1000 K with a formation of a constant alloy phase after long-term annealing at 1070 K. This alloy is identified as $Be_{12}W$.

3.2. Be films on W substrate

We have already presented XPS measurements in [2, 6, 7] and give here a short summary. After room temperature deposition of Be layers from submonolayer coverage up to 4 nm thickness, we observe a Be–W surface alloy restricted to the interface. The surface alloy is visible in both signals (<10% in Be 1s and W 4f). Be deposited in excess is in the metallic state. We observe also BeO (<10% on average) in the layer. Up to 670 K, the Be layer thickness and composition, respectively, remain constant. Above 670 K the Be layer thickness decreases and we observe an increase in the alloy intensities within the Be 1s (alloy at 111.1 eV, $\Delta BE = -0.7$ eV) and W 4f (alloy at 31.0 eV, $\Delta BE = -0.4$ eV) signals. The stoichiometric ratio of this alloy compound is $Be_{\leqslant 2}W$. The observation of a binding energy shift of -0.7 eV as compared to -0.5 eV, as given above for $Be_{12}W$, indicates the formation of a different alloy stoichiometry. From this observation and the stoichiometric ratio, we conclude the formation of Be_2W. The decrease of layer thickness depends on the initially deposited amount. Thin Be layers (up to 1.2 nm) show no Be loss. If the initial coverage ranges from 1.2 to ∼ 3.0 nm, the residual layer thicknesses are 1.4 nm at maximum. Thicker Be layers (>3.0 nm) show a decelerated decrease with a residual thickness above 1.6 nm. In all cases, an alloy phase (Be_2W) is observed at 970 K. Sputter depth profiles performed after the final annealing step indicate an intermixing of Be and W in restricted depth. Be diffusion into the W bulk is not observed. The Be loss during the thermal treatments is due to Be desorption rather than diffusion into greater depths.

For the XRD analysis, a thick Be film ($\gtrsim$50 nm) is deposited on a W substrate in UHV. The layer thickness after room temperature deposition exceeds the information depth of XPS analysis (several nanometres) and a thickness estimation using Be and W signal intensities is not possible. The Be amount decreases while annealing at 970 K for 90 min, but a layer thickness estimation using XPS intensities from Be 1s and W 4f signals is still not possible. The high resolution XPS measurements of the Be 1s and W 4f signals immediately after the thermal treatment are dominated by intensities from the metallic states. Since XPS measurements are surface sensitive, we cannot analyse the Be–W intermixing layer at the film–substrate interface. These observations for the

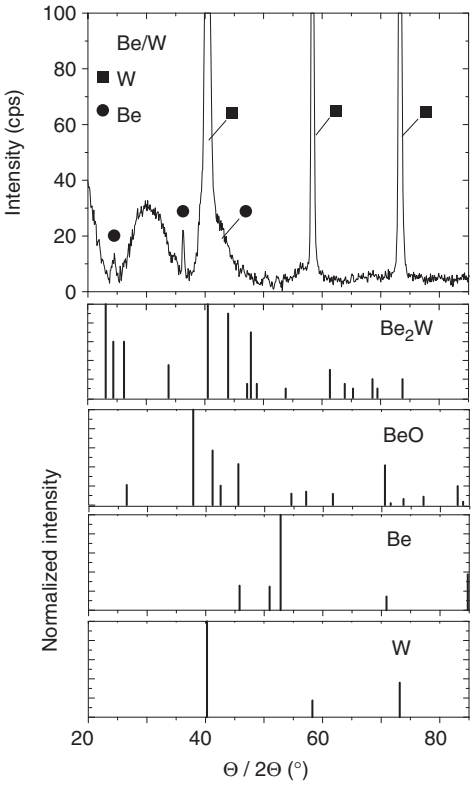

Figure 2. Analysis of a $\gtrsim$50 nm thick Be film on polycrystalline W after annealing at 970 K and the identification of W (■) and Be (●). Reference data for Be_2W, Be, W and BeO are given in the panels below. The broad signal at 30° is an artefact due to the sample holder.

$\gtrsim$50 nm Be film on W are compatible with and confirm the experiments described earlier [2, 6, 7]. During the thermal treatment at 970 K, we observe a decelerated Be loss compared to Be films of a few nm thickness. The detection of metallic states in both signals confirms the restriction of the Be–W intermixing to the interface at 970 K, as is observed after deposition of thin Be films on W. In particular, no alloy formation throughout a larger Be thickness is observed, as was shown for the first case (W on Be, see subsection 3.1). We gain more information concerning the Be–W layer and interface composition from XRD measurements. The XRD pattern of the sample is shown in the upper panel of figure 2. The measured diffraction pattern is compared with XRD patterns (lower panels in figure 2) taken from the JCPDS database and calculated by the software package Diamond. The respective crystal structure data are taken from the ICSD database. W has a cubic crystal structure (Im-3 m, $a = 3.1652$ Å), BeO has a tetragonal unit cell ($P4_2/mnm$, $a = 4.750$ Å, $c = 2.470$ Å) and Be_2W shows a hexagonal lattice structure ($P6_3/mmc$, $a = 4.437$ Å, $c = 7.347$ Å). The measured XRD pattern is dominated by the substrate (W). Additional reflexes with

minor intensities, however, cannot be explained by W. These reflexes originate from Be. The reflexes originating from Be and W are identified by measuring reference samples and a comparison with reference data, respectively. The residual reflexes observed in the measured pattern cannot be clearly identified as BeO or Be_2W by comparing their positions with powder patterns originating from the JCPDS database and the software package Diamond, respectively. These reference data are shown in the lower panels of figure 2. Diffraction patterns originating from $Be_{12}W$ are not observed. Since Be is deposited onto W, the XRD measurements are performed by using a fixed incident angle of 1° with respect to the surface. However, XRD analysis is applied for the structural investigation of bulk materials and is not sensitive to small amounts of components or thin films. From the observation of W and Be, we conclude again a restriction of the intermixing of Be and W limited to the film–substrate interface, as was already shown for the XPS measurements and sputter depth profiles of thin Be films on W. Alloy formation is observed in the XPS analysis, but the restriction to the interface does not allow an observation of the respective diffraction patterns in the XRD measurements.

After the XRD analysis, we perform a sputter depth profile in combination with XPS in high resolution mode. From this measurement, we gain information on the Be layer and, moreover, on the film–substrate interface composition. The near-surface region is dominated by contamination (C and O) due to transport through air for the XRD analysis. After removal of this contaminated layer, we observe Be (90%) and O (10%) within the Be film. The Be 1s signal is dominated by intensities originating from metallic (70–80%) and oxidic Be (10% in average). The remaining signal intensity is at the position of the alloy component ($\Delta BE = -0.65$ eV). The measured composition of the Be layer and Be 1s signal, respectively, are comparable to the values which are observed immediately after film deposition. After reaching the film–substrate interface, the intensity of the alloy component increases (60%). Metallic (30–40%) and oxidic Be (remaining intensity) are still observed. After removal of the Be–W intermixed layer, the Be 1s signal vanishes. Intensity originating from the W 4f signal is detected when reaching the film–substrate interface. In the W $4f_{7/2}$ signal, we observe metallic W (∼15%) and an alloy component (∼40%, $\Delta BE = -0.4$ eV). As was mentioned for the sputter depth profile for the W film on Be, we cannot determine the true stoichiometry of the alloy component with these measurements due to preferential sputtering effects. From the observation of an alloy component restricted to the film–substrate interface, we conclude again a limited diffusion of Be and W at 970 K. The observation of the chemical shifts within the Be 1s (−0.65 eV) and W 4f (−0.40 eV) signals and the stoichiometry of $Be_{<2}W$ indicates the formation of the ordered alloy Be_2W. Metallic Be is detected in the layer, as it is also measured in the XRD analysis.

From XPS measurements of thin Be films on W and a XRD analysis combined with a XPS sputter depth profile of a thick Be film, we conclude the formation of Be_2W is restricted to the film–substrate interface.

Thin Be films on W and the separately deposited Be film for XRD analysis are annealed up to 970 K. As shown in [6, 7], a thermal treatment up to 1070 K does not change the alloy amount within the Be 1s and W 4f signal significantly. Long-term annealing experiments for Be films on W at temperatures above 1000 K have not been applied up to now. The W films on Be are annealed up to 1070 K. Below this temperature no diffusion is observed. The W tiles in ITER are expected to operate at values below these temperatures. In addition, a Be deposition on W is more likely compared to W on Be. From a comparison of both experimental approaches, we conclude a limited diffusion of Be and W under ITER conditions and the formation of Be_2W rather than $Be_{12}W$ or $Be_{22}W$.

4. Summary

The crystallographic structure of the Be–W intermetallic system is analysed in detail in combination with additional qualitative and quantitative techniques. We deposit W films on Be and vice versa in order to determine diffusion and alloy formation of both metals. A W film on Be shows a Be–W intermixing above 1000 K and the final alloy is identified as $Be_{12}W$. This conclusion is drawn from the identification of the $Be_{12}W$ diffraction pattern in XRD measurements, the constant stoichiometry in the RBS measurements and a binding energy shift within the Be 1s signal in the XPS analysis.

Since Be deposition on W is more likely under ITER conditions, also Be layers on polycrystalline W are investigated. Independent from the initially deposited Be amount, the samples show a Be–W intermixing in restricted depth after annealing at 970 K. Be amounts in greater depth are not observed in sputter depth profiles after long-term annealing experiments up to 970 K. From the XRD analysis of a Be film after thermal treatment at 970 K and XPS binding energy shifts within the Be 1s and W 4f signals, the formation of Be_2W rather than $Be_{12}W$ or $Be_{22}W$ is concluded. The combination of XRD and XPS analysis affirms the observation of a restriction of Be–W intermixing.

Acknowledgments

We thank F Koch for the preparation of W films on Be. The cooperation of K Ertl and J Roth in the analysis of the RBS data of the W/Be system is greatly appreciated.

References

[1] Massalski T B, Okamoto H, Subramanian P R and Kacprzak L 1996 *Binary Alloy Phase Diagrams* 2nd edn (Materials Park, OH: ASM International)
[2] Linsmeier Ch, Ertl K, Roth J, Wiltner A, Schmid K, Kost F, Bhattacharyya S R, Baldwin M and Doerner R P *J. Nucl. Mater.* at press
[3] The International Centre for Diffraction Data (ICDD), PDF database 2000 available online at http://www.icdd.com
[4] Diamond 2006 Version 3.1d, Crystal Impact GbR, 2006
[5] Inorganic Crystal Structure Database 2004 Version 1.3.3, NIST, FIZ Karlsruhe, Germany
[6] Wiltner A and Linsmeier Ch 2005 *J. Nucl. Mater.* **337–339** 951
[7] Wiltner A and Linsmeier Ch 2006 *New J. Phys.* **8** 181

New Journal of Physics
The open-access journal for physics

Surface alloying of thin beryllium films on tungsten

A Wiltner and Ch Linsmeier[1]
Max-Planck-Institut für Plasmaphysik, EURATOM Association,
Boltzmannstr. 2, D-85748 Garching b. München, Germany
E-mail: linsmeier@ipp.mpg.de

New Journal of Physics **8** (2006) 181
Received 2 May 2006
Published 8 September 2006
Online at http://www.njp.org/
doi:10.1088/1367-2630/8/9/181

Abstract. The bimetallic system Be–W is studied after room temperature deposition of Be films on W and annealing experiments up to 1070 K using x-ray photoelectron spectroscopy (XPS). Already at room temperature an intermixing at the interface occurs. The amount of intermetallic compound increases during the annealing experiments, but is limited to ∼1.2 nm. The surface alloy formation is clearly visible as a binding energy (BE) shift of both core levels Be 1*s* and W 4*f*, and in the valence band (VB) region. The surface alloy is stable and the remaining layer thickness is independent of the initial Be layer thickness. Using a combination of sputter depth profiling before and after annealing and Monte Carlo simulation of the sputter process (TRIDYN) the depth scale of Be–W inter-diffusion is determined.

Contents

[1] Author to whom any correspondence should be addressed.

PII: S1367-2630(06)23685-1

1. Introduction

Thin metal-on-metal films are investigated in terms of growth mechanism, electronic structure or material aspects [1]–[3]. Generally, photoelectron studies of the surface alloying process are of great interest since both core level and valence band (VB) spectra are sensitively affected by the alloying process. The core level shift was detected, with subsequent alloying e.g. in systems like $Cu_xPd_{(1-x)}$ and $Ag_xPd_{(1-x)}$ [4, 5] and was found to be dependent on the stoichiometric ratio of the respective metals.

The Be–W intermetallic system is of special interest due to the application of both metals as first wall materials in a fusion device [6]. Surface alloying and therefore changed material properties result from alloy formation because of the exposure of these materials to high heat and particle fluxes at the first wall of fusion devices. Due to the different electronic structures of the transition element tungsten (delocalized *d* electrons dominate) and beryllium (*s* states dominate) a strong influence of the alloying both on the core levels and the valence levels is expected though modifications in the coupling of the *d* states [4, 7]. This paper describes the first observation of a surface alloy in the Be–W system and the application of x-ray photoelectron spectroscopy (XPS) as a sensitive tool for a detection of the alloying process.

Two metals can either form an ordered or an unordered alloy depending on atomic radius, chemical behaviour and metal lattices. Be and W show neither comparable atomic radii, chemical behaviour, nor identical lattice structures. The earth alkaline metal beryllium has an atomic radius of 0.1113 nm and crystallizes in the hcp structure. Tungsten is a transition metal with a bcc bulk structure and an atomic radius of 0.1442 nm. The Be–W phase diagram exhibits three stoichiometric compounds: $Be_{22}W$, $Be_{12}W$ and Be_2W with small phase widths [8]. The respective intermetallic compounds are examples for ordered alloys. There also exists a miscibility gap in the phase diagram. We deposit Be films on polycrystalline tungsten. If a reaction occurs, we expect the formation of Be_2W, since we approach the Be_2W phase in the phase diagram from the W-rich side. First measurements of the Be–W intermetallic system were published by Watts [9]. In his study, Be and W were mixed as powders, pressed and subsequently annealed. Vasina and Panov [10] reported on the Be–W alloy formation using crystallographic measurements. We presented first results of thin Be films on tungsten and the formation of a beryllide at the PSI-16 conference [11]. Doerner *et al* observed the formation of a tungsten-beryllide in a beryllium-seeded deuterium plasma (PISCES-B) using Auger electron spectroscopy (AES) sputter depth profiles [12]. They also reported on the Be–W alloy formation, while operating a tungsten effusion cell filled with Be. The alloy formation was analysed by wavelength dispersive spectroscopy and scanning electron microscopy, respectively. Zuber *et al* [13] investigated Be films on W(110) and W(100) using work function change measurements ($\Delta\phi$), low energy electron diffraction (LEED) and electron energy loss spectroscopy (EELS). The substrates were held between 300 and 1000 K. Schlenk and Bauer [14] deposited Be on the W(110) surface at room temperature and characterized the system using AES, EELS, $\Delta\phi$ measurements, LEED and thermal desorption spectroscopy (TDS). They found a layer growth mode with a dense packing of Be in each layer. Chrzanowski and Bauer [15] reported on the adsorption of Be on W(211) using LEED, AES, EELS, TDS and $\Delta\phi$ measurements. The Be–W alloy formation was not addressed in these publications describing thin Be films on different W planes.

Johansson *et al* [16] measured surface core level shifts (SCLS) of Be single crystals using synchrotron radiation and compared these experimental data with calculated results reported by Aldén *et al* [17]. Synchrotron radiation promises the highest surface sensitivity by tuning

the photon energy such that small photoelectron kinetic energies are achieved. To study surface alloying, we are more interested in the surface-near region and interface. XPS measurements using Al Kα radiation are particularly suitable for these requirements since the photoelectron kinetic energy originating from Be 1s core levels is around 1370 eV. At these energies the inelastic mean free path of electrons is 1.4 nm, resulting in a surface near information depth. Therefore XPS analysis provides both, a high surface sensitivity, and information about chemical interactions in the near-surface region. Especially in the case of surface alloying XPS promises direct information about alloy formation in this intermetallic system.

2. Experimental procedure

The experiments are performed in a commercial ESCA spectrometer (PHI ESCA 5600). Using the monochromatic x-ray source (Al Kα, 1486.6 eV) the best spectral resolution is 0.26 eV. The analysed area is 0.8 mm in diameter. XPS measurements are performed under a take-off angle of 22° with respect to the surface normal. We refer the binding energy (BE) scale to the Au $4f_{7/2}$ signal at 84.0 eV and calibrate it additionally with the Cu $2p_{3/2}$ and Ag $3d_{5/2}$ signals [18]. During the experiments, the pressure is better than 2×10^{-8} Pa. The polycrystalline tungsten is cleaned using alternating sputter (3 keV, Ar^+) annealing (up to 970 K) cycles until no impurities are detected in XPS survey scans. The analysis system is connected to a preparation chamber where the Be layer deposition is performed using a commercial evaporator (Omicron, EFM3). The Be (HEK GmbH, 99.999%) is suspended in a BeO crucible. During the evaporation process, the pressure is better than 4×10^{-8} Pa. Despite the low pressure, the deposited Be layers contain small amounts of oxygen (see below). After room temperature deposition and analysis, the samples are annealed in steps of 100 K at 30 min per step up to 1070 K. Annealing at higher temperatures is not performed by now, since the expected operation temperatures at the first wall in a fusion device are around 1100 K at maximum. The XPS measurements are carried out after cooling down to room temperature. In additional long-term annealing experiments, XPS analysis is performed at the respective elevated temperature. The layers are analysed in high resolution spectra (pass energy 2.95 eV) in order to resolve spectral details. Survey scans (pass energy 93.90 eV) are used for the quantitative determination of film thicknesses. The Be films are analysed with both, survey and high resolution scans, after room temperature deposition, after each annealing step and while annealing, respectively. Details of the film thickness determinations using the XPS intensities from both substrate and film signals are given elsewhere [19]. We assume a layer growth mode after room temperature deposition and annealing experiments as reported in [14]. Since no densities for Be–W alloys are available, the layer thicknesses after annealing experiments given here are calculated using the density of metallic Be (1.85 g cm^{-3}). One monolayer Be is then equivalent to a thickness of 0.2 nm.

3. Results and discussion

3.1. Be layers after room temperature deposition

Figure 1 shows a sequence of high resolution spectra with increasing Be layer thicknesses. For the Be 1s spectra, a Shirley background is used, whereas from the W $4f$ signal a linear background is subtracted. Despite the low sensitivity due to the small photoionization cross-section, the Be 1s

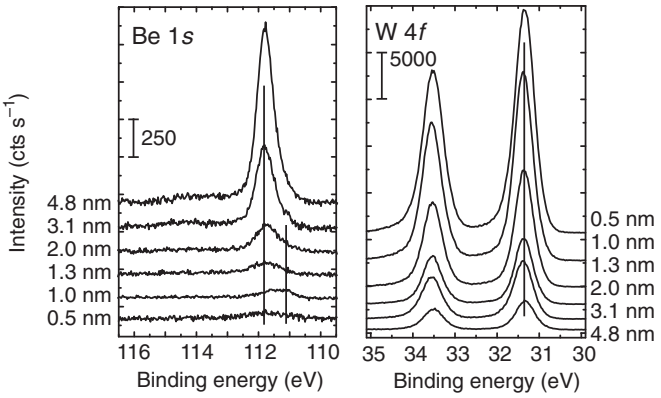

Figure 1. Be 1s and W 4f signals with increasing layer thicknesses after Be deposition at room temperature. The peak positions are marked at BEs of 111.8, 111.1 eV (Be 1s) and 31.4 eV (W 4f).

signals show a clearly visible fraction at lower BEs besides the metallic signal at 111.80 eV. As mentioned above, the layers are slightly contaminated with O and we find a small signal originating from BeO around 114.8 eV. The W 4f signals show no overall shift, but the full-width-at-half-maximum (FWHM) of the W 4$f_{7/2}$ peak increases slightly (0.05–0.10 eV, at the detection limit!) compared to the clean substrate.

The Be 1s signals are fitted by Gauss–Lorentz curves [20][2] with a Gaussian ratio of 80% and with fixed BEs for metallic Be (111.8 eV) and oxidic Be (114.8 eV) [21, 22]. Both fractions, metallic and oxidic Be, are taken as reference points for the third component which is observed at 111.1 eV. In case of the W 4$f_{7/2}$ signal, we position the metallic peak at 31.4 eV. The best agreement between data and fit curves is achieved using an additional peak at 31.0 eV. For the W 4f signals, we employ asymmetric Doniach–Šunjić functions [23] and keep the 7/2 and 5/2 spin–orbit splitting and area ratio constant at $\Delta = 2.18$ eV and 0.77, respectively. We assign the components at lower BEs in both the Be 1s and W 4f signals to a Be–W surface alloy. SCLS on clean Be substrates are in the same range (first layer: -0.82 eV, second layer: -0.57 eV, third layer: -0.26 eV [16]). However, using Al Kα radiation, we are sensitive for the whole near-surface region (several nanometres) and surface core levels can be excluded as origin of the additional peak in the Be 1s signal. To detect SCLS, the photoelectron kinetic energy must be close to the minimum of the electron escape depth. This is achieved by a photon energy around 135 eV, available at a synchrotron [16]. Using Al Kα radiation, however, we are not sensitive for SCLS and cannot resolve these BE shifts characteristic for the first atomic layers of a solid. Furthermore, we determine an additional signal in the W 4f signal by applying the peak fitting procedure, which cannot be explained by a SCLS within the W substrate signal. The alloy intensity in the Be 1s signal increases up to a deposition of ~4 ML (~0.8 nm) and is accompanied by a maximum in FWHM. In this film thickness region, the alloy contribution to the Be 1s intensity is ~50%. Further Be deposition leads to an increase in metallic Be intensity accompanied by a decrease in alloy intensity (see also [11]). This indicates that the Be–W alloy phase is only present at the

[2] This code uses a sum of Gauss and Lorentz functions to approximate the Voigt function.

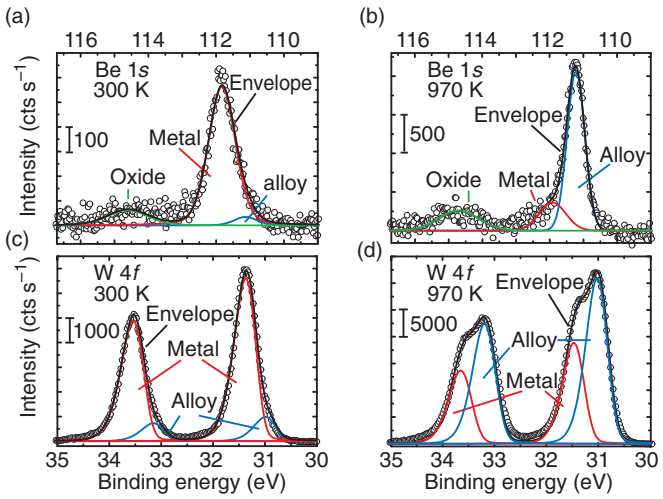

Figure 2. Be 1*s* and W 4*f* signals of a 2 nm Be film on W after room temperature deposition (panels (a) and (c)) and annealing at 970 K (panels (b) and (d)). The metal and alloy components (and the oxide in the Be 1*s* signals) are identified by fitting peaks representing metallic and alloy components to the data. Raw data are plotted as circles, the black line represents the sum of the fit functions.

interface between substrate and Be layer, since additionally deposited Be attenuates the alloy signal from the buried interface. The oxide concentration is nearly constant throughout the Be thickness series (∼10%), therefore the BeO is equally distributed in the whole Be layer. The alloy intensity in the W 4*f* signal amounts to 10 at-% at maximum. No additional components are identified besides metal and alloy. In particular, no oxide component or broadening due to a W–O surface layer [24][3] is observed. In that case even a submonolayer coverage would lead to a broadening or additional signal.

The VB spectra are dominated by the W substrate. A sharp feature at ∼2.3 eV and a broader signal around 5 eV are observed in good agreement with bulk W spectra [25]. A broad signal around 8 eV appears in XPS measurements of a clean Be substrate [26], which is not observed here. We also do not identify a O 2*p* signal (6–7 eV).

3.2. Annealing experiments

The peak fitting procedure as described and applied above becomes more evident when applied to the annealing experiments. Figure 2 shows Be 1*s* and W 4*f* signals measured at a 2 nm Be film on W after deposition at 300 K and after annealing to 970 K (remaining thickness 1.2 nm). From the raw data, a background is subtracted and peaks representing the elemental, alloy and oxide components are fitted (as described above, subsection 3.1). Whereas after 300 K deposition

[3] In separate measurements we adsorbed O_2 and atomic O on W_{poly}. In this case, the formation of a W–O first layer is clearly seen in a broadening of the W 4$f_{7/2}$ peak by 0.11 eV and in the appearance of intensity at the O 2*p* position at a BE of 6–7 eV, in accordance with this reference.

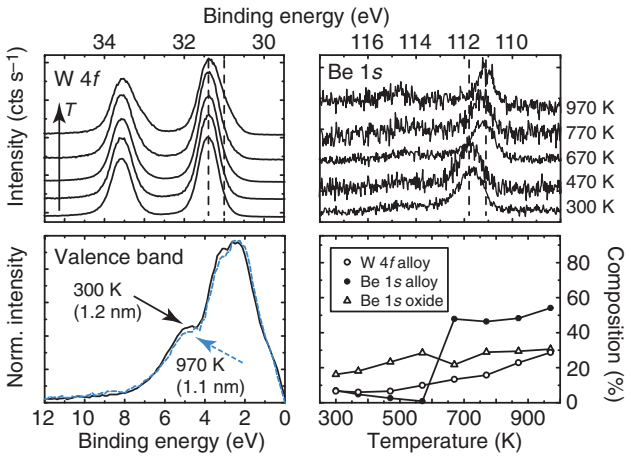

Figure 3. Be 1*s*, W 4*f* signals and the VB region of a 1.2 nm Be film, after the indicated annealing steps. In the Be 1*s* signal, a shift to the alloy position occurs at 670 K, whereas the changes in the W 4*f* peaks are gradual.

(spectra shown in panels (a) and (c) for Be 1*s* and W 4*f*, respectively) the necessity of the alloy peaks can still be challenged, it is obvious for the signals measured after the 970 K annealing step (see panels (b) and (d) for Be and W). When applying the fit parameters from the high-temperature step to the 300 K spectra, the data analysis becomes consistent in the whole temperature range. The Be 1*s* signal can be deconvoluted into a peak representing BeO, and peaks for Be in the metallic and in the alloy state. In the W 4*f* signal, two doublets are necessary to represent the experimental data which are assigned to W metal and W in a Be–W alloy.

The behaviour of the Be films upon annealing depends on the initial film thickness. Figure 3 summarizes the evolution of a Be layer with an initial film thickness of 1.2 nm (∼6 ML) with increasing annealing temperatures. The overall thickness of the Be layer decreases only marginally during the annealing series and amounts to 1.1 nm after 970 K. The signals in the Be 1*s*, W 4*f* and VB photoelectron energy regions are unchanged after 300 K deposition and annealing steps below 670 K. Above this temperature, a pronounced increase in the alloy fraction is observed in the Be 1*s* signal. After the final annealing step at 970 K, we determine 54% alloy and 31% oxidic fraction, respectively, in the Be 1*s* signal by applying the peak fitting procedure. 15% of the Be 1*s* signal are still in the metallic state. Due to the small layer thickness and the contribution of the substrate, the W 4*f* signal does not show an abrupt increase in the alloy component. However, the reaction between Be and W is unambiguously visible in a broadening towards lower BEs and finally leads to a shoulder after 970 K. After this annealing step, we examine 29% signal intensity originating from the alloy fraction within the W 4*f* signal. The residual signal intensity (71%) is in the metallic state. Additionally a small shift of 0.15 eV to lower BEs is noticeable in the VB.

In contrast to the almost unchanged Be thickness in this film, the Be intensity starts to decrease at 670 K in an annealing series starting with a 3.3 nm Be film. The results for this thick film are shown in figure 4. After the final annealing step at 1070 K, the residual film thickness

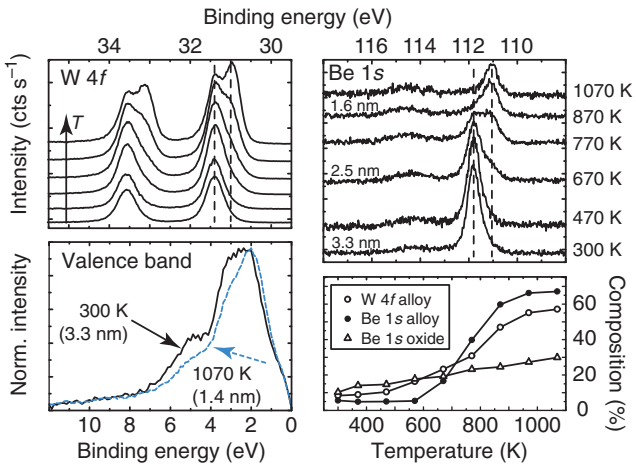

Figure 4. Thermal behaviour of a 3.3 nm thick film. The alloying reaction is clearly visible in all measured signals. In agreement with the Be film shown in figure 3 the alloy fraction increases above 670 K, accompanied by a decrease in film thickness.

amounts to 1.4 nm, which is clearly thinner than the initial film. All recorded XPS signals (Be 1*s*, W 4*f*, VB) unambiguously prove the alloy formation. After 1070 K, the Be 1*s* signal of the thick film is composed of about 67% alloy, 30% BeO and the remaining 3% are still in the metallic state. The appearance of the alloy peak in the W 4*f* signal is more pronounced than for the thin film: a second peak evolves which after 1070 K annealing is stronger than the metallic peak. We determine 57% alloy and 43% metal fraction intensity, respectively, within the W 4*f* signal. Also more pronounced are the changes in the VB region: the broad feature between 1 and 4 eV—characteristic for the tungsten *d* band—develops a maximum at 2 eV. The FWHM of this band decreases from 2.8 eV at 300 K to 2.6 eV after 1070 K. In the case of the 3.3 nm film, the band shift amounts to 0.15–0.20 eV, as determined from the low BE side of the VB spectra in figure 4.

The surface alloying between Be and W is further analysed in long-term annealing experiments, shown in figure 5. Be layers with increasing thicknesses are annealed at 770, 870 and 970 K, holding the samples at these elevated temperatures for several hours, without cooling to room temperature for XPS analysis. Due to the low sensitivity for the Be 1*s* signal exclusively, the W 4*f* signal is analysed in the high resolution mode. Spectra in survey resolution (for film thickness determination) and high resolution (W 4*f* for chemical analysis) are performed alternatingly. The decrease in film thickness (see table in figure 5) occurs already almost completely within the ramp-up time to the respective temperatures (10–13 min for 770–970 K). Immediately after reaching the annealing temperatures, the calculated Be thicknesses are between 1.0 and 1.2 nm. The film thickness then stays constant at these values. The remaining Be thickness in these experiments is comparable to that observed for the thin Be layer, shown in figure 3. The alloy intensity within the W 4*f* signal increases with temperature and changes then only marginally with annealing time. After the annealing experiments, the relative alloy concentrations

T (K)	770	870	970
d_{Be} (nm) at 300 K	1.3	1.5	2.0
d_{Be} (nm) at T	1.0	1.2	1.2
Alloy W 4f (%)	15	30	55

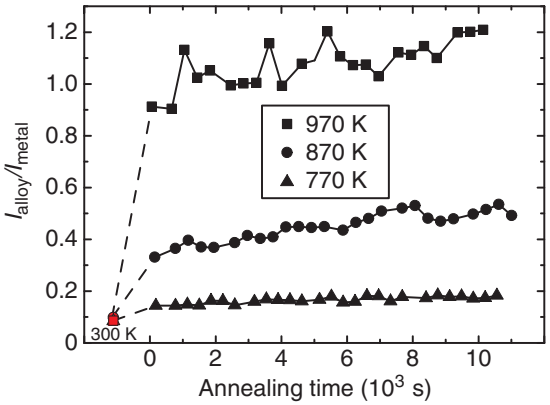

Figure 5. Ratio of alloy and metal intensities within the W 4f signals. The samples were held at the given elevated temperatures. The first data points indicate the intensity ratio after Be deposition at 300 K. The following data points are measured at elevated temperatures. Estimated layer thicknesses after room temperature deposition, while annealing and the relative alloy amount within the W 4f signal after annealing, respectively, are given in the table.

are determined from the W 4f signal (see table in figure 5). The absolute alloy amounts show also a clear tendency with a stoichiometric ratio representing Be_2W at 970 K.

3.3. Discussion

The XPS analysis of thin Be films on W indicates the formation of a surface alloy even after room temperature deposition. Both core levels show an additional signal intensity originating from the Be–W alloy. Since the VB spectra are not affected by this compound, the formation of a surface alloy is proved.

The survey scans after room temperature deposition are further analysed by comparing the inelastic background region around the W 4d signal. Tougaard reported on the influence of the surface morphology on the inelastic background in XPS spectra [27, 28]. An analysis of the background region around the W 4d signal in XPS spectra of Be films on W indicates a layer growth mode. This result in combination with measurements given in [14] justifies the determination of layer thicknesses with the assumption of layer-by-layer growth mode. The same procedure is used for the analysis of the surface morphology of Be films on W after thermal treatment. From the survey scans in both experimental procedures (temperature steps and long-term annealing) again an island formation is excluded which permits the film thickness estimation as mentioned above.

The thermal behaviour of thin Be films on W depends on the initially deposited layer thickness. In annealing experiments starting with different Be thicknesses, three coverage regions

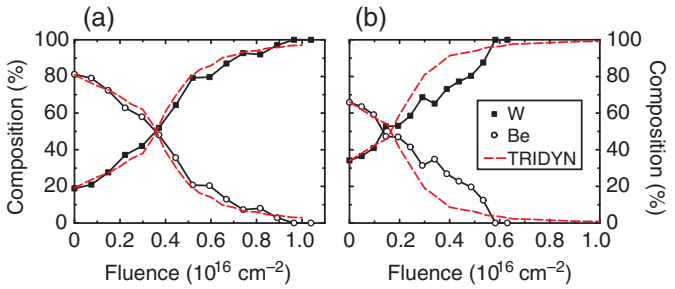

Figure 6. Comparison of the measured depth profiles of an untreated (a) and an annealed Be film (b), respectively, with TRIDYN results. The deposited film thickness is 1.9 nm (a), whereas the residual film after annealing at 970 K amounts to 1.2 nm (b).

can be distinguished: (i) $d_{Be} < 1.4$ nm, (ii) $d_{Be} = 1.4$–3.0 nm and (iii) $d_{Be} > 3.0$ nm. In region (i), the film thickness is not affected by annealing up to 970 K. Above 670 K, alloying sets in. The formed alloy is stable during further annealing and at 970 K, a Be_2W stoichiometry is measured. In XPS measurements, an overestimation of the W substrate is observed making the evaluation of the stoichiometric ratio within the alloy compound difficult. However, the absolute alloy amounts indicate a ratio of Be : W of $\sim$2 : 1 at 970 K rather than $Be_{12}W$ or $Be_{22}W$. In region (ii), the layer thickness decreases very fast and already within the temperature ramp-up time at the long-term annealing runs. The remaining layer thickness is 1.0 to 1.2 nm, both at elevated temperatures and after cooling to 300 K. The final alloy thickness is therefore comparable to the alloy thickness observed for region (i). Finally, region (iii) is characterized by a very slow decrease in Be thickness, starting at 670 K. For initial Be thicknesses above 3 nm, a Be thickness of >1.4 nm remains at 970 K. As in the two other regions, also a stable intermixing zone is observed.

In order to clarify whether Be diffusion or desorption leads to the observed decrease in film thickness in region (ii), sputter depth profiles are measured after the annealing experiments (3 keV Ar^+, 45° incidence). They are compared to a depth profile of a deposited Be layer (1.9 nm) without annealing. The ion–surface interactions are simulated using TRIDYN. This code accounts for kinematic collisional processes and adapts the sample composition dynamically [29]. Figure 6 compares the as-deposited case in (a) with an annealed film (thickness 1.2 nm after 970 K), shown in panel (b). The oxygen contamination is not considered here. The agreement between measured depth profile and TRIDYN simulation in (a) is very good and justifies again the assumption of a Be layer morphology. The apparent broadening of the film–substrate interface is an artefact due to ion-beam induced mixing and is well reproduced by the simulation [30]. In (b) a small deviation between the measured profile and the TRIDYN result is visible. The alloy formation leads to an intermixing within a restricted range. However, if diffusion of Be into the W substrate were the reason for the Be loss from the XPS analysis depth, Be intensity was to be found in greater depths than actually measured. Since the Be 1*s* signal vanishes for Ar^+ fluences above 6×10^{15} cm^{-2}, Be diffusion into the W bulk is excluded as reason for the Be losses from the surface. The only possible loss channel therefore is Be desorption.

The results presented here demonstrate for the first time the formation of a Be–W surface alloy during annealing of thin Be films on W. The alloy formation is verified in shifts both

Table 1. BEs used and determined (Be_2W alloy) in this work.

Core level	Chemical state	E_B(eV)
Be 1s	Metal	111.8
	Alloy (Be_2W)	111.1
	Oxide (BeO)	114.8
W 4$f_{7/2}$	Metal	31.4
	Alloy (Be_2W)	31.0

in the core level and the valence level BEs. The core level shifts are independent on the stoichiometry and amount to −0.7 eV (Be 1s) and −0.4 eV (W 4$f_{7/2}$), as compared to the respective metal values (see table 1). This is a clear indication for the formation of an ordered alloy with a fixed stoichiometry (Be_2W) as expected for the Be–W system. Random alloys or different stoichiometries ($Be_{12}W$, $Be_{22}W$) would lead to a continuous peak shift or additional signal intensities, respectively, in both core levels. Measurements of a W film (200 nm) on polycrystalline Be prove this result. In these measurements, we observe a formation of $Be_{12}W$ using a combination of RBS (Rutherford backscattering spectroscopy) and XPS [31]. The BE shift of that alloy compound within the Be 1s signal amounts to −0.5 eV, which is smaller than the result given above. Since the BE shift for thin Be films on W is constant within the Be 1s and W 4f signals after room temperature deposition and annealing experiments, respectively, the formation of a surface alloy is proved. The structure of this surface alloy has to be analysed with other techniques. The VB modifications are in accordance with calculations for other d band metals [7]. In addition to the core level shifts, the formation of a Be–W surface alloy is also detected by VB photoemission spectroscopy showing a reduced d band coupling due to the alloying of tungsten with the s metal beryllium. This behaviour is a clear indicator for a decreased d band coupling caused by the screening of the d orbitals by the Be s states [7]. Since coupling of d orbitals is best between alike atoms, the reduction of the d band width concludes the intermixing of Be and W atoms. This leads to a stronger localization of the W d states and to narrowing of the d band. This effect should be even more pronounced when the foreign atomic species is an s metal. The tendency to preserve the d band filling then leads to the shift which is observed experimentally.

4. Summary

Small alloy intensities are detected already after Be deposition on W at 300 K and increase significantly above 670 K. The onset of alloy formation is independent of the initial film thickness. In long-term annealing experiments, the alloy amount and reaction rate, respectively, do not further increase with annealing time. The alloy formation is limited to a thin layer of 1.0 to 1.2 nm. This observed intermixing layer thickness is comparable for all Be films described here. Additional metallic Be not incorporated in the alloy is desorbed from the surface rather than dissolved in the W substrate at elevated temperatures.

References

[1] Kolodziej J J, Madey T E, Keister J W and Rowe J E 2002 *Phys. Rev.* B **65** 075413
[2] Thayer G E, Ozolins V, Schmid A K, Bartelt N C, Asta M, Hoyt J J, Chiang S and Hwang R Q 2001 *Phys. Rev. Lett.* **86** 660
[3] Bischoff M M J, Yamada T, Quinn A J, van der Kraan R G P and van Kempen H 2001 *Phys. Rev. Lett.* **87** 246102
[4] Mårtensson N, Nyholm R, Calén H, Hedman J and Johansson B 1981 *Phys. Rev.* B **24** 1725
[5] Olovsson W, Abrikosov I A and Johansson B 2002 *J. Electron Spectrosc. Relat. Phenom.* **127** 65
Olovsson W, Abrikosov I A and Johansson B 2003 *J. Electron Spectrosc. Relat. Phenom.* **129** 81 (erratum)
[6] Parker R R 2000 *Nucl. Fusion* **40** 473
[7] Ganduglia-Pirovano M V, Kudrnovský J and Scheffler M 1997 *Phys. Rev. Lett.* **78** 1807
[8] Massalski T B, Okamoto H, Subramanian P R and Kacprzak L 1996 *Binary Alloy Phase Diagrams* 2nd edn (Materials Park, OH: ASM International)
[9] Watts C R 1968 *Int. J. Powder Metall.* **4** 49
[10] Vasina E A and Panov A S 1974 *Metally* **1** 197
[11] Wiltner A and Linsmeier Ch 2005 *J. Nucl. Mater.* **337–339** 951
[12] Doerner R P, Baldwin M J and Causey R A 2005 *J. Nucl. Mater.* **342** 63
[13] Zuber S, Sidorski Z and Polaǹski J 1979 *Surf. Sci.* **87** 375
[14] Schlenk W and Bauer E 1980 *Surf. Sci.* **94** 528
[15] Chrzanowski E and Bauer E 1986 *Surf. Sci.* **173** 106
[16] Johansson L I, Johansson H I P, Andersen J N, Lundgren E and Nyholm R 1993 *Phys. Rev. Lett.* **71** 2453
[17] Aldén M, Skriver H L and Johansson B 1993 *Phys. Rev. Lett.* **71** 2457
[18] Seah M P, Gilmore I S and Beamson G 1998 *Surf. Interface Anal.* **26** 642
[19] Wiltner A and Linsmeier Ch 2004 *Phys. Status Solidi* a **201** 881
[20] MultiPak, Ver. 6.1A, Physical Electronics 1999
[21] Goldstraß P and Linsmeier Ch 2000 *Nucl. Instrum. Methods* B **161–163** 411
[22] Linsmeier Ch and Wanner J 2000 *Surf. Sci.* **454–456** 305
[23] Doniach S and Šunjić M 1970 *J. Phys. C: Solid State Phys.* **3** 285
[24] Riffe D M and Wertheim G K 1998 *Surf. Sci.* **399** 248
[25] Moslemzadeh N, Barrett S D, Dhanak V R and Miller G 2003 *J. Electron Spectrosc. Relat. Phenom.* **130** 119
[26] Hüfner S 1995 *Photoelectron Spectroscopy* (Berlin: Springer)
[27] Tougaard S 1996 *J. Vac. Sci. Technol.* A **14** 1415
[28] Tougaard S 1998 *Surf. Interface Anal.* **26** 249
[29] Eckstein W 1991 *Computer Simulation of Ion–Solid Interactions* (Berlin: Springer)
[30] Schmid K, Wiltner A and Linsmeier Ch 2004 *Nucl. Instrum. Methods Phys. Res.* B **219–220** 947
[31] Linsmeier Ch, Ertl K, Roth J, Wiltner A, Schmid K, Kost F, Bhattacharyya S R, Baldwin M and Doerner R P 2006 *J. Nucl. Mater.* at press

Available online at www.sciencedirect.com
SCIENCE DIRECT®
Journal of Nuclear Materials 337–339 (2005) 951–955
journal of nuclear materials
www.elsevier.com/locate/jnucmat

Formation of a surface alloy in the beryllium–tungsten system

A. Wiltner *, Ch. Linsmeier *

Max-Planck-Institut für Plasmaphysik, EURATOM Association, Boltzmannstr. 2, D-85748 Garching b. München, Germany

Abstract

The interaction of beryllium and tungsten is investigated by deposition of thin beryllium layers (several nanometers) from the vapor phase onto polycrystalline tungsten substrates and analysis by means of X-ray photoelectron spectroscopy (XPS). Already after room temperature deposition we observe formation of a surface alloy, limited to the interface between the layer and the substrate. The alloy intensity increases continuously between 670 K and 1070 K. The alloy formation is restricted to a depth of 1.2 nm in maximum. Be in excess to this layer thickness desorbs from the sample surface. No Be diffusion or dissolution in the W bulk is observed. Sputter depth profiles before and after annealing experiments in combination with TRIDYN calculations demonstrate that Be is limited to the near-surface area of the tungsten substrate.

PACS: 68.35.−p; 71.20.Lp; 74.70.Ad; 82.80.Pv
Keywords: Beryllium; Tungsten; Surface analysis

1. Introduction

For future fusion devices (e.g. ITER) currently three elements are considered as wall materials [1]. Tungsten will be used in the divertor region, whereas beryllium lines the main chamber. At the strike points the present design considers carbon (carbon fiber-enforced material). Due to erosion processes, material transport and redeposition, in combination with energy input from the plasma, mixed materials will be formed. The investigation of binary model systems from the constituents of the wall materials is necessary to predict altered physical and chemical properties. We already investigate carbon films on Be and W using XPS as a surface sensitive tool [2,3]. Continuing the measurements of binary systems with respect to their use as wall materials we start to investigate the Be–W system. The Be–W phase diagram exhibits three compounds of known stoichiometry: $Be_{22}W$, $Be_{12}W$ and Be_2W [4]. Beside these compounds there exists a miscibility gap and regions of limited miscibility. Due to our applied experimental procedure we expect, if a reaction occurs, the formation of Be_2W. Besides these phase data, little is known in literature about the reactivity of Be and W. Especially XPS measurements which can reveal the alloy formation with high sensitivity are performed for the first time.

2. Experimental

The measurements are performed in an ultrahigh vacuum chamber consisting of an analysis and a preparation system. The analysis system (commercial PHI

* Corresponding authors. Tel.: +49 89 329 922 85; fax: +49 89 329 911 49.
E-mail address: linsmeier@ipp.mpg.de (Ch. Linsmeier).

0022-3115/$ - see front matter © 2004 Elsevier B.V. All rights reserved.
doi:10.1016/j.jnucmat.2004.08.021

ESCA 5600 system, base pressure $1-2\times10^{-8}$ Pa) is equipped with a standard (Mg Kα and Al Kα) and a monochromatic X-ray source (Al Kα, $h\nu = 1486.6$ eV). All measurements shown here are performed using the monochromatic X-ray source. We use pass energies of 93.9 eV for survey scans and 2.95 eV for high resolution measurements. The analysis spot is 0.8 mm in diameter and the energy resolution of the spectrometer system is 0.26 eV. We refer the binding energy scale to the Au $4f_{7/2}$ peak position at 84.0 eV. Furthermore, the analysis chamber is equipped with an ion gun (Specs IQE 12/38) for sample preparation. The polycrystalline tungsten samples are cleaned using alternating sputter (3 kV Ar^+) and annealing cycles (up to 970 K) until no impurities can be detected in the survey scans.

The film deposition is performed in a preparation chamber which is connected to the analysis system. We use a commercial electron beam evaporator (Omicron EFM3) and evaporate Be pieces (HEK GmbH, 99.999%) from a BeO crucible. During the deposition procedure the base pressure is better than 4×10^{-8} Pa. Due to the high reactivity of Be and O the deposited Be films contain a maximum oxygen contamination of 10%.

The experimental procedure is as follows. We deposit Be layers of different thicknesses (from a monolayer up to several nanometers) at room temperature followed by XPS analysis using survey and high resolution scans. The maximum layer thickness in our experiment is limited by the escape depths of the photoelectrons which are in the order of several nanometers. Annealing experiments are performed in two different ways. In procedure I the films are annealed in steps of 100 K up to 1070 K for 30 min per temperature step. The samples are measured by XPS after cooling down to room temperature. In procedure II the samples are annealed at 770, 870 and 970 K for several hours at each temperature while performing XPS analysis at the elevated temperatures. After the long term annealing steps sputter depth profiles (3 kV Ar^+, 45°) are recorded in order to analyze the Be diffusion depth.

3. Results and discussion

After room temperature deposition the Be layer thickness is determined using the procedure given in [5]. We use the density of metallic Be to calculate a Be layer thickness from the XPS intensities of both the substrate (W 4f) and layer signals (Be 1s). The high resolution spectra allow for the deconvolution of the photoelectron signals in components of different chemical species. Beside O no other impurities are detected in the Be layers. The fit procedures applied to deconvolute the Be 1s and W 4f signals are presented elsewhere [6].

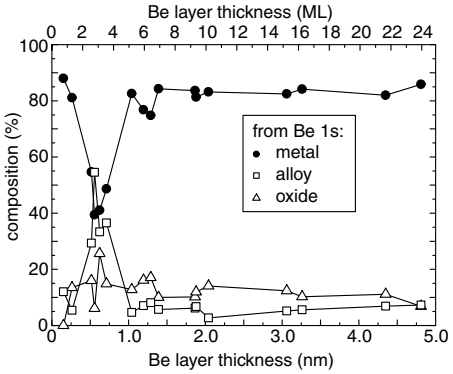

Fig. 1. Composition of Be layers after room temperature deposition. Within the Be 1s signal metallic (●) and oxidic (△) components are identified. Furthermore, a surface alloy (□) which is limited to the interface is observed.

The composition extracted from the Be 1s signal is shown in Fig. 1. Besides the BeO peak at 114.8 eV [7] the Be 1s signal exhibits a peak from metallic Be at 111.8 eV [3] and an additional signal at a lower binding energy of 111.1 eV. Within the substrate signal (W 4f) no oxide signatures (peak shift or broadening) are observed. The oxygen is completely bound to Be. The deconvolution of the W $4f_{7/2}$ signal results in the detection of a peak at 31.0 eV in addition to the peak at 31.4 eV originating from W metal [2]. These two new peaks shifted to lower binding energies compared to the metal signals in both the Be 1s and W 4f transitions are assigned to the formed Be–W surface alloy. As shown in Fig. 1, it is restricted to the interface and additionally deposited Be is predominantly in the metallic state. The oxide fraction is equally distributed in the whole layer and amounts to 10% in average. Due to the small photoemission cross section and therefore low intensity of the Be 1s signal the layer composition below 1 nm (four monolayers) has an error of ±5%. The W 4f substrate signal is dominated by the metallic W intensity from the substrate (>90%). Specifically in this coverage region (up to four monolayers) additional information regarding the layer composition is not obtainable.

3.1. Annealing experiments, procedure I

The layer compositions obtained from high resolution spectra after the annealing steps for two Be films of different initial thicknesses are shown in Fig. 2. In (a) a 1.2 nm thick film is annealed up to 970 K. The layer thickness calculated from the spectrum after the annealing step at 970 K is 1.1 nm. Therefore the Be layer is

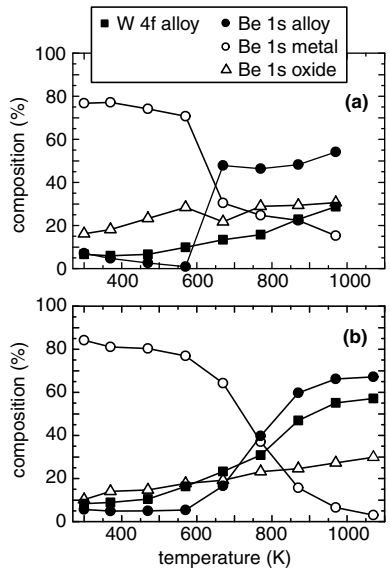

Fig. 2. Thermal behavior (procedure I) of 1.2 nm (a) and 3.3 nm (b) Be films. At 970 K the remaining layer amounts to 1.1 nm (a) and 1.6 nm (b), respectively. After the 1070 K step (b) the Be layer thickness is calculated to 1.4 nm. The alloy fraction intensity increases from 670 K.

stable during the annealing steps. Beginning at 670 K an increase in the alloy fraction is observed within both the Be 1s and W 4f signals. This increase is particularly well visible in the Be 1s signal. Despite the excellent base pressure and due to the high Be–O reactivity the BeO fraction increases slightly with each annealing step. In the substrate signal (W 4f) no oxide fraction is observed. The O 1s signal is broadened and shifted towards higher binding energy values. This observation is in agreement with measurements on the interaction of atomic and molecular O with W and Be surfaces [7].

Annealing of a 3.3 nm Be film leads to a smooth thickness decrease beginning at 570 K. The residual layer at 1070 K amounts to 1.4 nm which is comparable within the experimental precision to the remaining layer thickness of the measurement mentioned above (Fig. 2(a)). The alloy formation is observed in both the substrate and layer signals (Fig. 2(b)). In agreement with the 1.2 nm film the formation of additional Be–W alloy sets in at 670 K. The BeO concentration from the Be 1s signal increases likewise. Furthermore, no oxidic component within the W 4f signal is observed. The O 1s signal is broadened and shifted towards higher binding energy values, as reported above for the 1.2 nm Be film. In both experiments the stoichiometry at 970 K indicates the formation of Be_2W.

3.2. Annealing experiments, procedure II

In order to decide whether Be diffusion or desorption results in a decrease of the initially deposited layer thickness, the Be layers are annealed at elevated temperatures for several hours and subsequently analyzed by XPS sputter depth profiles. During annealing at elevated temperatures the sample composition is analyzed by alternating survey and high resolution scans. Due to the low sensitivity for the Be 1s signal we restrict the high resolution scans to the W 4f signal region. First we consider the changes in the Be layer thickness. The remaining layer thicknesses after the annealing procedures are similar for each experiment and amount to 1.0–1.2 nm, although the initial thicknesses range between 1.1 and 2.0 nm. The Be layer thickness decreases rapidly within the ramp-up to the annealing temperature and stays constant during annealing and after finally cooling down to room temperature.

Fig. 3 summarizes the change during annealing procedures. Fig. 3(a) and (b) shows the W 4f and Be 1s signals, respectively, before and after the 970 K experiment. In the W 4f spectra (3a) the alloy formation leads to the evolution of a second doublet at lower binding energies. The metallic substrate, still present, gives rise to a $W4f_{7/2}$

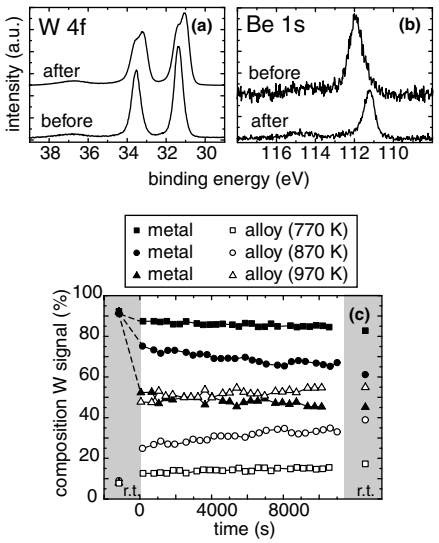

Fig. 3. Substrate (W 4f, a) and layer (Be 1s, b) signals before and after the continuous annealing (procedure II) at 970 K. The alloy formation is visible as an additional doublet (a) and peak shift (b), respectively, within both signals. The composition of the W 4f signal is shown in (c). The reactivity increases with annealing temperature.

peak at 31.4 eV, whereas now the alloy signal intensity at 31.0 eV dominates. The Be 1s peak (3b) shifts completely from the metallic position at 111.8 eV to the alloy signal at 111.1 eV indicating that the total remaining Be is bound in the alloy. As discussed above, a small BeO peak is nevertheless visible at 114.8 eV. The surface compositions obtained from the high resolution spectra in the W 4f region are shown in the central part of Fig. 3(c). The compositions before and after annealing are plotted in the highlighted areas. As indicated by the dashed lines, the bigger part of the alloy formation proceeds already during the ramp-up to the annealing temperatures. Only comparably small additional Be–W alloy is formed during the phases at constant temperatures. At 770 K additional changes are barely visible. At 870 K the alloying reaction proceeds clearly. Within the ramp-up to 970 K the alloy formation increases further, whereas the rate while annealing is comparable to the 870 K run. No alloy decomposition or other compositional changes are observed after cooling to room temperature. In agreement with the annealing experiments conducted by procedure I, the stoichiometry at 970 K indicates the formation of Be_2W.

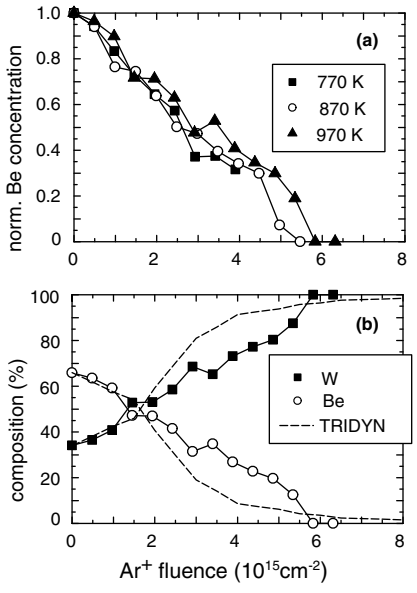

Fig. 4. XPS sputter depth profiles (3 kV Ar^+, 45° incidence) after annealing procedure II at 970 K (see Fig. 3) shown as normalized Be concentration (a). The comparison of a measured depth profile (1.2 nm) with the TRIDYN calculation indicates a limited Be–W intermixing (b).

After the annealing experiments the residual Be–W alloy layers are removed by sputtering while measuring depth profiles by XPS. In Fig. 4(a) the normalized Be depth profiles are plotted. The decrease of Be 1s intensity is comparable for all annealing temperatures, demonstrating equal final alloy layers. Fig. 4(b) shows the depth profile after annealing at 970 K (1.2 nm final Be film thickness) in comparison with a TRIDYN calculation. The TRIDYN code includes a kinematic ion–solid interaction model with a dynamic modification of the sample composition after each collision event [8]. For the TRIDYN calculation the O impurity is neglected. A depth profile of a Be layer, taken after 300 K deposition, shows perfect agreement with TRIDYN results for the measured Be layer thickness (not shown here). The TRIDYN curves in Fig. 4(b) represent a Be layer without intermixing (diffusion, reaction) of Be and W. The slope of the calculated profile is due to ion beam mixing effects and agrees very well with a depth profile of the untreated sample mentioned above [9]. Compared to the depth profile data (after annealing at 970 K) the deviation is small and only significant at fluences between 2 and 5.5×10^{15} $Ar^+ cm^{-2}$. This indicates that the modification of the Be depth distribution during the alloying procedure is small compared to a Be layer of nominally 1.2 nm thickness. The difference between the initially deposited 2.0 nm and the finally calculated 1.2 nm cannot be explained by diffusive Be loss into the W bulk. This would lead to a depth profile where Be extends deeper into the W bulk. The only remaining loss channel for Be is desorption.

4. Summary and conclusions

The Be–W intermetallic system is investigated by depositing thin Be films on polycrystalline tungsten substrates. Analysis of the alloy formation is performed by XPS. Already at room temperature an alloy at the Be–W interface is identified by photoelectron peaks shifted to lower binding energies both in the substrate W 4f and the overlayer Be 1s signals. The alloy signals appear at 111.1 eV (Be 1s) and 31.0 eV ($W 4f_{7/2}$). Despite the well-defined preparation conditions the Be layer contains a small amount of oxygen (approx. 10%) due to the high reactivity of Be. Oxygen is completely bound in BeO, no tungsten oxides are detected. However, the BeO shows no influence on the alloy formation in our experiments. Additional alloying sets in at 670 K, visible in both a decrease in the Be and W metallic peaks and an increase in intensity at the respective alloy binding energies. The alloy formation continues until 970 K where a stoichiometry of Be_2W is reached. The alloy formation at elevated temperatures is limited to a final thickness of approximately 1.2 nm, independent of the initially deposited Be layer thickness. For thicker deposited Be layers, desorption of Be is the proposed loss mechanism,

since sputter depth profiles indicate no Be diffusion into the W substrate. At 970 K, only a slightly widened depth distribution compared to the initial layer is measured. Implications for tungsten fusion first wall components are the decrease in melting point: according to the phase diagram, the Be_2W alloy has a melting temperature of 2500 K, compared to 3690 K of pure tungsten. However, the limited alloying only at the surface, together with the observation of no Be bulk diffusion, indicate that a modification of the tungsten bulk properties is not to be expected. The influence of the alloy formation on the hydrogen isotope retention and re-emission, as well as the changes in surface reactivity towards plasma impurities (carbon and oxygen), will be subject to further studies.

References

[1] R.R. Parker, Nucl. Fusion 40 (2000) 473.
[2] J. Luthin, Ch. Linsmeier, Surf. Sci. 454–456 (2000) 78.
[3] P. Goldstrass, K.U. Klages, Ch. Linsmeier, J. Nucl. Mater. 290–293 (2001) 76.
[4] T.B. Massalski, H. Okamoto, P.R. Subramanian, L. Kacprzak, 2nd Ed., Binary Alloy Phase Diagrams, Materials Park, 1996.
[5] A. Wiltner, Ch. Linsmeier, Phys. Status Solidi A 201 (5) (2004) 881.
[6] A. Wiltner, Ch. Linsmeier, submitted for publication.
[7] Ch. Linsmeier, J. Wanner, Surf. Sci. 454–456 (2000) 305.
[8] W. Eckstein, Springer Ser. Mater. Sci. 10 (1991).
[9] K. Schmid, A. Wiltner, Ch. Linsmeier, Nucl. Instrum. and Meth. B 219&220 (2004) 947.

Journal of Nuclear Materials 390–391 (2009) 975–978

Contents lists available at ScienceDirect

Journal of Nuclear Materials

journal homepage: www.elsevier.com/locate/jnucmat

Investigation of chemical phase formation in the ternary system beryllium, carbon and tungsten with depth-resolved photoelectron spectroscopy

F. Kost *, Ch. Linsmeier, M. Oberkofler, M. Reinelt, M. Balden, A. Herrmann, S. Lindig

Max-Planck-Institut für Plasmaphysik, EURATOM Association, Boltzmannstrasse 2, 85748 Garching b. München, Germany

ARTICLE INFO

PACS:
52.40.Hf
82.80.Pv
41.60.Ap
82.40.−g

ABSTRACT

Synchrotron radiation XPS with different photon energies is used to gain depth-resolved chemical information. The temperature-dependent evolution of a ternary system sample with beryllium, carbon and tungsten is investigated. Five temperature steps are performed in order to analyze the kinetic processes and chemical states, namely 300, 530, 850, 1020 and 1200 K. After each temperature treatment, the sample composition is analyzed using four different information depths.

1. Introduction

For the future fusion experiment ITER, the three elements beryllium, carbon and tungsten are planned to be used as first wall materials [1]. The interaction between these materials, in particular the developing compounds due to temperature treatments, are of major interest as they strongly influence fusion-relevant material properties such as erosion behaviour, melting point and hydrogen inventory. The knowledge of binary systems is well established (e.g. [2]), but the complexity increases considerably with the addition of a third component. In order to understand these interactions, model systems with thin elemental layers of a few nm thicknesses are prepared, annealed and analyzed by X-ray photoelectron spectroscopy (XPS). For the characterization of temperature-driven processes such as diffusion, the XPS technique is applied using synchrotron radiation. By changing the excitation energy in the XPS process, it is possible to gain information from within different depths of the sample [3–7]. Compared to sputter depth profiling, this method has the advantage of being non-destructive and therefore does not alter the chemical composition of the investigated system. Hence, it allows an elemental and chemical state analysis as a function of depth.

2. Experimental

A carbon–beryllium–tungsten (C/Be/W) ternary system is prepared using physical vapour deposition. Polished polycrystalline tungsten is used as substrate material and carbon acts as a passivating layer on the top in order to minimise the influence of oxygen contaminations since it is less reactive towards oxidation than W and, particularly, Be. The beryllium layer is intermediate between the substrate and the carbon layer. The film thicknesses are 2.4 nm for the beryllium layer and 1.5 nm for the carbon layer. The sample is prepared under vacuum conditions (p < 8E-7 Pa during evaporation) and then transferred to the synchrotron beamline via transport through air.

XPS measurements are performed using a hemispherical electron analyzer at the MUSTANG endstation at the RGBL-PGM of the synchrotron facility BESSY in Berlin. The angle between the incident X-ray and the photoelectron take-off direction is 45°. For all the measurements, the photoelectron take-off direction is normal to the sample surface and the pass energy is 2 eV. The binding energy regions Be 1s, C 1s and W 4f are measured.

The sample is annealed at different temperatures and the XPS measurements are performed after cooling to 300 K after each temperature treatment of 530, 850, 1020 and 1200 K. The annealing time is 30 min for each step. In the photo-ionisation process, the photoelectron kinetic energy is determined by the incident photon excitation energy and the core level of the element emitting the photoelectrons (Be 1s, C 1s and W 4f in this work). As the kinetic energy of the photoelectrons strongly influences the inelastic mean free path [8], the excitation energy is chosen such that the photoelectrons originate from within the same depths, i.e. the inelastic mean free path is equal for different elements. Four different information depths are chosen for analysis.

For each spectrum, the binding energies are calibrated by measuring the Au 4f signal. Assuming a homogenous material, the intensity $I(E_k,x)$ for a photoelectron peak of kinetic energy E_k excited from the level x is given by $I(E_k,x) = J(h\nu)\ N_i\ \sigma(h\nu,\theta,x)\ \lambda(E_k)\ T(E_k)$, where $J(h\nu)$ is the photon flux incident on the sample at the energy $h\nu$, N_i is the density of atoms of the ith species, $\sigma(h\nu,\theta,x)$

* Corresponding author.
E-mail addresses: florian.kost@ipp.mpg.de (F. Kost), linsmeier@ipp.mpg.de (Ch. Linsmeier).

0022-3115/$ - see front matter © 2009 Elsevier B.V. All rights reserved.
doi:10.1016/j.jnucmat.2009.01.251

is the photoelectron cross section for the level x of the ith species at energy $h\nu$ and electron ejection angle θ; $\lambda(E_k)$ is the inelastic mean free path in the sample for electrons of kinetic energy E_k and $T(E_k)$ is the transmission function of the analyzer. The photon flux and the analyzer transmission are defined by the experimental setup. The photoelectron cross section $\sigma(h\nu,\theta,x)$ is separated into an angle-independent part and an angle-dependent asymmetry factor L, $\sigma(h\nu,\theta,x) = \sigma(h\nu,x)\cdot L(h\nu,\theta,x)$. For the polarized light used at the synchrotron beamline, the asymmetry factor is $L(h\nu,\theta,x) = 1 + 0.5\beta(3\cos^2\theta - 2)$, where β is the asymmetry parameter [9]. For quantitative analysis, the peak areas are normalized against photo-ionisation cross section [9], asymmetry parameter [10], ring current, photon flux and analyzer transmission.

Since one element is measured with different photon energies, the electrons have different inelastic mean free paths λ. Hence, taking into account the exponential attenuation of the intensity with depth, $I = I_0 \exp(-d/(\lambda \cos\theta))$, absolute peak areas from the same depths d are not comparable. Therefore, relative signal intensities are considered, which are normalized against the total signal intensity, which is the sum over all contributions. As the exact information depths for the photoelectrons cannot be determined, it is necessary to refer to the different depths as $d1$ (near-surface region) to $d4$ (largest information depth). Taking into account the mean free path dependence on photon energy, the chosen photoelectron kinetic energies are 60 eV (near-surface region), 300, 480 and 700 eV (largest information depth). Since relative signal intensities are normalized against the sum over all contributions, it is possible to compare relative signal intensities of different depth regions (even though the inelastic mean free path changes from $d1$ to $d4$).

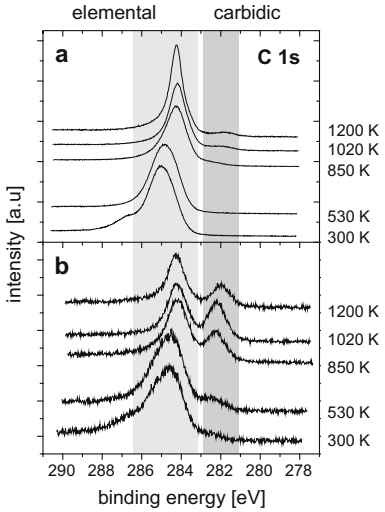

Fig. 1. XPS C 1s signal for 1.5 nm carbon and 2.4 nm beryllium layers evaporated on a tungsten substrate. The temperature steps are indicated on the right. The upper panel (a) shows measurements with a photoelectron kinetic energy of 60 eV (near-surface region, $d1$), while the lower panel shows data with a kinetic energy of 700 eV (largest information depth. $d4$). The beryllium carbide peak is developing at ~282 eV and expanding from the interface to the surface.

3. Results and discussions

Fig. 1 shows the C 1s signal after application of the previously described data treatments. Fig. 1(a) shows spectra in the C1s binding energy region with a photoelectron kinetic energy of 60 eV, while the measurements with a kinetic energy of 700 eV are shown in Fig. 1(b). The C 1s peak shape is fitted by background subtraction (Shirley background [11]) and three Gauss–Lorentz peaks: elemental carbon is described by a graphitic (E_B = 284.2 eV) and a disordered graphitic (E_B = 285.1 eV) contribution. The beryllium carbide peak is clearly visible in the binding energy region around 282 eV.

In the near-surface region (a), the carbide signal is not observed up to 850 K. At 1020 K, a small amount of Be_2C is detected. For the greater information depth (b), a certain amount of beryllium carbide is observed at room temperature. The carbide intensity rises during the temperature treatment and is most pronounced at 1020 K. At the last temperature, 1200 K, the beryllium carbide peak slightly shifts to lower binding energies. This binding energy shift might be due to the growth of Be_2C clusters and following cluster size effect. The cluster size is known to have an important influence on the binding energy [12]. The slight shift in the binding energy and peak shoulders at ~287 eV of the 300 and 580 K elemental carbon peaks indicates a surface contamination due to transport through air. This contribution is taken into account during the fitting procedure, but disregarded in the sample composition analysis.

The room temperature measurements are chosen to demonstrate the analysis of XPS spectra with different photon energies. The region $d1$ (photoelectron kinetic energy 60 eV) shows BeO with a relative signal intensity of 22% and elemental carbon with 78%. After sample preparation, no beryllium is present on the surface. This points to a Be diffusion (driven by the chemical gradient) to the surface when oxygen was available due to the transport through air.

The next information depth $d2$ (photoelectron kinetic energy 300 eV) shows 2% of metallic beryllium, 16% of BeO and 82% of elemental carbon. We want to emphasize here that the increasing kinetic energy of the photoelectrons increases the *information depth*, thus *adding* information of a greater depth to the overall measured relative elemental composition. Taking into account the exponential attenuation of the photoelectron intensity, the contribution from surface components is less influential as the information depth increases. Regarding the decreasing relative intensity of BeO for $d2$ from 22% to 16%, there is less BeO present in deeper regions. Vice versa, more elemental carbon is detected compared to $d1$. The relative signal intensities for $d3$ (photoelectron kinetic energy 480 eV) are 12% metallic Be, 3% beryllium carbide (Be_2C), 23% BeO and 62% elemental C. As there is a distinct contribution from metallic beryllium, the information depth now clearly exceeds the carbon overlayer. Both the Be and the BeO amounts increase for $d3$. As the relative signal intensity of BeO increases in measurement $d3$ compared to $d2$, this points not only to BeO at the surface but also to BeO in the metallic Be layer (below carbon). A small amount of Be_2C is detected at this information depth. Hence, the carbide formation at room temperature starts at the Be/C interface. Be_2C formation at room temperature has been investigated earlier [13]. The relative signal intensities for $d4$ (photoelectron kinetic energy 700 eV) are 18% metallic Be, 4% Be_2C, 25% BeO, 50% elemental carbon, and 2% metallic tungsten. Since the relative intensities for the beryllium components increase, there is more Be, Be_2C and BeO visible in $d4$. As there is a contribution from tungsten for $d4$, this information depth exceeds both the beryllium and carbon overlayers. The relative signal intensity of tungsten is not significant regarding the total sample composition, but nevertheless, metallic tungsten and a Be_2 W alloy are present.

The first annealing temperature is 530 K. The C 1s signal is taken as an example in Fig. 2 to point out the sample composition development during temperature treatments. The relative signal

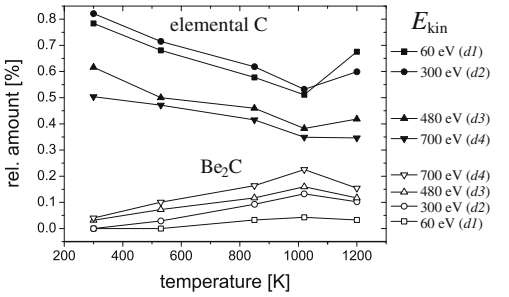

Fig. 2. Relative signal intensities of elemental carbon (solid symbols) and beryllium carbide (open symbols) as a function of temperature. The symbol shape indicates the photoelectron kinetic energy, as indicated on the right (*d*1 to *d*4 for near-surface and deepest analysis regions). The amount of beryllium carbide increases with increasing information depth. The change at 1200 K is due to a change in the surface morphology.

intensity of elemental carbon decreases from room temperature to the annealing step at 1020 K. The relative signal intensity is not maximal for *d*1, but for *d*2. This is due to the BeO overlayer, which is discussed above. As BeO is very prominent at the surface, the relative signal intensity of elemental carbon is smaller. Furthermore, the relative intensity of elemental carbon decreases from *d*2 to *d*4, since other contributions such as metallic Be and Be_2C become more prominent in greater depths. At the last temperature step, 1200 K, the relative signal intensity for elemental carbon is very prominent at the surface and decreases with increasing information depth. This might be due to carbon diffusion to the surface or a change in surface morphology, such as formation of island-like structures.

The relative signal intensity of Be_2C increases from *d*1 to *d*4. This indicates a beginning formation of beryllium carbide, starting at the Be/C interface and expanding to the surface. At the last temperature step, 1200 K, the overall relative signal intensity of Be_2C decreases. Since *relative* signal intensities are considered, the relative intensity of Be_2C is connected with that of elemental C.

At 530 K, the relative signal intensity of Be_2C increases for *d*3 and *d*4 and furthermore, Be_2C is detected in *d*2. This is another hint to beryllium carbide growth from the interface to the surface. According to an increasing Be_2C amount, the amounts of metallic Be and elemental carbon decrease. The amount of BeO at the surface is increasing due to rising pressure during temperature treatment, which gives rise to further oxide formation. Like for room temperature, a small contribution from tungsten is detected for *d*4 and the amount of the Be_2 W alloy is increasing.

At 850 K, the relative intensity of Be_2C increases for *d*2 to *d*4 and furthermore, Be_2C is detected in the near-surface region *d*1, giving another hint for carbide growth from the interface to the surface. The amount of BeO at the surface is increasing further and no metallic Be is left at this temperature step. As more Be_2C is forming, the total amount of elemental carbon decreases. At 850 K, the amount of Be_2 W is decreasing, whereas the onset of W_2C formation is observed.

At 1020 K, the relative intensity of Be_2C increases for *d*1 to *d*4. Furthermore, the amount of BeO at the surface increases. As no metallic Be is available to form additional Be_2C or BeO, this increase must be due to a change in surface morphology, thus giving more weight to near-surface components. According to the increase of Be_2C and BeO, the relative intensity of elemental carbon decreases for all depths. The relative signal intensity of tungsten is still not crucial regarding the total sample composition, but the amount of the Be_2 W alloy is further decreasing, whereas the amount of the subcarbide W_2C increases.

At 1200 K, the relative intensities of Be_2C and BeO decrease for *d*1 to *d*4, whereas the relative intensity of elemental carbon increases. As discussed for Fig. 2, this might be due to carbon diffusion to the surface or a change in surface morphology, such as formation of island-like structures. Furthermore, metallic tungsten and tungsten subcarbide W_2C is detected in the near-surface region *d*1. If tungsten diffusion was assumed, a carbide or alloy phase at the surface was expected. The presence of metallic tungsten can be ascribed to the appearing substrate which hints at the formation of island-like structures. At 1200 K, the Be_2 W alloy has completely vanished. The tungsten signal is composed of metallic and carbidic (W_2C) tungsten.

The results from the system Be/C/W are consistent with the analysis of binary systems. In experiments with carbon layers on a beryllium substrate, beryllium diffusion from the interface to the surface is observed [14]. At 770 K, Be_2C formation is complete [13]. Experiments with beryllium layers of a few nm thicknesses on a pyrolytic graphite substrate show island formation at 1070 K. In the ternary system, beginning formation of island-like structures is observed at 1020 K. Experiments with carbon layers on tungsten show C diffusion into the bulk material and W_2C formation starting at 870 K [15]. Alloy formation at room temperature is also observed in the binary system Be/W [16].

4. Summary

A layered system of beryllium, carbon and tungsten is prepared, annealed and analyzed by depth-resolved photoelectron spectroscopy. With this technique, it is feasible to characterize reactions by means of depth-resolved chemical information. Beryllium diffusion through carbon to the surface and BeO formation is observed at room temperature. The beryllium carbide formation starts at the interface and expands to the surface. It is complete at 850 K. Carbon diffuses into the bulk and starts forming W_2C at 850 K. At 1020 K, the analysis hints at a change in surface morphology. This effect is even more pronounced at 1200 K. The formation of a Be_2 W alloy is observed at room temperature. The alloy amount increases at 530 K; as the temperature rises to 850 K, the alloy amount is decreasing, whereas the amount of W_2C increases. The amount of tungsten carbide increases up to the last temperature 1200 K.

Acknowledgements

We thank Gianina Gavrialla, Maria Brzhezkinskaya and Mike Sperling for the support at the BESSY synchrotron beamline (RGBL-PGM).

References

[1] G. Federici, R. Anderl, J.N. Brooks, R. Causey, J.P. Coad, D. Cowgill, R. Doerner, A.A. Haasz, G. Longhurst, S. Luckhardt, D. Mueller, A. Peacock, M. Pick, C.H. Skinner, W. Wampler, K. Wilson, C. Wong, C. Wu, D. Youchison, Fus. Eng. Des. 39&40 (1998) 445.
[2] Ch. Linsmeier, AIP Conf. Proc. 740 (2004) 182.
[3] F. Esaka, K. Furuya, H. Shimada, M. Imamura, N. Matsubayashi, T. Sato, A. Nishijima, T. Kikuchi, A. Kawana, H. Ichimura, Surf. Sci. 377–379 (1997) 197.
[4] N. Matsubayashi, B.P. Singh, M. Imamura, T. Tanaka, Y. Sato, T. Ogiwara, M. Suzuki, S. Kiyota, Surf. Interface Anal. 36 (2004) 853.
[5] H. Shimada, N. Matsubayashi, M. Imamura, T. Sato, A. Nishijima, Appl. Surf. Sci. 100&101 (1996) 56.
[6] H. Shimada, K. Sato, N. Matsubayashi, M. Imamura, T. Saito, K. Furuya, Appl. Surf. Sci. 144&145 (1999) 21.
[7] M. Zier, S. Oswald, R. Reiche, K. Wetzig, Microchim. Acta 156 (2006) 99.
[8] M.P. Seah, W.A. Dench, Surf. Interface Anal. 1 (1979) 2.
[9] J.J. Yeh, I. Lindau, Atom. Data Nucl. Data 32 (1985) 1.
[10] M.P. Seah, I.S. Gilmore, Surf. Interface Anal. 31 (2001) 835.

[11] D.A. Shirley, Phys. Rev. B 5 (1972) 4709.
[12] M.G. Mason, Phys. Rev. B 27 (1983) 748.
[13] P. Goldstrass, K.U. Klages, Ch. Linsmeier, J. Nucl. Mater. 290–293 (2001) 76.
[14] J. Roth, W.R. Wampler, W.J. Jacob, J. Nucl. Mater. 250 (1997) 23.
[15] J. Luthin, Ch. Linsmeier, Surf. Sci. 454–456 (2000) 78.
[16] A. Wiltner, Ch. Linsmeier, J. Nucl. Mater. 337–339 (2005) 951.

ELSEVIER

Journal of Nuclear Materials 290–293 (2001) 121–125

journal of nuclear materials

www.elsevier.nl/locate/jnucmat

Influence of oxygen on the carbide formation on tungsten

J. Luthin, Ch. Linsmeier *

Max-Planck-Institut für Plasmaphysik, EURATOM Association, Boltzmannstrasse 2, D-85748 Garching bei München, Germany

Abstract

As a first wall material in nuclear fusion devices, tungsten will interact with carbon and oxygen from the plasma. In this study, we report on the process of thermally induced carbide formation of thin carbon films on polycrystalline tungsten and the influence of oxygen on this process. All investigations are performed using X-ray photoelectron spectroscopy (XPS). Carbon films are supplied through electron beam evaporation of graphite. The carbidization process, monitored during increased substrate temperature, can be divided into four phases. In phase I disordered carbon converts into graphite-like carbon. In phase II significant diffusion and the reaction to W_2C is observed, followed by phase III which is dominated by the presence of W_2C and the beginning reaction to WC. Finally in phase IV only WC is present, but the total carbon amount has strongly decreased. Different mechanisms of oxygen influence on the carbide formation are proposed and measurements of the reaction of carbon on tungsten with intermediate oxide layers are presented in detail. A WO_{2+x} intermediate layer completely inhibits the carbide formation, while a WO_2 layer leads to WC formation at temperatures above 1270 K.

Keywords: Carbon; Carbon-based materials; Coating; Composite materials; Deposition; Erosion; First wall materials; High-*Z* material; Material mixing; Oxidation; Plasma facing materials; Thermal desorption; Tungsten; XPS

1. Introduction

The carbide formation on tungsten as one of the favorite materials for the plasma-facing components in current and future fusion experiments [1,2] is an issue of great importance as long as both elements tungsten and carbon are present at the first wall of the vacuum vessel [3]. Changes of the material properties occur after tungsten has formed a chemical compound. Deposition of carbon, which is e.g. eroded from graphite tiles used in addition to the tungsten components, can lead to the formation of W_2C and WC [4], depending on the conditions like supply of thermal energy or particle bombardment. Besides carbon, oxygen is one of the main impurities of a fusion plasma and present when a fusion experiment is not evacuated. Different reaction scenarios between tungsten, carbon and oxygen can be envisaged. We investigate the influence of oxygen on the carbon deposition and carbide formation on tungsten. After presenting the carbide formation process in the binary system W–C the adsorption and reactions of oxygen on tungsten are reported. Furthermore we focus on the temperature-dependant behavior of carbon films on tungsten with intermediate tungsten oxide layers of different oxidation states.

2. Experimental

All measurements are carried out in a PHI 5600 ESCA X-ray photoelectron spectroscopy (XPS) system which is equipped with a monochromatic Al Kα radiation source, a hemispherical energy analyzer, a sample heater (max. 970 K) and an ion gun (0.5–5.0 keV). The XPS system is connected to a preparation chamber where carbon films can be prepared by electron beam evaporation of graphite [4,5]. Certain O_2 partial pressures can be adjusted and O atoms can be created by an oxygen source using a microwave discharge [6,7]. In the preparation chamber annealing up to 1670 K is possible

* Corresponding author. Tel.: +49-89 3299 2285; fax: +49-89 3299 2279.

E-mail addresses: jens.luthin@ipp.mpg.de (J. Luthin), linsmeier@ipp.mpg.de (Ch. Linsmeier).

0022-3115/01/$ - see front matter
PII: S0022-3115(00)00429-3

by electron beam heating. Base pressures in both chambers are in the 10^{-8} Pa range. Details of the experimental setup are presented elsewhere [8]. For this investigation polycrystalline tungsten samples are used which do not show any contamination after combined sputter/annealing cycles (5.0 keV Ar^+/970 K). Carbon deposition provides pure films within the XPS detection sensitivity [4]. The WO_2 and WO_{2+x} oxide films are prepared in an external furnace under atmospheric conditions. To analyze the acquired XPS spectra curve fitting procedures were carried out using the MultiPak software package [9] and the Spectral Data Processor [10]. All spectra presented in this paper are shown after a Shirley background subtraction [11]. Binding energies are calibrated with respect to the Au $4f_{7/2}$ core level at 84.0 eV.

3. Results and discussion

3.1. Carbide formation

Thin carbon films are evaporated onto clean tungsten substrates at room temperature (RT, approx. 300 K) and a systematic study of the temperature-dependant reactions is performed by annealing the samples under UHV conditions. At each step the desired temperature was reached within 10 min and held for 30 min. We already reported the characterization of the deposited carbon films and first results of the carbide formation on tungsten [4]. During the annealing of the carbon layers on tungsten from 300 to 1670 K four phases can be discriminated. The carbon film of the annealing experiment shown in Fig. 1 has an initial thickness of 1.5 nm, calculated from the attenuation of the substrate photoelectrons [12,13]. The energy analyzer is operated at 2.95 eV pass energy to achieve high energy resolution which is especially necessary to interpret the 300 K carbon 1s spectra. After carbon deposition we find a peak in the W $4f_{7/2}$ spectrum located at 31.4 eV binding energy (BE) which is identified as elementary tungsten. In Fig. 1 the carbon 1s peaks are shown with the results of the curve fitting procedures. At 300 K the peak consists of two major contributions from elementary carbon. The signal at 284.2 eV originates from graphitic carbon, whereas the peak at 285.2 eV is attributed to a disordered carbon fraction [4]. From measurements of carbon layers in the submonolayer range we know that already at RT a small amount of carbide (BE 281.9 eV) is formed directly at the carbon–tungsten interface [14]. This is difficult to detect here due to the attenuation by the covering elementary carbon. Annealing steps up to 870 K lead to a conversion of the disordered carbon into graphitic carbon [4] which is the dominating process within phase I. The total amounts of carbon and tungsten stay constant within this temperature range. Recent time-dependant

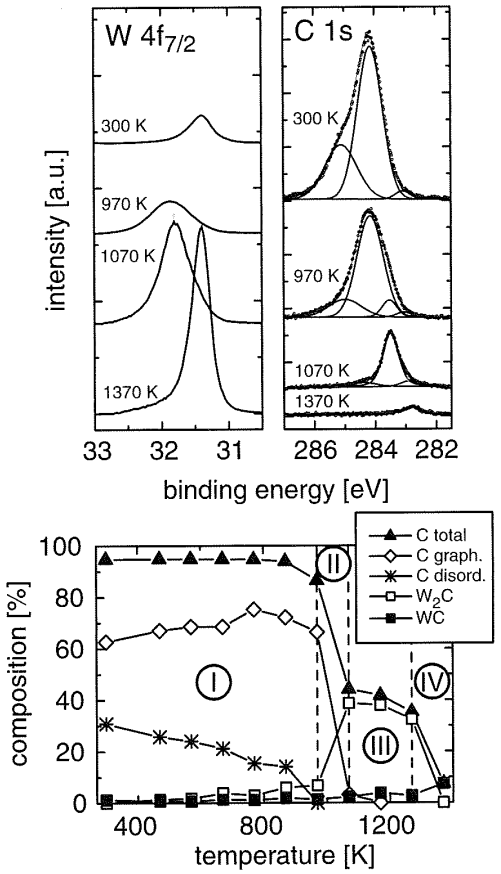

Fig. 1. W $4f_{7/2}$ and C 1s core level spectra and the surface layer composition of a carbon film on tungsten, monitored by XPS. Spectra are taken after annealing to the indicated temperatures. For the C 1s spectra the experimental data points are plotted as circles. The lines represent the peaks deconvoluted after fitting. The thin line beneath the data points is the sum of the deconvoluted peaks.

measurements have shown that diffusion below 870 K is very slow and increases significantly above this temperature [15]. This behavior is confirmed by simulations of carbon diffusion in tungsten [16]. The onset of phase II lies between 870 and 970 K. A part of the available carbon has reacted with the tungsten substrate to tungsten subcarbide (W_2C), indicated by a shift of 0.4 eV towards higher BE in the W $4f_{7/2}$ core level spectrum and a broadening of the C 1s peak. From that temperature on the amount of carbon is decreasing within the XPS detection depth and consequently that of tungsten is increasing. The C 1s spectrum recorded at 1070 K displays a shift of the peak maximum to 283.4 eV which agrees with the BE of W_2C. The W $4f_{7/2}$ spectrum has its

maximum at 31.8 eV with contributions of carbidic and metallic tungsten. At 1070 K we observe the transition between phases II and III of the carbidization process. Phase III is dominated by the presence of W_2C, which is formed by carbon atoms that occupy the octahedral sites of a hexagonal close-packed (hcp) W structure. Besides W_2C also WC can be found with a special WC structure, where the metal atoms form a hexagonal primitive packing and the carbon atoms are located in the middle of trigonal prisms built of tungsten atoms [17]. In phase III the reduction of the total carbon amount is slow compared to phase II. Above 1270 K (phase IV) we find the conversion of W_2C to WC which leads to a shift of the peak maximum in the C 1s region to 282.9 eV. This is accompanied by a further loss of carbon from the XPS analysis depth. The W $4f_{7/2}$ signal is shifted to 31.4 eV indicating that most of the intensity arises from elementary tungsten of the unreacted substrate. After all available carbon has reacted to WC, the process of carbide formation is complete.

3.2. Interaction with oxygen

An investigation of the ternary system C–O–W requires the consideration of various reaction paths. After presenting the process of carbide formation the interaction between oxygen and tungsten has to be discussed first. Many studies of oxygen adsorption on tungsten surfaces are reported which can be divided into different coverage ranges that are classified as chemisorption ($\leqslant 0.5$ monolayer (ML) oxygen coverage), two-dimensional oxidation (0.5–1.1 ML oxygen coverage) and bulk oxidation [18,19]. At RT exposure of tungsten to molecular oxygen results in dissociative chemisorption with oxygen atoms sitting at triply coordinated sites [20]. W $4f_{7/2}$ photoemission studies show that oxygen-induced features for $\leqslant 0.5$ ML oxygen coverage occur at ~0.3 eV higher binding energies than the signal from bulk tungsten [21,22]. We measured polycrystalline tungsten samples after 5–60 min at 1×10^{-5} Pa O_2 partial pressure and after exposure to O atoms created in a microwave discharge [6]. In all cases we observe an oxygen coverage of ~0.5 ML. The O 1s BE is located at 530.4 eV and the W 4f peaks are broadened. According to the literature, to achieve higher oxygen coverages the sample must be exposed either at elevated temperatures, for longer times or to higher oxygen pressures [23]. Annealing of the sample exposed 60 min at 1×10^{-5} Pa O_2 does not lead to changes in the tungsten/oxygen ratio up to 970 K. Above this temperature the oxygen amount decreases. However, after the last annealing to 1670 K an oxygen fraction of 10 at.% is still detected in the XPS signal. It is expected that atomic oxygen is the only desorption product for oxygen coverages below 0.5 ML [24]. With increasing coverage, a substantial part of oxygen can desorb as oxide [25]. We find that carbon deposition on chemisorbed oxygen and deposition of carbon in 1×10^{-5} Pa O_2 atmosphere with subsequent annealing do not reveal discrepancies in the process of carbide formation in the binary system W–C.

The influence of chemically bonded oxygen on the W–C interaction is studied at tungsten samples which are covered by thin oxide layers. Two different WO_x stoichiometries are examined. A WO_{2+x} with $x = 0.4$ is produced by annealing a sample (cleaned in vacuum as described above) in air for 60 min at 670 K. This treatment is carried out in a furnace under atmospheric conditions. The surface oxide exhibits a citric yellow color. After reinserting the sample into the UHV system XPS analysis results in a O/W ratio of 2.4 ($WO_{2.4}$). Annealing of the sample at 470 K for 10 min to remove volatile contaminations reduces the O/W ratio to 2.1. Since the substrate is pure W and the photoelectrons from W 4f have a higher kinetic energy than those from O 1s (1450 and 953 eV, respectively), the different attenuation lengths lead to an overestimation of the tungsten fraction in the O/W ratio. A ~1 nm thick carbon layer is evaporated on this oxide layer. The XPS results after annealing steps up to 1670 K are presented in Fig. 2. At RT the W $4f_{7/2}$ BE is 35.7 eV. With decreasing oxidation state the BE decreases, literature values are 35.8 eV for WO_3 and 32.8 eV for WO_2 [26]. The peak maximum for O 1s is at 530.5 eV and for C 1s at 284.2 eV. Annealing to 970 K does not change the detected amounts of the three elements but a second W 4f doublet indicates that a part of the tungsten is reduced. In the O 1s energy range a shoulder at higher BE is detected. Further investigations are necessary to clarify the local stoichiometry of the oxide film, to elucidate the chemical state of the tungsten and to determine the structure of this oxide. Annealing to 1170 K leads to significant changes. The carbon signal disappears completely and the W $4f_{7/2}$ peak maximum shifts to 31.4 eV which indicates the presence of metallic tungsten. Dean et al. proposed a two-stage mechanism for the reduction of higher tungsten oxides with carbon via WO_2 to W under the formation of CO and CO_2 [27,28]. This mechanism is partly able to explain the reactions in our experiments. However, another reaction path is necessary which explains the decrease of the remaining oxygen without the presence of carbon above 1170 K. We like to emphasize that the 1670 K spectra are identical to the final state of the adsorption experiment of oxygen on clean tungsten.

To separate the two stages of the tungsten oxide reduction mechanism a second oxide stoichiometry – WO_2 – is examined. WO_2 films are prepared by annealing a cleaned tungsten substrate first at 820 K for 15 min in air (sample color: purple) and then at 970 K, 60 min under UHV conditions. XPS analysis showed an O/W ratio of less than 2 but for the reasons mentioned above the sample surface is assumed to be WO_2. This is also

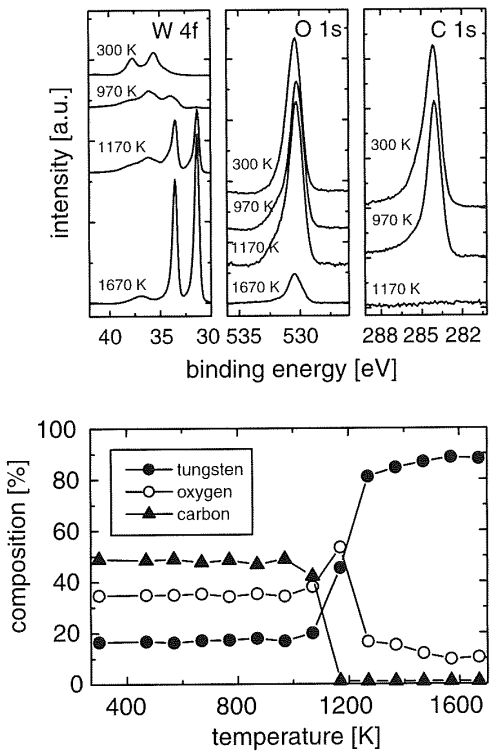

Fig. 2. XPS core level spectra and the surface layer composition as a function of the annealing temperature of a carbon film deposited on tungsten with a WO_{2+x} ($x = 0.4$) intermediate layer.

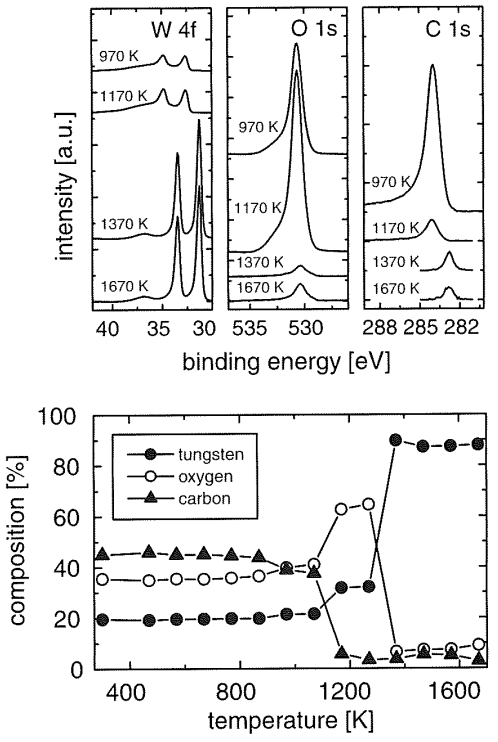

Fig. 3. XPS core level spectra and the surface layer composition as a function of the annealing temperature of a carbon film deposited on tungsten with a WO_2 intermediate layer.

confirmed by a W $4f_{7/2}$ BE of 32.8 eV, corresponding to the literature value. After carbon deposition annealing steps up to 970 K do not cause changes. Fig. 3 shows the XPS spectra and the surface composition during the subsequent annealing experiments. At 1170 K the tungsten is still present as WO_2, the carbon amount decreased again probably due to CO and CO_2 formation. However, in contrast to the $WO_{2.4}$ film, 6 at.% of graphitic carbon is left. The next annealing steps lead to a decrease in the oxygen amount but without a further decrease of the carbon intensity. Obviously, oxygen does not desorb from tungsten as a carbon compound at temperatures above 1170 K. We believe that the substitution $WO_2 \rightarrow WC$ is visible which is known for WO_2 reduction with CO [29,30]. At 1370 K all detectable carbon has completely reacted to WC indicated by a shift of the C 1s BE to 282.9 eV. Annealing to higher temperatures does not change the situation significantly. The final amount of oxygen is equal for all the other oxygen experiments. The reason for this similarity can be a very stable surface configuration at this oxygen concentration on tungsten.

4. Summary

We presented in detail the stepwise carbidization in the binary system W–C via W_2C to WC. An adsorbed oxygen layer or small amounts of oxygen during carbon film preparation on tungsten do not influence the process of carbide formation. However, intermediate oxide layers change the reaction behavior. A WO_{2+x} ($x = 0.4$) film inhibits the carbidization completely due to the reaction of carbon with oxygen. On a WO_2 layer carbon does not react with oxygen above 1170 K and with tungsten below 1370 K. At higher temperatures WC is formed without a W_2C subcarbide intermediate step. Further investigations will focus on the product spectrum and the mechanism of tungsten oxide reduction at temperatures above 1170 K. For the use of tungsten as first wall material in fusion devices we draw the conclusion that several reaction scenarios between W–O–C, depending on the initial conditions of the first wall, are

possible. This results in different surface layers with a broad variety of properties.

References

[1] J. Davis, V. Barabash, A. Makhankov, L. Plöchel, K. Slattery, J. Nucl. Mater. 258–263 (1998) 308.
[2] I. Kirillov, I. Danilov, S. Sidorenkov, Y. Strebkov, R. Mattas, Y. Gohar, T. Hua, D. Smith, Fusion Eng. Des. 39&40 (1998) 669.
[3] H. Maier, S. Kötterl, K. Krieger, R. Neu, M. Balden, ASDEX Upgrade-Team, J. Nucl. Mater. 258–263 (1998) 921.
[4] J. Luthin, Ch. Linsmeier, Surf. Sci. 454–456 (2000) 78.
[5] S. Schelz, T. Richmond, P. Kania, P. Oelhafen, H.-J. Güntherrodt, Surf. Sci. 359 (1996) 227.
[6] Ch. Linsmeier, J. Wanner, Surf. Sci. 454–456 (2000) 305.
[7] J. Jung, Max-Planck-Institut für Quantenoptik, MPQ-Report, 231, 1998.
[8] S. Miller, G. Berning, H. Plank, J. Roth, J. Vac. Sci. Technol. A 15 (1997) 2029.
[9] MultiPak Ver. 2.2, Physical Electronics, 1996.
[10] Spectral Data Processor, Ver. 2.1, XPS International, 1997.
[11] D. Shirley, Phys. Rev. B 5 (1972) 4709.
[12] M. Seah, Practical Surface Analysis, Wiley, Norwich, 1985.
[13] Ch. Linsmeier, Vacuum 6&7 (1994) 673.
[14] Ch. Linsmeier, J. Luthin, P. Goldstraß, these Proceedings.
[15] J. Luthin, K. Schmid, Ch. Linsmeier, J. Roth, to be published.
[16] K. Schmid, J. Roth, W. Eckstein, K. Ertl, these Proceedings.
[17] U. Müller, Anorganische Strukturchemie, Teubner, Stuttgart, 1992.
[18] T. Engel, H. Niehus, E. Bauer, Surf. Sci. 52 (1975) 237.
[19] E. Bauer, T. Engel, Surf. Sci. 71 (1978) 695.
[20] J. Feydt, A. Elbe, H. Egelhard, G. Meister, A. Goldmann, Surf. Sci. 440 (1999) 213.
[21] D.M. Riffe, G.K. Wertheim, Surf. Sci. 399 (1998) 248.
[22] C.H.F. Peden, N.D. Shin, Surf. Sci. 312 (1994) 151.
[23] H. Daimon, R. Ynzunza, J. Palomares, H. Takabi, C.S. Fadley, Surf. Sci. 408 (1998) 260.
[24] T. Engel, T. von dem Hagen, E. Bauer, Surf. Sci. 62 (1977) 361.
[25] D. Menzel, in: R. Gomer (Ed.), Topics in Applied Physics V.4. Interactions on Metal Surfaces, Berlin, 1975.
[26] J.F. Moulder, W.F. Strickle, P.E. Sobol, K.D. Bomben, in: J. Chastain (Ed.), Handbook of X-ray Photoelectron Spectroscopy, Perkin Elmer, MN, 1992.
[27] D.S. Venables, M.E. Brown, Thermochim. Acta 282&283 (1996) 251.
[28] D.S. Venables, M.E. Brown, Thermochim. Acta 282&283 (1996) 265.
[29] D.S. Venables, M.E. Brown, Thermochim. Acta 291 (1997) 131.
[30] T. Kodama, H. Ohtake, S. Matsumoto, A. Aoki, T. Shimizu, Y. Kitayama, Energy 25 (2000) 411.

ELSEVIER

Journal of Nuclear Materials 266–269 (1999) 581–586

journal of nuclear materials

Erosion of beryllium and deposition of carbon and oxygen due to bombardment with C^+ and CO^+ ions

P. Goldstraß, W. Eckstein, Ch. Linsmeier *

Max-Planck-Institut für Plasmaphysik, EURATOM-Association, Boltzmannstr. 2, D-85748 Garching, Germany

Abstract

The bombardment of clean, metallic beryllium with carbon and the co-bombardment with carbon and oxygen is investigated experimentally and by computer simulation. The experiments use C^+ and CO^+ ions with energies between 3 and 12 keV at normal incidence. The simulation is carried out with the Monte Carlo code TRIDYN. The results of carbon bombardment from experiment and simulation agree well and show the buildup of a carbon adlayer on the metal surface. After the carbon adlayer formation, no more Be is eroded. For C and O co-bombardment, carried out by CO^+ ion bombardment, simulation and experiment agree for low fluences. At higher fluences, another erosion channel besides kinematic sputtering is opened by the chemical interactions of C and O. This leads to a deposition/erosion equilibrium which is not predicted by the kinematic TRIDYN code. The formation of a ternary mixture layer on the Be target leads to a continuous erosion of the beryllium target.

Keywords: Beryllium; Erosion; Deposition; Carbon ions

1. Introduction

In the design of future fusion plasma devices like ITER several elements are regarded as possible first wall materials. Both, low-Z elements as Be and C, and heavy elements as Mo and W are under discussion. If these elements are eroded from walls or divertor plates, they will eventually lead to impurity contamination of the discharge. In this case plasma facing components will be bombarded simultaneously with hydrogen isotopes and these impurity species. Of the low-Z elements Be has been used in JET [1] and C in most fusion machines. Earlier investigations have shown that experimental data are well reproduced by simulations for the bombardment of W with C only [2]. Some information on Be is given in [3,4]. Therefore, in this paper the effects of a simultaneous bombardment of Be with C and O from CO^+ are investigated experimentally and compared to computer simulations to validate the modelling of this more complex situation.

* Corresponding author. Tel.: +49 89 3299 1263; fax: +49 89 3299 1149 e-mail: linsmeier@ipp.mpg.de

2. Experiment

A polycrystalline polished Be target was bombarded at normal incidence with 3 and 5 keV C^+ and 3, 5 and 12 keV CO^+ ions in the apparatus BOMBARDON [5]. The ions are produced by an electron impact source from CO gas (Linde 3.7) and subsequently mass-separated by a 80° magnetic deflection. The base pressure in the target chamber and during the RBS analysis was in the low 10^{-11} hPa range, during the implantation in the 5×10^{-11} hPa range. The Be target was cleaned by periodic 5 keV Ar^+ bombardment and annealing to 680 K. Analysis of the implanted C and O was performed by Rutherford backscattering spectroscopy (RBS) using 0.6 MeV $^4He^+$ at normal incidence. The detector was situated at a scattering angle of 163°. Implantation and subsequent RBS analysis were all carried out with the sample at room temperature.

Fig. 1 shows RBS spectra of the sample after cleaning (a) and after CO^+ implantation (b). The spectrum (a) of the clean sample exhibits the Be edge and peaks originating from Ar caused by the cleaning procedure, as well as a small signal from tantalum. The Ta surface contamination is caused by sputter deposition of Ta

0022-3115/99/$ – see front matter
PII: S0022-3115(98)00545-5

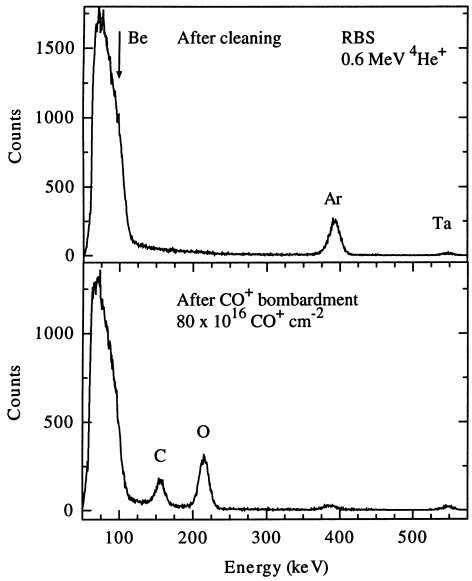

Fig. 1. Energy distributions of backscattered ^4He from a clean Be target (a) and a Be target bombarded with 5 keV CO^+ ions (b). The CO^+ fluence is 8.0×10^{17} cm^{-2}. Analysis is performed with 0.6 MeV $^4He^+$, the backscattering angle is 163°.

from an aperture used in early steps of the cleaning procedure. The Ta intensity corresponds to an amount of 6.0×10^{13} cm^{-2} (about 0.04 monolayers). No carbon and oxygen can be detected after the cleaning procedure. Spectrum (b) in Fig. 1 shows the RBS analysis of the Be target after bombardment with 8×10^{17} CO^+ cm^{-2} at 5 keV. It demonstrates well the separation of the C and O peaks and the Be edge. Due to the CO^+ bombardment, the Ar amount has decreased by a factor of about 26. The C and O amounts in the sample are determined by integration of the respective peak areas after background subtraction. The peak widths of both the C and O signals are comparable to the submonolayer signal from the Ta peak, which give an energy resolution of the detection system of 18.7 keV. The corresponding depth resolution of 650 Å (calculated for the stopping in Be metal) is not good enough to extract depth profiles from the measured spectra.

3. Simulation

The calculations were performed with the Monte Carlo program TRIDYN (version 40.3) [6,7]. This program takes into account all collisional effects as implantation, reflection, and sputtering. Target composition changes due to the bombardment are regarded as well, so that effects like sputter yields, reflection coefficients, and composition profiles can be determined as a function of the bombarding fluence. The program allows also simultaneous bombardment with several species of fixed energy or with a Maxwellian incident distribution. Surface binding energies, important for sputtering, are based on the elemental heats of sublimation and are interpolated due to the surface composition of the target [8]. Chemical erosion, diffusion and segregation are neglected. The sample is divided in thin layers of 2.5 Å thickness which may have different compositions. The output step is usually 1% of the total fluence applied. The composition of each layer is adjusted after processing every collision cascade. Thus, compositional changes due to the incoming ions are taken into account.

4. Results and discussion

4.1. C^+ implantation

The Be target was bombarded after cleaning with C^+ ions up to a fluence of 5.5×10^{17} cm^{-2}. The maximum fluence was determined by the lifetime of the ion source filament. Fig. 2 shows the calculated depth distribution of 5 keV C^+ implanted in beryllium for several fluences which correspond to the experimentally applied values. Beginning with 5×10^{16} cm^{-2}, carbon is deposited in a depth of roughly 200 Å with almost no carbon at the sample surface. For higher fluences, the carbon con-

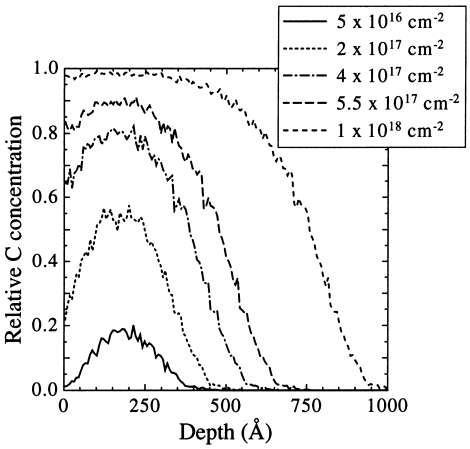

Fig. 2. Depth distributions of C in Be. Be is bombarded with 5 keV C^+ at normal incidence (TRIDYN). The calculated fluences correspond to the values of the experiments.

centration on the target surface increases up to almost unity and the buildup of a carbon layer with increasing thickness is expected. The further steps resulting in this adlayer formation are the erosion of the beryllium on the target surface above the implantation zone. During extended C^+ bombardment, the deposition zone with implanted carbon is finally reached. Since the self sputtering yield of C^+ on pure carbon is below unity [3], carbon then builds up a layer on the Be substrate. Under further C^+ ion bombardment, this carbon surface layer grows steadily.

The experimental results confirm the predictions from the TRIDYN simulation. Fig. 3 shows the deposited amount of carbon on the target as a function of the C^+ fluence. The lines represent the TRIDYN calculations for a primary energy of the C^+ ions of 3 and 5 keV. The data points are the measured carbon concentrations in the Be target after the C^+ bombardment. Each experiment consists of one or more series, each starting with a clean Be surface containing no carbon and oxygen (cleanliness corresponding to spectrum of Fig. 1(a)). The lines represent simulations with KrC [9] and ZBL [10] interaction potentials. The difference between them is negligible and not visible in the diagram. The amount of deposited carbon after ion bombardment is calculated from the carbon peak area in the RBS spectra after background subtraction. For 5 keV C^+ the agreement between simulation and experiment is excellent. For 3 keV a deviation between the Monte Carlo calculation and the data points from RBS analysis can be recognized. However, the shape of the calculated line fits very well to the data points if these are scaled by a factor of 1.3. The scaling can be done either on the C^+ fluence or on the intensity axis to achieve this agreement. Since the deposited fluence is determined experimentally by integrating the current collected on the target and the surrounding Faraday cup during implantation, an error in the current measurement leads to an error in the C^+ fluence determination. Therefore, the agreement between the TRIDYN simulation and the RBS measurement can be regarded as satisfiable for both primary energies. The error bars at the experimental data points in Fig. 3 account only for the statistical error in the RBS spectra and do not reflect uncertainties in the current measurement.

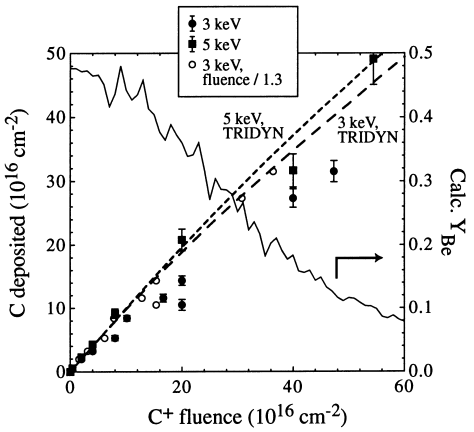

Fig. 3. Deposited C on the Be target versus the C^+ fluence due to the bombardment with 3 and 5 keV C^+ at normal incidence. The TRIDYN calculations are performed with the KrC and ZBL interaction potentials. The difference between the two interaction potentials is negligible and not shown in the diagram. Also shown is the calculated sputtering yield of Be considering the compositional changes due to the C^+ bombardment.

As predicted by the simulation, the experiments show the buildup of a carbon layer on the sample surface. In the studied fluence range no saturation in the deposited amount of carbon is found. The carbon layer thickness at the maximum experimental C^+ fluence of 5.48×10^{17} cm^{-2} is 483 Å, calculated for a graphite density of 2.26 g cm^{-3}. This is in good agreement with the result from the calculation (Fig. 2), where the carbon concentration starts to decrease at a depth of about 500 Å. However, the maximum carbon concentration in the calculation is only 98%, but the additional carbon in deeper layers leads to a total amount of carbon comparable to that detected in the RBS experiments. The carbon layer at the maximum fluence after 3 keV C^+ bombardment (4.73×10^{17} cm^{-2}) reaches a thickness of 417 Å.

Both experiment and TRIDYN simulation in Fig. 3 show a change in the slope of the C amount with increasing fluence. This can be attributed to a compositional change in the surface layer during C^+ implantation. The carbon peak deposition zone is in a depth of approximately 200 Å. The sputtering process due to the collision cascades takes place at the outermost layers. This leads to an erosion of the mixed Be–C layer at the surface above the C implantation zone. This process continues until the surface layer consists predominantly of carbon. The gradual change in the composition results in an increase of the C^+ reflection. However, the reflected fraction of primary ions stays well below 0.2% for both primary energies. For high C concentrations after greater fluences, the erosion of the Be–C mixed layer decreases and the C adlayer formation continues. This leads finally to a surface layer consisting almost exclusively of carbon, and as a consequence to the continuous build-up of a carbon layer on the beryllium substrate.

4.2. CO^+ implantation

Since the CO^+ currents from the ion source are much larger than for C^+, implantation fluences up to

2×10^{18} cm^{-2} are accessible in the experiment. Compared to the C^+ beams, the carbon and oxygen atoms impinging on the surface from CO^+ beams have lower energies. The kinetic energy is split between the atoms in the CO^+ molecule according to their mass ratio of C (3/7) and O (4/7). Therefore, carbon possesses energies around 1.286, 2.143 and 5.145 keV for the 3, 5 and 12 keV primary beams, whereas oxygen has energies of 1.714, 2.857 and 6.855 keV, respectively.

At low fluences below approximately 1×10^{17} cm^{-2}, the experimentally measured amounts of deposited carbon and oxygen in the sample increase according to the calculations by the TRIDYN program, see Fig. 4. This behaviour is similar to that of the C^+ bombardment and can be explained by the implantation of both C and O in the Be matrix. The ion bombardment also leads to a simultaneous sputtering of beryllium. Both carbon and oxygen are deposited in an implantation zone below the surface. The depth and width of this zone depend on the primary energy of the CO^+ ions. Fig. 5 shows TRIM.SP results for CO^+ ions, impinging on Be at three different energies, respectively. In contrast to TRIDYN, TRIM.SP does not account for compositional changes in the target due to ion bombardment. Since the kinetic energy splits asymmetrically between C and O upon CO^+ impact on the surface and these two species exhibit different stopping cross-sections on their path through the target, their depth distribution depends on the CO^+ primary energy. For 3 keV CO^+, the peak implantation zone is around a depth of 60 Å. Oxygen is implanted slightly deeper than carbon. For 5 keV CO^+, the implantation maximum is around a depth of 80 Å. Again, oxygen is deposited slightly deeper than carbon. The difference in implantation depth between C and O vanishes for a primary CO^+ ion energy of 12 keV and the maximum of the deposition zone lies around 200 Å. It can also be noted that the width of the implantation zones increases strongly with increasing CO^+ primary energy. The calculation pictured in Fig. 5 reflects the very beginning of the CO^+ implantation and corresponds to zero fluence, since no compositional changes due to the ion beam are taken into account by TRIM.SP. For continued CO^+ bombardment, the beryllium above the C and O deposition zones is eroded by sputtering. The actual sample surface recesses and subsequent C and O are deposited accordingly in greater depths. This will lead eventually to the formation of a mixed layer consisting of the three elements C, O and Be which starts at the surface and extends into the sample. In contrast to the C^+ implantation scenario, the ternary system of C, O and Be is expected to show a more complex behaviour, which is demonstrated in the experimental results.

The C and O concentrations start to saturate at a fluence which depends on the CO^+ primary energy. Fig. 4 shows a deviation of the RBS results from the TRIDYN calculations at fluences between 4×10^{16} cm^{-2} and 3×10^{17} cm^{-2}, depending on the CO^+ energies. Only shown is the TRIDYN calculation for 5 keV CO^+ ions, since the difference for 3 and 12 keV in the valid fluence regime below approx. 1.5×10^{17} cm^{-2} is negligible. The C

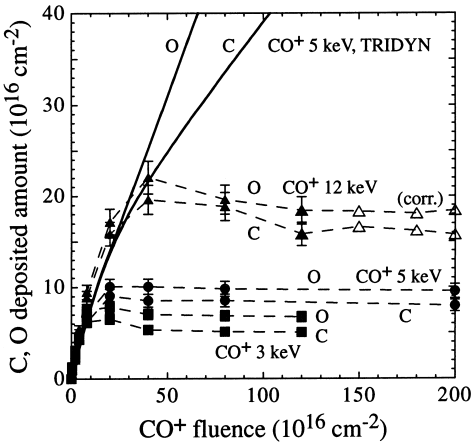

Fig. 4. Deposited C and O in the Be target versus the fluence due to the bombardment with 3, 5 and 12 keV CO^+ at normal incidence. Lines between the experimental data points are drawn to guide the eye. (The 12 keV CO^+ data points at fluences $>1.3\times10^{18}$ cm^{-2} (open symbols) are corrected due to an error in the current measurement.)

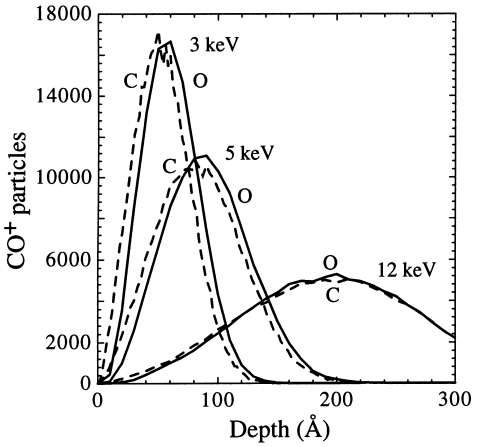

Fig. 5. Implantation zones for carbon and oxygen at 3, 5 and 12 keV, resulting from the asymmetric splitting of the kinetic energy of the CO^+ ion upon target impact and subsequent stopping in beryllium. Calculations are carried out by TRIM.SP and represent the zero fluence case (no compositional changes in the target due to the ion beam are considered).

and O concentrations start to saturate and reach an energy-dependent, constant value. The measurements also suggest that the amounts of deposited C and O pass through a maximum before reaching their saturation value. This saturation effect cannot be explained by mere atomic collisions and is therefore not predicted by the TRIDYN calculations. The experiments demonstrate that after a certain transition fluence an erosion mechanism other than collisional sputtering sets in. It leads to a constant C/O ratio and to a constant C and O inventory in the ternary compound formed on the beryllium target. This erosion mechanism releases C and O in equal amounts and is presumably of chemical nature. In experiments dealing with carbon erosion by oxygen, an erosion yield of about unity is found [3,11,12]. The formation of CO and CO_2 by chemical erosion of graphite and beryllium was observed under O^+ irradiation [13,14]. As observed in the O^+ ion experiments [14] this process may also be effective here only after an appreciable C concentration has been accumulated on the surface and after this layer is saturated in oxygen.

The reason for the initial increase in deposited carbon and oxygen, as predicted by the kinematic simulations, is the implantation of C and O in deeper layers. For the erosion mechanism via the formation of CO molecules and their subsequent desorption, a sufficiently high density of both C and O in the Be matrix is necessary. Moreover, the loss of CO by desorption is only possible at the outermost surface. Therefore, two criteria have to be fulfilled before CO erosion can take place and the observed deposition/erosion equilibrium sets in: (1) accumulation of C and O in a sufficiently high density for the formation of the CO molecules. This implies also that the substrate temperature (always room temperature in these experiments) may play an important role, since elevated temperatures will increase the mobility of implanted C and O species. Criterion (2) is the possibility for formed CO to desorb. This can only take place for CO reaching the target surface, either by the formation of CO molecules at the very surface or by diffusion of CO molecules from their formation location to the outermost surface. The increasing onset fluence, the increasing overall C and O inventories and the observed increasing C/O ratios for increasing CO^+ ion energies support this interpretation, as will be discussed in the following paragraphs.

The onset fluence for CO desorption reflects the depth of the implantation zone for C and O. For greater CO^+ primary energies this depth is larger and therefore a greater fluence is necessary to erode the overlying Be layer. Only after the implantation zone is sputtered, C- and O-containing material reaches the surface (CO formation at the surface) or the CO diffusion path length is long enough for CO to reach the surface (CO formation in deeper layers).

The increasing overall C and O inventory for increasing CO^+ primary energies is a consequence of the broader depth distribution for CO^+ ions with higher energies, see Fig. 5. This broader distribution leads to a greater thickness of the C–O–Be ternary mixture layer on the Be target and consequently to a greater C and O equilibrium concentration. Experimentally, the thickness of the ternary adlayer on the Be substrate is reflected in the shift of the Be edge in the RBS spectra. However, the edge shift compared to the edge of the clean Be sample is at the limit of the experimental resolution and may only be taken as a supportive argument.

The different C/O equilibrium ratios for the examined primary energies result from the difference in ion ranges and stopping cross-sections for C^+ and O^+ at their respective energies. For low primary energies, oxygen is implanted at slightly greater depths than carbon. After extended bombardment (after erosion of the Be layer above the implantation zone), the oxygen zone extends further into the sample than the carbon zone. This difference vanishes with increasing CO^+ primary energy, as shown in Fig. 5 by the TRIM.SP simulation. The different thicknesses of the C- and O-containing layers at equilibrium lead to the different average C/O ratios of 0.75, 0.85 and 0.90 for the three respective CO^+ primary energies of 3, 5 and 12 keV. For higher ion energies, the C/O ratio approaches 1, since the implantation depths of C and O become equal.

The consequence of the equilibrium concentrations in the case of a C and O co-bombardment is an equilibrium composition of a ternary adlayer of finite thickness. This implies a continuous erosion of Be in addition to the CO desorption. Therefore, the chemical CO formation process, accompanied by kinematic sputtering, results in a continuous Be target erosion. The different steps in the CO^+ interaction with the beryllium target are summarized in Fig. 6. Step 1 depicts the low fluence regime, where incoming CO^+ are implanted in the Be matrix. CO^+ also leads to sputtering of Be at the surface. This leads to an erosion of the original sample surface. The full separation of the C- and O-containing zones in this picture is for clarification of the process only. For continued CO^+ bombardment (step 2 in Fig. 6), the implantation zone is extended into the Be sample, since the surface is continually eroded. The carbon- and oxygen-containing implantation zones start to overlap in this model. In reality, however, both implantation layers will be overlapping already from the beginning, as is shown in Fig. 5 according to the TRIM.SP calculations. As long as there is a Be layer above the implantation zones, all incoming CO^+ are trapped (except the very small amount of reflected particles, well below 0.2% according to the calculations). This regime corresponds to the low fluences in Fig. 4, which is well reproduced by the TRIDYN simulations. When the implantation zones reach the sample surface (step 3 in Fig. 6), the emission of CO starts and deposition and erosion equilibrate.

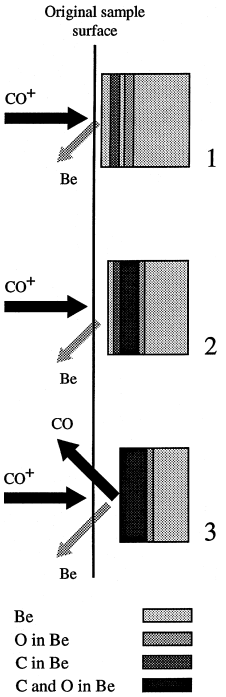

Fig. 6. Schematic description of the CO^+ ion-target interaction. Step 1: Implantation of C and O in different depths, according to their respective energies and stopping cross-sections. Step 2: Continued erosion of Be above the implantation regimes, extended implantation in deeper layers. Step 3: Start of CO erosion, continued Be erosion. Deposition/erosion equilibrium sets in.

This regime finally leads to the constant ternary layer composition, which is found in the experiments.

5. Conclusions

It is shown that the experimental data are in good agreement with results calculated by the kinematic Monte Carlo code TRIDYN for 3 and 5 keV C^+ ions bombarding a clean beryllium target under perpendicular incidence. The interaction of the incoming ions with the target is fully explained by kinematic processes like implantation, reflection and sputtering. A carbon layer of increasing thickness is formed on top of the beryllium metal. After a fluence of approximately 1×10^{18} cm^{-2} no more Be is eroded.

Co-bombardment of beryllium with carbon and oxygen, simulated by the implantation of CO^+ ions in Be, shows a different behaviour. For low fluences, depending on the CO^+ primary energy, a kinematic description of the ion-target interaction is sufficient. TRIDYN simulation and experiment both agree in the accumulation of carbon and oxygen in the Be target. However, after an energy-dependent fluence, another – presumably chemical – erosion mechanism dominates the ion-target interaction. This leads to a constant composition in the target surface layers. Both the composition and the thickness of the formed layer depend on the energy of the incoming CO^+ ions. The absolute amounts of C and O reach constant values for extended CO^+ implantation which means that the Be target surface is continuously eroded. The underlying chemical processes for this behaviour, which may imply the formation of BeO, Be_2C and additional compounds in the ternary layer, and the formation and transport of CO molecules as the desorbing species in the erosion process, are not yet identified and subject to further studies.

Acknowledgements

The authors thank R. Bastasz for the polished Be target.

References

[1] The JET team: presented by P.R. Thomas, J. Nucl. Mater. 176&177 (1990) 3.
[2] W. Eckstein, J. Roth, Nucl. Instr. and Meth. B 53 (1991) 279.
[3] W. Eckstein, C. Garcá-Rosales, J. Roth, W. Ottenberger, IPP-Report 9/82, Garching, 1993.
[4] J. Roth, W. Eckstein, M. Guseva, Fus. Engi. Design 37 (1997) 465.
[5] M. Mayer, W. Eckstein, B.M.U. Scherzer, J. Appl. Phys. 77 (1995) 6609.
[6] W. Eckstein, Computer Simulation of Ion–Solid Interaction, Springer, Berlin, 1991.
[7] W. Möller, W. Eckstein, J.P. Biersack, Comput. Phys. Commun. 51 (1988) 355.
[8] W. Eckstein, M. Hou, V.I. Shulga, Nucl. Instr. and Meth. B 119 (1996) 477.
[9] W.D. Wilson, L.G. Haggmark, J.P. Biersack, Phys. Rev. B 15 (1977) 2458.
[10] J.F. Ziegler, J.P. Biersack, U. Littmark, in: J.F. Ziegler (Ed.), The Stopping and Range of Ions in Matter, vol. 1, Pergamon, New York, 1985.
[11] J. Roth, J. Nucl. Mater. 145–147 (1987) 87.
[12] V. Vietzke, T. Tanabe, V. Philipps, M. Erdweg, K. Flaskamp, J. Nucl. Mater. 145–147 (1987) 425.
[13] V. Vietzke, A. Refke, V. Philipps, M. Hennes, J. Nucl. Mater. 220–222 (1995) 249.
[14] A. Refke, V. Philipps, E. Vietzke, M. Erdweg, J. von Seggern, J. Nucl. Mater. 212–215 (1994) 1255.

Towards a detailed understanding of the mechanisms of hydrogen retention in beryllium

M. Oberkofler[1], M. Reinelt[1], A. Allouche[2], S. Lindig[1], and Ch. Linsmeier[1]

[1] ***Max-Planck-Institut für Plasmaphysik, EURATOM Association, Boltzmannstraße 2, 85748 Garching b. München, Germany***

[2] ***Physique des Interactions Ioniques et Moléculaires, CNRS and Université de Provence, Campus Scientifique de Saint Jérôme, service 242, 13397 Marseille Cedex 20, France***

*Towards a detailed understanding of the mechanisms of hydrogen retention in beryllium*2

Abstract. In this paper we present new temperature programmed desorption measurements from implanted single and polycrystalline beryllium as well as new computational results on the diffusion of interstitials through an undisturbed beryllium lattice. The threshold fluence for the appearance of a low-temperature desorption region around 460 K after implantation of 1 keV D ions into polycrystalline beryllium is determined to 1.2×10^{21} m^{-2}. In the high temperature release region an implantation energy-dependent shift in desorption temperatures is observed after implantation to very low fluences. It is explained by the variation of the mean distance from the surface for atoms implanted at different energies rather than by changes in the activation energy for detrapping. Morphological investigations of the surface of polycrystalline beryllium after several implantation and annealing cycles show a strong dependence of the damage on the surface-orientation of grains. This dependence correlates with the preferred diffusion of interstitials parallel to basal planes of the beryllium lattice as calculated within the formalism of density functional theory.

PACS codes: 61.80.Jh; 61.72.Hh; 68.43.Vx; 68.55.Ln; 82.20.Pm; 66.30.je; 71.15.Mb; 71.15.Nc; 28.52.-s

1. Introduction

Understanding of the main mechanisms responsible for the retention of hydrogen atoms implanted into beryllium (Be) is a field of ongoing research. In order to gain further insight in the relevant processes at atomic scale, models have to be developed and tested. However, impure sample surfaces, poorly defined defect densities, and other sources of uncertainty often make it difficult to compare experimental data with values from simulations. Our experimental approach in the past years has been to simplify the system under investigation in order to rule out as many experimental uncertainties as possible. To this aim we have performed measurements on single crystalline Be with well-defined surface oxygen coverages as low as 0.3 monolayers as the only remaining impurity [1]. Temperature programmed desorption (TPD) spectra recorded after implantation of hydrogen into these well-defined specimens show a sequential release of the retained hydrogen in several temperature steps. These release temperatures are governed by activation energies for the various processes occurring during annealing: detrapping, diffusion, retrapping of hydrogen and self interstitials and, finally, recombination and desorption of hydrogen from the surface. By modelling the release based on rate equations we can extract values for such activation energies from our experiments. Activation energies for individual processes can be calculated ab initio within density functional theory (DFT). This allows a direct comparison of experimental findings with atomistic calculations. This comparison of the experimental and ab initio parameters ultimately should lead to a consistent picture for the hydrogen-related processes in Be.

This work summarizes our recent progress in singling out parameters that influence the observed desorption temperatures. Two topics are addressed. First, we discuss the observed appearance of a low-temperature release peak in the TPD spectra after implantation above the corresponding threshold fluence and compare these new results

from experiments on polycrystalline Be with previously published results from Be($1\,1\,\bar{2}\,0$) single crystals. Second, TPD experiments with implantation energy-dependent release temperatures performed with a single crystalline sample after implantation up to very low fluences ($\sim 10^{19}$ m^{-2}) are presented. They are discussed in relation to TPD results from single and polycrystalline samples implanted to higher fluences.

Furthermore, recent results from DFT calculations on the diffusion of hydrogen interstitials as well as Be self interstitials in Be are presented. The influence of the resulting diffusional anisotropy on the morphology of the sample surface observed experimentally after numerous implantation and annealing cycles is discussed.

2. Experimental and computational details

For the shown TPD spectra polycrystalline or single crystalline samples are implanted with mass-separated deuterium ions (D_3^+ or D_2^+) at 1 keV and 3 keV per atom, up to fluences ranging from 2.5×10^{19} m^{-2} to 2.0×10^{21} m^{-2}. The surface orientation of the single crystalline Be is ($1\,1\,\bar{2}\,0$) i.e. the crystal is cut orthogonally to the basal planes. Previous to implantation the surfaces of the samples are cleaned by repeated sputtering with argon ions and subsequent annealing. As observed with in situ X-ray photoelectron spectroscopy (XPS), the only remaining impurity during the whole course of the experiments is a constant amount of beryllium oxide. On the polycrystal the ratio of the relevant XPS signal intensities (Be 1s and O 1s) corresponds to sub-monolayer oxygen coverage. Even though the surface oxygen content of the single crystal was higher than in earlier experiments [2], no influence of this oxide layer on the desorption peaks was observed. Detailed description of the experimental procedure is given elsewhere [2]. The shown spectra from single crystalline beryllium are recorded after implantation with an improved beam spot. The implanted fluence is verified to be homogeneous over an

area of 4×4 mm^2 with a steep descent to zero fluence outside this area. The desorption flux is calibrated via the charge collected during implantation with the underlying assumption (verified in [1]) that the retention at small fluences amounts to 80% of the irradiated fluence. Furthermore, the desorption experiments on the single crystal are performed by using a newly commissioned controller (SCHLICHTING HS170) for obtaining the linear temperature ramp. The heating rate is 42 K/min in all shown TPD spectra.

Scanning electron microscopy (SEM) and electron back-scatter diffraction (EBSD) measurements are performed in a field emission gun scanning electron microscope (Helios FEI). To obtain the SEM micrographs the secondary electron signal is recorded with an in-lens detector. EBSD patterns are recorded using a Norlys II detector (HKL/Oxford Instruments).

The simulations of TPD spectra are performed with the rate equation-based code TMAP7 [3]. The implantation depth profiles used in the simulations are calculated with the Monte Carlo code SDTrim.SP [4, 5]. The computational details for the studies within the framework of density functional theory are given in [6]. In these calculations the stationary state structures are optimized using a quasi-Newton generalized algorithm. All energy calculations are carried out using the Quantum-Espresso package [7]. Activation energies are calculated using the Nudged Elastic Band (NEB) algorithm [8, 9, 10] implemented in the Quantum-Espresso package.

3. Results

3.1. Threshold fluence for the low-temperature release peak

Figure 1 shows the temperature dependent release of D from a Be polycrystal previously implanted with 1 keV D ions up to different fluences. The desorption peak around 460 K

features a threshold behaviour with respect to the irradiated fluence. The peak is absent up to a fluence of 1.17×10^{21} m^{-2} and appears at a fluence of 1.31×10^{21} m^{-2} and higher. An analogous parameter study was performed by Reinelt et al. [1] on single crystalline Be cut parallel to the $(1\,1\,\bar{2}\,0)$ plane. There, the broad high temperature release region was ascribed to detrapping of D from ion-induced defects (point defects or small clusters) and the low temperature region around 470 K to the release from regions which have become structurally modified due to implantation above a threshold fluence of 1.22×10^{21} m^{-2}. The structural modifications are supposed to take place in regions of the implantation zone which become supersaturated with D in the course of the irradiation. The same interpretation applies to the spectra recorded from polycrystalline Be shown here.

The very similar desorption temperatures suggest that the release from both the polycrystalline and the Be $(1\,1\,\bar{2}\,0)$ occurs from traps of the same nature. The threshold fluence for the release in the low temperature region of the spectrum apparently is not influenced by the presence (or absence) of grain boundaries in the poly- and single crystalline samples. This analogous behaviour can be explained by assuming the supersaturation to take place in the volume of crystallites of the polycrystal. In the inner of crystallites conditions equivalent to the ones present in the single crystal are assumed at the onset of irradiation. It has been argued before that when the kinetic energy of the implanted D falls below the displacement threshold, the impurity atom is trapped after very short diffusion on an atomic length scale. The new results support this assumption: If D diffusion to grain boundaries of the polycrystal is inhibited, similar D concentrations are reached in the volume of crystallites of the polycrystal as in the single crystal at similar fluences.

Furthermore, insight into the possible role of grain boundaries as traps for D in Be can be gained from the shown spectra. If grain boundaries act as additional traps

with an activation barrier higher than the one for the ion induced traps, we expect a corresponding additional release peak at a higher temperature. The fact that such an additional release is not observed leads to the conclusion that if D is trapped at grain boundaries, the release from there happens at lower temperatures than the release from the ion-induced traps. D atoms possibly released from grain boundaries at lower annealing temperatures could be retrapped in ion-induced defects on their way towards the surface. In this case the release from grain boundaries would remain unobserved.

The fraction of D detrapping from polycrystalline Be in this low temperature region seems to be higher than for the measurements on the single crystal. This shall, however, not be discussed here since the surface area which was irradiated with a fluence above the threshold is not well known in these experiments. A quantitative analysis of the fractions desorbing in each temperature region will be performed in the future, facilitated by the improved well-defined implantation spot.

3.2. Dependence of release temperatures on implantation energy

In a previous publication we discussed the shift of the maximum release temperature observed in TPD spectra from polycrystalline Be after implantation with D at 1, 2 and 3 keV per atom up to fluences of 2×10^{21} m^{-2} [11]. As can be seen in figure 1, at these fluences the low temperature release region around 460 K is well established. Furthermore, the high temperature release region features at least two energetically different release peaks. The nature of these is discussed in [11] and a possible explanation for the shift is given there.

In this work in order to address the retention and release mechanisms leading to the broad desorption region at temperatures around 700–800 K, we record the desorption from a single crystal after implantation up to fluences of 7.8×10^{20} and 7.5×10^{20} m^{-2} with 1 and 2 keV energy per atom, respectively (spectra not shown).

The low temperature release peak is absent in these spectra as the fluence is below the threshold for supersaturation. By choosing this fluence we eliminate a possible influence of D desorbing at lower temperatures on the release at higher temperatures. In these measurements we find a shift in the maximum release temperature of approx. 40 K. This shift is somewhat smaller (although in the same range) as observed in the experiments on polycrystalline beryllium.

In order to further simplify the initial microscopic configuration at the onset of a desorption experiment, as well as to reduce the number of processes involved during annealing, we further reduce the implantation fluence. The intent is to prepare a parameter region for the defect and hydrogen densities in which only the detrapping and retrapping from and into one single kind of trap with a single activation energy for detrapping controls the observed desorption flux. Figure 2 shows TPD spectra recorded from single crystalline Be$(1\,1\,\bar{2}\,0)$ after implantation of D with energies of 1 and 3 keV per atom up to a fluence of 2.7×10^{19} m^{-2}. At these small fluences the TPD spectra feature a single peak at a temperature around 750 K, i.e. in the lower range of the high temperature region. The shift in the desorption temperature between the two spectra is 24 K.

Assuming only one kind of trap to be responsible for the retention at these low fluences, it is possible to simulate these TPD spectra with one single activation energy. To reproduce the spectra in simulations with TMAP7 we use an activation energy for detrapping of 1.9 eV. Upon implantation, irradiation induced point defects and D atoms will stabilize each other, forming immobile traps near the position where the D atoms are stopped [2]. If this trapping mechanism is assumed to be the only one active for implantation up to very low fluences then the initial trap depth profile corresponds to the implantation depth profile as calculated with SDTrim.SP.

The maxima of the implantation profiles are at 26 nm (peak atomic concentration: 0.0065) and at 86 nm (peak atomic concentration: 0.0035), for implantations with 1 keV and 3 keV, respectively. Only isotropic diffusion can be treated in TMAP7. The experimental values for the parameters of the isotropic diffusion coefficient $D = D_0 \exp(-E_D/RT)$ were used, i.e. $D_0 = 6.9\times10^{-9}$ m^2 s^{-1} for the prefactor and $E_D = 0.29$ eV for the diffusion activation energy [12]. Using those input parameters, the calculations lead to a shift between the two simulated desorption peaks of 30 K (figure 2) which is in fairly good agreement with the experiment.

Although the TMAP7 simulations provide some insight into the parameters affecting the observed release temperatures, we are not able to reproduce all features of the measured spectra. A main reason for this seems to be that TMAP7 cannot take into account any evolution of the structure and therefore of the trap mobility, and possibly also the trap nature (and therefore of the activation energy for detrapping) in the course of an annealing experiment. Surface morphology investigations hint at structural changes induced in the material in the course of implantation and annealing. In the next paragraph we present our recent results from such investigations.

3.3. DFT results and orientation dependent morphology

The NEB calculated barrier for diffusion of a self-interstitial atom in the undisturbed Be lattice is 0.12 eV in the [110] direction, i.e. parallel to the basal planes, and 0.97 eV along the [001] direction, i.e. orthogonal to the basal planes. These low values, in good agreement with the experimental value of 0.15 eV, are due to the small crystal cohesion: the Be-Be bonds are so weak that the crystal can adapt itself to the self-interstitial displacement.

The activation barriers for hydrogen diffusion are 0.41 and 0.74 eV for parallel and orthogonal diffusion (with respect to the basal plane), respectively. A hydrogen atom

can find its path through the crystal at an energy cost comprised between these two limits. This result also is in good agreement with the reported experimental values of 0.29 eV for deuterium diffusion in high-purity Be [13] or 0.32 eV from laser desorption studies of D implanted Be [14].

These anisotropic results for the various diffusion mechanisms are reflected in the surface morphology of the sample developing during repeated bombardment with deuterium (up to fluences above the threshold fluence for structural modifications) followed by annealing up to temperatures well above half the melting point of Be. The left part of figure 3 shows an SEM image of the implanted region of the polycrystalline sample after several experimental runs. The maximum fluence before each TPD run is around or below 2×10^{20} m^{-2}, while the cumulative fluence (summed over all experimental runs) amounts up to approx. 5×10^{22} m^{-2}. Clearly grains with different damage in form of craters of roughly 1 μm in diameter are identified. E.g., the marked region to the upper left (full line) exhibits much less defects than the region to the right (broken line). The fact that the dark features visible in the SEM image are holes, not protrusions, is confirmed by atomic force microscopy measurements (not shown here). Outside of the implantation zone no such craters where observed. In the EBSD image of the same region, shown in the right part of figure 3, the orientation of the grains with respect to the basal plane is colour coded. White areas exhibit a (0 0 0 1) orientation parallel to the surface, dark red areas an orientation of the (0 0 0 1) plane perpendicular to the surface. A comparison of the two images leads to the conclusion that the damage induced in each grain strongly depends on the orientation of its surface with respect to the basal plane. This correlation points to a considerable influence of the calculated anisotropy in activation energies for diffusion of interstitials on the structural evolution of the material. Such surface orientation-

dependent morphology changes might go along with surface orientation-dependent trap evolution during implantation and/or annealing. This will be further investigated by comparing these results with measurements on single crystals with different surface orientations (e.g. $(0\,0\,0\,1)$, $(1\,0\,\bar{1}\,0)$, $(1\,1\,\bar{2}\,0)$).

4. Summary

TPD spectra have been recorded from polycrystalline Be and single crystalline Be with a $(1\,1\,\bar{2}\,0)$ surface orientation after implantation to various fluences. The threshold fluence for the appearance of the low-temperature release peak is the same for the two different specimens. Also, the influence of implantation energy on the release temperatures is similar. A shift in the desorption maximum from the single crystalline sample after implantation up to very low fluences with varying implantation energy is reproduced in TMAP7 simulations by assuming the initial deuterium and trap depth profile for each implantation energy to be equivalent to the implantation depth profiles as calculated by SDTrim.SP. It is concluded that the shift after implantation with different energies at very small fluences is a consequence of the different mean distances of the deuterium atoms to the surface. New DFT results on anisotropic diffusion of interstitials in bulk Be are presented and allow an interpretation of the differences in surface morphology evolution during implantation and release cycles on differently oriented grains.

References

[1] M. Reinelt and Ch Linsmeier. Temperature programmed desorption of 1kev deuterium implanted into clean beryllium. *Physica Scripta*, T128:111–114, 2007.

[2] M. Reinelt, A. Allouche, M. Oberkofler, and Ch. Linsmeier. Retention mechanisms and binding states of deuterium implanted into beryllium. *New Journal of Physics*, 11(4):043023, 2009.

[3] J.A. Ambrosek and G.R. Longhurst. Verification and validation of tmap7. Technical Report INEEL/EXT-04-01657, Idaho Falls, September 2004.

[4] W. Eckstein. *Computer Simulation of Ion-Solid Interactions*, volume 10. Springer Series in Materials Science, 1991.

[5] A. Mutzke W. Eckstein, R. Dohmen and R. Schneider. Sdtrimsp: A monte carlo code for calculating collision phenomena in randomized targets. Report IPP 12/3, 2007.

[6] A. Allouche and Ch. Linsmeier. Quantum study of tungsten interaction with beryllium (0001). *Journal of Physics: Conference Series*, 117:012002–, 2008.

[7] website http://www.quantum-espresso.org.

[8] Weinan E, Weiqing Ren, and Eric Vanden-Eijnden. String method for the study of rare events. *Phys. Rev. B*, 66(5):052301, August 2002.

[9] Y. Kanai, A. Tilocca, A. Selloni, and R. Car. First-principles string molecular dynamics: An efficient approach for finding chemical reaction pathways. *J. Chem. Phys.*, 121(8):3359–3367, August 2004.

[10] G. Henkelman and H. Jonsson. A dimer method for finding saddle points on high dimensional potential surfaces using only first derivatives. *J. Chem. Phys.*, 111(15):7010–7022, October 1999.

[11] M. Oberkofler, M. Reinelt, S. Lindig, and Ch. Linsmeier. Structure-dependent deuterium release from ion implanted beryllium: Comparison between be(1 1 -2 0) and be(poly). *Nuclear Instruments and Methods in Physics Research Section B: Beam Interactions with Materials and Atoms*, 267(4):718–722, February 2009.

[12] E. Abramov, M. P. Riehm, D. A. Thompson, and W. W. Smeltzer. Deuterium permeation and diffusion in high-purity beryllium. *J. Nucl. Mater.*, 175(1-2):90–95, December 1990.

[13] A. Kh. Klepikov, I. L. Tazhibaeva, O. G. Romanenko, Y. V. Chikhray, V. P. Shestakov, and E. A. Kenzhin. Influence of loading method on hydrogen retention and release from beryllium. *Journal of Nuclear Materials*, 258-263(Part 1):798–802, October 1998.

[14] D. Kéroack and B. Terreault. Laser desorption study of deuterium implanted in beryllium. *Journal*

*Towards a detailed understanding of the mechanisms of hydrogen retention in beryllium*13

of Nuclear Materials, 212-215(Part 2):1443–1447, September 1994.

Figure captions

Figure 1

Signal at 4 amu/q as a function of the sample surface temperature, recorded during annealing of a polycrystalline Be sample previously implanted at room temperature with 1 keV deuterium ions up to various fluences. The linear heating rate is 42 K/min.

Figure 2

Calibrated deuterium desorption spectra after implantation at room temperature in single crystalline Be $(1\,1\,\bar{2}\,0)$ sample up to a fluence of $2.7{\times}19$ m^{-2} at two different ion energies. The smooth curves are the respective simulations with TMAP7.

Figure 3

SEM (left) and EBSD (right) images of the surface in the implantation zone of polycrystalline Be after numerous implantation/desorption cycles. In the EBDS image, white pixels correspond to a $(0\,0\,0\,1)$-oriented surface. The angle of deviation from this orientation is colour-coded in red. Not indexed pixels are in black. Two grains are highlighted in each image for comparison: The grain in the upper-left part is oriented orthogonal to the $(0\,0\,0\,1)$ plane (full line), the grain to the right has $(0\,0\,0\,1)$ orientation (broken line).

Figure 1.

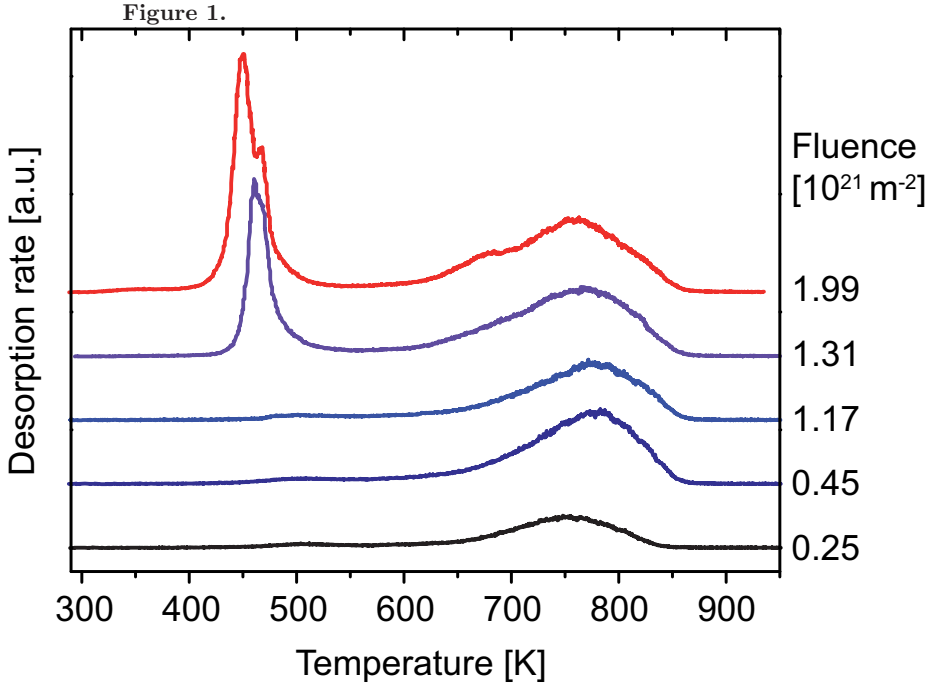

Figure 2.

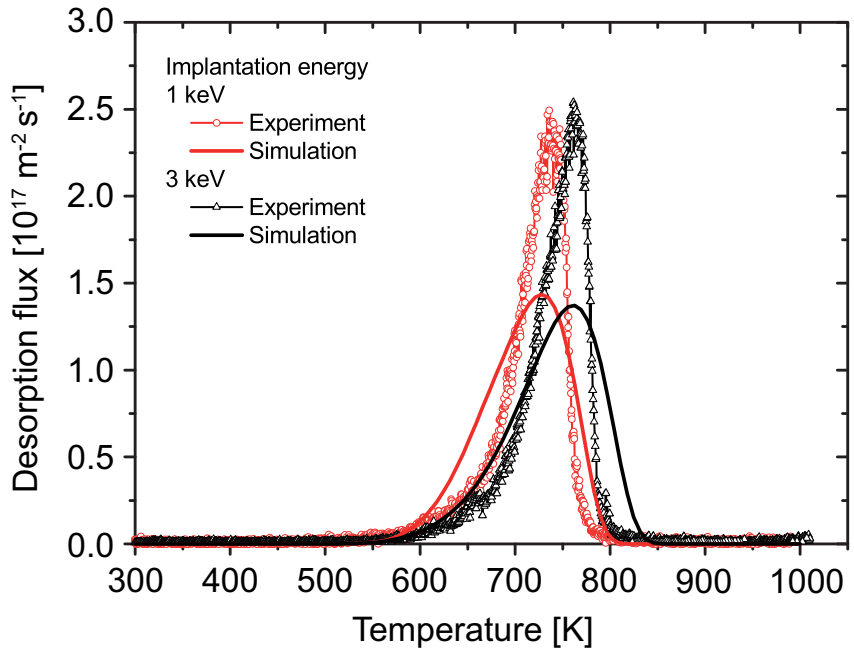

Figure 3.

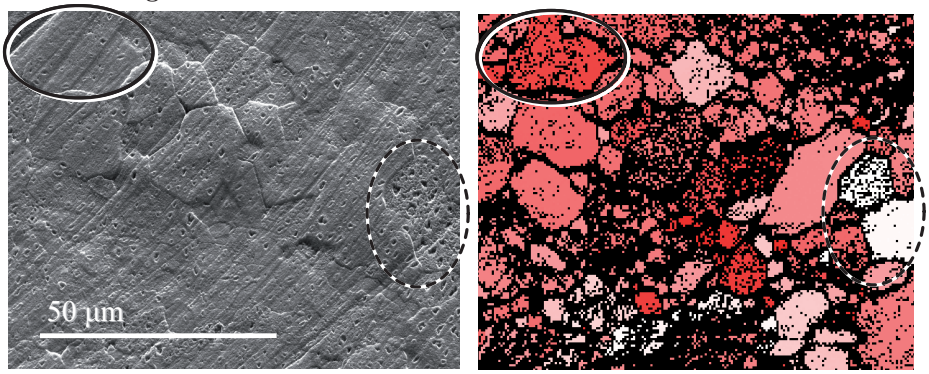

Nuclear Instruments and Methods in Physics Research B 267 (2009) 718–722

Contents lists available at ScienceDirect

Nuclear Instruments and Methods in Physics Research B

journal homepage: www.elsevier.com/locate/nimb

Structure-dependent deuterium release from ion implanted beryllium: Comparison between Be(11$\bar{2}$0) and Be(poly)

M. Oberkofler, M. Reinelt, S. Lindig, Ch. Linsmeier *

Max-Planck-Institut für Plasmaphysik, EURATOM Association, Boltzmannstr. 2, 85748 Garching b. München, Germany

ARTICLE INFO

Article history:
Received 7 November 2008
Received in revised form 14 November 2008
Available online 27 November 2008

PACS:
61.80.Jh
61.72.Hh
68.43.Vx
68.55.Ln
82.20.Pm

Keywords:
Beryllium
Deuterium inventory
Implantation
Trapping
Defects
Thermal desorption

ABSTRACT

The temperature-driven release of deuterium implanted as keV ions into metallic beryllium is measured by temperature-programmed desorption (TPD). TPD spectra from single and polycrystalline Be implanted with 1 keV ions are compared. The high-temperature desorption stage ($T > 700$ K) is attributed to the release of deuterium trapped at several types of energetically different ion-induced defects. A release peak around 850 K is recorded in the single crystal, while in the polycrystal all deuterium desorbs below this temperature. An increase in the maximum release temperature is observed after implantation of the polycrystal with higher ion energies (2 and 3 keV). We propose an interpretation of the experimental results based on two types of traps, with depth distributions adapted to the implantation energy. Preliminary TMAP7 calculations qualitatively reproduce the shifts in the maximum desorption temperature, observed in the polycrystal at different implantation energies. The difference between the single and the polycrystal is explained by a higher density of surviving defects in the single crystal. Diffusion of mobile defects to grain boundaries and subsequent annihilation is proposed as the dominant mechanism for differences in deuterium desorption from Be(11$\bar{2}$0) and Be(poly).

1. Introduction

Metallic beryllium is planned as an inner vacuum vessel cladding for the international fusion experiment ITER, covering an area of 690 m^2 of the plasma-facing first wall [1]. During operation with a deuterium or a deuterium/tritium plasma, the first wall materials are subjected to elevated heat loads and energetic particle fluxes of hydrogen isotopes (D and T at energies from eV to keV and fluences greater than 1×10^{17} cm^{-2}). This leads to implantation and accumulation of hydrogen in the material far from thermodynamic equilibrium. To control fuel balancing and minimize the retention of radioactive T in the plasma vessel, the temperature-dependent recycling process is of great concern. The surface temperature of the Be is expected to range from room temperature up to the melting point (during off-normal events such as disruptions). The planned bake-out temperature for ITER is 530 K. The thermal release ('outgassing') of implanted hydrogen depends strongly on the binding energy of hydrogen to the metal matrix. High activation energies for desorption (above 1 eV) can be associated to the release of hydrogen from traps with high binding energies. Detrapping into mobile states occurs at correspondingly high temperatures. Investigations of the thermal release of implanted deuterium from single crystalline and chemically pure Be show a number of binding states with a fluence-dependent occupation. Release peaks are recorded at temperatures of 440, 470, 770 and 840 K [2]. Diffusion of D through unirradiated Be is fast at room temperature with an activation barrier of only 0.29 eV [3], as it is common for most metals. Therefore, the peaks in the TPD spectra can be attributed to release of D from irradiation-induced traps. The experimentally investigated systems consist purely of Be and D. Thus, the nature of the traps only depends on the structure of the Be–D material (with possible formation of beryllium hydride [4,5]). To gain further information about the nature of the different sites, we compare the thermal release of D implanted into single and polycrystalline Be substrates at different ion energies. In this way we vary the depth distribution of the defects generated in the collision cascades, as well as the available sinks (surface and grain boundaries) for mobile defects. We present experimental results and discuss an interpretation based on TMAP7 modelling.

* Corresponding author. Tel.: +49 89 32992285; fax: +49 89 3299962285.
E-mail address: linsmeier@ipp.mpg.de (Ch. Linsmeier).

0168-583X/$ - see front matter © 2009 Published by Elsevier B.V.
doi:10.1016/j.nimb.2008.11.015

2. Experimental procedures

The results from temperature-programmed desorption (TPD) studies on single crystals (sc) have been published before [2,4]. Experimental details for the polycrystal (pc) measurements are identical. In brief, a polished sc disc (diameter of 14 mm, thickness less than 1 mm and $(11\bar{2}0)$ surface orientation) and a polished pc sample ($10.5 \times 10.5 \times 0.5$ mm^3) are sputter-cleaned by 3 keV Ar^+ bombardment and subsequently annealed up to 1000 K to gain sub-monolayer oxygen coverage as the only remaining impurity visible by in situ performed X-ray photoelectron spectroscopy (XPS). These well established surfaces are then implanted with deuterium ions at room temperature. The sc Be sample is implanted with a 3 keV monoenergetic and mass-selected D_3^+ beam up to a fluence of 2×10^{17} D cm^{-2}. Instantaneous dissociation of the molecule at the surface can be assumed, resulting in an effective energy per D atom of 1 keV. The pc sample is implanted in the same way with a 3 keV or 6 keV D_3^+ or a 6 keV D_2^+ beam to obtain energies per atom of 1, 2 and 3 keV, respectively.

The samples are then heated to 1000 K with a linear temperature ramp and the desorbing species are recorded with a quadrupole mass spectrometer (QMS) positioned in line-of-sight geometry in front of the sample. The TPD spectra shown in this work are recorded at 4 amu/e, corresponding to D_2. Other deuterium-containing species are either not observed during TPD (D, HDO, D_2O) or show a signal intensity more than one order of magnitude lower than molecular deuterium (as in the case of HD). Hence, it can be assumed that deuterium desorbs as D_2 molecules.

The temperature ramps for the TPD experiments are 1 K/s for the sc and 0.73 K/s for the pc. From measurements with a ramping rate of 1.34 K/s on the pc sample (not shown) it can be inferred that the difference in the temperature ramps does not account for the main effects in the comparison of pc and sc observed in this work. In order to exclude an influence of the sample history, the desorption of 1 keV implanted deuterium from the pc was carried out at the beginning of the experimental campaign and again repeated at the end of it. The spectra perfectly match, therefore no influence of the experimental series on the conditions of the pc sample and hence the resulting TPD spectra is observed.

After the last annealing cycle the samples were investigated ex situ by electron backscattered diffraction (EBSD) mapping. These measurements were performed in a field emission gun scanning electron microscope (Helios FEI) using a Norlys II detector (HKL/Oxford Instruments). For the single crystal, the recorded Kikuchi patterns confirmed the Be$(11\bar{2}0)$ orientation of the surface. The averaged relative deviation from this orientation is significantly lower than 0.5° over the examined area of 128×128 μm^2. The results for the polycrystal are shown in Fig. 1. The colours correspond to different orientations of crystallites. Three reference orientations are assigned the primary colours[1] red, green and blue; other orientations result in secondary colours. A band contrast picture is overlaid to the colour map. In such a band contrast picture the contrast of the Kikuchi patterns is assigned a grayscale, yielding darker pixels where the patterns are more diffuse. Grain boundaries are thus highlighted. Grains up to 20 μm in diameter with various orientations are visible.

3. TPD measurements

Fig. 2 shows TPD spectra from single and polycrystalline beryllium, respectively, implanted with 1 keV D. Two distinct temperature regions of deuterium release can be identified. For the single crystal the broad high-temperature release stage has been assigned to deuterium detrapping from defect sites, created upon irradiation [2,4]. This is in agreement with the finding that irradiation-induced defects in beryllium strongly influence the lattice site occupation of implanted impurities [6], especially of deuterium [7]. We call these traps 'ion induced', as they originate from the collision cascade initiated by ions hitting the metal surface. The more sharply peaked release stage around 450 K appears only at higher fluences. The threshold fluence for the occurrence of this low-temperature release stage lies around 1×10^{17} cm^{-2} for both the single and the polycrystal. It has been argued [2,4] that deuterium released in this temperature regime originates from supersaturated (Be/D > 0.4), and thereby structurally modified Be–D areas. The TPD spectrum from the polycrystal, just as the one from the single crystal, also shows the two mentioned distict release stages.

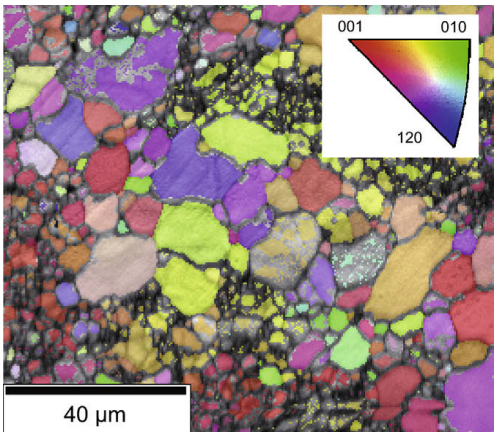

Fig. 1. EBSD map of the surface of the polycrystalline sample. The orientation of crystallites is colour-coded. Grain boundaries appear dark due to overlay of a band contrast picture.

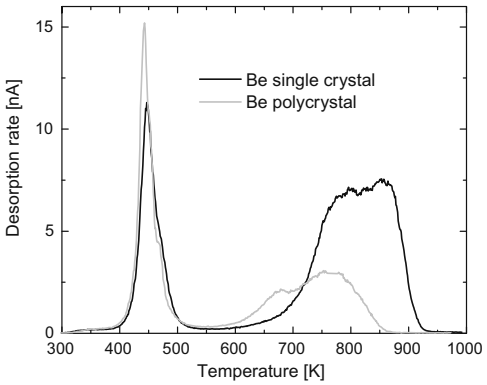

Fig. 2. TPD spectra from D-implanted single and polycrystalline Be. The samples were implanted at room temperature up to a fluence of 2×10^{17} D cm^{-2}. The energy per implanted atom was 1 keV. The signal of the quadrupole mass spectrometer at $m/e = 4$ (corresponding to D_2) is plotted against the temperature of the sample surface. The temperature ramping rates are 0.73 K/s and 1 K/s, respectively. This difference in ramps does, however, not account for the observed shift of the highest recorded release temperature.

[1] (For interpretation of the references to the color in this figure legend, the reader is referred to the web version of this article.)

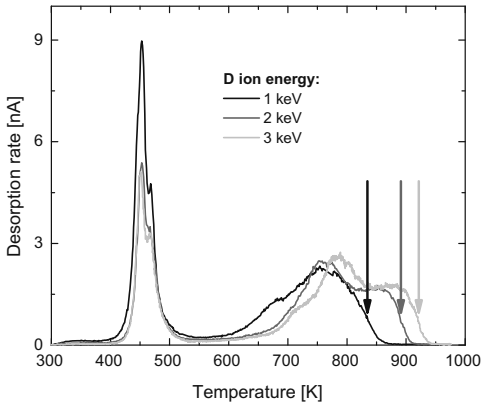

Fig. 3. TPD spectra from polycrystalline Be implanted with D at various ion energies. The samples were implanted at room temperature up to a fluence of 2×10^{17} D cm^{-2}. The signal of the quadrupole mass spectrometer at $m/e = 4$ (corresponding to D_2) is plotted against the temperature of the sample surface. The temperature ramping rate is 0.73 K/s.

Still, some differences can be noticed. First, the ratio between the integrated areas of the high and low-temperature regimes differs between the single and the polycrystal. This difference indicates that in the polycrystal a bigger fraction of the retained deuterium is released from supersaturated areas. Yet this might not be an effect of the difference in crystallinity, as it could be caused by differences in the implantation beam profile. Second, the release from the ion-induced traps happens at lower temperatures in the polycrystal as compared to the single crystal. An interpretation of this shift of the high temperature edge of the spectra is presented in Section 4.

Fig. 3 shows TPD spectra from the polycrystalline sample after implantation with deuterium ions at energies of 1, 2 and 3 keV per atom. The spectra vary slightly, the most prominent difference being a shift in the high-temperature edge of the release from ion-induced traps. The shift amounts to 50 K between the implantations with 1 and 2 keV per atom, and another 25 K between the implantations with 2 and 3 keV. Assuming various trap sites in the implanted material, different peaks in the TPD spectra can be assigned to detrapping from sites with different activation energies. Thus a shift in the highest desorption temperature could be explained by a change in the nature of the traps, e.g. different sizes of clustered vacancies. However, it is also possible to explain such a shift by assuming unaltered traps (i.e. activation energies) and instead adapting the depth distribution of the traps to the respective implantation energy. In the following section we present a plausibility model taking into account energy-dependent density profiles of ion-induced traps. This model is implemented in TMAP7 [8]. This code includes treatments of temperature transport, trapping, diffusion and surface recombination. The shift with implantation energy in the maximum release temperature as calculated by TMAP7 is compared to the experimental findings.

4. Discussion of the high-temperature edge shift

Upon irradiation of beryllium with 1, 2 or 3 keV deuterium, a large number of Frenkel pairs is created in collisional cascades. Molecular dynamics simulations show that a large fraction of these Frenkel pairs has recombined by the time the cascade has cooled down (for a review see for example [9] and [10]). At maximum primary knock-on energies of 600 eV (for 1 keV D on Be) to 1800 eV (for 3 keV D on Be) the surviving defects are primarily point defects, i.e. single vacancies or self interstitials. Irradiation-induced defects have been shown to be mobile in beryllium at room temperature [11,12] and can therefore diffuse to sinks such as the surface or grain boundaries to annihilate, or face annihilation upon encountering an anti-defect. Some defects will be trapped by forming immobile impurity-defect complexes with the implanted projectile [13], preferably at the end of the collision cascade. Deuterium atoms implanted into beryllium have been shown to be trapped near the site where they are stopped [14]. Depth distributions trapped deuterium can therefore be calculated using the Monte Carlo simulation program SDTrim.SP [15,16]. This program is an extension of the TRIM code [17] to allow for material accumulation (and erosion) in the implanted sample. It is based on the binary collision approximation and considers a deuterium projectile to be stopped in the beryllium when its kinetic energy falls below a given cut-off energy (here 2 eV) due to energy losses. The resulting implantation profile for each implantation energy can roughly be approximated by a Gaussian, truncated due to the intersection with the surface. The maxima of the fitted Gaussians lie at 37 nm (1 keV), 66 nm (2 keV) and 94 nm (3 keV), their root mean square deviations being 21 nm, 30 nm and 33 nm, respectively. These profiles are used as input for the TMPA7 simulations.

Moreover, some of the point defects will form clusters (dislocation loops or fine cavities, as observed for example by Yoshida et al. [18] and Chernikov et al. [19]). These represent a second kind of trap for diffusing deuterium atoms. At fluences of 10^{17} atoms cm^{-2}, as applied in our experiments, hundreds of collision cascades will overlap spatially. Cascades produced in the debris of earlier cascades will heal parts of the clustered defects and their density will eventually saturate. In the qualitative picture drawn here, by the end of the implantation a constant density of surviving defect clusters will have evolved up to a depth that can be estimated from the range of a Frenkel defect depth profile, accessible again by a calculation with SDTrim.SP. As this depth varies with the energy of the incident deuterium, the total number of these traps also scales with the implantation energy. After implantation, and before the onset of a TPD experiment, these cluster traps may be empty or partially filled with deuterium. During a TPD experiment, however, they are assumed to be filled up by retrapping of some of the deuterium released from traps with lower activation energies, such as those in the low-temperature region of the shown spectra.

The above considerations can be summarized in the following model. We assume two kinds of ion-induced traps responsible for the high temperature release stage of the TPD spectra. The first kind arises from a deuterium atom merging with a nearby defect at the implantation site, directly after it is stopped. A second kind of traps is represented by small defect clusters. The density of these traps is assumed to be constant, up to a depth dependent on the Frenkel pair depth profile (and therefore of the energy of the implanted deuterium) and zero beyond that depth.

In a first attempt to simulate the TPD spectra of the polycrystal shown in Fig. 3, the trap profiles (both dependent on the implantation energy) are used as input to the program TMAP7. All traps are assumed to be saturated with deuterium at the onset of the high temperature release stage. The clustered defects are assigned a somewhat higher activation energy than the implantation sites. The resulting spectra clearly show a shift in the high-temperature edge as a function of implantation energy. The shift is of the right order of magnitude (50 K and 25 K) and about twice as big between the 1 keV and the 2 keV implanted spectra than between the 2 keV and the 3 keV implanted spectra. This model would also provide an explanation for the spectra recorded by Markin et al. [20], where the highest release temperature reaches up to 1000 K for beryllium implanted with deuterium at an energy per atom of 5 keV. The

absolute release temperatures in the simulations are still different from the experiment, indicating that some of the TMAP7 input parameters need further optimization. The reproduction of the temperature shift, however, demonstrates the validity of the defect distribution assumption.

It is realized and emphasized that the illustrated model is oversimplified. For example, any evolution of the microstructure during the heating of the samples is neglected. Nevertheless, the simulations show the possibility to explain the shift in the high-temperature edge of the TPD spectra by simply adapting implantation and damage profiles to the used implantation energy. No additional traps with different detrapping energies are needed in our model for the 2 keV and 3 keV implanted TPD spectra as compared to the 1 keV implanted. The identical activation energies are applicable to all three implantation energies. It is important to notice that two consequences of varying the implantation energy cause the shift. First, the larger range of the vacancy cluster traps for higher implantation energy – the trap density being held constant over this range – implies a larger total amount of such traps, available for deuterium atoms to be trapped in. Second, the fact that the trap profiles are shifted further into the bulk for higher implantation energies results in a longer path towards the surface for detrapped atoms before they can recombine and desorb. The simulations reveal that the latter effect is smaller than the first. It should be mentioned here, that, as discussed in [2], surface recombination is not considered to be a rate limiting step for the release of D implanted into Be.

Now we turn to the comparison of the polycrystal with the single crystal. We see from Fig. 2 that there is a shift in the maximum temperature at which release is observed in TPD measurements. Assuming the same nature of traps in both specimens, we try an interpretation based on the difference in crystallinity. The implantation profiles and Frenkel defect production during the collision cascades can be considered to be independent of crystallinity. However, grain boundaries have been shown to play an important role in the evolution of the initially generated defects. Several authors (among others, Hudson et al. [21], Norris [22] and Zinkle et al. [23]) have observed zones denuded of voids near grain boundaries in various irradiated materials. Singh et al. [24] calculated a decrease in void concentration with decreasing grain size in austenitic stainless steel irradiated with 1 MeV electrons. We therefore assume a reduced trap density in the irradiated pc beryllium as compared to the sc: single defects created upon irradiation might diffuse to grain boundaries of the pc where they face annihilation. Moreover, stresses originating from the misorientation at grain boundaries in the pc might attract defect clusters otherwise immobile in the sc. On the contrary, in the sc, mobile defects could survive longer and travel further until they finally form immobile compounds. These mechanisms lead to an increased defect density, and thus, to a higher number of available traps for deuterium in the sc. Deuterium might possibly even be trapped at greater depths than in the pc due to the greater distance defects can travel without annihilating at grain boundaries. Our TMAP7 calculations have shown that both an increased number of traps, as well as their distribution deeper into the bulk contribute to a shift of the highest release peak observed in TPD spectra towards higher temperatures. It is therefore possible, that the shift observed in the comparison of the TPD spectra from the single and the polycrystal in Fig. 2 is due to differences in the defect evolution depending on the absence or presence of grain boundaries.

5. Summary

The retention behaviour of deuterium implanted polycrystalline beryllium is compared to that of the single crystal. In both cases, release takes place in two stages. The sharp low-temperature peak is attributed to deuterium trapped in regions where the beryllium lattice is structurally modified due to supersaturation. It only appears above a fluence of $1 \times 10^{17}\,\mathrm{cm}^{-2}$. At higher temperatures deuterium is released from non-supersaturated regions where it is trapped in ion-induced defect sites.

For the observed shift of the high-temperature edge to lower temperatures in the case of the polycrystal as compared to the single crystal, a possible explanation is proposed. This shift could be the consequence of a reduced density of the traps with the highest activation energy. A possible mechanism leading to such a reduction is the diffusion of vacancies towards grain boundaries in the polycrystal.

In the polycrystal sample, it is observed that upon raising the implantation energy, the high-temperature edge of the TPD spectrum shifts to higher temperatures.

On the basis of a model with two kinds of traps and trap distributions which depend on the implantation energy, this feature can be qualitatively reproduced in simulations, without changing the nature (i.e. the activation energies) of the traps.

References

[1] J. Roth, E. Tsitrone, A. Loarte, Plasma-wall interaction: a complex combination of surface processes critical for thermo-nuclear fusion, J. Phys.: Conf. Ser. 100 (6) (2008) 062003.
[2] M. Reinelt, Ch. Linsmeier, Temperature programmed desorption of 1 keV deuterium implanted into clean beryllium, Phys. Scripta T 128 (2007) 111.
[3] E. Abramov, M.P. Riehm, D.A. Thompson, W.W. Smeltzer, Deuterium permeation and diffusion in high-purity beryllium, J. Nucl. Mater. 175 (1–2) (1990) 90.
[4] M. Reinelt, A. Allouche, M. Oberkofler, Ch. Linsmeier, Retention mechanisms and binding states of deuterium implanted into beryllium, New J. Phys., submitted for publication.
[5] G. De Temmerman, Insight into the codeposition of deuterium with beryllium: influence of the deposition conditions on deuterium retention and release, J. Nucl. Mater., submitted for publication.
[6] J. Hanßmann, O. Meyer, G. Linker, Influence of vacancy mobility and volume size mismatch energy on the lattice site occupation of implanted species in beryllium single crystals, Nucl. Instr. and Meth. B: Beam Interact. Mater. Atom. 122 (4) (1997) 635.
[7] R. Vianden, E.N. Kaufmann, J.W. Rodgers, Impurity lattice location in ion-implanted beryllium: measurements and systematics, Phys. Rev. B 22 (1) (1980) 63. July.
[8] J.A. Ambrosek, G.R. Longhurst, Technical Report INEEL/EXT-04-01657, Idaho Falls, September 2004.
[9] Bachu Singh, Damage production accumulation and materials performance in radiation environment, J. Comput.-Aided Mater. Des. 6 (2) (1999) 195.
[10] T. Diaz de la Rubia, N. Soneda, M.J. Caturla, E.A. Alonso, Defect production and annealing kinetics in elemental metals and semiconductors, J. Nucl. Mater. 251 (1997) 13.
[11] J.C. Nicoitd, J. Delaplace, J. Hillairet, D. Schumacher, Y. Adda, Etude des defauts crees dans le beryllium par irradiation a basse temperature, J. Nucl. Mater. 27 (2) (1968) 147.
[12] J. Delaplace, J.C. Nicoud, D. Schumacher, G. Vogl, Low-temperature neutron radiation damage and recovery in beryllium, Phys. Status Solidi 29 (1968) 819.
[13] W.R. Wampler, Trapping of deuterium in beryllium, J. Nucl. Mater. 196–198 (1992) 981.
[14] V.Kh. Alimov, V.N. Chernikov, A.P. Zakharov, Depth distribution of deuterium atoms and molecules in beryllium implanted with d ions, J. Nucl. Mater. 241–243 (1997) 1047.
[15] W. Eckstein, Computer Simulation of Ion–Solid Interactions Volume 10 of Springer Series in Materials Science, Springer, Berlin, 1991.
[16] W. Eckstein, R. Dohmen, A. Mutzke, R. Schneider, Report IPP 12/3, IPP, 2007.
[17] J.P. Biersack, L.G. Haggmark, A monte carlo computer program for the transport of energetic ions in amorphous targets, Nucl. Instr. and Meth. 174 (1–2) (1980) 257.
[18] N. Yoshida, S. Mizusawa, R. Sakamoto, T. Muroga, Radiation damage and deuterium trapping in deuterium ion injected beryllium, J. Nucl. Mater. 233–237 (Part 2) (1996) 874.
[19] V.N. Chernikov, V.Kh. Alimov, A.N. Markin, A.P. Zakharov, Gas swelling and related phenomena in beryllium implanted with deuterium ions, J. Nucl. Mater. 228 (1) (1996) 47.
[20] Andrey V. Markin, Vladimir N. Chernikov, Sergey Yu. Rybakov, Andrey P. Zakharov, Thermal desorption of deuterium implanted into beryllium, J. Nucl. Mater. 233–237 (Part 2) (1996) 865.
[21] J.A. Hudson, D.J. Mazey, R.S. Nelson, Void formation in nickel during 20 MeV C^{++} irradiation at 525 °C, J. Nucl. Mater. 41 (3) (1971) 241.

[22] D.I.R. Norris, The use of the high voltage electron microscope to simulate fast neutron-induced void swelling in metals, J. Nucl. Mater. 40 (1) (1971) 66.
[23] S.J. Zinkle, K. Farrell, Void swelling and defect cluster formation in reactor-irradiated copper, J. Nucl. Mater. 168 (3) (1989) 262.
[24] B.N. Singh, A.J.E. Foreman, Calculated grain size-dependent vacancy supersaturation and its effect on void formation, Philos. Mag. 29 (4) (1974) 847.

Journal of Nuclear Materials 390–391 (2009) 568–571

Contents lists available at ScienceDirect

Journal of Nuclear Materials

journal homepage: www.elsevier.com/locate/jnucmat

Ion implanted deuterium retention and release from clean and oxidized beryllium

M. Reinelt, Ch. Linsmeier *

Max-Planck-Institut für Plasmaphysik, EURATOM Association, Boltzmannstrasse 2, 85748 Garching b. München, Germany

ARTICLE INFO

PACS:
52.40.Hf
68.43.Vx
61.80.Jh
66.30.je
79.20.Rf

ABSTRACT

The deuterium retention and thermal recycling behavior of clean and oxide-covered beryllium is investigated by a combination of temperature programmed desorption, X-ray photoelectron spectroscopy and other methods. From the experimental results, the retention mechanisms are deduced and activation energies for the release processes are obtained from modeling. Implanted deuterium at 1 keV kinetic energy is trapped locally in ion-induced defects with a release temperature above 700 K. At a local deuterium concentration greater than 0.35 D/Be, the beryllium bulk is supersaturated. This leads to the formation of additional binding states with a release temperature of 450 K and formation of BeD_2, which decomposes at 570 K. The amount of deuteride formed is influenced by the target temperature during implantation. The Be surface and BeO surface layers have no rate-limiting influence on the thermal release process.

1. Introduction

The main wall of ITER's plasma vessel is planned to be covered with beryllium as a plasma-facing material [1]. During operation, intense fluxes of hydrogen isotopes are implanted and retained in the plasma-facing material. Sputtering and high temperature lead to a release of retained hydrogen into the plasma or transport inside the component. Especially from a safety point of view, a detailed knowledge on the hydrogen recycling behavior in Be is needed to predict the machine's total tritium inventory. For this, characteristic values describing the recycling like diffusivity, solubility and detrapping energies are needed. Usually, these values are gained from modeling experimental data. Although a large number of studies have been dedicated to this issue in the past, the details of the mechanisms governing the retention are still unclear. This can be seen primarily in a large scatter of the characteristic values. Even the reported retained areal densities vary up to two orders of magnitude [2]. Three possible reasons should be considered.

1.1. Sample crystallinity

The defect density or grain size distribution of the Be samples under investigation can have a significant influence on the trap site density or diffusivity of hydrogen. As quantitative results require modeling, uncertainties in the sample structure can lead to misinterpretation of experimental data. The experiments described in this work are performed with single crystalline Be. Defects created in the course of the experiments are annealed by temperature treatment assuring the structural integrity of the sample.

1.2. Chemical composition of the Be surface

Be reacts very quickly with oxygen or water forming a closed BeO surface layer even under good vacuum conditions [3]. Because the release process of implanted hydrogen has to occur via the substrate surface, the chemical condition of the surface can have a significant influence. It can introduce an additional energy barrier for coverages even below one monolayer (ML). This is especially important for permeation or, as in this work, for desorption experiments, where a superposition of all (release-) rate-limiting processes is measured. Up to now, no experimental data for hydrogen retention implanted into oxygen-free Be (i.e. Be without a BeO-covered surface) was reported.

1.3. Retention mechanisms

In order to extract quantitative results from experiments involving the temperature-driven transport of hydrogen inside and out of beryllium metal by modeling, the rate-limiting steps have to be identified. Evaluation of experimental data of the temperature-dependent release of hydrogen requires the assignment of observed peaks to rate-limiting mechanisms such as detrapping, diffusion or recombination ($2D \rightarrow D_2$).

2. Experimental

The Be sample under investigation is a single crystalline disk with a diameter of 14 mm and a thickness of 0.5 mm. The single

* Corresponding author.
E-mail addresses: matthias.reinelt@ipp.mpg.de (M. Reinelt), linsmeier@ipp.mpg.de (Ch. Linsmeier).

0022-3115/$ - see front matter © 2009 Elsevier B.V. All rights reserved.
doi:10.1016/j.jnucmat.2009.01.103

crystallinity is confirmed by Laue diffractography and shows an orientation of the mirror-polished surface of $(11\bar{2}0)$ with a miss-cut of less than 1°. The surface of the Be sample is cleaned under UHV conditions by cycles of bombardment with a scanned 3 keV Ar^+ ion beam 45° to the surface at room temperature and subsequent annealing up to 1000 K. The chemical surface composition is monitored by X-ray photoelectron spectroscopy (XPS) and low energy ion scattering spectroscopy (LEIS). LEIS is performed with a 480 eV He ion beam at a scattering angle of 135°. A minimal residual oxide coverage of 0.2 ML on the sample surface as the only contamination could be achieved and maintained for 12 h at a base pressure of 2×10^{-11} mbar. The cleaned sample is bombarded by a mass-separated, monoenergetic 3 keV D_3^+ ion beam under perpendicular angle of incident. This corresponds to a kinetic energy of 1 keV per deuterium atom. TPD experiments are performed by heating the sample at a linear ramp with electron impact from the back. The sample temperature is measured by a thermocouple spot-welded to the sample surface at a position where it is not irradiated by the ion beams. The effusing gas flux is detected by a differentially pumped quadrupole mass spectrometer (QMS) in the line-of-sight geometry. The amount of surface oxide does not change during implantation and TPD experiments. The deuterium flux is calibrated by measuring the retained deuterium areal density after implantation in situ by nuclear reaction analysis (NRA). The reaction $D(^3He,p)^4He$ with 800 keV $^3He^+$ ions from a 3 MV tandem accelerator is used [4]. After TPD experiments up to 1000 K, no residual D can be detected in the sample both by NRA, and by successive TPD runs. Desorption of oxygen-containing molecules such as HDO and D_2O is not observed. The flux of HD formed during desorption is two orders of magnitude lower than the effusing D_2 flux and is therefore ignored in the following. All experiments, except scanning electron microscopy (SEM) shown in Fig. 1(b) and (c) are performed in situ in an experimental setup described elsewhere in detail [5].

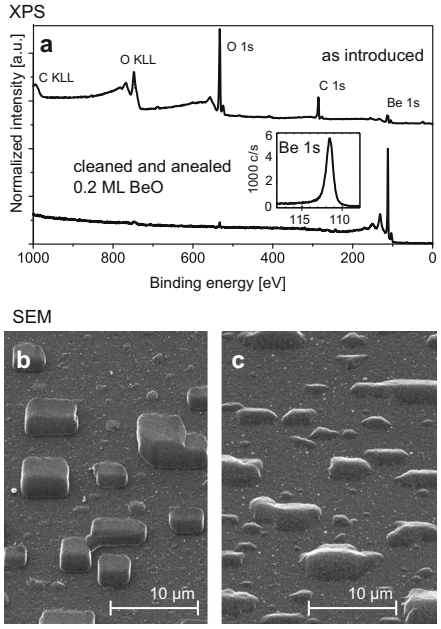

Fig. 1. In situ XPS spectra of the Be sample, as introduced and after cleaning and annealing. The insert shows the Be 1s binding energy region of the clean, annealed and D-implanted Be surface (a). Ex situ SEM image of the annealed Be sample (b). Ex situ SEM image of the cyclically sputtered (Ar ions) and annealed sample surface (c).

3. Results

3.1. Substrate characterization

Fig. 1(a) shows normalized XPS spectra of the Be sample surface as introduced (upper spectrum) and after many cleaning and annealing cycles (lower spectrum). The residual oxygen contamination of the cleaned sample surface corresponds to an equivalent of 0.2 monolayers BeO. The insert shows the photoelectron peak of the Be 1s binding energy region of the cleaned sample. The binding energy is 111.8 eV of the clean metal. Although the Be sample is originally a single crystal, its near-surface region is severely damaged by the Ar bombardment of the cleaning process. Flash heating the sample up to 1000 K can anneal these defects and recrystallize the sample surface. By this procedure, implanted Ar is also removed from the near-surface region. TPD spectra after temperature treatment up to 1000 K show no desorbing gaseous species from the sample (Ar or hydrogen in any form). The effect of the recrystallization is directly visible by SEM imaging (Fig. 1(b)) on the sample surface, which was heated cyclically from RT to 1000 K under UHV conditions (without ion bombardment). Micrometer-sized facetted Be crystallites are formed on the initially flat sample surface. The uniform alignment of the facetted structures across the whole sample additionally indicates the single crystallinity of the bulk material. The 30° tilted facets have an orientation of $(10\bar{1}0)$. The sides (left and right of each crystallite in Fig. 1(b)) are oriented (0001). Driving force of this mass transport is the minimization of the surface energy. Electron backscattering diffraction (EBSD) shows that the crystallographic structure and orientation of the crystallites and original sample surface are identical, which means that the crystal develops a facetted surface under these conditions without loosing the bulk single crystallinity. Cycles of ion bombardment and annealing lead to a roughening of the surface by recrystallization and simultaneous erosion of the recrystallized structures (Fig. 1(c)) This roughness increases the (flat) projected surface area of the irradiated surface region up to a factor of 1.2, as measured by atomic force microscopy (AFM). LEIS measurements after increasing annealing temperatures show, that Be from the bulk segregates through thin BeO surface layers, forming a (metallic) Be-terminated surface above a temperature of 900 K. The original BeO surface layer is thus covered by at least one ML of metallic Be. This surface is stable at lower temperatures, until oxidized by residual gas. Such a mechanism is in agreement with results from ^{18}O marker experiments performed by Roth et al. [6]. On the basis of those observations, the conclusions can be drawn that annealing of the cleaned Be sample leads to a recrystallization of the surface. The chemical surface composition and sample crystallinity are therefore well defined for thermal release experiments of implanted deuterium.

3.2. Deuterium retention mechanism at fluences below 1.0×10^{21} m^{-2}

A TPD spectrum ($m/q = 4$, D_2) of implanted D reveals several release steps (Fig. 2(a) and (b)). Below fluences of 1.0×10^{21} m^{-2}, D is trapped in two types of bulk sites, related to defects created by the implantation cascade with release temperatures of 780 and 850 K (denoted as release states 1 and 2 in Fig. 2). Fig. 2(a) shows a TPD spectrum after bombarding the sample at RT with a fluence of 6.5×10^{20} m^{-2}. A lateral scan of the sample with NRA reveals

a D distribution similar to the intensity profile of the implantation beam. The release from the ion-induced trap sites involves detrapping to a solute (mobile) state, diffusion through the bulk lattice, recombination to molecular D_2 at the surface and finally desorption into vacuum. All steps can influence the observed peak temperature, although detrapping is the rate-limiting step. To include all these processes into a model, TMAP7 is used [7]. This code includes diffusive and surface processes. For the model, the diffusivity from Abramov et al. [8] is used. It is given as $6.7 \times 10^{-9}\exp(-0.29\ \mathrm{eV}/kT)\ [\mathrm{m^2\ s^{-1}}]$, which corresponds to a diffusion length of micrometers (per second) already at room temperature. The solubility is taken from Shapovalov and Dukel'ski [9] and the surface recombination barrier for D on pure Be as 0.87 eV from Lossev and Küppers [10]. The D concentration profile is taken from a static SDTrim.SP calculation, a Monte Carlo code that can model kinematic processes of ion implantation into a solid material [11]. A manual adjustment of the calculated desorption flux to the TPD experiments yields activation energies of 1.88 eV and 2.05 eV for the detrapping from the ion-induced sites (1) and (2).

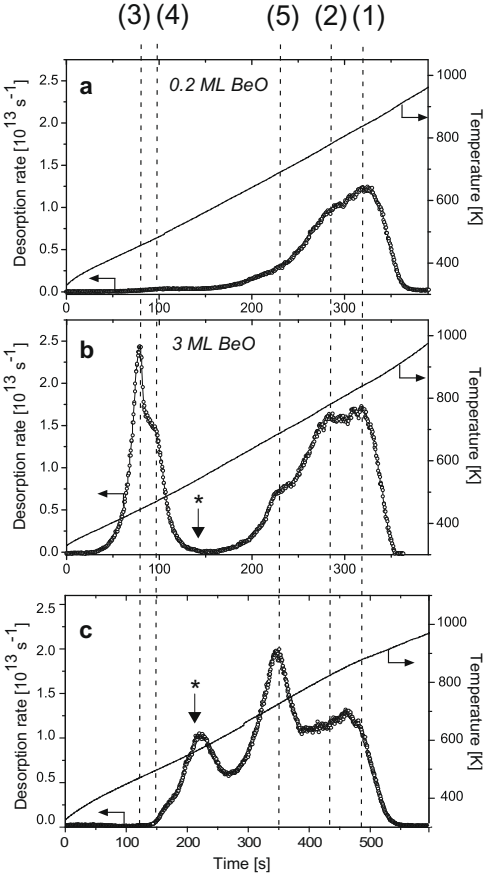

Fig. 2. TPD spectra (m/q = 4, D_2) after implantation of different deuterium fluences: (a) $6.5 \times 10^{20}\ \mathrm{m^{-2}}$ and (b) $1.8 \times 10^{21}\ \mathrm{m^{-2}}$. The asterisk indicates the decomposition temperature of BeD_2. The spectrum (c) is recorded after implantation at a substrate temperature of 530 K.

3.3. Deuterium retention mechanism at higher fluences

Above a fluence of $1.0 \times 10^{21}\ \mathrm{m^{-2}}$ (Fig. 2(b)), additional binding states with release temperatures of 440 K and 480 K are created due to a D accumulation in the bulk. These binding states show a sharp threshold behavior and appear only above an irradiation fluence of $1.0 \times 10^{21}\ \mathrm{m^{-2}}$. In Fig. 2(b) these states are denoted as (3) and (4). The local supersaturation enforces nanoscaled structural modifications in the Be lattice. Release from these states is energetically different from detrapping from states (1) and (2), resulting in a lower peak temperature. Simulations of a first order release reaction [12] with a frequency factor of $10^{13}\ \mathrm{s^{-1}}$ by a rate equation yield activation barriers of 1.25 eV and 1.33 eV for states (3) and (4), respectively. Above the threshold fluence for the appearance of release peaks (3) and (4), SEM and AFM images show protrusions on the D-irradiated sample surface with a size of about 100 nm. Cracking of the surface is not observed. Depth profiles from SDTrim.SP calculations, which allow an accumulation of D in the Be bulk show, that D reaches a local concentration of 0.26 at.% in a depth of 40 nm at an irradiation fluence of $1.0{\cdot}10^{21}\ \mathrm{m^{-2}}$. This corresponds to a maximum Be/D ratio of 0.35, which is in the range of values for the maximum D concentration given in previous studies [2]. The sample retention reaches steady-state at irradiation fluences above $2.0 \times 10^{21}\ \mathrm{m^{-2}}$, where 30% of the retained amount is trapped in the supersaturated states. The maximum retained areal density is $2.0 \times 10^{21}\ \mathrm{m^{-2}}$. This is in good agreement to earlier investigations by Haasz and Davis [13].

3.4. Influence of a thin BeO surface layer

To investigate the influence of a BeO-covered surface, the sample is thoroughly cleaned, annealed and implanted with deuterium. XPS shows an oxygen contamination equivalent to 0.2 monolayers BeO on the surface after the implantation. The sample is stored overnight under UHV conditions to allow the growth of a closed BeO surface layer of 3 monolayer thickness from the residual gas (reactive species: water). A successive TPD experiment is directly compared with an experiment with the same cleaning procedure and irradiation fluence, but TPD immediately after the implantation. For the first experiment, all desorption occurs via the BeO-covered surface, while for the latter, the surface is fully Be-terminated, as discussed above. Any difference in the spectra can hence be directly related to the influence of the oxide coverage. The segregation of metallic Be to cover the BeO surface layer during the temperature ramp of the TPD experiment occurs above 900 K, where D is already released from the sample. Assuming that D_2 (as a molecule) does not diffuse through the Be lattice, the last step for the release processes of any retained D is recombination to D_2 on the sample surface. If the chemical surface composition is changed from Be to BeO, the energetic conditions change for this step. The recombination process itself can be limited, for example, by the surface diffusivity for adsorbed D atoms and its activation barrier. Changing the chemical composition of the outermost ML would consequently result in a shift of the measured temperature of any release peak limited by such a recombination process. The experiments show, however, that none of the peaks (1)–(4) is influenced by the chemical composition of the surface, hence none of the peaks is recombination-limited. Instead, increased amounts of D are released from state (5) in the TPD experiment with oxide-covered beryllium. Since the amount released in peak (5) is influenced by the areal density of BeO, it is concluded that D is bound to BeO on the surface, presumably as a hydroxide.

3.5. Implantation at elevated temperature

Elevated substrate temperatures during implantation can alter the retention mechanism. To investigate the influence of elevated substrate temperatures on the retention mechanisms, the sample is kept at 530 K during implantation. The substrate temperature is, hence, above the release temperatures of states (3) and (4). As a consequence, these states cannot be occupied at fluences above 1×10^{21} m^{-2}. The chemical surface composition is monitored by XPS and does not change during the experiments. A successive TPD experiment (Fig. 2(c)) starting at room temperature shows a peak at 570 K, which is a dominant release peak in this case (its position is indicated by an asterisk in Fig. 2). Also, increased amounts are released at 680 K, the decomposition temperature of the surface hydroxide. The ion-induced trap sites (1) and (2) are not affected in position and occupation by the increased substrate temperature. A possible explanation for the formation of surface hydroxide despite the constant clean sample surface in the irradiation zone, is an increased diffusivity of D during the implantation. This allows D to reach (uncleaned) outer sample regions or the sample back to form the hydroxide. Although states (3) and (4) are not occupied at implantation temperatures above 500 K, the retention of the sample is not reduced proportionally. Deuterium, which is bound in the supersaturated areas at room temperature implantation, is instead bound to a state with a release temperature of 570 K. This can be explained by the increased substrate temperature, which allows a phase formation of beryllium deuteride BeD_2 upon local supersaturation of the bulk during the implantation. It is reported that BeH_2 (and accordingly BeD_2, under the assumption of similar isotope behavior) decomposes above 570 K [14], which is the dominant release temperature observed in this experiment. A chemical shift of the Be 1s binding energy due to the hydride formation [15] is not observed by XPS, which indicates that the hydride is formed below the information depth of XPS. This is consistent with the formation of the hydride in the supersaturation zone in a depth of 40 nm, which is well beyond the XPS information depth of about 20 nm.

4. Summary

The investigation of deuterium retention by a combination of TPD and surface analytical techniques reveals qualitatively the retention mechanisms and release processes of deuterium implanted into beryllium. This allows modeling of the experimental results and thus obtaining quantitative values such as activation energies. At low fluences, deuterium is trapped in ion-induced defects. The release from these binding states has activation barriers of 1.88 eV and 2.05 eV, respectively. Above a fluence of 1×10^{21} m^{-2}, which corresponds to a local concentration of 0.35 D/Be in a depth of 40 nm, local supersaturation of the bulk leads to the creation of binding states with a lower release temperature similar to surface desorption. The activation energies for the release from these states are 1.25 eV and 1.33 eV, respectively for a first order release-reaction mechanism. With increasing implantation temperature, implanted D above the saturation concentration forms increasing amounts of BeD_2, which decomposes again above 570 K. The sample surface (metallic Be or BeO) has no rate-limiting influence on the thermal release, because all deuterium implanted with an energy of 1 keV is retained and released from binding states in the bulk.

References

[1] G. Federici, R. Anderl, J.N. Brooks, R. Causey, J.P. Coad, D. Cowgill, R. Doerner, A.A. Haasz, G. Longhurst, S. Luckhardt, D. Mueller, A. Peacock, M. Pick, C.H. Skinner, W. Wampler, K. Wilson, C. Wong, C. Wu, D. Youchison, Fus. Eng. Des. 39&40 (1998) 445.
[2] R.A. Anderl, R.A. Causey, J.W. Davis, R.P. Doerner, G. Federici, A.A. Haasz, G.R. Longhurst, W.R. Wampler, K.L. Wilson, J. Nucl. Mater. 273 (1999) 1.
[3] S. Zalkind, M. Polak, N. Shamir, Surf. Sci. 385 (1997) 318.
[4] V.K. Alimov, M. Mayer, J. Roth, Nucl. Instrum. and Meth. B 234 (2005) 169.
[5] Ch. Linsmeier, P. Goldstrass, K.U. Klages, Phys. Scr. 2001 (2001) 28.
[6] J. Roth, W.R. Wampler, W. Jacob, J. Nucl. Mater. 250 (1997) 23.
[7] J.A. Ambrosek, G.R. Longhurst, INEEL/EXT-04-01657, 2004.
[8] E. Abramov, M.P. Riehm, D.A. Thompson, W.W. Smeltzer, J. Nucl. Mater. 175 (1990) 90.
[9] V.I. Shapovalov, Y.M. Dukel'ski, Russ. Met. 5 (1984) 210.
[10] V. Lossev, J. Küppers, Surf. Sci. 284 (1993) 175.
[11] W. Eckstein, Computer Simulation of Ion–Solid Interactions, Springer-Verlag, Berlin, 1991.
[12] A.M. de Jong, J.W. Niemantsverdriet, Surf. Sci. 233 (1990) 355.
[13] A.A. Haasz, J.W. Davis, J. Nucl. Mater. 241–243 (1997) 1076.
[14] P.E. Barry, J.S. Bowers, R.G. Garza, P.C. Souers, J.S. Cantrell, T. Beiter, J. Nucl. Mater. 173 (1990) 142.
[15] G. De Temmerman, M.J. Baldwin, R.P. Doerner, D. Nishijima, R. Seraydarian, K. Schmid, J. Nucl. Mater. 390–391 (2009) 564.

New Journal of Physics
The open–access journal for physics

Retention mechanisms and binding states of deuterium implanted into beryllium

M Reinelt[1], **A Allouche**[2], **M Oberkofler**[1] **and Ch Linsmeier**[1,3]

[1] Max-Planck-Institut für Plasmaphysik, EURATOM Association, Boltzmannstrasse 2, 85748 Garching b. München, Germany
[2] Physique des Interactions Ioniques et Moléculaires, CNRS and Université de Provence, Campus Scientifique de Saint Jérôme, Service 242, 13397 Marseille Cedex 20, France
E-mail: linsmeier@ipp.mpg.de

New Journal of Physics **11** (2009) 043023 (19pp)
Received 31 December 2008
Published 17 April 2009
Online at http://www.njp.org/
doi:10.1088/1367-2630/11/4/043023

Abstract. The retention of 1 keV D^+ ions implanted into clean and oxidized single crystalline Be at room and elevated temperatures is investigated by a combination of *in situ* analytical techniques including temperature programmed desorption (TPD), nuclear reaction analysis, low-energy ion spectroscopy (LEIS) and x-ray photoelectron spectroscopy. For the first time, the whole temperature regime for deuterium release and the influence of thin oxide films on the release processes are clarified. The cleaned and annealed Be sample has residual oxygen concentration equivalent to 0.2 monolayer (ML) BeO in the near-surface region as the only contamination. LEIS shows that Be from the volume covers thin BeO surface layers above an annealing temperature of 1000 K by segregation, forming a pure Be-terminated surface, which is stable at lower temperatures until again oxidized by residual gas. No deuterium is retained in the sample above 950 K. By analyzing TPD spectra, active retention mechanisms and six energetically different binding states are identified. Activation energies (E_A) for the release of D from binding states in Be are obtained by modelling the experimental data. Two ion-induced trap sites with release temperatures between 770 and 840 K ($E_A = 1.88$ and 2.05 eV, respectively) and two trap sites (release between 440 and 470 K) due to supersaturation of the bulk above the steady state fluence of 2×10^{17} cm^{-2} are identified. None of the release steps shows a surface recombination limit. A thin BeO surface layer introduces an

[3] Author to whom any correspondence should be addressed.

additional binding state with a release temperature of 680 K. Implantation at elevated temperatures (up to 530 K) changes the retention mechanism above the saturation limit and populates a binding state with a release temperature of 570 K.

Contents

1. Introduction

Currently, the material of choice for the plasma facing first wall of ITER's main chamber is beryllium (Be). Fuels for a fusion reactor are the heavy hydrogen isotopes deuterium (D) and tritium (T). Escaping energetic hydrogen isotopes from the plasma are implanted into the first wall materials. As Be will cover an area of almost 700 m^2, large amounts of tritium could be retained in the material or lost by permeation into structural components of the vessel. Increased temperatures can release implanted hydrogen again [1]. Reliable predictions of this recycling behaviour of the complete first wall require a detailed understanding of the interactions of hydrogen and Be. Although much experimental data have been acquired in the past [2]–[6], the details of the processes that influence the recycling are still unclear. This can be seen particularly in the widely differing values of hydrogen isotope retention and release (diffusivity, solubility, detrapping energies, etc) [7]. Three possible reasons for the disagreeing results are considered:

Firstly, unknown chemical compositions of the samples, especially oxidized surfaces, can influence thermally activated release processes. Desorbing gaseous species have to pass the surface and, especially in the case of hydrogen, must recombine to molecules (within the expected relevant temperature range) in order to desorb. The release rate can therefore be limited by surface processes. Even a closed monolayer (ML) impurity coverage can thereby introduce an energetic barrier to recombination. The surface of Be is quickly covered by a closed beryllium oxide (BeO) layer [8] introducing a factor of uncertainty to the analysis of experimental retention data. According to the results from Zalkind *et al* [8], BeO grows quickly initially from the gas phase in the form of islands, which leads to a closed BeO surface at a coverage of 3 ML (after exposure to only tens of Langmuirs), when the growth mechanism changes and the rate slows down. The fast growth rate at sub-ML coverages makes experiments with clean Be surfaces technically very demanding, even under good UHV conditions.

Secondly, hydrogen transport in Be is influenced by the substrate structure. The crystalline configuration is especially of importance, because diffusivities through an undisturbed lattice

and along grain boundaries can differ significantly. Before hydrogen exposure, an unknown density and character of defects in the Be lattice can constitute possible trap sites for hydrogen, introducing an additional factor of uncertainty to models and simulation.

Finally, in order to obtain characteristic values describing the hydrogen recycling, the retention mechanisms must be identified to apply the appropriate modelling, from which quantitative activation barriers for hydrogen release are determined.

Due to these considerations, this work places special emphasis on the structure and the chemical composition of the substrate and the identification of the retention mechanisms in the experiments.

One way to obtain characteristic values, especially activation energies, is to model the temperature- and therefore energy-dependent release of implanted hydrogen. By heating an implanted Be sample in a controlled, preferably linear manner (temperature programmed desorption, TPD), spectra of hydrogen desorption rate versus time, and therefore temperature, can be measured. Unlike the desorption of adsorbed molecules from a surface, the release of implanted gaseous species from within a bulk material is influenced by a combination of bulk- and surface-controlled processes. By minimizing the experimental uncertainties in surface composition and sample structure, single processes can be separated and identified. We discuss the experimental results from a phenomenological point of view to derive the retention mechanisms and the processes that govern the temperature-dependent release of implanted D. The qualitative models are then cast into quantitative TMAP7 [9] modelling and rate equations in order to obtain activation energies from the experimental TPD data. Density functional theory (DFT) calculations of the structural evolution of the Be lattice and hydrogen-bonding upon increasing D concentration allow further insights. The binding energies obtained from these calculations, which directly picture the system after implantation, are related to the activation energies obtained from the modelling of the release processes. This provides the possibility of drawing conclusions about the retention mechanism itself.

2. Experimental procedure

The Be sample under investigation is a single crystalline disc of 0.4 mm thickness and 14 mm in diameter. The single crystallinity was confirmed by Laue diffractography and shows an orientation of the mirror-polished surface of $(11\bar{2}0)$ with a deviation of less than 1°. The surface of the Be sample was cleaned under UHV conditions by numerous cycles of bombardment with 3 keV Ar^+ ions under 45° incident angle at room temperature and underwent subsequent annealing up to 1000 K. The chemical surface composition is monitored by x-ray photoelectron spectroscopy (XPS) and low-energy ion spectroscopy (LEIS). The LEIS spectra are recorded with a 480 eV He ion beam under an angle of incidence of 45°. XPS measurements are performed with a non-monochromatic x-ray source with Mg Kα radiation. For both analytical techniques a hemispherical analyzer (model PHI 10-360) is used. A minimal residual oxide coverage of 0.2 ML on the annealed sample as the only contamination is achieved and maintained for several hours at a base pressure of 2×10^{-11} mbar in the vacuum chamber. The sample is thoroughly degassed, so that during annealing up to 1000 K, the pressure in the chamber does not rise above 1×10^{-9} mbar and thus no additional oxygen uptake on the sample surface is observed by XPS. Higher oxygen coverages (up to 3 ML) are obtained by storing the sample under UHV conditions for more than 24 h, allowing a BeO layer to grow

from the residual gas. The sample is prepared as described and bombarded by a mass-separated, monoenergetic 3 keV D_3^+ ion beam incident perpendicular to the surface. This molecular kinetic energy corresponds to a kinetic energy of 1 keV per D atom. The beam profile and irradiation fluence are measured using a Faraday cup with a pinhole opening of 0.5 mm diameter. As far as it is detectable by XPS, the chemical composition of the cleaned sample surface does not change with implantation. TPD experiments are performed by heating the sample with a linear rate from the back via electron impact. The surface temperature is measured by an Ni/CrNi thermocouple spot welded to the sample surface. Pre-programmed and optimized temperature ramps of 0.5, 1.0 and 4.0 K s^{-1} are used. The released gas flux is detected by a differentially pumped quadrupole mass spectrometer (modified Balzers QMG 422) in line-of-sight geometry. The desorbing deuterium flux is calibrated by measuring the retained deuterium areal density after implantation *in situ* by nuclear reaction analysis (NRA). Details are given in Reinelt and Linsmeier [10]. The reaction $D(He^3, p)^4He$ with 800 keV $^3He^+$ ions from a 3 MV tandem accelerator is used [11]. The integrated TPD flux is set equal to the measured areal density by NRA. After a TPD experiment up to 1000 K, no residual D can be detected in the sample either by NRA or by successive TPD runs. The complete experimental set-up is described elsewhere in detail [12].

3. Results and discussion

3.1. Sample surface characterization

To gain information on the evolution of the surface composition during the temperature treatments, LEIS spectra are recorded at different substrate temperatures to show the composition of the first ML of the sample. For this experiment, the sample surface is covered by a closed, 3 ML thick BeO layer grown from the residual gas during 24 h. Figure 1 shows the corresponding LEIS and XPS O 1s spectra after flash heating the sample to the denoted temperature. After switching off heating, LEIS and XPS spectra are recorded during cooling down. At temperatures below 1005 K, LEIS shows a clear peak at $0.36E/E_0$, which is assigned to oxygen. The indication of a shoulder at $0.17E/E_0$, almost covered by the background of secondary ions, is assigned to Be. The relative Be and O intensities reflect qualitatively the composition of the first ML of the sample. The corresponding O 1s binding energy region measured by XPS is shown in the right panel of figure 1. In contrast to LEIS, XPS probes not only the first atomic layer, but a surface region up to a depth of several nm. After heating the sample to temperatures above 875 K, LEIS and XPS spectra show different compositions of the sample's first layer (LEIS) and the near-surface region (XPS). The oxygen in the first ML vanishes and a clear peak at $0.17E/E_0$ indicates a Be-terminated surface. Simultaneously, the intensity of the O 1s peak in the XPS spectra decreases and exhibits a shift of 0.8 eV to higher binding energies. These observations are explained by segregation of metallic Be from the bulk through the BeO surface layer above 875 K, taking into account that BeO cannot evaporate at this temperature (melting point $T_M(\mathrm{BeO}) = 2851$ K). The metal-terminated surface is stable at lower temperatures, until again oxidized by oxygen or water from the residual gas. The decrease of the O 1s intensity in the XPS spectra is caused by the covering of the outermost oxygen, attenuating the photoelectron intensity and changing the chemical state of the surface oxygen atoms. The shift in the binding energy of the total O 1s peak can therefore be explained by assuming that the total O 1s peak is composed of two oxygen species with different O 1s binding

IOP Institute of Physics DEUTSCHE PHYSIKALISCHE GESELLSCHAFT

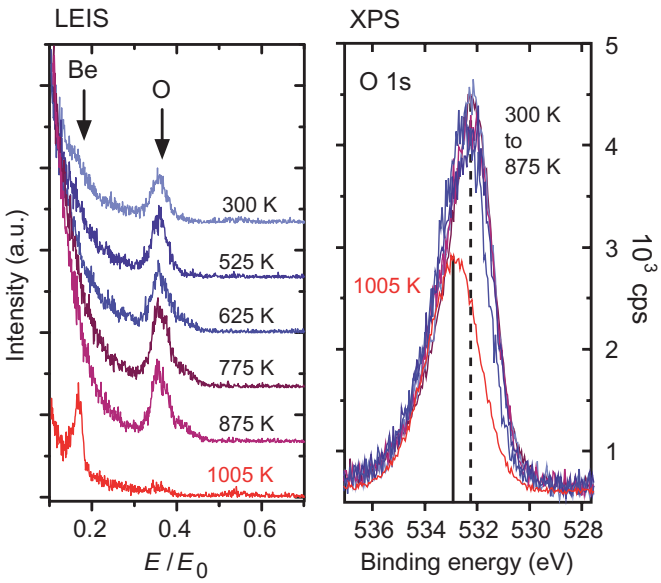

Figure 1. LEIS (left) and XPS (right) spectra of a BeO-covered (3 ML) Be sample, flash heated sequentially to the indicated temperatures. Above 875 K, Be from the bulk segregates towards the surface, burying the oxide layer. The photoelectron intensity of the O 1s core levels is attenuated by this overlayer. The shift in the binding energy indicates two oxygen-binding states (vertical lines), one associated with oxygen at the surface (dashed line).

energies. The binding energy of the species corresponding to surface oxygen is shifted towards higher binding energy when covered with beryllium. This interpretation is in agreement with the previous observation in ^{18}O marker experiments [13] investigating the growth mechanism of BeO. The conclusion of these observations is the onset of Be diffusivity at about 900 K, clearly below the bulk melting temperature of Be metal, T_M(Be) = 1551 K.

Ex situ SEM images of the single crystal surface without any treatment by ion bombardment, but several heating cycles up to 100 K, show the formation of large crystallite structures (up to 100 μm) with uniform geometry and alignment across the sample surface. The 30° tilted surfaces of the crystallite facets have a $(10\bar{1}0)$ orientation. The front facet of the crystallites shows the (0001) surface, as indicated in figure 2(a). According to the conclusions from the LEIS and XPS measurements, the crystallites are formed by a recrystallization process to lower indexed surfaces when the sample is heated up to 1000 K, driven by the reduction of surface energies for low-indexed facets. The size of the structures indicates a considerable mass transport. From these observations, we conclude that after cleaning and annealing up to 1000 K, the sample surface region is structurally and chemically well defined with a Be-terminated surface, that defects due to ion bombardment are annealed and that the sample is in a single crystalline state.

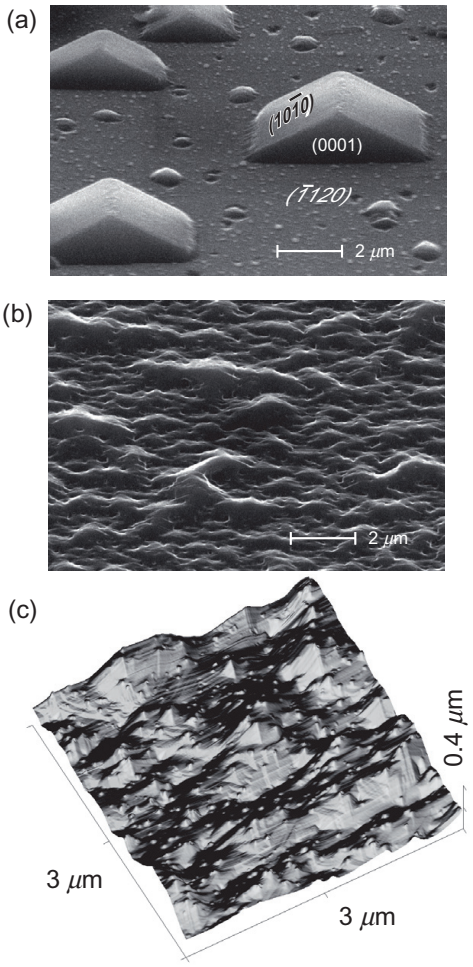

Figure 2. SEM images of the (a) cyclically annealed (1000 K) and (b) annealed, D irradiated and degassed single crystalline Be surface. Recrystallization forms large crystallites with lower surface energies. D sputtering competes against recrystallization and forms structural modifications. Their morphology can be seen as nm-sized protrusions in the AFM image in (c).

After several D^+ irradiations, TPD experiments and cleaning cycles, the sample surface exhibits a heavily modified microscopic structure, as shown in the SEM image in figure 2(b). However, a large part of the roughness is caused by the recrystallization process described above, as there is a clear transition from well-shaped crystallites to rough and eroded structures along the sample surface. This lateral transition of the surface morphology is related to the locally applied ion fluence (Ar and D bombardment). Small protrusions (up to 100 nm in

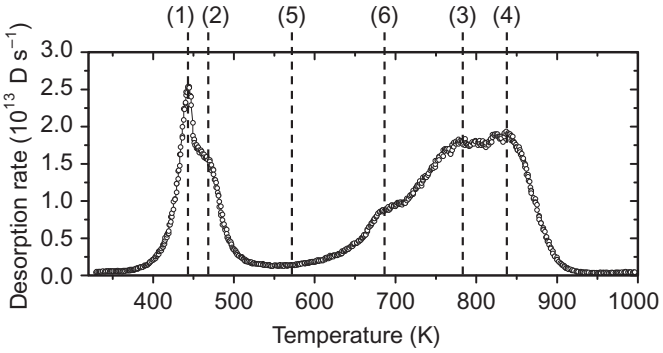

Figure 3. TPD spectrum of $m/q = 4(D_2)$, acquired with a heating rate of $1\,K\,s^{-1}$, measured after an incident D fluence of $2 \times 10^{17}\,cm^{-2}$, implanted at room temperature into an annealed single crystalline Be sample. The sequential release occurs at six different temperatures indicating six energetically different activation energies.

diameter) can be found on the D irradiated surface. Although these modifications appear as small holes in the SEM image in figure 2(b), their real morphology is revealed by atomic force microscopy (AFM). AFM imaging (figure 2(c)) in contact mode shows the topography of the microfacetted and partially recrystallized surface, which is covered with D-induced protrusions. The nature of these modifications will be discussed below.

3.2. Retention mechanisms

3.2.1. Implantation at room temperature. A typical TPD spectrum (figure 3) of $m/q = 4(D_2)$ with a heating rate of $1\,K\,s^{-1}$ after an incident D fluence of $2 \times 10^{17}\,cm^{-2}$, implanted at room temperature, shows a sequential release of D in two temperature regions. The contribution of HD to the overall deuterium release ($m/q = 3$) is two orders of magnitude lower due to the low H_2 background pressure in the chamber and shows mainly a peak at 470 K, which is omitted in the further discussions. A release of other species (D_2O, HDO, etc) was not observed. No background is subtracted from the spectra, because the rate drops quickly to the initial background pressure after complete desorption (above 950 K). The release peak at low temperatures (400–500 K) is composed of two distinct peaks: peak (1) at a temperature of 440 K and peak (2) at 470 K. Release of deuterium in this temperature region was previously reported by Markin *et al* [14]. A broad release feature at high temperature is composed of peak (3) at 770 K and peak (4) at 840 K. A shoulder at a temperature of 680 K indicates an additional peak (6). Between the main peaks (1, 2) and (3, 4), an increased background (5) hints at additional release peaks with low occupation. To model this experimental spectrum, the nature of the rate-limiting step for each of the release peaks (1)–(6) has to be identified.

A lateral analysis of the irradiation spot with NRA shows a deuterium distribution in the form of the lateral ion implantation profile. This means that D is retained locally at its implantation position and does not diffuse or dissolve in the Be bulk. TPD spectra with increasing incident fluence exhibit a sequential occupation of the binding states (figure 4) from

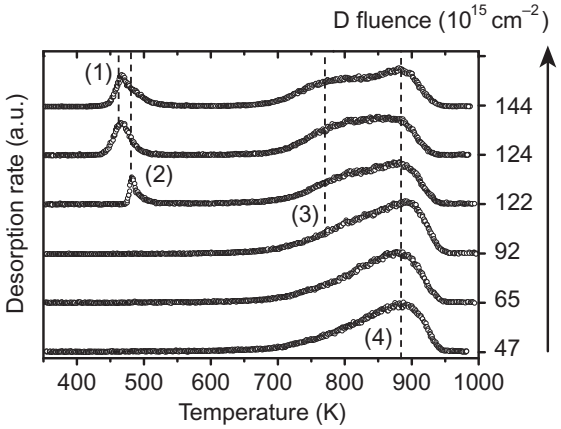

Figure 4. Series of TPD spectra with varying incident deuterium fluences implanted at room temperature. The release states are occupied sequentially from (4) to (1), indicating local saturation of the binding sites. States (1) and (2) show a threshold behaviour. The spectra are measured at random fluence steps.

higher (state 4) to lower release temperatures (state 1). This behaviour can be explained by a saturation of the available binding sites, as lower release temperatures indicate lower activation energies and therefore energetically unfavourable sites. The ratio of occupation of states (3) and (4) changes with increasing fluence. A constant retention of $78 \pm 5\%$ is measured up to an incident fluence of 1×10^{17} cm^{-2}.

Based upon the conclusions from the sample characterization, the Be lattice is in an undisturbed and single crystalline state when, at very low irradiation fluences, the first hydrogen atoms are implanted. Due to the collision cascades initiated by the impinging D ions, defects are created in the lattice which can act as trap sites with a higher binding energy for hydrogen. At the end of the atom trajectories (where most of their kinetic energy is dissipated by collisions) D is not necessarily bound to such a high-energy trap (state 3 or 4), but can diffuse freely through the bulk, until trapped by one of these two types of trap sites. This retention mechanism explains why the ratio of occupation changes with increasing fluence. This description also agrees with an apparently fast diffusivity at room temperature [15]. Gas-loaded Be samples examined by Macaulay-Newcombe *et al* [16] also show a release in two peaks at temperatures similar to those of peaks (3) and (4) observed in this work. The amount and ratio of occupation depends on the fabrication method of the Be samples. Neutron-irradiated samples show a release of hydrogen starting at a temperature of at least 775 K [17], above the temperature of peak (3). These observations support the assignment of release peaks (3) and (4) to detrapping from defects in the lattice, which are created by the collision cascade due to D implantation. These types of trap sites can also be intrinsically present in materials, depending on the structure, or can be created by neutron irradiation.

In contrast to the release from high-energy traps, the release from low-temperature states (1) and (2) shows a threshold behaviour as a function of implantation fluence. Above a fluence of 1×10^{17} cm^{-2}, initially state (2) is occupied and at higher fluences, predominantly state (1) is

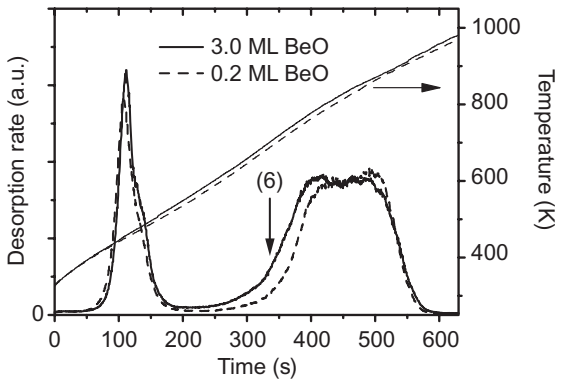

Figure 5. TPD spectra of cleaned (0.2 ML residual oxygen coverage) Be and release via a closed BeO-covered surface (3 ML). None of the release peaks is influenced by changing the surface composition and, thus, the processes are not recombination limited. State (6) shows a slightly increased occupation, indicating the decomposition of a surface hydroxide.

occupied. The spectrum series in figure 4 was recorded in random order after intermittent sample preparation to prevent the influence of sample history. Implantation of fluences lower than 1×10^{17} cm^{-2} does not lead to the formation of states (1) and (2). It is therefore concluded that these states are created due to a deuterium concentration build-up in the sample. Although the release temperatures of (1) and (2) are similar to desorption from a surface, the amount originating from these states is 60 times the saturation coverage of a Be surface with D [18], which cannot be explained by surface roughness alone. AFM measurements (figure 2(c)) indicate a surface roughness, which increases the (flat) projected surface area by not more than a factor of 1.2. Therefore, surface desorption processes from adsorbed D as rate limiting processes are excluded here. The released D_2 originates from D retained in the collision-cascade-modified Be lattice.

3.2.2. Influence of a BeO-covered surface. Under normal operation conditions in ITER, the Be first wall will be covered by various compound surface layers, one of them being BeO. As already pointed out, even one closed ML of a different material on a Be surface could represent an energy barrier for the recombination process of hydrogen, altering the release parameters. To investigate this issue, a TPD spectrum is recorded in the described manner with an incident D fluence of 2×10^{17} cm^{-2} and a BeO coverage of 0.2 ML. For a second experiment, the cleaned and annealed Be is implanted with the same incident fluence. In this experiment, however, after loading the substrate with D, a 3 ML closed BeO surface layer is allowed to grow from the residual gas in the UHV chamber. The segregation of Be bulk material to form the Be-terminated surface takes place above 900 K, which means that desorption in a TPD experiment with this sample preparation must occur via a completely BeO-covered surface. Both TPD spectra (shown in figure 5) are recorded with the same temperature ramp of 1 K s^{-1}. Any difference in the two spectra obtained by the two experiments can hence be directly related to the influence of the thin

BeO layer. If one of the observed release states (1)–(4) were rate limited by a surface process (such as recombination), a change of the surface composition from Be to BeO would shift the corresponding activation energy for this surface process (e.g. surface diffusivity). This would then alter the measured peak temperature. However, none of the binding states (1)–(4) is shifted or changed significantly. Instead, for the sample with 3 ML BeO a slightly increased amount of D is bound in state (6), indicated by an arrow in figure 5. A release of D in the form of D_2O or HDO is not observed. Three conclusions can be drawn from this experiment. Firstly, the retention is not significantly influenced by a thin 3 ML BeO coverage on the surface. This is to be expected for the discussed retention mechanisms in the Be bulk. Secondly, none of the peaks is shifted in its temperature, which would be expected if any of the states were limited by a surface process. From this it can be concluded that the activation energy for the reaction $2D \rightarrow D_2$ on Be and BeO surfaces is lower than the barriers for the release processes observed in these experiments. In TDS experiments [18], desorption of (chemisorbed) D from a clean Be surface was seen to start at 400 K, whereas from an oxidized surface, desorption was observed already at 300 K. Thirdly, release peak (6) is related to the BeO-covered surface. It stands to reason that D is bound as BeO–D at the surface and that decomposition of this surface hydroxide (to BeO and D_2) leads to release peak (6). TPD spectra of oxidized Be samples [4] show an increased release at about 700 K, the temperature region of release peak (6).

3.2.3. Retention of deuterium. A major issue in plasma–wall interaction in fusion reactors is the retention behaviour of the first wall materials. The retention behaviour is the basis for estimating fuel recycling and safety limits regarding tritium accumulation. From integration of calibrated TPD fluxes, the retention of D implanted into clean Be at room temperature can be obtained. Figure 6(a) shows the measured retained deuterium areal density (circles) as a function of deuterium irradiation fluence. Each circle represents the retained D fluence from one integrated TPD experiment, performed after preparation of a clean Be surface. At a fluence of $2 \times 10^{17}\,\mathrm{cm}^{-2}$, the deuterium retention in the sample reaches a steady state. This value is in good agreement with previous studies [7, 19]. Below the steady state fluence, the retention (retained areal density/incident fluence) is $78 \pm 5\%$, obtained from a linear fit to the data points (not shown). Figure 6(c) shows D depth profiles of a dynamic SDTrim.SP calculation (a Monte Carlo code simulating the kinematic interactions of a particle impinging on a solid target based on the binary collision approximation [20, 21]), in which accumulation of D in the Be matrix by implantation is allowed. The profiles show that the concentration build-up by implantation in the bulk is faster than the loss of D by sputtering. This leads to a local concentration of 20–25 at% deuterium in a depth of 40 nm in the Be bulk at an incident fluence of $1 \times 10^{17}\,\mathrm{cm}^{-2}$. The experimentally determined fraction of retained deuterium released from states (1) and (2) in figure 6(b) shows that this is the threshold fluence for creation of binding states (1) and (2). At this implantation fluence (and therefore local D concentration of 20–25 at% in the bulk), the Be bulk reaches local saturation, i.e. all locally available ion-induced defects are occupied. Additional implanted deuterium leads to the creation of binding states (1) and (2), which exhibit a lower release temperature. This means that the states are created due to local supersaturation of the bulk. Because the resulting structural modifications (also seen in the AFM image in figure 2(c) as small protrusions) cannot be accounted for by SDTrim.SP, the local concentration is limited to 0.26 at% deuterium in the simulation. The sample saturation is reached at higher fluences ($>2 \times 10^{17}\,\mathrm{cm}^{-2}$). The maximum local concentration of $D/Be = 0.35$ is also in good agreement with the literature values [7]. Because the concentration in the SDTrim.SP calculation

IOP Institute of Physics DEUTSCHE PHYSIKALISCHE GESELLSCHAFT

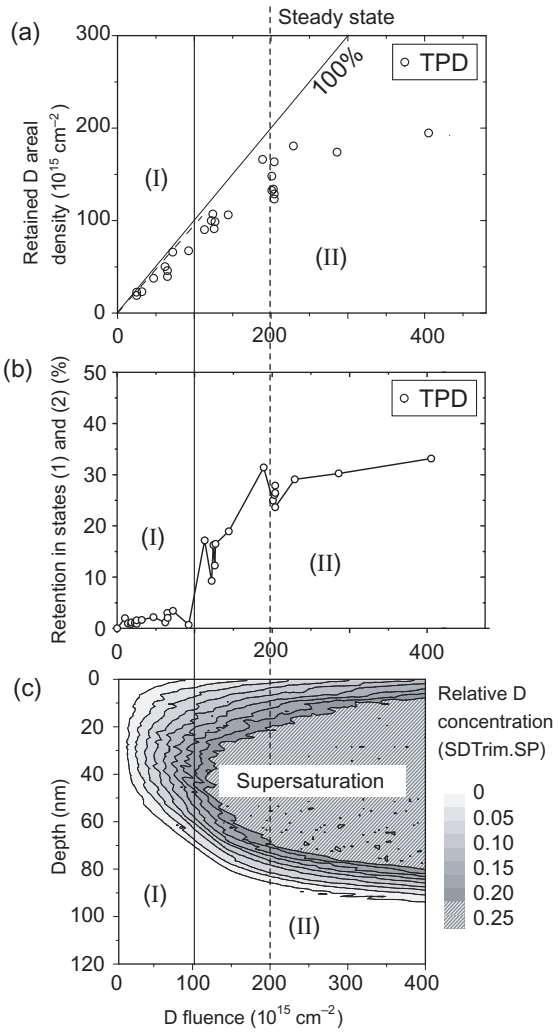

Figure 6. (a) Experimentally measured (by TPD) retained D areal density as a function of incident fluence. The fraction of deuterium retained in binding states (1) and (2) is illustrated in (b), showing a threshold behaviour. The experimental result is compared with a dynamic SDTrim.SP [21] calculation (c), which allows the accumulation of D in Be up to a local concentration of 0.26. This value is reached at a depth of 40 nm, as illustrated by the calculated concentration depth profiles (c) at an irradiation fluence just above 1×10^{17} cm^{-2}. The SDTrim.SP calculation is only valid in the fluence region denoted by (I). In region (II), states (1) and (2) appear in TPD spectra due to local supersaturation.

is clipped at this value, ignoring all additionally stopped D at this depth, the calculation is only valid below an incident fluence of 1×10^{17} cm^{-2} (denoted by region (I)). Region (II) indicates a supersaturated and structurally modified Be bulk.

According to transmission electron microscopy (TEM) imaging performed by Chernikov *et al* [22], nanostructural modifications in the form of cavities (diameter below 1 nm) appear in the Be lattice in the fluence region below 1×10^{17} cm^{-2}. It was deduced from TEM and secondary ion mass spectrometry (SIMS) experiments that D is present in the form of molecular deuterium (D_2) in closed cavities above the saturation limit. The D_2 pressure in the cavities was calculated to be in the range of GPa. However, if the assignment of the structural modifications to binding states (1) and (2) is correct, the release temperature of 470 K does not allow molecular D_2 to reabsorb as D into the Be bulk by dissociation. This step, however, is required for the diffusion to the sample surface and subsequent release into the vacuum. This step would consequently be rate-limiting requiring an activation energy above 2 eV per D atom (breaking of the D–D bond). Molecular deuterium does not chemisorb on Be [18], so the re-adsorption of D_2 from gas-filled bubbles into the Be lattice is not possible at 470 K. The release temperatures of (1) and (2) are also too low for a release mechanism involving crack formation in the bulk material due to a pressure increase. Because of the size of the structural modifications and the concentration in the supersaturated regions at fluences slightly above 2×10^{17} cm^{-2}, we conclude that the actual equilibrium concentration of molecular D_2 in the supersaturated regions must be close to zero. Deuterium is probably present in the form of a 'destabilized Be/D amorphous material', in which D is bound in a form energetically related to the adsorbed state on a surface. This explains the similarity of the release temperatures for states (1) and (2) and desorption from a Be surface. The temperature-dependent release process starts for both cases from a similar binding state of D to Be. For adsorbed deuterium on the sample surface, the release proceeds towards D_2 and desorption into vacuum. The release from the supersaturated regions (states 1 and 2) corresponds to a release of atomic deuterium into a solute (mobile) state in the Be bulk. The appearance of D_2 in SIMS and cavities in TEM [22] might be due to interference of the (destructive) analytical methods with the actual retention condition described above. Release of pressure from the system by sputtering during SIMS or thinning for TEM can, as a consequence, lead to the appearance of D_2 gas-filled cavities. Applying much higher fluences than performed in the experiments described here leads to the formation of a porous open network structure with channels of micrometre radius [23], although the maximum retention does not change significantly. High fluences relate to increasing damage and disordering of the material. The consequence is a restructuring of the (at first nanosized) supersaturated regions by aggregation to big cavities and channels, which are then filled with D_2 gas or are open to the vacuum.

3.2.4. Implantation at elevated temperatures. Implantation at elevated substrate temperatures is a common situation for plasma–wall interaction in a fusion experiment, as radiation and high particle fluxes impose a massive heat load on the material. At temperatures above 480 K, which is the expected normal operation temperature of the ITER Be first wall [1], binding states (1) and (2) cannot be occupied. Based on the previous discussion, one would expect that all implanted D is retained in binding states (3) and (4) and therefore released above 700 K. Instead, a TPD spectrum at an implantation temperature of 530 K shows that increased amounts of D are released from states (5) and (6), as shown in figure 7. This spectrum is directly compared with an experiment with implantation of the same deuterium

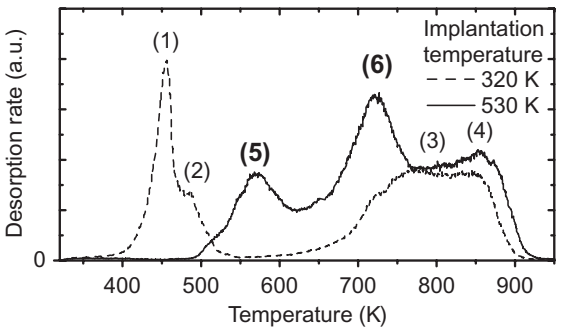

Figure 7. TPD spectra of D implanted into Be at temperatures of 320 and 530 K. Retention in the ion-induced trap sites (3) and (4) is not affected. The low-temperature binding states (1) and (2) are not occupied in the 530 K implantation experiment. Instead, increased amounts of D are retained in states (5) and (6).

fluence (2×10^{17} cm^{-2}) at 320 K. The condition of the substrates with respect to structure and chemical composition is identical for both experiments. The retention in states (3) and (4) seems to be unaffected, which is to be expected, if these peaks are governed by release from trap sites in the bulk. From this comparison, it can be concluded that the retention mechanism for an implantation fluence above the bulk saturation changes with an increase in implantation temperature. Binding state (5) is only noticeable as an increased background in room temperature implantation experiments. A hint about the nature of binding state (5) can be found in Barry *et al* [24] where the dissociation of beryllium hydride was investigated. Several investigations report a decomposition temperature of beryllium hydride, BeH_2, from 500 to 600 K, the peak temperature of state (5) [24]–[26]. Although no direct experimental data for BeD_2 are available, it can be assumed that the decomposition temperatures of BeH_2 and BeD_2 are similar. An elevated substrate temperature during implantation can allow a phase transition above the fluence threshold for the appearance of binding states (1) and (2) from a supersaturated Be lattice to BeD_2. However, this can only occur within a narrow temperature range, as the deuteride starts to decompose above 500 K. This explains why the occupation of state (5) is temperature dependent. Also during the run of a TPD experiment (after RT implantation), the elevated temperatures allow only small amounts of BeD_2 to be formed, as the majority of D from the supersaturated states, binding states (1) and (2), is already released at the formation temperature. During implantation at elevated substrate temperatures, most of the locally retained fluence above bulk saturation is retained as BeD_2. In this case, the hydride phase is formed during implantation. This also explains why in many experiments reported in [7], retention is rather constant up to an implantation temperature of 700 K, when finally occupation of states (5) and (6) is no longer possible. A persistent background at a temperature above 500 K is also observed in TDS experiments of adsorbed D atoms on a clean Be surface [18]. In [18], this was attributed to absorption of D in subsurface sites. In light of the present conclusions, this background is explained by a phase transformation of adsorbed D to BeD_2 during the desorption experiment, followed by subsequent decomposition of BeD_2 and release of D_2.

Increased amounts of deuterium are also released from state (6), assigned in the discussion above to release from an oxidized Be surface. Although the surface composition in the

irradiation spot does not show an increased BeO coverage, as measured by XPS, a higher diffusivity of D might allow D to reach uncleaned (BeO-covered) sample regions and form hydroxides, which can explain the increased amounts of D bound in state (6).

3.3. Modelling

3.3.1. Modelling of deuterium release. As a consequence of the qualitative assignment of the release peaks observed by TPD to retention mechanisms and binding states of D in Be, the spectra can be modelled using hydrogen transport and trapping codes. TMAP7 [9, 27] includes treatment of temperature transport, diffusion, surface recombination and trapping and is thus applicable for modelling the release from the ion-induced defects in release peaks (3) and (4). The code numerically solves the diffusion equation and applies flux equilibria as boundary conditions. The diffusivity is included as

$$\mathrm{D}(T) = 6.7 \times 10^{-9}\ \exp\left(\frac{-0.29\,\mathrm{eV}}{kT}\right) \tag{1}$$

from permeation experiments by Abramov *et al* [15]. The recombination on the clean surface follows the values given in [18] with an activation energy of desorption of 0.87 eV. Two types of trap sites in the bulk are used in the model, corresponding to release peaks (3) and (4). The trap concentration profiles are determined by the implantation collision cascades and therefore taken from implantation profiles calculated by static SDTrim.SP. For the TMAP7 simulation, these profiles are approximated by Gaussian-shaped distributions due to insignificant deviations in the calculation. All trap sites are filled with D at the beginning of the temperature ramp. The number of traps and therefore the overall retained amount of deuterium is taken from the experiment. The temperature is varied linearly according to the respective experiment. Desorption occurs via recombination into a vacuum volume with a constant partial pressure of 10^{-10} mbar (re-adsorption is negligible). The flux from the sample surfaces (front and back) is assumed to correspond to the TPD spectrum. The calculation shows that the flux contribution from the back of the sample is 5 orders of magnitude lower and thus negligible. A manual adjustment of the simulated flux to the TPD experiment by varying the activation energy for detrapping in the model yields activation energies of 1.88 eV for the release from trap site (3) and 2.05 eV for site (4). The model shows good agreement for different temperature ramps (0.5–4 K s^{-1}) and different incident fluences below 1×10^{17} cm^{-2}. Results of the TMAP7 simulation are shown in figure 8(a), together with the experimental data for D^+ implanted into clean Be at room temperature.

For the release peaks (1) and (2), TMAP7 cannot be used because dynamic changes of the substrate (i.e. structural modifications by supersaturation as discussed above) are not implemented in the code. For the release from this region of the TPD spectrum (350–550 K), a simple model is applied, which is based on rate equations [28] in the form of

$$R(T, N) = -\frac{\partial N}{\partial T}\frac{\partial T}{\partial t} = N^r \nu\ \exp\left(-\frac{E_\mathrm{A}}{kT}\right). \tag{2}$$

Several assumptions must be considered. First, the release rate R is determined by one rate-limiting step. Furthermore, this step must be temperature dependent and described by equation (2), where $\nu \approx 10^{13}\,\mathrm{s}^{-1}$ is a frequency factor, r the reaction order ($r = 1$ for this case) and E_A the activation energy of the release process. N is the deuterium amount in the

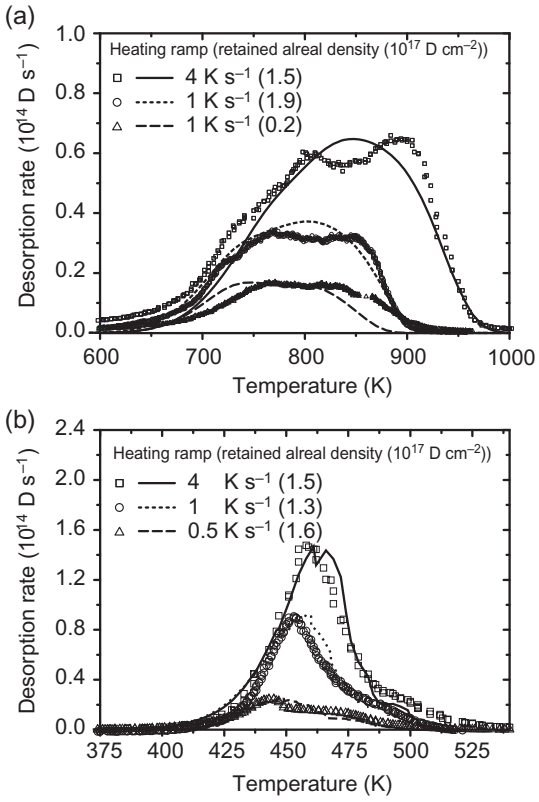

Figure 8. Experimental and simulated TPD spectra for D^+ implantation into clean Be at room temperature. (a) Comparison of simulated D release rates (TMAP7 model) from the ion-induced trap sites with experimental TPD spectra measured with varying D implantation fluence and heating rates. The differences in the peak temperatures between experiment and simulation are due to deviations of the temperature ramps. (b) Measured release rates from supersaturated states are compared with calculations based on a simple rate equation model at different heating rates. The experimental heating rates are included in these calculations. The symbols represent experiments and the lines TMAP7 simulations. The measured total retained D areal densities for each experiment are given in brackets.

sample. The first assumption is arguable, because the peak temperature is in a region where diffusion, although quite fast, might have an influence on the measured desorption rate by superposition of the release processes from states (1) and (2). The measured temperature ramp of the TPD experiment is considered in the calculation of the release rate, allowing more accurate comparisons but introducing noise to the simulation. A manual adjustment of the release rates

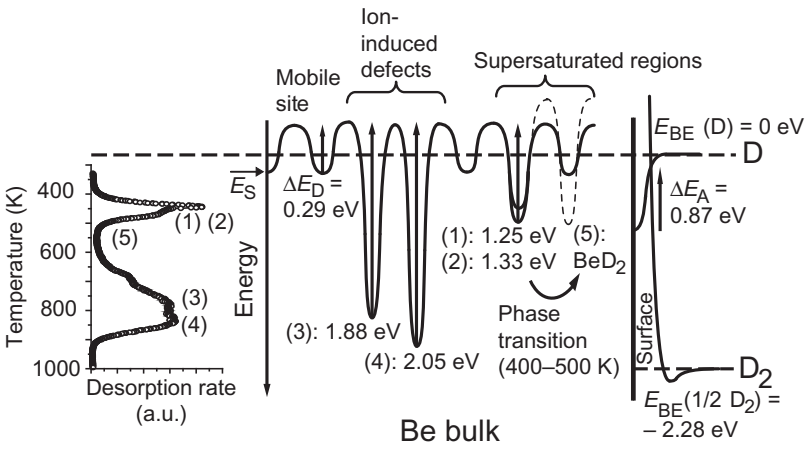

Figure 9. Schematic energy diagram (not to scale) illustrates the activation energies obtained from TPD experiments and calculations. Reference energy is free atomic D (= 0 eV). On the left side, a TPD spectrum shows the temperature dependence of the release from the binding states (1)–(5) for comparison with the determined activation energies. Surface desorption processes are illustrated on the right side.

of the model to the TPD experiments in the spectrum regions between 400 and 500 K yields activation energies of 1.25 and 1.33 eV for states (1) and (2), respectively. Different amounts N and heating rates $\partial T/\partial t$ result in good agreement between simulated and experimental rates as shown in figure 8(b). Nevertheless, the simulated release peaks are slightly broader than the experimental results, independent of the fit parameters E_A and the reaction order r. Inclusion of diffusive processes broadens the peaks even more. However, a frequency factor of $10^{20}\,s^{-1}$ calculates a spectrum with a peak width that gives better agreement with the experimental data (not shown). Such a high-frequency factor is physically unrealistic, as ν is usually related to the attempt frequency of a process. For this case, ν relates to the thermal vibration of a deuterium atom in the bulk. This indicates that the assumptions used in this model might be reasonable but incomplete. The release of deuterium from the supersaturated zone is not sufficiently described by a mere thermally activated process, but can additionally be influenced by the high D concentration and forces in the destabilized regions. This agrees with the qualitative picture drawn above on the nature of release states (1) and (2).

Based on the determined activation energies for the release processes from the various binding states of deuterium in Be, a schematic energy diagram is drawn in figure 9 (not to scale). Reference energy of a free D is set to 0 eV (upper horizontal line). The second reference energy is the binding energy of D in molecular form (D_2), which corresponds to an energy of −2.28 eV per D atom. Within the Be bulk, the activation energy for diffusion ($\Delta E_D = 0.29$ eV) represents the height of the energy barrier between two mobile sites, i.e., movement of D through the undisturbed Be lattice. The binding energy of D in a mobile (= solute) site is given by the dissolution energy E_S. Several values for E_S are given in the literature and vary between

0.1 eV [7, 29] and 1 eV [30]. According to this picture, the activation energy for the release of D bound in ion-induced trap sites (3) and (4) is the difference between its binding energy and $E_S + \Delta E_D$. Qualitatively, the activation energies for the different rate-limiting steps correspond to the peaks observed in a TPD spectrum (shown on the left side of figure 9). With increasing fluence, all available ion-induced trap sites (3) and (4) are saturated, such that the bulk lattice becomes locally supersaturated upon further D implantation. States (1) and (2) are created and lead to activation energies for the deuterium release of 1.25 and 1.33 eV, respectively. Elevated substrate temperatures (above RT, but below 570 K) can initiate a phase transition of the supersaturated areas into BeD_2, which decomposes at 570 K. The activation energy for $2D \rightarrow D_2$ recombination is $\Delta E_A = 0.87$ eV [18], leading to a desorption temperature similar to the release temperatures of state (1) or (2). However, as stated above, this recombination step is not a rate-limiting energy barrier for the release of implanted deuterium.

3.3.2. Modelling of retention by DFT. The models discussed above allow only indirect conclusions about the retention mechanism itself. A direct experimental characterization of the situation right after implantation is not possible by means of thermally activated release, as only activation energies for these processes and not the actual binding states and binding energies are accessible. First-principle calculations based upon spinpolarized gradientcorrected DFT can provide these insights [31, 32]. The link between activation energies for the various release processes and actual binding energies is illustrated in figure 9. Given a dissolution energy of $E_S = -0.1$ eV [7] (as assumed in figure 9), the binding energy of a D atom bound in a state corresponding to the release peak (i) would be $|E_{BE(i)}| = \Delta E_{A(i)} - \Delta E_D - E_S$. As an example for $i = 4$ one gets $\Delta E_{A(4)} = 1.86$ eV for the activation energy for the release from binding state (4). This binding energy can be compared with the interaction energy ΔE_{INT} of a single hydrogen atom with the rest of the calculation slab obtained from DFT. ΔE_{INT} is defined as $\Delta E_{INT} = E(m\mathrm{Be} + n\mathrm{H}) - E(m\mathrm{Be} - (n-1)\mathrm{H}) - E(\mathrm{H})$, where m is the number of Be atoms in the slab and n is the number of H atoms. The different hydrogen isotopes are considered to be identical. Energetically stable structures are obtained up to a ratio of $\mathrm{H/Be} \approx 3$. The average cohesive energy per atom of the system decreases linearly from $-2.7\,\mathrm{eV\,atom^{-1}}$ ($\mathrm{H/Be} = 1$) to $-1.5\,\mathrm{eV\,atom^{-1}}$($\mathrm{H/Be} = 3$). The minimum interaction energy of the single hydrogen atoms decreases from 1.7 eV at $\mathrm{H/Be} = 1$–0.2 eV at $\mathrm{H/Be} = 2.96$, corresponding to a decrease of the binding energy of hydrogen in the calculated structure. Within the structure, ΔE_{INT} exhibits variations of about 1 eV. However, such high interaction and thus binding energies suggest a smaller value for E_S in figure 9. For these calculations, the volume of the cell is kept constant. This would only approximate the real situation, where a certain swelling is observed in the AFM measurements in the form of protrusions, but on the other hand, free relaxation is inhibited by the surrounding material. Figure 10 illustrates the positions of the atoms (big spheres are Be, small ones hydrogen) in the cell with a ratio $\mathrm{H/Be} = 1$ and allowed volume expansion. The (originally) hexagonal Be lattice is dissolved. Nevertheless, this structure is energetically stable and gives a qualitative picture of the structure of the structural modifications in the supersaturated regions.

4. Summary

Based upon qualitative and quantitative evaluation of TPD spectra on clean and oxidized single crystalline Be, the retention mechanisms for implanted deuterium are identified. D is trapped in

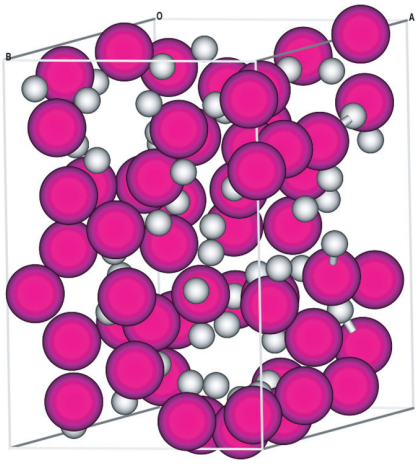

Figure 10. Calculated structure of a material with H/Be = 1 by DFT. The volume of the slab was allowed to expand. The original hexagonal Be lattice structure is dissolved by increasing the number of hydrogen atoms. This structure is energetically stable and gives an impression of the nature of the supersaturated regions created by ion implantation.

the Be bulk in defects created by the collision cascade and, at higher fluences, in destabilized (supersaturated) Be–D regions. A steady state is reached at a fluence of 2×10^{17} cm^{-2}. An oxidized sample surface does not limit the thermally activated release rate. Provided there is enough thermal energy (implantation above RT), the supersaturated regions can transform into BeD_2, which starts to decompose above 500 K.

The investigations in this work provide for the first time experimental data for deuterium retention and thermal release of clean beryllium. It could be shown that the influence of surface oxide layers on the release of implanted deuterium is of minor importance. The experimental simplification of the investigated system with respect to surface and bulk chemistry (pure beryllium, pure monoenergetic deuterium implantation) and structure (single crystalline and annealed beryllium bulk) allows the thermal release to be modelled and thus leads to an understanding of the basic processes that govern deuterium retention.

The real Be first wall of ITER is different from the experimental conditions and sample structure in the experiments performed here. However, the results obtained here in well-defined single crystalline beryllium can be regarded as an upper limit for the expected retention of the real wall and allow a quantitative estimation. Lower deuterium energies or smaller angles of incidence to the surface will shift the implantation cascades towards the surface, leading to a shallower D profile and therefore a lower retained deuterium amount. For the case with the highest expected retention, such as areas where the wall is at low temperatures, so that all binding states can develop, a maximum amount of 7 g of hydrogen can accumulate in a (hypothetically) clean ITER Be wall with an area of 700 m^2. This is also the upper limit for the contribution of the pure metallic main wall to the overall tritium inventory of ITER under the assumption of negligible isotope effects on the retention. Although thin BeO surface layers do

not influence retention in Be and release from Be itself, thicker BeO layers or other compound surface layers could still strongly influence the recycling behaviour. If hydrogen is implanted into these materials, their respective retention mechanisms could govern the recycling processes and require further investigations.

References

[1] Federici G *et al* 1998 *Fusion Eng. Des.* **39–40** 445
[2] Alimov V K, Chernikov V N and Zakharov A P 1997 *J. Nucl. Mater.* **241–3** 1047
[3] Doerner R P, Grossman A, Luckhardt S, Seraydarian R, Sze F C, Whyte D G and Conn R W 1998 *J. Nucl. Mater.* **257** 51
[4] Haasz A A and Davis J W 1997 *J. Nucl. Mater.* **241–3** 1076
[5] Wampler W R 1992 *J. Nucl. Mater.* **196–8** 981
[6] Won J, Doerner R P and Conn R W 1998 *J. Nucl. Mater.* **256** 96
[7] Anderl R A, Causey R A, Davis J W, Doerner R P, Federici G, Haasz A A, Longhurst G R, Wampler W R and Wilson K L 1999 *J. Nucl. Mater.* **273** 1
[8] Zalkind S, Polak M and Shamir N 1997 *Surf. Sci.* **385** 318
[9] Longhurst G 2004 INEEL/EXT-04–02352
[10] Reinelt M and Linsmeier C 2007 *Phys. Scr.* T **128** 111
[11] Alimov V K, Mayer M and Roth J 2005 *Nucl. Instrum. Methods Phys. Res.* B **234** 169
[12] Linsmeier C, Goldstrass P and Klages K U 2001 *Phys. Scr.* **T94** 28
[13] Roth J, Wampler W R and Jacob W 1997 *J. Nucl. Mater.* **250** 23
[14] Markin A V, Chernikov V N, Rybakov S Y and Zakharov A P 1996 *J. Nucl. Mater.* **233–7** 865
[15] Abramov E, Riehm M P, Thompson D A and Smeltzer W W 1990 *J. Nucl. Mater.* **175** 90
[16] Macaulay-Newcombe R G and Thompson D A 1994 *J. Nucl. Mater.* **212–5** 942
[17] Barabash V, Federici G, Linke J and Wu C H 2003 *J. Nucl. Mater.* **313–6** 42
[18] Lossev V and Küppers J 1993 *Surf. Sci.* **284** 175
[19] Wampler W R 1984 *J. Nucl. Mater.* **123** 1598
[20] Eckstein W 1991 *Computer Simulation of Ion–Solid Interactions* (Berlin: Springer)
[21] Eckstein W, Dohmen R, Mutzke A and Schneider R 2007 *IPP Report* 12/3
[22] Chernikov V N, Alimov V K, Markin A N and Zakharov A P 1996 *J. Nucl. Mater.* **228** 47
[23] Anderl R A, Hankins M R, Longhurst G R, Pawelko R J and Macaulay-Newcombe R G 1992 *J. Nucl. Mater.* **196–8** 986
[24] Barry P E, Bowers J S, Garza R G, Souers P C, Cantrell J S and Beiter T 1990 *J. Nucl. Mater.* **173** 142
[25] Baker R W, Brendel G J, Lowrance B R, Mangham J R, Marlett E M and Shepherd L H 1978 *J. Organomet. Chem.* **159** 123
[26] Maienschein J L, Bowers J S, Beiter T A and Cantrell J S 1993 *J. Alloys Compd.* **196** 1
[27] Ambrosek J A and Longhurst G R 2004 INEEL/EXT-04-01657
[28] de Jong A M and Niemantsverdriet J W 1990 *Surf. Sci.* **233** 355
[29] Shapovalov V I and Dukel'ski Y M 1984 *Russ. Metall.* **5** 210
[30] Swansiger W A 1986 *J. Vac. Sci. Technol.* A **4** 1216
[31] Allouche A 2008 *Phys. Rev.* B **78** 085429
[32] Allouche A and Linsmeier C 2008 *J. Phys.: Conf. Ser.* **117** 012002

IOP Publishing Physica Scripta
Phys. Scr. **T128** (2007) 111–114 doi:10.1088/0031-8949/2007/T128/022

Temperature programmed desorption of 1 keV deuterium implanted into clean beryllium

M Reinelt and Ch Linsmeier

Max-Planck-Institut für Plasmaphysik, EURATOM Association, Boltzmannstrasse 2, 85748 Garching b. München, Germany

E-mail: linsmeier@ipp.mpg.de

Received 27 October 2006
Accepted for publication 8 December 2006
Published 8 March 2007
Online at stacks.iop.org/PhysScr/T128/111

Abstract
Beryllium is planned as a plasma-facing material for ITER covering most of the inner wall of the plasma vessel. It is thus subjected to intense fluxes of escaping hydrogen ions from the plasma, which are implanted and retained in the plasma-facing material. As beryllium reacts very quickly with oxygen and especially with water, forming a surface oxide layer even under good vacuum conditions, previous studies of the interaction of deuterium and beryllium had to deal with oxygen contamination as a factor of uncertainty. To rule out the influence of a BeO-covered surface, the retention and release of 1 keV deuterium ions implanted in clean beryllium at room temperature are investigated by temperature programmed desorption (TPD). The surface composition is measured by x-ray photoelectron spectroscopy (XPS). The outline of a retention mechanism is developed by discussing the thermal release behaviour as a function of increasing deuterium fluence.

PACS numbers: 52.40.Hf, 61.80.Jh, 66.30.Jt, 79.20.Rf

1. Introduction

Although a large number of earlier studies have been dedicated to the retention behaviour of hydrogen in beryllium [1], the details of the mechanism are still unclear. Moreover, there is a large scatter in the experimentally evaluated parameters such as detrapping energies, diffusivity, solubility and recombination rates. These values are especially important for ITER, curently under construction in Cadarache, France, to estimate the tritium accumulation in the first wall material, which is an important safety issue. This raises two questions: what are the reliable characteristic values that describe the interaction between D and Be and why is there such poor agreement between different experiments? In this context, the retention and desorption behaviours of D implanted into Be are investigated and conclusions about a retention mechanism are drawn from the results. Special emphasis is put on the control of the elemental surface composition to exclude an influence of contaminated surface layers.

2. Experimental

The sample under investigation is a polished beryllium disc with a diameter of 14 mm and a thickness of less than 1 mm. One sample was used for all experiments described here. Laue diffraction measurements at various positions on the sample indicate full single crystallinity with an orientation of $(11\bar{2}0)$ and a miss-cut of less than 1°. The surface is cleaned by cycles of 3 keV Ar^+ bombardment under 45° incidence and annealing. The surface composition is monitored by x-ray photoelectron spectroscopy (XPS). The cleaning cycles are repeated until less than 0.2 monolayers (ML) of residual oxygen as the only remaining impurity are detected by XPS. Even though the preparation is performed under UHV conditions with a base pressure better than 3×10^{-11} mbar, an oxygen contamination of 1 ML is accumulated over a period of a few hours demanding further cleaning and annealing prior to each experiment. A fluence of 1×10^{-17} Ar cm^{-2} is needed to regain sub-ML oxygen

coverage. Annealing the sample at 1000 K removes implanted Ar. The background pressure in the experimental chamber stays below 4×10^{-10} mbar at this sample temperature. The cleaned sample is implanted at room temperature with a 3 keV monoenergetic and mass-selected D_3^+ ion beam under normal incidence. This corresponds to a kinetic energy of 1 keV per D atom. The beam is not masked by an aperture to prevent contamination of the surface by sputter deposition of aperture material. The beam is scanned over the target by deflection plates (100 V) flattening the implantation profile from the Gaussian-shaped beam over a width of 5 mm. From the measured ion current onto the target, the incoming absolute amount of deuterium ions is determined. The fluence profile is measured by scanning the beam with a Faraday cup with a 0.5 mm opening mounted on the sample manipulator. The increased background pressure of 2×10^{-9} mbar during implantation is due to molecular deuterium. Temperature programmed desorption (TPD) is performed by positioning the target in front of a differentially pumped funnel that shields both a quadrupole mass spectrometre (QMS) in line-of-sight geometry and the target. The target is heated by electron impact from the backside, increasing the temperature linearly from room temperature to 1000 K at 0.5, 1 or 4 K s^{-1}. The temperature ramps are pre-programmed and optimized for linearity. The sample temperature is measured by a thermocouple spot-welded to the surface. XPS measurements show that one implantation and subsequent TPD up to 1000 K do not increase the oxygen contents of the cleaned Be surface. The absolute retained amount of deuterium and retained fluence in the maximum of the implantation spot are measured by nuclear reaction analysis (NRA) using the $D(^3He, p)^4He$ reaction at 800 keV. This amount is used to calibrate the deuterium desorption rate measured by TPD. All experiments are performed *in situ* in a set-up described elsewhere in detail [2].

3. Results

3.1. Retention

Figure 1 shows the retained deuterium fluence measured by TPD plotted versus the implanted fluence (in the maximum of the ion beam profile). The order in which the fluence steps were implanted was chosen randomly to exclude an influence of the sample history. Below fluences of 1.5×10^{17} D cm^{-2}, a linear fit to the data shows that $78 \pm 3\%$ of the implanted deuterium is retained in the sample. As expected, the retention tends to saturate at higher fluences. In the steady state, the amount of deuterium lost by erosion from the D-enriched Be region is in equilibrium with the retained amount. The data points are in good agreement with earlier retention measurements [3, 4], although the surface in those experiments was not free of BeO.

3.2. Desorption characteristics

The thermally activated deuterium release of a saturated sample occurs mainly in two stages: a broad structured stage at a temperature above 700 K and a sharp double peak around 480 K (figure 2). The high temperature stage consists of at least two peaks (1 and 2). The low temperature stage is

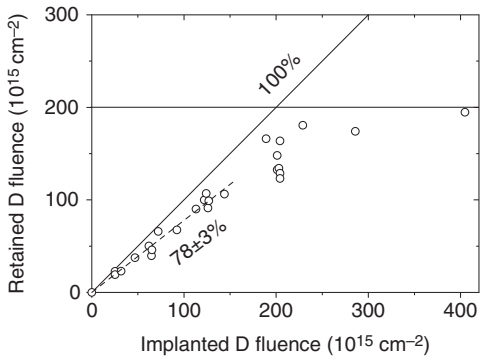

Figure 1. Retention of 1 keV deuterium implanted into clean beryllium at room temperature. The dashed line is a linear fit to the data points at low fluence and indicates a retention of $78 \pm 3\%$. The steady state fluence is above 2×10^{17} D cm^{-2}. The data points are obtained from TPD measurements calibrated *in situ* by NRA.

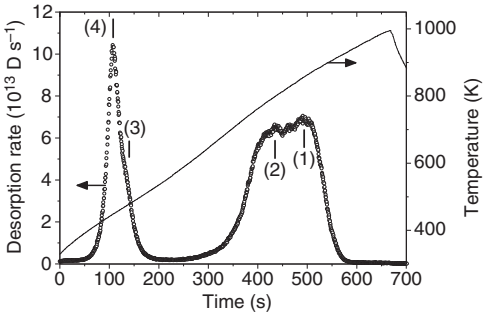

Figure 2. Typical TPD spectrum ($m/z = 4$) of 2.6×10^{16} deuterium ions (fluence in maximum 2.04×10^{17} D cm^{-2} at 1 keV) implanted into single crystalline beryllium at room temperature with 0.1 ML residual BeO surface coverage. The heating ramp is 1 K s^{-1}. Four release peaks are apparent (labelled 1–4), separated into a high temperature stage (peaks 1 and 2) and a low temperature stage (peaks 3 and 4).

composed of a sharp peak (4) with a shoulder at a higher temperature (3). More than 99% of deuterium is released as D_2, the rest (< 1%) as HD molecules due to low water and H_2 background pressures. The release of atomic D, D_2O and HDO was not observed. Heating the sample up to 950 K is enough to remove all retained deuterium. This was confirmed by NRA of a degassed sample. Additionally, no further deuterium is released in subsequent TPD experiments. Such TPD measurements without prior deuterium implantation also indicate that a background correction of the spectra is not necessary, because in that case the signals for D_2 and HD are near the detection limit of the QMS. Figure 3 shows a series of TPD spectra with D fluences between 4.7×10^{16} and 1.44×10^{17} D cm^{-2}. All fluences in figure 3 are below the saturation of the sample. At low fluences (up to 1×10^{17} D cm^{-2}), only the high temperature states (1) and (2) are populated with maxima of the release rate at 800 and 880 K, respectively. The deuterium

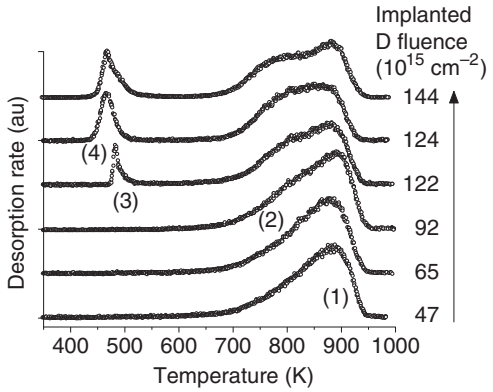

Figure 3. Series of TPD spectra with increasing deuterium fluences below saturation. The release states are occupied sequentially from the highest to lower temperatures. The low temperature states are absent at low fluences. The spectra are measured at random order.

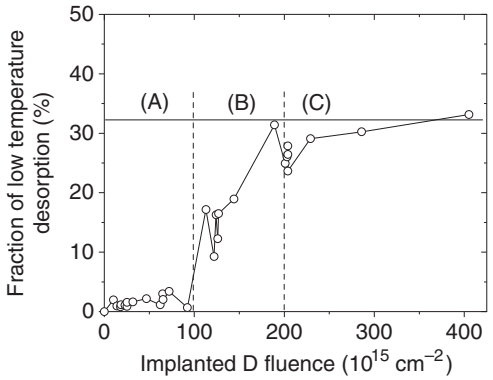

Figure 4. The fraction of deuterium released from the low temperature states (3) and (4) as a function of implanted fluence. These states are not occupied at fluences below 1×10^{17} D cm^{-2} (region A). The deuterium retention of the sample and accordingly the retention in the low temperature states saturate in region C.

inventory in these states increases with the fluence. Above 1×10^{17} D cm^{-2}, an additional low temperature release stage appears, consisting of peaks 3 and 4. Initially, state 3 is populated. The retention in state 4 increases rapidly and finally retains more deuterium than state 3. The fraction of deuterium in states 3 plus 4 is plotted in figure 4 versus the implanted fluence. The low temperature stage appears after the threshold fluence of 1×10^{17} D cm^{-2}. The retention behaviour can therefore be divided into three phases. In phase A, only the high temperature states are occupied. In phase B, retention in the low temperature states increases rapidly. The system is in steady state in phase C.

4. Discussion

The TPD spectra of implanted hydrogen show a superposition of the temperature (and therefore energy) dependence of all release-determining processes. Activation energies for the release-determining processes can thus be obtained from the temperature of release stages. This, however, implies knowledge of the character of the processes and therefore the mechanisms that govern the trapping and release of deuterium. Without prior qualitative assignment of the observed release stages to corresponding release-determining processes, quantification is not possible.

Three principle processes can provide energy barriers for the release of implanted deuterium into the vacuum: diffusion, surface recombination and detrapping from defects. The diffusion barrier for deuterium in beryllium is very low (0.29 eV [5]) and deuterium diffuses very fast even at room temperature. For this reason, diffusion is no release-determining effect for the experimental conditions discussed here. Deuterium has to form D_2 molecules in order to desorb into vacuum within this temperature range. The recombination rate depends on surface diffusivity and surface binding energies and is therefore directly influenced by the surface chemical composition. TPD spectra (not shown here) demonstrate that none of the observed release stages is directly influenced by changing the chemical surface composition of the sample from Be to more than 1 ML BeO. This indicates that recombination is no limiting effect either. The third and remaining process is detrapping. Therefore, one can suggest that the peaks measured by TPD are caused by the thermally activated detrapping from sites in the Be bulk.

At fluences far below 1×10^{17} D cm^{-2}, deuterium is implanted into an undisturbed bulk lattice. This assumption is justified, because the sample is single crystalline and annealed before each implantation at a temperature above half of the melting point [6]. An implantation profile with a maximum at a depth of 30 nm results from calculations by SDTRIM [7], a kinetic Monte Carlo code. Two explanations for the high temperature states are possible. They can be due to either intrinsic trap sites or sites created by the collision cascade. If both types of trap sites are intrinsic in the Be lattice, they would be abundant throughout the bulk and their ratio of concentration would be constant. Trapping of stopped deuterium at the end of its collision cascade would occur in the nearest possible trap site (which is accessible by diffusion) leading in average to a constant occupation ratio between state 1 and 2 with increasing fluence. The increase of the temperature up to 800 K during a TPD experiment mobilizes D bound in state 2, enables diffusion through the bulk, and finally trapping again in an unoccupied state 1. If this state is intrinsic, there are always unoccupied sites available. This means that state 2 would never be observed in a TPD experiment. Because it is observed and the ratio of occupation between the two states changes with fluence, at least site 1 is ion induced and must be limited in its concentration. Increasing the fluence means that the D concentration is locally increased, which leads to a saturation of the trap sites available within the implantation zone. Unoccupied states with the highest binding energy being locally accessible are occupied by diffusion. This explains the behaviour of the system shown in figure 3, where at first state 1 and subsequently increasing amounts of state 2 are occupied.

If all possible trap sites are occupied, the local oversaturation enforces a structural modification in the bulk. This

occurs at 1×10^{17} D cm^{-2} and explains the sharp threshold fluence observed for the appearance of release states 3 and 4. Lossev *et al* [9] performed thermal desorption spectroscopy (TDS) of adsorbed atomic deuterium on clean Be surfaces and found a dominant desorption peak at 425 K, which was assigned to surface recombination. Although the low temperature release stage observed in our experiments has almost the same temperature, it is not identical. First of all, the measured release peaks are much sharper than the peaks observed for surface desorption [9]. Under the assumption of a saturated Be surface, the amount released from the low temperature states must be correlated to the sample surface. The fraction of low temperature desorption presented in figure 4 is determined from the ratio of the desorbed absolute amounts from high and low temperature stages measured by TPD. Due to the implantation method, the lateral deuterium concentration in the sample is not homogeneous. Instead, the concentration is smaller in the outer regions of the implantation spot. If the low temperature states are created in the centre of the irradiation spot, they are not yet created in the outer regions. This means that the fractions shown in Figure 4 underestimate the amount released from the low temperature stage above 1×10^{17} D cm^{-2}. Accordingly, earlier TPD experiments [10] show a higher peak at low temperature. Hence, a lower limit of 6×10^{16} D cm^{-2} can be given for the release from the low temperature stage in steady state, which is more than 30% of the overall retained amount. The D areal density of a saturated Be surface is 1×10^{15} D cm^{-2} [9]. If the low temperature release stage originates from a surface, this surface would accordingly be 60 times larger than the projected (flat) sample surface. *Ex situ* atomic force microscopy (AFM) measurements, however, indicate that the true surface area of the sample is in the range of 1.1–1.2 times the projected surface area. This means that release stages 3 and 4 are energetically similar to surface desorption but are not related to the actual sample surface.

There is agreement in the literature that the maximum concentration of D in Be is roughly 0.4 [8], which would equal a formal stoichiometry of $Be_{2.5}D$. The inventory of 2×10^{17} D cm^{-2} observed here in steady state, together with an implantation profile calculated by SDTRIM leads a maximum stoichiometry of $Be_{2.85}D$. Such a high D concentration cannot be realized by evenly distributed point defects. Assuming only intrinsic traps like interstitial sites, those lattice positions would correspond to e.g. 1/5 of all tetrahedral holes or 2/5 of all octahedral holes within the hcp Be lattice, which had to be occupied by D. Another possibility is that D is not evenly distributed but the concentration of 0.4 is realized by bulk areas of a much higher D concentration (>0.4) and areas of saturated Be grains. The saturation of the Be grains (with a D concentration <0.4) is reached at 1×10^{17} D cm^{-2}. Regarding these considerations and the above discussions of the TPD results, we suggest that D is bound primarily in ion induced defect sites.

5. Conclusion

The retention of 1 keV deuterium implanted into clean, single crystalline beryllium at room temperature is investigated by TPD up to saturation of the sample. The chemical composition of the near surface region is controlled by XPS and kept below 1 ML residual BeO coverage. About 78% of the implanted deuterium is retained below a fluence of 2×10^{17} D cm^{-2}. Above, the sample saturates retaining a D areal density of 2×10^{17} D cm^{-2}. The release is not surface-recombination limited. It is suggested that the release-determining processes are detrapping from bulk sites. Four different trap sites are proposed. The two high temperature traps have a release temperature of 800 and 880 K, respectively. At least one of them is created by ion implantation. Two additional trap sites are supposed to be formed due to structural modifications provoked by local oversaturation of the bulk above a fluence of 1×10^{17} D cm^{-2}. The respective release temperatures are 450 and 470 K. They are energetically similar to surface desorption states, but are not related to the sample surface.

References

[1] Anderl R A *et al* 1999 *J. Nucl. Mater.* **273** 1
[2] Linsmeier Ch, Goldstraß P and Klages K U 2001 *Phys. Scr.* T **94** 28
[3] Alimov V Kh, Chernikov V N and Zakharov A P 1997 *J. Nucl. Mater.* **241–243** 1047
[4] Wampler W R 1984 *J. Nucl. Mater.* **122–123** 1598
[5] Abramov E, Riehm M P and Thompson D A 1990 *J. Nucl. Mater.* **175** 90
[6] Knözinger H and Taglauer E 1993 *Catalysis* **10** 1
[7] Eckstein W 1991 *Computer Simulation of Ion–Solid Interactions* (Berlin: Springer)
[8] Causey R A 2002 *J. Nucl. Mater.* **300** 91
[9] Lossev V and Küppers J 1993 *Surf. Sci.* **284** 175
[10] Haasz A A and Davis J W 1997 *J. Nucl. Mater.* **241–243** 1076